

POLITECNICO DI MILANO
SCUOLA DI INGEGNERIA INDUSTRIALE E DELL'INFORMAZIONE
DIPARTIMENTO DI CHIMICA, MATERIALI E INGEGNERIA CHIMICA "G. NATTA"

A Lumped Condensed-Phase Kinetic Model for Plastic Waste Thermochemical Recycling

From Pyrolysis towards Gasification



DOCTORAL DISSERTATION FOR DEGREE OF DOCTOR OF PHILOSOPHY IN
INDUSTRIAL CHEMISTRY AND CHEMICAL ENGINEERING

Author:

Andrea LOCASPI
951216

Supervisor:
Prof. Tiziano FARAVELLI
Dott.ssa Silvia GIACOBBE

Tutor:
Prof. Roberto PIAZZA

Head of the Doctoral Program:
Prof. Carlo CAVALLOTTI

Cycle XXXV 2020-2023

September 2023

*Out of the cradle
onto dry land
here it is
standing:
atoms with consciousness;
matter with curiosity.*

*Stands at the sea,
wonders at wondering: I
a universe of atoms
an atom in the universe.*

— Richard P. Feynman (1955)

ABSTRACT

In a circular economy perspective, plastic waste (PW) is a valuable source of chemicals, energy vectors, and fuels. Thermochemical recycling technologies as pyrolysis, gasification, and partial oxidation are promising processes able to valorize complex and polluted waste streams. In this context, Computational Fluid Dynamics and chemical kinetics are valuable tools that aid in designing and optimizing valorization processes.

The present PhD thesis proposes a kinetic framework to describe the condensed-phase thermal degradation of PW for reactor-scale simulations. These condensed-phase models aim at capturing the key aspects of the degradation process, i. e., characteristic condensed-phase degradation times, detailed product distribution, and energy requirements. The functional groups approach proposed in literature for poly(vinyl chloride) (PVC) pyrolysis is employed and expanded, focusing first on the pure polymers. High-molecular-weight chains are described through several mid- and end-chain pseudo-species representative of the polymer chemical moieties. Conversely, low-molecular-weight compounds are represented similarly to conventional gas-phase kinetic models for pyrolysis and combustion. The reaction network employs a reaction classes approach, where all species undergo the same types of reactions with reactivity-specific corrections. Defining the elementary steps and their rates relies on existing models of polymer degradation when available. Otherwise, the model development leverages analogies with gas-phase compounds of similar chemical moieties. The kinetic mechanism is complemented by the defining the thermochemical and transport properties for both gas and condensed-phase species. Phase-change phenomena, such as melting and boiling, are incorporated through volumetric chemical reaction.

The proposed methodology is validated on polyethylene (PE) pyrolysis, employing experimental data and detailed kinetic models both from literature. Hundreds of experimental mass-loss data are investigated, while data on volatile yields and heat fluxes are scarce. The semi-detailed model proves able to describe the phenomena involved within experimental and author-to-author variability, achieving an accuracy comparable to detailed models.

Building on the semi-detailed model predictions, this work proposes two reduced-order kinetic models: a reduced semi-detailed model and a multi-step fully lumped model. The former lumps all radical isomers, reducing the number of species by 60% for PE. The latter describes the complex radical reactivity through few global steps, reducing the number of species by 92% for PE. Both models are assessed with the semi-detailed model and literature experimental data, proving able to reproduce the key features of the mechanism. Due to the strong lumping employed, the multi-step

mechanism cannot reproduce the detailed carbon distribution, and limits at predicting the formation of petroleum cuts.

Following this methodology, this thesis proposes condensed-phase kinetic models also for polypropylene (PP), polystyrene (PS), and poly(ethylene terephthalate) (PET). The reaction network for PP and PS relies on existing kinetic models to define the elementary steps. Conversely, to the author's knowledge, no PET pyrolysis model has been proposed in the scientific literature. The PET kinetic mechanism builds on reaction pathways proposed by other authors, quantitatively assessing their relevance through analogies with gas-phase model compounds. Both molecular and radical degradation pathways are considered, the former being responsible for oligomers, while the latter resulting in char and short chain compounds. The interplay of molecular and radical mechanisms describes mass-loss profiles, volatile distribution, char yields, and char composition.

The single polymers kinetic models serve as basis for describing PW mixture degradation. Considering vinyl polymers, literature investigations highlight the immiscibility of the polymers in the molten phase. The model captures literature mass-loss profiles neglecting interactions, although a high author-to-author variability is observed. More complex behaviours arise when considering mixtures involving PET-PVC, which exhibit relevant condensed-phase interactions. The present thesis proposes a degradation mechanism involving both molecular and radical pathways to explain the formation of chloro-esters experimentally observed.

The conclusive chapter outlines the relevance of this thesis and further works to expand the applicability of the proposed framework. All 13 proposed kinetic models are freely available on GitHub as public repositories and are merged in the CRECK kinetic framework.

SINOSSI

Nell'ottica di una economia circolare, il rifiuto plastico (plastic waste, PW) può essere una fonte di composti, vettori energetici e carburanti. Tecnologie di riciclo chimico quali pirolisi, gasificazione e ossidazione parziale sono promettenti per valorizzare rifiuti complessi e contaminati. La fluidodinamica computazionale (Computational Fluid Dynamics, CFD) e la cinetica chimica sono strumenti indispensabili per progettare e ottimizzare questi processi industriali.

La presente Tesi di dottorato propone una metodologia per modellare la cinetica in fase condensata del degrado termico del PW. Lo sviluppo dei meccanismi cinetici ha come obiettivo l'applicazione in simulazioni CFD di reattori su scala industriale, offrendo quindi un compromesso tra il costo computazionale ed il dettaglio della descrizione fisico-chimica del processo. I parametri di interesse che i modelli descrivono sono dunque i tempi caratteristici del degrado in fase liquida, la descrizione dettagliata dei prodotti rilasciati ed il costo energetico del processo. La modellazione cinetica sfrutta ed espande l'approccio a gruppi funzionali (functional groups, FG), proposto in letteratura per descrivere il degrado termico del poli(vinil cloruro) (PVC). Seguendo questo approccio, per ogni polimero le catene polimeriche sono distinte in specie ad alto e basso peso molecolare. Le prime sono descritte tramite pseudo-specie di centro e fine catena rappresentative della natura chimica del polimero, le seconde sono invece modellate con un dettaglio comparabile ai modelli convenzionali per pirolisi e ossidazione in fase gas. Il meccanismo di reazione è sviluppato secondo una logica a classi, ovvero tutte le specie reagiscono attraverso reazioni simili ma con correzioni basate sulla specificità del sito reattivo. Le reazioni elementari sono definite partendo da modelli di letteratura sul degrado del polimero, quando disponibili. In mancanza di dati di letteratura, i parametri cinetici sono determinati tramite analogie con composti in fase gas caratterizzati da funzionalità chimiche simili. Il meccanismo cinetico è completato attraverso la stima di proprietà termochimiche e di trasporto sia per le specie gassose che in fase condensata. Fenomeni di transizione di fase, quali fusione ed ebollizione, sono rappresentati tramite delle reazioni volumetriche.

La metodologia proposta è validata sul caso di pirolisi di polietilene (PE) mediante il confrontandosi con dati sperimentali e modelli cinetici dettagliati proposti in letteratura. La validazione dei tempi caratteristici di degrado sfrutta un centinaio di dati sperimentali, mentre sono limitati i dati disponibili per il confronto riguardante la distribuzione di prodotti e i flussi di calore. Il modello cinetico semi-dettagliato proposto si dimostra in grado sia di descrivere le osservazioni sperimentali, considerando la variabilità intrinseca ai diversi studi sperimentali di letteratura, che di riprodurre gli andamenti previsti dai modelli dettagliati.

I risultati di questa metodologia sono impiegati per derivare due meccanismi ridotti. Il primo, un modello ridotto semi-dettagliato, rappresenta ogni gruppo di radicali isomeri attraverso una singola specie, e ottiene una riduzione del numero di specie del 60% per il PE. Il secondo meccanismo è invece della tipologia "multi-step" e "fully lumped", il quale rappresenta la reattività radicalica attraverso reazioni globali, e raggiunge una riduzione del numero delle specie pari al 92%. Entrambi i modelli sono validati mediante il confronto con il meccanismo semi-dettagliato, dimostrando di replicare ragionevolmente gli aspetti chiave di quest'ultimo. Ciò nonostante, per via delle significative semplificazioni apportate, il modello multi-step non è in grado di descrivere la distribuzione di carbonio dettagliata, e si limita a riprodurre la formazione dei principali tagli petroliferi del processo.

La metodologia proposta è sfruttata per proporre modelli cinetici in fase condensata anche per polipropilene (PP), polistirene (PS) e poli(etilene tereftalato) (PET). Mentre lo sviluppo del meccanismo cinetico per PP e PS si basa su modelli pubblicati in letteratura, per quanto a conoscenza dell'autore, nessun modello è stato proposto per il degrado termico di PET. La cinetica di pirolisi è quindi costruita attraverso cammini reattivi di natura molecolare e radicalica proposti nella letteratura scientifica, sfruttando analogie con composti in fase gas per quantificare l'effettiva importanza di tali reazioni. Il modello cinetico così ottenuto si dimostra in grado di descrivere sia i profili di massa che la distribuzione e caratterizzazione quantitativa dei volatili e del residuo solido.

I modelli cinetici sviluppati per i polimeri puri sono opportunamente accoppiati per descrivere il degrado di miscele polimeriche rappresentative del PW. E' stato verificato in letteratura che le interazioni tra polimeri differenti siano relative alla miscibilità dei materiali fusi. Per quanto riguarda miscele di polimeri vinilici, l'immiscibilità dei polimeri fusi risulta in interazioni binarie di entità trascurabile. Il modello di miscela riesce infatti a descrivere il degrado di PW trascurando interazioni in fase condensata, sebbene la variabilità tra studi sperimentali di autori differenti sia maggiore che nel caso dei polimeri puri. Miscele contenenti PET e PVC mostrano interazioni in fase condensata di entità considerevole. In questa tesi viene proposto un meccanismo di interazione basato su reazioni molecolari e radicaliche che spiegano la giustificazione di cloro-esteri osservati sperimentalmente.

Nel capitolo conclusivo vengono discusse la rilevanza della metodologia proposta e suggerimenti per estendere l'applicabilità dei modelli cinetici sviluppati. I 13 modelli cinetici sono disponibili gratuitamente su GitHub e sono inclusi nell'insieme di modelli cinetici CRECK.

All models are wrong, but some are useful — George E. P. Box

ACKNOWLEDGEMENTS

The author wishes to express his thanks to the persons who contributed to this Ph.D. journey. First of all, Professor Tiziano Faravelli for the support and invaluable insights, but also for the challenging questions and stimulus. Professor Kevin M. Van Geem for welcoming me in Gent, but also for broadening my outlook on and the depth of my understanding of my research topic. Dott.ssa Silvia Giacobbe and ENI S.p.A. for the opportunity to perform the current Ph.D.

Thanks are due to the entire CRECK modeling Lab, specifically to Matteo Pelucchi and Alessio Frassoldati for their support. Among the Ph.D. students, the utmost sincere gratitude goes to Andrea, Edoardo, and Francesco for sharing the office and the stimulating discussions. Thanks go also to Alessandro, Timoteo, Dong-Sheng, Romina, Clarissa, Riccardo, Niccold, and Francesco. The author thanks all the LCT group, particularly Oguzhan, Victor, Tamas, Rejish, Gust, Moe, Lowie, Daniel, Afroditi, Michiel, and Jeroen.

The author extends gratitude to their family and friends, who gave continuous support and encouragement during these years.

PUBLICATIONS AND CONFERENCES PARTICIPATION

PUBLISHED PAPERS:

- **Locaspi, Andrea**, Matteo Pelucchi, and Tiziano Faravelli, "Towards a lumped approach for solid plastic waste gasification: Polystyrene pyrolysis", *Journal of Analytical and Applied Pyrolysis* 171 (2023): 105960.
- **Locaspi, Andrea**, Matteo Ferri, Francesco Serse, Matteo Maestri, and Matteo Pelucchi, "Chemical kinetics of catalytic/non-catalytic pyrolysis and gasification of solid plastic wastes", *Advances in Chemical Engineering*. Vol. 60. No. 1. Academic Press, 2022. 21-76.
- **Locaspi, Andrea**, Matteo Pelucchi, Marco Mehl, and Tiziano Faravelli, "Towards a lumped approach for solid plastic waste gasification: Polyethylene and polypropylene pyrolysis", *Waste Management* 156 (2023): 107-117.
- **Locaspi, Andrea**, Paulo Debiagi, Matteo Pelucchi, Christian Hasse, and Tiziano Faravelli, "A predictive physico-chemical model of biochar oxidation", *Energy & Fuels* 35.18 (2021): 14894-14912.
- Afessa, Million Merid, Venkata Ramayya, Derese Nega, Henok Mossisa, **Andrea Locaspi**, and Tiziano Faravelli, "Investigation of Kinetic, Thermodynamic and Performance Parameters during Devolatilization of Agricultural biomass Waste via TGA", *Ethiopian Journal of Applied Science and Technology* (2023): 16-24.
- Yönder, Özlem, Gunnar Schmitz, Christof Hättig, Rochus Schmid, Paulo Debiagi, Christian Hasse, **Andrea Locaspi**, and Tiziano Faravelli, "Can small polyaromatics describe their larger counterparts for local reactions? A computational study on the H-abstraction reaction by an H-atom from polyaromatics", *The Journal of Physical Chemistry A* 124.46 (2020): 9626-9637.

IN PREPARATION:

- **Locaspi, Andrea**, Oguzhan Akin, Mohammadhossein Havaei, Robin Jhon. Varghese, Alessio Frassoldati, Luna Pratali Maffei, Matteo Pelucchi, Marco Mehl, Kevin M. Van Geem, and Tiziano Faravelli, "Thermochemical recycling of polyethylene terephthalate: condensed-phase kinetic modelling and experimental investigation", *Chemical Engineering Journal* (2024).

- **Locaspi, Andrea**, and Tiziano Faravelli, "Reduced-order condensed-phase kinetic models for thermochemical recycling of polyethylene, polypropylene and polystyrene", Chemical Engineering Journal (2024).
- **Locaspi, Andrea**, Federico Pelizza, Samuele Fontolan, Gianmaria Gardoni, Samuele Delfino, Mattia Sponchioni, Marco Mehl, Matteo Pelucchi, Davide Moscatelli, and Tiziano Faravelli, "Thermochemical recycling of poly(methylmethacrylate): condensed-phase kinetic modelling and experimental investigation", Polymer Degradation and Stability (2024).

OTHER PUBLICATIONS:

- **Locaspi, Andrea**, Matteo Pelucchi, Marco Mehl, Alessio Frassoldati, Alberto Cuoci, Tiziano Faravelli, "La plastica da rifiuto a risorsa: il ruolo del riciclo chimico", RiEnergia - Staffetta Online, Ottobre 2021.

CONFERENCE AWARDS:

- **Best Oral Standard Award** - Locaspi, Andrea *et al.*, WasteEng22, DTU, Denmark, June 2022
- **Best Poster Award** - Locaspi, Andrea *et al.*, Iscre27, Quebec City, June 2023.

ORAL PRESENTATIONS:

- **Locaspi, Andrea**, Federico Pelizza, Samuele Fontolan, Gianmaria Gardoni, Samuele Delfino, Mattia Sponchioni, Marco Mehl, Matteo Pelucchi, Davide Moscatelli, Tiziano Faravelli, "Kinetic and Experimental Investigation of Waste Plastics Thermochemical Recycling: Polymethylmetacrylate Pyrolysis". PRE2023, Potsdam, September 2023.
- **Locaspi, Andrea**, Oguzhan Akin, Mohammadhossein Havaei, Marco Mehl, Matteo Pelucchi, Robin John Varghese, Kevin M. Van Geem, Tiziano Faravelli, "Thermochemical Recycling of Polyethylene Terephthalate: Experimental and Kinetic Investigation". 45th Meeting of the Italian Section of the Combustion Institute, Firenze, Italy, May 2023.
- Giudici Clarissa, Davide Cafaro, Andrea Nobili, Daniele Micale, **Andrea Locaspi**, Francesco Serse, Matteo Ferri, Mauro Bracconi, Matteo Maestri, Matteo Pelucchi, "Kinetic modelling of the formation and growth of single walled carbon nanotubes (SW-CNTs) in floating catalyst chemical vapour deposition". 32nd International Conference on Diamond and Carbon Materials. Lisbon, Portugal, September 2022.

- **Locaspi, Andrea**, Matteo Pelucchi, Marco Mehl, Tiziano Faravelli, "A lumped kinetic approach for solid plastic waste chemical recycling: polyethylene, polypropylene and polystyrene pyrolysis". WasteEng22, DTU, Denmark, June 2022 - **Best Oral Standard Award**
- **Locaspi, Andrea**, Matteo Pelucchi, Marco Mehl, Tiziano Faravelli, "A lumped kinetic approach for solid plastic waste chemical recycling: polyethylene, polypropylene and polystyrene pyrolysis". 44th Meeting of the Italian Section of the Combustion Institute, Napoli, Italy, June 2022.
- **Locaspi, Andrea**, Matteo Pelucchi, Tiziano Faravelli, "A lumped kinetic approach for polystyrene pyrolysis". Pyro22, Gent, Belgium, May 2022.
- **Locaspi, Andrea**, Matteo Pelucchi, Roberto Batista da Silva Junior, Marco Mehl, Alberto Cuoci, Alessio Frassoldati, Alessandra Beretta, Luca Lietti, Tiziano Faravelli. "Thermal degradation of nylon-6 and real mixtures of solid plastic waste. An experimental and kinetic modelling study", 43rd Meeting of the Italian Section of the Combustion Institute, Ischia, Italy, October 2021.
- Serse, Francesco, Andrea Locaspi, Andrew Ure, Matteo Pelucchi, Stephen Dooley, Alberto Cuoci, Tiziano Faravelli, Alessio Frassoldati, "Experimental and theoretical study of cellulose pyrolysis", 43rd Meeting of the Italian Section of the Combustion Institute, Ischia, Italy, October 2021
- Debiagi Paulo, **Andrea Locaspi**, Christian Hasse, Tiziano Faravelli. "A fundamental model of char oxidation". Bad Honnef, Germany. In: 715-WE-Heraeus Seminar, March 2020.

POSTER PRESENTATIONS:

- **Locaspi, Andrea**, Marco Mehl, Matteo Pelucchi, Tiziano Faravelli, "Kinetic Modelling of Plastic Waste Thermochemical Recycling: Polyethylene Terephthalate Pyrolysis". Iscre27, Quebec City, June 2023 - **Best Poster Award**

CONTENTS

ABSTRACT	v
SINOSI	vii
ACKNOWLEDGEMENTS	ix
PUBLICATIONS AND CONFERENCES PARTICIPATION	xi
TABLE OF CONTENTS	xv
1 PLASTIC WASTE: ISSUES AND OPPORTUNITIES	1
1.1 Plastic waste and current recycling technologies	2
1.2 Aim of the Ph.D. Thesis	5
2 CHEMISTRY AND KINETICS OF THERMOCHEMICAL RECYCLING	9
2.1 Condensed-phase physical-chemistry	10
2.1.1 Polymer thermochemistry	12
2.1.2 Backbone degradation	14
2.1.3 Side-group elimination	16
2.1.4 Condensation polymers	17
2.1.5 Plastic waste mixtures	20
2.2 Condensed-phase kinetic models	21
2.2.1 Global kinetic models	21
2.2.2 The Discrete Section Method	22
2.2.3 The Method-of-Moments	24
2.2.4 The functional groups Approach	25
2.2.5 The kinetic Monte Carlo	25
2.3 Gasification and Catalytic Conversion	26
2.3.1 Gasification of volatiles and char	26
2.3.2 Catalytic pyrolysis	28
2.4 Perspectives and challenges	31
3 DEVELOPMENT OF A GENERALIZED KINETIC MODEL: POLYETHYLENE	33
3.1 Semi-detailed Kinetic Model: PE-125-3500	34
3.1.1 Species Definition	35
3.1.1.1 <i>High molecular weight species</i>	36
3.1.1.2 <i>Low molecular weight species</i>	38
3.1.1.3 <i>Number Average Molecular Weight</i>	41

3.1.2 Reaction Network	42
3.1.2.1 Elementary Reaction Rates	43
3.1.2.2 Internal radicals: backbone degradation	47
3.1.2.3 Resonance stabilization: allyl-type radicals	55
3.1.2.4 Terminal radicals: unzipping and backbiting	57
3.1.2.5 Weak-Links: LDPE correction	61
3.1.3 Phase-change phenomena: melting and boiling	62
3.1.3.1 Melting kinetics	63
3.1.3.2 Bubble physical-chemistry	64
3.1.3.3 Average bubble distribution and boiling kinetics	66
3.1.4 Thermochemistry and transport properties	68
3.1.4.1 LMW thermochemistry	69
3.1.4.2 HMW thermochemistry	73
3.1.4.3 Species transport properties	76
3.2 Model Validation	80
3.2.1 Physical and numerical model	81
3.2.2 Model performances: Curve Matching Score	82
3.2.3 Characteristic degradation times: mass-loss profiles	84
3.2.4 Products selectivity: volatile yields	89
3.2.5 Energy requirements	93
3.3 Reduced-Order Models	94
3.3.1 Reduced Semi-Detailed Model: PE-50-480	95
3.3.1.1 Species definition	95
3.3.1.2 Radical isomer lumping	96
3.3.1.3 Reaction lumping	98
3.3.2 Multi-step Fully Lumped Model: PE-10-10	100
3.3.2.1 Species definition	100
3.3.2.2 Multi-step kinetic mechanism	101
3.3.3 Models validation and comparison	105
3.3.3.1 Characteristic degradation times	105
3.3.3.2 Products selectivity: volatile yields	108
3.3.3.3 Energy requirements	110
3.4 Conclusions and Further Work	111
4 POLYPROPYLENE	115
4.1 Semi-detailed Kinetic Model: PP-240-13000	116
4.1.1 Species Definition	117
4.1.2 Reaction Classes	119
4.1.2.1 Elementary Steps	119
4.1.2.2 Backbone Degradation Mechanism	121
4.1.2.3 Allylic position, terminal radicals, and weak-links	125

4.2	Reduced-Order Models	127
4.2.1	Reduced Semi-Detailed Model: PP-130-2500	128
4.2.2	Multi-step Fully Lumped Model: PP-10-12	129
4.3	Model Validation	132
4.3.1	Characteristic degradation times: mass-loss profiles	132
4.3.2	Products selectivity: volatile yields	136
4.3.3	Energy requirements	141
4.4	Conclusions and Further Work	142
5	POLYSTYRENE	143
5.1	Semi-detailed Kinetic Model: PS-55-500	144
5.1.1	Species Definition	145
5.1.2	Reaction Classes	146
5.1.2.1	<i>Elementary Steps</i>	147
5.1.2.2	<i>Backbone Degradation: Lumping and delumping by aromatic ring number</i>	148
5.1.2.3	<i>Terminal and allyl-type radicals</i>	153
5.2	Reduced-Order Models	155
5.2.1	Reduced Semi-Detailed Model: PS-40-300	155
5.2.2	Multi-step Fully Lumped Model: PS-7-6	156
5.3	Model Validation	157
5.3.1	Characteristic degradation times: mass-loss profiles	158
5.3.2	Products selectivity: volatile yields	163
5.3.3	Energy requirements	167
5.4	Conclusions and Further Work	168
6	POLY(ETHYLENE TEREPHTHALATE)	171
6.1	Semi-detailed Kinetic Mechanism: PET-85-700	172
6.1.1	Species Definition	173
6.1.2	Reaction Classes	176
6.1.2.1	<i>Molecular Degradation Mechanism</i>	177
6.1.2.2	<i>Radical Degradation Mechanism</i>	185
6.2	Model Validation	195
6.2.1	Methods and Materials	195
6.2.2	Characteristic degradation times: mass-loss profiles	197
6.2.3	Products selectivity: volatile yields and char characterization	201
6.2.4	Sensitivity analysis	205
6.3	Conclusions and Further Work	208
7	PLASTIC WASTE THERMOCHEMICAL RECYCLING	211
7.1	Mixture thermodynamics	212
7.1.1	Binary interaction parameters	213
7.2	Vinyl polymers	215

7.2.1	Literature degradation models	215
7.2.2	Validation of mixture degradation	216
7.3	Condensation polymers	220
7.3.1	On the interactions in PET-PVC blends	221
7.3.2	On the interactions of polyamides with PET and PVC	224
7.4	Conclusions	225
8	PERSPECTIVES AND FURTHER WORK	227
8.1	Towards a new state-of-the-art	227
8.2	Perspectives and Outlooks	228
8.2.1	On the condensed-phase degradation of plastic waste	229
8.2.2	On the secondary reaction of volatiles from plastic waste	230
8.2.3	On the secondary reaction of plastic char	231
8.3	Conclusions	233
	BIBLIOGRAPHY	235

LIST OF FIGURES

Figure 1.1	European Union Waste Hierarchy. Figure from Waste Framework Directive ¹⁶	3
Figure 1.2	Schematic representation of the technological aspects of the present work. Thermochemical recycling processes complement other recycling and management strategies.	6
Figure 2.1	Plastic waste composition from different sources and years ⁴⁴⁻⁴⁶	11
Figure 2.2	Different phenomena taking place in the volatilization process of polymers, adapted from Dogu <i>et al.</i> ¹⁵	12
Figure 2.3	An overview of the multi-scale nature of plastic gasification. Adapted from Madanikashani <i>et al.</i> ³⁴	12
Figure 2.4	Flux unit characterization in polymer melt, adapted from Marongiu <i>et al.</i> ⁵⁶	14
Figure 2.5	Schematic representation of the backbone degradation mechanism with side-group G = H, CH ₃ , C ₆ H ₅ for PE, PP, and PS respectively. Adapted from Locaspi <i>et al.</i> ⁷⁴	16
Figure 2.6	Schematic representation of the side-group degradation reaction classes. Adapted from Marongiu <i>et al.</i> ³⁵	18
Figure 2.7	Schematic representation of the molecular degradation mechanism involved in degradation of: a) PET, b) PA. Adapted from Locaspi <i>et al.</i> ⁴²	19
Figure 2.8	Discrete section kinetic models for pyrolysis of PE, PP and PS. Comparison of: a) PE mass-loss profiles ⁵⁵ ; b) PS mass-loss profiles ⁶⁶ ; c) PE gas product distribution ⁶⁵ ; d) PE mass-loss profiles considering different evaporation models ⁶⁵ . Adapted from Locaspi <i>et al.</i> ⁴²	23
Figure 2.9	Method of Moment kinetic models for pyrolysis of PE, PP and PS. Comparison of: a) PS mass-loss profiles ⁶¹ ; b) PS molecular weights distribution evolution ⁷³ ; c) PE total gas, alkane, and alkene yields ⁶⁷ ; d) PE mass-loss profiles for MoM (--) and discrete section methods (-) ⁵⁷ . Adapted from Locaspi <i>et al.</i> ⁴²	24
Figure 2.10	Functional groups kinetic model for pyrolysis of PVC and PCP. Comparison of: a) PVC conversion ³⁵ and b) PCP mass-loss profiles ³⁶ . Adapted from Locaspi <i>et al.</i> ⁴²	25
Figure 2.11	Kinetic Monte Carlo kinetic model for pyrolysis of polyolefins. Comparison of: a) PS gas molar fractions ⁷² and b) PSP molar yields ⁷⁹ . Adapted from Locaspi <i>et al.</i> ⁴²	26
Figure 2.12	Schematic representation of: left) physical structure of a char particle with volume V _p , porosity ϵ , and intrinsic surface area S; right) chemical structure of char at the gas-solid interface. Adapted from Locaspi <i>et al.</i> ¹⁶⁷	27
Figure 2.13	Proposed reaction mechanism for catalytic pyrolysis of polyolefins. Adapted from Abbas-Abadi <i>et al.</i> ¹⁸¹	30

Figure 2.14	Schematic representation of the comprehensive kinetic mechanism to be developed for mixture thermochemical recycling	32
Figure 3.1	Modelling polymer degradation through the functional groups approach ⁷⁴ . . .	35
Figure 3.2	Schematic representation of a polymer chain represented through mid-chains (blue) and end-chains (red) moieties	37
Figure 3.3	Schematic representation of the stable and radical pseudo-species introduced to describe long polymer chains (HMW). The distinction between crystalline and molten/amorphous pseudo-species is also shown.	38
Figure 3.4	Representation of the experimental product distribution of Michajlov <i>et al.</i> ²²⁵ employing different ULMW (blue) and ULLMW+RLMW (red lines in the green area). Details are given in the text.	41
Figure 3.5	Schematic representation of the degradation of the initial mid-chain pseudo-species to form LMW products. The MC species undergoes random scission forming terminal radicals which recombine, backbite, H-abstract, or unzip. . .	44
Figure 3.6	Schematic representation of a supported random scission reaction consuming a mid-chain pseudo-species (SPU) to form 2 end-chains.	49
Figure 3.7	Schematic representation of a supported β scission reaction of a mid-chain radical consuming a mid-chain pseudo-species (SPU) to form 2 end-chains. . .	51
Figure 3.8	Schematic representation of the lumping of formation and stabilization of $\dot{\text{C}}_3\text{H}_7$. The ULMW species is assumed to stabilize converting any stable species RH to its corresponding radical R. The elementary steps are represented in italic, while the bold arrows correspond to the lumped reaction introduced in the mechanism.	52
Figure 3.9	Schematic representation of the lumping of formation and stabilization of $\dot{\text{C}}_3\text{H}_7$. The ULMW species is assumed to stabilize converting any stable species RH to the corresponding radical R. The elementary steps are represented in italic, while the bold arrows correspond to the lumped reaction introduced in the mechanism.	53
Figure 3.10	Schematic representation of radical-radical recombination reactions increasing the average chain length.	54
Figure 3.11	Schematic representation of the main reactions involving allyl-type radicals. .	56
Figure 3.12	Schematic representation of the main reactions involving terminal radicals. .	57
Figure 3.13	Schematic representation of 1-5 backbiting from the EC terminal radical employing an MC unit as SPU.	58
Figure 3.14	Schematic representation of unzipping reaction from the EC terminal radical employing an MC unit as SPU.	61
Figure 3.15	Morphological changes during pyrolysis of Polyethylene (left) and Polypropylene (right) by high-speed infrared camera. Figure taken from Wang <i>et al.</i> ²⁵⁰	62

Figure 3.16	Thermodynamic parameters per unit mass of C ₁₆ H ₃₄ (L) evaluated for gas (blue) and liquid (red) phase compared to the values employed in the model (black). The results are compared with experimental data ¹⁰⁰ (marks) and the Ruzicka-Domalski correlation ^{285,287}	73
Figure 3.17	Thermodynamic parameters per unit mass evaluated for different n-alkanes as described in Section 3.1.4.1. The reported experimental data are from the NIST webbok ¹⁰⁰	74
Figure 3.18	Thermodynamic parameters per unit mass evaluated for the crystalline (purple) and amorphous/molten (red) mid-chain species compared to literature experimental data ^{100,232,291–296} (dashed-lines and marks).	77
Figure 3.19	Comparison of different models and experimental data showing: a) the pitfall of point-wise approaches ³¹³ ; b) typical fuel mole fractions in isothermal flow reactors ³¹²	83
Figure 3.20	Sample mass-loss profiles of PE subjected to different temperature profiles. Comparison among the present work (solid lines), the detailed model of Faravelli <i>et al.</i> (dashed lines) and literature experimental data (marks). The Curve Matching score (CM) is reported for both models with the same colour legend as the plots.	86
Figure 3.21	Parity plots for the semi-detailed model (blue squares) and the detailed model of Faravelli <i>et al.</i> (yellow circles) with literature data on HDPE and LDPE degradation temperatures (top) and times (bottom) at sample mass (m _L) 0.9, 0.5 and 0.1.	87
Figure 3.22	Comparison of SciExpeM indices on all mass-loss profiles investigated for the proposed model and the detailed model of Faravelli <i>et al.</i>	88
Figure 3.23	HDPE sample mass-loss (m _L) and average chain length (L _{av}) profiles at HR=1-50°C/min. Comparison among the present work (solid and dashed-dotted lines) and the detailed model of Faravelli <i>et al.</i> ⁶⁵ (dashed and dotted lines) and mass-loss literature experimental data (marks). The CM score on mass-loss is reported for both models with the same colour legend as the plots.	88
Figure 3.24	Comparison of volatiles molar yields of the present model (lines) and experimental data ^{65,227} (marks). Model predictions are normalized on the volatiles experimentally measured.	91
Figure 3.25	Comparison of species mass yields for the present model (full), the detailed model by Faravelli <i>et al.</i> (full) and experimental data (patched).	92
Figure 3.26	Comparison of predicted (solid lines) and measured (symbols) profiles for HDPE mass-loss (black) and yields (coloured) at: left) 390°C, right) 410°C. The predictions of the detailed model by Faravelli <i>et al.</i> (dashed lines) are reported as well.	93
Figure 3.27	Comparison of predicted (solid lines) and measured (symbols) heat-flux profiles for HDPE and LDPE.	94

Figure 3.28	Schematic representation of the radical isomer lumping for end-chain paraffin radicals. The isomers P-NC ₄₀ H ₈₀ and P-NC ₄₀ H ₈₀ _T are described by the species P-NC ₄₀ H ₈₀ only (purple)	97
Figure 3.29	Schematic representation of the multi-step reaction mechanism.	102
Figure 3.30	Sample mass-loss profiles of PE subjected to different temperature profiles. Comparison among the semi-detailed (solid lines), reduced (dashed lines), and multi-step (dotted lines) models and literature experimental data (marks). The Curve Matching score (CM) is reported for the three models with the same colour legend as the plots.	106
Figure 3.31	Parity plots for HDPE and LDPE degradation temperatures (top) and times (bottom) at sample mass (m_L) 0.9, 0.5 and 0.1 of the semi-detailed (blue squares), reduced (yellow circles) and multi-step (red triangles) models with literature experimental data	107
Figure 3.32	Comparison of SciExpeM indices (Section 3.2.2) on all mass-loss profiles investigated for the semi-detailed, reduced, and multi-step model. The detailed model of Faravelli <i>et al.</i> ⁶⁵ is also reported as comparison.	107
Figure 3.33	HDPE sample mass-loss (m_L) and average chain length (L_{av}) profiles at HR=1-50°C/min. Comparison among the semi-detailed (solid and dashed-dotted lines) and the reduced (dashed and loosely dashed lines) models and mass-loss literature experimental data (marks).	108
Figure 3.34	Comparison of volatiles molar yields of the semi-detailed (solid lines) and reduced (dashed lines) models and experimental data (marks). Model predictions are normalized on the volatiles experimentally measured.	109
Figure 3.35	Comparison of species mass yields for the semi-detailed, reduced and multi-step mechanism (full) and experimental data (patched).	110
Figure 3.36	Comparison of predicted (lines) and measured (symbols) profiles for HDPE mass-loss (black) and yields (coloured) at: left) 390°C, right) 410°C.	110
Figure 3.37	Comparison of semi-detailed (solid lines), reduced (dashed lines) and multi-step (dotted lines) models and measured (symbols) heat-flux profiles for HDPE and LDPE.	111
Figure 4.1	Schematic representation of the stable pseudo-species introduced to describe long polymer chains (HMW).	117
Figure 4.2	Schematic representation of the stable head and tail configurations of LMW species. C ₁₂ is employed as an example	118
Figure 4.3	Comparison of predicted and experimental ³³⁵ thermodynamic parameters per unit mass for the crystalline (P-IC ₄₅ H ₉₀ -P_S) and amorphous/molten (P-IC ₄₅ H ₉₀ -P) mid-chain polymeric species	120
Figure 4.4	Schematic representation of the degradation of the initial mid-chain pseudo-species to form LMW products. The MC species undergoes random scission forming terminal radicals which recombine, backbite, H-abstract, or unzip.	123

Figure 4.5	Sample mass-loss profiles of PP subjected to different temperature profiles. Comparison among the present work for iPP (solid lines), the model for aPP (dashed dotted lines), the detailed model of Ranzi <i>et al.</i> (dashed lines) and literature experimental data (marks). The Curve Matching score (CM) is also reported.	133
Figure 4.6	Sample mass-loss profiles of PP subjected to different temperature profiles. Comparison among the semi-detailed (solid lines), reduced (dashed lines) and multi-step (dotted lines) model and literature experimental data (marks). The Curve Matching score (CM) is also reported.	134
Figure 4.7	Parity plots for iPP and aPP degradation temperatures (top) and times (bottom) at sample mass (m_L) 0.9, 0.5 and 0.1 of the semi-detailed (blue squares), reduced (yellow circles), multi-step (red triangles), detailed model of Ranzi <i>et al.</i> (green diamonds), and literature experimental data.	135
Figure 4.8	Comparison of SciExpeM indices (Section 3.2.2) on all mass-loss profiles investigated for the semi-detailed, reduced, and multi-step model. The detailed model of Ranzi <i>et al.</i> is also reported as comparison.	136
Figure 4.9	iPP mass-loss (m_L) and number average molecular weight ($MW_{n,av}$) profiles at $HR=10^\circ\text{C}/\text{min}$. Comparison among the semi-detailed, reduced, and detailed model of Faravelli <i>et al.</i> and mass-loss and number average molecular weight literature experimental data.	137
Figure 4.10	Comparison of total carbon weight yields of the semi-detailed and reduced models (solid and dashed lines) and experimental data (marks). Model results are normalized on the predictions of volatiles experimentally measured. . . .	138
Figure 4.11	Comparison of species mass yields for the semi-detailed, reduced, and multi-step models (full) and experimental data (patched).	140
Figure 4.12	Comparison of predicted (solid lines) and measured ^{318,348,354} (symbols) heat-flux profiles.	141
Figure 5.1	Schematic representation of the stable and radical pseudo-species introduced to describe long polymer chains (HMW).	146
Figure 5.2	Thermodynamic parameters per unit mass evaluated for the mid-chain polymeric species (solid red lines) compared to experimental data ³⁶² (dashed lines) and the Ruzicka-Domalski correlation. The glassy state properties are reported in purple.	147
Figure 5.3	Schematic representation of the degradation of the initial mid-chain pseudo-species to form LMW products. The MC species undergoes random scission forming terminal radicals which recombine, backbite, H-abstract, or unzip. The lumping and delumping discussed in the this sections is included in this representation.	149

Figure 5.4	Examples of lumping by aromatic ring number for the trimer. Random scission reactions in the represented position leads to formation of three different trimer configurations, which are however represented by a single lumped species labelled $\text{C}_{24}\text{H}_{23}$	150
Figure 5.5	Examples of delumped reactions forming: a) toluene (C_7H_8); b) α -methyl styrene (C_9H_{10}); c) diphenyl propane ($\text{C}_{15}\text{H}_{16}$). The balancing error is dumped on formation of benzene (C_6H_6), ethylbenzene (C_8H_{10}), cumene (C_9H_{12}), diphenyl butane ($\text{C}_{16}\text{H}_{18}$), and light olefins	152
Figure 5.6	Schematic representation of: a) β -scission reaction involving instantaneous stabilization of the LMW product; b) supported β -scission reaction occurring on an end-chain to release a LMW. The end-chain functional group is reformed consuming the “support” mid-chain unit (SPU)	154
Figure 5.7	Mass-loss profiles of PS subjected to different temperature profiles. Comparison among the semi-detailed model (solid lines), the detailed one of Faravelli <i>et al.</i> (dashed lines) and literature experimental data (marks). The Curve Matching score (CM) is also reported.	159
Figure 5.8	Mass-loss profiles of PS subjected to different temperature profiles. Comparison among the present semi-detailed (solid lines), reduced (dashed lines) and multi-step (dotted lines) mechanisms with literature experimental data (marks). The Curve Matching score (CM) is also reported.	160
Figure 5.9	Parity plots of the present work prediction (blue squares), the detailed model of Faravelli <i>et al.</i> (yellow circles) and literature experimental data for polymer degradation temperatures (top) and times (bottom) at sample mass (m_L) 0.9, 0.5 and 0.1.	161
Figure 5.10	Comparison of SciExpeM indices (Section 3.2.2) on all mass-loss profiles investigated for the semi-detailed, reduced, and multi-step model. The detailed model of Faravelli <i>et al.</i> is also reported as comparison.	161
Figure 5.11	PS mass-loss (m_L) and number average molecular weight ($\text{MW}_{n,\text{av}}$) profiles at 350°C from different initial molecular weights. Comparison among the semi-detailed, reduced, and detailed model of Faravelli <i>et al.</i> and mass-loss and number average molecular weight literature experimental data.	162
Figure 5.12	Parity plots of final gas-phase yields of C_8 , C_{16} , and C_{24} . Comparison of the present semi-detailed (blue squares), reduced (yellow circles), multi-step (red triangles), and detailed model of Faravelli <i>et al.</i> (green diamonds) and literature experimental data.	164
Figure 5.13	Comparison of mass yields of volatiles among the semi-detailed model, the detailed one of Faravelli <i>et al.</i> and experimental data (patched bars).	166
Figure 5.14	Comparison of mass yields of volatiles among the semi-detailed, reduced and multi-step models with experimental data (patched bars).	167
Figure 5.15	Comparison of predicted (solid lines) and measured ^{318,358,369,372,374} (symbols) heat-flux profiles.	168

Figure 6.1	Schematic representation of the PET semi-detailed model according to the functional groups approach.	173
Figure 6.2	Schematic representation of the stable and radical HMW species included in the present kinetic model. Further details on the nomenclature are given in the text.	174
Figure 6.3	Schematic representation of the monomer and dimers considered in the present work (except for the cyclic dimer CYEDGE). Both stable and radical species are presented with their labels.	176
Figure 6.4	Schematic representation of the proposed molecular (blue) and radical (red) degradation mechanism.	178
Figure 6.5	Schematic representation of the degradation of the 6-centred syn elimination to form vinyl and carboxylic end-chains employing two terephthalic units as SPUs (dashed lines).	179
Figure 6.6	Schematic representation of the syn elimination occurring near a carboxylic end-chain.	179
Figure 6.7	Schematic representation of the ethyldene methyl syn elimination to form vinyl and carboxylic end-chains.	181
Figure 6.8	Schematic representation of the ethyldene syn elimination to form phenyl anhydride and acetaldehyde.	182
Figure 6.9	Schematic representation of carboxylic acids dimerization.	183
Figure 6.10	Schematic representation of vinyl-ester isomerisation and decarbonylation.	184
Figure 6.11	Schematic representation of the random scission on the OC-CO bond of the glycol mid-chain moiety to form two end-chain methyl ester radicals.	187
Figure 6.12	Schematic representation of the random scission on the CO-OC bond of the vinyl ester end-chain moiety to form acetaldehyde, CO, and a phenyl end-chain.	187
Figure 6.13	Schematic representation of the β -scission of the glycol COO-C bond to form a vinyl ester and a benzyloxy radical.	188
Figure 6.14	Schematic representation of the β -scission of the glycol CO-OC bond a methyl ester, a phenyl radical and 2 CO.	189
Figure 6.15	Schematic representation of all types of β -scission reactions considered in the present work.	189
Figure 6.16	Schematic representation of isomerisation of the glycol secondary radical to the primary ethyldene position. The reverse step is represented through a separate reaction.	190
Figure 6.17	Schematic representation of glycol radical additions on carbonyl positions of the vinyl ester end-chain.	192
Figure 6.18	Schematic representation of glycol radical aromatic additions on the mid-chain aromatic rings.	192
Figure 6.19	Schematic representation of phenyl additions to carbonyl groups considered in the present work.	193

Figure 6.20	Schematic representation of LMW phenyl radicals additions to mid-chain aromatic rings.	194
Figure 6.21	Schematic diagram of the micropyrolyzer reactor with a comprehensive analytical section comprising ToF-MS, FID and PDD detectors	196
Figure 6.22	Mass-loss profiles of PET in dynamic conditions. Comparison among the present work (solid lines) and literature experimental data ^{87,99,139,400,432–437} (marks).	199
Figure 6.23	Mass-loss profiles of PET in isothermal conditions. Comparison among the present work (solid lines) and both literature ^{99,434} and new experimental data (marks).	201
Figure 6.24	Parity plots of model prediction with literature ^{87,99,139,400,432–437} and new experimental data for polymer degradation temperatures (top) and times (bottom) at sample mass (m_L) 0.9 and 0.5 and char yield.	202
Figure 6.25	Comparison of SciExpeM indices (Section 3.2.2) on all mass-loss profiles investigated.	203
Figure 6.26	Comparison of mass yields of volatiles for the proposed model and both new and literature ^{99,101} experimental data (patched bars).	205
Figure 6.27	Comparison of char elemental composition for the present model (solid bars) and both literature ^{405,406,438} and new experimental data (patched bars).	206
Figure 6.28	Sensitivity analysis for the temperatures 0.1 and 0.5 liquid conversion are achieved ($T_{(m_L=0.9)}$ and $T_{(m_L=0.5)}$) and the final char yield.	207
Figure 6.29	Sensitivity analysis for the final mass yields of the major volatiles.	208
Figure 7.1	Comparison of predicted (solid lines) and measured (symbols) mass-loss profiles for PE, PP, and 50-50 mixtures.	218
Figure 7.2	Comparison of predicted (solid lines) and measured (symbols) mass-loss profiles for 50-50 mixtures of PE and PS with PVC at HR=10°C/min.	219
Figure 7.3	Comparison of predicted (solid lines) and measured (symbols) mass-loss profiles plastic mixtures at HR=10°C/min.	220
Figure 7.4	Comparison of predicted (solid lines) and measured (symbols) mass-loss profiles of a 35LDPE-35HDPE-10PP-10PS-10PVC mixture at various HR.	220
Figure 7.5	Comparison of predicted (solid lines) and measured (symbols) mass-loss profiles for: a) 25HDPE-25PP-25PS-25PET HR=40°C/min ⁴⁵¹ ; b) 20LDPE-20PP-20PS-20PET-20PVC HR=10°C/min ⁴⁶⁹	221
Figure 7.6	Experimental mass-loss profiles at HR=10°C/min for: a) 50PET-50PVC mixture ⁴⁶⁹ ; b) different PCL-PVC mixtures ¹²² . Solid lines are the experimental results, while dashed lines are obtained as linear combination of the pure polymer behaviours.	223
Figure 7.7	Proposed radical-molecular interaction mechanism between PET and PVC.	224
Figure 8.1	Comparison of predicted and experimental yields for HDPE pyrolysis in a spouted bed reactor at different operating temperatures.	231

Figure 8.2 Oxidation step of chars obtained by direct oxidation of PET at different heating rates.Comparison of model predictions (lines) and literature⁴³² experimental results (marks) 232

LISTINGS

PLASTIC WASTE: ISSUES AND OPPORTUNITIES

PLASTICS have become ubiquitous in the contemporary era, revolutionizing numerous facets of daily life across diverse industries. Their versatility, durability, and cost-effectiveness have propelled innovation in packaging, construction, healthcare, and transportation. Today, it is nearly impossible to imagine a world without plastics^{1,2}. For instance, plastics compose roughly 15 wt.% of cars and 50 wt.% of the Boeing Dreamliner^{1,3}. However, the very characteristics that make plastics so useful have contributed to a growing environmental crisis, i. e., plastic waste (PW).

Global plastic production has witnessed an exponential rise in recent decades⁴. Over half of all plastic ever produced was manufactured after the year 2000, and current projections estimate a doubling of global plastic production by 2050⁵. Plastics account for 4-8% of the global oil consumption², and throughout their lifecycle contribute to 3.4% of global greenhouse gas emissions⁶. Conversely, the current capability to manage this plastic influx lags significantly, and this trend is an environmental threat. Recycling rates remain low, with only 9% of plastic ever produced being recycled⁴. Incineration accounts for a further 12%, but this method has limitations and raises environmental concerns⁷. The remaining PW is either still in use or has been improperly disposed of in landfills or released into the environment⁵. Terrestrial and aquatic ecosystems are increasingly choked by plastic debris, disrupting vital natural habitats and jeopardizing biodiversity⁸. Additional issues arise from microplastics impacting human health as they enter the food chain⁹⁻¹².

New perspectives are required to tackle both the waste management problem of plastics and climate change contributions². The business-as-usual outlook is unsustainable and strong global policies are required¹³. In this context, additional waste valorization policies and recycling technologies are of paramount importance. This is crucial since traditional management methods, such as landfilling and incineration, present significant drawbacks^{7,14,15}. The European Union has taken several steps towards a circular economy through several directives and policies¹⁶. However, despite achieving a plastic recycling rate of 18.7% in 2022, fossil fuels remain the dominant source material, exceeding 80%⁴. Tackling plastic waste requires a multifaceted approach, involving both technological advancements and also socio-political considerations. This includes reducing the amounts of waste and enforcing robust collection and sorting policies². Among the technological issues, development of sustainable materials and recycling processes hold paramount importance, and these advancements

are inherently interconnected^{17,18}. Currently, most biodegradable plastics are obtained from fossil resources or are compostable only under controlled conditions². Similarly, existing recycling technologies struggle to handle the complexity and variability of waste feedstocks^{7,15,19}.

The present Ph.D. thesis is a small step towards a circular and sustainable plastic economy. The following Sections discuss the currently available recycling processes, highlighting their limitations, challenges, and potential advancements. The aim and outline of the current work are then presented.

1.1 PLASTIC WASTE AND CURRENT RECYCLING TECHNOLOGIES

Plastic is defined as a "*polymeric material that has the capability of being moulded or shaped, usually by the application of heat and pressure*"²⁰. Each plastic material consists of a distribution of macromolecules with similar chemical functionalities but different chain lengths. Both the monomers and chain length distribution affect the physico-chemical properties of the material. Additives are commonly introduced to further tune processing and final properties of the desired product²¹.

On a global scale, the plastics with the highest production in 2022²² are polyethylene (PE, 26.3%), polypropylene (PP, 18.9%), poly(vinyl chloride) (PVC, 12.7%), poly(ethylene terephthalate) (PET, 6.2%), polyurethanes (PU, 5.3%), and polystyrene (PS, 5.2%). These materials alone account for ~82% of all plastics from fossil-based fuels (>90% of the global production). Plastics account for 6% of the global oil consumption², and of the 402 Mt of plastics produced globally, 58.8 Mt were made in Europe⁴. The geographical distribution of plastic production varies significantly, but the dominant polymer types remain consistent across regions. Similarly, the composition of plastic waste exhibits significant geographical variation and depends heavily on the source of the waste^{7,15}. Post-industrial PW are manufacturing scrapes typically recycled within the production facility itself. Post-consumer waste is a mixed plastic stream often contaminated with organic and inorganic materials. Packaging materials are a major contributor to PW due to their widespread use and short lifespans¹⁵. Consequently, the composition of municipal and household plastic waste reflects the commonly used packaging polymers. Several of these polymers are partially sorted for mechanical recycling processes, resulting in a typical composition of 70-75% PE-PP, 5-10% PS, 5-10% PET, and 0-4% PVC²³. In several instances, PVC content in plastic waste is significantly higher (15-25%)^{7,24}, highlighting the inherent variability in composition.

The *Waste Framework Directive*¹⁶ (WFD-2008/98/EC) defines the waste management principles towards a circular economy. The directive addresses several socio-political issues introducing concepts such as the "*polluter pays principle*" and "*extended producer responsibility*". From a technological standpoint, it establishes a hierarchical framework for the valorization of PW, as illustrated in Figure 1.1. This hierarchy prioritizes waste

management options according to their complexity and environmental impact, aiming at maximizing material recovery while minimizing energy requirements and waste generation. The highest priority objective is prevention, both in terms of promoting repair and re-use but also in terms of product design. Implementing policies to eliminate superfluous plastic items is also a key step to effectively decrease waste generation. The second preferred option is to recover and prepare waste for further re-use. This approach is preferred as it employs less energy and fewer resources, reducing CO₂ and pollutant emissions¹⁹. Recycling, recovery, and disposal represent the subsequent hierarchical steps to reprocess waste. Recycling is usually distinguished in sublevels^{19,25}:

- Primary recycling* (in-plant recycling) involves employing as raw materials products that cannot satisfy market specification. This pathway is performed for post-industrial waste, which is often a pure high quality stream⁷.
- Secondary recycling* (e.g., mechanical recycling), which involves only physical transformation to convert PW into similar products.
- Tertiary recycling* (chemical recycling), which involves chemical transformations of plastic waste to obtain new chemicals.
- Quaternary recycling*, also known as energy recovery, which converts waste into energy.

Among the disposal pathways, landfilling is the most common^{26,27}. This pathway however results in significant losses in terms of energy and chemicals, but also in severe contamination of the environment^{15,26,27}. Energy recovery allows better exploiting PW, but it poses environmental concerns due to release of CO₂ and several pollutants^{7,28}.



Figure 1.1: European Union Waste Hierarchy. Figure from Waste Framework Directive¹⁶.

Mechanical recycling is a well-established technology that has been studied since the 1970s¹⁹. It is currently the most widespread recycling technology, accounting for ~18.5% of the plastics produced in 2022 in Europe⁴. Considering the global plastic

production, in 2022 only 9% was from mechanical recycling²². This process centers on heating PW to its melting point to reprocess it into new materials. Several challenges are still present^{7,15,19,25}. During their lifetimes, waste plastics are typically exposed to a variety of environmental stresses such as heat, oxygen, radiation, and mechanical ones. These factors, coupled to the moderately high process temperatures, induce partial degradation of the material. This phenomenon translates to a decrease in physical properties of the recycled product compared to its virgin counterpart¹⁴. Considering mixed waste, the process temperature must be the highest among the polymers melting point. In presence of high melting point materials (e.g., PET), plastics with low degradation temperatures (e.g., PVC) thermally decompose during the recycling⁷. Furthermore, the resulting blend requires appropriate additives to have suitable properties. For these reasons, mechanical recycling requires pure uncontaminated streams, and is often hindered by the sorting capability¹⁹. Strategies such as solid-state post-condensation or addition of chain-extenders partly recover the loss in physical properties⁷. In this context, the design of novel polymers and materials suitable for mechanical recycling is of paramount importance.

Chemical recycling emerges as a strategic complement to mechanical recycling, particularly for addressing complex or contaminated PW streams. The term chemical recycling encompasses all processes that alter the chemical structure of the waste¹. Each process yields a diverse range of valuable products, including monomers, oil-like mixtures, and energy carriers. These products essentially constitute the fundamental building blocks utilized by the chemical industry, offering a pathway to reintegrate plastic waste into the value chain. Several research is underway to develop new recycling technologies^{15,25}, such as solvent extraction and hydrothermal liquefaction. Solvent extraction involves fully or partially depolymerizing plastic materials to the initial monomers or pre-polymers suitable for subsequent polymerization processes²⁹. Glycolysis is the most widely spread technology, although methanolysis, hydrolysis, and aminolysis are emerging as well. The main drawback of these processes is that they can be employed only for condensation polymers (e.g., PET) and involve expensive purification and upgrading of the monomers²⁵. Furthermore, the relatively high process temperatures (150–300°C²⁵) can induce degradation of other polymers present within the mixed waste. The presence of additives and contaminants in PW further complicates product purification and treatment. Hydrothermal liquefaction is a type of thermochemical recycling that employs sub- or supercritical water to produce gas, oil, and char³⁰. The scalability of the process is however hindered by the high operating pressures (~300 bar), long residence times, and high amounts of process water¹⁵.

¹ Technically, the WFD-2008/98/EC¹⁶ categorizes this among the "Recovery Operations" (Annex II). Specifically, it defines "*R3 - Recycling/reclamation of organic substances which are not used as solvents (this includes preparing for re-use, gasification and pyrolysis using the components as chemicals and recovery of organic materials in the form of backfilling)*"

Currently, pyrolysis and gasification (thermochemical recycling) are the most promising technologies for waste valorization^{7,15,19}. The reason is that they are able to accommodate the high variability and amounts of contaminants characteristics of PW feedstocks. Gasification is especially promising for mixed plastic - municipal solid waste (MSW)¹⁵. Pyrolysis typically involves thermal decomposition in an inert environment at T=300-700°C. This process results in formation of light gases, pyrolysis oil, and char³¹. Conversely, gasification is a partial oxidation process performed at T=700-1500°C under H₂O, CO₂, or O₂. The main product of the process is syngas, i.e., a gaseous mixture primarily composed of CO, H₂, CO₂, and CH₄²⁸. A critical challenge associated with both pyrolysis and gasification is achieving optimal product selectivity while minimizing pollutant formation and energy consumption. For instance, formation of high amounts of tars leads to undesirable coke deposit. Mitigation strategies involve decoupling condensed-phase pyrolysis from product upgrading (e.g., ex-situ catalysis). Additionally, the presence of PVC leads to release of high amounts of hydrochloric acid. Implementing a low temperature degradation step beforehand allows collecting HCl in appropriate equipment without compromising the desired products. Minimizing the formation of other pollutants such as NOx and SOx emissions is also crucial for ensuring environmentally sound operation of these technologies.

Pyrolyzers and gasifiers are well-established technologies to convert oil, coal, and biomass into valuable products³². However, current conversion processes often rely heavily on "heuristic approaches", i.e., empirical methods based on experience and trial-and-error. While effective to some extent, these methods provide limited insights into the underlying phenomenology. Although numerous studies are underway to improve these processes, a significant portion focuses primarily on establishing input-output relationships. This approach neglects detailed investigations and quantifications of the complex phenomena involved. Conversely, the considerable variability in feedstock requires an accurate characterization of the chemico-physical transformations to develop next-generation reactors¹⁵. Chemical kinetics and computational fluid dynamics (CFD) modelling tools offer valuable methodologies to address this limitation. These in-silico approaches allow performing numerical experiments, aiding in the interpretation of physical experiments³³. A comprehensive understanding of the underlying phenomena aids optimizing product distribution, designing experiments, reactors, and processes, and controlling pollutant formation^{7,34}.

1.2 AIM OF THE PH.D. THESIS

The present PhD thesis contributes to the development of alternative recycling technologies for plastic waste. As previously highlighted, PW is a valuable feedstock to produce valuable chemicals, energy carriers, and fuels. In this context, thermochemical

recycling offers a complementary approach to mechanical, solvent, and other recycling processes as shown in Figure 1.2.

The condensed-phase chemical kinetics of the process proposing models for the degradation of common plastics are investigated.¹³ Kinetic models are proposed for the most common polymers present in PW, i.e., LDPE, HDPE, PP, PS, PET. The functional groups approach proposed in the scientific literature for halogenated polymers^{35,36} and biomass³⁷ is employed and further expanded. This methodology allows obtaining low computational mechanisms suitable for reactor-scale CFD simulations. Additional theoretical lumping techniques are proposed to further reduce the computational cost. All the kinetic models are validated with literature experimental data on polymer degradation and, when available, also with detailed literature models. The targets the models aim at describing are the characteristic degradation times, product distribution, and energy fluxes. The kinetic models find application in the degradation of waste polymers, which have unknown origin and cannot be characterized. Therefore, the mechanisms focus on predicting the *average reactivity* of the constituents in PW.

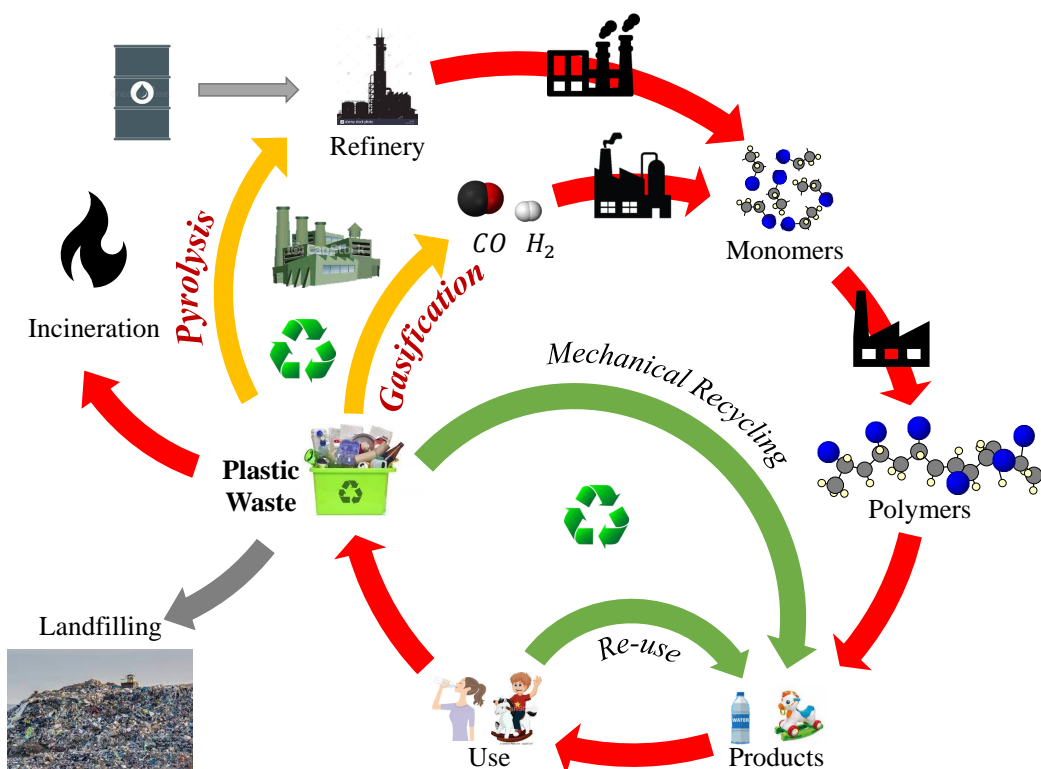


Figure 1.2: Schematic representation of the technological aspects of the present work. Thermochemical recycling processes complement other recycling and management strategies.

The thesis is organized by polymer investigated, presenting a semi-detailed kinetic model for each plastic type while discussing its peculiarities. Several methodologies are shared between each chapter, and therefore they are described in-depth once and

then briefly reiterated in the other chapters. Specifically, the discussion is organized as follows:

- *Chapter 2* presents a comprehensive review of the current **state-of-the-art** for kinetic modelling of condensed-phase polymer pyrolysis. Both the physico-chemical phenomena and models proposed in literature are discussed highlighting the advantages and limitations. A brief outline also of secondary gas-phase and catalytic reactions is also presented.
- *Chapter 3* discusses the development of a functional groups approach condensed-phase kinetic model. The methodology is described in-depth employing **PE** as case study since it is the simplest in terms of chemical functionalities. First a semi-detailed kinetic mechanism is developed, also presenting an estimation of the species thermochemical and physical properties. The model is validated with literature experimental data and other established detailed models. The results are then employed to derive reduced-order models that offer a balance between accuracy and computational efficiency.
- *Chapter 4* presents the kinetic model for **PP**. Building on PE's model, this chapter tailors the kinetics for PP, focusing on managing head and tail terminations. A reduced and fully lumped model are also proposed, complemented by polymer thermochemistry.
- *Chapter 5* presents the kinetic model for **PS**. The "*lumping by aromatic ring number*" approach is introduced to further decrease the computational cost of the kinetic mechanism. In line with PE and PP, a reduced and a fully lumped model are also proposed together with the polymer thermochemistry.
- *Chapter 6* presents the kinetic model for **PET**. Considerable attention is given to critically assess the molecular and radical degradation pathways proposed in the scientific literature. The thermochemical properties are not accounted for due to the scarce literature on phenyl esters thermochemistry.
- *Chapter 7* demonstrates how to employ the kinetic models to **PW** mixtures. Vinyl polymers are presented first, discussing their immiscibility and the interactions observed in experimental data. Interactions in mixtures involving PET and PA are then presented, proposing reaction pathways to explain the cross-products.
- *Chapter 8* briefly resumes the **conclusions** of the current work. Further challenges and opportunities are then proposed.

The developed kinetic models find application in various thermochemical conversion processes, including pyrolysis, gasification, and combustion, when coupled with suitable complementary gas-phase models. Indeed, condensed-phase pyrolytic degradation is the first hierarchical step and is similar across all thermochemical processes.

The difference among pyrolysis, gasification, and energy conversion lies in the gaseous environment during each conversion process. Coupling these kinetic models with analogous ones for other polymers and biomass allows consistently addressing both PW and PW/MSW valorization. The developed kinetic models are provided in CHEMKIN-like format and are freely available as a public GitHub repository². All the experimental data employed for the validation are also reported in the repository in "json" format. The kinetic models are also integrated in the comprehensive GitHub repository of the CRECK Modeling Lab³. These models aid in designing and optimizing large-scale thermochemical conversion reactors for plastic waste valorization, ultimately promoting a more circular economy for plastic materials.

² Available at <https://github.com/Alocaspi/Polymers-Kinetic-Mechanisms>

³ Available at <https://github.com/CRECKMODELING/Kinetic-Mechanisms>

CHEMISTRY AND KINETICS OF THERMOCHEMICAL RECYCLING

CHEMICAL recycling of plastic waste (PW) is of paramount importance to meet sustainability targets in both the chemical and energy industries^{19,38}. As previously discussed, plastic waste is a complex mixture of different polymers, additives, inorganics, and contaminants with a time- and location- varying composition and availability. Thermochemical conversion processes such as pyrolysis and gasification allow to achieve the flexibility required to handle these complex feedstocks^{28,39,40}. According to the desired target, vastly different product spectra can be obtained adapting reactor conditions (e.g., temperature, residence time, catalyst). Modelling the physico-chemical transformation of the reacting mixture is a key requirement to control and optimize the process. Particularly, fluid dynamics and chemical kinetic modelling tools aid reactor and process design, but also performances optimization and pollutant formation mitigation^{7,15,34}.

Describing the chemistry and characteristic times of the thermochemical process is challenging. The plastic waste is a solid-phase feedstock, which upon heating melts and decomposes to form a multi-phase and multi-component product mixture. For this reason, describing the process requires suitable condensed- and gas- phase models⁴¹. Additionally, according to the PW composition, formation of significant amounts of a char-inorganic solid matrix can take place further increasing the complexity of the reacting environment. The impact of conversion of such solid residue during gasification should be also accounted for since it affects the product distribution, the quality (e.g., H₂/CO ratio in syngas), and acts as the rate determining step in certain conditions³².

The present Chapter presents a review of the state-of-the-art approaches to kinetic modelling of plastic waste thermochemical recycling. To the author's knowledge, few studies on plastic waste mixtures have been presented only recently^{15,34,42}, while extensive focus has been given to single polymer pyrolysis to decouple mixture complexity and secondary gas-phase cracking, catalytic, gasification, and oxidation reactions. Gasification and catalytic-upgrading processes involve first a condensed-phase pyrolytic step followed by secondary gas-, gas-solid, or liquid-solid reactions that can be studied separately employing appropriate pyrolysis models. For this reason, the mechanism and kinetics involved in the recycling technologies are discussed in a hierarchical approach. Thermal degradation is first addressed followed by a brief outline of gasification and then catalytic conversion. To aid the reader, the discussion follows a

mechanistic approach presenting first the degradation mechanisms and then the state-of-the-art kinetic models developed in the past years.

2.1 CONDENSED-PHASE PHYSICAL-CHEMISTRY

Thermochemical conversion of plastic waste, even without the presence of a catalyst, is a multi-component, multi-phase and multi-scale problem^{15,34,41,43}. Modelling the degradation of the PW requires characterizing its thermophysical properties and constituents.

Figure 2.1 shows the main constituents of PW from European and American sources from 1995 until 2019. High variability is observed in terms of amounts of the polymer constituents, but similar characteristic materials are found. Notably, the amounts of PVC across these studies vary considerably, as German waste in 1995⁴⁴ has high amounts in the range of 15% of PVC, while in more recent studies^{45,46} amounts of 1-4% are found. In general, the variability of the PW feedstock can be described using few reference constituents, i. e., creating a surrogate³⁷. According to the desired level of detail, the mixture can be represented as a single pseudo-species⁴⁷ or accounting for the polymers and additives included⁴⁸. The complexity and accuracy of the model increase according to the number of reference species accounted for, including polymers, impurities, and additives. The level of detail employed in characterizing the mixture also affects the level of accuracy in modelling its evolution. In general, the mixture behaviour cannot be assumed as a linear combination of its constituents^{49,50} and cross-interactions can lead to different final products which may require further downstream processing to treat the flue-streams.

As shown in Figure 2.2, the PW partially melts upon heating (e. g., T=140-280 °C for the most common commercial polymers and polyolefins) and decomposes (e. g., T=250-500 °C) forming smaller species. The released intermediates cover a wide distribution of molecular weights, resulting in simultaneous formation of solids, liquids, vapours, and supercritical gases. The coexistence of multiple phases requires estimation of their contact areas and their characteristic times. For instance, formation of bubbles in the liquid melt can enhance mass and heat exchange in the reactor, while proper quantification of contact times with solid ashes present in the feedstock is necessary for evaluating catalytic effects. Secondary gas-phase cracking or cross-linking reactions also contribute to alter the expected product distribution. The multi-phase nature can result in additional transport limitations, which lead to formation of by-products that further increase mass and heat transfer resistance in a complex interplay. As with the multi-component nature of the system, the multi-phase system can be simplified considering only global behaviours that reduce the complexity at the expenses of some loss in accuracy of model predictions³⁴.

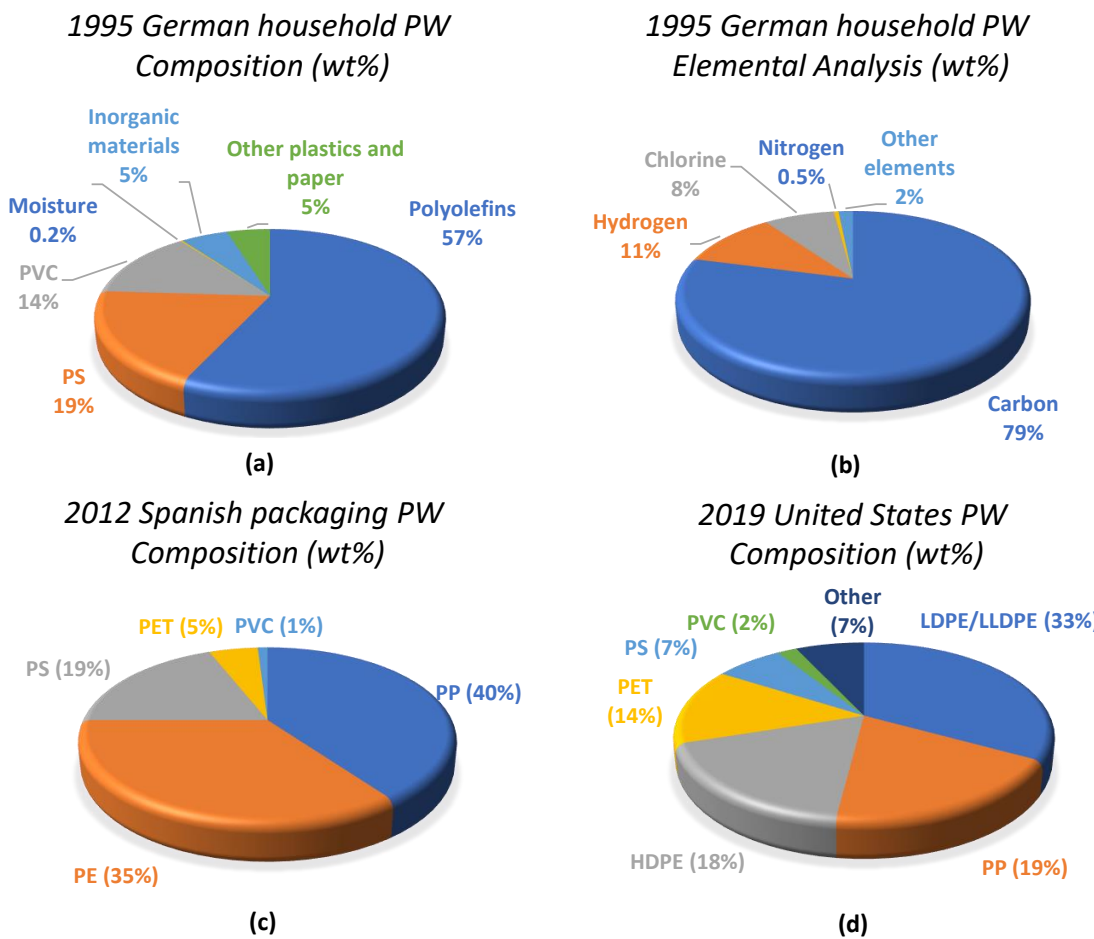


Figure 2.1: Plastic waste composition from different sources and years^{44–46}.

The description of the entire process requires proper characterization of different time- and length-scales due to the different physico-chemical phenomena involved as shown in Figure 2.3. The smallest scale involved is the chemical reactions' one, taking place at the Angstrom scale, whereas physico-chemical transformation occur at the nanoscale. These molecular transformations concur with bubble and particle evolution at the micro- or millimetre scale and with the reactor itself that is at the meter scale. Simultaneous description of all the scales involved requires modelling up to the largest scale (10^0 m) with the characteristic length-scale of the smallest one (10^{-10} m)⁵¹. To model the process, the different scales must be bridged in a multi-scale framework, where the reactor and particle scale employ subgrid models able to represent the complex physical behaviour⁵².

Describing the conversion process is performed employing different sub-description of the physico-chemical phenomena involved. In this context, thermodynamic and kinetic models act as a bridging strategy between molecular and reactor scale. The first describe the properties of the compounds involved and the energy fluxes, while the latter describe the transformation of chemical species and the rates involved. The aim of both

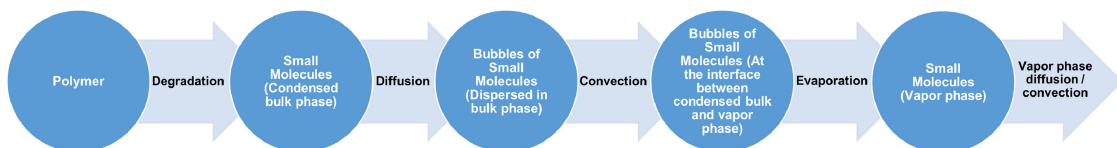


Figure 2.2: Different phenomena taking place in the volatilization process of polymers, adapted from Dogu *et al.*¹⁵

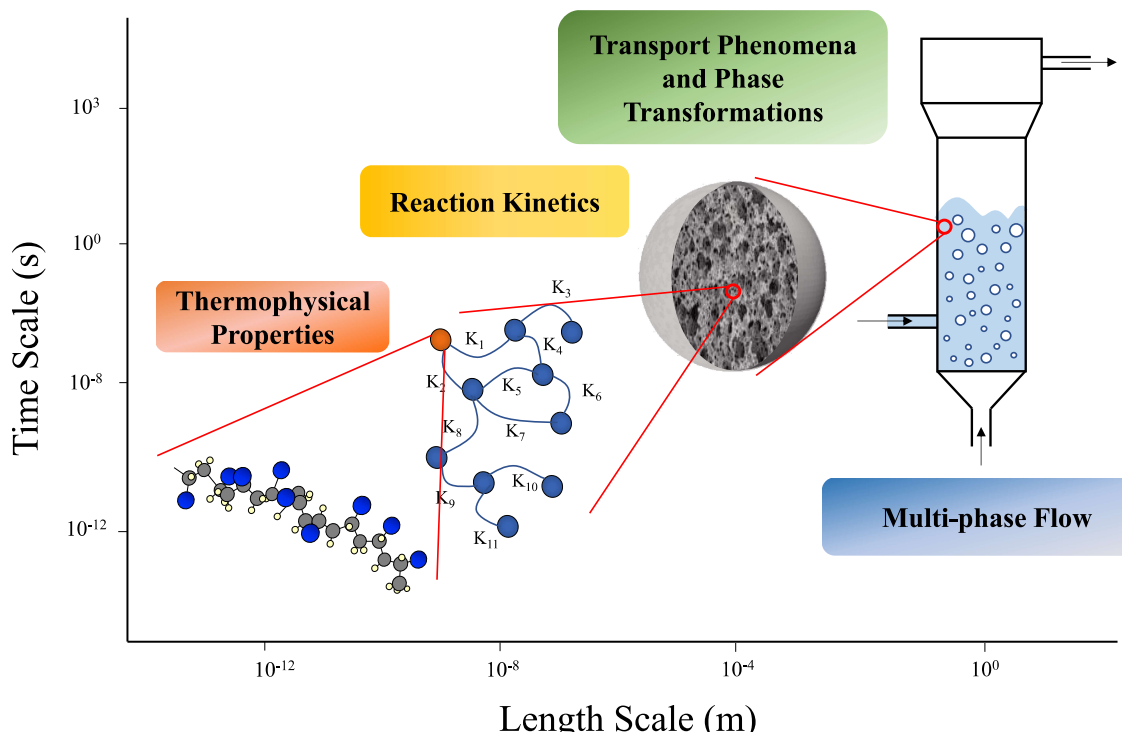


Figure 2.3: An overview of the multi-scale nature of plastic gasification. Adapted from Madanikashani *et al.*³⁴

models is to represent the stochastic nature of the physico-chemical transformation with simplified terms to be employed in particle and reactor governing equations^{53,54}.

The following Sections present a brief overview of the phase-transition and degradation chemistry involved in plastics thermochemical recycling. Upon heating, polymers first undergo phase transition to a molten state. In this liquid-like condition, they decompose according to two main mechanisms: backbone degradation and side-groups elimination. Non-vinyl polymers exhibit specific reactivity related to the presence of heteroatoms along the polymer backbone.

2.1.1 Polymer thermochemistry

A plastic material consists of a distribution of chains with varying lengths but similar chemical functionalities. These polymeric chains are essentially macromolecules, each comprising thousands of atoms interconnected by covalent bonds, forming lin-

ear, branched, or intricate 3-D networks. Notable examples of natural macromolecules include proteins and cellulose. In contrast, synthetic macromolecules exhibit simpler structures, composed of few types of constitutional repeating units.

Polymeric materials are characterized by a chemical structure and a molecular weight distribution pattern: the first relates to the chains molecular structure, while the latter to the chains' ensemble. The interplay of these determines the physico-chemical properties of the material, such as cohesive forces, molecular mobility, and morphology. Each macromolecule consists of a backbone, either linear or branched, and peripheral atoms or atom groups (the side-groups). The chemical structure is generally related to the nature of the repeating units, the end-groups type, the branches and cross-links, and the nature of structural defects. The molecular weight distribution on the other hand is controlled mainly by the synthesis process. Mechanical and bulk properties are largely determined by the weight average molar mass, while thermodynamic properties are dependent on the number average.

Polymeric materials, upon heating from room temperature, exhibit several phase transitions. In its solid state, the material can be partly crystalline, rubbery, or glassy. Melting is the only thermodynamic phase-transition, while all others are not thermodynamically stable states with well-defined transition temperature²¹. Above the melting point polymeric chains behave similarly to a liquid, although exhibiting viscoelastic properties, i. e., polymer properties vary with deformation conditions. The dynamic properties of a polymer can be interpreted with the hole-theory of Eyring^{21,55}. A liquid contains unoccupied sites through which molecules can diffuse. The energy barrier required to jump from one vacancy to the other is related to the heat of vaporization, where the similarity stems from both processes involving removal of a molecule from its neighbours⁵⁶. This value in a polymer has an asymptotic value independent on the molecular weight. The reason is that polymeric chains above the melting point do not move as single macromolecules but through flux units as shown in Figure 2.4. These are rigid segments interconnected by flexible joints that allow the angle between nearest neighbour segments to take different values. Rheology measurements allow to estimate the heat of evaporation of the flux unit⁵⁶, and the critical length of the flux unit can be estimated through the Trouton-Meissner rule.

The concept of flux unit is employed also in determining the activation energies of the degradation process⁵⁵. Chemical reactions are local phenomena, but in liquid-phase neighbouring molecules affect reactants, products, and transition state conformation. As few reliable data for liquid-phase kinetics are available, analogy rules can be employed through the flux unit and solvation corrections from gas-phase data on similar model compounds^{57,58}.

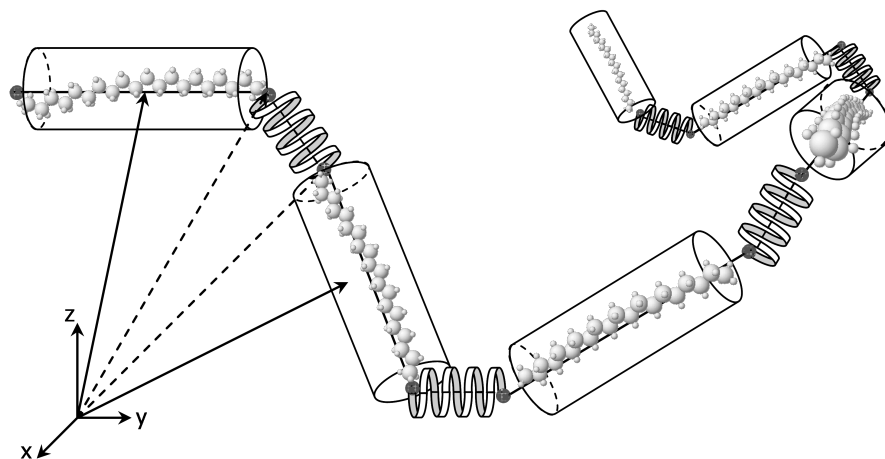


Figure 2.4: Flux unit characterization in polymer melt, adapted from Marongiu *et al.*⁵⁶

2.1.2 Backbone degradation

Breaking the polymer's backbone results in formation of fragments with a chemical structure similar to the reactant⁵⁷. These smaller chains then undertake similar reactions recursively. Backbone degradation is the main decomposition pathway for polymers characterized by side-groups with chemical bonds stronger than the backbone C-C bonds. The main ones are polyethylene (PE), polypropylene (PP), polystyrene (PS), and poly(methyl methacrylate) (PMMA). Studies on thermal degradation kinetics of these polyolefins started in the late 1940s⁵⁹, although only in the late 1990s the first mechanistic kinetic models were proposed^{55,60}.

Pyrolysis of long hydrocarbon chains can be broadly represented through initiation, propagation, and termination reactions. Backbone initiation reactions are high-temperature random scission reactions that form the first radicals triggering the radical decomposition mechanism. These reactions involve high activation energies ($E_a=60\text{-}90 \text{ kcal mol}^{-1}$ ^{57,61}) and impact product distributions only at $T>1000^\circ\text{C}$. Nevertheless, they significantly affect the degradation process as they control the onset of the radical pool. Presence of weak links such as peroxides impurities^{62,63} or defects from the specific polymerization process⁶⁴ facilitate the onset of polymer degradation. The presence of double bonds (e.g., allylic terminal positions) or catalyst impurities also contributes to increasing the initiation rates⁶⁵. Conversely, termination reactions inhibit the growth of the radical pool as they convert two highly reactive radicals to stable molecules. The main termination pathways are radical-radical recombination and disproportionation reactions, where the first results in a single longer molecule while the latter in an unsaturated and a saturated molecule. While these reactions involve significantly lower activation energies ($E_a=2\text{-}20 \text{ kcal mol}^{-1}$ ^{66,67}), the low radical concentrations make them comparable to random scission rates.

While initiation and termination reactions affect the overall radical concentration, propagation reactions are the rate determining steps at typical operating conditions. These pathways dominate both degradation process and product selectivity, the most important propagation channels being β -scission, chain transfer, and isomerisation. β -scission forms an unsaturated molecule and a terminal radical of shorter length and is characterized by activation energies in the range of $E_{act}=20\text{-}40 \text{ kcal mol}^{-1}$ ^{68,69}. Compared to gas-phase pyrolysis, liquid-phase reactions involve higher concentrations, resulting in a higher importance of bimolecular reactions with respect to the gas-phase counterparts⁵⁵. Bimolecular H-transfer are characterized by low activation energies ($E_{act}=6\text{-}15 \text{ kcal mol}^{-1}$ ^{66,67}), while bimolecular radical additions are the reverse step of β -scission reactions and have activation energies similar to terminations ($E_{act}=1\text{-}6 \text{ kcal mol}^{-1}$ ^{67,70}). For terminal radicals, intramolecular radical additions can result in the formation of cyclic compounds, while terminal β -scission (unzipping) results in monomer formation. Backbiting isomerisation corresponds to an intramolecular H-transfer reaction proceeding through the formation of 3 to 7 member rings transition states. The activation energies are in the range $E_{act}=10\text{-}40 \text{ kcal mol}^{-1}$ ^{57,71,72} according to the strain involved in ring formation. While formation of small rings results in high strain energies, high-membered rings require a specific arrangement of multiple atoms in place and therefore is entropically limited. The most favoured isomerisation is 1-5 backbiting, i. e., formation of a 6-member ring able to preserve bond angles at low entropic cost. These reactions are responsible for preferential formation of specific compounds such as n-hexene from PE and trimers from PP and PS^{65,66,73}. The presence of double bonds plays an important role in the reaction mechanism as the stabilization from resonance effects increases the formation rate of allylic radicals.

The degradation mechanisms of the most common polyolefins (e. g., PE, PP and PS) can be represented similarly, as shown in Figure 2.5. The main differences arise from variation in the kinetic parameters of the reactions involved⁵⁷, together with the monomers molecular weight. For instance, the higher stability of benzyl radicals results in a lower decomposition temperature for PS. Terminal radicals undergo unzipping before intermolecular chain-transfer, resulting in a monomer yield for PS of 70-90 wt.% in the 500-800°C temperature range^{61,66}. PP has a higher thermal recalcitrance than PS, although lower than PE due to the presence of tertiary alkyl radicals. A key difference also for PP and PS with respect to PE is the presence of head and tail configurations^{61,66}, which can result in significantly more complex kinetic mechanisms and spiked product distributions.

The similarity between reaction mechanisms originates from the assumption of inert side-groups. This assumption fails at higher temperatures, where additional compounds are experimentally observed⁷⁵. To overcome this simplification, the side-group mechanism discussed in the following paragraph could be considered also for these polymers, resulting however in significantly more complex reaction networks. The presence of impurities can also result in additional reactive pathways that alter product

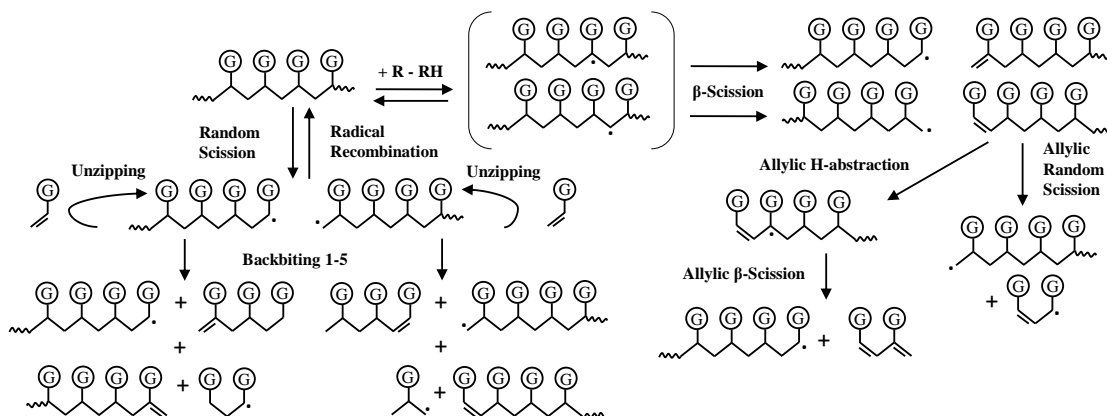


Figure 2.5: Schematic representation of the backbone degradation mechanism with side-group $G = H, \text{CH}_3, \text{C}_6\text{H}_5$ for PE, PP, and PS respectively. Adapted from Locaspi *et al.*⁷⁴

selectivity. Several shortcomings arise when adopting these mechanisms. The main difference with experimental data is these mechanisms do not explain char formation and predict equimolar amounts of paraffins and α - ω dialkenes⁷⁴. The former possibly results from catalytic effects of ashes or side-group reactions not considered in pure model polymers. Experimentally, few authors measure formation of diolefins, observing a 1:1:0 paraffin:olefin:diolefin ratio. This violates the elemental balances, unless formation of highly unsaturated carbonaceous structures occurs, which however is not observed in significant quantities. The discrepancy possibly relates to diolefin cross-linking on tube reactors or cyclization of olefins and diolefins to naphthenes. Additional modelling and experimental studies can aid in improving the understanding of the underlying physico-chemical phenomena⁷⁶.

The backbone degradation mechanism is also dominant for other polymers such as polyisobutylene (PIB)⁷⁷ and polyalphamethylstyrene ($\text{P}\alpha\text{MS}$)⁶⁰. In the case of PMMA, the presence of heteroatoms in the side-group further enhances formation of tertiary backbone radicals through resonance stabilization. This results in high selectivity towards unzipping reactions that lead to MMA yields >95 wt.%⁷⁸. Similarly, in the case of polystyrene peroxide (PSP), the oxygen atoms along the backbone chain enhance the decomposition rate but do not alter the mechanism with respect to polystyrene⁷⁹.

2.1.3 Side-group elimination

Breaking the side-group bond changes the chain moieties while preserving the chain-length. As the chain functionality varies, the reactivity of the products differ from the reactant's. The side-group degradation mechanism is the main decomposition pathway for polymers with chemical bonds in the side groups which are weaker than the C-C backbone bonds³⁵. Polymers of this class are halogenated vinyl-polymers such as poly(vinyl chloride) (PVC), poly(vinyl bromide) (PVBr), and polychloroprene (PCP).

PVC is among the main commodity polymers and has been extensively studied in the past decades⁸⁰. Other halogenated polymers have received less consideration due to their niche application (e.g., flame retardants such as PVBr). These polymers are of relevance as formation of halogenated products requires specific reactors, purification units and, in general, downstream equipment. However, few modelling activities have been performed due to the complexity resulting from the side-group degradation mechanism¹⁵. This reaction network also comprises radical pathways which can be distinguished in initiation, propagation, and termination steps, although additional molecular pathways must be accounted for. Figure 2.6 shows the main reaction classes typical of the side-group degradation mechanism. Radical initiation mainly occurs through backbone - side-group bond cleavage, i.e., C-Cl for PVC ($E_{act} \sim 55$ kcal mol⁻¹³⁵), forming a carbon chain radical and a side-group radical. The main propagation reactions are the side-group radicals' stabilizing through H-abstractions on the polymer chain and then evaporating. In PVC and PVBr, this dehydrohalogenation step is responsible for the initial >50 wt.% mass loss³⁶ and leads to formation of stable polyene structures. Mid-chain radicals tend to undergo β -scission breaking the side-group bond and forming mid-chain unsaturations. These in turn enhance the formation of other neighbouring mid-chain radicals through allylic resonance stabilization. The dehydrohalogenation process can also take place through a 4-centered molecular reaction⁸¹. These polyenes then undergo intra- and inter-molecular Dies-Alder reactions that form aromatic and alkyl-aromatic groups. Further condensation and dealkylation of these structures leads to the second mass-loss step forming a char residue and releasing small olefins and aromatic compounds³⁵. Chlorine and bromine can also interact with the polyene and aromatic structures leading to formation of toxic species as chlorobenzenes. For polychloroprene (PCP), the dehydrochlorination and condensation step partially overlap due to the stronger vinyl - Cl bond³⁶.

The side-group mechanism involves reaction classes that alter the polymer structure leading to a broad range of classes of compounds¹⁵. As previously mentioned, these classes can be coupled with the backbone mechanism to improve model predictions although at higher computational cost. For instance, these reactions account for the formation benzene and polyaromatics from PS pyrolysis. These reactions are also responsible for formation of CO, CO₂, and small olefins during thermal degradation of PMMA. Similarly, the backbone degradation is a key pathway in PCP degradation due to the lower difference in backbone and side-groups bond strength³⁶.

2.1.4 Condensation polymers

Contrary to polyolefins, non-vinyl polymers such as polyesters, polyamides, and polyurethanes do not involve a paraffinic backbone chain. This has a significant technological advantage, because the properties of the polymer can be tailored through the

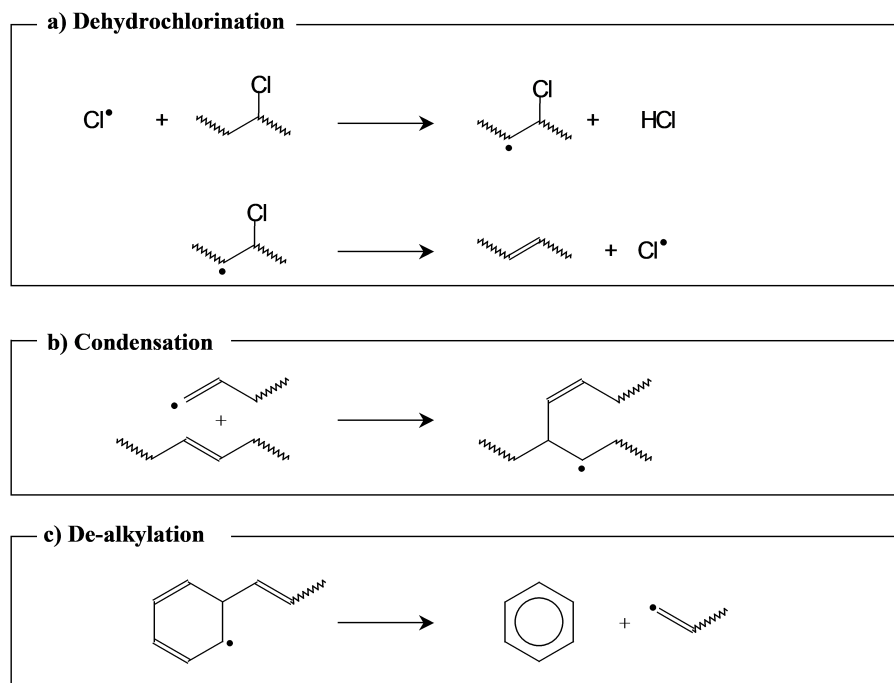


Figure 2.6: Schematic representation of the side-group degradation reaction classes. Adapted from Marongiu *et al.*³⁵

backbone structure. Additionally, they can be decomposed and recycled more easily as discussed in Chapter 1.

The reactivity of heteroatom-containing polymers is not fully described by the decomposition mechanisms previously discussed. In general, the presence of non-carbon atoms has a weakening effect on the chemical bonds⁸² and allows for additional competitive four- or six-centred molecular reactions^{81,83–85}. For instance, dehydrohalogenation can occur by both a radical mechanism and a low-temperature 4-centered concerted molecular pathway⁸¹. Similarly, molecular reactions are responsible for cyclization, dealkylation, and further dehydrogenation of polyene structures³⁵. For condensation polymers, to the best of the author's knowledge, no mechanistic kinetic model has been proposed, although several possible reaction pathways have been discussed^{86–89}.

In general, ester, amide, or urethane functionalities allow intra- and inter-molecular concerted H-abstractions that lead to formation of vinyl ends and specific functional groups. For instance, ester functionalities in polyethylene terephthalate (PET) are hypothesized to undergo intramolecular syn-elimination to form a vinyl and a carboxyl end^{90–98} as shown in Figure 2.7a. These reactions are usually assumed the main pathways leading to monomer, dimer and trimer formation, while additional decarboxylation reactions are considered responsible for formation of other aromatic compounds as benzoic acid, small olefins, and acetylene⁹⁹. These decomposition reactions however involve high activation energies ($E_{\text{act}}=50\text{--}80 \text{ kcal mol}^{-1}$ ^{82,83,100}) which do not explain the high yields of CO_2 and char experimentally observed^{99,101}. While molecular re-

actions have an important role, the C-C bond strength of PET is comparable to the other polymers (~80 kcal mol⁻¹⁸⁵), suggesting the possibility of competing radical degradation pathway similar to lignin degradation¹⁰². The low energy barriers of radical decarboxylation ($E_{act}=15\text{-}20 \text{ kcal mol}^{-1}$ ^{83,103}) and radical addition reactions ($E_{act}=5\text{-}20 \text{ kcal mol}^{-1}$ ^{104,105}) explain the high low temperature yields of major products such as acetaldehyde and char.

Concerted molecular reactions are also hypothesized as the main depolymerization reactions for polyamides¹⁰⁶. Four-member interactions among nitrogen, hydrogen, and ketone functionalities lead to formation of cyclic monomers and dimers¹⁰⁷ as shown in Figure 2.7b. As with PET, the backbone bond dissociation energies are similar to polyolefins, suggesting the possibility of competing radical degradation pathways at high temperatures. Monomer selectivity is extremely high at low temperatures (>95 wt.%), and no formation of char is generally observed¹⁰⁸.

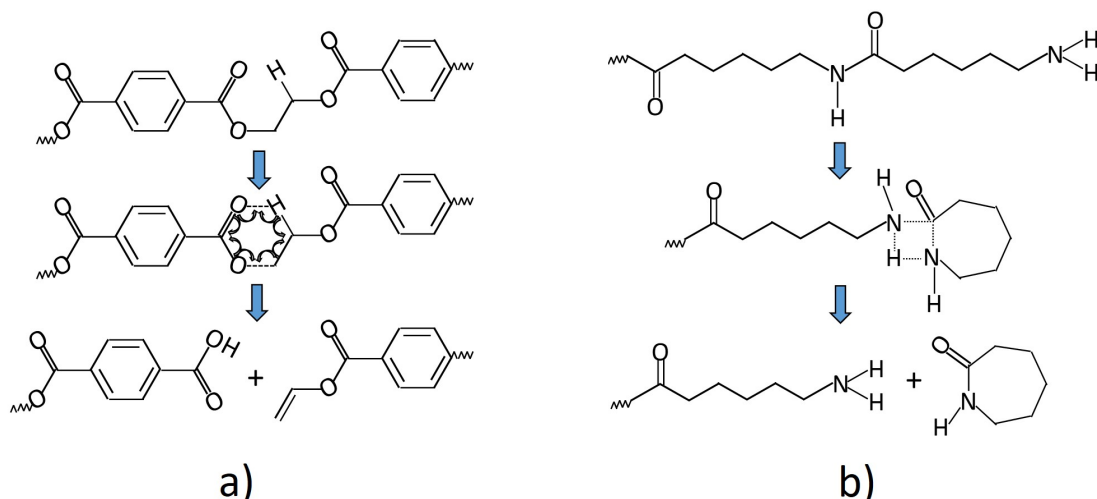


Figure 2.7: Schematic representation of the molecular degradation mechanism involved in degradation of: a) PET, b) PA. Adapted from Locaspi *et al.*⁴²

The term “polyurethanes” refers to a broad class of polymers with significantly different chemical structures, usually involving ester or ether linkages and aromatic or aliphatic segments¹⁰⁹. While the degradation mechanism depends on the polyurethane monomers, the first degradation step can be related to molecular decomposition of the urethane linkages, forming either isocyanate, amine, or imine ends^{89,110,111}. According to the molecular structure, the amounts of char experimentally observed vary from 0¹⁰⁹ to 40 wt.%¹¹². Similar to PET and lignin degradation, this may result from further dehydrogenation and addition reactions.

2.1.5 Plastic waste mixtures

Several studies on pure polymers' degradation were performed in the past decades, but fundamental understanding of condensed-phase decomposition of plastic mixture is lacking. Modelling the pyrolysis of real mixtures requires considering both the main constituents and their cross-interactions, i.e., the interactions between polymers, additives, and inorganics.

Most of the studies targeting this topic in the scientific literature are limited to binary mixtures of PE, PP, and PS. In general, independent decompositions are observed because of the immiscibility of the polymers, which prevents molecular-scale interactions¹¹³. Their interactions result from the similar radical pathways involving the same small radicals as reactants or products. For instance, radicals formed from PS pyrolysis can diffuse in the PE/PP melt enhancing their degradation if a PS/PE/PP mixture is considered. Nevertheless, few interactions are observed because of the low solubility and molecular diffusivities¹¹⁴ and accurate description of mixing phenomena are required to model the co-pyrolysis³⁴.

Considering other polymer binary or higher order mixtures, no modelling activity has been performed to the author's knowledge. Experimental investigation on PVC interactions with PE, PP, and PS show that interactions are negligible, and the polymers can be assumed reasonably independent^{115,116}. On the other hand, experimental results on PVC-PET-PA mixtures show that PET and PA decomposition are significantly enhanced^{49,50,117,118} and cross-interaction products are identified^{119–121}. The solubility of these polymers with PVC is complex to measure experimentally because of the low degradation temperatures of the latter³⁵ combined with the high melting temperature of the former²¹. PVC is miscible with only few polyesters¹²², but the miscibility increases with the chlorine content¹²³. Polycaprolactone (PCL) is the polyester which shows the highest degree of compatibility with PVC, which however has been reported not to interact with PVC¹²⁴. Blends of polyamides and PVC also show similar behaviours^{125–129}. As with polyesters, polycaprolactame is reported as immiscible with PVC but shows considerable cross-interactions^{50,117,124}. The synergistic behaviour could also stem from the interactions between HCl released from PVC and PET ester groups or PA amide groups. However, liquid-phase concentrations of hydrogen chloride are expected to be negligible because of its high evaporation rates ($T_{b,n}=200\text{K}$, $T_{crit}=325\text{ K}$ ¹⁰⁰).

The effect of additives and inorganic matter in the feedstock also requires further in-depth characterization, both from an experimental and modelling point of view. In general, experimental results show cellulosic impurities increase char yield, form an aqueous phase, CO, and CO₂, result in a lower heating-value for gases, and a higher separation costs for liquids⁷. CaCO₃ was found to affect the pyrolysis of PA and polycarbonates (PC), possibly due to the interactions with amide groups¹³⁰. Calcium

carbonate also acts as a chlorine-capture agent⁴⁹, although it increases the chlorine content of the liquid fraction¹³¹.

2.2 CONDENSED-PHASE KINETIC MODELS

A kinetic mechanism is a network of chemical reactions describing the transformation of reactants into products and the various intermediates involved. To describe the dynamics of the reactive system, the kinetic model requires defining the thermodynamic and transport properties of each species and the rate of each reaction⁴³. According to the level of detail, the reaction network can span from 10^0 to $>10^9$ number of reactions¹³². The peculiarity of polymeric systems stems from the high molecular weight and polydispersity of the polymeric material which, coupled with the complex free-radical mechanism, results in enormous and hardly manageable networks of reactions¹³³. The broad product spectrum from plastic pyrolysis¹⁵ is consequence of the various isomers and classes of compounds that form during the process which, in theory, must all be considered.

Kinetic models can be classified in two macro-kinds¹³²: global and mechanistic. The first class aims at representing the overall behaviour through few simplified global reactions. On the other hand, the latter tries to describe the underlying physico-chemical phenomena to achieve a more comprehensive description although at higher computational cost. A detailed description of the proposed reaction mechanisms requires characterizing the reactivity of all compounds involved, i. e., reactants, intermediates, and products. This detailed approach results in a network of elementary reactions which, in principle, is independent of the feedstock and allows for extrapolation. However, the detailed model of a single polymer necessitates describing all chain-lengths and their potential isomers. Such reaction networks require a number of species (N_s) $>10^7$ for each polymeric constituent, resulting in mechanisms that are unsuitable for systems characterized by complex fluid dynamics such as industrial reactors. In the past decades, several modelling approaches have been developed to simplify the involved chemistry while preserving the desired accuracy as discussed in the following paragraphs.

2.2.1 Global kinetic models

The focus of global models is to describe the overall decomposition rate of the reacting mixture. These models are generally obtained fitting rate equations to the experimental weight loss profiles. While these models are extremely simple and flexible, they yield case-specific reaction parameters as they are generally obtained from thermogravimetric analyses (TGA) with no possibility to decouple reaction kinetics from transport phenomena^{134–136}. Indeed, since weight-loss occurs only due to evaporation of suffi-

ciently small fragments, one-step global models describe the global evaporation rate¹³⁷ without characterizing the sequential occurrence of cracking and evaporation, nor the chemical dynamics of product release.

Several authors report significantly different kinetic parameters even for single polymers investigated in similar conditions^{71,76,86,138–140}. The differences can be attributed to variation in the properties and characteristic of the polymers investigated⁵⁷ or to the presence of different additives, impurities or weak links resulting from the specific production process⁶¹. Nevertheless, these discrepancies result also from the diversity in experimental conditions investigated as these models are valid only in a small range of operating conditions and conversion levels¹⁵.

In general, one-step models assume a power-law dependence on the mass conversion, α , of the kind:

$$\frac{d\alpha}{dt} = k(T) \cdot f(\alpha) \quad (2.1)$$

where $k(T)$ is the rate constant, usually evaluated with an Arrhenius form, and $f(\alpha)$ is the conversion dependence. For polymers such as PE, PP, PS, a simple first-order law can represent the overall behaviour. Nevertheless, for more complex systems as PVC, PU or plastic mixtures, more complex functions are required to capture the multi-step degradation. A different approach instead of defining a conversion function consists in the “Distributed Activation Energy Models” (DAEM)¹⁴¹. These models assume the process as characterized by a continuous distribution of activation energy representative of the different constituents involved. They often consider a Gaussian distribution whose parameters are determined by experimental fitting¹⁴².

The main interest of plastic thermal degradation is the released products, but one-step global models focus only on the weight-loss profiles. To this aim, more complex global models have been developed that consider multiple reactions. The Independent Parallel Reactions (IPR) formulation has been employed to model different polymers and mixtures^{143,144}, while other authors⁴⁷ employ a more complex network accounting also for formation of gas, liquid and solid compounds. More intricate models can be developed introducing global stoichiometric coefficients accounting for the condition dependent (i.e., mainly temperature and residence time) product distribution⁷¹. However, most of these models do not distinguish between condensed and gas-phase reactivity, limiting their extrapolation capability. The main advantage of these models is their simplicity, which however still results in an extremely limited range of applicability.

2.2.2 The Discrete Section Method

The first detailed kinetic models employed for polymer pyrolysis date to the late 1990s⁵⁵. These models consider every stable polymeric chain and introduce the quasi

steady-state assumption (QSSA) for propagating radicals. The resulting kinetic models involve $N_s \sim 10^6$ but enable non-stiff algorithms that decrease the overall computational cost. These models have been successfully validated for PE^{55,65,69,145}, PP⁵⁵, and PS⁶⁶ as shown in 2.8, both in terms of mass-loss profiles and product distribution. A free-radical backbone degradation mechanism is assumed, and the side-groups for PP and PS are assumed inert^{57,71}. Faravelli *et al.*⁶⁵ (2.8d) also highlighted the importance of considering separate models for reaction kinetics and evaporation rates. Not considering appropriate phase-change models can result in dumping mass-transfer limitations on kinetic parameters resulting in less generalizable predictions³⁴.

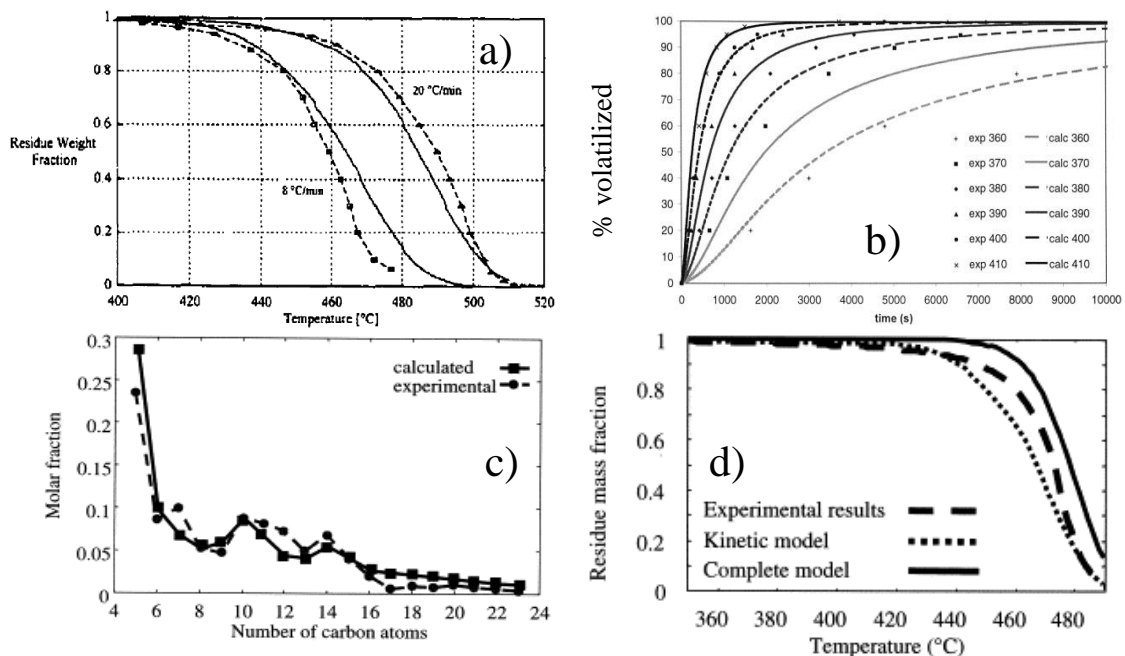


Figure 2.8: Discrete section kinetic models for pyrolysis of PE, PP and PS. Comparison of: a) PE mass-loss profiles⁵⁵; b) PS mass-loss profiles⁶⁶; c) PE gas product distribution⁶⁵; d) PE mass-loss profiles considering different evaporation models⁶⁵. Adapted from Locaspi *et al.*⁴²

The issue with these models lies in the scalability to complex reactors and more complex reaction mechanisms. To reduce the computational cost, a vertical lumping approach¹⁴⁶ has been employed for PE⁵⁷ and PS⁶⁶. This method, employed also to describe particulate matter formation in combustion devices¹⁴⁷, describes the chain distribution through few carbon numbers while the other chain-lengths are assumed as mixture of the chosen carbon numbers. This approach reduces the number of species involved without significant losses in terms of accuracy⁴³. The complete distribution is recovered in post-processing through appropriate delumping techniques¹⁴⁶.

2.2.3 The Method-of-Moments

The method of moments (MoM) approach was first introduced in the 1950s¹⁴⁸. Population balances are coupled to the theory of reactions in “continuous” mixtures¹⁴⁹ to represent the chain-length distribution through its statistical moments. This allows to simplify a theoretically infinite number of mass balance equations in a significantly smaller subset¹⁵⁰. Nevertheless, different distributions must be defined for chains with different structural characteristics, e. g., unsaturation and branching. In general, only the first three statistical moments are tracked per distribution, which however requires appropriate closure techniques^{57,68}. This approach is extremely powerful in describing the polymer chain-distribution evolution and has been successfully employed for PE⁶⁷, PP⁶⁸, PS^{61,73}, and P α MS⁶⁰ as shown in Figure 2.9. Marongiu *et al.*⁵⁷ compared the MoM and discrete section models applied to HDPE and PS pyrolysis obtaining similar results as shown in Figure 2.9d. This method has been employed also for soot predictions¹⁵¹ and shares the same limitations as the discrete sections. While this approach yields extremely detailed results at low computational costs, the main issue lies in the need of a distribution for each different structural chain. For polymers as PVC, where significant formation of polyene and aromatic structures occurs, the method of moments requires a significant increase in number of equations to be considered³⁵.

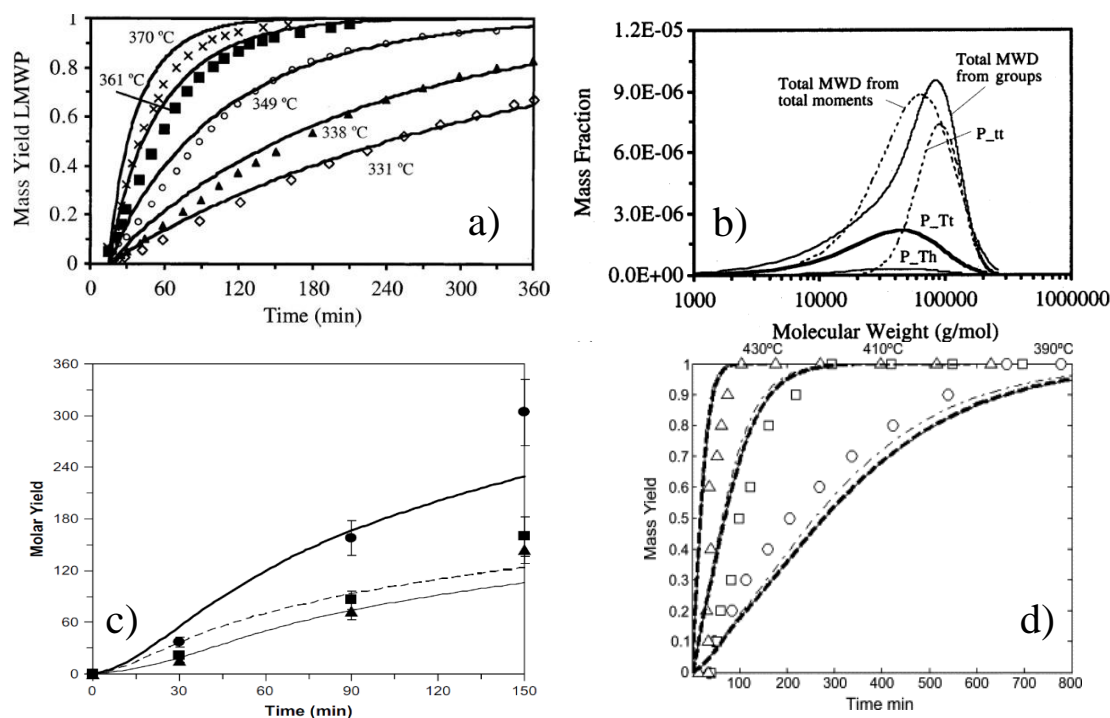


Figure 2.9: Method of Moment kinetic models for pyrolysis of PE, PP and PS. Comparison of:
a) PS mass-loss profiles⁶¹; b) PS molecular weights distribution evolution⁷³; c) PE total gas, alkane, and alkene yields⁶⁷; d) PE mass-loss profiles for MoM (---) and discrete section methods (—)⁵⁷. Adapted from Locaspi *et al.*⁴²

2.2.4 The functional groups Approach

Chemical reactions are local phenomena that involve only the nearest neighbors⁵⁸. Therefore, above a certain monomer-number, the elementary step does not depend on the chain-length but only on the neighbouring chemical groups. The evolution of the polymer melt can be related to the reactivity of the chemical moieties of the chain and not to the distribution itself. This approach discards information about the chain distribution but allows to track different chemical structures at a low computational cost. The only chain-distribution information required is the distinction between mid- and end-chain chemical moieties because of their different selectivity to low molecular weight products. This distinction also allows to recover the number average molecular weight⁷⁴. The functional groups Approach has been successfully employed to model halogenated polymers as PVC³⁵, PVBr³⁶, and PCP³⁶, and also to model biomass pyrolysis^{37,152}. To the authors' knowledge, this is the only mechanistic approach developed for PVC pyrolysis. Figure 2.10 shows the models' predictions for different polymers in terms of mass-loss profiles, although satisfactory results are obtained also for gas-phase profiles.

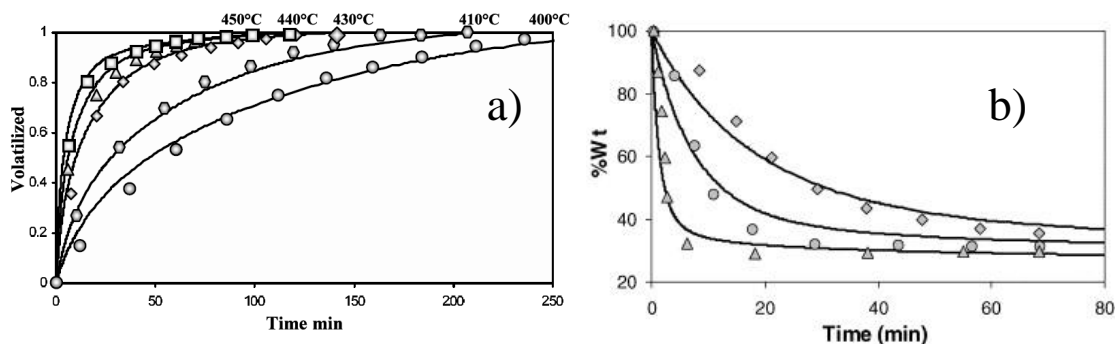


Figure 2.10: Functional groups kinetic model for pyrolysis of PVC and PCP. Comparison of: a) PVC conversion³⁵ and b) PCP mass-loss profiles³⁶. Adapted from Locaspi *et al.*⁴²

2.2.5 The kinetic Monte Carlo

The kinetic Monte Carlo (kMC) algorithm employs a stochastic approach in contrast to the continuum deterministic modelling approaches previously described^{153–155}. This approach is a proven solution of the Chemical Master Equation (CME) and is able to describe explicitly every species in the system through a microscale homogeneous reaction volume⁷⁹.

The main drawback is the computational cost which is unfeasible for polymeric systems due to the huge number of atoms involved. Nevertheless, hybrid kMC methodologies allow to reduce the computational cost and are commonly employed to describe polymerization processes. kMC also for polymer pyrolysis have been successfully im-

plemented for PE^{77,156}, PP¹⁵⁷, PS^{72,76,158,159}, PIB⁷⁷, P α MS¹⁶⁰, PSP¹⁵⁸, and PMMA¹⁶¹ as shown in Figure 2.11. Machine Learning algorithms can be employed to integrate kMC predictions with computationally expensive fluid dynamics simulations¹⁶².

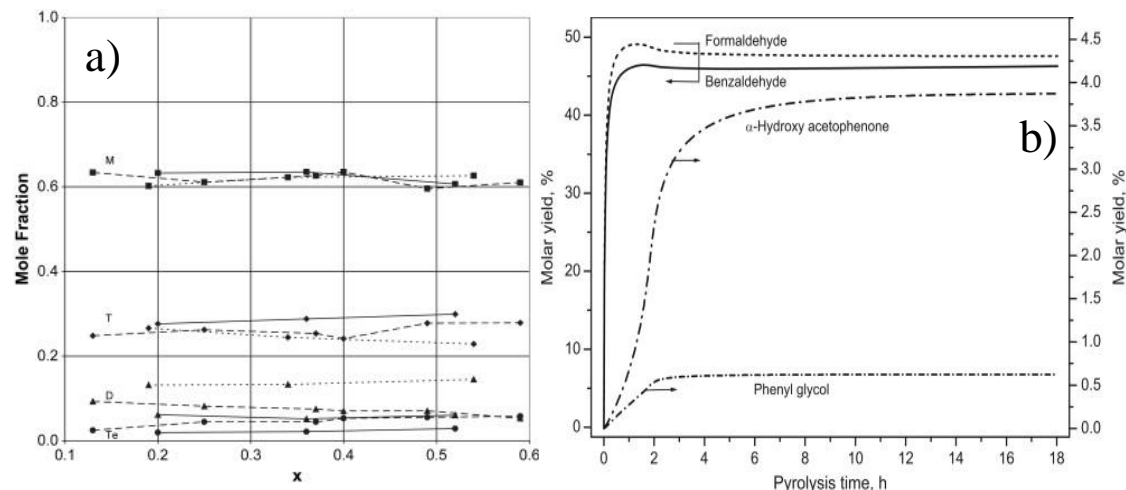


Figure 2.11: Kinetic Monte Carlo kinetic model for pyrolysis of polyolefins. Comparison of: a) PS gas molar fractions⁷² and b) PSP molar yields⁷⁹. Adapted from Locaspi *et al.*⁴²

2.3 GASIFICATION AND CATALYTIC CONVERSION

The pyrolytic mechanisms discussed in the previous sections characterize the polymer degradation. The low molecular weight compounds that form can nucleate homogeneously or heterogeneously to form bubbles that grow and break-up on the liquid surface⁶⁵. Secondary gas-phase reactions can play an important role both in bubble-phase and in the gas-phase exiting the reactor altering the product selectivity, and therefore proper quantification of bubble and gas-phase residence times are also required³⁴.

Product selectivity varies significantly also in the presence of gasifying agents or catalysts. The first allows to convert the pyrolysis products to a mixture of H₂ and CO (syngas), while the latter increases selectivity to specific high value products like olefins or aromatics. Catalysts can be employed in-situ also to lower process temperatures, enabling parallel competing degradation mechanism.

2.3.1 Gasification of volatiles and char

PW gasification can be regarded as a combination of polymer pyrolysis and secondary reactions, where the products further react with gas-phase oxidizing agents. The discussed pyrolysis models can be coupled with gasification subsets to extend the range of operating conditions. However, the high temperatures involved in gasification can

decrease model reliability due to the increased importance of alternative chemistry pathways³⁴, e.g., the side-groups cannot be assumed inert. Experimental studies show that the concentration of oxygen in the gasifying agent can affect also melt decomposition and evaporation¹⁶³. However, further studies are required to understand the extent of liquid-phase kinetic effects compared to local gas-phase hot-spots near the gas-liquid interface. Gasification generally involves gas-phase homogeneous reactions of volatiles species, and gas-solid heterogeneous reactions of the solid residue (char). Because of the low solubility of gasifying agents in the polymer melt and the high Stefan-flow, liquid-phase gasification reactions are expected to be of negligible importance. With respect to volatiles gasification, several detailed models have been developed for gas-phase kinetics¹⁴⁶, although care must be given to obtain mechanisms compact enough for reactor scale CFD simulations.

Several polymers produce a solid residue, known as char, which is an amorphous carbonaceous structures containing residual amounts of oxygen and hydrogen, together with minor quantities of nitrogen and sulfur. Different quantities of inorganics (ashes) are also present in significant amounts (2-40 wt.%). Figure 2.12 schematically sketches the complex physical and chemical structure of a biochar particle. For plastic chars, few characterization data are available in literature. Overall, most polymers have low char yield (~2 wt.%), mainly formed as consequences of inorganics in the feedstock¹⁵. The only polymers with significant char formation are PVC, PET, and polyurethanes, with yields ranging from 10 to 50 wt.%. Compared to biochars, plastic-derived char have generally higher amounts of ashes due to the low initial fixed carbon¹⁶⁴. Furthermore, non-negligible amounts of chlorine are found if no dehydrochlorination of PVC is performed. Plastic chars also exhibit low specific surface areas^{164,165}, and only at severe reaction conditions the devolatilization process yields a well developed micro and meso-porous network¹⁶⁶.

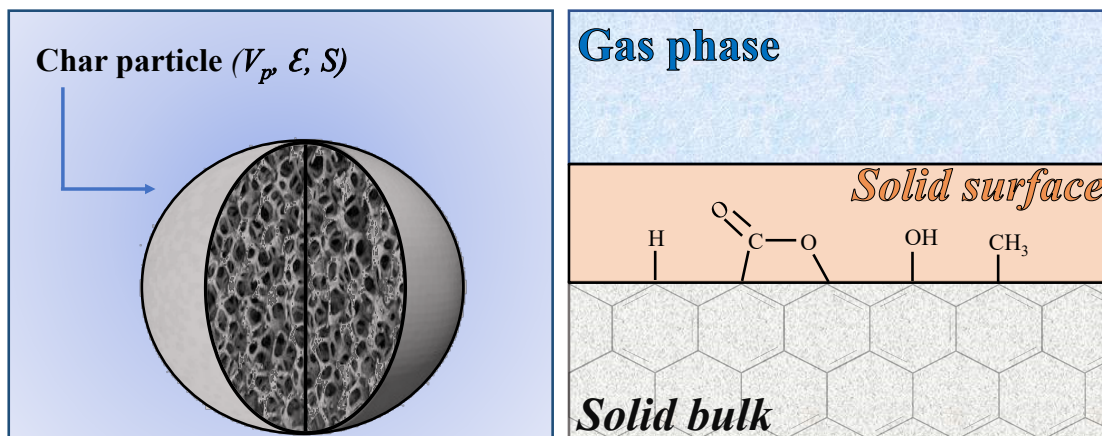


Figure 2.12: Schematic representation of: left) physical structure of a char particle with volume V_p , porosity ϵ , and intrinsic surface area S ; right) chemical structure of char at the gas-solid interface. Adapted from Locaspi *et al.*¹⁶⁷

Char conversion involves mainly gas-solid heterogeneous surface reactions¹⁶⁷. For this reason, the evolution of the solid residue depends not only on its chemical composition but also on its structural evolution, i.e., its pore network. In the past decades, several models were developed to describe oxidation of coal and biomass chars. The simplest empirical models consider a single n-th order reaction, assuming a constant ratio of conversion of carbon into both CO and CO₂. These approaches are rather limited in their validity, as the selectivity of CO/CO₂ formation is very sensitive to the reaction temperature¹⁶⁸. Furthermore, these models cannot be directly applied to plastic chars. More advanced models couple simple one-step kinetics to complex descriptions of the physical evolution. The pore size distribution, i.e., the internal surface, is described in terms of grain^{169,170} or pore models^{171–173}.

The most advanced char conversion models available consider a limited degree of complexity in chemical kinetics^{168,174–177}. Models using Langmuir-Hinshelwood or Elay-Rideal reaction mechanisms are widely used because of their improved physical description and capability to predict char conversion rates over wider ranges of temperature and pressure. Such models consider both the adsorption/desorption process in surface reaction kinetics and the physical evolution of the char particle, which strongly increases their comprehensiveness. A more complex chemical description was formulated by Haynes and co-workers^{178,179}, defining the concepts of turnover models for char oxidation, and explaining how surface reactions expose unreactive carbon to the gaseous environment. In this case the reactivity of different structures is described by means of a continuous distribution of activation energies. The most comprehensive models couple complex description of physical and chemical evolution to achieve a wide range of extrapolation^{142,167}.

Although several model families have been developed to describe coal- and bio-char oxidation and gasification, to the author's knowledge, no model has been assessed with plastic char oxidation/gasification. Furthermore, data on characterization and oxidation of plastic char are still scarce in literature. Nevertheless, char gasification is usually the rate determining step, impacting product selectivity significantly and thereof downstream processing costs¹⁸⁰. As with PW, mechanistic kinetic models, coupled with structural information on pore-evolution and diffusion limitations, are required to model the overall process³⁴.

2.3.2 Catalytic pyrolysis

Catalysts can be employed to crack the polymer feedstock (in-situ) or to upgrade the released volatiles (ex-situ). While the first allows to reduce reaction temperatures and requires less process equipment, the molten plastic significantly hinders mass transfer to the catalyst and causes pore blockage¹⁸¹. Catalytic upgrading on the other hand offers significant benefits when non-volatile contaminants are present. Since PW contains

several contaminants, catalyst poisoning is a key issue to be addressed. The most common catalyst families are zeolites, silica-alumina catalysts, and fluid catalytic cracking (FCC) catalysts^{182,183}.

Zeolites are alumino-silicates with a well-defined crystal structure. They are composed of T-O₄ tetrahedral structural unit, where T is the central atom (i.e., Si or Al) surrounded by O atoms connecting the units together. The building blocks interconnection results in a variety of 3-D microporous networks and specific structural properties¹⁸⁴. The Si/Al ratio determines the number of surface acid sites, and in turn the overall reactivity. The most used zeolite catalyst is the HZSM-5 which has been employed for the pyrolysis of HDPE^{185–194}, LDPE^{193,195–198}, and PP¹⁹³, due to its high catalytic activity, better selectivity and limited deactivation. Other commonly adopted zeolites are HUSY^{190,192,199,200}, H β ^{201,202}, HY^{201,203,204}, HZSM-11²⁰², and HMOR²⁰⁵.

Amorphous silica-alumina catalysts contain Bronsted and Lewis acid sites, with an ionizable hydrogen atom and an electron accepting site, respectively. The acidity of the catalyst is determined by the SiO₂/Al₂O₃ mole ratio oppositely to zeolite, i.e., high ratios indicate high acidity. The degree of acidity strongly influences the end product of plastic pyrolysis²⁰⁶. Another frequently used catalyst in the pyrolysis of plastics is MCM-41, a non-zeolite mesoporous material of the family of silicate and aluminosilicate characterized by a regular arrangement of cylindrical mesopores^{187,199,207–210}.

FCC catalysts consist in a zeolite crystal and a non-zeolite acid matrix¹⁸². FCC catalysts that have been used in refinery processes, known as spent FCC catalysts, can be reused in the plastic pyrolysis process. The usage of FCC catalyst is encouraged to maximize the liquid product, and a catalyst/polymer ratio <20 wt.% is required to minimize formation of coke and gaseous product^{211,212}.

The degradation mechanism is similar to the thermal one as shown in Figure 2.13. The main accepted pathways are the monomolecular Haag-Dessau mechanism coupled with bimolecular ion transfers^{181,213}. The initial step is agreed to be the adsorption of the reactant on the acid site and the production of a carbenium ion, which promotes the cracking of the molecule. The carbenium ion is produced either by abstraction of hydride ion at the Lewis acid site or by the proton addition to the polymer by Bronsted acid site. The acidity of the catalyst strongly affects the reaction rate and mechanism. When the acidity is strong, the catalytic cracking proceeds by end-chain scission, forming olefins. Conversely, in weak acidic catalysts, the cracking process occurs via random scission, leading to the formation of waxes. The carbenium ions are also believed responsible for cyclization of diolefins and formation aromatics. The final product composition is strongly influenced by the operating parameters and the catalyst physico-chemical structure.

To the author's knowledge, in the scientific literature mainly global and lumped models have been presented⁴². For in-situ and ex-situ catalytic cracking different approaches must be considered, as the catalyst interacts directly with the molten polymer in the first case and with the volatiles in the latter. Because of the widely different

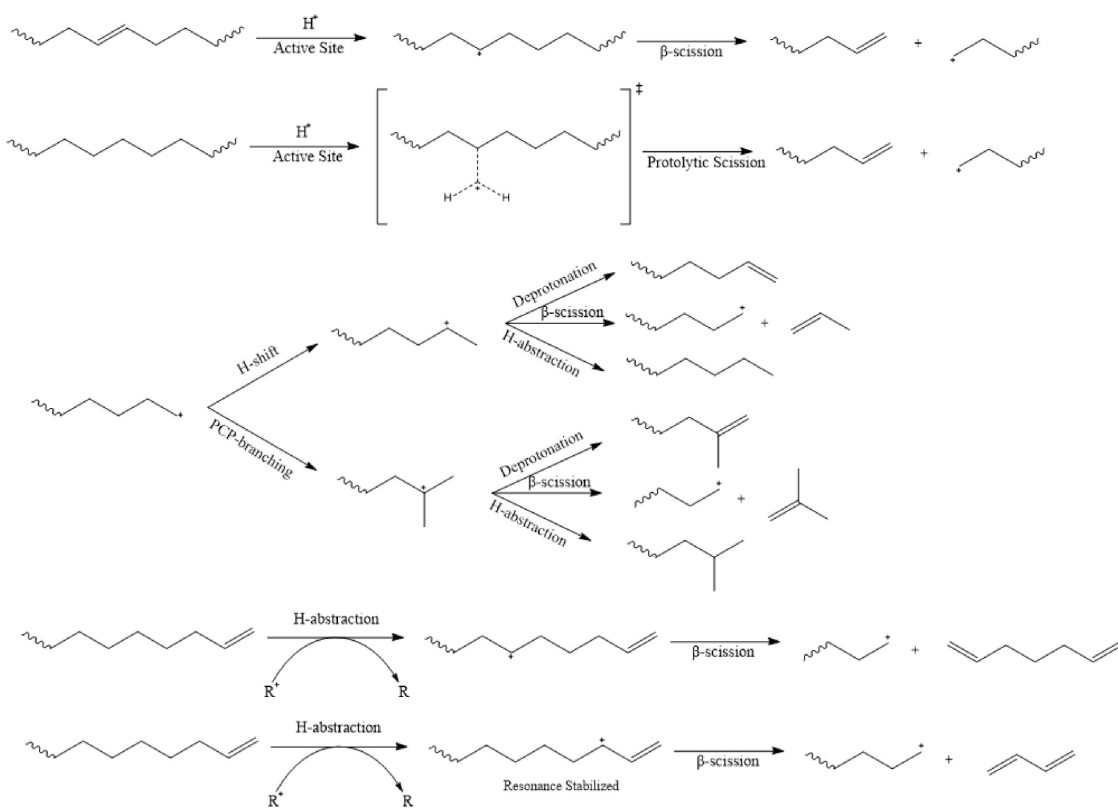


Figure 2.13: Proposed reaction mechanism for catalytic pyrolysis of polyolefins. Adapted from Abbas-Abadi *et al.*¹⁸¹

catalysts' structures and composition, global models are extremely case-specific. The micro and mesoporous structure, the effective diffusivity, the active site density and distribution, and pore-blocking are additional phenomena that must be accounted for but are complicated to quantify. Considerable work has been performed by Marcilla *et al.*^{210,214–217} to model in-situ pyrolysis through multi-step global models for different catalysts. Several models of increasing complexity were proposed by the authors, with reaction parameters obtained from regressions on experimental data. Lumped models have also been proposed^{188,199,200,218–221}, accounting for formation of the different products.

To the author's knowledge, a single mechanistic kinetic model has been proposed in the scientific literature²²². The model is developed analogously to the discrete section method employed for radical degradation^{55,65,66}, with carbenium and carbonium ions taking the place of radicals. In the proposed mechanism, the initiation step is the protonation by Bronsted sites of olefins and paraffins, forming respectively carbenium and carbonium ions. Termination occurs by desorption or deprotonation of the chains, restoring the original active site on the catalyst surface, while propagation reactions involve β -scissions and hydride ions abstractions. Similarly to the detailed radical degradation mechanisms, secondary reactions are neglected. Nevertheless, cyclization, aromatization, and coke formation in catalytic pyrolysis considerably affect product

yields. Additionally, the catalytic kinetic model is assumed volumetric although catalysts involve surface reactions^{53,167}.

2.4 PERSPECTIVES AND CHALLENGES

Various technologies have been developed in the past decades to recycle plastic waste. The advantage of thermochemical conversion pathways is that no separation is required, and few pretreatment steps are needed, like dehydrochlorination of PVC. Several kinetic models have been published in the scientific literature, but, to the author's knowledge, all of them are limited to single polymers.

The aim of the present thesis is to create a framework suitable to predict the degradation kinetics of PW for CFD applications. As discussed in the previous sections, the method of moments is the most widely spread kinetic model with the lowest computational cost. Unfortunately, it is not suitable to describe halogenated polymers, and therefore it is not relevant to the purposes of the present work. The kinetic models aim at describing the degradation of waste polymers, which have unknown origin and cannot be characterized. Therefore, the focus lies in predicting the *average reactivity* of PW constituents. As schematically shown in Figure 2.14, the kinetic mechanism is developed starting from elementary quantum-chemical information and is then coupled to suitable multiphase transfer model in reactor-scale simulations. Appropriate mixture degradation mechanisms are required, featuring polymer subsets developed with the same formulation and low computational cost. The targets of the models are the characteristic degradation times of the polymer, the detailed products yields, and the heat requirements of the process. In practice, this corresponds to answering the following questions: "*how long does it take?*", "*what comes out?*", and "*what's the energy cost?*".

The functional groups approach is chosen for its versatility. This methodology allows to model each polymer separately, address their cross-interactions, and extend the models for municipal solid waste (MSW) valorization. The following chapters first present a generalized framework for developing kinetic models through the FG approach. The discussion details several key aspects such as species definition, reaction representation, lumping techniques, and rate constants estimation. This thesis employs first polyethylene pyrolysis as reference to better explain the practical implications of the methodology and assumptions introduced. The mechanisms for polypropylene and polystyrene are developed following the same rules, although polymer-specific lumping techniques are introduced. While the mechanisms for PE, PP, and PS are built following studies in literature, the model for PET pyrolysis is developed from scratch. The models are complemented defining the thermochemistry of the species involved and are validated with literature experimental data. Following the results of the semi-detailed mechanisms, the present work proposes a methodology to derive two types of

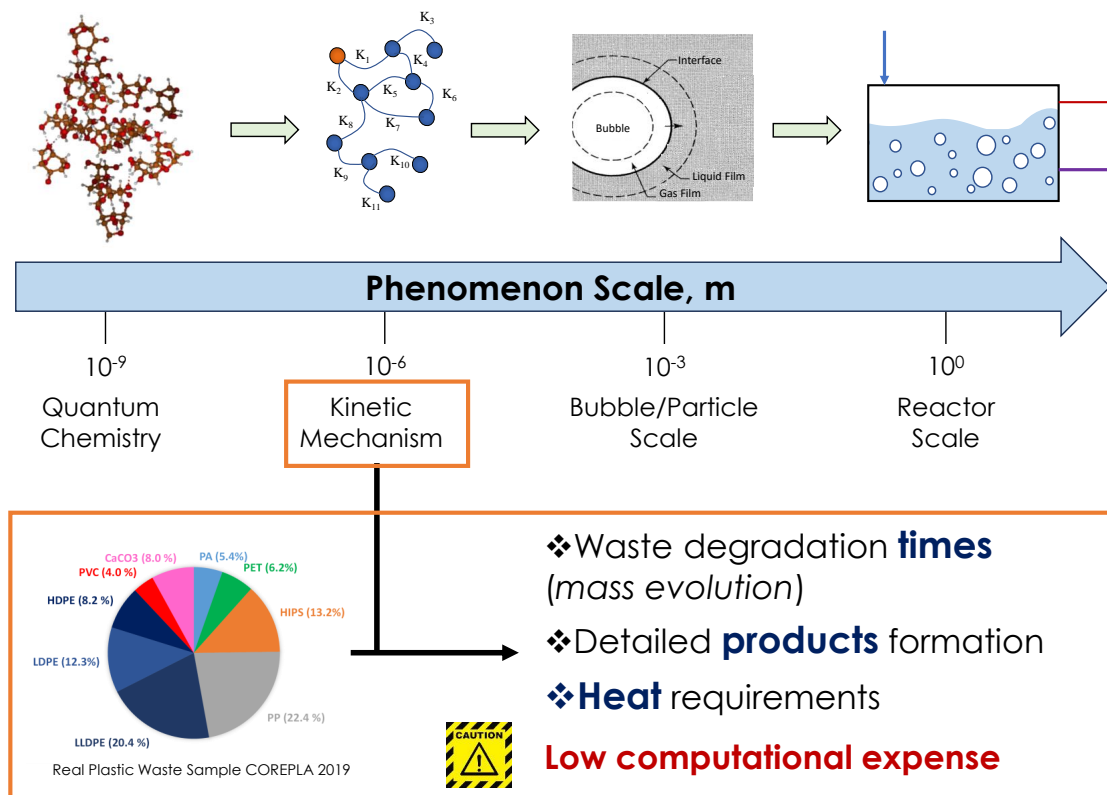


Figure 2.14: Schematic representation of the comprehensive kinetic mechanism to be developed for mixture thermochemical recycling

reduced-order kinetic models. The developed models are then coupled with the PVC one³⁵ to investigate mixture degradation.

3

DEVELOPMENT OF A GENERALIZED KINETIC MODEL: POLYETHYLENE

POLYETHYLENE (PE) is the largest volume commodity thermoplastic in the world⁴ and is among the most widespread polymers^{7,15}. PE is a light and versatile synthetic resin employed mainly for packaging as food wrap, shopping bags, and detergent bottles, but also as high speciality materials²²³. Polyethylene blends are mainly used for packaging due to their barrier properties toward oxygen and water and chemical resistance to aqueous systems, edible fats, and oils²²⁴. Additionally, PE as a blend component improves several properties such as flow, impact and chemical resistances and environmental stress cracking sensitivity at low price.

PE was first industrialised in the late 1930s, but the production considerably increased only in the late 1950s. The versatility of PE polymerization processes results into a spectrum of products with distinct properties and applications. Commercial products are categorized according to their density, which typically ranges from 0.88 to 0.95 g/cm³²²⁴. The prevalent PE grades are high-density (HDPE), low-density (LDPE), and linear low density (LLDPE). Nevertheless, several other grades like very low-density (VLDPE) or ultra high molecular weight (UHMWPE) are commercially relevant. The various PE resins differ by molecular weight, crystallinity, and branching, although they share the same molecular formula. HDPE is a rigid, opaque, white solid that forms films characterized by a turbid appearance and a crisp feel²²³. It exhibits low branching and high degree of crystallinity, resulting in a glass transition temperature (T_g) ~120°C and a melting point (T_m) of 120–140°C²¹. These properties make HDPE rigid and impermeable, ideal for products and packaging. LDPE and LLDPE are translucent, whitish solids with higher flexibility compared to HDPE. Films from these grades exhibit a limp feel and are transparent with only a slight milkeness²²³. These properties make HDPE rigid and impermeable, ideal for products and packaging. LDPE's high branching enhances flexibility over HDPE but reduces strength and heat resistance. LLDPE, an ethylene-based copolymer, offers a balance between these properties, making it ideal for films.

The degradation behaviour of the different polyethylenes is quite similar. The low degree of branching of HDPE and UHMWPE results in higher thermal recalcitrance. LDPE and LLDPE have degradation temperatures (T_d) ~20°C lower, although still above 450°C^{55,67,74}. The decrease in T_d relates to branches acting as weak points in the polymer structure. Specifically, CH-CH₂ carbon bonds are easier to break with

respect to CH₂-CH₂ ones¹⁴⁶ resulting in larger radical pools. Nevertheless, the different transport properties, chain mobility, and presence of impurities also contribute to the variations in T_d^{71,74}. LDPE and LLDPE involve also formation of higher amounts of branched hydrocarbons²²⁵. As discussed in Section 2.2, the kinetic modelling of thermal degradation of PE has been extensively studied in the past decades. However, the developed models are not suitable for modelling PW degradation due to several limitations. Discrete section^{55,65} and kinetic Monte Carlo⁷⁶ (kMC) models exhibit high computational cost, while global models suffer from insufficient accuracy¹³⁷. The method of moments (MoM) models satisfy these requirements^{57,67}, but they are not suitable to consider interactions with other waste components and are of difficult scalability⁴².

The following Chapter presents a detailed description of the functional groups (FG) approach. It details how to employ this methodology to develop a condensed-phase kinetic model for polymer thermal degradation, highlighting the description of the involved chemical compounds and their reactivity. The approach is demonstrated for PE thermal degradation to show the practical implications and outcomes of each assumption. The extensive research conducted for PE pyrolysis serves as benchmark for the model development. The performances of the resulting semi-detailed kinetic model are assessed by comparison with literature experimental data on mass-loss profiles, product yields, and heat-fluxes. The detailed kinetic model of Faravelli *et al.*⁶⁶ is also employed as validation target to evaluate the robustness of the proposed approach. The model proves able to describe the average behaviour of PE degradation, consistently with the aim of PW valorization. The developed semi-detailed model is employed to obtain two further lumped mechanisms, a semi-detailed and a fully lumped one. The performance of these reduced-order models is evaluated through validation against the semi-detailed mechanism and literature experimental.

The kinetic mechanisms are written automatically through a Python code according to the assigned species and elementary rate parameters. The mechanisms follow the CHEMKIN-like²²⁶ format and are publicly available as a GitHub repository¹.

3.1 SEMI-DETAILED KINETIC MODEL: PE-125-3500

The present Section describes the formulation of the semi-detailed kinetic mechanism for PE condensed-phase thermal degradation. As shown in Figure 3.1, the aim of the proposed mechanism is reproducing the main features of the degradation process at low computational cost. This consists in describing the characteristic degradation times (mass-loss profiles), product distribution, and heat requirements. The chemical changes in the reacting mixture are modelled with a complex network of reactions that convert one compound to another.

¹ Freely available at <https://github.com/Alocaspi/Polymers-Kinetic-Mechanisms>

The following Sections present the general formulation of the functional groups approach, i.e., how the polymer chains and their transformations are represented. The generalized aspects are described showing their application to the case of polyethylene. Firstly, the definition of pseudo-species is introduced, highlighting the distinction of polymeric chains between High and low molecular weight species. Compared to previous models^{35,37}, the present work expands the FG methodology distinguishing between mid- and end-chain fragments. This distinction improves the description of short compounds of interest, while preserving information on the average molecular weight of the mixture. Subsequently, the degradation mechanism is described, outlining reaction classes, rate constants, and variations in reactivity among different species. The reaction network is built assuming ideal polymeric chains (polymethylene) and then incorporates corrections for branches and impurities in the matrix. Finally, physical transformations as melting and boiling are presented together with their representation in the kinetic mechanism.

In the following, all compounds that evaporate from the molten to the gas- phase at reaction temperature are defined as “gas species”. These are further categorized as light or condensable (tars) gases according to their physical state at room temperature.

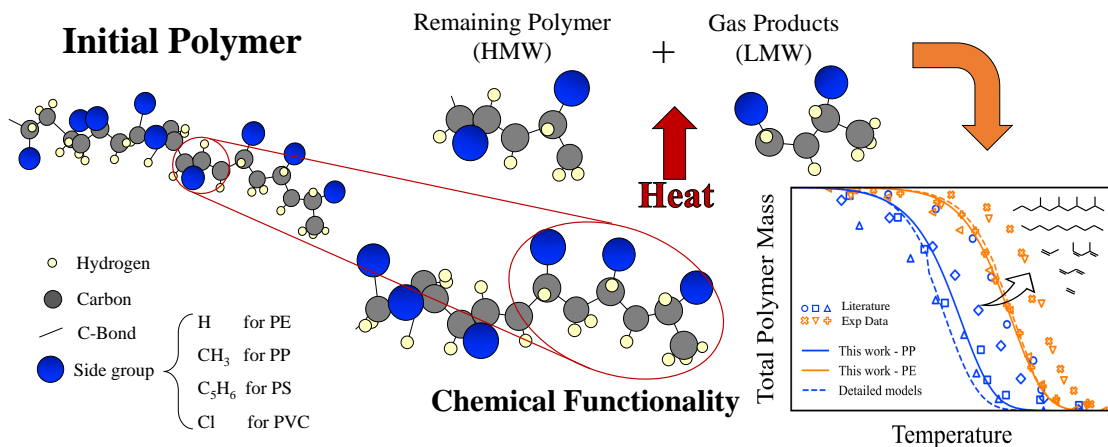


Figure 3.1: Modelling polymer degradation through the functional groups approach⁷⁴.

3.1.1 Species Definition

The polymer chain distribution is composed of chains with different lengths but similar functionalities. The FG approach categorizes these chains in high molecular weight (HMW) and low molecular weight (LMW) species. The former subset consists of the chains described by their chemical moieties, while the latter are the products of interest described with high accuracy. Within the FG formulation, only LMW species are able to evaporate forming stable gaseous products.

A threshold carbon number (N_c^*) differentiates HMW and LMW subsets. This value represents the longest polymeric chain that might evaporate in the FG framework. Chains with $N_c > N_c^*$ are classified as HMW, while shorter chains fall under the latter. This distinction is based on experimental observations of gas-phase products reported in the literature^{65,225,227–229}. The longest chains observed vary according to the operating conditions, while the model implements a clear cut-off. Considering a higher N_c^* allows to describe formation of longer gas-phase chains, but it also increases computational cost. Conversely, employing a low N_c value might limit the model applicability.

3.1.1.1 High molecular weight species

According to its chain length, each polymeric chain involves a different number of repeating units with identical chemical functionalities (the monomers). As schematically shown in Figure 3.2, any polymeric chain can be represented by a combination of mid-chain (MC) and end-chain (EC) chemical moieties. HMW species, while exhibiting varying chain lengths, share identical functional groups. This characteristic allows describing the entire HMW chain-distribution using just MC and EC fragments. Specifically, chains with similar chemical moieties but differing lengths are represented by the same pseudo-species, although in distinct amounts. Conversely, chains of same length but distinct moieties have similar Mid-to-end-chain ratios but involve distinct pseudo-species.

The mid- and end-chain functional groups can represent any chain longer than 2 EC units. Consequently, the length of end-chains (L_{EC}) is defined as $L_{EC} = 0.5 \cdot N_c^*$. The length of mid-chain units (L_{MC}) does not involve any physical boundary, and in the present work it is chosen $L_{MC}=L_{EC}$. The constraint on EC length does not affect model predictions. A model that involves formation of short chain compounds longer than 2 EC units is able to reproduce the desired targets. However, the overlap of the HMW and LMW subsets introduces errors when recovering the mixture's average molecular weight (Section 3.1.1.3).

Pseudo-species are introduced to represent the chemical moieties found in both the initial polymer and its degradation intermediates. All pseudo-species are identified by the prefix “P-”, with mid-chains also having a terminal “-P” in their name. The “P” in the label represents the pseudo-species being bonded within the polymer chain. Consequently, pseudo-species exhibit a slight hydrogen deficiency compared to their isolated counterparts. For instance, the polyethylene structural unit ($-\text{CH}_2-$) is represented as P-CH₂-P in the present approach. This pseudo-species has two H atoms less than the closest real equivalent (CH₄) as the “P” groups represent bonds with other segments. Linear hydrocarbons have an “N” in their label to highlight their configuration.

The initial chain-distribution depends on the polymerization process. Considering PE, it is assumed to contain solely paraffinic moieties. Conversely, the moieties of the

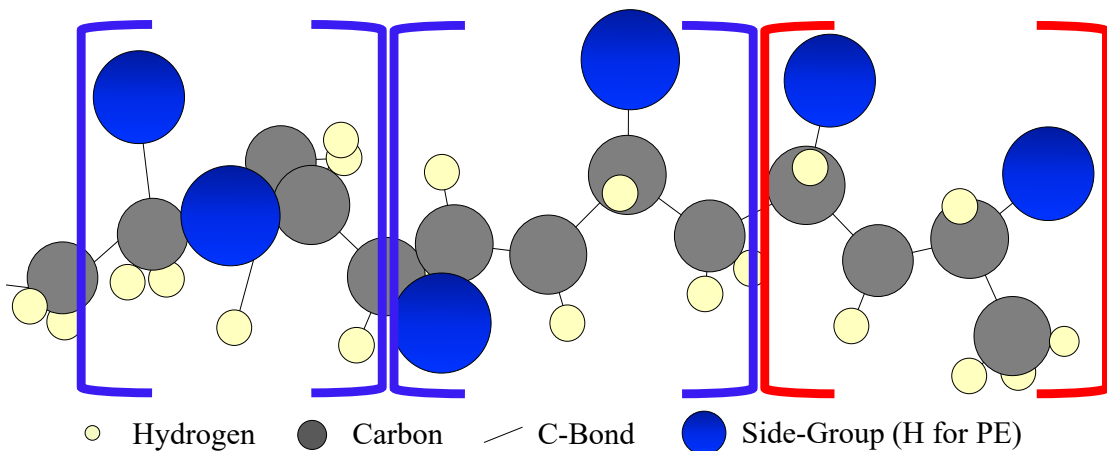


Figure 3.2: Schematic representation of a polymer chain represented through mid-chains (blue) and end-chains (red) moieties

intermediates depend on the degradation mechanism. As described in the next Sections, the radical mechanism is assumed to generate double bonds only within the terminal groups of PE chains²³⁰. Consequently, the evolution of PE chains is described through blends of three stable pseudo-species: a single stable paraffinic MC and a pair of stable ECs, one paraffinic and one olefinic. All chains with a normal boiling point ($T_{b,n}$) $< 750^\circ\text{C}$ are assumed able to evaporate allowing to describe formation of heavy waxes at low temperature^{228,231}. This corresponds to a threshold carbon number for the PE model of $N_c^* = 80$. The functional groups are therefore labelled " $P-NC_{40}H_{80}-P$ " the mid-chain, " $P-NC_{40}H_{81}$ " the paraffin end-chain, and " $P-NC_{40}H_{79}$ " the olefin end-chain. Figure 3.3 schematically represents all the pseudo-species introduced to represent the HMW distribution.

Polymer degradation typically occurs in the molten-phase. The initial stages upon heating involve either melting or glass transition according to the material's properties. The evaluation of the overall energy requirement of the process relies on the polymer state at room-temperature. As previously mentioned, polyethylene²¹ at room temperature is in a semi-crystalline state, with a crystallinity dependent on the grade. The mechanism describes the initial material through two components representative of the crystalline and amorphous parts, respectively. The latter exhibits similar thermodynamic properties to the molten state²³². Consequently, only an additional species representative of the crystalline part is introduced, labelled " $P-NC_{40}H_{80}-P_S$ ".

The most important reaction intermediates of the semi-detailed model are the radical species. Each pseudo-species requires multiple radical isomers to accurately describe its reactivity. Considering PE, since the chemical moieties are similar across the different chains, lumping approaches are implemented⁴³. For instance, a mid-chain unit has N_c^* radical isomers, all characterized by the same reactivity in terms of reaction products and rate. To reduce the number of species (N_s) involved, a single lumped

radical ($P-\dot{N}C_{40}H_{79}-P$) represents these isomers. Similarly, a single species represents all internal secondary alkyl radicals of each end-chain. These pseudo-species are labelled respectively " $P-NC_{40}H_{80}$ " and " $P-NC_{40}H_{78}$ " and have an even number of hydrogens due to the " $P-$ " prefix. End-chain paraffins and olefins also exhibit specific position-related reactivity. For paraffinic ECs, terminal primary alkyl radicals have a lower stability and higher mobility. The resulting different selectivity compared to internal radicals is represented by the " $P-NC_{40}H_{80-T}$ " species. Similarly, olefinic ECs involve resonantly stabilized allyl-like positions. These decrease the process apparent activation energy and form preferentially butadiene at low temperatures. The species " $P-NC_{40}H_{78-A}$ " represents this position-specific reactivity. In general, the labels " $_T$ " and " $_A$ " are employed to identify terminal and allylic radicals, respectively. Formation of vinyl radicals is neglected because of the higher activation energies involved¹³³.

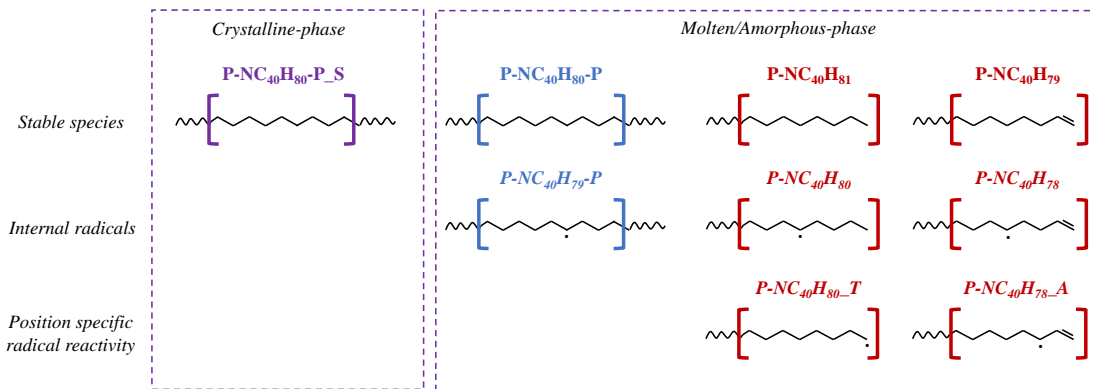


Figure 3.3: Schematic representation of the stable and radical pseudo-species introduced to describe long polymer chains (HMW). The distinction between crystalline and molten/amorphous pseudo-species is also shown.

The FG approach employs these pseudo-species to describe the initial polymer and its degradation until LMW chains. With respect to PE, the model describes the evolution of the entire HMW distribution using only 4 stable pseudo-species alongside 5 radical counterparts. Consequently, the model requires a number of mass balances similar to the method of moments, resulting in significantly less computational effort. In contrast, fully detailed models^{55,57,65} involve a number of equations of 10^6 - 10^7 . Section 3.3.1.2 presents additional lumping techniques to further reduce the computational cost associated to the proposed kinetic model.

3.1.1.2 Low molecular weight species

Low molecular weight compounds are the products of interest, ranging²²⁸ from non-condensable gases (e.g., methane) to heavy waxes of $MW > 600 \text{ g mol}^{-1}$. LMW species form through decomposition of HMW chains, and, to properly describe the product distribution, their reactivity must be accurately characterized. The model describes liquid- and gas-phase LMW compounds similarly to conventional semi-detailed mod-

els for combustion and pyrolysis of gaseous and liquid fuels^{43,146}. Chains with a critical temperature (T_c) lower than 400°C rapidly exit the reactive liquid-phase, due to their volatility. Conversely, heavier waxes can undergo partial cracking before evaporation. This competition depends on the operating pressure and temperature.

To reduce the computational cost while preserving the physical interpretation, two lumping techniques are implemented within the PE model⁴³. Compounds with $12 < N_c < N_c^*$ are described by a vertical lumping methodology¹⁴⁶, i. e., few lumped N_c are employed to represent the entire carbon spectra (Section 3.1.2.2). Conversely, real species describe chains shorter than C_{12} . The fast evaporation of light compounds is represented through a lumping technique as well. As with the N_c^* value, the model implements a clear cut-off although the competition degradation-evaporation depends on the operating conditions. The present model assumes species with $T_{b,n} < 250^\circ\text{C}$ not to undergo further reaction in the condensed-phase. Since they are $> 100^\circ\text{C}$ above their boiling temperatures¹⁰⁰, they are assumed to form directly as stable gas-phase compounds. For LMW with $T_{b,n} > 250^\circ\text{C}$, the radical reactivity is characterized through the same secondary, primary (_T), and allyl-like (_A) radicals introduced for HMW species. Each carbon number with an explicit characterization of the reactivity requires 10 additional liquid-phase species (20 liquid+gas species). This stems from the model introducing 7 radicals per carbon number: 2 radicals for the alkane (internal and terminal), 3 for the alkene (allylic, internal, and terminal), and 2 for the dialkene (allylic and internal).

Overall, the PE model categorizes the LMW product distribution into three classes based on carbon chain length and reactivity. Real species whose condensed-phase reactivity is neglected ($C < C_{12}$) are referred to as "*Unreactive LMW*" (ULMW). Lumped compounds whose condensed-phase reactivity is neglected ($C < C_{15}$) are referred to as "*Unreactive Lumped LMW*" (ULLMW). Lumped species whose reactivity is considered ($C > C_{15}$) are referred to as "*Reactive LMW*" (RLMW). The choice of LMW classification depends on the desired level of detail and computational resources available. Extending the spectrum covered by ULMW increases products detail without significant additional computational cost with respect to the condensed-phase. However, the computational cost associated to the secondary gas-phase reactivity increases as ULMW degradation cannot be neglected. Furthermore, this limits the applicability of the model at high pressure and high temperature where the fast evaporation assumption fails. Conversely, extending the carbon spectrum covered by RLMW compounds allows for simulating a broader range of operating conditions. This however comes with an increase in computational cost both in condensed- and gas-phase. Indeed, the number of liquid-phase reactions (N_r^L) scales $\propto (N_s)^2$ because of bimolecular reactions. Most importantly, the computational cost of micro-kinetic models scales $\propto (N_s)^n$ with $n \in [1, 2]$ according to the numerical methodology²³³.

The practical implications of the choice of ULMW, ULLMW, and RLMW are schematically represented in Figure 3.4. The kinetic model describes in detail all the compounds within the ULMW region (light blue area), while only the formation of the

red bars within the combined ULLMW and RLMW region (green area) is explicitly modelled. For instance, a model employing $C < C_{10}$ as ULMW limit and C_{15} , C_{20} , C_{25} , and C_{30} for RLMW species (Figure 3.4a) predicts preferential formation of C_6 but not C_{15} . While delumping techniques allow recovering the ULLMW-RLMW distribution (thin red lines), they assume a linear mass relation between the lumped carbon numbers. This model involves a compromise in detail and cost, as it considers $N_s=120$ and $N_r^L=3800$.

The model shown in Figure 3.4b employs a higher ULMW limit together with 4 ULLMW-RLMW species. It predicts preferential formation of both C_6 and C_{15} , but its applicability at high P and T is limited by neglecting secondary cracking of diesel-cuts. Considering a broader range of ULMW species has minor impact on the condensed-phase computational cost ($N_s=140$, $N_r^L=4000$). Since the model neglects their radical reactivity, they increase the number of mass balances without affecting the complexity and stiffness of the radical system. On the other hand, increasing the number of RLMW species considerably impacts the computational expenses.

The model shown in Figure 3.4c involves C_5 as ULMW limit with 6 ULLMW-RLMW. This allows accurately describing a broad range of operating conditions, but it involves higher demand as RLMW radical reactivity must be included ($N_s=140$, $N_r^L=7500$). Furthermore, since it lumps the gasoline cuts in the ULLMW-RLMW range, it is not able to describe preferential formation of C_6 nor C_{15} .

Reducing the number of both ULMW and ULLMW-RLMW considerably simplifies the kinetic model. The model shown in Figure 3.4d employs C_5 as ULMW limit and 2 lumped carbon numbers to describe the ULLMW-RLMW range. This mechanism employs $N_s=70$ and $N_r^L=1500$, but it captures only the key features of the product distribution. Nevertheless, this model is already close to being compact enough for reactor-scale CFD application of pure PE. In essence, the choice between model complexity and computational efficiency depends on the desired level of detail in the product distribution and the specific operating conditions of interest.

This thesis proposes a semi-detailed model that balances between accuracy, flexibility, and computational efficiency. Considering experimental product distribution data on PE, the developed model considers $C < C_{13}$ (ULMW), no ULLMW, and the reactivity of C_{16} , C_{30} , C_{45} , and C_{60} (RLMW). This approach results in a model with 130 liquid+gas species, which is significantly lower than detailed models (10^2 vs 10^6). However, the proposed mechanism still presents computational challenges for reactor-scale CFD simulations of PW. Nevertheless, appropriate model reduction tools^{234,235} allow achieving a computational cost manageable for reactor scale CFD simulations, i. e., 30-50 species. In this context, Section 3.3 presents two reduced-order models with lower computational cost. Specifically, section 3.3.1 discusses a reduced model with less carbon numbers that further lumps the radical isomers. Similarly, Section 3.3.2 presents the derivation of a multi-step kinetic mechanism (i. e., 4-10 species). This strongly simpli-

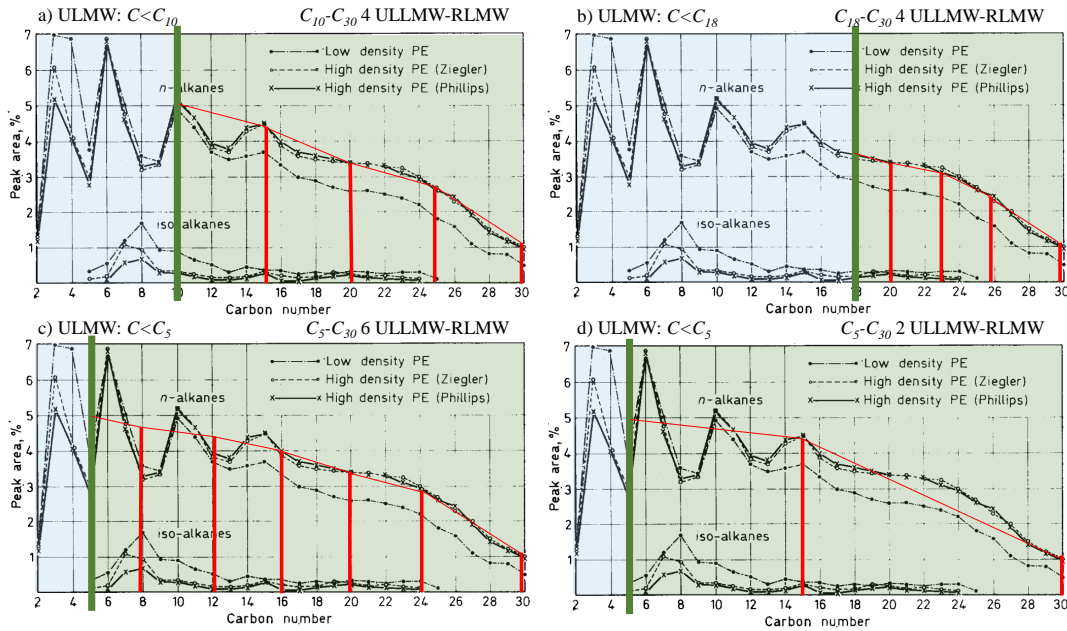


Figure 3.4: Representation of the experimental product distribution of Michajlov *et al.*²²⁵ employing different ULMW (blue) and ULLMW+RLMW (red lines in the green area). Details are given in the text.

fied mechanism offers a more in-depth description compared to TGA-derived fitting models.

3.1.1.3 Number Average Molecular Weight

The description through the chemical moieties of the polymer simplifies the different chains in a few functional groups. Nevertheless, the distinction in mid- and end-chain moieties relates to the average chain distribution. The initial quantities of MC and EC are evaluated according to the chain distribution resulting from the polymerization process. For PE, a Schultz distribution of polymeric chains is considered²³⁶. At increasing initial average molecular weight, the mass fraction of MC groups tends to unity to represent infinitely long chains.

Each polymeric chain is composed of two end-chain functionalities. Therefore, the initial moles of end-chains (n_{EC}^0) are evaluated as:

$$n_{EC}^0 = 2 \sum_{l=N_c^*}^{\infty} f(\chi, l) \quad (3.1)$$

where χ is the degree of polymerization and $f(\chi, l)$ is the chain-length distribution. The former is evaluated through the monomer (MW_m) and polymer initial number average molecular weight (MW_{av}^0) as:

$$\chi = MW_{av}^0 / MW_m \quad (3.2)$$

The function $f(\chi, l)$ depends on the polymerization process. As previously mentioned, for PE a Schultz distribution is assumed²³⁶ and therefore:

$$f(\chi, l) = \frac{4l}{(\chi - 1)^2} \left(\frac{\chi - 1}{\chi + 1} \right)^l \quad (3.3)$$

The initial moles of mid-chains pseudo-species (n_{MC}^0) represent the portion of polymer not included in the end-chains nor LMW species. This value is calculated based on the total mass of HMW chains not contained in the end-chain groups:

$$n_{MC}^0 = \frac{1}{MW_{MC}} \left(\sum_{l=N_c^*}^{\infty} f(\chi, l) MW_l - n_{EC} MW_{EC} \right) \quad (3.4)$$

Following the degradation process, the number average molecular weight (MW_{av}) can be reconstructed based on the mid-to-end-chain ratio. As previously mentioned, each real polymeric chain is composed of two end-chain units. For this reason, the moles of ECs are related to the total HMW moles and MW_{av} is evaluated as:

$$MW_{av} = \frac{m_L}{0.5n_{EC} + \sum n_{LMW}} \quad (3.5)$$

where m_L is the total Liquid mass and n_{LMW} the moles of liquid-phase low molecular weight species. The approach proposed to reconstruct the polymer degradation requires to distinguish between mid- and end-chain moieties.

3.1.2 Reaction Network

The model employs a detailed reaction mechanism to represent the various transformations that degrade the polymer. Each reaction introduced aims at representing the elementary steps involved in the breakdown process. The network development follows a reaction class approach, i. e., all the reactions are generated from a small set of elementary steps. The considered elementary pathways characteristic of each polymer moiety derive from studies on the polymer or analogous compounds. The mechanism includes both molecular and radical reactions according to the polymer functionalities.

Chemical reactions are localized phenomena⁵⁸. Consequently, the elementary reaction classes defined for individual molecules are directly applicable to the pseudo-species representative of polymer fragments. However, as discussed in the next sections, the FG methodology requires appropriate corrections to consider the presence of neighbouring polymer fragments. Each elementary step requires to define the reaction rate and the species involved (i. e., the stoichiometric coefficients). Gas-liquid analogies⁵⁵ are used to determine reaction constants, while lumping methodologies^{43,146} provide the basis for reactant and product definitions. When available, specific studies on the polymer degradation are also employed.

The reaction mechanism employs volumetric reactions followed by interface evaporation of LMW species. The liquid-phase reactions involve homogeneous reactants and

form two types of products: HMW and RLMW compounds as liquid-phase species, while ULMW and ULLMW compounds as gas-phase species. Other authors^{237,238} propose a volumetric polymer degradation followed by interface cracking at the polymer end-chains. These surface phenomena are concurrent with the volumetric reactions and dominate at high specific surfaces and interface end-chain fractions. The specific surface increases because of boiling phenomena consequent to formation of light volatiles in the liquid bulk. Similarly, end-chains originate from polymer degradation in the liquid bulk. The relevance of this interface cracking increases with polymer conversion, and it is expected to impact mainly the end of the degradation process. However, modelling these phenomena requires accurate descriptions of the liquid-vapour interface, which is outside the scope of this work.

With respect to PE, a purely radical degradation mechanism is introduced. Figure 3.5 schematically shows the reaction pathways that lead to LMW formation from HMW stable species for PE degradation. In general, mid-chains decompose to form end-chains which in turn release LMW products. These further react or stabilize and evaporate to stable gas-phase products. The same reaction classes proposed by other authors for PE are considered^{55,65,67,76}, and the main reaction products are alkanes, α -alkenes, and $\alpha - \omega$ dialkenes. Radical initiation occurs with random-scission reactions to form terminal radicals that either propagate or terminate¹⁵⁶. The propagation reactions considered in the model are H-abstractions, β -scissions, unzipping, and backbiting. Only termination by radical-radical recombination is included²³⁹.

The following sections discuss the elementary steps and the associated kinetic parameters. The first subset presented is the backbone degradation, which is characteristic of internal radicals. Particular focus is given on the reaction formulation to account for the stabilization of ULMW and the representation of the chain-length variation. Subsequently, the reaction pathways specific to allyl-like and terminal radicals are discussed.

3.1.2.1 Elementary Reaction Rates

The reaction network builds on the definition of the elementary reaction classes and their rates. As previously mentioned, studies on the polymer itself serve as the basis for this definition. Investigations on model compounds with similar functionalities can also be applied to polymer systems⁹¹. The extensive scientific literature published since the 1950s¹⁰⁰, coupled with recent advanced quantum chemical calculations, allows for highly accurate estimations of the rate parameters. According to the methodology, the calculation of gas-phase rate constants can fall within a factor of 2 uncertainty²⁴⁰. The comparisons with gas-phase data enables quantitative assessment of proposed reaction mechanisms in the scientific literature.

While gas-phase kinetic parameters can be estimated with high accuracy, accurately determining the liquid-phase counterparts is challenging. Unlike gas-phase reactions,

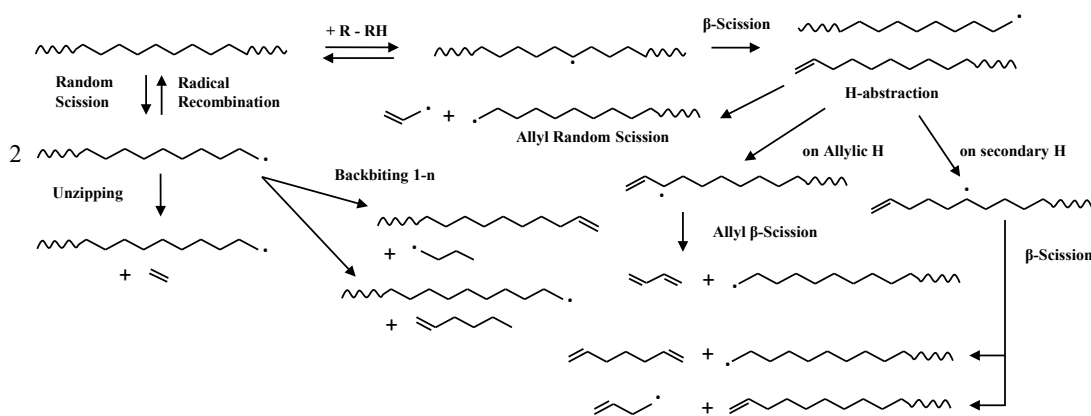


Figure 3.5: Schematic representation of the degradation of the initial mid-chain pseudo-species to form LMW products. The MC species undergoes random scission forming terminal radicals which recombine, backbite, H-abstract, or unzip.

solvent interactions significantly influence reaction rates in the condensed phase. To the author's knowledge, a comprehensive theory for predicting liquid-phase rates is currently lacking. Theoretically, gas-phase rate constants can be translated to liquid-phase employing solvation energies⁵⁸. However, defining solvation energies for radicals and transition state configurations often proves difficult. Recent advancements in coupling quantum chemistry with continuum solvation methods offer promising solutions in this regard²⁴¹. Additionally, studies utilizing metadynamics are proving valuable for defining liquid-phase reaction rates²⁴².

Polymer degradation is far from being an ideal system. While the kinetic models assume ideal polymeric chains, real-world degradation involves the presence of weak-links, impurities, and inorganic matter. These phenomena cannot be assessed *a priori* through theoretical ideal systems, as their exact nature and occurrence is not known¹⁶⁷. The proposed rate constants indirectly account for these phenomena and their impact on the overall degradation rate. Due to the complexity of the reacting system, this work relies on simplified approaches based on analogous compounds. The resulting rate parameters represent the complex molecular scale phenomena in a simplified approach. Each rate constant accounts for angle orientations, steric hindrances, nearest-neighbours, and solvent effects. This work employs modified-Arrhenius laws for the rate constants, where the temperature exponent (n_A) is null for most reactions. An exception is made for reactions where $n_A \neq 0$ is theoretically motivated, such as termination reactions. These reactions are diffusion controlled²⁴³, and their rate is estimated through the Free Volume Theory^{55,244}. For this reason, a value $n_A=1$ is considered following the theoretical derivation. Conversely, H-abstractions rate parameters typically exhibit $n_A > 1$. However, because of the investigated low-to-mid temperature range (between 300 and 1000°C), for H-abstraction n_A is set to 0. This simplification allows

for straightforward use of analogies based on bond dissociation energies (BDE) and reaction entropies²⁴⁵.

In this work, the gas-liquid transposition follows the solvation correction proposed by Ranzi *et al.*⁵⁵. The polymer itself acts as solvent in the degradation environment, and viscosity data enable to estimate polymer solvation energies. This correction primarily impacts reactions where the reverse reaction has a negligible energy barrier⁵⁷. Radical initiations and β -scission reactions fall within this category, as the energy barriers for radical termination and additions are lower than the forward ones. For these reactions, the solvation correction leads to a decrease in the activation energy. This gas-to-liquid analogy is not applicable to all reaction types. In the present work, reactions such as molecular ones and methathesis employs selectivities similar to the gas-phase counterparts. Considering H-abstractions and intramolecular isomerisation, the model employs the selectivity proposed by Mehl *et al.*²⁴⁶. Table 3.1 reports the elementary selectivity according to the type of hydrogen and radical involved in the H-abstraction reaction. The values reported are defined with respect to H-abstraction of a secondary alkyl radical (R_2) on a secondary alkyl hydrogen (H_2). For instance, H-abstraction of R_2 on CH (H_3) has 2.5 kcal mol⁻¹ lower activation energy compared to R_2 on CH_2 (H_2). The corrections in Table 3.1 do not account for the total number of available hydrogens. For example, H-abstraction on CH_2 has a twice higher frequency factor compared to reactions with CH due to the presence of 2 abstractable hydrogens per carbon atom. The model employs the approach proposed by Ranzi *et al.*²⁴⁵ to estimate the reverse reaction.

Table 3.1: H-abstraction correction to rate parameters according to the type of hydrogen and radical involved (units cal, mol), with respect to a secondary alkyl radical H-abstracting a secondary alkyl hydrogen (R_2+H_2)²⁴⁶.

TYPE	Primary	Secondary	Tertiary	Allylic
$Hydrogen_j+R_2$	$E_{act}+2000$	1	$E_{act}-2500$	$E_{act}-2500$
$Radical_j+H_2$	$E_{act}-1000$	1	$E_{act}+500$	$E_{act}+8000$

Considering PE, Table 3.2 reports the elementary reaction classes and their modified-Arrhenius. The rate constants presented in this thesis have been updated compared to the published model⁷⁴ to incorporate new experimental data on product distributions. The proposed parameters derive from previous literature studies^{55,57,65,67,76}, but several modifications are considered.

With respect to random scission reactions, the model employs the solvation correction estimated by Ranzi *et al.*⁵⁵. This results in a decrease of ~5 kcal mol⁻¹ in E_{act} compared to the gas-phase counterpart. The frequency factor (A) also decreases because of the loss of internal motions due to the presence of the solvent⁵⁷. The rate parameters

herein employed are the same as Ranzi *et al.*⁵⁵ and Faravelli *et al.*⁶⁶. Conversely, Levine and Broadbelt⁶⁷ use values similar to gas-phase initiations¹⁰⁰.

The E_{act} proposed for β -scission reactions is lower than the one suggested by Faravelli *et al.*⁶⁵ and aligns with the value of Levine and Broadbelt⁶⁷. The decrease compared to Faravelli *et al.*⁶⁶ accounts for the solvent effect also on these reactions⁵⁵. These solvent effects vary according to the chain-length of the compounds involved. Short compounds exhibit higher mobility within the polymer melt and are less affected by the repulsive force of the surrounding solvent (the polymeric chains). In gas-phase reactions, the formation of CH_3 radicals involves $\sim 2.3 \text{ kcal mol}^{-1}$ higher E_{act} compared to formation of R_1 . This results in methane formation being negligible at process temperatures, contrary to experimental data on PE degradation²²⁸. The liquid-phase "cage-effect" is assumed responsible for the increased formation of methane. This phenomenon involves both enthalpy changes, due to the electronic repulsion of solvent molecules, and entropy changes, as low molecules have higher mobility. The model employs for CH_4 same activation energy of other β -scission reactions, which corresponds to a decrease of $2.3 \text{ kcal mol}^{-1}$ compared to gas-phase. Additionally, the frequency factor for this reaction is increased by a factor of 10 to represent higher mobility. All reactions that form short chain products should account for the lower cage-effect, but further work is required.

Among the various β -scission reactions, unzipping plays a key role. Unzipping is a β -scission reaction that releases the monomer starting from a terminal radical. For PE, this involves a primary alkyl radical forming ethylene. Formation of C_2H_4 is favoured because of the higher reactivity of the primary radical and the lower cage-effect. To represent these phenomena, a decrease of 3 kcal mol^{-1} is introduced with respect to mid-chain β -scissions. Additionally, the frequency factor is increased by a factor of 2 to account for the higher mobility of the short-chain product.

The model accounts for both intra- and intermolecular H-transfer reactions. These reactions employ similar parameters to the gas-phase counterparts. Table 3.2 reports the values for H-abstraction of a secondary hydrogen by a secondary radical. The selectivity to the different hydrogen and radical types are estimated with the values reported in Table 3.1. With respect to radical isomerisation (backbiting), only formation of 5-, 6-, and 7-membered rings are considered. These ring sizes represent the most favorable conformations as they compromise between ring-strain and the number of hindered rotors. Compared to other literature studies^{55,57,66,67}, the present model assumes 1-6 backbiting (7-member ring) to occur through out-of-plane bending. This conformation allows preserving bond angles and therefore does not involve ring-strain compared to 1-5 backbiting. Conversely, the frequency factor is decreased by $10^{0.8}$ due to the additional hindered rotor¹⁴⁶. The model also includes consecutive backbiting to account for preferential formation of long-chain hydrocarbons (Section 3.1.2.4).

Recombination reactions are fast reactions with null activation energy. As mentioned, in liquid-phase, the rate determining step is the diffusion of the radicals towards each

other²⁴⁷. As highlighted by Poutsma⁷⁶, the rate of termination increases with conversion as the viscosity of the polymer melt decreases. The model accounts for the difference in diffusivity between polymer chains of varying lengths. Different frequency factors are considered according to the species chain-length as described by Kruse *et al.*⁶¹. The lower limit for recombination rates is set through the flux units evaluated by Ranzi *et al.*⁵⁵. The corresponding rate parameters are reported in Table 3.2.

The present work also includes a chemical reaction to represent the polymer melting from crystalline to amorphous phase. This phase-transition is modelled with high activation energies and frequency factors to ensure it occurs within a narrow temperature range near T_m of PE (130°C). Further details regarding the representation of physical phenomena through chemical reactions are given in Section 3.1.3.

Table 3.2: Modified-Arrhenius parameters for elementary reactions classes (units cm, mol, s, cal). Parameters for recombination reactions refer to the polymer flux unit, while H-abstraction refers to a secondary radical (R_2) abstracting a secondary hydrogen (H_2).

Reaction	A	n _A	E _{act}
Random scission	8.00E+14	0	78000
β -scission	2.00E+13	0	28000
CH_3 formation	2.00E+14	0	28000
Unzipping	3.00E+13	0	25000
H-abstraction R_2+H_2	3.00E+11	0	13500
Backbiting 1-4	5.00E+10	0	20600
Backbiting 1-5	7.50E+09	0	14500
Backbiting 1-6	1.50E+09	0	14500
Radical recombination	5.00E+10	1	6000
Melting	1.00E+18	0	37000

3.1.2.2 Internal radicals: backbone degradation

The backbone degradation mechanism describes the variation of units inside the polymeric chains. All the radicals along the backbone involve the same chemical moieties but form products of different chain length. Reactions occurring close to the end-chain groups result in formation of LMW products. The FG framework employs several lumping techniques to describe the reactions of the pseudo-species. The kinetic model for PE serves as basis to describe the general formulation of the approach. All internal radical positions are equivalent, allowing the present Chapter to focus only on the mechanism formulation. Chapter 4 and 5 describe how to consider the presence of two different types of internal radicals. Chapter 6 describes how to employ the FG

approach to copolymers and, more in general, to polymers that break in compounds smaller than the starting monomers.

The backbone degradation results in equimolar formation of chains of different lengths, i.e., similar amounts of any chain from C₂ to C₈₀. This stems from the H-abstraction rate for internal hydrogens being independent on its chain position⁵⁵. Long chains are not observed in significant molar amounts in gas-phase because of their high boiling points and slow evaporation rates. Conversely, preferential formation of specific short-chain compounds (e.g., ethylene, propane, butadiene, hexene) is due to the reactivity of terminal and allylic radicals discussed in the next Sections. This section discusses the formulation of reactions within the FG approach. The same reaction classes are defined also for all RLMW radical species, although not reported here. The RLMW reactivity represents the main computational cost of the kinetic model.

The rate determining step depends on the polymer. Considering PE, the polymer reaction times are primarily controlled by two aspects: HMW β-scission reactions and the radical pool concentration. The latter depends on the ratio of random scission to radical recombination reactions^{55,65}. Conversely, inter- and intra-molecular H-abstractions impact the gas-phase products selectivity. The mechanism predicts formation of paraffins:olefins:diolefins in 0.25:0.5:0.25 molar ratio, satisfying the hydrogen balance⁷⁴. To reduce the number of reactions and isomers, the model does not consider reaction pathways of low importance at the temperatures of interest^{57,67,71,146}. Specifically, because of the higher BDE involved, the model neglects formation of H and vinyl radicals and neglects H-abstractions on primary hydrogens. The latter is also statistically less probable considering PE. The mechanism also neglects radical addition to double bonds and termination by disproportionation, due to low importance compared to β-scission and recombination reactions^{55,65}.

As mentioned, the degradation starts with a unimolecular random scission on the mid-chain pseudo-species ("P-NC₄₀H₈₀-P") forming two end-chain terminal radicals ("P-N·C₄₀H₈₀-T"). Figure 3.6 schematically shows the initiation reaction. Using a limited set of functional groups to describe the degradation of polymeric chains poses a conundrum. The FG approach describes all HMW chain structures with units that have the same carbon number. During the degradation, these units are consumed in reactions that form light products and chain units of same length as the reactant. To conserve atomic and radical balances, the concept of "*Supporting Polymer Unit*" (SPU) is introduced. Decomposition reactions involving mid- or end-chain units consume additional chain units (SPU) to account for the chain length decrease. This approach allows to preserve the physical interpretation of the FG approach while also describing the chain-length variation. The latter is represented by the ratio of mid-to-end-chain units as discussed in Section 3.1.1.3.

As reaction proceeds, the average polymer chain length decreases and the ratio mid-to-end chain reduces as well. Consequently, the probability to have end-chains neighbouring to the reacting functionality increases. To represent this phenomenon,

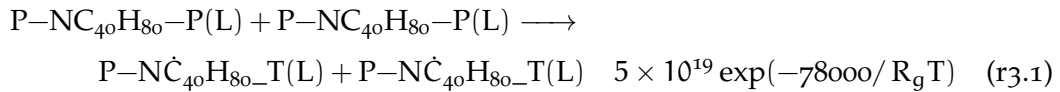
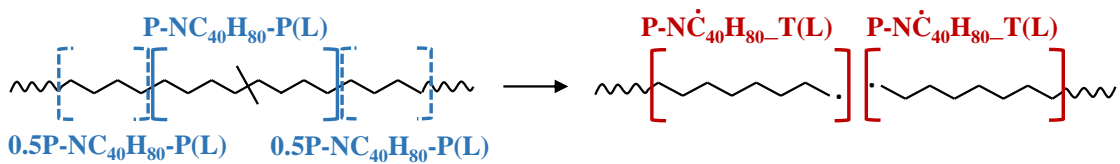
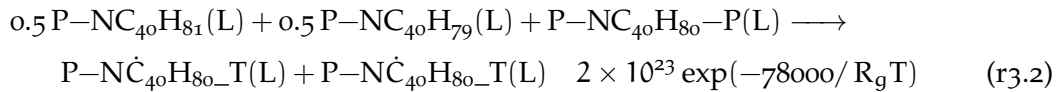


Figure 3.6: Schematic representation of a supported random scission reaction consuming a mid-chain pseudo-species (SPU) to form 2 end-chains.

the model considers also pairs of end-chains as SPU. This reaction preserves the degree of unsaturation of the mixture (H/C ratio) while consuming end-chains. The reaction has the same representation as Figure 3.6, but it is written as:



The kinetic parameters of both initiation reactions derive from the values reported in Table 3.2. Nevertheless, corrections are introduced to reduce the number of reactions and preserve the SPU interpretation. The same elementary step can occur on all 40 carbon bonds in the mid-chain species yielding the same products. These 40 elementary steps are lumped in the same reaction with a pre-exponential factor 40 times faster than the single elementary step.

The difference between the two reactions lies in the SPU. Both reactions are unimolecular and do not directly involve the supporting unit in the transition state. Nevertheless, the reactions must consider a selectivity to the SPU representative of the probability the reactive site and the support are adjacent. However, this probability should not affect the total rate of consumption of the reactive site and alter the unimolecular nature of the reaction. The probability to employ the supporting unit "i" (γ_{SPU_i}) corresponds to the moles of SPU_i to the total moles of SPU available. For pure polymers, this corresponds to the mixture molar fraction, as functional groups during the degradation account for >95% of the mixture. This Supporting Polymer Unit mimics the effect of bulk activities in surface decomposition reactions^{167,226}.

The CHEMKIN format does not consider this complex behaviour and accounts for dependences only on the species concentrations. To conform with this format, the reaction frequency factor is modified by a species-dependent parameter, γ_{SPU_i} , defined through the species concentration as:

$$\gamma_{SPU_i} = \frac{MW_{SPU_i}}{\rho_L} \frac{1}{\sum_{SPU_j \in e} \omega_{SPU_j}^0} \quad (3.6)$$

where ρ_L is the polymer density at reaction conditions (0.76 g cm^{-3} for PE⁵⁵) and MW_{SPU_i} is the molecular weight of unit i . The term $\sum_{SPU_j \in e} \omega_{SPU_j}^0$ accounts for the initial mass fraction all units that can be employed as SPU in reaction e . This value is 1 for polyolefins, while being less than unity for copolymers (e.g., PET). The kinetic rate is modified introducing a γ_{SPU_i} correction for each SPU_i involved. Considering reaction r_{3.1}, the reaction rate computed following the CHEMKIN format (r) is:

$$\begin{aligned} r &= k_{RS}^{SPU_{MC}} \cdot C_{MC} \cdot C_{SPU_{MC}} = k_{RS} \gamma_{SPU_{MC}} \cdot C_{MC} \cdot C_{SPU_{MC}} = \\ &= k_{RS} \cdot C_{MC} \frac{\omega_{SPU_{MC}} \rho_L}{MW_{SPU_{MC}}} \frac{MW_{SPU_{MC}}}{\rho_L} \frac{1}{\sum_{SPU_j \in e} \omega_{SPU_j}^0} = \\ &= k_{RS} \cdot C_{MC} \cdot \frac{\omega_{SPU_{MC}}}{\sum_{SPU_j \in RS} \omega_{SPU_j}^0} \end{aligned} \quad (3.7)$$

where $k_{RS}^{SPU_{MC}}$ the rate constant employed in the model accounting for the SPU considered, k_{RS} is the random scission elementary rate constant reported in Table 3.2, and MC is the mid-chain unit P–NC₄₀H₈₀–P. C_{MC} and $C_{SPU_{MC}}$ are respectively the concentrations of the MC acting as reactive site and the MC acting as SPU_{MC} , while $\omega_{SPU_{MC}}$ is the mass fraction of the MC employed as SPU.

Equation 3.7 shows that this approach introduces a dependence of the reaction rate on the mass fraction of the SPU. This is an approximation as the probability relates to the molar fraction of the SPU. As MC and EC have similar molecular weight, the pseudo-species mixture has an approximately constant molecular weight. Therefore, the error in approximating molar fractions with mass ones is deemed acceptable. Because of the different SPU involved, reaction r_{3.1} and r_{3.2} involve different frequency factors. Specifically, considering the kinetic model for PE $\gamma_{SPU_{EC}} \approx \gamma_{SPU_{MC}} = 736.8 \text{ mol cm}^{-3}$. Since reaction r_{3.1} employs a single SPU, its frequency factor (A) is $A_{r3.1} = 8 \times 10^{14} \cdot 40 \cdot 736.8 \approx 5 \times 10^{19} \text{ cm}^3 \text{ mol}^{-1} \text{ s}^{-1}$. Conversely, reaction r_{3.2} employs two SPU, and therefore $A_{r3.2} = 8 \times 10^{14} \cdot 40 \cdot (736.8)^2 \approx 2 \times 10^{23} \text{ cm}^6 \text{ mol}^{-2} \text{ s}^{-1}$. As mentioned, these frequency factors do not have physical meaning but try to represent the elementary behaviour following the CHEMKIN format. The reaction is first-order in each SPU unit through the keyword "FORD".

The terminal radicals undertake H-abstractions on any neighbouring hydrogens as discussed in Section 3.1.2.4. Initially, only mid-chain hydrogens are available resulting in formation of a mid-chain secondary radical P–N \dot{C}_{40} H₇₉–P. This pseudo-species represents all 40 radical positions in the MC unit and it either stabilizes by H-abstraction, recombines with other radicals, or undergoes β -scissions. Figure 3.7 schematically represents the β -scission reaction to form a terminal end-chain double bond (P–NC₄₀H₇₉) and a terminal radical (P–NC₄₀H₈₀–T). As with random scissions, an SPU is required to form the end-chain moieties while preserving the propagation aspect of the reaction (i.e., a constant number of radicals). The model also introduces additional reactions involving pairs of end-chains as SPU. The kinetic parameters of the reaction are cor-

rected with the γ_{SPU} as shown in equation 3.6 and 3.7. Compared to reaction r3.1, the 40 equivalent radical isomers are accounted for through the higher formation rate and species concentration.

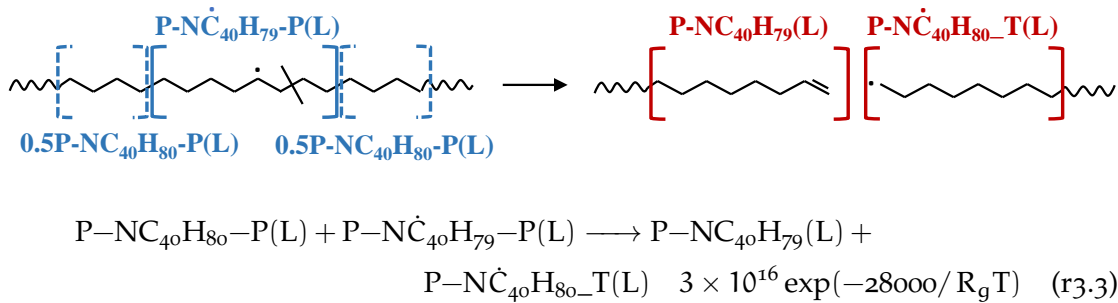
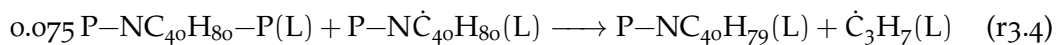


Figure 3.7: Schematic representation of a supported β scission reaction of a mid-chain radical consuming a mid-chain pseudo-species (SPU) to form 2 end-chains.

As polymer degradation proceeds, the amounts of end-chain units in the polymeric melt increases. This leads to an increase in the formation of internal EC radicals. When these radicals undergo β -scission reactions, they release volatiles of interest represented through LMW species. As with mid-chain units, all internal radical positions are represented through a single pseudo-species. Figure 3.8 schematically shows the β -scission of the 5th carbon radical to form C_3 . The product of the elementary β -scission reaction is the propyl radical (\dot{C}_3H_7), but the model neglects radicals of species with $C < C_{20}$ (Section 3.1.1.2). To this aim, the formation of the radical and its stabilization are lumped in a single reaction. The formation step (the β -scission) employs a mid-chain SPU to generate the end-chain olefin " $P-NC_{40}H_{79}$ " and it would be written as:



The 0.075 of the SPU is required to satisfy the elemental balances, and its reaction order is enforced unitary with the CHEMKIN keyword *FORD/P-NC₄₀H₈₀-P 1/*. The stabilization of the propyl radical can occur on any stable species RH belonging to the HMW and RLMW subsets. A separate reaction is required to account for the different RH terms, and all bimolecular stabilization would be written as:



where C_3H_8 forms directly as a gas-phase species.

The two elementary reactions are lumped in a single step as shown in Figure 3.8. As mentioned, the stabilization step can take place through any stable species (RH) with a radical counterpart (HMW and RLMW species), and the model introduces a separate reaction for each RH species considered. The mechanism assumes formation only of the most likely radical, which in the case of PE is the internal radical for all species. The formation of the LMW radical is the rate determining step of the reaction⁵⁵, and the

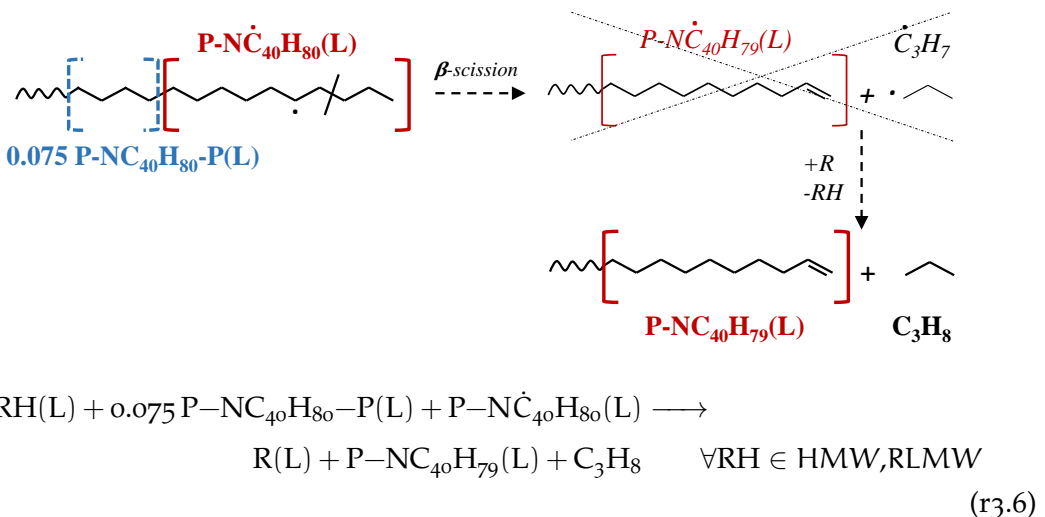
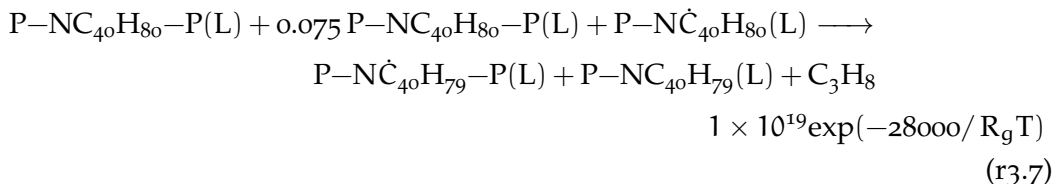


Figure 3.8: Schematic representation of the lumping of formation and stabilization of $\dot{\text{C}}_3\text{H}_7$.

The ULMW species is assumed to stabilize converting any stable species RH to its corresponding radical R. The elementary steps are represented in italic, while the bold arrows correspond to the lumped reaction introduced in the mechanism.

parameters of β -scission reactions reported in Table 3.2 are employed. Nevertheless, the frequency factor is modified to account for the SPU_i introduced through the factor γ_{SPU_i} . The model also exploits the same γ correction to account for the selectivity to RH_i . For instance, the reaction introduced in the model for stabilization through a mid-chain species is:



where the frequency factor of the reaction is evaluated as $A = A_\beta \cdot \gamma_{\text{SPU}_{MC}} \gamma_{\text{RH}_{MC}} = 2 \times 10^{13} \cdot 736.8 \cdot 736.8 = 1 \times 10^{19}$. Compared to γ_{SPU_i} , the correction γ_{RH_i} correctly accounts for the fraction of hydrogen in the mixture.

The same elementary reaction can occur also from a radical in the 13th position to form $\text{C}_{14}\text{H}_{28}$ and terminal end-chain radical ($\text{P-NC}_{40}\text{H}_{80}-\text{T}$). As discussed in Section 3.1.1.2, the chain distribution for $\text{C}_{12}>\text{C}_{16}$ is represented through a vertical lumping procedure¹⁴⁶. This consists in representing any species as a mixture of compound with the same chemical functionalities but different chain length. Formation of $\text{C}_{14}\text{H}_{28}$ is represented through a mixture of the adjacent carbon number included - C_{12} and C_{16} . In general, a C_n species with $12 < n < 16$ is represented through the lever rule as:

$$n_{\text{C}_{12}} = n_{\text{C}_n} \cdot \frac{16-n}{16-12} \quad n_{\text{C}_{16}} = n_{\text{C}_n} \cdot \frac{n-14}{16-12} \quad (3.8)$$

Therefore, instead of forming $C_{14}H_{28}$, the model considers formation of $0.5C_{12}H_{24} + 0.5C_{16}H_{32}$. Figure 3.9 schematically represents the reaction introduced in the model. The rate constant is evaluated following the same approach as reaction r3.3, as it employs a SPU but not a stabilization step.

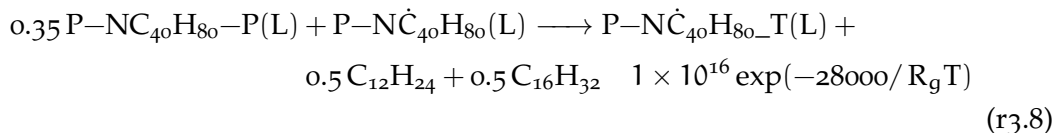
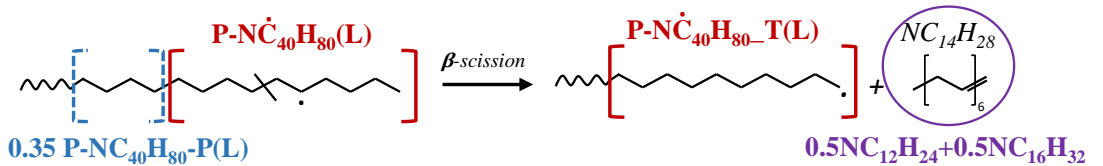
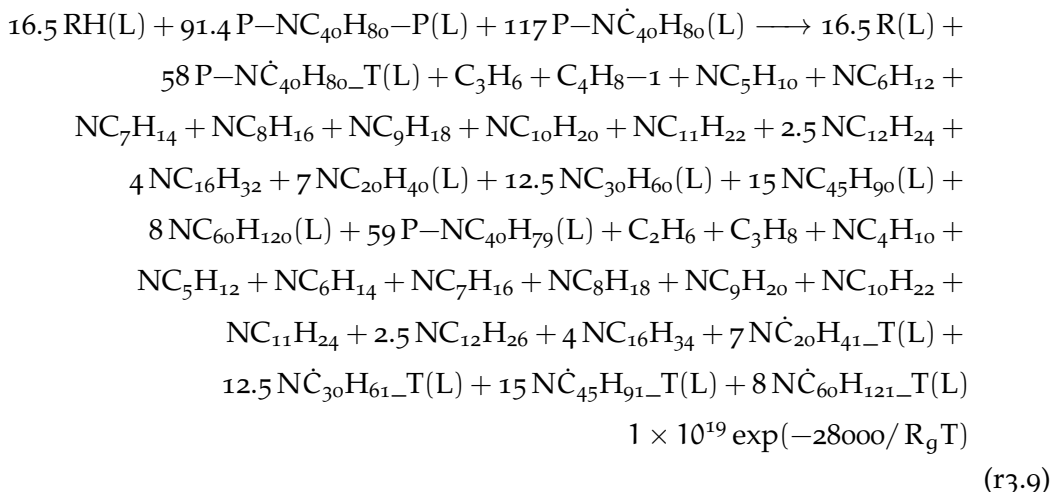


Figure 3.9: Schematic representation of the lumping of formation and stabilization of C_3H_7 . The ULMW species is assumed to stabilize converting any stable species RH to the corresponding radical R. The elementary steps are represented in italic, while the bold arrows correspond to the lumped reaction introduced in the mechanism.

End-chain units have different radical isomers, each with similar reactivity but leading to products with different chain lengths. For instance, the paraffinic end-chain " $P-NC_{40}H_{81}$ " can form a radical on either the 5th or 10th carbon with equal likelihood. While both radicals undergo β -scission, the resulting products differ based on the scission position. The 5th carbon scission yields C_6H_{12} or C_3H_7 , while the 10th carbon scission produces $C_{11}H_{22}$ or C_9H_{19} . As previously mentioned, these radicals have the same reactivity and are represented by the same pseudo-species: $P-\dot{N}C_{40}H_{80}$ for paraffins, $P-\dot{N}C_{40}H_{78}$ for olefins. To reduce the number of reactions, a single reaction represents all the elementary β -scission events of the same EC radical⁴³. The stoichiometric coefficients are obtained as the sum of the elementary coefficients²⁴⁸ and result in formation of species ranging from C_2 to C_{80} . The reaction incorporates the formulation previously described, such as the supporting unit, stabilization, and vertical lumping. The complete β -scission reaction introduced in the kinetic mechanism for $P-\dot{N}C_{40}H_{80}$ is:



The reaction employs the same nomenclature of the CRECK gas-phase mode¹³³ version 2310² for species already present in the mechanism. The resulting reaction is far from being an elementary step, although it derives from them. The model employs the "FORD" keyword to enforce the reaction orders required to employ the γ correction of equation 3.7. All reactants have unitary reaction order.

The model considers only termination by radical-radical recombination^{55,65}. As mentioned, these reactions impact the total radical concentration and the characteristic degradation times. Recombination reactions lead to an increase in the average polymer chain-length contrary to decomposition reactions. To reflect this behaviour, the model represents reaction products with $\text{C}>\text{N}_c^*$ as a mixture of MC and EC units. The first describes the increase in chain-length while the latter the chemical functionality. For instance, Figure 3.10 shows the recombination of $\text{N}\dot{\text{C}}_{30}\text{H}_{61}-\text{T}$ with $\text{P-NC}_{40}\text{H}_{80}-\text{T}$. The formation of $0.75\text{P-NC}_{40}\text{H}_{80}-\text{P}$ represents the increase in chain length, while $\text{P-NC}_{40}\text{H}_{81}$ preserves the paraffinic functionality of the original reactant.

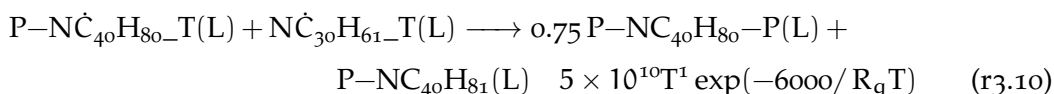
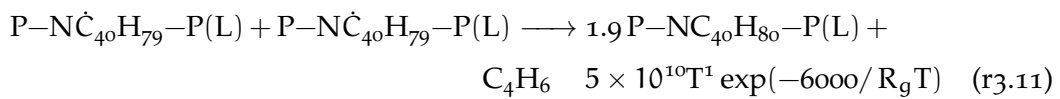


Figure 3.10: Schematic representation of radical-radical recombination reactions increasing the average chain length.

² Freely available at <https://github.com/CRECKMODELING/Kinetic-Mechanisms>

Several recombination reactions lead to formation of branched or unsaturated functionalities. These chemical structures have lower hydrogen content with respect to the pseudo-species introduced in the kinetic model. While formation of these structures impact the chain distribution and material properties, they have negligible impact on volatile distribution and degradation times. For this reason, the model neglects the formation of these branched and unsaturated species and dumps the balancing error on LMW unsaturated species. With respect to PE degradation, the error is dumped on the smallest diolefin (C_4H_6) as it has the lowest H/C ratio. For instance, recombination of 2 mid-chain radicals ideally results in a mid-chain quaternary carbon. However, the model instead represents this structure through formation of C_4H_6 and 1.9 stable MC. The reaction introduced is therefore:



As mentioned, this simplification introduces an error. Through a global Rate of Production Analysis, this error is quantified being <0.1%, an acceptable trade-off.

3.1.2.3 Resonance stabilization: allyl-type radicals

The backbone degradation mechanism predicts in equimolar amounts of all oligomers. However, this is not consistent with experimental observations. The presence of the double bond affects the reactivity, both in terms of characteristic degradation times and product distribution. Alkenes have lower oxidation rates with respect to alkanes at the considered reaction temperatures. For this reason, they are often employed to increase the octane number of gasolines²⁴⁶.

Figure 3.11 shows the allyl-type reaction pathways introduced in the present mechanism. In the present kinetic model, allyl-types undergo the same reactions as other radicals, but at different rates. The double bond increases the stability of radicals in α -position through a resonance effect¹⁰⁰. This effect increases the total radical concentration, but the slower decomposition of resonance stabilized radical reduces the degradation rates²⁴⁶. Indeed, allyl-type radicals are easier to form, but also act as radical sink. In PE degradation, the allyl-type reactivity justifies the preferential formation of C_3H_6 and C_4H_6 . The former is mainly consequence of β -scission reactions near the double bond, while the latter results from β -scission of the allylic radicals themselves.

Table 3.3 reports the variation in reactivity compared to the values reported in Table 3.2. These rates and product selectivities are similar to those proposed by Mehl *et al.*²⁴⁶. Chain fission to form allylic radicals involve lower BDE due to the resonance stabilization. This translates to a decrease in activation energy with respect to the backbone random scission. However, the frequency factor also decreases due to the loss of a rotor in the transition state and a reduced chain mobility⁵⁷. As previously mentioned, the allylic radicals affect β -scission reactions in two different ways. As with random

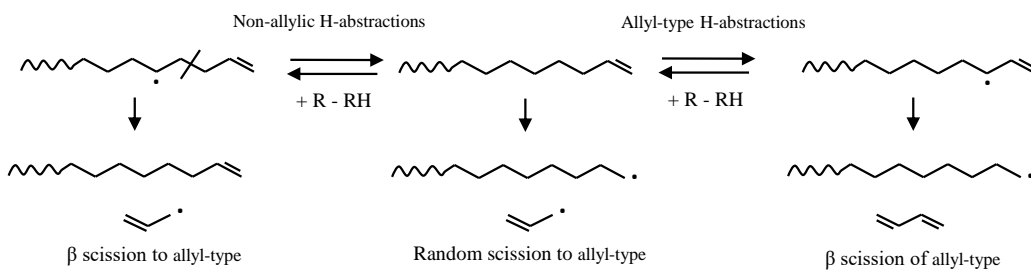


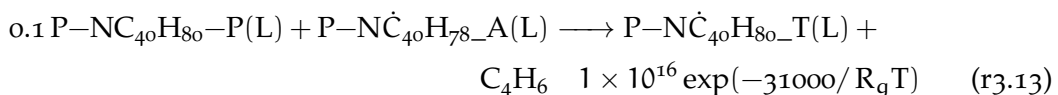
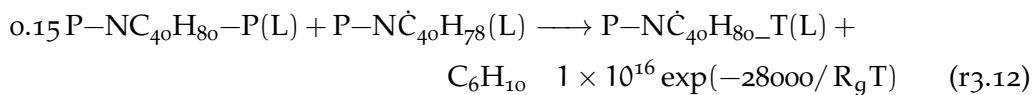
Figure 3.11: Schematic representation of the main reactions involving allyl-type radicals.

scissions, the β -scission of a radical that forms the allyl one (C_3H_5) is favoured. The rate constant for this reaction is modified considering the lower BDE and the reduced cage-effect for small molecules. Conversely, the higher stability results in higher energy barriers for β -scission of allylic radicals to form C_4H_6 . Compared to the selectivity proposed by Mehl *et al.*²⁴⁶, a lower increase in E_{act} is introduced. This accounts for a reduced cage-effect on small compounds as discussed in Section 3.1.2.1. Termination reactions are diffusion-limited, and therefore the higher stability does not affect the rate constants.

Table 3.3: Allylic corrections to modified-Arrhenius parameters²⁴⁶. The “0” subscript refers to the elementary reference parameters reported in Table 3.2 (units mol, cal).

Reaction	A _{allyl}	n _{allyl}	E _{allyl}
Random scission	0.2·A ₀	0	E ₀ -11000
β -scission of allylic	A ₀	0	E ₀ +3000
β -scission to C_3H_5	0.5·A ₀	0	E ₀ -5000
H-abstraction by R _{allylic}	A ₀	0	E ₀ +8000
H-abstraction of H _{allylic}	A ₀	0	E ₀ -2500

To exemplify the impact of these corrections on reaction rates, consider the elementary step leading to C_6H_{10} and C_4H_6 from end-chain olefin radicals. The two elementary reactions and their rate constants are:



The former reaction involves a secondary alkyl radical $P-NC_{40}H_{78}$, while the latter considers the allylic radical $P-NC_{40}H_{78}-A$. Both reactions employ the correction accounting for the SPU, while no stabilization step is required. As reported in Table 3.3, the β -scission of $P-NC_{40}H_{78}-A$ employs an activation energy 3 kcal mol⁻¹ higher

compared to P–N⁺C₄H₇8. Conversely, the model does not consider any modification to the frequency factor. The correction introduced lowers the rate constant for butadiene formation. Nevertheless, the high concentration of allylic radicals results in high selectivity towards C₄H₆ at low temperatures.

3.1.2.4 Terminal radicals: unzipping and backbiting

Backbone radicals are easier to form due to the lower BDE, but terminal radicals are the primary products of scission reactions. The selectivity among their reaction pathways strongly impacts the product distribution.

Figure 3.12 schematically shows the reaction rates considered for terminal radicals. H-abstractions are the most important mechanism at low temperature. Compared to gas-phase mechanisms, the high liquid-phase concentrations result in strong effect of bimolecular reactions. Stabilization of the terminal radicals forms backbone radicals that undergo the backbone degradation. This pathway is the main responsible for the high amounts of waxes observed at low temperatures. The model considers intramolecular H-transfer through backbiting isomerisation. As discussed in the following paragraphs, the model considers both single and consequent backbiting steps. These are medium temperature pathways that result in preferential formation of gasoline and diesel-cuts. At high temperature, the main reaction is unzipping to form the monomer. Formation of terminal double bonds releasing the side-groups are not included as they are not relevant at the considered operating conditions^{55,57,65,67,76}. The following paragraphs discuss these reaction classes for PE pyrolysis.

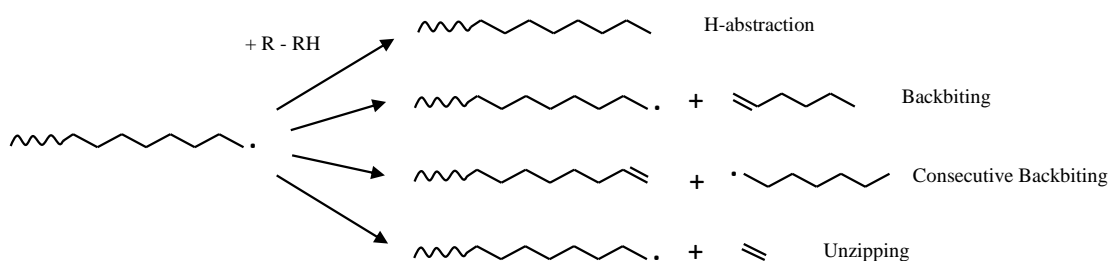


Figure 3.12: Schematic representation of the main reactions involving terminal radicals.

Backbiting reactions are competing pathways responsible for preferential formation of propane, 1-hexene, heptane, 1-decene, and others. These reactions involve the rearrangement of radicals from their current position on the chain to a different internal location. The most important backbiting steps involve primary radicals isomerizing to any internal position " n " (i.e., 1- n transfer). This work incorporates separate backbiting reactions for all HMW and LMW terminal radicals. Each of them undergoes up to 1-16 isomerisation through multiple consecutive transfer. Further intra-chain transfers are possible but decrease in importance due to lower probability. Table 3.2 reports the rate parameters for isomerisation of a primary alkyl to a secondary alkyl radical.

The model employs the same selectivity of H-abstractions to evaluate isomerisation involving other radical types (Table 3.1). In general, isomerisation from unstable to stable radicals are more favoured.

The backbiting reaction consists of an isomerisation followed by a β -scission reaction. This work lumps the two steps in a single reaction as schematically shown in Figure 3.13. The model assumes the isomerisation being the rate determining step compared to the bond-scission, and the reaction employs the backbiting kinetic parameters. The frequency factor is multiplied by the hydrogen sites available for the H-transfer reactions, which is 2 for PE.

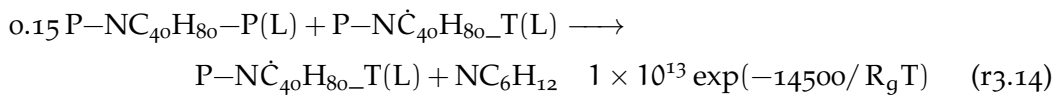
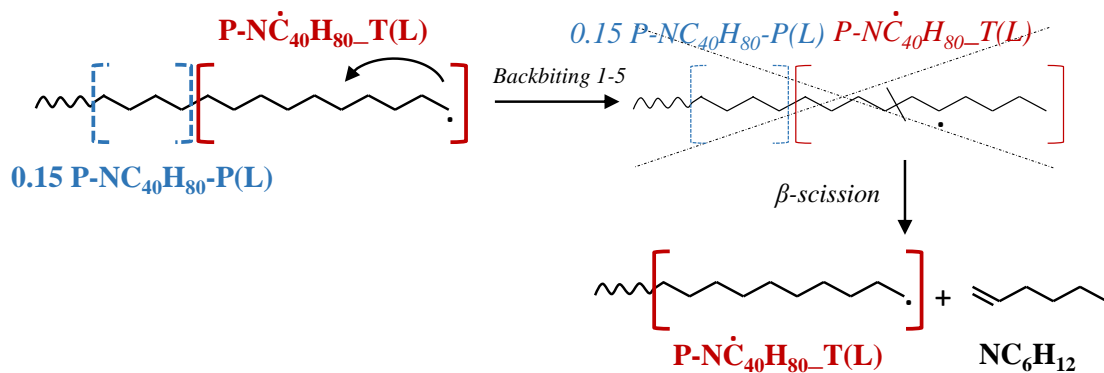
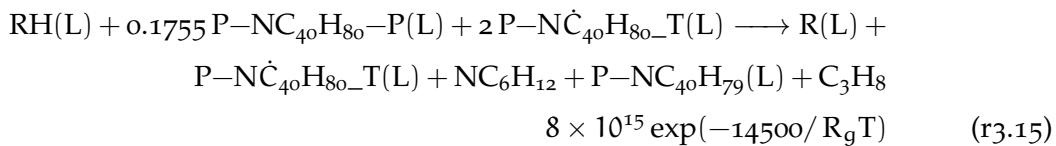


Figure 3.13: Schematic representation of 1-5 backbiting from the EC terminal radical employing an MC unit as SPU.

The internal radical formed through the isomerisation has equal probability to break either the left or right C-C bond. To reduce the number of reactions, both steps are lumped in the same reaction as:



where the stabilization step is lumped in the reaction to avoid introducing the radical $\dot{\text{C}}_3\text{H}_7$ (Figure 3.8). The frequency factor for r3.15 is 736.8 times higher than the one for r3.14 as here γ_{RH} must be introduced.

The most favoured isomerisation is 1-5 as it is the smallest ring that preserves bond angles. On the other hand, 1-4 backbiting involves one less hindered rotor but higher activation energy because of the ring strain. 1-2 and 1-3 hydrogen-shifts are even less favourable due to the substantial strain in 3- and 4- membered rings^{72,146}. Higher order backbiting (1-6 and beyond) exhibits similar trends. While activation energies might be

comparable to 1-5, the presence of more hindered rotors progressively reduces the entropy contribution¹³³. Backbiting reactions with $n > 6$ are assumed resulting from multiple consecutive isomerisation steps. For instance, 1-7 isomerisation results from 2 consecutive 1-4 H-transfers. For consecutive backbiting, the model employs the elementary rate constant modulated by a backbiting probability factor, $\alpha_{bb_{n,i}}$, defined as:

$$\alpha_{bb_{n,i}} = \frac{k_{bb_{n,i}}}{\sum_j k_{bb_{j,i}} + \sum_j k_{i,H_j} C_{H_j} + k_{RR} C_{R_{tot}}} \quad (3.9)$$

This probability represents the likelihood of a radical at position " i " undergoing a "1- n " H-transfer compared to all competing pathways for the radical in position n . The available reaction pathways are all elementary backbiting, H-abstractions on any hydrogen type " j ", and recombination reactions. The elementary backbiting constants are adjusted to account for the stability of the formed radical. As mentioned, the model employs the same selectivity introduced for H-abstractions (Table 3.1). The type j hydrogen concentration (C_{H_j}) is assumed constant and evaluated at the mixture density. The total radical concentration ($C_{R_{tot}}$) is evaluated through the steady-state approximation⁵⁵ as:

$$C_{R_{tot}} = \sqrt{\frac{k_{RS} C_{C-C}}{k_{RR}}} \quad (3.10)$$

where k_{RS} and k_{RR} are respectively the elementary random scission and radical recombination constants reported in Table 3.2. C_{C-C} is the concentration of aliphatic bonds on which initiation can occur. This is evaluated as ρ_L/MW_{CH_2} assuming only secondary carbons are present in the polymer melt.

To illustrate the application of backbiting probability factors, consider the following example of a 1-9 intramolecular H-transfer. This backbiting can occur through multiple pathways: two consecutive 1-5 isomerisations, a 1-4 followed by a 1-6 transfer, or a 1-6 followed by a 1-4 hydrogen H-shift. The rate constant of each pathway is computed multiplying the initial backbiting constant by the probability the subsequent step occurs. For instance, the constant of the 1-6 transfer followed by a 1-4 isomerisation, $k_{bb_9}^{1-4/1-6}$, is:

$$k_{bb_9}^{1-4/1-6} = k_{bb_6} \cdot \alpha_{bb_{4,6}} \quad (3.11)$$

In this equation, $\alpha_{bb_{4,6}}$ is evaluated considering the reaction pathways available to the radical on the 6th carbon. Specifically, it represents the probability the radical undergoes a further 1-4 backbiting with respect to its stabilization or decomposition. The total 1-9 rate constant, k_{bb_9} , is then obtained summing the rates for the three pathways:

$$k_{bb_9} = k_{bb_5} \cdot \alpha_{bb_{5,5}} + k_{bb_6} \cdot \alpha_{bb_{4,6}} + k_{bb_4} \cdot \alpha_{bb_{6,4}} \quad (3.12)$$

The resulting rate constant is then regressed to an Arrhenius form. Table 3.4 reports all the consecutive backbiting reactions and their Arrhenius parameters. These rates already include the per site hydrogen concentration. Overall, the 1-5 backbiting is the most important in the range of temperatures of interest, followed by the 1-6 and 1-4 transfer. The latter becomes the most important at $T > 1000^\circ\text{C}$. Multiple backbiting reactions are in general less favoured with respect to the single ones. Among them, the most favoured is 1-9 isomerisation, as it results from two consecutive 1-5 transfers. This reaction explains the preferential formation of n-heptane and 1-decene observed experimentally. Other favoured reactions are the 1-10 and 1-8 hydrogen shifts as they involve at least one 1-5 isomerisation.

The kinetic parameters account for the probability a radical completes the further isomerisation after the first one. While crossing the first energy barrier corresponds in enough energy for both steps, the model accounts for the intermediate radical's stability. For instance, backbiting 1-7 results from two consecutive 1-4 transfers. Under the rate-determining step assumption, both steps would have the same activation energy. However, the model assigns a higher barrier for 1-7 backbiting. This reflects the possibility that the intermediate radical (formed after the first 1-4 transfer) stabilizes before undergoing the second isomerisation. At moderate temperatures, even if the reactant crosses the initial barrier, the intermediate product can stabilize before completing the entire 1-7 rearrangement. The proposed kinetic parameters reflect this phenomenon through a higher energy barrier for 1-7 backbiting compared to 1-4 isomerisation ($\sim 7.6 \text{ kcal mol}^{-1}$). As a matter of fact, this value is roughly equivalent to the energy difference between 1-4 transfer and H-abstraction (around $7.1 \text{ kcal mol}^{-1}$), representing the competition between these pathways for the intermediate radical

Table 3.4: Arrhenius parameters of consecutive backbiting reactions obtained from regression (units s, cal, mol).

Reaction	A	E_{act}
Backbiting 1-7	1.92E+11	28200
Backbiting 1-8	5.77E+10	22100
Backbiting 1-9	5.93E+09	16400
Backbiting 1-10	2.00E+09	162900
Backbiting 1-11	2.42E+09	19300
Backbiting 1-12	3.93E+10	23900
Backbiting 1-13	4.08E+09	18200
Backbiting 1-14	1.69E+09	18300
Backbiting 1-15	2.12E+09	20500
Backbiting 1-16	2.23E+10	24500

Unzipping is the most important reaction at high temperatures for all vinyl polymers. Unzipping reactions are "auto-catalytic", as the radical reactant is also among the products of this reaction. The ratio between unzipping and stabilization rate is the polymer zip-length. Considering PE degradation, this reaction pathway is the sole responsible for formation of C_2H_4 . Figure 3.14 schematically shows the unzipping reaction of an EC terminal radical using a mid-chain as SPU. As previously mentioned, the rate constant reported in Table 3.2 is modified to account for γ_{SPU} . Unzipping reactions are introduced for RLMW radicals.

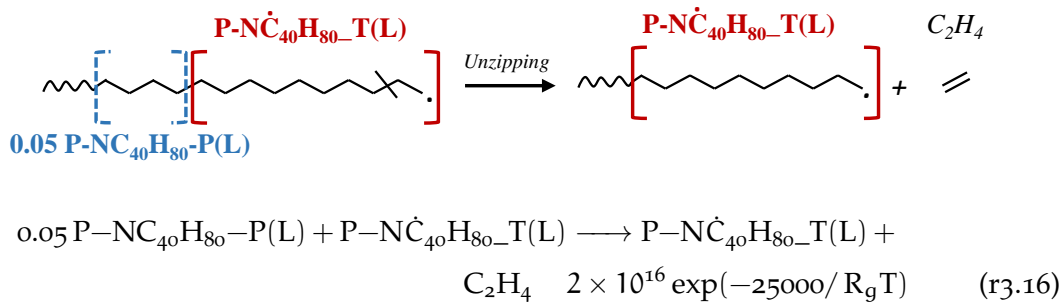


Figure 3.14: Schematic representation of unzipping reaction from the EC terminal radical employing an MC unit as SPU.

3.1.2.5 Weak-Links: LDPE correction

As mentioned, the kinetic model is developed assuming ideal polymeric chains. Nevertheless, because of imperfections in the polymerization process, life-time degradation, and the presence of impurities, polymers are seldom ideal chains.

The provided kinetic descriptions assume ideal, unbranched polymer chains (poly-methylene). While these constants can predict degradation profiles for HDPE, they underestimate LDPE reactivity. The lower degradation temperature of LDPE is generally consequence of branches and melt mobility⁷¹. The presence of branches along the polymer backbone introduces weak-points along the chain. As with allyl-types, these act both as radical initiation points and also reduce the energy barrier for β -scissions near the branches. To account for the lower degradation temperatures observed in LDPE, a correction factor is applied to the activation energy of mid-chain random scission (ΔE_{MC}^{RS}). This correction is based on the sample density, ρ_L , as:

$$\Delta E_{MC}^{RS} = -2000 \frac{\rho_L - 970}{910 - 970} \quad (3.13)$$

where units are kcal, mol, kg, and m^3 . This correlation relates the presence of branches to the sample weight. The maximum decrement is based on the difference in energy barriers to form a primary and a secondary radical instead of two primary ones²⁴⁹. For LDPE samples with unknown density, the model employs a value of $\Delta E_{MC}^{RS} = -1000$.

A more comprehensive approach is describing these phenomena through the presence of polypropylene fragments within the backbone of PE. This approach allows for predicting formation of branched products as well, but it requires accounting for interactions between the MC and EC units of PE and PP. The resulting kinetic scheme would involve higher computational cost without significant increase in accuracy however.

3.1.3 Phase-change phenomena: melting and boiling

The behaviour of a polymeric material in pyrolysis conditions involves a complex interplay of physical and chemical transformations. As temperature increases, polymer chains gain mobility, leading to significant changes in the physical properties of the melt.

Figure 3.15 shows the morphological changes for PE and PP granules upon heating²⁵⁰. The process can be broadly divided into three stages. Initially, the polymer melts forming a homogeneous liquid phase. Upon reaching the degradation temperature, the polymer breaks down into short chain compounds. Several of these species are hundreds of Celsius above their critical temperature point and boil within the reacting melt. In the last decomposition stages, ash deposition and may occur according to the impurities and metals in the polymer matrix through secondary tar reactions²⁵¹.

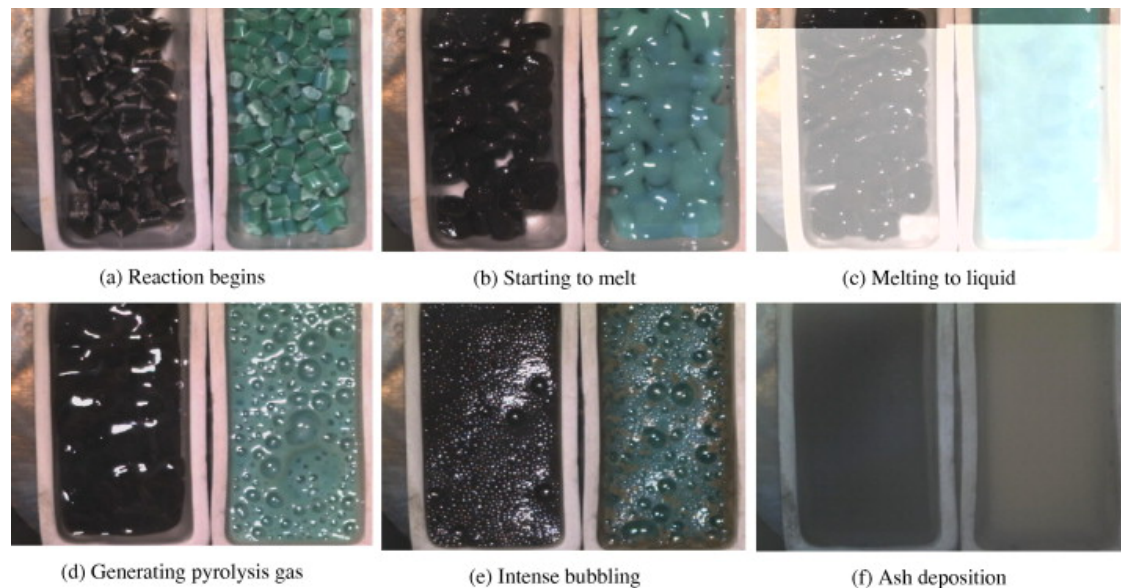


Figure 3.15: Morphological changes during pyrolysis of Polyethylene (left) and Polypropylene (right) by high-speed infrared camera. Figure taken from Wang *et al.*²⁵⁰

While melting occurs at lower temperatures than decomposition, accurate quantification the gas-liquid phase-change is crucial. The competition with degradation determines whether long-chain molecules decompose further or form stable gas-phase products Secondary cracking can occur both in the liquid- and gas-phase. The latter

occurs both inside the bubbles in the melt and in the reactor's bulk gas-phases before volatiles cool down. These three cracking environment have distinct selectivity.

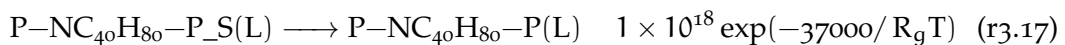
Because of the lower concentrations, gas-phase reactions have higher selectivity towards unimolecular pathways such as unzipping and reactions forming short-chain products. Condensation to polycyclic aromatic hydrocarbons (PAHs) and soot occurs mainly in gas-phase or through heterogeneous wall reactions. Notable exceptions are polymers with aromatic rings in their backbone or strong cross-linking (e.g., PET and PU) and those that form complex polyene structures (e.g., PVC). To accurately predict product selectivity, all relevant timescales need to be accurately quantified. The equipment vessel and mass-flows control the reactor gas residence times, while phase-change phenomena impact liquid and bubble cracking. The following sections provide a simplified approach to model these transfer rates and incorporate them into the overall pyrolysis description.

The proposed kinetic model represents phase-change through chemical reactions placed at the beginning of the mechanism. These kinetics can be removed if other phase-change models are available.

3.1.3.1 Melting kinetics

According to the starting material, different phase transition can take place upon heating. For instance, polypropylene is characterized by several types of solid-phases and the corresponding phase-transitions²⁵². Conversely, polystyrene is generally in the glass state at room temperature²¹. Polyethylene is a semi-crystalline material, i.e., it is characterized by the coexistence of an amorphous and a crystalline region. Upon heating, the first physico-chemical transformation of the polymer is melting of the crystalline phase. In the case of HDPE, this first-order phase transition occurs at 130°C in a narrow temperature range²¹.

To avoid considering a ternary phase system (solid, liquid, and gas), both crystalline, amorphous, and molten state are represented as liquid-phase species. As mentioned, the same mid-chain species " $P-NC_{40}H_{80}-P$ " describes the amorphous and molten state as they have similar thermodynamic properties^{21,232}. Conversely, the crystalline phase is represented by the additional species " $P-NC_{40}H_{80}-P_S$ ". The model incorporates a melting reaction to represent the phase transition of the form:



The model employs an activation energy of 37 kcal mol⁻¹, although the melting energy barrier is ~8 kcal mol⁻¹^{21,232}. This is because melting is an isothermal and isobaric process²¹. To capture this behaviour in the model, the proposed kinetic parameters allow the transition to occur within a narrow temperature range. As the melting temperature is 130°C, the rate employs a correspondingly high frequency factor. DSC and DTA experimental data could be employed to derive fitting-kinetics analogously to

one-step TGA models. However, the scarcity and scattering of experimental data in the scientific literature hinders reasonable application of this methodology.

The effectiveness of this approach is demonstrated in Section 3.2. Considering HDPE, good agreement between predicted and experimental melting profiles (DSC and DTA) is achieved. The model employs a combination of the crystalline and molten species according to the material initial crystallinity. LDPE has a lower crystallinity compared to HDPE²¹. While this approach allows to consider the difference in heat-flux profiles, it does not account for LDPE having a lower melting temperature. On the one hand, melting can be represented through bimolecular reactions, such that T_m decreases with the amorphous-phase content. However, as melting has low enthalpy changes, the impact of this improvement is expected to mildly affect model predictions.

3.1.3.2 Bubble physical-chemistry

An accurate description of the phase-change consequent to short-chain products volatilization requires evaluation of several crucial phenomena. Bubbles both facilitate mass transport of volatiles and influence heat transfer. Their presence reduces local thermal conductivity, induces internal convection circulations, and alters radiation absorption²⁵³. Bubble bursting also creates locally higher surface areas, enhancing interface mass and heat transfer. To the author's knowledge, few studies in literature have addressed the complexity of the phenomena involved⁶⁵. Wichman²⁵⁴ proposed a 1-D model accounting for the key global quantities involved, but lacked experimental validation. Butler²⁵³ proposed an in-depth analysis of the physical phenomena in microgravity combustion. The author employs a 1-D model coupled with a Lagrangian description of bubbles in the polymer melt.

Bubble evolution generally involves four distinct stages: nucleation, growth, migration, and burst²⁵³. The initial stage corresponds to the homogeneous nucleation of a bubble consequent to volumetric liquid-phase reactions. The degradation forms clusters of volatiles that act as seed for bubble nucleation. These clusters can surpass a critical size and progress to growth if they continue to collide with surrounding liquid volatiles. The critical size for bubble nucleation (the formation of a physical interface) corresponds to the bubble-liquid thermal, chemical, and mechanical equilibrium. Heterogeneous nucleation on surfaces and impurities involves lower energy barriers but has lower importance. As incondensable gases act as nucleation seeds, homogeneous nucleation is the dominant pathway during polymer degradation^{253,255}. Once nucleated, the bubble expands by colliding with and absorbing additional volatile molecules, while buoyancy and internal recirculations cause the bubble to rise. Bubbles burst upon reaching the polymer-gas interface, releasing the trapped gas to the environment.

Classical Nucleation Theory^{256,257} (CNT) provides a framework to estimate homogeneous nucleation rates per unit volumes (r_{cnt}). These rates are expressed through an Arrhenius-like equation as:

$$r_{\text{cnt}} = \sqrt{\frac{2\sigma}{\pi m_{\text{mol}}}} \exp\left(-\frac{16\pi\sigma}{3k_b T(P_{\text{eq}} - P_l)^2}\right) \quad (3.14)$$

where σ is the surface tension, m_{mol} the molecular mass, k_b the Boltzmann constant, and P_{eq} and P_l are the equilibrium and liquid pressure respectively. The frequency factor is in the order of 10^{11} s^{-1} , while the activation energies are in about 10-20 kcal mol $^{-1}$ ²⁵³. While CNT offers a starting point, it often overestimates nucleation due to its simplified nature. More complex models have been proposed to account for additional factors like elastic stress and macromolecular presence^{258,259}, but these often require empirical constants and lack general predictive power^{253,255}.

Once a bubble nucleates, it grows by mass transfer of volatile species from the surrounding liquid. The Epstein-Plesset law²⁶⁰ estimates this mass flux for any volatile species " j " (\dot{m}_{ev}^j) as:

$$\dot{m}_{\text{ev}}^j = \mathfrak{D}_j \cdot 4\pi r^2 \left(\frac{1}{r} + \frac{1}{\sqrt{\pi \mathfrak{D}_j t}} \right) (\rho_j^L - \rho_j^{IL}) \quad (3.15)$$

where " r " is the bubble radius and " t " the time since the bubble has nucleated. ρ_j^L and ρ_j^{IL} are respectively the density in the liquid bulk and liquid interface for species " j ". The interface concentration can be estimated assuming thermodynamic equilibrium, allowing even low boiling point components to contribute to bubble growth²²⁸.

The Epstein-Plesset equation employs several species properties. Equilibrium information such as vapour pressures or Henry parameters are reported in the NIST database¹⁰⁰ or can be estimated with Nannoolal's group contribution method²⁶¹. The liquid-phase diffusivity of species " j ", \mathfrak{D}_j , are estimated with the Free Volume Theory^{244,262-264} (FVT) applied to solvents in amorphous polymers^{65,263} as:

$$\mathfrak{D}_j = \mathfrak{D}_{0j} \exp\left(-\frac{\beta V_j^{0K}}{T + k_{22} - T_{g2}}\right) \quad (3.16)$$

where β and k_{22} are polymer-specific parameters related to the WLF theory^{244,264,265}. V_j^{0K} is the 0K molar volume of the volatile which can be evaluated through group contribution methods²⁴⁴. \mathfrak{D}_{0j} is the compound specific pre-exponential factor that requires experimental estimation. Values of \mathfrak{D}_{0j} not tabulated are estimated the approach proposed by Faravelli *et al.*⁶⁵ by linearization on their molar volume at 0K. Specifically, given two reference compounds values A and B, the diffusivity of any species j is evaluated as:

$$\mathfrak{D}_j = \exp\left(\ln(\mathfrak{D}_B) + \frac{\ln(\mathfrak{D}_B) - \ln(\mathfrak{D}_A)}{V_B^{0K} - V_A^{0K}} (V_j^{0K} - V_A^{0K})\right) \quad (3.17)$$

Bubble growth is also influenced by phenomena beyond simple diffusion^{266–269}. Buoyancy-driven convection, wake entrainment, and secondary nucleation induced by the growing bubble itself can all play a role. Additionally, bubble migration through mechanisms like buoyancy or Marangoni effects can occur, but the high viscosity of the polymer melt often limits their significance. Coalescence of bubbles during their rise can also reduce the overall gas-liquid exchange surface area. A crucial parameter in this process is the bubble pressure. Due to surface tension, smaller bubbles experience a higher internal pressure compared to larger ones. This pressure impacts the degradation pathways of volatile species within the bubble due to the increase in concentrations.

3.1.3.3 Average bubble distribution and boiling kinetics

Modelling the complete volatile phase-change process is beyond the scope of this work. The rate-limiting step depends on the specific compound involved. For small volatiles, nucleation and bubble growth might be equally important. Conversely, long-chain species are unable to act as nucleation seeds and evaporate through diffusion to existing bubbles. This work proposes a simplified approach based on bubble nucleation and growth phenomena.

The macroscopic phenomenon consequent to the volatilization phenomenon is the mass-loss curve. The bubbles formed during the degradation profiles are different, but share the average behaviour. The degradation curves allow to recover "*a posteriori*" the average bubble history. Several assumptions are made to simplify the problem. N_b bubbles per unit mass are considered, all with identical and simultaneous behaviour. Each bubble forms at its nucleation radius, and grows according to a bubble mass balance of the form:

$$\frac{dr}{dt} = \frac{\dot{m}_{ev,b}}{4\pi r^2} \frac{R_g T}{MW_{ev} P(r)} \quad (3.18)$$

where MW_{ev} is the average molecular weight of the evaporating mixture (represented by $C_{30}H_{62}$), and $\dot{m}_{ev,b}$ is the evaporating mass flux per bubble. The total mass evaporation flux is estimated in post-processing from the results of the detailed model of Faravelli *et al.*⁶⁵. All bubbles simultaneously burst when the gas volume is 10% of the liquid one, and immediately nucleate again at the critical radius.

Each bubble shares the same history as the others, but each begins at a distinct point in time. Therefore, the average properties of each bubble are equivalent to the instantaneous distribution-average properties. The distribution per unit mass is considered to account for the variation in the polymer mass. As mentioned, the impact of the phase-change is the strongest for long-chain compounds. Bubble growth is the rate determining step for their evaporation, and the model employs the Epstein-Plesset

equation to describe their phase-change. The functional form employs the conversion-average distribution parameters computed from the single bubble evolution as:

$$\dot{m}_{ev}^j = \mathfrak{D}_j \cdot \left(\frac{S}{r} \Big|_{av} + \frac{S}{\sqrt{t}} \Big|_{av} \frac{1}{\sqrt{\pi \mathfrak{D}_j}} \right) (\rho_j^L - \rho_j^{LL}) \quad (3.19)$$

The specific average bubble transport parameters are then evaluated averaging the bubble history over the polymer mass conversion (χ). For instance, the S/r parameter per unit mass is obtained integrating:

$$\frac{S}{\sqrt{t}} \Big|_{av, m_L} = \int_{\chi=0}^{\chi=1} 4\pi \frac{r}{m_L} d\chi \quad (3.20)$$

Considering mass loss profiles in the temperature range 400-900°C and assuming $N_b = 10^5$ bubbles kg⁻¹, the following values are estimated:

$$\frac{S}{r} \Big|_{av, m_L} = 10^4 \text{ m kg}^{-1} \quad (3.21)$$

$$\frac{S}{\sqrt{t}} \Big|_{av, m_L} = 10^5 \text{ m}^2 \text{s}^{-0.5} \text{kg}^{-1} \quad (3.22)$$

$$P_b \Big|_{av} = 1.3 P_{ext} \quad (3.23)$$

$$V_b \Big|_{av, m_L} = 10^{-4} \text{ m}^3 \text{kg}^{-1} \quad (3.24)$$

To obtain real-time values for the average bubble parameters, they are multiplied by the instantaneous polymer mass. The total number of bubbles per unit mass is assigned "*a priori*" and assumed constant in time. Varying N_b of orders of magnitude, the resulting transport parameters have been verified to not be significantly affected.

The proposed approach requires calculating the bubble phase composition, which can be computationally expensive. This is because it involves assuming thermodynamic equilibrium at the interface, doubling the number of equations to solve and potentially leading to numerical stiffness. To address this challenge and promote broader applicability, a kinetic approach is employed. Indeed, boiling is a volumetric phenomenon characteristic of the reacting system, and is therefore reasonable to represent it through the volumetric reactions. As discussed in Section 3.1.1.2, ULMW and ULLMW compounds in the mechanism directly form as gas-phase stable species. For each RLMW compound, the model introduces a single irreversible reactions representative of the proposed boiling model. For instance, phase-change of C₃₀H₆₀ is represented through the reaction:



The kinetic parameters for these reactions are obtained through simulation of the kinetic mechanism coupled with the separate boiling model. Each species evaporation rate is regressed to an Arrhenius form across a temperature range of 400-900°C. The resulting activation energies (15-40 kcal mol⁻¹) are higher than to typical evaporation

enthalpy changes (5-15 kcal mol⁻¹). However, these parameters reflect the competition of kinetics and evaporation phenomena. At low temperatures, the rate determining step is volatiles formation (40-60 kcal mol⁻¹^{15,42}). Conversely, boiling is the controlling factor at higher temperatures.

Table 3.5: Kinetic parameters of evaporation reactions for RLMW species (units cm, mol, s, cal).

RLMW species	A	E _{act}
NC ₁₆ H ₃₄	2.95E+05	14300
NC ₁₆ H ₃₂	3.94E+05	15000
NC ₁₆ H ₃₀	4.48E+05	15400
NC ₃₀ H ₆₂	1.87E+06	20700
NC ₃₀ H ₆₀	1.44E+06	20100
NC ₃₀ H ₅₈	1.66E+06	20500
NC ₄₅ H ₉₂	1.21E+07	27800
NC ₄₅ H ₉₀	9.33E+06	27200
NC ₄₅ H ₈₈	1.05E+07	27500
NC ₆₀ H ₁₂₂	1.99E+07	31200
NC ₆₀ H ₁₂₀	1.83E+07	31000
NC ₆₀ H ₁₁₈	1.92E+07	31200

3.1.4 Thermochemistry and transport properties

The kinetic mechanisms describes the changes in the reacting mixture in terms of chemical composition. This composition allows for estimating the instantaneous mixture properties from data on pure substance properties and appropriate mixing rules. According to the CHEMKIN format, the reaction mechanism is complemented by the definition of the thermodynamic and transport properties of the pure substances.

The proposed kinetic mechanism involves only irreversible reactions. While not essential for the kinetic mechanism itself, thermodynamic property estimation allows for energy balance calculations. The main parameters of interest are therefore reaction and phase-change enthalpies.

The following Sections describe the definition of the thermodynamic properties for LMW and HMW compounds. A brief description on evaluation of gas- and liquid-phase transport properties is also given.

3.1.4.1 LMW thermochemistry

For low molecular weight species, both gas- and liquid-phase thermochemical properties are required. First gas-phase properties of radicals and stable LMW are evaluated. These are then employed to estimate the liquid-phase values from phase-change data. For liquid-phase properties, the critical temperature (T_c) constitutes a discontinuity which requires appropriate consideration.

The gas-phase thermochemistry is evaluated according to the group-contribution method proposed by Benson⁵⁸ with updated values^{270–272}. Currently, more accurate methods like quantum-chemical calculations or machine learning are available in the scientific literature^{273–275}. However, considering uncertainties in polymer characterization and plastic waste variability, the current approach offers acceptable accuracy, particularly for simple molecules.

Group contribution methods decompose molecules into functional groups with assigned enthalpies, entropies, and heat capacities. Each atom's environment (nearest neighbors) defines its group type. Non-next-nearest Neighbour Interactions (NNNI) are incorporated through corrections such as gauche (1-4) and pentane (1-5) interferences^{58,271}. For instance, n-hexadecane ($C_{16}H_{34}$) is represented by a combination of 14 "C/C₂/H₂" (secondary carbon) and 2 "C/C/H₃" (primary carbon) groups. The notation defines the central atom, followed by the number and type of bonded neighbors. For instance, the group "C/C₂/H₂" represents an alkyl carbon (C) bound to 2 alkyl carbons (C₂) and 2 hydrogens (H₂), i. e., a secondary carbon. Different bond types (e. g., single, double) are also considered. For example, the group "CD/H₂" represents a terminal double bond with two hydrogens.

The thermodynamic properties of the molecule are then obtained by summation of the groups' values. For instance, the formation enthalpy of n-hexadecane ($\Delta h_{C_{16}H_{34}}^{f,0}$) is obtained as:

$$\Delta h_{C_{16}H_{34}}^{f,0} = 14\Delta h_{C/C_2/H_2}^{f,0} + 2\Delta h_{C/C/H_3}^{f,0} = -90.0 \frac{\text{kcal}}{\text{mol}} \quad (3.25)$$

The value computed through this methodology is within ~ 0.5 kcal mol⁻¹ from the experimental values^{100,276}. The high-temperature limit of the heat capacity (c_p) accounts for the number of internal rotors in the molecule²⁷⁷. The number of rotors reduces the number of vibrational modes and the high temperature value of c_p .

The thermochemistry properties of radicals are derived from the stable counterparts. This involves modifying group contributions based on the radical location. Appropriate groups are introduced for both the radical center and the nearest neighbours. For instance, the secondary radical of n-hexadecane ($C_{16}H_{33}$) is described by "C./C₂/H" (the radical site) and "C/C/C./H₂" (the adjacent carbon). The formation enthalpy is calculated as:

$$\Delta h_{C_{16}H_{33}}^{f,0} = \Delta h_{C_{16}H_{34}}^{f,0} - (3\Delta h_{C/C_2/H_2}^{f,0}) + \Delta h_{C./C_2/H_2}^{f,0} + 2\Delta h_{C/C/C./H_2}^{f,0} \quad (3.26)$$

The computed value is -44.0 kcal mol⁻¹, which is similar to the one estimated by RMG²⁷³ of -43.2 kcal mol⁻¹. The error is higher than the molecule counterpart, but still lower than 1 kcal mol⁻¹.

The evaluated thermochemical properties are regressed to a NASA polynomials format as required by the CHEMKIN format²²⁶. These polynomials are defined such that:

$$\frac{c_p}{R_g} = a_1 + a_2 T + a_3 T^2 + a_4 T^3 + a_5 T^4 \quad (3.27)$$

$$\frac{h}{R_g} = a_1 T + \frac{a_2}{2} T^2 + \frac{a_3}{3} T^3 + \frac{a_4}{4} T^4 + \frac{a_5}{5} T^5 + a_6 \quad (3.28)$$

$$\frac{s}{R_g} = a_1 \ln(T) + a_2 T + \frac{a_3}{2} T^2 + \frac{a_4}{3} T^3 + \frac{a_5}{4} T^4 + a_7 \quad (3.29)$$

where c_p is the molar specific heat capacity, h the specific molar enthalpy, s the specific molar entropy, and R_g the ideal gas constant. The CHEMKIN format employs two sets of parameters to describe a broad temperature range of 300-5000K. In the present work, a single set is employed to cover a more limited temperature range of 300-2000K. Further work will address extension of the temperature range appropriately differentiating the parameters in two sets²⁷⁷.

Estimating liquid-phase thermodynamic properties is more challenging due to limited literature compared to gas-phase data. With respect to polymer degradation, the key parameters affecting the process are the reaction and evaporation enthalpies. The standard NASA polynomial format used for gas-phase species is not well-suited for representing liquid-phase properties, particularly near the critical point where specific heat capacity diverges²⁷⁸. This work employs a combined approach to include liquid-phase species in the CHEMKIN format. Above the critical temperature, gas-phase NASA-polynomials are considered. On the other hand, for $T < T_c$ the parameters are estimated from phase-change thermochemistry. The transition between the two sets of NASA polynomials is defined breakpoint temperature ($T_{L \rightarrow G}$)

The difference between gas and liquid molecules is related to the solvation energy. Estimation of Gibbs free solvation energies is a reliable method to properly assess liquid-phase thermochemistry²⁷⁹. As mentioned, the kinetic mechanism employs only irreversible reactions. Consequently, the focus is estimating species heat capacities and enthalpies, and in turn reaction and phase-change enthalpies. Condensed-phase properties are typically solvent-dependent. However, for polymers characterized by oligomers formation, the functional groups remain largely unchanged across the degradation process. The species thermochemical properties do not vary considerably, and the pure component data also represent evaporation from the polymer melt.

The molar liquid-phase enthalpy of species "j", h_L^j , is estimated from the gas-phase (h_G^j) and evaporation (Δh_{ev}^j) enthalpies:

$$h_L^j(T) = h_G^j(T) - \Delta h_{ev}^j(T) \quad (3.30)$$

where gas-phase enthalpies are determined as previously described. Normal vaporization enthalpies ($\Delta h_{ev}^j(T_{b,n})$) and entropies ($\Delta s_{ev}^j(T_{b,n})$) are computed through the group-contribution method proposed by Kolska *et al.*²⁸⁰. The method proposed by Mehandoust *et al.*²⁸¹ offers an alternative approach when an exact chemical structure is complex to define. The normal and critical temperatures are obtained from databases¹⁰⁰ or evaluated through the group contribution methods proposed by Nannoolal *et al.*^{282,283}. The vaporization enthalpy for $T < T_c$ is evaluated through the Watson correlation^{284,285}:

$$\Delta h_{ev}^j(T) = \Delta h_{ev}^j(T_{b,n}) \left(\frac{T_c - T}{T_c - T_{b,n}} \right)^{0.38} \quad (3.31)$$

where the temperature exponent of $n = 38$ has been evaluated as appropriate for aliphatic hydrocarbons^{285,286}. Considering n-hexadecane, the approach results in $\Delta h_{ev}(T_{b,n}) = 13 \text{ kcal mol}^{-1}$ and a $\Delta h_{ev}(298K) = 18 \text{ kcal mol}^{-1}$. The estimated liquid-phase formation enthalpy of $C_{16}H_{34}(L)$ ($108.0 \text{ kcal mol}^{-1}$) shows good agreement ($\sim 1 \text{ kcal mol}^{-1}$) compared to the NIST database value ($-109.0 \text{ kcal mol}^{-1}$). For $T > T_c$, the liquid-phase enthalpies are assumed equal to the gas-phase ones.

To this aim, the liquid heat capacity is computed through two complementary methodologies. At $T < 490\text{K}$ the Ruzicka-Domalski correlation²⁸⁷ is employed, while at $T > 490\text{K}$ $c_{p,L}$ is computed from dh_L/dT . To obtain meaningful parameters, the liquid-phase NASA-polynomials are obtained regressing $c_{p,L}$ for $T < 0.97T_c$ to avoid the divergence at the critical temperature²⁷⁸. The other NASA parameters are then evaluated from evaporation enthalpies and entropies. The transition temperature between the liquid and gas polynomials (T_{LG}) is defined such that enthalpies are continuous. Since $c_{p,L}$ is underestimated approaching T_c , this results in a discontinuity of c_p at T_{LG} and the latter being $\approx 20 \text{ K}$ higher than T_c .

Direct regression using the liquid-phase enthalpy to obtain NASA polynomials leads to unphysical results for liquid-phase specific heat capacity ($c_{p,L}$) and entropy (s_L). To address this, a combined approach is employed to derive the heat capacities. The low temperature value ($T < 490\text{K}$) is calculated through the Ruzicka-Domalski group-contribution method²⁸⁷. At $T > 490\text{K}$, $c_{p,L}$ is obtained from the derivative of the liquid enthalpy:

$$c_{p,L}^j(T) = \frac{dh_L^j(T)}{dT} = \frac{d}{dT} \left(h_G^j(T) - \Delta h_{ev}^j(T) \right) \quad (3.32)$$

Considering short chain compounds, the calculation of $c_{p,L}$ at $T < 490\text{K}$ is equivalent for the two methodologies. Conversely, for long chain compounds extrapolation of estimated $\Delta h_{ev}(T_{b,n})$ values with the Watson correlation has low accuracy²⁸⁰. The issue lies both in the uncertainty to determine $T_{b,n}$, T_c , and $\Delta H_{ev,n}$. To improve the accuracy, the vaporization enthalpy is computed from $\Delta h_{ev}(298\text{K})$ for compounds with $T_c/T_{b,n} < 1.2$ (e.g., $C > C_{50}$). In this context, the method of Kolska *et al.*²⁸⁰ is employed.

The kinetic model does not necessitate the liquid-phase entropies. Therefore, it is estimated assuming that the liquid and gas entropy are equal at the breakpoint temperature. Further evaluation of the accuracy of this approach is discussed in the next paragraphs. Similar to the gas-phase approach, low-temperature liquid-phase NASA polynomials are obtained through a regression. As mentioned, to ensure physically meaningful coefficients, the regression is performed on the specific heat capacity. The resulting coefficients are then employed to estimate the enthalpy and entropy coefficients.

Figure 3.16 shows the estimation of thermochemical properties for $\text{NC}_{16}\text{H}_{34}(\text{L})$. The plot shows the comparison in terms of NASA polynomials (solid lines) for c_p , h , and s . The liquid-phase parameters evaluated from Δh_{ev} (Equation 3.30) are also reported (dashed-line). Literature data are reported when available (markers)¹⁰⁰, together with the Ruzicka-Domalski correlation extrapolated above 490K²⁸⁷. The color legend is employed to group the data by type: blue for gas-phase values, red for liquid- and extrapolated values, and black for the values employed in the kinetic model. Vertical lines are reported also to emphasize T_c (dashed-line) and $T_{\text{L}\rightarrow\text{G}}$ (dashed-dotted line).

In the current approach, $c_{p,L}$ (Figure 3.16a) is obtained as the derivative of the liquid-phase enthalpy (red dashed-line). The specific heat capacity of the liquid phase exhibits a characteristic divergence as it approaches T_c ²⁷⁸. This behaviour cannot be accurately captured by the 4th-order polynomials used in the NASA format, while maintaining good agreement across other temperature ranges. To address this limitation, the NASA regression on $c_{p,L}$ is performed for $T < 0.97T_c$, ensuring a monotonic behaviour of the functional form (solid red-line). As previously mentioned, the liquid-phase enthalpy (3.16b) and entropy (3.16c) are then recovered from these parameters.

At $T > T_c$, the species behaves as a dissolved gas. The gas-phase polynomials are employed as high temperature NASA set, neglecting any influence of dissolved gases solvation enthalpies. Additionally, considering $T_{\text{L}\rightarrow\text{G}} = T_c$ results in a discontinuity in the thermodynamic functions. The breakpoint temperature is therefore defined as the temperature where the extrapolated h_L intersects with h_G . While this approach introduces a slight overestimation of properties above T_c , it ensures continuity.

With respect to the experimental data, the proposed approach shows good agreement for c_p and h , but it overestimates the s_L . This overestimation has minimal impact on model performance because the kinetic mechanism only considers irreversible reactions.

The same methodology is employed to estimate the liquid-phase thermochemistry of radicals. Similar to stable species, gas-phase radical thermochemistry is employed and corrected with phase-change properties. To the author's knowledge, no phase-change data is available for radical species, and the vaporization properties of stable molecules are employed. This assumption implies similar reactivity for radicals in both gas and liquid-phase. Unlike ions, which benefit from charge delocalization and increased stability in condensed phases²⁸⁸, radicals are not expected to experience significant sta-

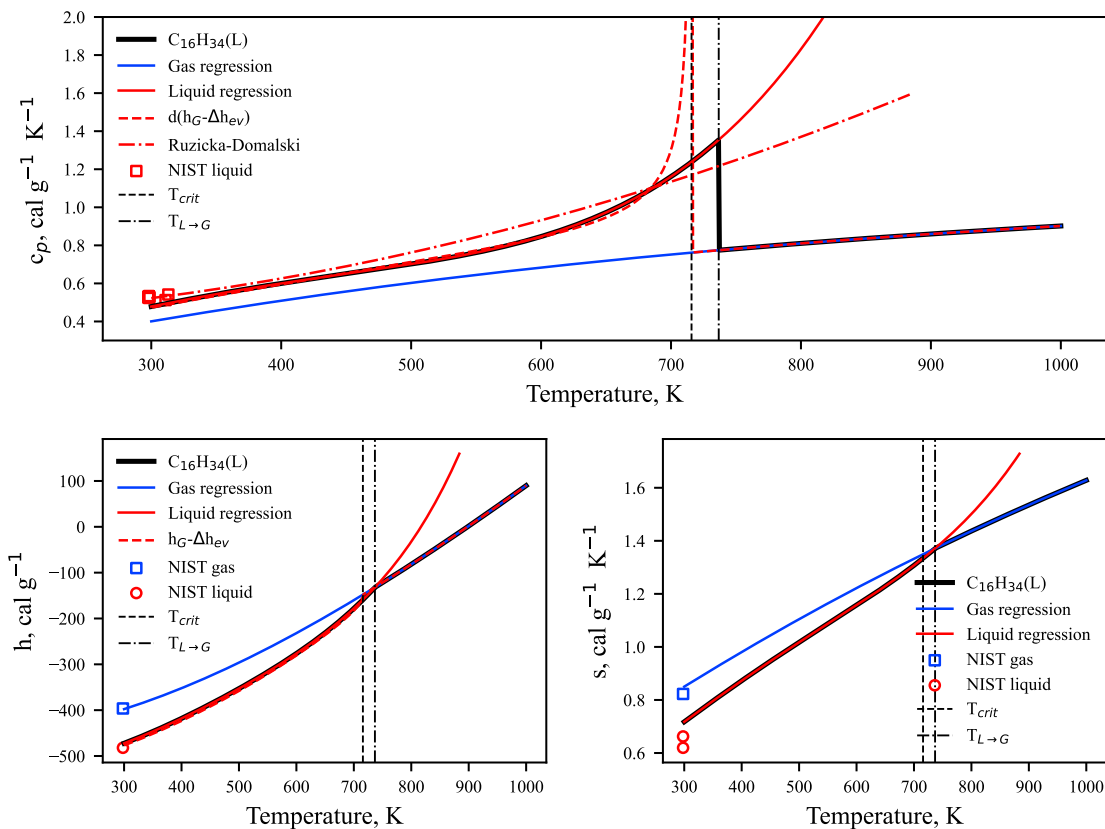


Figure 3.16: Thermodynamic parameters per unit mass of $C_{16}H_{34}(L)$ evaluated for gas (blue) and liquid (red) phase compared to the values employed in the model (black). The results are compared with experimental data¹⁰⁰ (marks) and the Ruzicka-Domalski correlation^{285,287}

bilization from solvent interactions^{43,56,146}. The evaluation of differences in stabilities due to the gas-liquid transposition requires further theoretical studies. Nevertheless, as shown in Section 3.2, the present approach provides accurate predictions for the heat requirements of the pyrolysis process.

3.1.4.2 HMW thermochemistry

Accurate estimation of thermochemical properties for HMW pseudo-species is crucial for the process. Indeed, the main energy requirement of the process is the heat to decompose long polymeric chains into low molecular weight compounds. These pseudo-species represent only fragments of the polymeric chains, and the approach proposed for LMW compounds requires specific tuning.

As shown in Figure 3.17, the thermodynamic properties per unit mass approach the same value asymptotically with increasing chain length. The sole difference lies in the critical point, which affects the breakpoint temperatures. Additionally, the Watson correlation predicts at increasing T_c a lower difference in gas and liquid

heat capacities. Two separate approaches are implemented to estimate the liquid-phase properties of molten HMW species.

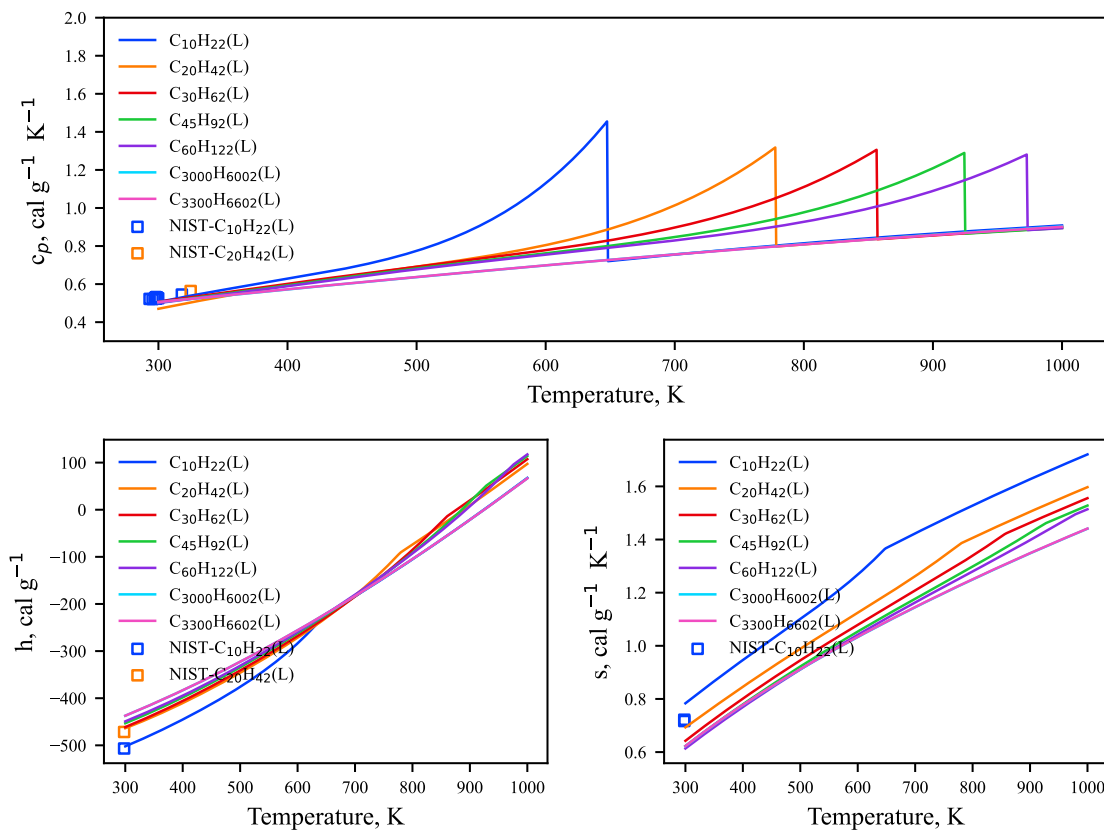


Figure 3.17: Thermodynamic parameters per unit mass evaluated for different n-alkanes as described in Section 3.1.4.1. The reported experimental data are from the NIST webbok¹⁰⁰

Specific heats and enthalpies are estimated following the group contribution of Benson⁵⁸ and Kolska *et al.*²⁸⁰. The groups defining the chain units account for them being bound to other parts of the polymer. For instance, the mid-chain species P–NC₄₀H₈₀–P is composed of 40 "C/C₂/H₂" groups. Similarly, the paraffin end-chain P–NC₄₀H₈₁ has 39 "C/C₂/H₂" and 1 "C/C₃H₃". The enthalpy of the fictitious gas-phase species is then translated to the liquid-phase through the evaporation enthalpies at 298K²⁸⁰. As with long LMW chains, the specific heat is evaluated with the Ruzicka-Domalski correlation at low T²⁸⁷ and from the enthalpy derivative at T>490K.

Conversely, entropy is estimated from two reference chains ("ref₁" and "ref₂") with similar functionalities but slightly different chain lengths. The first one is composed of 100 chain-units, while the latter has exactly 10 units more. These chains are chosen with a T_c>2000K to avoid overlapping with the operating conditions of interest. The thermochemical parameters of these reference are obtained as described for other LMW and are reported in Figure 3.17 as well.

The difference in entropy between "ref₁" and "ref₂" is attributed to the variation in chain-lengths, which corresponds to the different number of mid-chain units. The MC entropy is therefore recovered as difference in number of units as:

$$s_L^{MC}(T) = \frac{s_L^{ref_2}(T) - s_L^{ref_1}(T)}{10} \quad (3.33)$$

where 10 is the difference in number of mid-chain units between the two reference species. The same comparison is introduced to evaluate h_L^{MC} and s_L^{MC} . Similarly, end-chain properties are determined by subtracting the number of MC units in ref₁ (i. e., 100-2 = 98) from the corresponding reference paraffin or olefin. The paraffin end-chain is obtained from the ref₁ paraffin ("C₄₀₀₀H₈₀₀₂"), while the olefin end-chain is obtained from the ref₁ diolefin ("C₄₀₀₀H₇₉₉₈") as:

$$s_L^{P-NC_{40}H_{81}}(T) = \frac{s_L^{C_{4000}H_{8002}}(T) - 98 \cdot s_L^{MC}(T)}{2} \quad (3.34)$$

$$s_L^{P-NC_{40}H_{79}}(T) = \frac{s_L^{C_{4000}H_{7998}}(T) - 98 \cdot s_L^{MC}(T)}{2} \quad (3.35)$$

This approach can result in unphysical behaviour for ECs entropy (e. g., non-monotonic increase of entropy). The issue possibly lies in numerical errors involved in the estimation of the mid-chain which affect the end-chains. In such cases, to preserve a physical behaviour, the end-chain entropies are estimated starting considering the same gas-phase difference between the corresponding Benson groups. Nevertheless, as previously mentioned, the entropy has no impact on the model predictions. The thermochemistry of radicals is estimated with the same approaches previously discussed, i. e., from gas-phase differences between stable and radical counterpart.

The pyrolysis process also requires energy for the solid polymer to transition to a molten state. For PE, the crystalline phase is represented by the mid-chain species P-NC₄₀H₈₀-P_S, while the amorphous phase is described with P-NC₄₀H₈₀-P. As mentioned, the latter represents also the molten phase due to the similar thermochemical properties²³². For the crystalline phase, an approach similar to the gas-liquid transposition is employed. However, experimental data on heat capacities and melting enthalpy are incorporated to improve the accuracy²³².

Experimental data for the crystalline phase is limited to the theoretical melting temperature ($T_m=414.6$ K²³²) since this phase doesn't exist above that point. Using only this low-temperature data leads to unrealistic values at higher temperatures, causing issues for simulations. To this aim, the high temperature crystalline specific heat ($c_{p,c}$) is represented through the functional dependency of the Einstein theory²⁸⁹. While the Debye theory²⁹⁰ has better quantitative agreement, both theories converge at high temperatures.

The crystalline enthalpy and entropy are determined from the corresponding melting values (Δh_m and Δs_m). The entropy is estimated from the melting enthalpy at

the theoretical melting point as no literature data was found. Specifically, since at the phase-transition the Gibbs free energy is null:

$$\Delta s_m = \frac{\Delta h_m}{T_m} \quad (3.36)$$

Employing the Einstein and Debye theories for specific heat result in melting being exothermic at $T > 700\text{K}$. This theoretical prediction has no impact on the model simulations as the actual melting temperature for polyethylene is lower (414 K).

Figure 3.18 shows the evaluated (solid lines) thermodynamic properties of the amorphous (red) and crystalline (purple) phase compared to literature experimental data^{100,232,291–296} (marks). The dashed lines represent the critical review of experimental data proposed by Gaur and Wunderlich²³². A significant scattering in experimental data is observed. For instance, the formation enthalpy of PE obtained from combustion experiments varies from -1500 cal g^{-1} ²⁹⁷ to 50 cal g^{-1} ²⁹⁸, possibly owing to the different additives and inorganics in the polymer. Small errors also on the calorific value (<5%) translate in significant differences in the polymer formation enthalpies (400%). Similar variations are observed also for the polymer specific-heat, likely due to differences in degrees of crystallinity not reported.

The proposed approach has reasonable agreement over the investigated temperature range. The key parameter is the phase-change enthalpies which are coherent with experimental data as well²³². With respect to the crystalline specific heat, introducing a low temperature set of NASA polynomials is expected to improve model predictions. This would allow capturing the inflection observed at 300–400K temperature range while preserving a physical description at $T > T_m$. The entropy of the amorphous-phase is overestimated as previously described for liquid-phase compounds. Nevertheless, since the entropies are not employed in the kinetic mechanism, this error has no impact on model performances.

3.1.4.3 Species transport properties

Transport limitations, such as diffusion and heat transfer, can significantly affect product distributions and reaction times in complex reactors. Conversely, these phenomena are negligible in the simple systems considered in this work.

For more complex reactor modeling, transport properties like conductivities (k), viscosities (μ), densities, and diffusivities (\mathfrak{D}) are needed for both gas and liquid phases. The CHEMKIN format is employed for gas-phase properties, requiring parameters like collision diameters and dipole moments. These are then used to estimate transport properties through theoretical methods²²⁶. For liquid-phase properties, an in-depth study of estimation of transport properties is not performed as it does not affect the conditions of interest. Nevertheless, several correlations are employed to estimate the transport properties of the pure components. Further work is required to assess these properties in real systems and include appropriate mixing rules.

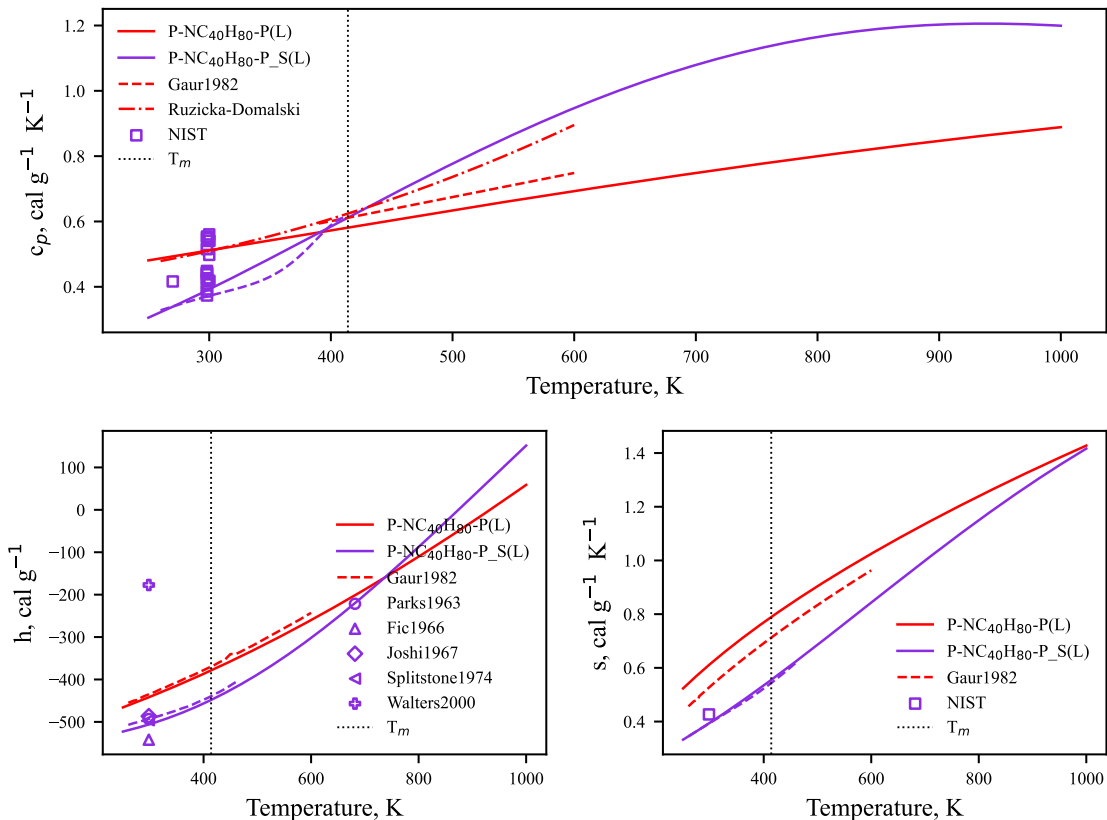


Figure 3.18: Thermodynamic parameters per unit mass evaluated for the crystalline (purple) and amorphous/molten (red) mid-chain species compared to literature experimental data^{100,232,291-296} (dashed-lines and marks).

The Nannoolal group contribution method is employed to boiling temperatures²⁸², critical properties²⁸³, vapour pressures²⁶¹, and viscosities²⁹⁹. The normal boiling point $T_{b,n}$ of each species is estimated as:

$$T_{b,n} = 59.344 + \frac{\sum N_i C_i + GI}{n^{0.6713} + 1.4442} \quad (3.37)$$

where N_i is the number of groups with contribution C_i , GI second order-corrections, and n the total number of atoms except hydrogen. The evaluated boiling temperature in K. The second order corrections GI are evaluated as:

$$GI = \frac{1}{n} \sum_i^m \sum_j^m \frac{C_{i,j}}{m-1} \quad (3.38)$$

where n is the total number of atoms except hydrogen, m the total number of interaction groups in the molecule, and $C_{i,j}$ the interaction between two different groups. Specifically, $C_{i,j}=C_{j,i}$ and $C_{i,i}=0$.

As mentioned, the critical properties are also evaluated from the Nannoolal group contribution method²⁸³ as:

$$T_c = T_{b,n} \left(0.6990 + \frac{1}{0.9889 + (\sum N_i C_i + GI)^{0.8607}} \right) \quad (3.39)$$

$$P_c = \frac{MW^{-0.14041}}{(0.00939 + \sum N_i C_i + GI)^2} \quad (3.40)$$

$$V_c = \frac{\sum N_i C_i + GI}{n^{-0.2266}} + 86.1539 \quad (3.41)$$

where the critical temperature T_c is in K, the critical pressure P_c in kPa, and the critical molar volume in $\text{cm}^3 \text{ mol}^{-1}$. The second order contribution GI are evaluated with equation 3.38 also in this case. Notably, the proposed method predicts for high molecular weights a value of $T_c < T_b, n$.

The boiling and critical properties are employed to estimate the acentric factor (ω) through the Lee and Kesler correlation³⁰⁰:

$$\omega = \frac{-\ln P_c - 5.92714 + 6.09648 \frac{T_c}{T_{b,n}} + 1.28862 \ln \left(\frac{T_{b,n}}{T_c} \right) - 0.169347 \left(\frac{T_{b,n}}{T_c} \right)}{15.2518 - 15.6875 \frac{T_c}{T_{b,n}} - 13.4721 \ln \left(\frac{T_{b,n}}{T_c} \right) + 0.435777 \left(\frac{T_{b,n}}{T_c} \right)} \quad (3.42)$$

The estimation of the acentric factor heavily relies on the accuracy of the critical properties²⁸⁵.

The critical point and ω are employed to evaluate the gas-phase Lennard-Jones parameters through the correlation of Holley *et al.*³⁰¹:

$$\sigma_{LJ} = (2.3511 - 0.0874\omega) \left(\frac{T_c}{P_c} \right)^{\frac{1}{3}} \quad (3.43)$$

$$\frac{\epsilon_{LJ}}{k_b} = (0.7915 + 0.1693\omega) T_c \quad (3.44)$$

where σ_{LJ} is the Lennard-Jones collision diameter in Angstroms, and ϵ_{LJ}/k_b is the Lennard-Jones potential well depth in K. These parameters are reported in the CHEMKIN transport file and allow estimating conductivities, diffusion coefficients, and viscosities for gas-phase species²²⁶. Currently, this work considers null values for the dipole moment and polarizability.

Vapour pressures (P_{ev}) are also evaluated through the group contribution method proposed by Nannoolal²⁶¹ as:

$$\log_{10} P_{ev}(T) = (4.1012 + dB) \left(\frac{T - T_{b,n}}{T - 0.125T_{b,n}} \right) \quad (3.45)$$

where the evaluated pressure is in atm, and the dB is a molecule parameter evaluated as:

$$dB = \left(\sum N_i C_i + GI \right) - 0.176055 \quad (3.46)$$

The values of the group contribution are specific for vapour pressures, while the second-order corrections are evaluated as equation 3.38. The vapour pressures are then regressed to the Yaws form³⁰²:

$$\log_{10} P_{ev}(T) = a_0 + \frac{a_1}{T} + a_2 \log_{10}(T) + a_3 T + a_4 T^2 \quad (3.47)$$

where the vapour pressure is in mmHg and the temperature in K.

Liquid viscosities (μ_L) are also evaluated with the Nannoolal group contribution method²⁹⁹. A similar functional dependence to the vapour pressure is proposed:

$$\ln \left(\frac{\mu_L(T)}{1.3} \right) = -dB \left(\frac{T - T_\mu}{T - 0.0625T_\mu} \right) \quad (3.48)$$

where the liquid-phase viscosity is in cP and the temperatures are in K. The dB values are evaluated similarly to the vapour pressures as well with the following correlation:

$$dB = 3.777 + \frac{\sum N_i C_i + GI}{n^{-2.5635} + 0.0685} \quad (3.49)$$

employing equation 3.38 for evaluation of the second order interaction contribution GI. T_μ is the viscosity reference temperature, which is also estimated with group contribution methods:

$$T_\mu = 21.8444 T_{b,n}^{0.5} - 231.1361 + \frac{(\sum N_i C_i + GI)^{0.9315}}{n^{0.6577} + 4.9259} \quad (3.50)$$

The evaluated viscosities are then regressed to the Yaws form³⁰²:

$$\log_{10} \mu_L(T) = a_0 + \frac{a_1}{T} + a_2 T + a_3 T^2 \quad (3.51)$$

where the viscosity is in kPa s and the temperature in K.

Additional properties of interest are liquid-phase densities (ρ_L), conductivities (k_L), and diffusivities (D_L). The first is evaluated with the group contribution method proposed by Elbro *et al.*³⁰³ as:

$$\rho_L(T) = \frac{MW}{\sum N_i (A_i + B_i T + C_i T^2)} \quad (3.52)$$

The group contribution is validated in the temperature range of 200-500 K but proves able to predict also polymer densities³⁰³. The obtained density is then regressed to the Yaws form³⁰²:

$$\rho_L(T) = a_0 a_1^{-\left(1 - \frac{T}{T_c}\right)^{a_2}} \quad (3.53)$$

The liquid-phase thermal conductivity is estimated through the group contribution method proposed by Sastri and Rao³⁰⁴. In this approach, the thermal conductivity at the boiling point is first evaluated and then its temperature dependence is considered similarly to the Watson correlation²⁸⁴. The resulting equation employs first order (C_i) and second order additive corrections ($C_{i,c}$) as:

$$k_L(T) = \left(\sum N_i C_i + \sum N_{i,c} C_{i,c} \right) \cdot 0.160^{1 - \left(\frac{T_c - T}{T_c - T_{b,n}} \right)^{0.2}} \quad (3.54)$$

The evaluated conductivity is then regressed to the Yaws functional form³⁰²:

$$\log_{10} k_L(T) = a_0 + a_1 \left(1 - \frac{T}{a_2}\right)^{\frac{2}{7}} \quad (3.55)$$

As discussed in Section 3.1.3, liquid-phase diffusivities are evaluated with the Free Volume Theory^{244,262–264}. Additional correlations have been proposed in literature³⁰⁵, but most of them are suitable for solvent and solutes of similar sizes. The present approach simplifies the estimation of diffusivities considering solutes significantly smaller than the solvent.

3.2 MODEL VALIDATION

The proposed kinetic model is validated with a wide range of experimental data reported in the scientific literature. Significant data scattering is observed, possibly because of both plastic-to-plastic variability and experimental setup employed. The former results from each polymer exhibiting different amounts of weak-links, impurities, additives, and initial molecular weight. These differences primarily impact the onset degradation temperature⁶⁵, which generally shows the highest variability. The experimental facility also affects the degradation profiles. The temperature has the strongest effect, but the carrier gas flowrate, sample pan, and instrument geometry can introduce shifts of $\sim 10^\circ\text{C}$ ^{306,307}.

To minimize the influence of these factors, the validation focuses on experimental facilities (e.g., TGA, pyroprobes, micropyrolyzers) where transport phenomena and secondary cracking of released volatiles are negligible. The temperature range where these assumptions hold true varies depending on the polymer. For instance, heat transfer limitations for PE become relevant at 550°C in isothermal TGAs³⁰⁸ and at 600°C in pyroprobes³⁰⁹. The relevance of secondary gas-phase cracking reactions also increases with temperatures as consequence of high Stefan flows (low dilution) and low gas-phase degradation times. Specifically, at 600°C the characteristic degradation time of long normal hydrocarbon is about few seconds²⁵¹ and it decreases to milliseconds at 800°C ¹³³.

The following sections assess the semi-detailed kinetic model previously described with experimental data. Model simulations are performed through the OpenSMOKE++³¹⁰ numerical framework, and model performances are quantitatively assessed through the Curve Matching Score^{311,312}. The validation is performed in terms of characteristic degradation times (mass-loss profiles), product yields, and heat requirements. A comparison with the detailed model of Faravelli *et al.*⁶⁵ is also shown.

3.2.1 Physical and numerical model

The model considers the initial polymer to be in a semi-crystalline state at room temperature. The initial quantities of mid- and end-chains are evaluated from the initial average molecular weight as reported in Equation 3.1 and 3.4. The relative quantities of crystalline and amorphous phase are estimated from the polymer crystallinity. The initial amounts of weak-links is evaluated from the sample density as shown in Equation 3.13. When no information on the sample is available, the model considers average polymer values^{21,224}. Specifically, a value $MW_{av}^0 = 80 \text{ kg mol}^{-1}$ is considered⁵⁵. Similarly, for HDPE the model assumes a crystallinity of 80% and no weak-links ($\Delta E_{MC}^{RS} = 0$). With respect to LDPE, the initial crystallinity assumed is 50% together with a value of $\Delta E_{MC}^{RS} = -1000 \text{ kcal mol}^{-1}$.

The model treats the polymer sample as a zero-dimensional homogeneous system (a well-mixed semi-batch reactor). Mass balances are written for each species "j" in the liquid (m_L^j), bubble (m_B^j), and gas (m_G^j) phases:

$$\frac{dm_L^j}{dt} = -\dot{m}_{ev}^j + MW_j R_L^j V_L \quad (3.56)$$

$$\frac{dm_B^j}{dt} = \dot{m}_{ev}^j - \dot{m}_{out}^j + MW_j R_L^j V_L + MW_j R_B^j V_B |_{av} \quad (3.57)$$

$$\frac{dm_G^j}{dt} = \dot{m}_{out}^j \quad (3.58)$$

where R_L^j are the formation rates of species j due to liquid-phase reactions and R_B^j the homogeneous gas-phase reactions occurring in bubble-phase. \dot{m}_{ev}^j and \dot{m}_{out}^j are the mass flowrate entering and leaving the bubble-phase, respectively. If evaporation reactions are employed, formation of gas compounds in the bubble-phase is due to the term R_L and $\dot{m}_{ev}=0$. The total flowrate exiting the bubble-phase, \dot{m}_{out} is evaluated such that the average bubble pressure is constant in time.

The heat gain of the process, \dot{Q}_{out} , is evaluated from the energy balance on the sample (liquid + bubble-phase). The model assumes thermal equilibrium among liquid, bubble, and gas-environment, therefore a single temperature T is defined. The sample temperature profile is known "*a priori*" as it is set by the experimental facility. The energy balance equation is solved separately from the material balances to recover \dot{Q}_{out} :

$$\begin{aligned} -\dot{Q}_{out} = & \sum_i r_L^i \Delta H_{r_L}^i V_L + \sum_i r_B^i \Delta H_{r_B}^i V_b |_{av} + \\ & \sum_j \dot{m}_{ev}^j \Delta h_{ev}^j(T) + \left(\sum_j m_{Lj} c_{p,L}^j + \sum_j m_{Bj} c_{p,G}^j \right) \frac{dT}{dt} \end{aligned} \quad (3.59)$$

where r_L and r_B are respectively the reaction rates of the liquid and bubble-phase mechanism, ΔH_{r_p} the reaction enthalpies of phase P, and dT/dt is the known temperature

profile of the system. The sample energy balance does not account for the gas-phase as volatiles leave the reacting environment as they form. As previously mentioned, the kinetic model considers the crystalline polymer as a liquid-phase species and it represents melting heat through liquid-phase reaction enthalpies (ΔH_{rL}). Employing evaporation reactions involves a $\dot{m}_{ev}^j = 0$, while ΔH_{rL} accounts for evaporation enthalpies. The degradation process is endothermic, and the resulting heat gain is negative ($\dot{Q}_{out} < 0$). Charification reactions may cause exothermicity¹⁵², but these phenomena are not considered for PE.

The model represents secondary cracking occurring in bubble-phase through a simplified gas-phase kinetic mechanism analogous to the liquid-phase one. This mechanism employs the CRECK kinetic mechanism version 2301³ to describe the degradation of ULMW compounds. The same elementary kinetic parameters used in the CRECK mechanism for n-hexadecane are employed, while the same hydrogen and allylic selectivities as liquid-phase are considered.

The numerical integration is performed utilizing a robust stiff BDF integrator from the OpenSMOKE++ suite³¹⁰. This library provides advanced tools for simulating complex chemical reaction systems. The developments to perform 0D-simulations for this work are merged in the 0.21.0 version. The software is freely available for academic users⁴.

3.2.2 Model performances: Curve Matching Score

Model performance can be evaluated qualitatively (visual inspection) or quantitatively (metrics). The former relies on expert judgment to compare simulations with experiments. However, this approach is subjective to the differences in user background³¹³.

Quantitative assessment is generally performed with point-wise approaches such as the R^2 score. These methodologies define a set of score functions to measure the similarity between experimental and simulated datasets. The error is then estimated through a point by point comparison. For datasets with different x-coordinates, the simulated one is represented through cubic splines. These are then employed to recover the same x-values defined in the experimental dataset. These approaches are computationally efficient, but have several limitations. Point-wise approaches overlook trends and the chemical-physical behaviours inherent of experimental measurements. High scores are obtained even for considerable differences in model trends, making the approach potentially misleading. Figure 3.19a shows an example of this pitfall. The two models presented have similar point-wise scores, but only Model 1 captures the experimental trend. Point-wise approaches also struggle to discriminate between the models reported in Figure 3.19b. From a graphical comparison, model 1 proves to have better

³ available on GitHub at <https://github.com/CRECKMODELING/Kinetic-Mechanisms>

⁴ Available online at <https://www.opensmokepp.polimi.it/>

performances than model 2, with only a slight delay in reactivity. On the other hand, model 2 significantly anticipates the reactivity, overestimating the fuel degradation by ~ 100 K.

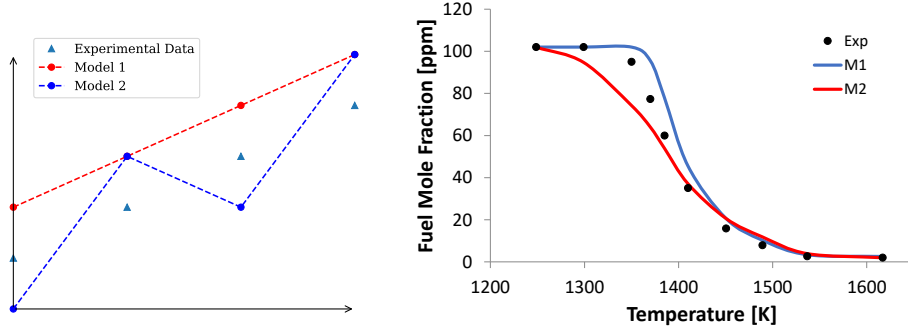


Figure 3.19: Comparison of different models and experimental data showing: a) the pitfall of point-wise approaches³¹³; b) typical fuel mole fractions in isothermal flow reactors³¹².

The Curve Matching Score (CM) is a quantitative trend approach that addresses limitations of point-wise methods^{311,312}. This methodology quantifies errors in terms of difference between functions and their derivatives, preserving the physical interpretation of the trends³¹². The CM score combines five individual indices that measure dissimilarities related to translation, dilatation, and shift between two curves representing the experimental and simulated data. Two curves F and G are generated using cubic spline interpolation of experiment and model data points, with their first derivatives labelled respectively F' and G'. The CM approach defines the following dissimilarities measurements.

$d_{L_2}^0$ is the generalization of the Sum of Squared Errors (SSE) to the continuous case as:

$$d_{L_2}^0(F, G) = \frac{1}{1 + \frac{\|F - G\|}{D}} \in (0, 1) \quad (3.60)$$

$d_{L_2}^1$ is a similar generalization of SSE but applied to the first derivatives of the two functions. This index is invariant to vertical translation but quantifies the dissimilarities between the slopes.

$$d_{L_2}^1(F, G) = \frac{1}{1 + \frac{\|F' - G'\|}{D}} \in (0, 1) \quad (3.61)$$

$d_{P_e}^0(F, G)$ and $d_{P_e}^1(F, G)$ are the Pearson correlation index respectively applied to F and G and their derivatives, which measures the disagreement between the trends of two curves.

$$d_{P_e}^0(F, G) = 1 - \frac{1}{2} \left\| \frac{F}{\|F\|} - \frac{G}{\|G\|} \right\| \in (0, 1) \quad (3.62)$$

$$d_{P_e}^1(F, G) = 1 - \frac{1}{2} \left\| \frac{F'}{\|F'\|} - \frac{G'}{\|G'\|} \right\| \in (0, 1) \quad (3.63)$$

The shift S measures the dissimilarities in terms of horizontal translation of the two functions and is defined as:

$$S = \max\left(1 - \frac{\delta}{D}, 0\right) \in (0, 1) \quad (3.64)$$

where δ is the horizontal shift obtained maximizing the sum of the previous indices

$$\delta = \operatorname{argmax}_{\delta} (d_{L_2}^0 + d_{L_2}^1 + d_{P_e}^0 + d_{P_e}^1) \quad (3.65)$$

The global Curve Matching index is the arithmetic average of the five values, where S is weighted twice to account for both left and right shifts as:

$$CM(F, G) = \frac{d_{L_2}^0 + d_{L_2}^1 + d_{P_e}^0 + d_{P_e}^1 + 2S}{6} \quad (3.66)$$

The Curve Matching index accounts for experimental uncertainty through a bootstrapping procedure. When no information on the uncertainty is available, a default value of $\sim 10\%$ is considered³¹³.

Similar to squared error, a score close to unity represents a perfect match, while values close to 0 imply significant deviations. The threshold to define a model as satisfactory varies according to the data type. For dynamic mass-loss profiles, $CM < 0.9$ corresponds to significant deviations. Conversely, in isothermal conditions a $CM > 0.8$ typically indicates good agreement with experimental data.

3.2.3 Characteristic degradation times: mass-loss profiles

Mass-loss profiles are the most common experiments performed in the scientific literature. These data involve heating the polymer at a controlled rate and recording the variation of total mass as function of time. Considering PE, the current validation considers approximately 100 mass-loss profiles datasets^{55,115,214,249,251,307,308,314–328}. The detailed model of Faravelli *et al.*⁶⁶ is reported for comparison as well.

Figure 3.20 shows the mass-loss profiles of HDPE and LDPE subjected to different thermal histories. Literature data exhibit a variability of $\sim 10\text{--}20^\circ\text{C}$ depending on the study. The difference becomes more pronounced at higher heating rates, reaching a discrepancy of 50°C at $HR=50^\circ\text{C}/\text{min}$ for both HDPE (Figure 3.20a) and LDPE (Figure 3.20b). Internal transport limitations caused by improper setting of the experimental setup might be responsible for these deviations. The semi-detailed model reproduces the detailed model across the entire investigated temperature range, although with a lower apparent activation energy. This discrepancy arises from the different kinetic parameters adopted in the two models. Additionally, the present work incorporates unzipping reactions, a crucial degradation pathway not considered by Faravelli *et al.*⁶⁶. Both models accurately describe HDPE mass-loss profiles (Figure 3.20a), within experimental uncertainty, as evidenced by the high CM scores. For LDPE degradation (Figure

3.20b), the simple correction introduced effectively captures the decrease in apparent activation energy.

Model performances are assessed also in isothermal conditions at atmospheric (Figure 3.20c) and vacuum (Figure 3.20d) pressure. While the temperature dependence is described with reasonable accuracy, both mechanisms underestimate the low temperature reactivity and predict higher apparent activation energies. Accounting for metal impurities and their low temperature catalytic pathways could improve model predictions. Pressure has negligible effect on liquid-phase kinetics, but it impacts evaporation of LMW products. For instance, under vacuum conditions the product distribution will shift towards heavier compounds as they evaporate before further decomposition. The primary source of discrepancies between the two kinetic models lies in the different phase-change description. The detailed model by Faravelli *et al.*⁶⁵ predicts shorter degradation times due to the formation of C₁₀₀-range compounds. Similarly, it predicts longer degradation times at higher pressures (not reported here). Conversely, the evaporation kinetics described in Section 3.1.3 are pressure-independent irreversible reactions. Consistent with experimental measurements, the present model does not predict significant variations in mass-loss profiles between atmospheric and vacuum conditions. Even for isolated droplets, the effect of pressure on evaporation is not straightforward³²⁹, and accounting for multiple complex phenomena is necessary. Further validation at non-atmospheric conditions, particularly focusing on product distribution, is required for a more comprehensive assessment of model predictions.

Figure 3.21 presents parity plots comparing for the onset ($m_L=90\%$), half-conversion ($m_L=50\%$), and final-conversion ($m_L=10\%$) temperatures (T) and times (t). Both HDPE and LDPE data are considered, demonstrating the effectiveness of the weak-links correction. While a wide scatter is observed particularly for onset temperatures, both the detailed and semi-detailed models exhibit good agreement across the investigated operating conditions. The semi-detailed model achieves higher average R^2 values, but the results are comparable overall.

At high T and HR, both mechanisms overestimate the reactivity. For dynamic conditions (Figure 3.21a), the model predicts a maximum half-conversion temperature of ~500°C. This occurs because the degradation times become faster than the rate of temperature increase. This trend emerges also in isothermal conditions (Figure 3.21b). Both models predict an exponential decrease in conversion times, whereas experimental observations show smaller variations. This discrepancy possibly arises from transport limitations in experimental setups, which are not accounted for in the models. Mass-loss profiles are affected by factors such as flow-rates, sample pan size, and initial polymer mass, although these phenomena are seldom studied^{307,316}. Even in pyroprobes, heat transfer limitations are observed for PE at T>600°C³⁰⁹. If transport limitations are neglected, the kinetic models predict mass-loss to occur in <1 s at 700°C. To model the non-uniform heating of the particle, more complex multidimensional models should be employed.

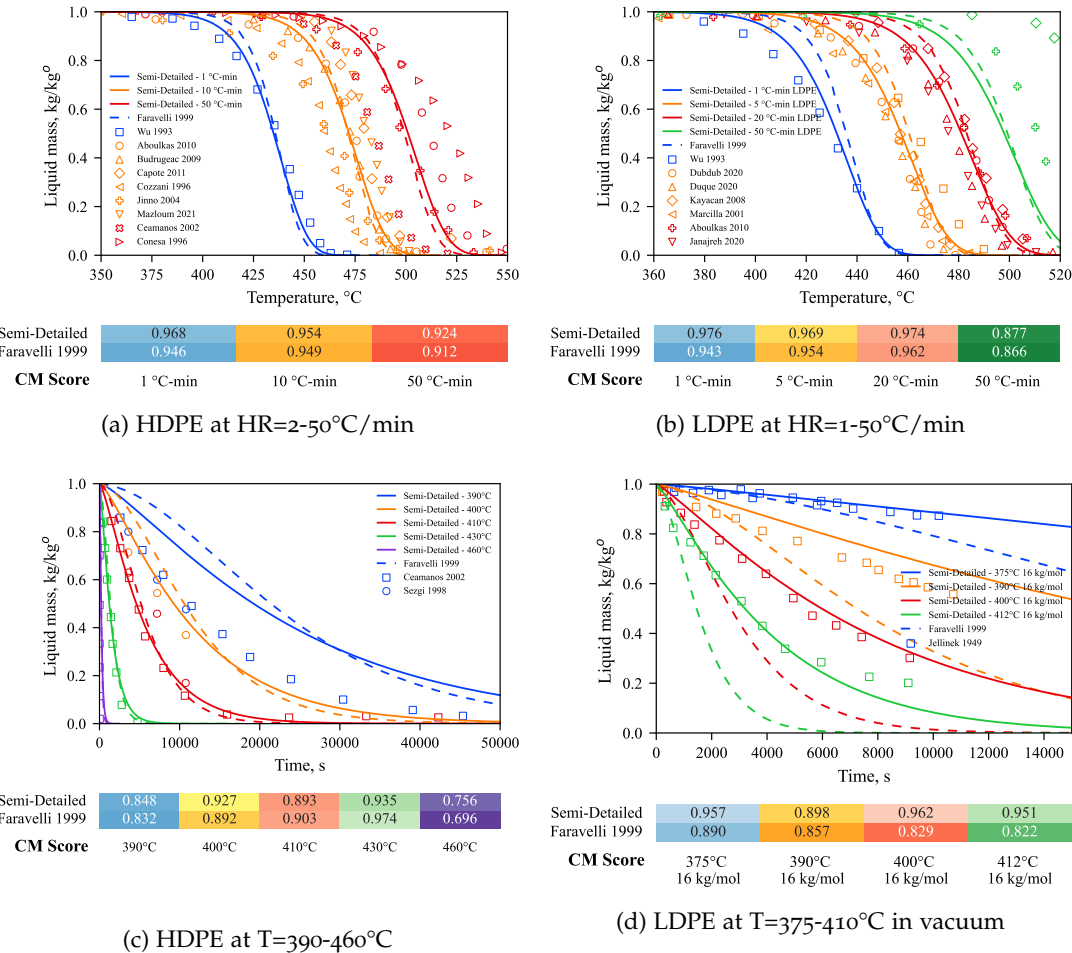


Figure 3.20: Sample mass-loss profiles of PE subjected to different temperature profiles. Comparison among the present work (solid lines), the detailed model of Faravelli *et al.* (dashed lines) and literature experimental data (marks). The Curve Matching score (CM) is reported for both models with the same colour legend as the plots.

Model predictions are evaluated through the multi-index Curve Matching approach, considering both HDPE and LDPE data under dynamic and isothermal conditions. As described in Section 3.2.2, this method employs 5 different indices to quantify the dissimilarities between two functions and their derivatives. While overall CM scores were presented in previous figures for clarity, a more detailed analysis is provided in Figure 3.22. The semi-detailed and detailed models have similar CM scores, supporting the validity of the proposed approach to model degradation times. As with the parity plots, the former achieves higher scores, but the differences are negligible. Analysing the individual indices offers a more in-depth assessment of model predictions. Both mechanisms achieve high L^2 indices, indicating satisfactory agreement in terms of overall curve shapes. Conversely, lower values are observed for d_{Pe}^1 and shift. The latter possibly reflects the wide experimental scatter in degradation temperatures. As previously discussed, individual variations within polymer samples lead to differences

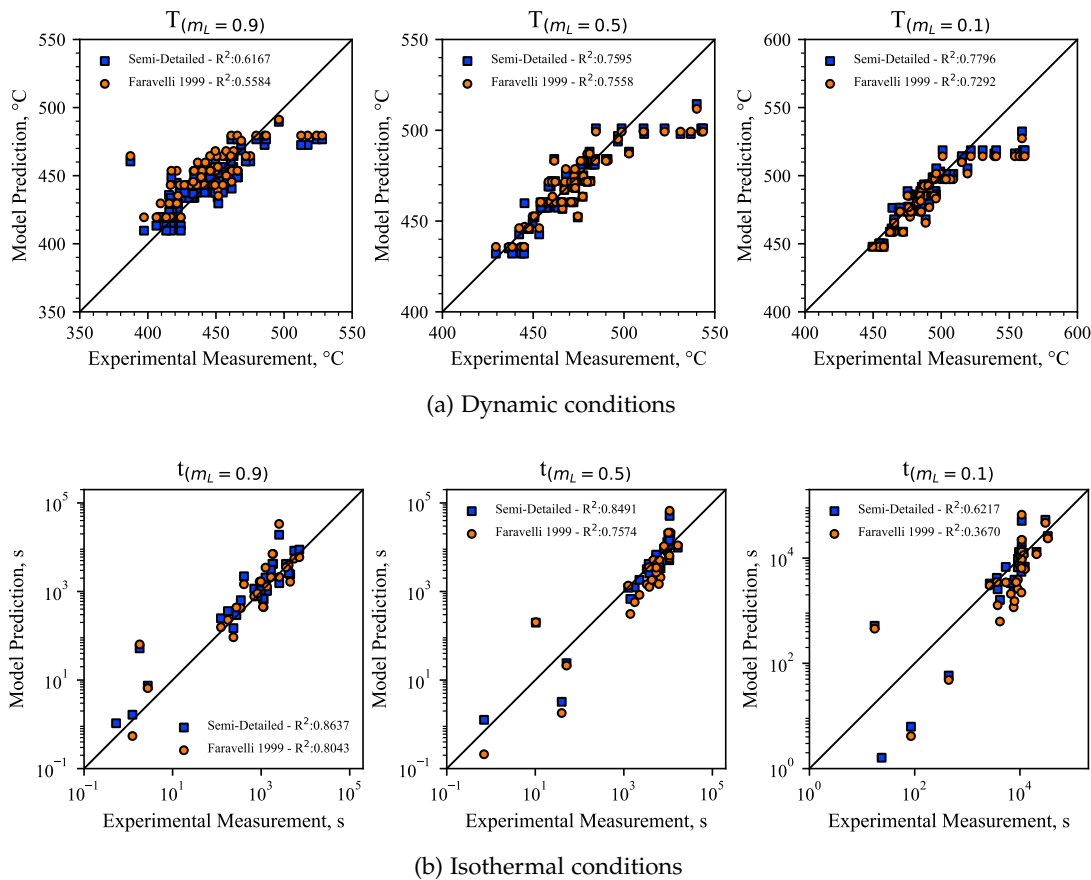


Figure 3.21: Parity plots for the semi-detailed model (blue squares) and the detailed model of Faravelli *et al.* (yellow circles) with literature data on HDPE and LDPE degradation temperatures (top) and times (bottom) at sample mass (m_L) 0.9, 0.5 and 0.1.

in degradation temperatures. Overall, the model correctly captures the degradation trend. While individual polymer properties affect prediction of the specific different degradation temperatures, they do not impact considerably the apparent activation energy of the process.

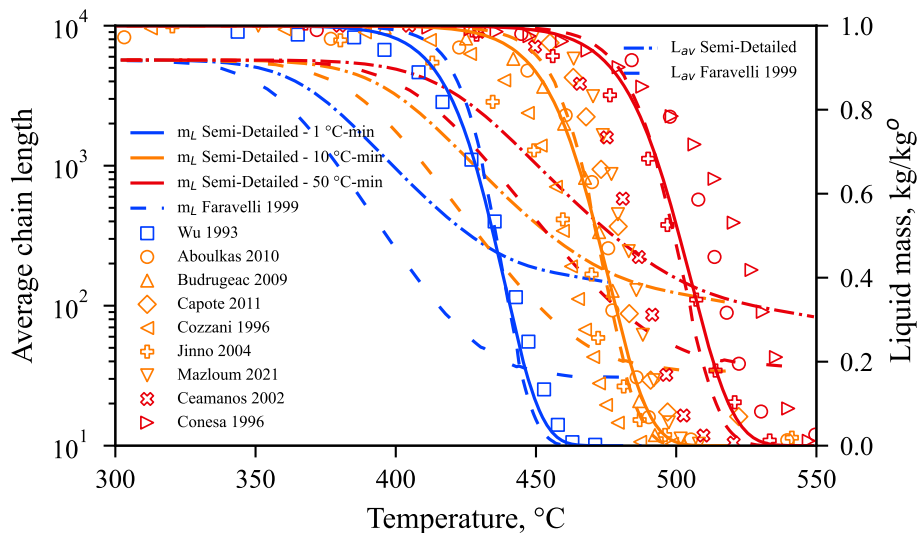
Polymer mass-loss occurs when the chains become small enough to escape the polymer melt. However, the degradation of the polymeric chains begins before volatiles are released. While the observed mass-loss of PE starts above 400°C, according to the kinetic models the variation in molecular weight starts as early as 350°C. The proposed kinetic model simplifies the description of the chain-length distribution by focusing on the polymer evolution in terms of its chemical moieties. Nevertheless, as discussed in Section 3.1.1.3, MW_{av}^0 affects model predictions as it relates to the amounts of end-chains present⁷⁴.

Figure 3.23 compares the reconstructed number average chain-length (L_{av}) of the present work (dashed-dotted lines) and the values predicted by the detailed model of Faravelli *et al.*⁶⁵ (loosely dashed lines). The present approach exhibits good agreement with the detailed model. The differences in chain-length decrease result from the

	CM	$d_{L_2}^0$	$d_{L_2}^1$	d_{Pe}^0	d_{Pe}^1	shift
Semi-Detailed	0.894	0.973	0.963	0.948	0.902	0.789
Faravelli 1999	0.879	0.978	0.967	0.935	0.875	0.760

Figure 3.22: Comparison of SciExpeM indices on all mass-loss profiles investigated for the proposed model and the detailed model of Faravelli *et al.*..

competition between unzipping and β -scission reactions. The former shorten chains by one monomer unit, while the latter halve the chains. The detailed model predicts a sharper decrease as it does not consider unzipping reactions. Towards the end of the degradation process, the semi-detailed model predicts a higher L_{av} due to the faster evaporation of C₃₀-C₆₀ chains. Nevertheless, validation of model predictions require ad hoc experimental data in controlled conditions.



Semi-Detailed	0.968	0.954	0.924
Faravelli 1999	0.946	0.949	0.912
CM Score	1 °C-min	10 °C-min	50 °C-min

Figure 3.23: HDPE sample mass-loss (m_L) and average chain length (L_{av}) profiles at HR=1-50°C/min. Comparison among the present work (solid and dashed-dotted lines) and the detailed model of Faravelli *et al.*⁶⁵ (dashed and dotted lines) and mass-loss literature experimental data (marks). The CM score on mass-loss is reported for both models with the same colour legend as the plots.

3.2.4 Products selectivity: volatile yields

A key aspect of the proposed model is its capability to predict the detailed product distribution. Characterizing the distribution of compounds from plastic waste is notoriously complex, leading to limited speciation data availability in the scientific literature. Most existing studies focus on identifying the compounds involved without quantification. While such data provides valuable insights into degradation processes, it does not allow for evaluation of model predictions. Less detailed speciation data classifies the product distribution in terms of petroleum cuts. Typically, volatiles are categorized according to their boiling temperatures in gases, oils, or waxes. While these data are usually quantitative, discrepancies arise according to the specific study. The responsibility possibly lies in secondary cracking reactions occurring within large experimental equipment²⁵¹.

Model predictions are compared with literature detailed speciation data. Figure 3.24 shows the comparison of predicted and measured molar yields at different temperatures. A normalization is performed to compare the model predictions with the reported data. All predicted products are referenced against the total amount of species experimentally quantified species. For instance, experimental data of De Witt and Broadbelt²²⁷ (Figure 3.24a) only measure the C₀-C₅ and C₈-C₃₅ carbon ranges. This normalization allows for meaningful comparison with the experimental data, while presenting also predictions of unquantified compounds. The normalized model molar yields of species *i*, n_{*i*}ⁿ, are therefore evaluated as:

$$n_i^n = \frac{n_i}{\sum_{i \in C_0-C_5, C_8-C_{35}} n_i} \quad (3.67)$$

where n_{*i*} are the real moles of species *i* computed by the model. Detailed experimental mass yield data does not require this normalization. However, data from De Witt and Broadbelt²²⁷ does not report the evaluation of the polymer moles. Similarly, the data reported by Faravelli *et al.*⁶⁵ are normalized molar fractions.

The comparisons presented in Figure 3.24 are obtained through a vertical delumping procedure¹⁴⁶. The semi-detailed kinetic models consider formation only of specific carbon numbers (ULLMW and RLMW) to describe the C₁₂-C₆₀ carbon range. Nevertheless, the remaining part of the distribution is obtained assuming no preferential formation occurs. A linear vertical delumping is performed, where the mass of each ULLMW-RLMW compounds is split between the others. For instance, the mass of C₁₆H₃₄ is split among the compounds comprised between C₁₂H₂₆ and C₂₀H₄₂ as. The mass of C₁₆H₃₂ contained in each compound *i* ∈ [12, 20] (m_{*i*}^{C₁₆H₃₂}) is evaluated as:

$$m_i^{C_{16}H_{34}} = \frac{\nu_{i/16}}{\sum_{i=12}^{20} \nu_{i/16}} m_{C_{16}H_{34}}^{\text{lump}} \quad (3.68)$$

where the ν_{*i*/16} are the lumping coefficient obtained through the lever rule (Equation 3.8) and m_{C₁₆H₃₂}^{lump} is the model output mass of C₁₆H₃₄. The values of ν_{*i*} depend on the

lumped species the delumping starts from. For example, $\nu_{17/16} = 0.75$ while $\nu_{17/20} = 0.25$, but their sum is 1. The delumped mass of compound i is then calculated summing the values obtained from two adjacent ULLMW-RLMW carbons. For instance, the mass of C₁₈H₃₈ is computed from:

$$m_{C_{18}H_{38}} = m_{C_{18}H_{38}}^{C_{16}H_{34}} + m_{C_{18}H_{38}}^{C_{20}H_{42}} \quad (3.69)$$

The delumping is performed between carbon numbers with the same functionalities. Indeed, the procedure shown previously involves only paraffins. The same lever rule can also distinguish between different configurations as shown in Chapter 4 for polypropylene.

Figure 3.24a compares predicted and measured volatiles' normalized molar fractions at T=420°C for different reaction times. The experimental procedures of De Witt and Broadbelt²²⁷ involves pyrolyzing 10-30 mg of HDPE in a sealed ampule for 30-150 minutes. The released gases are collected at 30, 90, and 150 min. The present model predicts near-complete conversion within 90 minutes, aligning with data from Ceamanos *et al.*²⁴⁹, Sezgi *et al.*³²⁵, and Jellinek³²⁸. Consequently, the comparison does not consider data at 150 minutes as any variation results from secondary gas-phase reactions. The model describes the product distribution with considerable agreement.

Gas products (C₀-C₅) are described at 30 minutes (blue marks) well within experimental uncertainty. Specifically, the model captures the formation of ethylene from unzipping, C₃ from backbiting and allyl stability, and C₄ from allylic radicals β-scissions. The latter is underestimated, although better agreement is observed compared to other data³³⁰ shown in the following paragraphs. C₆ and C₇ were not experimentally measured, but the model predicts them as major products from backbiting pathways. The model captures the C₁₀-C₁₂ peak from sequential backbiting steps, but not the C₁₅ peak as it is recovered from delumping as previously mentioned. For the C₂₀-C₃₅ range, the model predicts equimolar formation of heavy products due to their fast evaporation compared to secondary liquid-phase cracking at the considered temperatures. The model does not predict significant variations with reaction time, while experiments show a significant increase in light gases. This discrepancy might be attributed to secondary gas-phase reactions within the reaction environment or the pressure increase in the sealed vessel.

Figure 3.24b shows the comparison for unsaturated volatiles molar fractions at T=500 and T=600°C⁶⁵. The authors⁶⁵ report only data in the C₄-C₂₅ carbon range, while the Figure also shows model predictions of light gases. In general, the model accurately predicts the effect of backbiting reactions that lead to preferential formation of C₆H₁₂. The C₅ peak observed at 500°C is underestimated because the favoured backbiting reaction (1-5) leads to C₆ formation. Similarly, the model underestimates the preferential formation of C₄ at 600°C. However, the experimental results are in contrast with other literature data³³⁰.

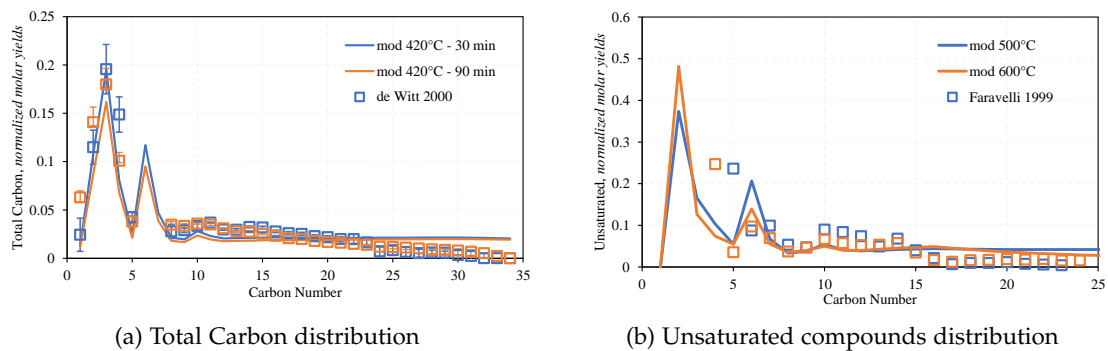
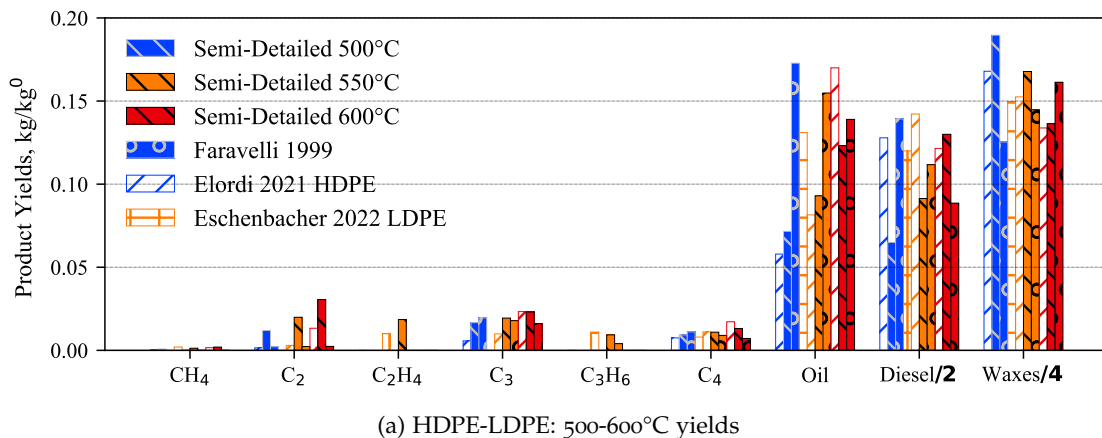


Figure 3.24: Comparison of volatiles molar yields of the present model (lines) and experimental data^{65,227} (marks). Model predictions are normalized on the volatiles experimentally measured.

Model predictions are validated against experimental mass yields of various carbon fractions. Figure 3.25a shows the comparison of the semi-detailed and detailed models with experimental data at T=500–600°C. As previously mentioned, most of the literature data employ large reactors and high temperatures, where secondary cracking reactions are relevant²⁵¹. This leads to significant scatter in product yields according to the facility employed. For instance, the oil fraction measured at 550°C (orange) by Eschenbacher *et al.*²²⁸ is considerably lower than that measured by Elordi *et al.*²²⁹. This discrepancy possibly arises from the latter employing a fluidized bed reactor, where secondary reactions are more prominent. Conversely, the total yield of C₂ hydrocarbons reported by Elordi *et al.*²²⁹ is lower than the yield of ethylene quantified by Eschenbacher *et al.*²²⁸.

Overall, both models correctly capture the observed trends in product fraction yields across the considered temperature range. The semi-detailed models predicts higher yields of light gases with respect to the detailed one of Faravelli *et al.*⁶⁵. This results from unzipping being a significant pathway for C₂H₄ formation, coupled to explicitly considering allylic radicals which results in higher yields of C₃H₆ and C₄H₆. The detailed model predicts waxes yields (C₂₁₊) increasing with temperature due to evaporation of longer chains at higher temperatures. Consequently, it predicts a decrease in the yield of oil (C₅–C₁₀) and diesel (C₁₁–C₂₀) fractions. Conversely, the semi-detailed model predicts an increase of lighter compounds at high temperatures due to wax liquid-phase cracking. This work underestimates diesel fraction at low temperature, possibly because of neglecting backbiting longer than 1–16 (see Section 3.1.2.4). However, these same backbiting reactions are responsible for the overestimation of oil yields at low temperature. Neither model can predict the experimental maximum in diesel yields at T=550°C, which is possibly due to secondary gas-phase cracking reactions.

Figure 3.25b shows the comparison for pyroprobes yields of light gases (C₀–C₄) and condensable species (C>C₅)³⁰⁶. At T=500°C, the model significantly underestimates



product yields. This results from the experimental residence time is only 20 s, whereas the characteristic degradation time of PE at these temperatures are of the order of minutes²²⁸. At T=600°C, the model underestimates light gases formation, possibly because of secondary cracking reactions similar to those involved in the experiments by Elordi *et al.*²²⁹ and Krishna *et al.*³⁰⁹. At 700°C, both models severely underestimate the secondary cracking of heavier fractions (by ~20 wt.%), probably occurring in gas-phase. As previously mentioned, the characteristic gas-phase degradation time at 700°C is lower than 0.1 s¹³³.

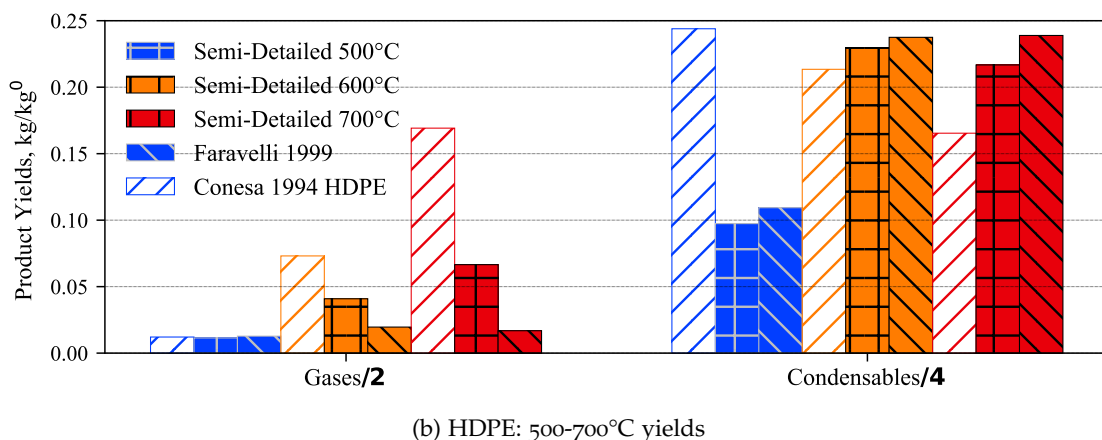


Figure 3.25: Comparison of species mass yields for the present model (full), the detailed model by Faravelli *et al.* (full) and experimental data (patched).

The model is validated also with experimental product distribution time-profiles. Figure 3.26 shows the time-evolution of light gases and heavier compounds at T=390 and T=410°C. At low temperatures, both models underestimate the polymer reactivity, although overall yield trends are properly captured. The underestimation of gas yields is possibly related to low temperature pathways involving metal impurities acting as catalysts¹⁵. Additionally, secondary gas-phase reactions could also be relevant due to the relatively long experimental residence times (40 s). For reference, the CRECK gas-

phase mechanism¹³³ predicts a molar conversion of 3% for pure normal hexadecane at 400°C in 40 s. This conversion translates to an increase of few % of light gases, partially explaining the observed higher yields.

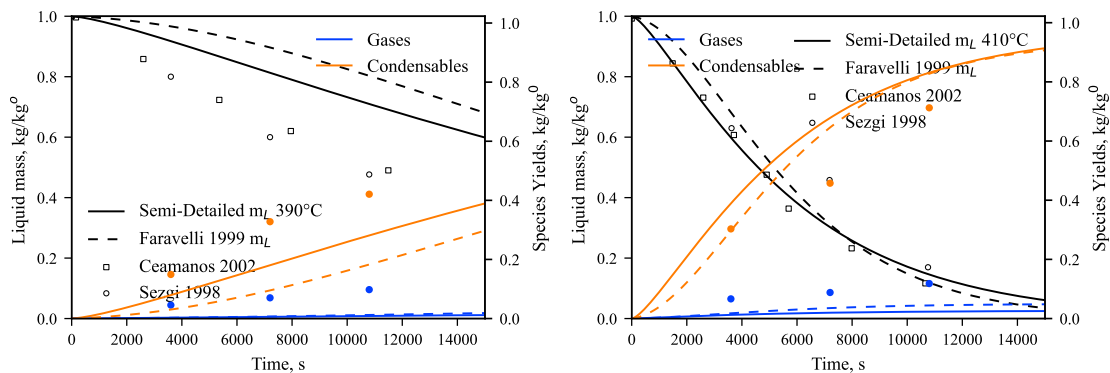


Figure 3.26: Comparison of predicted (solid lines) and measured (symbols) profiles for HDPE mass-loss (black) and yields (coloured) at: left) 390°C, right) 410°C. The predictions of the detailed model by Faravelli *et al.*(dashed lines) are reported as well.

3.2.5 Energy requirements

The proposed thermochemistry is validated against experimental data on heat flux profiles. These experiments involve measuring the heat flow required to maintain the assigned temperature profiles within the sample. In general, TG/DSC and TG/DTA calorimetry data are employed. The heat release profiles are inherently related to the mass-loss ones, for which model validation has already been discussed.

Figure 3.27 shows the comparison of experimental and predicted heat-fluxes for HDPE and LDPE. Two distinct endothermic peaks are observed, relative to melting and polymer degradation, respectively. Considering HDPE profiles (Figure 3.27a), the model reasonably captures the peaks magnitudes and amplitude, although significant experimental scattering is observed. The kinetic parameters used for the melting reaction result in a predicted $T_m \sim 120-150^\circ\text{C}$, consistent with experimental data. As the model represents melting through a chemical reaction, increasing HR shifts the peak at higher temperatures, although still at $T < 150^\circ\text{C}$. The model underestimate \dot{Q}_{out} for $T=200-400^\circ\text{C}$. This discrepancy might result from two factor. On the one hand, the model might be underestimating the extent of chain-length degradation, predicted to start at $T \sim 350^\circ\text{C}$ ⁶⁵. On the other hand, the issue might lie in the high experimental uncertainty involved, as measurements of different authors vary by a factor of 2 at 10°C/min in this temperature range. For the heat required for polymer degradation, the proposed approach captures the heat fluxes within the range of experimental uncertainty.

A considerably higher scattering is observed for LDPE samples, as shown in Figure 3.27b. While the degradation peak is described with reasonable accuracy, considerable differences are observed for the melting and heating fluxes. The model predicts a lower melting heat requirement for LDPE than HDPE due to its lower crystallinity. However, as mentioned, the melting reaction is not able to describe the decrease in T_m for LDPE. Introducing a different melting reaction for the LDPE mechanism could potentially address this behaviour, but there is limited data available for such purpose. Significant variations exist also among experimental data of different authors at identical operating conditions. For instance, at 20°C/min (red) Duque *et al.*³²² report negligible heating between 200-400°C, while Janajreh *et al.*³²⁴ measure a constant heat flux of 3 kW kg₀⁻¹. Overall, the data from Janajreh *et al.*³²⁴ appear to exhibit a constant baseline during the heating process and a low influence of HR.

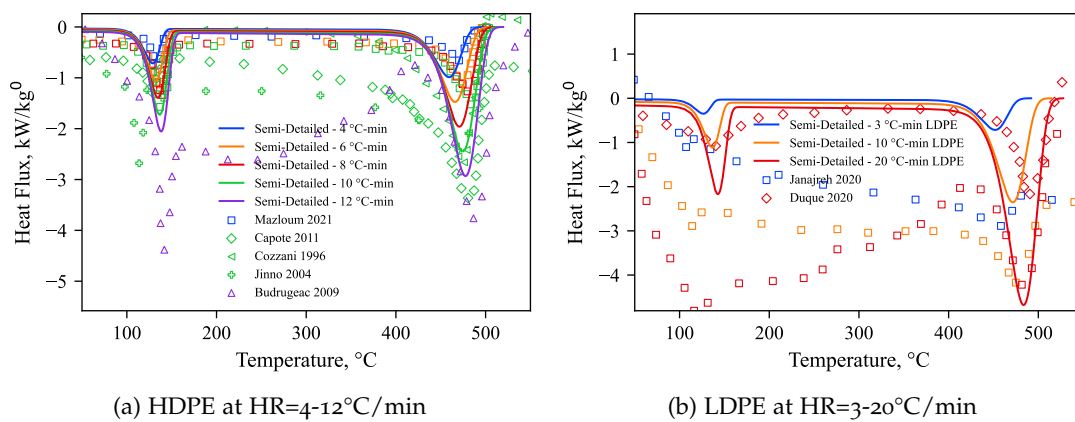


Figure 3.27: Comparison of predicted (solid lines) and measured (symbols) heat-flux profiles for HDPE and LDPE.

3.3 REDUCED-ORDER MODELS

The proposed kinetic mechanism achieves comparable accuracy in predicting the characteristic degradation times and product distribution to more computationally expensive detailed models^{55,65,76}. The FG approach allows for reducing the computational cost, but CFD applications for PW valorization involve multiple polymers and a detailed gas-phase reactivity. To this aim, the present work employs further lumping techniques to reduce the number of species (N_s) and reactions (N_r) considered.

The following sections present two reduced-order models. First, the derivation of a reduced semi-detailed kinetic mechanism is proposed. The reduction procedure simplifies the description of the radicals types lumping all isomers in a single species. The mechanism introduces specific corrections to preserve the original selectivity. Additionally, as the main computational cost results from the description of LMW species, the distribution is lumped in fewer representative carbon numbers. Following these

results, a multi-step (fully lumped) model is presented. This model neglects all radical intermediates and simplifies the reaction pathways in few lumped steps. The rate parameters account for the complex radical reactivity. These are obtained from theoretical assumptions and analysing the selectivity of the reduced model. The mechanism are reported as well on the GitHub repository⁵. The methodology is applied to PE, but it can be extended to other polymers.

3.3.1 Reduced Semi-Detailed Model: PE-50-480

As mentioned, the main computational cost of the semi-detailed kinetic mechanism stems from the accurate description of LMW reactivity. A decrease in computational cost is achieved simplifying the number of tracked species and their condensed-phase reactivity. This approach lumps all radical isomers dumping the difference in reactivities in the rate parameters. Models that employ few radical isomers (e.g., PET in chapter 6) mildly benefit from this methodology.

According to the starting mechanism, the proposed methodology achieves different levels of reductions. With respect to PE-125-3500 (Section 3.1), the lumping procedure simplifies it to 50 species and 480 reactions (PE-50-480). The lumping techniques described in the following Sections achieve a decrease of $N_s \sim 60\%$ and $N_r \sim 85\%$. These techniques involve defining smaller species subsets, but also ad hoc approaches for reaction lumping.

PE-50-480 has a N_s lower than the fully lumped model developed for biomass pyrolysis⁴¹. Nevertheless, it involves higher N_r and a stiff system due to radicals being explicitly considered.

3.3.1.1 Species definition

The semi-detailed model defines two categories of polymeric chains: HMW and LMW species. The first are described with ~ 10 pseudo-species, while the latter through ~ 120 compounds. The LMW category is further classified as unreactive (ULMW), lumped unreactive (ULLMW), and reactive (RLMW) species.

Compared to the semi-detailed model, fewer compounds are considered to simplify product distribution. Real species (ULMW) are used to track light gases ($C < C_6$, while all longer chains are represented by a smaller number of lumped species based on carbon number. Specifically, C_{16} is chosen to represent diesel cuts, C_{30} for light waxes, and C_{60} for heavy waxes. The first one is assumed unreactive, while the reactivity of the latter two (C_{30} and C_{60}) is described in detail, as discussed in the next section. To summarize, the reduced model uses $C < C_6$ as ULMW, C_{16} as ULLMW, and C_{30} and C_{60} as RLMW. Since this model tracks the same carbon range ($C < C_{80}$) as the semi-detailed model, the predicted results are similar.

⁵ Freely available at <https://github.com/Alocaspi/Polymers-Kinetic-Mechanisms>

The high number of reactions stems from the various radicals considered and the corresponding reactions. Bimolecular reactions (e.g., H-abstractions and recombinations) account for the majority of the total number of reactions. To reduce the computational burden, all radical isomers are represented by a single pseudo-species. For each introduced RLMW species, this approach considers only three stable species and three radical species.

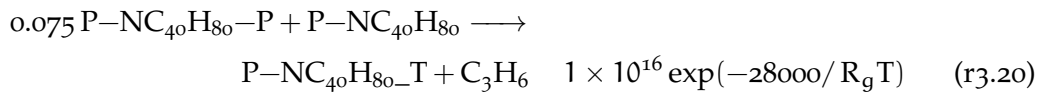
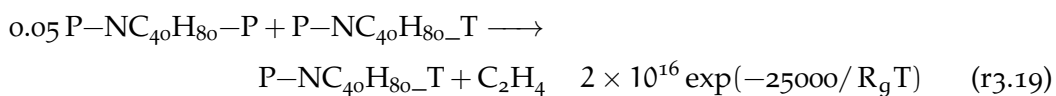
Overall, the number of species employed in the reduced model is 50 (liquid+gas). Compared to the semi-detailed model, the total number is decreased by 61%. However, this number does not consider gas-phase intermediates from gas-phase reactions of ULMW and ULLMW compounds. Further work will address developing a reduced gas-phase mechanism to be coupled with the present one.

An additional lumping methodology for reducing N_s involves further simplifying the description of long-chain hydrocarbons. At high molecular weight, the distinction among paraffin, olefin, and diolefin narrows, and the reactivities become similar. Therefore, a further reduction could be achieved introducing a single species per carbon number, representative of the paraffin, olefin, and diolefin. Combining this approach with the radical lumping previously discussed, only a stable and a radical species would be introduced instead of 6. This approach has not been introduced in the present work still. Unlike the lumped radical, these species are not isomers and involve different elemental composition. Nevertheless, this approach is expected to considerably reduce the model computational cost both in terms of N_s and N_r .

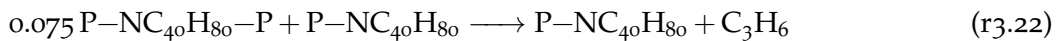
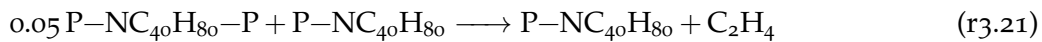
3.3.1.2 Radical isomer lumping

As mentioned, the reduced model lumps all radical isomers in a single pseudo-species. This is schematically represented in Figure 3.28. The lumped pseudo-species accounts for the reactivity of the original isomers, appropriately weighted by their relative abundance and selectivity. Any reaction forming either isomer will instead form the lumped radical, and the latter will undergo all reactions of the real isomers.

For instance, the elementary steps involving formation of C_2H_4 and C_3H_6 from $P-NC_{40}H_{80}-T$ and $P-NC_{40}H_{80}$ respectively are:



where the SPU are included as discussed in Section 3.1.2.2. Lumping the radical isomers involving introducing the following reactions:



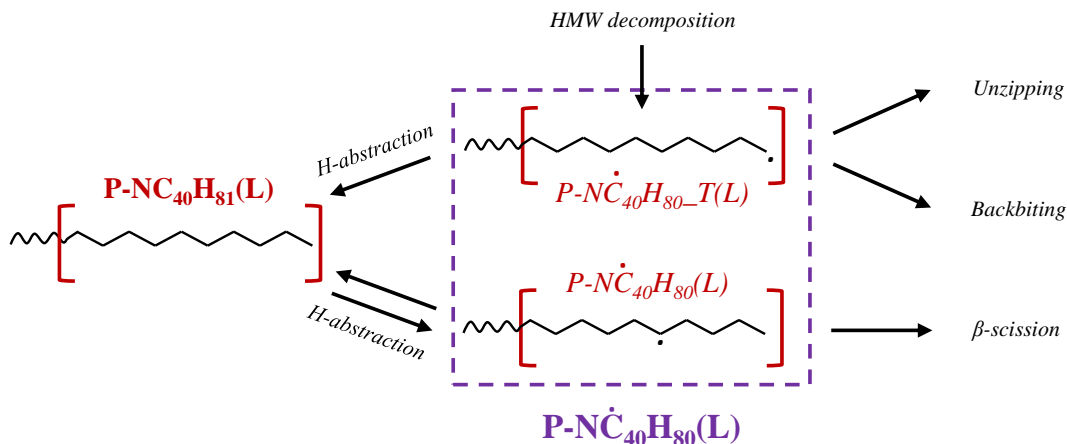


Figure 3.28: Schematic representation of the radical isomer lumping for end-chain paraffin radicals. The isomers $P\text{-NC}_{40}\text{H}_{80}$ and $P\text{-NC}_{40}\text{H}_{80}\text{-T}$ are described by the species $P\text{-NC}_{40}\text{H}_{80}$ only (purple)

where no formation of terminal radicals takes place and the unzipping reaction starts from the lumped radical $P\text{-NC}_{40}\text{H}_{80}$.

The key-point is estimating the rate parameters that preserve the selectivity of the semi-detailed model. Recently, a theoretical lumping methodology based on master equations has been proposed and validated³³¹. However, it cannot be employed in the present case as the radical isomers belong to different Potential Energy Surfaces (PES). This limitation arises because the formation pathways for the different radical isomers are intricately linked to other reactions in the system. Their formation and decomposition channels are opposite. For instance, β -scission reactions consume internal radicals to form terminal ones, while H-abstractions consume terminal radicals to form internal ones.

To address these issues, the present work employs an alternative approach based on the relative abundance (branching fractions) of each isomer³³². In this context, *a priori* pseudo-steady-state approaches fail as the isomers exhibit different time-varying profiles. Additionally, the relative abundance of terminal and secondary radicals necessitates information of the time-varying EC-to-MC ratio. The relative abundance of the isomers significantly depends on the choice of N_c^* , as it affects the number of internal hydrogens in the EC species.

To this aim, the branching fractions of isomer class are computed in post-processing. Isothermal simulations of the semi-detailed model are performed across a temperature range of 300–1100°C. The average branching fractions (BFs) for each isomer class are then calculated at different temperatures. Four classes of radicals are considered: primary alkyl radicals, secondary paraffin radicals, secondary olefin radicals, and allylic radicals. For each simulation, the instantaneous relative amounts of isomer j (x_j) are evaluated. This is achieved considering the concentration of radicals belonging to class j , normalized on the total radical concentration. The corresponding

branching fraction of isomer j at temperature T ($BF_j(T)$) is then computed through the time-integral over the total degradation time ($t_d(T)$):

$$BF_j(T) = \frac{1}{t_d(T)} \int_0^{t_d(T)} x_j(t) dt \quad (3.70)$$

These integral branching fractions represent the relative pseudo-steady-state abundance of the different isomers.

The reduced model kinetic parameters are obtained combining the original parameters and the computed branching fractions. Reactions that involve formations of any specific radical isomer are not modified. Conversely, reactions involving decompositions of the lumped radical (R_L) to any species S ($k_{R_L \rightarrow S}(T)$), are calculated through the decomposition rates ($k_{R_j \rightarrow S}(T)$) of the individual isomers (R_j) as:

$$k_{R_L \rightarrow S}(T) = \sum_j BF_j(T) k_{R_j \rightarrow S}(T) \quad (3.71)$$

Table 3.6 reports the calculated rate constants regressed to an Arrhenius form.

This approach preserves the selectivities within each isomer class. For instance, the relative importance of unzipping with respect to backbiting reactions is the same of the semi-detailed model (Section 3.1.2.4). The introduced branching fractions delineate the low and high temperature reaction mechanisms. For instance, for paraffin radicals, the regressed parameters correctly predict wax formation at low temperature through the "Paraffin β -scission" reaction. The resulting parameters are far from being elementary ones. Indeed, β -scission reactions have parameters similar to H-abstraction reactions, as the rate determining step is the stabilization of the terminal radicals. This also explains the large variation in monomer yields with increasing temperature. At higher temperatures, C_2H_4 formation and backbiting become more important as primary radicals tend to decompose rather than stabilizing. The low and high temperature mechanism for olefin radicals are the opposite. As the allylic radicals are energetically favoured, they characterize the low temperature degradation. For this reason, preferential formation of waxes from olefin radicals is a high temperature reaction. This appears contradicting with the lower amounts of waxes experimentally observed at high T . However, formation of olefin radicals occurs mainly at low T , as unzipping becomes the main decomposition pathway.

3.3.1.3 Reaction lumping

Further decrease in the computational cost is achieved also simplifying several reaction pathways.

As polymer degradation temperatures are relatively low, propagation reactions are the rate determining steps. Initiation and termination impact the total radical pool, but they do not directly influence product selectivity. The dominant radicals in the system are HMW ones. While RLMW radicals control the degradation of their corresponding species, their overall impact on the degradation process is minimal. For

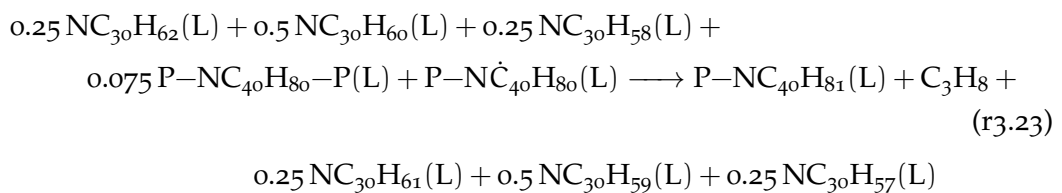
Table 3.6: Modified-Arrhenius parameters of radical lumped reactions obtained from regression (units cm, mol, s, cal).

Reaction	A	n _A	E _{act}
Unzipping	4.33E+13	0	29800
Backbiting 1-4	7.22E+10	0	25400
Backbiting 1-5	1.10E+10	0	19300
Backbiting 1-6	2.20E+09	0	19300
Paraffin β -scission	9.60E+07	0	13800
Olefin β -scission	6.00E+12	0	32600
Olefin allylic β -scission	1.80E+13	0	30900
H-abstraction by paraffin	6.00E+11	0	14000
H-abstraction by olefin	2.50E+11	0	19100

this reason, the radical pool is considered resulting only from the reactivity of HMW species. Neglecting initiation and termination of RLMW species results in a significant decrease in N_r without significant loss in accuracy.

An additional simplification involves backbiting reactions. Backbiting reactions that form RLMW species can be lumped together with appropriate stoichiometric coefficients. For instance, reactions forming C₁₅ and C₁₄ produce the same species in similar amounts. This lumping leads to a considerable reduction in N_r, particularly for models with significant vertical lumping of species.

As discussed in Section 3.1.2.2 (Figure 3.8), the stabilization of ULMW and ULLMW radicals is lumped in their formation. This step can involve any stable species and a separate reaction is required for each "RH" considered. Since species with similar carbon number have similar boiling points, a single reaction is written for stabilization on all RLMW with a specific carbon number. For instance, instead of Reaction 3.6, a single reaction is introduced for N_c=30:



where the stoichiometric coefficients represent the expected 1-2-1 molar ratio or paraffin-olefin-diolefin⁶⁵. The reaction rate is assumed to be first order only in the paraffin molar fraction, while the presence of the other species acts as an on/off switch for the reaction rate. This simplification is necessary as paraffinic species form as radicals. Therefore, at high temperatures, the paraffin radicals decompose to shorter chains before stabiliz-

ing. Conversely, diolefin species form as stable species and before decomposing require undergoing H-abstraction reactions, while olefins have an in-between behaviour.

3.3.2 Multi-step Fully Lumped Model: PE-10-10

The reduced kinetic model offers a significant reduction in computational cost compared to the semi-detailed model. This allows for direct application in CFD and reactor-scale simulations of PE thermochemical recycling. However, addressing PW requires defining similar models also for the other polymers involved. Additionally, for high temperature and long residence times applications, the secondary gas-phase reactivity requires appropriate characterization. A comprehensive mechanism for multiple polymers is expected to involve ~50–100 gas+liquid species per polymer, leading to significantly higher computational costs.

To this aim, the reduced model serves as a foundation for deriving a multi-step condensed-phase kinetic mechanism. This multi-step model also aims at predicting the key physico-chemical aspects of the degradation, i.e., residence times, heat requirements, and product distribution. This is achieved simplifying the complex radical reactivity into few lumped steps, resulting in a less computationally expensive and non-stiff kinetics. Considering PE, with respect to the semi-detailed and reduced models, PE-10-10 achieves a decrease in N_s of 92% and 80%, respectively. Similarly, by neglecting radical reactions, N_r reduces of 99.7% and 97.9%, respectively.

The proposed model involves only unimolecular reactions. As described in Chapter 7, this allows employing a single kinetic model representative of the pseudo-phase occurring in PW degradation^{113,114}. Coupling this model with similar models for other polymers and biomass⁴¹ allows consistently describing thermochemical valorization of complex waste mixtures (e.g., PW/MSW mixtures). These combined models can then be used to evaluate factors like particle size distribution, reactor geometry, and transport phenomena. This information is valuable for designing, modeling, and optimizing industrial reactors like pyrolyzers and gasifiers.

3.3.2.1 Species definition

As with the semi-detailed (Section 3.1.1) and reduced (Section 3.3.1) models, the model classifies species in HMW and LMW subsets.

The HMW distribution is described by using only two mid-chain pseudo-species: crystalline ($P-NC_{40}H_{80}-P_S$) and amorphous/molten ($P-NC_{40}H_{80}-P$) phases. These represent the material's chemical moieties and physical state, while end-chain pseudo-species are excluded for a compact mechanism. The choice of chain-length of polymer species aligns with the semi-detailed and reduced kinetic model. The multi-step model employs the same carbon numbers, assuming that species with $C > C_{80}$ cannot evaporate to stable gas-phase species. The initial pseudo-species quantities are determined

through the polymer crystallinity, without considering molecular weight variations in this approach. As the model does not include end-chain species, the average molecular weight cannot be recovered in post-processing.

Volatiles (LMW) are described similarly to the other models, although with a reduced number of species. Permanent gases (ULMW) are described by C_2H_4 , C_3H_6 , C_3H_8 , and C_4H_6 . The first two are olefin of interest, while C_3H_8 and C_4H_6 represent saturated and unsaturated low molecular weight compounds. Additionally, C_4H_6 is a key soot and PAHs precursor¹⁴⁷. For longer chains, few lumped species represent the different oil fractions. However, the model considers only the olefin for each specific carbon number, and no long chain paraffin/diolefin is introduced. Oil cuts (C_5 – C_{10}) are represented by NC_6H_{12} , diesel cuts (C_{11} – C_{20}) by $NC_{16}H_{32}$, and waxes (C_{21+}) by $NC_{30}H_{60}$. The carbon numbers introduced are analogous to the semi-detailed and reduced kinetic models. Species with $T_{b,n} < 350^\circ C$ are assumed unreactive due to their rapid evaporation and form as gas-phase species (ULLMW). The model considers the liquid-phase species and reactivity only for compounds with $T_{b,n} > 350^\circ C$ (i.e., $NC_{30}H_{60}$) (RLMW). Cracking of C_{16} and shorter chains is attributed to gas-phase reactions not considered in the present work.

The multi-step model includes 7 gas-phase and 3 liquid-phase species. As mentioned, this approach achieves a considerable decrease in N_s compared to the other kinetic mechanisms. For instance, all waxes are represented by C_{30} , and only few light gases are explicitly tracked. Conversely, the delumping techniques previously employed are not applicable here. A more detailed description could involve additional species at the extremes of the distribution (e.g., C_4H_8 for light gases and $C_{60}H_{120}$ for heavy waxes). Nevertheless, this model effectively captures the main product ranges. For a more accurate description of the product distribution, the reduced or semi-detailed models are recommended.

3.3.2.2 Multi-step kinetic mechanism

As previously mentioned, the present model simplifies the complex reactivity in few lumped single-step reactions. Figure 3.29 schematically represents the complete reaction mechanism. These lumped steps start from the mid-chain molten species resulting in formation of gas-species and liquid-phase waxes. The latter undergoes the same reaction classes of the molten polymer releasing other LMW compounds or evaporates to gas-phase.

Radical species are not explicitly tracked. The model accounts for their reactivity and selectivity through the rate parameters introduced. Table 3.7 summarizes the reaction classes introduced, together with their rate parameters. To avoid unnecessary complexity inconsistent with the strong simplifications, an Arrhenius equation is employed.

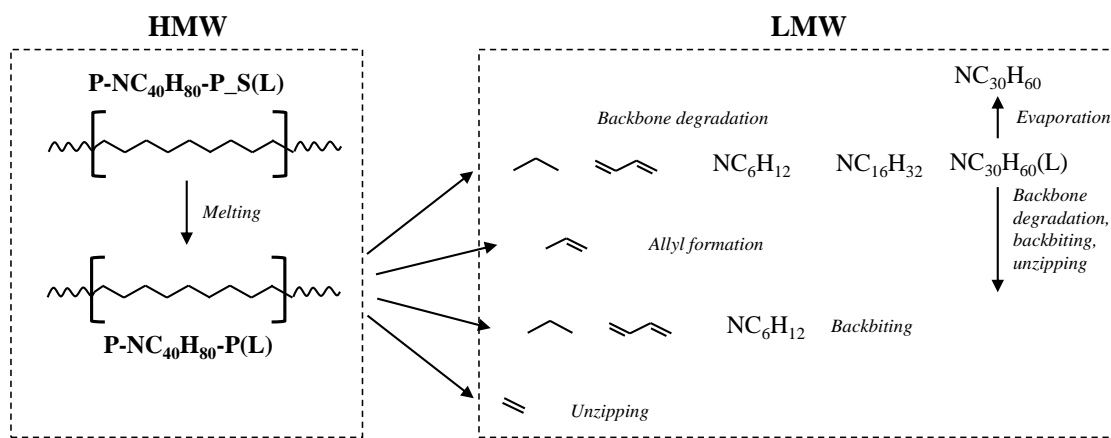
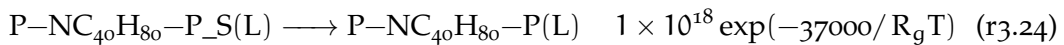


Figure 3.29: Schematic representation of the multi-step reaction mechanism.

Table 3.7: Reaction classes of the multi-step model and their Arrhenius parameters (units s, cal, mol)

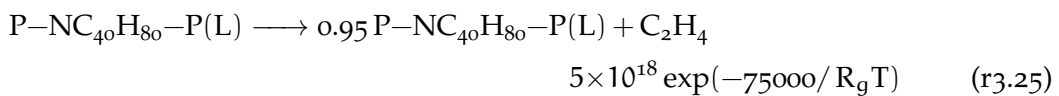
Reaction (number)	A	E _{act}
Melting (r3.24)	1.0E+18	37000
Backbone degradation (r3.27)	1.0E+16	62500
Propylene formation (r3.28)	2.0E+14	59500
Backbiting (r3.26)	2.5E+15	64500
Unzipping (r3.25)	5.0E+18	75000
Waxes evaporation (r3.30)	1.0E+06	23000

Similar to the semi-detailed model (Reaction r3.17), the first transformation upon heating involves melting the crystalline phase. This process is represented by a single homogeneous reaction:



The melting reaction utilizes the same kinetic parameters as the semi-detailed model (Table 3.2).

The molten polymer decomposes through four pathways. On molar basis, the dominant reaction pathway is unzipping. The model represents this decomposition reaction with a single step starting from the stable mid-chain as:



The rate parameters of this reaction are obtained from the pseudo-steady-state assumption on the total amounts of terminal radicals. Neglecting the presence of allylic pos-

itions, the concentration of terminal radicals τ can be determined a priori from the conservation equation:

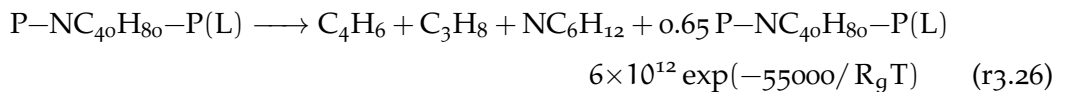
$$\frac{dC_\tau}{dt} = k_\beta (C_{R_{tot}} - C_\tau) - k_{H_2,R_\tau} C_\tau \quad (3.72)$$

where the kinetic constants are those employed in the semi-detailed model and $C_{R_{tot}}$ is the total amounts of radicals, which is determined from the pseudo-steady-state assumption⁵⁵ as well. Unzipping and backbiting reactions are not considered as they do not change the total amounts of terminal radicals in the system. The total rate of unzipping can be estimated multiplying the unzipping constant by the total amount of terminal radicals. Dividing this by the concentration of mid-chain units allows the determination of the multi-step unzipping constant ($k_{3.25}$). Overall, the rate constant is evaluated as:

$$k_{3.25} = \frac{1}{C_{CH_2} N_c^*} k_{UZ} \frac{k_\beta}{k_\beta + k_{H_2,R_\tau} C_{H_2}} \sqrt{\frac{k_{RS} C_{CH_2}}{k_{RR}}} \quad (3.73)$$

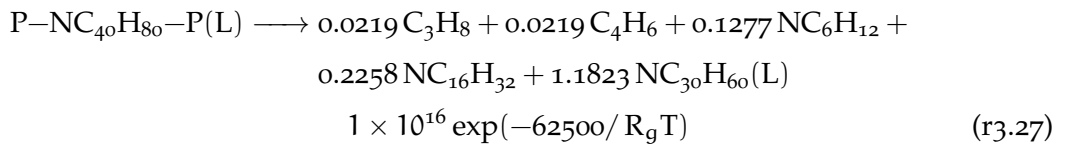
where the kinetic constants on the right-hand-side refer to semi-detailed kinetic model (Table 3.2). Conversely, $C_{CH_2} = \rho_L / 14$ is the monomer liquid-phase concentration, $C_{H_2} = 2C_{CH_2}$ is the concentration of secondary hydrogens, and $C_{CH_2} N_c^*$ the concentration of mid-chain units. The resulting expression is regressed to an Arrhenius form as reported in Table 3.7

Terminal radicals can further decompose through backbiting reactions before stabilizing. As shown in Figure 3.12, this results in formation of oil-cuts and light gases at low T. To represent this class of reactions, a single lumped step is considered:



For PE, the multi-step model does not consider formation of diesel-cuts through multiple backbiting as it involves 3 or more intramolecular H-transfers.

On mass basis, the dominant reaction pathway is the backbone degradation. The model employs a single reaction that produces an equimolar distribution of chains from C_3 to C_{80} . This step represents the reactivity characteristic of internal radicals (Section 3.1.2.2) and it is written as:

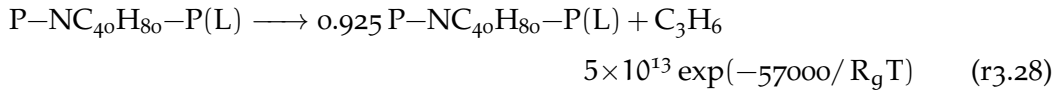


The stoichiometric coefficients account for the vertical lumping methodology presented in Figure 3.9. These coefficients reflect the fraction of carbon ending up in each product size range. As previously mentioned, smaller molecules ($C < C_{30}$) are directly formed as gas-phase compounds. The rate parameters of this reaction are obtained

assuming stabilization of terminal radicals is rate determining for the formation of the internal end-chain radicals. The kinetic constant of the backbone degradation mechanism ($k_{3.27}$) is estimated from the ratio between unzipping and stabilization of the semi-detailed model as:

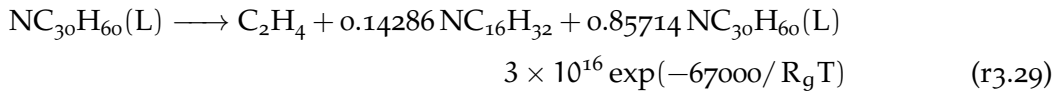
$$k_{3.27} = k_{3.25} \frac{k_{H_2,R_1} C_{H_2}}{k_{UZ}} \quad (3.74)$$

Propylene formation is favoured due to the stability of the allyl radical. As shown in Figure 3.11, this is consequence of β -scission reactions of olefin radicals forming C_3H_5 . To account for the increased rate of this reaction pathway, the model considers a separate homogeneous reaction:



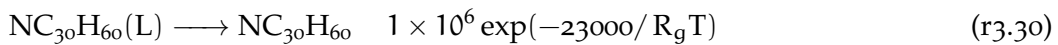
The rate parameters of this reaction are similar to reaction (r3.27). However, this step occurs only $1/N_c^*$ times compared to the backbone degradation, although with a lower energy barrier due to the formation of a more stable radical.

In the present work, the compounds released to gas-phase do not undergo further cracking. On the other hand, liquid-phase species can further decompose through the same four reaction classes introduced (Reactions r3.25 - r3.27). While the pathways are the same, different stoichiometric coefficients are required to represent the reduction in chain length. For instance, the reaction to represent unzipping of $C_{30}H_{60}$ is:



where the vertical lumping represents the long chain product (C_{28}) as a combination of C_{16} and C_{30} . The Arrhenius parameters of this reaction are the same as unzipping of the polymer chain. Conversely, backbone degradation of $NC_{30}H_{60}(L)$ is $27/80$ times slower due to the shorter chain-length.

As with the semi-detailed and reduced models, a volumetric phase-change reaction represents waxes evaporation as:



Evaporation rate parameters are obtained in post-processing following the same approach described in Section 3.1.3. These differ from the semi-detailed model as C_{30} lumps chains of significantly different lengths.

Overall, propylene formation and backbiting are important at low temperatures, while at $T > 600^\circ C$ unzipping becomes dominant. At low temperatures, most waxes evaporate before decomposing, but at $T > 500^\circ C$ secondary liquid-phase cracking becomes important. To account for the lower degradation temperature of LDPE, a similar

approach to the one employed for the semi-detailed mechanism is used. Specifically, the value of $k_{3.27}$ is modified introducing a lower apparent activation energy as:

$$k_{3.27,\text{LDPE}} = k_{3.27} \cdot 0.5 \exp(1500/R_g T) \quad (3.75)$$

which corresponds to a 1.5 kcal mol⁻¹ lower activation energy and a halved frequency factor. As mentioned, LDPE can be described as a combination of PP and HDPE. This methodology accounts for formation of branched products²²⁵, but it has not been tested yet in the present work.

3.3.3 Models validation and comparison

Both the reduced and multi-step kinetic models are validated against literature experimental data and the semi-detailed model predictions. The validation focuses on the key degradation parameters: characteristic degradation times (i.e., mass-loss profiles), product yields, and heat requirements. The reduced model is assessed for the same targets as the semi-detailed model. Conversely, the multi-step mechanism has several limitations. As previously mentioned, it cannot employ delumping techniques nor track the average molecular weight. The detailed model of Faravelli *et al.*⁶⁵ is not reported for clarity reasons.

3.3.3.1 Characteristic degradation times

As with the semi-detailed model, the reduced-order mechanisms are assessed with ~100 mass-loss experimental data in the scientific literature^{55,115,214,249,251,307,308,314–328}.

Figure 3.30 shows the comparison for data on HDPE and LDPE of the semi-detailed (solid lines), reduced (dashed lines), and multi-step (dotted lines) models. Overall, all models capture the influence of operating conditions as reflected by the high CM scores. At low temperatures, the reduced model predicts slightly longer degradation times, possibly because of underestimation of allylic reactivity. The multi-step model predicts a smoother degradation profile, as the simplified reaction kinetics do not account for the time-varying reactivity. All models overestimate the polymer reactivity considering LDPE at 50°C/min (Figure 3.30b). The weak-links correction introduced results in a higher reactivity than HDPE samples, consistently with low heating rates experiments. On the other hand, experimental data measure for LDPE a higher T_d than HDPE at 50°C/min. This difference may result from not proper setting of experimental equipment resulting in transport phenomena not considered in the present work.

Figure 3.31 shows parity plots comparing predicted onset ($m_L=90\%$), half-conversion ($m_L=50\%$), and final-conversion ($m_L=10\%$) temperatures (T) and times (t). Both data on HDPE and LDPE are considered, highlighting the capability of the simple correction in describing the process. All models show similar predictions for degradation temperatures and times, with R^2 values differing by only a few percent. In general,

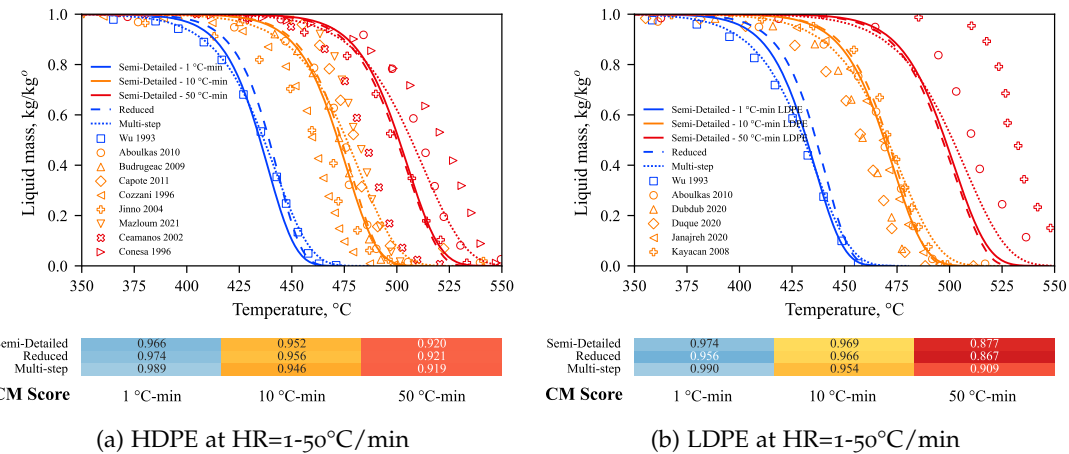
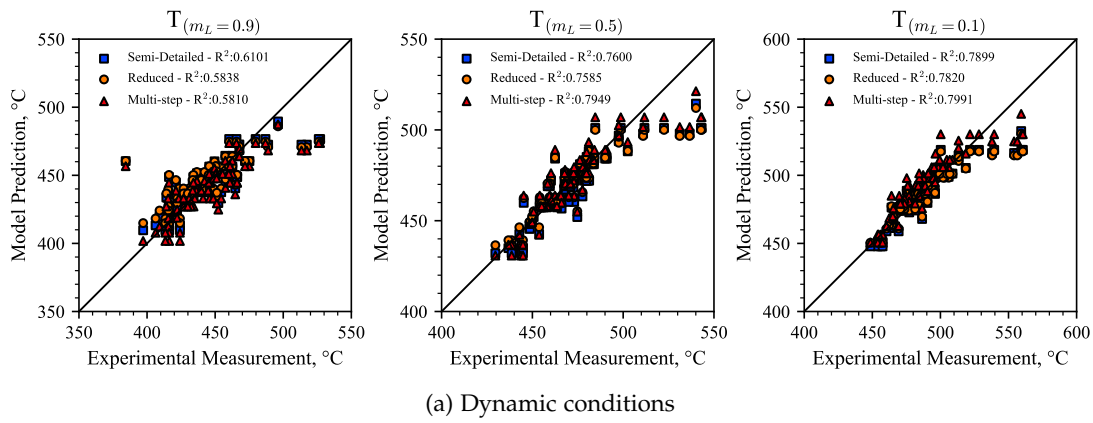


Figure 3.30: Sample mass-loss profiles of PE subjected to different temperature profiles. Comparison among the semi-detailed (solid lines), reduced (dashed lines), and multi-step (dotted lines) models and literature experimental data (marks). The Curve Matching score (CM) is reported for the three models with the same colour legend as the plots.

the multi-step model slightly underestimates onset temperatures while overestimating the final conversion ones. The reduced model predicts a higher apparent activation energy compared to the semi-detailed mechanism. This translates to overestimating onset temperatures and underestimating the final degradation ones. Considering isothermal conditions (Figure 3.31b), all models underestimate degradation times at high temperature. Internal transport limitations in the sample are probably the reason. Similar trends to the dynamic conditions are observed for the isothermal data. Specifically, the reduced model underestimates the onset reactivity, while the multi-step mechanism overestimates it.



A more detailed analysis of mass-loss profiles is performed using the multi-index curve matching approach. Figure 3.32 shows the comparison among the kinetic models and the detailed one by Faravelli *et al.*⁶⁵. All models achieve similar CM scores, in-

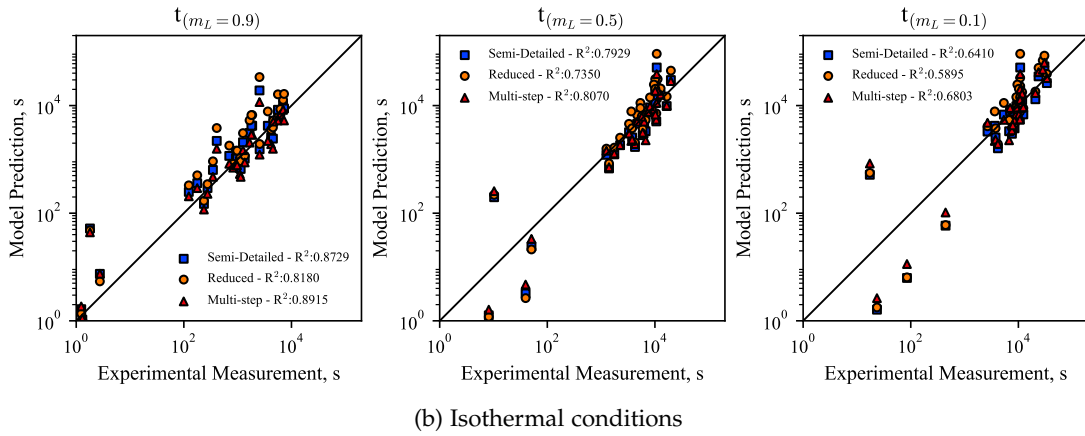


Figure 3.31: Parity plots for HDPE and LDPE degradation temperatures (top) and times (bottom) at sample mass (m_L) 0.9, 0.5 and 0.1 of the semi-detailed (blue squares), reduced (yellow circles) and multi-step (red triangles) models with literature experimental data

dicating that they effectively capture the experimental characteristic degradation times. The differences in CM scores are negligible, with the reduced model even achieving the highest CM score. The reduced and multi-step model reproduce the predictions of the semi-detailed model also in terms of indices. Specifically, the mechanisms show good agreement for L^2 indices, which represent the overall curve similarity. Conversely, a lower agreement for d_{Pe}^1 and shift are observed, although in line with the semi-detailed model. Overall, the proposed lumping approaches preserve the predictions of characteristic degradation times. Any improvement made to the semi-detailed model are expected to be reflected in the reduced and multi-step mechanisms as well.

	CM	$d_{L_2}^0$	$d_{L_2}^1$	d_{Pe}^0	d_{Pe}^1	shift
Semi-Detailed	0.894	0.973	0.963	0.948	0.902	0.789
Reduced	0.900	0.972	0.962	0.939	0.919	0.805
Multi-step	0.886	0.966	0.951	0.934	0.891	0.787
Faravelli 1999	0.879	0.978	0.967	0.935	0.875	0.760

Figure 3.32: Comparison of SciExpeM indices (Section 3.2.2) on all mass-loss profiles investigated for the semi-detailed, reduced, and multi-step model. The detailed model of Faravelli *et al.*⁶⁵ is also reported as comparison.

Figure 3.33 shows the comparison of the reconstructed number average chain-length (L_{av}) of the semi-detailed and reduced mechanism. The corresponding mass-loss profiles are also reported as comparison. Both semi-detailed and reduced models show similar trends in predict L_{av} . The multi-step model cannot be used for chain length reconstruction because it does not distinguish between mid-chain and end-chain func-

tionalities. As mentioned, to the author's knowledge no experimental data on MW_{av} in controlled conditions is available. The semi-detailed model predictions were assessed against the ones of the detailed model by Faravelli *et al.*⁶⁵ (Figure 3.23). The reduced model shows similar predictions to the semi-detailed one, except for the last stages of conversion. This is possibly due to the lower stabilization rate of chains in the C₃₀-C₆₀ range.

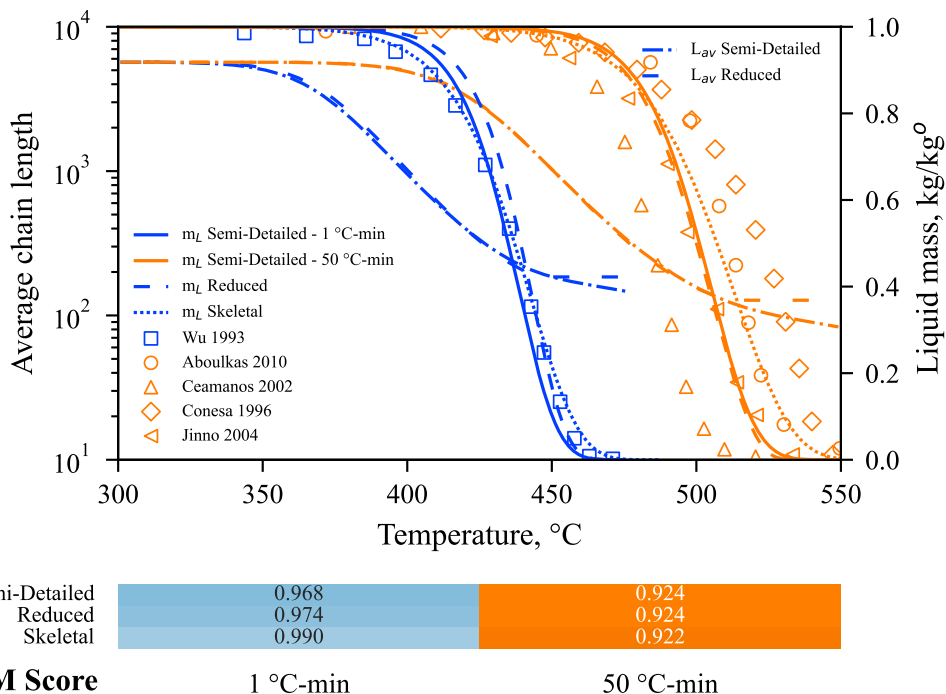


Figure 3.33: HDPE sample mass-loss (m_L) and average chain length (L_{av}) profiles at $HR=1-50^\circ\text{C}/\text{min}$. Comparison among the semi-detailed (solid and dashed-dotted lines) and the reduced (dashed and loosely dashed lines) models and mass-loss literature experimental data (marks).

3.3.3.2 Products selectivity: volatile yields

All models achieve good accuracy in describing the mass-loss profiles. The reason is that the model predictions are similar granted that the same range of products can evaporate to gas-phase. The differences between the mechanisms arise when considering the description of the product distribution.

Figure 3.34 shows the comparison of the semi-detailed and reduced models prediction of the product distribution^{65,227}. The two models show several key differences in predictions. For instance, the reduced model predicts double the ethylene yield compared to the semi-detailed mechanism. The discrepancy results from the strong simplification in the selectivity between terminal and internal radicals. To this aim, the procedure proposed by Pegurri *et al.*³³² is expected to improve the reduced model's

predictions. Reducing them optimizing the lumped rate constants on the semi-detailed model predictions allows for recovering the predicted selectivity. Another key difference lies in the description of longer hydrocarbons. The reduced model is not able to describe the preferential formation of C_6 and C_{10} , as the C_6-C_{10} distribution is represented through a vertical lumping. This translates in the reduced model predicting an increase in the oil cuts, without pinpointing which compounds are formed preferentially. As previously mentioned, the multi-step model cannot employ delumping techniques and is therefore not included in the present comparison.

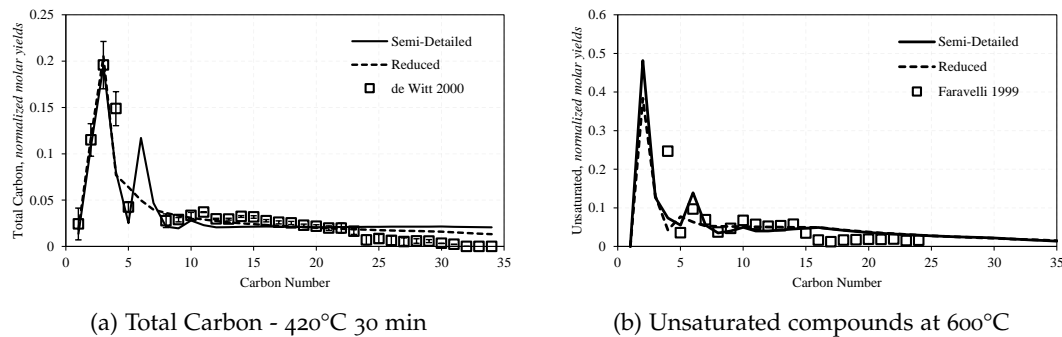


Figure 3.34: Comparison of volatiles molar yields of the semi-detailed (solid lines) and reduced (dashed lines) models and experimental data (marks). Model predictions are normalized on the volatiles experimentally measured.

All condensed-phase models are validated against mass distribution data^{228,229,306}. Figure 3.35 shows the comparison with experimental data in the 500-600°C temperature range. Overall, all models capture the trend in the variation of product yields across the considered temperature range. As with the other comparisons, several discrepancies are observed. For instance, the multi-step model does not consider methane formation. The reduced model slightly overestimates the yields of ethylene, consistently with the results shown in Figure 3.34. Considering C_3 yields, the semi-detailed and reduced model show similar predictions, while the multi-step mechanism overestimates them. The main issue of the multi-step model is its considerable underestimation of oil-cuts at high temperatures. This is possibly consequence of the strong lumping of the distribution, which is not able to properly account for the differences in product formation. This also might be the cause for the high diesel-cuts yields. The higher oil yields of the reduced model are consequence of the strong simplification in selectivity between terminal and internal radicals. With respect to waxes formation, the reduced model predicts lower variation with temperature. This results from waxes stabilizing before decomposing at higher temperatures. As mentioned, the methodology proposed by Pegurri *et al.*³³² is expected to improve the reduced model predictions.

The models are validated also against experimental data on the time-evolution of distribution profiles³²⁵. Figure 3.36 shows the evolution of light gases and heavier compounds at 390 and 410°C. The primary discrepancies between the models stem from

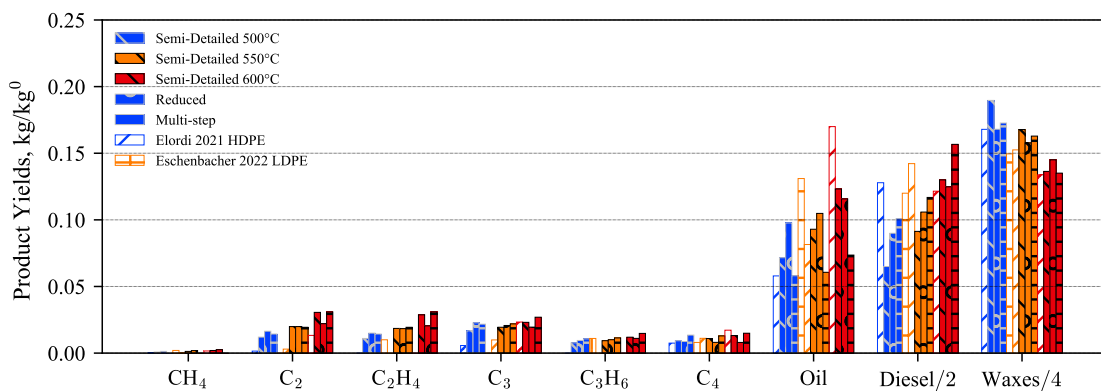


Figure 3.35: Comparison of species mass yields for the semi-detailed, reduced and multi-step mechanism (full) and experimental data (patched).

the previously discussed differences in mass-loss profiles. At low temperatures, the three models underestimate the polymer reactivity and formation of light gases. The latter is possibly due to low temperature pathways involving metal impurities acting as catalyst¹⁵. Secondary gas-phase reactions could also be relevant due to the long experimental residence times (40 s). As previously mentioned, the reduced model predicts a higher apparent activation energy and underestimates the low T reactivity.

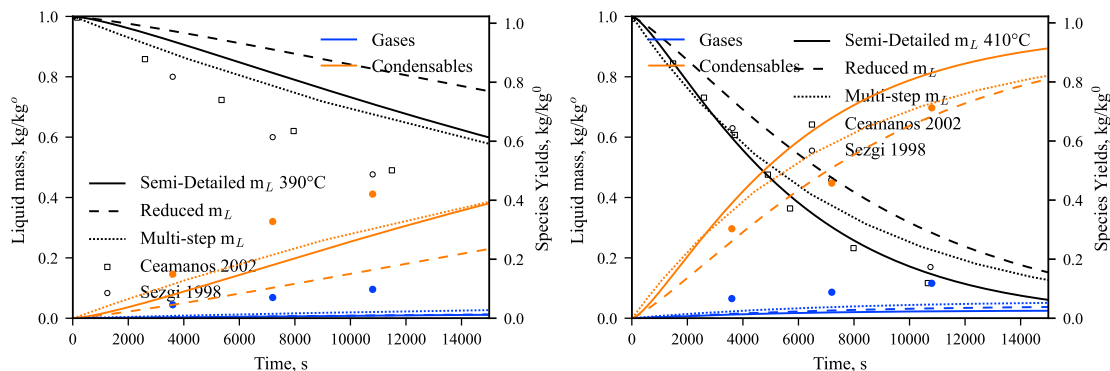


Figure 3.36: Comparison of predicted (lines) and measured (symbols) profiles for HDPE mass-loss (black) and yields (coloured) at: left) 390°C, right) 410°C.

3.3.3.3 Energy requirements

Figure 3.37 compares the predicted heat-fluxes with respect to experimental data on HDPE^{251,317–319} and LDPE^{322,324}. Overall, the predicted energy requirements across the three models are quite similar. The similarity stems from the three models employing the same melting reaction and thermochemistry. Consequently, they predict identical endothermic peaks for the melting phase-transition and similar heating profiles in the 200–400°C range. Differences in the predicted pyrolysis heat fluxes arise primarily from variations among the mass-loss profiles. For instance, the multi-step model predicts a

broader peak due to its lower predicted apparent activation energy, resulting in slower degradation process. The reduced model shows similar profiles to the semi-detailed one, although with a slight delay.

The same trends are observed considering LDPE data (Figure 3.37b). As previously mentioned, the proposed correction for LDPE is not able to explain the significant scattering in experimental data.

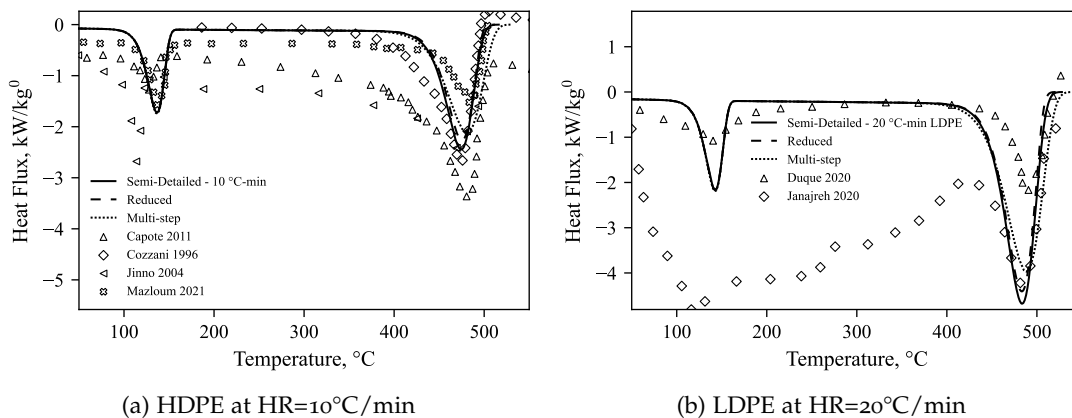


Figure 3.37: Comparison of semi-detailed (solid lines), reduced (dashed lines) and multi-step (dotted lines) models and measured (symbols) heat-flux profiles for HDPE and LDPE.

3.4 CONCLUSIONS AND FURTHER WORK

The present Chapter presents the development of a polymer condensed-phase kinetic model following the functional groups approach. The proposed general methodology is applied to Polyethylene degradation to aid the reader in understanding the assumptions introduced.

The functional groups approach aims at describing the characteristic degradation times, volatiles released, and energy requirements. This methodology simplifies the description of high molecular weight chains into a limited number of lumped pseudo-species with specific chemical functionalities. These pseudo-species are distinguished according to the location in the chain among mid- and end-chain species. This distinction allows tracking preferential formation of short-chain compounds and the number average molecular weight. The model describes also the solid-state of the polymer through an additional mid-chain species. Low molecular weight products are described with lumping approaches analogous to gas-phase kinetic mechanisms. The accurate description of the volatile distribution is the main responsible for the computational cost of the model.

The FG methodology builds the reaction network through a reaction-class approach, where the identified elementary steps are applied to both HMW and LMW species.

Appropriate corrections for the reactants and products reactivity are included, considering similar gas-phase reference compounds. Considering PE degradation, the kinetic mechanism leverages on established reaction classes. The rate parameters of these classes are obtained from analogies to gas-phase compounds, including corrections for the presence of the solvent. The discussion distinguishes the reactivity of internal, terminal, and position specific radicals, also describing in detail the lumping techniques employed to reduce the number of reactions. A correction is introduced also to account for the lower degradation temperature of LDPE samples.

The kinetic model incorporates both melting and boiling phase-change models through appropriate chemical reactions. The definition of the species thermochemistry complements the reaction mechanism allowing for describing the heat requirements involved in the process. The liquid-phase thermochemical properties are derived from literature phase-change correlations. Conversely, experimental data on solid polymers serve as basis to define the solid-phase thermochemistry.

The semi-detailed model is validated with an extensive set of experimental data from the scientific literature and the detailed model by Faravelli *et al.*⁶⁵. Model simulations are performed through an in-house C++ code, while the model's results are quantitatively assessed through a multi-index Curve Matching score. The proposed model accurately captures the characteristic degradation time compared to the detailed model, even across hundreds of mass-loss profiles. High accuracy is achieved also when comparing with data on volatile distribution, capturing both valuable compounds (e.g., C₂H₄, C₃H₆) and long-chain cuts. TG/DSC data allow for validating the proposed thermochemistry. While reasonable accuracy is achieved considering HDPE heat profiles, further experimental and modelling work is required to investigate LDPE profiles due to the high experimental scattering.

The present chapter also proposes a methodology to derive reduced-order kinetic models, where the semi-detailed model serves as basis to obtain two further lumped models: a semi-detailed reduced and a fully-lumped multi-step model. The former employs additional assumptions to further reduce both the number of species and reactions involved. While it tracks in detail the radical species, a reduction methodology is introduced to represent radical isomers with lumped species. Conversely, the multi-step model simplifies the radical chemistry in few global steps that account for the main reaction classes. This fully lumped mechanism allows coupling with other similar models to describe complex PW and PW/MSW mixtures at low computational cost. However, due to the considerable simplifications introduced, it cannot reproduce all degradation targets of the semi-detailed model. Both reduced-order kinetic models are validated against the semi-detailed mechanism, proving able to describe mass-loss profiles with the same accuracy. However, when compared with volatile distribution profiles, differences are observed due to the significant lumping involved. The reduced model does not predict preferential formation of several long chain hydrocarbons. Additionally, it overestimates the importance of the terminal radicals reactivity at low

temperature. The multi-step model cannot predict the carbon distribution, and it limits at describing the petroleum cuts.

Different mechanisms are proposed for HDPE and LDPE, resulting in a total of 6 mechanisms. All the kinetic mechanism follow the CHEMKIN format and are freely available on GitHub⁶.

The proposed kinetic models address only the condensed-phase reactivity. As discussed in Chapter 8, further work will incorporate secondary gas-phase reactions. As mentioned several times in the present Chapter, gas-phase cracking significantly affects the product distribution. For instance, gas-residence times of ~20 seconds lead to >50%wt cracking of heavy waxes at 500°C. Coupling the proposed condensed-phase model with appropriate gas-phase mechanisms allows also describing the gasification reactivity.

⁶ Available at <https://github.com/Alocaspi/Polymers-Kinetic-Mechanisms>

4

POLYPROPYLENE

POLOPROPYLENE (PP) ranks as the second most widely produced commodity plastic, making it one of the most prevalent polymers alongside polyethylene and polystyrene^{7,15}. This thermoplastic material is employed mainly for food packaging and containers but also in pipes construction³³³. Notably, it boasts the lowest density among all commodity plastics³³³. A large application of PP is also fibre productions for fabrics, construction, and medical purposes³³⁴. Its popularity stems from advantageous properties such as toughness, resilience, water resistance and chemical inertness. Compared to polyethylene (PE) it has lower chemical resistance but higher mechanical and thermal resistance³³³. Copolymers of PE and PP are usually tough and flexible.

Polypropylene was first industrialised in 1957 through to the Ziegler-Natta catalysts (1954²²⁴). The key aspect in polymerization processes is achieving high control of the polymer stereochemistry. In perfectly isotactic PP, the monomers are arranged in regular head-to-tail configurations without any branching or 1,3-additions. According to the catalyst employed, occasional errors of 0.3-1.5% occur in some chains. Metallocene catalysts allow to reduce the number of imperfections and distribute them uniformly across the chains. Not controlling the stereochemistry results in atactic polymers, which are incapable of crystallizing. These products have low molecular mass and are usually employed only in adhesives. Ziegler-Natta catalysts produce a $MW_w/MW_n \sim 5-10$, while metallocene ones allow to have narrower distributions with $MW_w/MW_n \sim 2-4$.

The mechanical properties of polypropylene result from a matrix of interlocking crystallites. A highly isotactic polymer forms helical coils with 3 monomers per turn, which stack in thin lamellar crystallites²²⁴. Three crystalline forms are known for PP, but other metastable states are also found²⁵². The theoretical³³⁵ melting point of polypropylene is about 188°C, but at normal heating rates a $T_m \approx 160-170^\circ\text{C}$ is observed²¹. Crystallization of the molten polymer is hindered by chain entanglements and helices folding. For this reason, even highly stereoregular polymer usually result in commercial articles with a crystallinity of 30-60%. Specific purified and annealed samples are able to exceed 70% of crystallinity²²⁴.

The degradation behaviour of polypropylene closely resembles polyethylene. PP has a higher melting point, but its decomposition temperature is approximately 50°C lower than that of PE. This temperature difference arises from the tertiary carbons bonds which are easier to break compared to the secondary ones. The different repetitive unit

also results in a notably more intricate product distribution, together with the higher chain mobility and metal impurities in the polymer matrix⁷¹. Atactic polypropylene has a generally lower degradation temperatures³³⁶ because of an even higher melt mobility and presence of defects⁷¹.

As discussed in Section 2.2, polypropylene has received less consideration than the other polymers in the past decades. Furthermore, the developed models are not suitable for modelling plastic waste (PW) degradation because of their high computational cost (e.g., discrete section⁵⁵) or low accuracy (global models¹³⁷). The method of moments (MoM) allows developing mechanisms that satisfy these requirements⁶⁸. However, this approach is not suitable to consider interactions with PVC as well⁴² and therefore not of interest in the present work. In the following Sections, a kinetic mechanism for PP pyrolysis is presented based on the functional groups approach previously discussed. The model is developed assuming perfectly ideal polymeric chains (i.e., isotactic polypropylene) and corrections are then introduced to consider branches and impurities in the matrix. The present Chapter follows the same methodology presented in Chapter 3 for PE degradation. First the definition of species is introduced, followed then by the degradation mechanism and the reduced-order models. Compared to the previous chapter, the description focuses only on the differences with respect to PE (mainly considering head and tail configurations). The three proposed kinetic models are then validated in terms of mass-loss profiles, product distribution, and energy requirements. A Python code was developed to automatically write the kinetic mechanisms at assigned carbon numbers. The mechanisms are developed in CHEMKIN format and are freely available on GitHub¹.

4.1 SEMI-DETAILED KINETIC MODEL: PP-240-13000

This Section outlines the development of the kinetic mechanism. The chemical transformations within the reacting mixture are delineated through a network of reactions that convert one compound into another. The subsequent subsections elaborate on the formulation of the functional groups approach, encompassing how polymer chains and their changes are taken into account. First the species definition is introduced, highlighting the different description of long polymeric chains and volatiles of interest. The development of the reaction network is then discussed employing a hierarchical reaction-families approach. Physical transformations such as melting and boiling are incorporated in the kinetic mechanism. As mentioned, the same procedure is described in more detail for polyethylene. For this reason, the discussion focuses mainly on the key differences, such as accounting for the reactivity of internal radicals isomers and head and tail terminations. The kinetic mechanism has been validated and published⁷⁴, but it is here updated in analogy to PE following additional experimental data on

¹ Available at <https://github.com/Alocaspi/Polymers-Kinetic-Mechanisms>

product distribution. Both the choice of species and rate parameters have been modified.

4.1.1 Species Definition

The polymer chain distribution is categorized in High and low molecular weight species, respectively labelled HMW and LMW. A threshold carbon number $N_c^* = 90$ is defined: longer chains are considered part of the HMW subsets while shorter ones are part of the latter in agreement with experimental data on gas-phase products^{68,231,336–341}. The chosen N_c^* has the same normal boiling point as in the case of PE ($\sim 750^\circ\text{C}$).

HMW polymeric chains are represented by Mid-chain (MC) and End-chain (EC) components (Figure 4.1). The former characterize the chain's length, while the latter the terminal moieties. For polypropylene (PP), end-chain groups are classified into "tail" and "head" terminations, designated as "t" and "h" respectively. Tail terminations refer to species with a methyl group on the second chain carbon and have distinct products selectivity (Section 4.1.2). Assuming the methyl side-groups being inert^{55,57,68}, the double bonds form only on the chain-carbons and therefore tail and head olefins are 1- and 2-alkenes respectively. The polymer at room temperature is in the semi-crystalline state, and an additional species is introduced to represent the crystalline phase ($\text{P}-\text{IC}_{45}\text{H}_{90}-\text{P}_S$). No distinction is made among the different crystalline phases, nor between amorphous and molten-phase³³⁵.

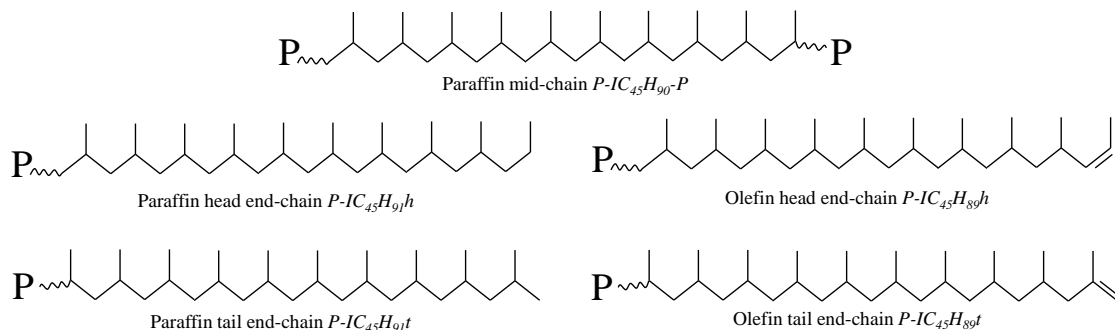


Figure 4.1: Schematic representation of the stable pseudo-species introduced to describe long polymer chains (HMW).

LMW compounds in both liquid and gas phases are modeled in a manner similar to conventional detailed models, and two lumping techniques^{43,146} are applied to minimize the number of species. The C_1-C_{16} range is represented by real species assumed to be unreactive due to their rapid evaporation (ULMW)¹⁰⁰. The $\text{C}_{17}-\text{C}_{89}$ distribution is represented by a vertical linear lumping procedure considering three lumped N_c : C_{30} , C_{48} , and C_{72} . Chains with $T_{b,n} > 250^\circ\text{C}$ are referred to as reactive LMW (RLMW) and have a well characterized reactivity. To model the spiked product distribution of PP, multiple series are required: "head-head", "head-tail", and "tail-tail" configurations. As

shown in Figure 4.2, these configurations exhibit similar reactivity but differ in carbon numbers. For instance, the "head-head" configuration of $C_{12}H_{26}$ is $C_{11}H_{24}$. This results in PP requiring three times the number of species compared to PE for each additional lumped carbon number considered. Head configurations in Figure 4.2 are represented in the trans conformer as usually shown in chemistry databases. The "head-tail" olefin involves a double bond either on the head or tail termination, but the two configurations are lumped into a single species⁶⁸. Because of the higher stability of tertiary radicals, the main configurations are head-head for paraffins, head-tail for olefins, and tail-tail for diolefins.

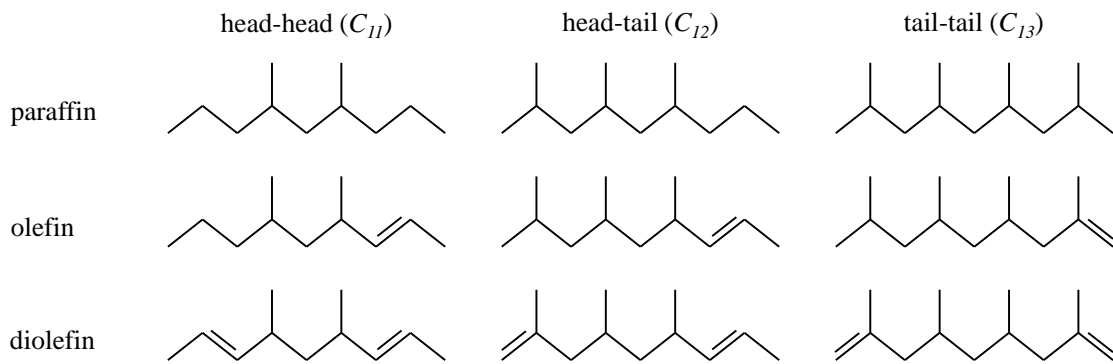


Figure 4.2: Schematic representation of the stable head and tail configurations of LMW species. C_{12} is employed as an example

The reactivity of both HMW and RLMW is characterized by internal and position-specific radicals (terminal and allylic). The former are either secondary or tertiary ones, but are represented by a single lumped species ($P-IC_{45}H_{89}-P$) that accounts for the reactivity of both positions. Terminal radicals ($_T$) in tail configurations are primary alkyl radicals, while for head configurations they are secondary alkyl radicals. Similarly, allyl-like radicals ($_A$) are secondary or tertiary allylic ones for tail and head configurations respectively.

The total number of liquid+gas species introduced is 240, where only 14 are HMW species. A significantly lower number of species compared to detailed models (10^2 vs 10^6) is employed, but they are still demanding for CFD simulations. As discussed in Section 4.2, a semi-detailed reduced and a multi-step model with lower number of species and reactions are validated.

The thermodynamic, transport, and critical properties are evaluated as discussed in Section 3.1.4. The main parameters of interest are thermochemical properties of stable species and vaporization enthalpies to perform reactor-scale energy balances. Briefly, gas-phase properties are estimated with group-contribution methods^{270–272}. Discrepancies are observed at increasing chain-length with the approach implemented in RMG²⁷³, but no experimental data for these long highly branched hydrocarbons is available for validation. Liquid-phase NASA polynomials are estimated from vaporization enthalpies^{280,284} and liquid heat capacities²⁸⁷. For LMW species, above the critical

temperature (T_c) the gas-phase parameters are employed, where the transition temperature (T_{LG}) is defined such that enthalpies are continuous. Since $c_{p,L}$ is underestimated approaching T_c , this results in a discontinuity of c_p at T_{LG} and the latter being $T_{LG} \approx T_c + 20$ K. Enthalpy (h_L) and specific heats of amorphous polymer species are obtained with the same procedure. On the other hand, entropy (s_L) is estimated from the NASA-polynomials of two fictitious reference carbon numbers C_{3000} and C_{3300} . This approach is quite sensitive to small numerical errors, resulting in not so accurate values for the species entropies. Nevertheless, as the mechanism employs only irreversible reactions, these uncertainties do not affect model predictions. The crystalline properties are estimated from experimental data on crystalline specific heats³³⁵. Above the melting temperature (T_m), the Einstein functional form is employed to ensure meaningful physical bounds to the heat capacity²⁸⁹. The crystalline enthalpy (h_c) is then estimated from the experimental melting enthalpy²¹, while s_c at 298 K is obtained from experimental data³³⁵.

Figure 4.3 shows the comparison of predicted properties for the mid-chain species with experimental values³³⁵. The proposed approach has good agreement over the experimentally investigated temperature range. With respect to the amorphous polymer, excellent agreement with experimental heat capacities and enthalpies is observed while entropy is overestimated. The issue lies in the complexity of estimating liquid-phase entropies far from the boiling point. Data on solvation energies can be employed to improve the agreement with experimental data, but model predictions will not be affected. With respect to the crystalline phase, good agreement is observed as the experimental data are employed to recover the thermochemical properties.

4.1.2 Reaction Classes

The proposed degradation mechanism operates on a radical basis, resulting in the formation of alkanes, 1- or 2-alkenes, and $\alpha - \omega$ dialkenes. The model is constructed through a hierarchical approach to reaction classes, where the entire network is derived from families of reactions proposed by other authors^{55,68}. This section first presents the considered reaction classes, their elementary steps, and the associated kinetic parameters. The reaction network is built from these families and involves ~ 13000 liquid-phase reactions. These are mainly H-abstractions and recombination reactions, but also stabilization of ULMW results in a higher number of backbiting reactions.

4.1.2.1 Elementary Steps

Homogeneous liquid-phase reactions lead to the formation of liquid-phase species or directly to gas-phase ULMW/ULLMW species. The elementary reaction classes, along with their modified-Arrhenius parameters, are reported in Table 4.1. The rate constants proposed here have been revised from the published model⁷⁴, reflecting updates due

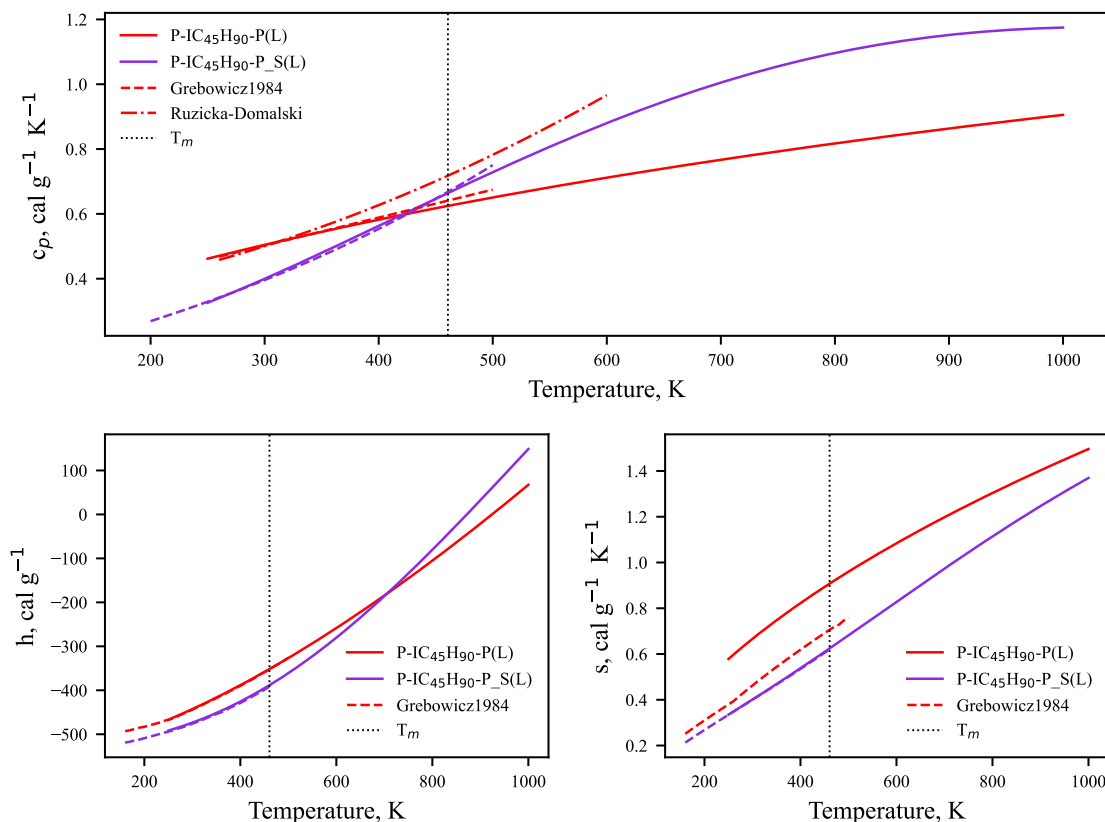


Figure 4.3: Comparison of predicted and experimental³³⁵ thermodynamic parameters per unit mass for the crystalline ($P-IC_{45}H_{90}-P_S$) and amorphous/molten ($P-IC_{45}H_{90}-P$) mid-chain polymeric species

to newly available experimental data on product distributions. These parameters are derived from previous studies in the literature^{55,57,68}, with some variations incorporated.

Considering chain initiation, a solvation correction using the flux unit proposed by Ranzi *et al.*⁵⁵ is applied, resulting in a decrease of ~ 8 kcal mol⁻¹ in activation energy. Consequently, this leads to lower activation energies for random scission reactions when compared to other works⁶⁸ and a 5 kcal mol⁻¹ lower activation energy than PE. The difference in reactivity between PE and PP is about 3 kcal mol⁻¹ lower than the gas-phase difference between branched and normal alkanes¹⁴⁶.

Regarding the proposed β -scission, lower activation energies are suggested compared to other literature studies^{55,68} but more in line with PE. A decrease of 1 kcal mol⁻¹ is considered due to formation of a primary and secondary radical instead of two primary radicals. This value also accounts for the starting radical being more stable and therefore less reactive. The unzipping rate constant has a 1 kcal mol⁻¹ decrease with respect to β -scission due to the lower stability of the reacting radical. Short compounds, characterized by higher mobility in the polymer melt, are less influenced by the repulsion of polymeric chains acting as a solvent. The high yield of C_3H_6 is

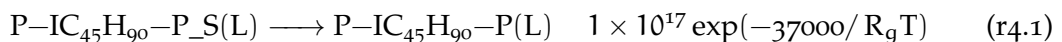
attributed also to a lower cage effect and an additional reduction of 2 kcal mol⁻¹ is introduced to account for the lower cage effect. Similarly, an increase to the frequency factor is considered to represent the higher mobility of the short segment. Compared to PE, this results in a higher selectivity to the monomer consistent with experimental observations.

With respect to H-abstraction reactions, similar rate parameters to gas-phase reactions are employed. Table 4.1 provides the values for H-abstraction of a secondary hydrogen by a secondary radical. The same gas-phase selectivity¹⁴⁶ to the abstracting radical and abstracted hydrogen as in gas-phase reactions (see Table 3.1). Regarding radical isomerisation, specifically backbiting, only the formation of 5-, 6-, and 7-member rings is considered as they balance between the number of hindered rotors and ring strain. In contrast to other literature studies, the present work considers that 1-6 backbiting (7-member ring) does not involve higher strain energies compared to 1-5, as bond angles are preserved through out-of-plane bending. Consecutive backbiting is also incorporated to account for the preferential formation of long-chain hydrocarbons, as discussed in more detail in Section 4.1.2.3. Table 4.1 reports the values for isomerisation of a primary radical to a secondary position. The difference in reactant and product radical are accounted for through the same corrections for H-abstraction reactions.

Recombination reactions are fast, but in the liquid phase the rate-determining step is the approach of two radicals, and therefore, they are assumed to be diffusion-controlled²⁴⁷. The difference in diffusivity between chains is evaluated by considering different frequency factors based on the species' chain lengths, following the description by Kruse *et al.*⁶¹. The flux units assessed by Ranzi *et al.*⁵⁵ serve as the lower limit for recombination reactions, and the corresponding values are presented in Table 4.1. Polymer melting is represented through a chemical reaction from the crystalline to the molten phase. High activation energies and pre-exponential factors are employed to ensure the phase transition occurs within a narrow range near the polypropylene melting temperature (180°C).

4.1.2.2 Backbone Degradation Mechanism

Upon heating, the first transformation the polymer undergoes is melting of the crystalline phase, represented by the liquid-phase reaction:



The reaction employs high activation energy and frequency factors to represent the quasi isothermal phase-transition at 180°C.

Heating further the molten polymer, the radical degradation starts through backbone random-scission reactions forming terminal radicals¹⁵⁶. These radicals then undertake propagation reactions as H-abstraction, β-scission, unzipping, and backbiting, while

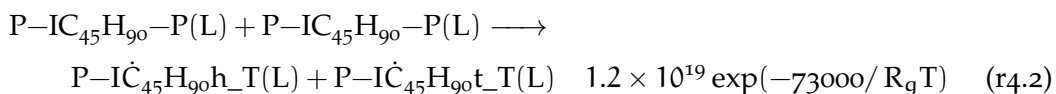
Table 4.1: Modified-Arrhenius parameters for elementary reactions classes (units cm, mol, s, cal). Parameters for recombination reactions refer to the polymer flux unit, while H-abstraction refers to a secondary radical (R_2) abstracting a secondary hydrogen (H_2). Unzipping reaction parameters refer to head radicals

Reaction	A	n_A	E_{act}
Random scission	5.00E+14	0	73000
β -scission R_3	1.00E+13	0	27000
β -scission R_2	1.00E+13	0	28000
Head unzipping	3.00E+13	0	24000
H-abstraction R_2+H_2	2.00E+11	0	13500
Backbiting 1-4	5.00E+10	0	20600
Backbiting 1-5	7.50E+09	0	14500
Backbiting 1-6	1.50E+09	0	14500
Radical recombination	2.00E+10	1	6000
Melting	1.00E+17	0	37000

only termination by radical-radical recombination is included²³⁹. Figure 4.4 schematically shows the reaction pathways leading to LMW formation from HMW stable species. The kinetic mechanism is more complex than PE as the head and tail end-chains undergo the same reactions although with different product selectivity. The random scission mechanism predicts equimolar formation of chains of different lengths, i.e., similar amounts of any chain from C_2 to C_{60} . Preferential formation of specific short-chain compounds such as propylene, 2-pentene and the trimer is due to the reactivity of primary and allylic radicals discussed in the next Sections.

The rate determining steps are HMW β -scission reactions^{55,65}, while the gas-phase products selectivity is primarily affected by the end-group functionalization. Nevertheless, the ratio initiation-to-termination controls the radical pool and considerably affects mass-loss profiles. To simplify the mechanism, primary Hydrogens are assumed unreactive and methane formation is neglected^{55,57,68}. Radical addition to double bonds and termination by disproportionation are not considered because of their lower importance with respect to β -scission and recombination reactions^{55,65}.

Radical initiation involves random scission on the mid-chain to form a head and a tail end-chain radicals:



where this reaction lumps all elementary initiation reactions occurring on the mid-chain species and a mid-chain unit is employed as Supporting Polymer Unit (SPU)

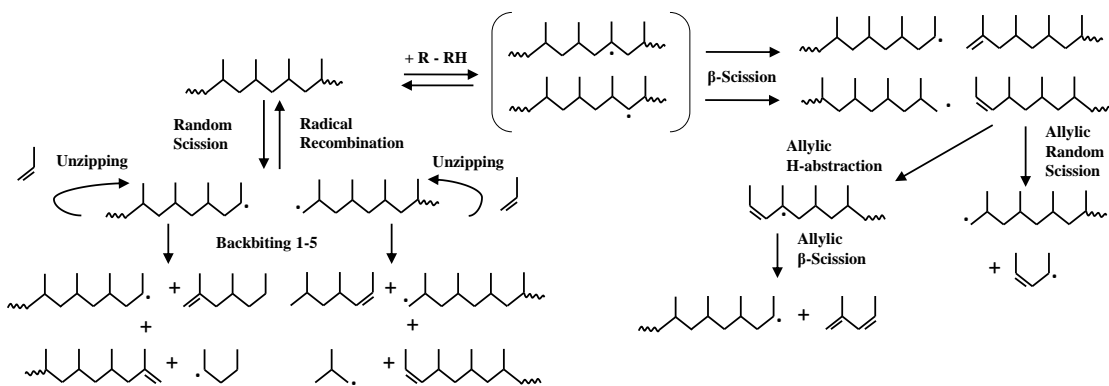
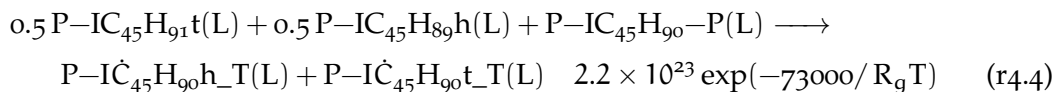
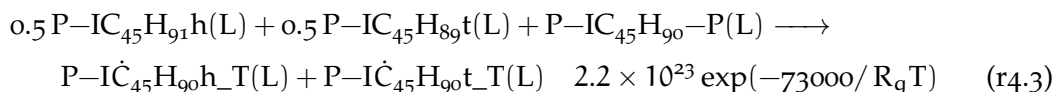


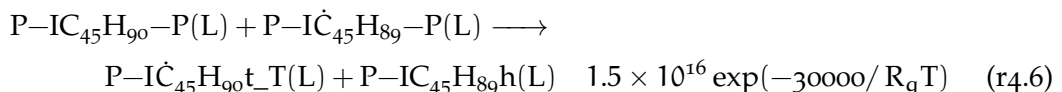
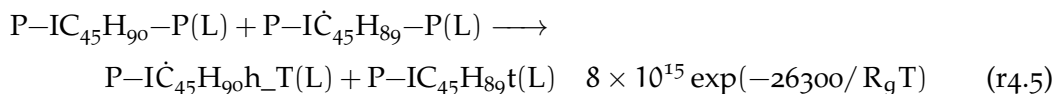
Figure 4.4: Schematic representation of the degradation of the initial mid-chain pseudo-species to form LMW products. The MC species undergoes random scission forming terminal radicals which recombine, backbite, H-abstract, or unzip.

(Figure 3.6). This additional chain-unit allows to conserve atomic and radical balances preserving the mechanism physical interpretation. To represent the possibility of having a neighbouring end-chain to the reacting functionality pairs of end-chains are also introduced as SPU. For PP, two pairs of head-tails conformations are considered:



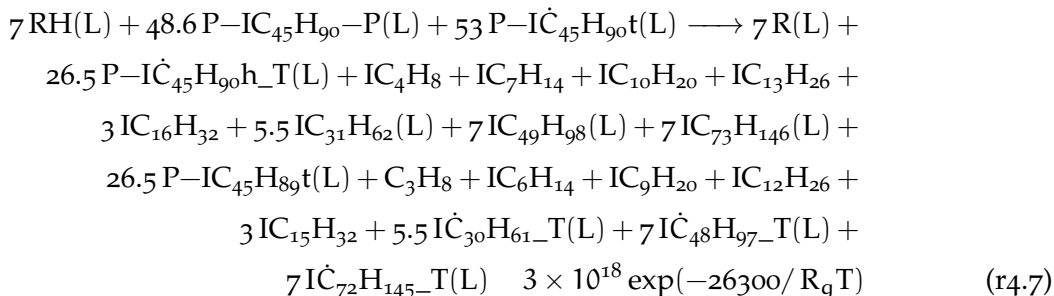
The selectivity to the SPU is included through the SPU molar fraction. To conform with the CHEMKIN format, the reaction rate constant is modified by a species-dependent parameter, γ_{SPU} , based on the SPU concentration (Equation 3.6).

The terminal radicals can stabilize through H-abstractions on the chain backbone. Reactions with mid-chain pseudo-species form mid-chain radicals ($P-\dot{I}C_{45}H_{89}-P$), which lump both secondary and tertiary positions. Following the lumping approach¹⁴⁶, H-abstractions forming either isomer are lumped in a single step with rate constant obtained as the weighted sum of the other two. On the other hand, two different decomposition reactions are included to account for the different product selectivity. β -scission of tertiary radicals form head paraffins and tail olefins, while secondary ones form the opposite as:



The rate parameters are modulated by the probability to form a secondary or tertiary radical⁴³. The former involves 2 hydrogens, but the latter is energetically favoured. For

instance, the rate constants of the reactions proceeding from tertiary radicals are modified considering the probability for the H-abstraction to occur on the tertiary hydrogen among all available positions (i.e., tertiary and secondary)¹⁵⁷. With respect to end-chain radicals, two separate β -scission reactions are also introduced to represent both internal positions. For instance, the reaction representing decomposition of a tertiary radical on the tail paraffin end-chain ($P-\dot{I}C_{45}H_{90}t$) is:



This reaction lumps all the elementary steps of the tertiary radical that releases species from C_3 to C_{90} through a vertical lumping procedure (Figure 3.9). The reaction also considers the proper configuration of the products, resulting in formation of head-tail paraffins (e.g., C_3H_8 and $IC_{15}H_{32}$) and tail-tail olefins (e.g., IC_4H_8 and $IC_{16}H_{32}$). ULMW and ULLMW species form directly as stable gas-phase species, assuming their formation is rate determining. The required hydrogen is taken from any neighbouring species RH converting it to the corresponding radical (Figure 3.8). To reduce the number of reactions, stabilization on RLMW with same carbon number are lumped together (see Section 3.3). The selectivity to the molar fraction of RH is introduced modifying the rate constant with a species-dependent γ_{RH} coefficient similarly to the SPU (Equation 3.6).

Termination by recombination leads to an increase in average chain-length³⁴². Therefore, when the reaction product is an HMW species, it is represented as a mixture of MC and EC units (Figure 3.10). This class of reactions also leads to formation of branched or unsaturated species which have lower hydrogen content compared to the considered compounds. To avoid introducing such species, the balancing error is dumped on the smallest diolefin (IC_6H_{10}). This simplification introduces an error that, using a global Rate of Production Analysis, was quantified in an increase of C_6 diolefin formation lower than 0.1%, an acceptable trade-off.

The same reaction classes are introduced also for RLMW species. The stable species can undergo H-abstractions forming internal radicals which can decompose through β -scission reactions, where the reaction products are represented through vertical lumping. An additional reaction is also introduced to represent their evaporation with reaction parameters obtained from a bubble-evaporation model (Section 3.1.3). The resulting boiling activation energies account for kinetics being controlling at low temperatures while boiling becomes determining at higher temperatures. Additionally, longer

chain compounds are characterized by low temperatures reaction rates as they are more prone to secondary degradations at higher temperatures.

4.1.2.3 Allylic position, terminal radicals, and weak-links

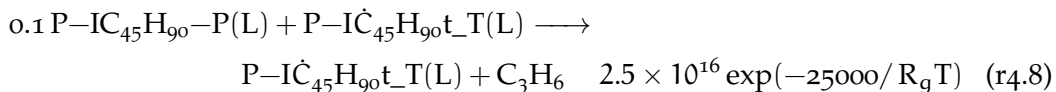
The backbone degradation mechanism predicts an equimolar release of LMW products not consistent with the experimental observations. The uneven distribution is assumed resulting from specific functionalization as allyl-type and terminal radicals.

The increased stability of the allylic radical justifies the preferential formation of isobutene (IC_4H_8), 2-pentene ($\text{C}_5\text{H}_{10}-2$), and 2-methyl-1,3-pentadiene (IC_6H_{10}). These radicals undergo the same elementary steps reported in Table 4.1 but with different rates. The correction with respect to secondary alkyl radicals are the same reported in Table 3.3. The higher stability results in an increase of both random and β -scissions but also H-abstractions that form them. On the other hand, reactions of these radicals are slower due to their higher stability. Nevertheless, formation of IC_6H_{10} is enhanced because of formation of conjugated double bonds. Since termination reactions are assumed diffusion-limited, the higher radical stability does not affect the rate constant.

In polypropylene, allyl-like radicals are secondary and tertiary allylic in tail and head configurations, respectively. The resonance stability also favours H-abstractions on the methyl groups next to the double bond resulting in primary allylic hydrogens with lower BDE than the backbone ones. While these should be considered because of the higher reactivity, the primary allylic radical can only undergo β -scission reactions forming an allene structure in tail configurations. This step requires breaking the bond in the vinyl position, which is unfavoured due to the higher activation energy involved⁴³. On the other hand, in head configurations the primary allylic radical has a resonant form that can decompose breaking the chain bonds to form 1,3-pentadiene (C_5H_{8-3}). While this pathway is important with respect to the backbone mechanism, it is not considered due to the ~ 4 kcal mol⁻¹ lower stability of primary radicals with respect to tertiary ones¹⁴⁶. For the same reason, formation of head allyl-type radicals has a 2 kcal mol⁻¹ activation energy lower with respect to tail allylic ones.

Contrary to allyl-types, terminal radicals are less stable than the backbone ones. However, these form through backbone decomposition reactions and before stabilizing they can undertake different reaction pathways. The most important decomposition pathways for both configurations are unzipping and backbiting. The first one is responsible for preferential formation of propylene, while the latter for formation of the trimer (IC_9H_{18}). As discussed in-depth in section 4.1.2.1, according to literature experimental data the monomer molar yield is higher than the one in polystyrene. This is possibly consequence of lower cage-effects or formation of double bonds on the

side-groups which ease formation of C₃H₅. In the present work, these phenomena are represented through unzipping reactions of the form:



The same reaction is introduced also for head and RLMW terminal radicals, neglecting differences in reactivities between head and tail conformations. The reported kinetic constant has a 1 kcal mol⁻¹ higher E_{act} compared to Table 4.1 as it forms a primary radical from a primary radical.

All terminal radicals can undergo up to backbiting 1-12. The model assumes isomerisation being rate determining, and therefore the decomposition step of the formed radical is lumped in the backbiting reaction. As mentioned, the Arrhenius parameters reported in Table 4.1 refer to the isomerisation of a primary to a secondary radical. Isomerisation involving other radicals are modified with the same corrections employed also for H-abstraction reactions¹⁴⁶. For each consecutive transfer, the rate constant is modulated through a backbiting probability, $\alpha_{bb_n,i}$, defined as:

$$\alpha_{bb_n,i} = \frac{k_{bb_n,i}}{\sum_j k_{bb_j,i} + \sum_j k_{i,H_j} C_{H_j} + k_\beta + k_{RR} C_{R_{tot}}} \quad (4.1)$$

which represents the probability that the radical in position *i* undergoes a 1-*n* H-transfer compared to the available reaction pathways of radical *i*, where *n* refers to the elementary backbiting considered in Table 4.1. Both H-abstraction and backbiting constants depend on the type of radical *i*, and the latter also depends on the resulting radical. The possible radical pathways are all elementary backbiting, H-abstractions on any hydrogen type *j*, β-scissions or recombination reactions. The hydrogen concentration of type *j* (C_{H,j}) are assumed constant and evaluated at the monomer concentration, while the total radical concentration (C_{R,tot}) is estimated with the pseudo-steady-state assumption⁵⁵. The rate constant of backbiting 1-*n* is then evaluated summing all pathways leading to that isomerisation and regressing it to an Arrhenius form. The rate of each pathway is estimated modulating the first backbiting step with the probability $\alpha_{bb_n,i}$ (Section 3.1.2.4).

Head and tail configurations have different selectivities, and therefore the rate constants are evaluated separately. Table 4.2 reports the resulting rate constants for head and tail backbiting reactions. The 1-5 backbiting of head radicals is the most favoured one. For the tail configuration, the 1-6 backbiting has lower activation energy than 1-5 as it forms a tertiary radical. Nevertheless, its frequency factor is lower both because of the higher number of hindered rotors and lower hydrogens per carbon (i.e., there are two secondary hydrogens and a single tertiary one). Similarly, tail 1-6 backbiting has 1 kcal mol⁻¹ lower than 1-5 head due to the lower stability of the starting radical. Backbiting 1-7 has significantly higher activation energy as the 1-4 energy barrier is modulated by the probability a second backbiting occurs with respect to the stabilisation of the radical in 5th position. Indeed, the increase of ~10 kcal mol⁻¹ obtained

by linear regression is consistent with the difference of ~ 8 kcal mol $^{-1}$ between backbiting 1-4 and H-abstraction. The main products from backbiting reactions of both head and tail configurations are the trimer (IC_9H_{18}) and C_4 – C_6 paraffins. Formation of the tetramer ($\text{IC}_{12}\text{H}_{24}$) and pentamer ($\text{IC}_{15}\text{H}_{30}$) are also enhanced. However, the latter is represented through a vertical lumping procedure and therefore its specific peak is underestimated in the present model.

Table 4.2: Arrhenius parameters of backbiting reactions obtained from regression (units s, cal, mol).

Reaction	Head		Tail	
	A	E_{act}	A	E_{act}
Backbiting 1-4	1.00E+11	21600	5.00E+10	18400
Backbiting 1-5	7.50E+00	13300	1.50E+10	14500
Backbiting 1-6	3.00E+09	15500	1.50E+09	12300
Backbiting 1-7	4.88E+11	30500	1.13E+11	24800
Backbiting 1-8	4.07E+10	20500	8.14E+10	21700
Backbiting 1-9	6.51E+09	16100	8.05E+09	15500
Backbiting 1-10	1.47E+09	14600	3.26E+09	16000
Backbiting 1-11	2.00E+10	22800	2.36E+09	16500
Backbiting 1-12	4.00E+10	21800	1.27E+11	24100

The description reported refers to ideal isotactic polymeric chains. In case of atactic samples, the higher reactivity is attributed to defects as head-head configurations or heteroatoms weak-links and a higher melt-mobility^{71,224}. Similarly to LDPE, a correction to the activation energy of mid-chain random scission ($\Delta E_{\text{MC}}^{\text{RS}}$) is considered. The decrease is based on the sample density, ρ_L^0 , as:

$$\Delta E_{\text{MC}}^{\text{RS}} = -4000 \frac{\rho_L^0 - 985}{895 - 985} \quad (4.2)$$

where units are kcal, mol, kg, and m 3 . In general, for APP samples with unknown density a value of $\Delta E_{\text{MC}}^{\text{RS}} = -2000$ is employed.

4.2 REDUCED-ORDER MODELS

Despite a significant reduction in computational cost, applying Computational Fluid Dynamics (CFD) to plastic waste valorization demands description of multiple polymers and detailed characterization of gas-phase reactivity. The kinetic model for PP is especially expensive due to both a high number of species and reactions, and therefore additional lumping techniques are employed to decrease them.

In the following sections, two reduced models are introduced in line with Section 3.3. A semi-detailed model that simplifies the radical description is first presented. The selectivity of the different radical isomers are then employed to obtain a multi-step (fully lumped) mechanism. This model omits all radical intermediates and simplifies the intricate reaction pathways into a few lumped steps.

4.2.1 Reduced Semi-Detailed Model: PP-130-2500

The main computational cost of the proposed kinetic mechanism stems from the detailed characterization of the radical reactivity. To this aim, both the species and reactions considered are further lumped.

Compared to the model for PE, the selected species for PP are close to the minimum necessary to portray the product distribution. Lumping the distribution of C<C₁₂ does not allow to evaluate preferential formation of C₉, which is the main product after propylene. A small decrease in the number of species is achieved considering one less RLMW. Therefore, the reduced model employs C<C₁₆ as ULMW, and C₃₀ and C₆₀ as RLMW. Additional reduction techniques are expected to further decrease the computational cost but have not been considered in the present work. For instance, lumping the head-tail configurations can significantly reduce the number of species involved. Additionally, long-chain paraffins, olefins, and diolefins can be further lumped due to their similar reactivity. With respect to the considered radicals, all isomers are represented in a single pseudo-species and one radical per stable species is considered. Overall, the reduced model incorporates a substantial reduction in the number of species, decreasing it from 240 to 130 (liquid+gas) (55%). While the kinetic mechanism still involves three times the number of species introduced for the reduced PE model, significant progress has been made compared to the starting mechanism.

The radical lumping is performed following the approach proposed by Pegurri *et al.*³³² as discussed for PE in Section 3.3.1.2. The branching fraction (BF) of each class of radicals are evaluated in post-processing and are employed to weight the elementary rate constants. These are then regressed to an Arrhenius form and are reported in Table 4.3. As a first approximation, no distinction is made between head and tail radicals while estimating BFs, but the lumped rate constants preserve the configuration selectivity of the semi-detailed model. For instance, estimating the lumped rate constant of backbiting 1-5 from a head radical employs the head backbiting constant and the branching fraction of terminal radicals. On the other hand, the backbiting 1-5 from a tail radical employs the same BF value but the rate constant of tail 1-5 backbiting. Compared to values obtained for PE (Table 3.6), several differences are observed. Unzipping rate constants are similar, while the lower selectivity to waxes is reflected in a significantly lower rate constant for paraffin β-scissions. For this reason, backbiting reactions in PP are intermediate temperature reactions contrary to PE. Lower import-

ance of allylic radicals is observed for PP, possibly because of the higher stability of the tertiary position.

Table 4.3: Modified-Arrhenius parameters of radical lumped reactions obtained from regression (units s, cal, mol).

Reaction	A	n _A	E _{act}
Paraffin β -scission	3.00E+07	0	11000
Olefin β -scission	8.00E+12	0	32500
Olefin allylic β -scission	7.20E+12	0	29800
H-abstraction by paraffin	6.00E+11	0	12700
H-abstraction by olefin	7.20E+11	0	17800
Unzipping	1.50E+14	0	30300
tail Backbiting 1-5	1.05E+11	0	20800
tail Backbiting 1-6	1.05E+10	0	18600
tail Backbiting 1-9	4.20E+10	0	21800
tail Backbiting 1-10	1.62E+10	0	22300
head Backbiting 1-5	3.60E+10	0	19600
head Backbiting 1-6	1.50E+10	0	21800
head Backbiting 1-9	3.00E+10	0	22400
head Backbiting 1-10	7.50E+09	0	20900

Additional steps are also taken to reduce the number of reactions. Since propagation reactions are rate determining and the radical pool is controlled by HMW species, RLMW species undergo only propagation reactions. Furthermore only the most important backbiting reactions are considered. Due to the high activation energy, backbiting 1-4, 1-7, and 1-8 are not included. On the other hand, backbiting longer than 1-10 are neglected because of the high entropic requirements. These lumping techniques result in the reduced model involving 2500 reactions, which is significantly lower than the starting 13000.

4.2.2 Multi-step Fully Lumped Model: PP-10-12

The reduced mechanism achieves a significant reduction in computational cost compared to the semi-detailed one, but it is still far from application for PW valorization. The results of the reduced model are employed to derive a multi-step version where the complex radical reactivity is simplified in few lumped steps, resulting in a non-stiff kinetic mechanism. The aim is still being able to predictively describe the key physico-

chemical steps of the degradation, i. e., residence times, heat requirements, and product distribution.

The polymer chain distribution is represented only by a crystalline and an amorphous/molten mid-chain species ($P-IC_{45}H_{90}-P_S$ and $P-IC_{45}H_{90}-P$). The initial composition depends only on the polymer crystallinity, while any dependence on the average molecular weight is neglected. With respect to the volatile compounds (LMW), light gases are represented only by C_3H_6 , IC_4H_8 , and C_5H_{12} (ULMW). The first is the main high-temperature product, while the other two represent short chain products formed by allylic radicals and backbiting reactions respectively. The shortest diolefin introduced is IC_6H_{10} , which is the equivalent of C_4H_6 for PE, and acts as precursor for both soot and tar¹⁴⁷. Longer chains are represented through lumped species representative of various petroleum fractions, with only the olefin specific to that particular carbon number taken into consideration. Consequently, oil cuts (C_7-C_{11}) are embodied by IC_9H_{18} , diesel cuts ($C_{12}-C_{20}$) by $IC_{15}H_{30}$, and heavy waxes (C_{21+}) by $IC_{30}H_{60}$. All species except for $IC_{30}H_{60}$ form directly in gas-phase, while the latter can further decompose in liquid-phase to shorter chains. The total number of species introduced is 10, where only 3 are liquid-phase ones.

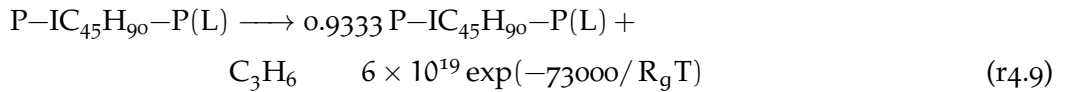
As previously mentioned, the present model simplifies the complex reactivity in few lumped single-step reactions representative of the elementary acts involved. Radicals are not explicitly considered but are accounted for through the proposed Arrhenius parameters. The introduced reaction classes and their rate parameters are summarized in Table 4.4.

Table 4.4: Reaction classes of the multi-step model and their modified-Arrhenius parameters (units cm, mol, s, cal)

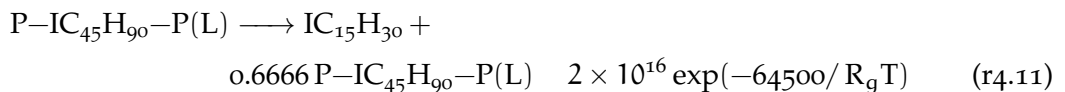
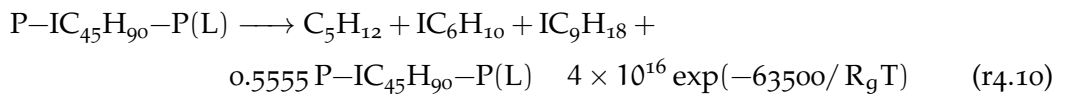
Reaction (number)	A	E
Melting	1.0E+17	37000
Backbone degradation	1.5E+16	60300
IC_4H_8 formation	1.5E+14	57000
Backbiting	4.0E+16	63500
Multi-Backbiting	2.0E+16	64500
Unzipping	6.0E+19	73000
Evaporation of waxes	5.0E+06	17000

The first phenomenon occurring is melting of the crystalline phase, which is represented with the same reaction as the semi-detailed model. The molten polymer then decomposes along five main routes. The high temperature pathway is unzipping, whose

rate is determined a priori neglecting the presence of allylic radicals. The unzipping reaction introduced is:

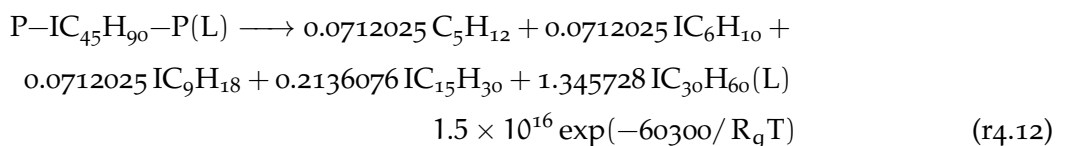


The Arrhenius parameters of this reaction are obtained assuming steady-state terminal radicals and employing the unzipping rate constant. The rate constant is evaluated as the concentration of terminal radicals per mid-chain unit multiplied the unzipping rate constant (Equation 3.27). Compared to PE, a higher selectivity to the monomer is obtained introducing both a lower activation energy and higher frequency factor. With respect to the reactivity of terminal radicals, reactions representing single and multiple backbiting are introduced. Indeed, the first corresponds to formation of short chain compounds and the trimer (oil cuts), while the latter results in higher diesel cuts yields. Compared to PE, formation of diesel cuts results from only two consecutive backbiting and are therefore relevant at reaction conditions. To summarise, the reactions introduced to describe the reactivity of terminal radicals are:



The kinetic parameters of these reactions are obtained from the selectivity of the semi-detailed model.

The low temperature pathway is the backbone degradation mechanism, which results in formation of chains from C_5 to C_{90} as:



The rate parameters of this reaction are obtained assuming the stabilization of the terminal radical is rate determining for the backbone degradation mechanism. Compared to PE, a lower activation energy is obtained analogously to the faster unzipping reaction. The reactivity of allylic radicals is considered in the backbone degradation mechanism as formation of unsaturated compounds is lumped in the single degradation step. On the other hand, formation of isobutene is consequence of preferential formation of allylic radicals, and is represented with a separate reaction. The rate constant employs the same selectivity to propylene formation from PE. As previously mentioned, these kinetic parameters represent complex lumped pathways and do not correspond to elementary step parameters.

The same reaction classes are introduced also to represent secondary liquid-phase cracking of waxes. Therefore 5 additional reactions are considered also for $\text{IC}_{30}\text{H}_{60}(\text{L})$, employing the same selectivity. Evaporation of waxes is represented as well through a chemical reaction. Overall, the mechanism considers 12 liquid-phase reactions.

4.3 MODEL VALIDATION

The performances of the proposed kinetic models are assessed through a wide range of literature experimental data. The data exhibits notable variability, attributed potentially to both variations in the plastic composition and differences in the employed experimental setups¹⁵. The former source of variability arises from each polymer possessing distinct quantities of weak links, impurities, additives, and initial molecular weights. These factors predominantly impact the onset temperature⁶⁵, contributing to the observed high scattering. The latter source of variability stems from the experimental facility itself. While temperature remains the most influential factor, variations in carrier gas flow rate, sample pan design, and instrument geometries and materials can lead to temperature shifts of approximately 10°C ^{306,307}.

Model validation is performed in terms of characteristic degradation times (i.e., mass-loss profiles), volatile yields, and energy requirements. Setups where transport phenomena and secondary cracking reactions can be reasonably neglected (e.g., TGAs, pyroprobes, micropyrolyzers) are considered. If no information on the polymer is reported, an initial number average molecular weight of 80 kg mol^{-1} is considered. Similarly, the initial $\Delta E_{\text{RS}}^{\text{MC}}$ correction employs a value of 0 and $-2000 \text{ kcal mol}^{-1}$ for isotactic and atactic polypropylene respectively. The initial composition is evaluated from the Schultz distribution²³⁶ assuming only olefins are present in the reacting mixture. If no information on the crystallinity is reported, a value of 0.5 is considered for isotactic PP while the atactic polymer is assumed purely amorphous²²⁴. The same physical and numerical model described in Section 3.2.1 is employed. A comparison with the detailed model of Ranzi *et al.*⁵⁵ is also shown, and the mechanism performances are assessed through the Curve Matching (CM) score (Section 3.2.2).

4.3.1 Characteristic degradation times: mass-loss profiles

Mass-loss profiles constitute the most prevalent experiments conducted in scientific literature, and approximately 70 mass-loss profiles^{55,115,215,314,318,327,336,337,339,343–354} have been utilized in the present validation. Literature data show a variability of $\sim 10\text{--}20^\circ\text{C}$ according to the experimental study, although average degradation temperatures are quite consistent.

Figure 4.5 shows the comparison of mass-loss profiles for isotactic (iPP) and atactic polypropylene (aPP) for the semi-detailed and detailed models. The former is able to

reproduce the latter both at dynamic (Figure 4.5a) and isothermal (Figure 4.5b) conditions, as highlighted by the high curve matching scores of both models. The present mechanism predicts a slightly lower apparent activation energy, due to the different kinetic parameters employed. The semi-detailed model is able to describe the mass-loss profiles of aPP (dashed-dotted lines) through the simple correction introduced. However, the mechanism cannot reproduce experimental data of Kiang *et al.*³³⁶ at HR=30°C/min. Indeed, the kinetic mechanism predicts a monotonic increase in reaction temperature at higher heating rates. For this reason, it is not able to predict for the HR=30°C/min sample having a lower degradation temperature with respect to the HR=5°C/min one. The data of Kiang *et al.*³³⁶ have also a 60°C lower degradation temperature compared to measurements of Abbas-Abadi *et al.*³⁵⁵ in similar conditions. This discrepancy between experimental data is the reason for the low CM score at HR=30°C/min. While the mechanism underestimates the reactivity of both iPP and aPP, it captures the difference between the samples' degradation temperature also at these conditions. Considering isothermal conditions, the semi-detailed model predicts slightly higher degradation times with respect to the detailed one. Nevertheless, both models have high CM score.

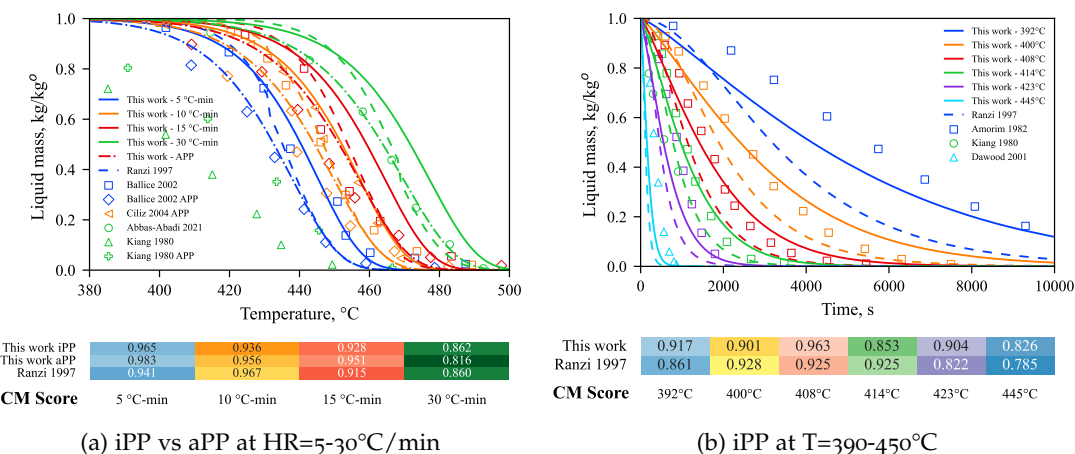


Figure 4.5: Sample mass-loss profiles of PP subjected to different temperature profiles. Comparison among the present work for iPP (solid lines), the model for aPP (dashed dotted lines), the detailed model of Ranzi *et al.* (dashed lines) and literature experimental data (marks). The Curve Matching score (CM) is also reported.

Figure 4.6 shows the comparison of the three models with experimental data on PP. Considering dynamic conditions (Figure 4.6a), a higher data scattering is observed compared to PE. Specifically, at HR=10°C/min the measured onset temperature varies of 50°C according to the study. The three models predict comparable profiles with differences <5°C in terms of temperatures and are in agreement with experimental data as highlighted by the high CM scores. The semi-detailed model predicts a delayed onset but a higher global reactivity. On the contrary, the reduced and multi-step mechanisms

simplify the radical description resulting in smoother profiles. The reduced model also predicts slightly higher apparent activation energies, possibly because of an excessive importance of unzipping reactions at low temperature. All models overestimate the reactivity at $HR=50^{\circ}\text{C}/\text{min}$, but further validation is required. Similar behaviours are observed also in isothermal conditions, where the semi-detailed mechanism predicts steeper degradation profiles compared to the other two. The CM scores in isothermal conditions exhibit quite different values, but no significant difference in predictions is observed. All models predict similar behaviours with respect to aPP profiles.

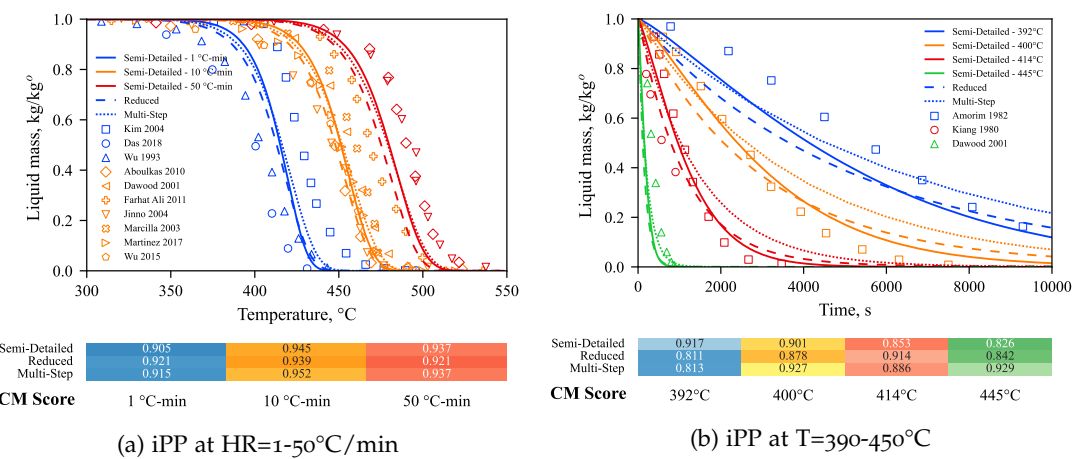


Figure 4.6: Sample mass-loss profiles of PP subjected to different temperature profiles. Comparison among the semi-detailed (solid lines), reduced (dashed lines) and multi-step (dotted lines) model and literature experimental data (marks). The Curve Matching score (CM) is also reported.

Figure 4.7 presents parity plots comparing predicted and experimental onset ($m_L=90\%$), half-conversion ($m_L=50\%$), and final-conversion ($m_L=10\%$) temperatures (T) and times (t). The parity plot incorporates data for both iPP and aPP, showcasing the efficacy of the simple correction in capturing the differentities. While a noticeable scattering is observed, particularly in terms of onset temperatures, both the detailed and semi-detailed models exhibit good agreement overall under the investigated operating conditions. The semi-detailed model generally boasts higher average R^2 values, although the results from all models are comparable. Specifically, in dynamic conditions (Figure 4.7a) it predicts higher onset temperatures ($<5^{\circ}\text{C}$) and lower final conversion temperatures ($<5^{\circ}\text{C}$). The reduced model has the higher apparent activation energy, resulting in 5°C lower onset temperature and final-conversion temperatures. The semi-detailed models have general better agreement considering isothermal conditions (Figure 4.7b), but the other mechanisms do not significantly differ. At high temperatures, all models predict an exponential increase in degradation rates.

Model predictions are further evaluated using the multi-index approach of Curve Matching, considering both iPP and aPP data in dynamic and isothermal conditions.

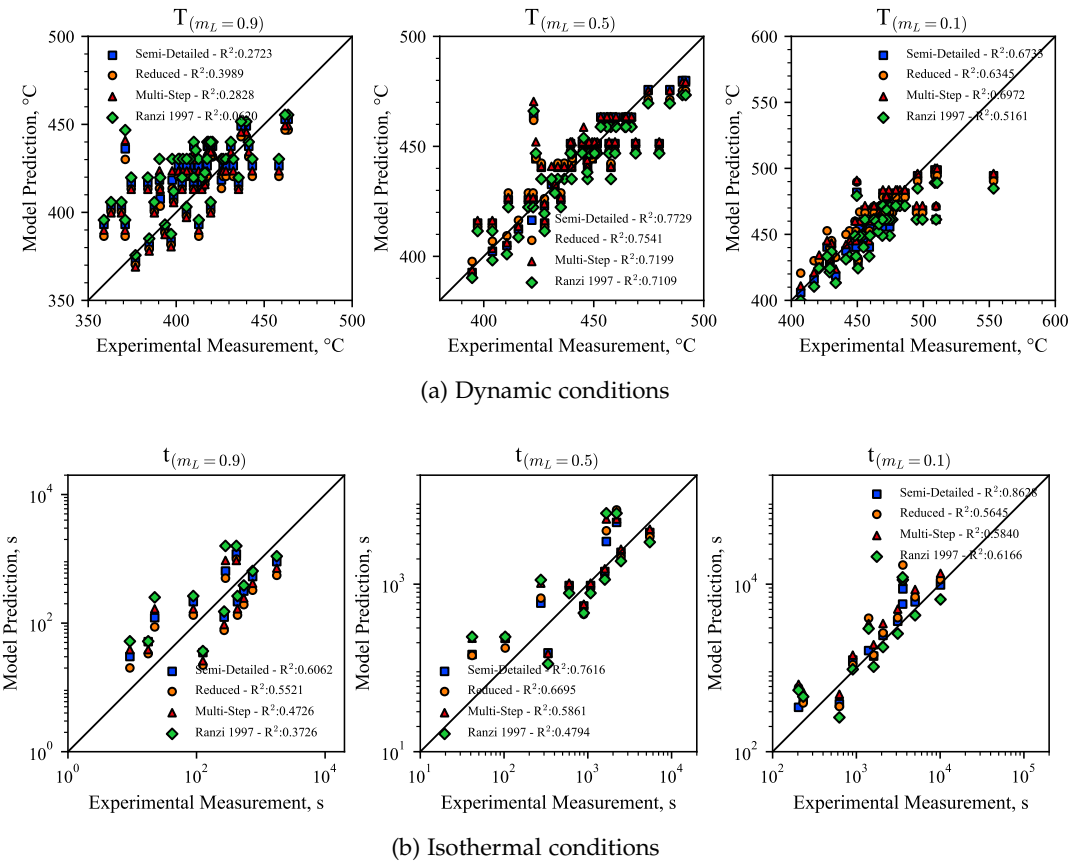


Figure 4.7: Parity plots for iPP and aPP degradation temperatures (top) and times (bottom) at sample mass (m_L) 0.9, 0.5 and 0.1 of the semi-detailed (blue squares), reduced (yellow circles), multi-step (red triangles), detailed model of Ranzi *et al.* (green diamonds), and literature experimental data.

Figure 4.8 shows both the CM score and the 5 different indices introduced. The semi-detailed and detailed models exhibit similar CM scores, emphasizing the reliability of the proposed approach in terms of characteristic degradation times. Although the former has slightly higher scores, the difference is negligible. On the other hand, the reduced and multi-step model have higher curve matching scores compared to both the semi-detailed and detailed mechanisms. Analyzing different indices provides a more comprehensive assessment of model predictions. Semi-detailed and detailed mechanisms show high L^2 indices, while lower values are observed for d_{pe}^1 and shift. The latter are a consequence of the wide experimental scattering in terms of degradation temperatures. As discussed in previous paragraphs, individual differences in polymer samples result in variations in degradation temperatures. The higher values of these indices are the reason for the higher CM score of the reduced-order models. The semi-detailed model proves better in isothermal operating conditions, and possibly the lack of these data penalizes it compared to the other two models. Overall, the models correctly captures the degradation trend, with polymer-specific differences mainly af-

fecting the prediction of different degradation temperatures rather than the apparent activation energy of the process.

	CM	$d_{L_2}^0$	$d_{L_2}^1$	d_{Pe}^0	d_{Pe}^1	shift
Semi-Detailed	0.904	0.994	0.987	0.954	0.894	0.798
Reduced	0.923	0.992	0.988	0.936	0.919	0.851
Multi-Step	0.928	0.991	0.988	0.933	0.910	0.872
Ranzi 1997	0.874	0.988	0.976	0.929	0.852	0.750

Figure 4.8: Comparison of SciExpeM indices (Section 3.2.2) on all mass-loss profiles investigated for the semi-detailed, reduced, and multi-step model. The detailed model of Ranzi *et al.* is also reported as comparison.

Polymer mass-loss is a result of the formation of species short enough to escape the polymer melt. However, the degradation of polymeric chains initiates before volatiles are released. In the case of PP, even though the observed mass-loss starts above 400°C, the variation in molecular weight begins as early as 300°C according to the models. The proposed kinetic mechanisms simplify the description of the chain-length distribution while portraying the polymer evolution in terms of its chemical moieties. Nonetheless, as discussed in Section 3.1.1.3, the initial average molecular weight influences model predictions, as it correlates with the amounts of end-chains in the system⁷⁴. Figure 4.9 illustrates the comparison between the reconstructed number average molecular weight $MW_{n,av}$ in the semi-detailed and reduced models and the values predicted by the detailed model of Ranzi *et al.*⁵⁵. The present approach demonstrates substantial agreement with the detailed model. The observed difference in chain-length reduction is a consequence of the higher significance of unzipping reactions compared to β -scissions. Unzipping reactions reduce chain lengths by one monomeric unit, while β -scissions halve the chains. Toward the end of the degradation, the semi-detailed model predicts a higher L_{av} due to faster evaporation of chains in the C₃₀-C₆₀ range. Validation of predictions from all models requires data on average molecular weight under controlled conditions. The reduced model has similar results compared to the semi-detailed one.

4.3.2 Products selectivity: volatile yields

The crucial aspect of the proposed models lies in their ability to depict detailed product distributions. As mentioned earlier, characterizing the compound distribution of plastic waste is exceedingly complex, leading to a scarcity of speciation data in the scientific literature. Furthermore, most studies focus solely on identifying the compounds involved, often without providing quantification. While these data aid in comprehending

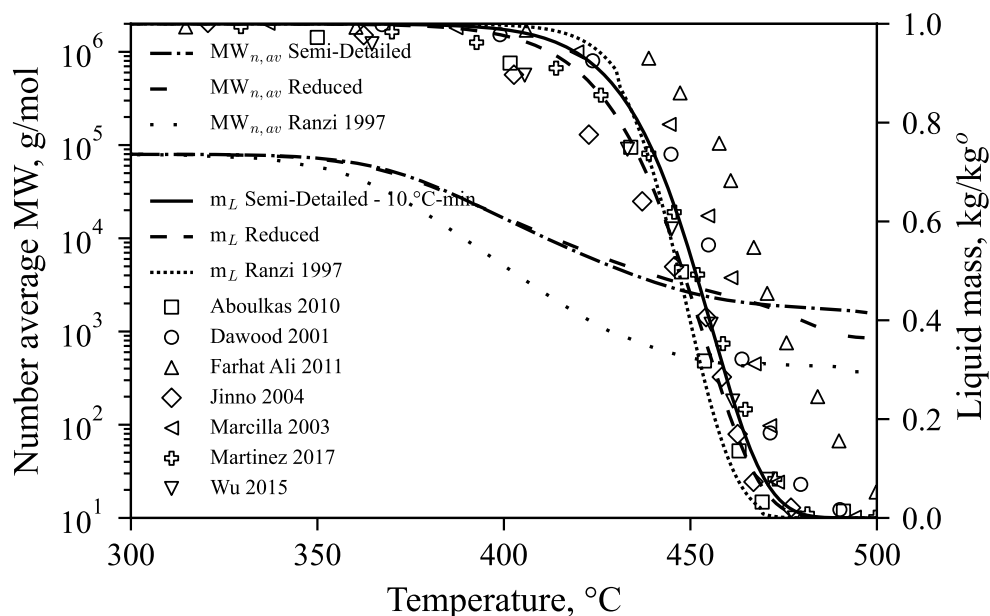


Figure 4.9: iPP mass-loss (m_L) and number average molecular weight ($MW_{n,av}$) profiles at $HR=10^\circ\text{C}/\text{min}$. Comparison among the semi-detailed, reduced, and detailed model of Faravelli *et al.* and mass-loss and number average molecular weight literature experimental data.

the processes occurring during degradation, they are insufficient for validating model predictions. Less detailed speciation data involve characterizing the product distribution in terms of petroleum cuts, categorizing volatiles based on their boiling temperatures into light gases, oils, or waxes. Although these data are typically quantitative, discrepancies typically arise due to experimental variations possibly due to secondary cracking reactions²⁵¹.

Figure 4.10 shows the comparison of the semi-detailed and reduced models in estimating the weight carbon distribution at 410, 438, and 600°C. The figures show the comparison of selectivity to the considered product, i. e., model predictions are normalized on the identified volatiles. This procedure allows to have a meaningful comparison with the experimental data in terms of selectivity, while showing also the predicted values of compounds not quantified. If detailed mass yield data are available, the total yields are compared as they are. Both models are able to represent the product selectivity at the different temperatures, although specific different behaviours are observed. The semi-detailed model captures the high selectivity to trimer formation (C_9) and its relative decrease at higher temperatures. Similarly, the increase in monomer formation is well captured at the three temperatures of interest. On the other hand, the model does not consider methane formation and underestimates formation of C_2 hydrocarbons. As with PE, formation of both products are possibly due to a lower cage effect. These phenomena can be considered, resulting however in a significantly more expensive mechanism. As the model already involves a high number of reactions, it is chosen

to neglect them. The reduced model predicts a lower selectivity to propylene at higher temperatures. The reason is that the lumped kinetic parameters are not able to predict comparable yields at both 410°C (Figure 4.10a) and 600°C (Figure 4.10c). Similarly, it does not properly quantify the allylic radicals' reactivity resulting in underestimation of C₆ at high temperatures. The higher observed yield in C₉ is consequence of a lower selectivity to unzipping reactions. The reduced model kinetic parameters can be optimized to better reproduce the semi-detailed one³³², but the current results are already within experimental uncertainty.

While good agreement is observed for product selectivity at 410°C (Figure 4.10a), the models predict low absolute yields (i. e., kg/kg⁰) of the shown components. The reason lies in the predicted high yields of waxes (>60 wt.%) analogously to polyethylene (Section 3.2). High wax yields and formation of long-chain hydrocarbons (C>C₅₀) are measured also by other authors at higher temperatures²³¹. Given that wax formation is favoured at low temperatures²²⁸, higher yields at 410°C can be expected as measured by Wong *et al.*³⁵⁶. The extended residence times in the fixed bed reactor (approximately 1 minute) or high sample masses (0.25 g) could potentially lead to the cracking of C>C₂₀ hydrocarbons. Similarly, the elevated C₁₃ yield in comparison to data at 438°C³³⁶ (Figure 4.10b) might be explained by multiple gas-phase backbiting. Unlike in the liquid phase, these reactions encounter fewer hindrances as no solvent is present.

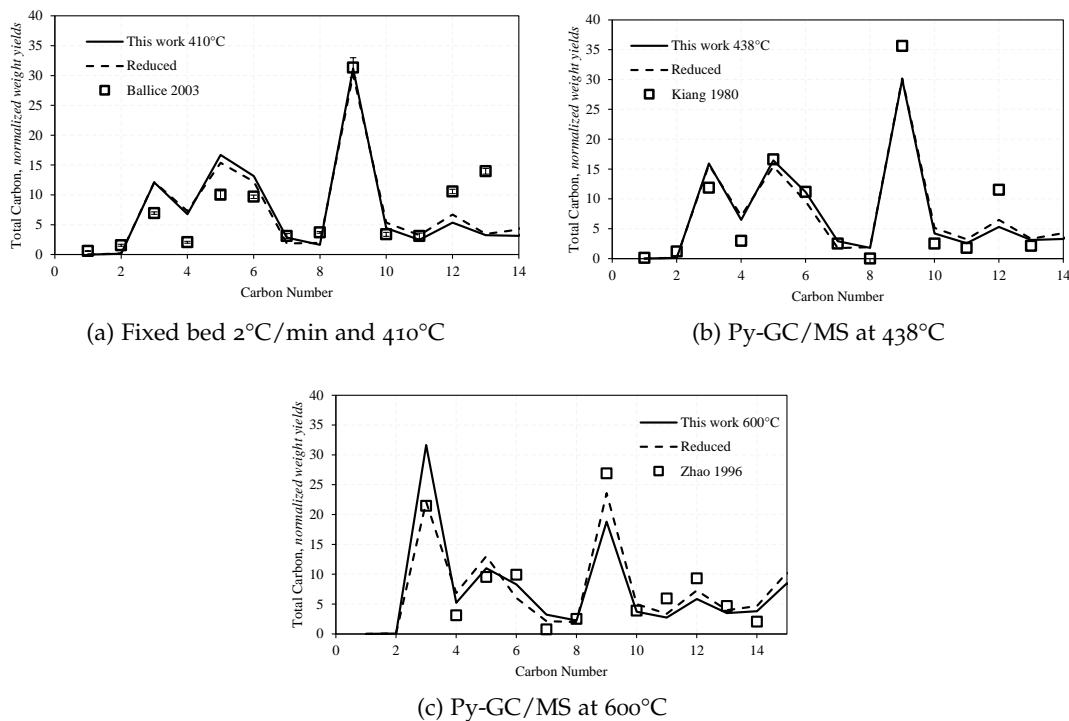
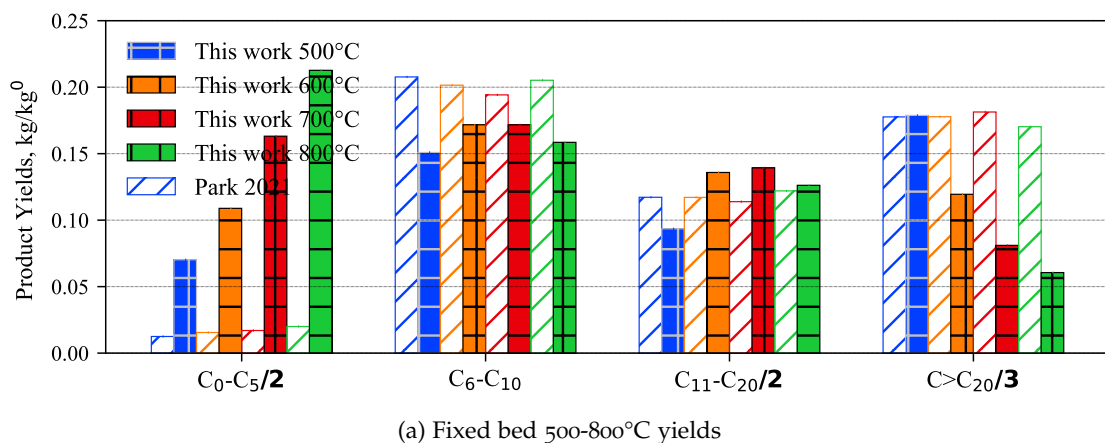


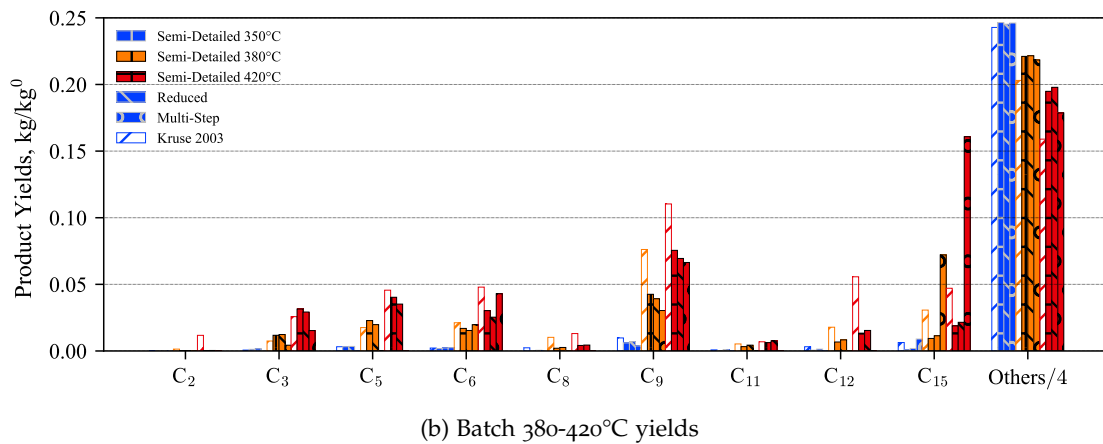
Figure 4.10: Comparison of total carbon weight yields of the semi-detailed and reduced models (solid and dashed lines) and experimental data (marks). Model results are normalized on the predictions of volatiles experimentally measured.

The models are validated also with mass yields of various carbon ranges with respect to the initial polymer mass (Figure 4.11). Similar trends to the previous comparisons are observed. Figure 4.11a shows the comparison of model predictions with yields measured in a fixed bed by Park *et al.*³⁴⁰. The mechanism correctly captures the variation in yields of the C₆–C₂₀ hydrocarbons. On the other hand, it significantly overestimates formation of light gases as consequence of lower predicted waxes yields, consistently with data of De Amorim *et al.*³³⁸ (Figure 4.11c). The data of Park *et al.* show quite unexpected behaviours. For instance, the experimental carbon distribution (not reported here) measures preferential formation of C₁₀ and C₁₁, although those are not relevant products^{55,57,68,336–338,354}. Furthermore, the yields are almost constant at increasing reactor temperature. A possible explanation lies in the experimental procedure. Since the sample is inserted in the cold furnace, complete degradation probably occurs during the heating phase before reaching the set-temperature. Indeed, as shown in Figure 4.6a, even at 50°C/min the final degradation temperature is ~500°C. The authors however do not report the heating profile and therefore more appropriate comparisons cannot be performed. Even considering decomposition occurring at significantly lower temperatures than the reactor's, the light gases yields are notably lower than the ones measured by Kruse *et al.*⁶⁸ at 420°C.



Considering low temperature yields (Figure 4.11b), all three models correctly describe the variations of most compounds. Differences in yields are also the result of different mass-loss profiles between models and experimental data as the former predicts slightly longer degradation times. As previously mentioned, experimental results measure high amounts of waxes in contrast with data of Ballice and Reimert³³⁷. The semi-detailed model overestimates formation of waxes at high temperatures, while underestimating yields of compounds in the C₆–C₁₅ range. Secondary gas-phase cracking reaction or the increase in pressure occurring in the batch vessel experimentally employed could explain these discrepancies. The reduced model has similar predictions to the semi-detailed one, while the multi-step one has several key differences. For instance, it does not predict formation of C₅, C₈, C₁₁, C₁₂ and overestimates formation

of C_{15} . The former are not considered due to the lumping to reduce the number of species which in turns results in an increase of the latter which lumps together all species in the range C_{12} – C_{20} . Considering yields of individual components, the multi-step model underestimates both the propylene and trimer yield, but it captures correctly the yield of waxes.



Considering higher temperature yields (Figure 4.11c), the semi-detailed model correctly describes the increase in light gases yield with temperature. On the other hand, the trimer and tetramer yields appear underestimated by all models. The discrepancies are in line with data of Zhao *et al.*³⁴¹, although the underestimation is higher according to the present data. The reduced model predicts low amounts of the C_1 – C_8 range, possibly because of the simplified backbiting considered and lower selectivity towards unzipping.

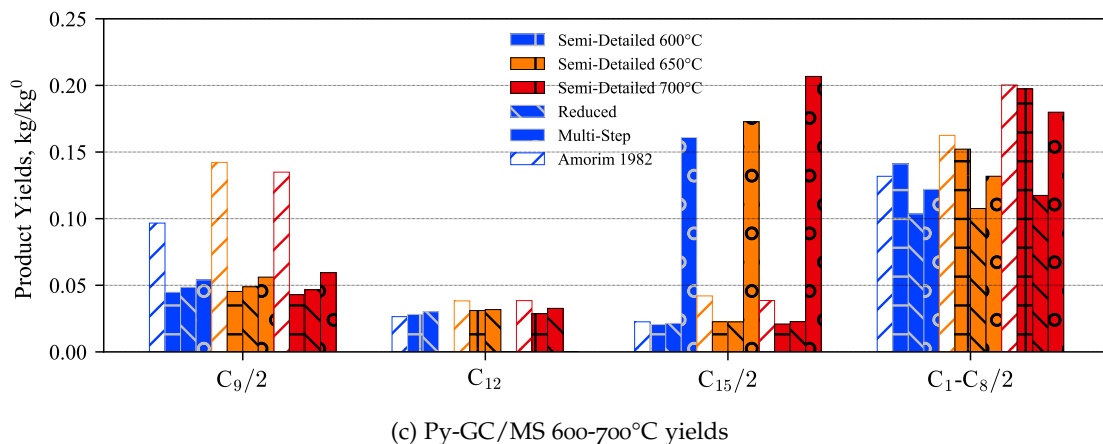


Figure 4.11: Comparison of species mass yields for the semi-detailed, reduced, and multi-step models (full) and experimental data (patched).

4.3.3 Energy requirements

The thermodynamic properties are validated using experimental data derived from heat profiles. These experiments entail measuring the heat fluxes necessary to maintain assigned temperature profiles for the sample. Typically, TG/DSC and TG/DTA calorimetry data are utilized for this purpose. The heat release profiles are consequently related to the mass-loss profiles.

Figure 4.12a shows the comparison for iPP heat flux profiles for the semi-detailed model and experimental data. While the different models show similar predictions (Figure 4.12b), high scattering of experimental data is observed. For instance, measurements of Zhang *et al.*³⁵⁴ do not perceive variations due to the increase heating rate. With respect to these data the model overestimates the increase heat-flux peak. On the other hand, compared to data of Jinno *et al.*³¹⁸, the model underestimates both melting and degradation endothermic peak and their variation at increasing HR. Additionally, both data measure the energy-fluxes required to heat the molten polymer to the degradation temperature being similar to the melting peak. On the contrary, the model estimates the melting peak being significantly more important consistently with data of Farhat Ali *et al.*³⁴⁸. The difference in degradation peak is related to Farhat Ali *et al.* measuring higher degradation temperatures for polymer mass-loss (see Figure 4.5a). Overall, there are few experimental data in literature on heat-fluxes and no quantitative agreement is observed. These data are not sufficient to validate the proposed thermochemistry and a targeted experimental campaign is required to supplement the lack of literature data.

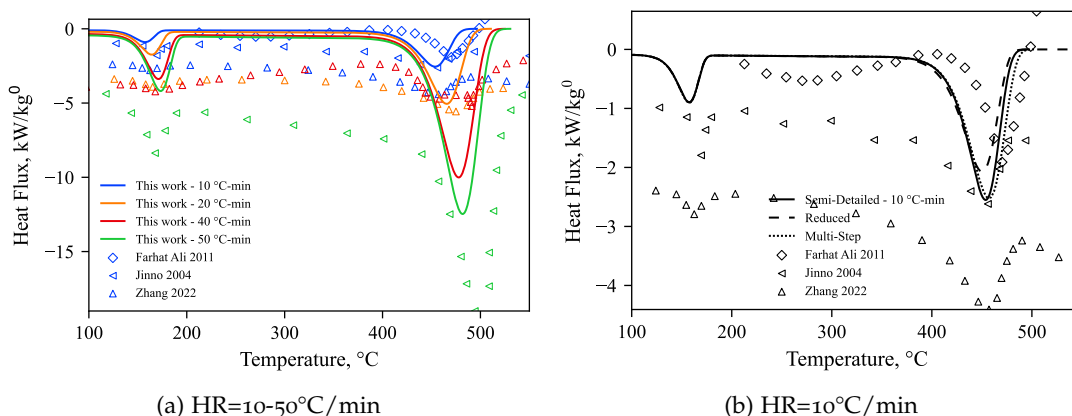


Figure 4.12: Comparison of predicted (solid lines) and measured^{318,348,354} (symbols) heat-flux profiles.

4.4 CONCLUSIONS AND FURTHER WORK

In this Chapter, a condensed-phase kinetic model for Polypropylene degradation is proposed and validated. The mechanism is formulated using the functional groups approach, aiming at characterizing degradation times, released volatiles, and energy requirements. High molecular weight chains are simplified into a few lumped pseudo-species with specific chemical functionalities, while low molecular weight products are treated with greater detail. The kinetic mechanism adopts reaction classes from the scientific literature, employing various lumping techniques to reduce the number of reactions. The kinetic mechanism is complemented by defining species thermochemistry to account for the heat requirements in the process. Liquid-phase properties are derived from phase-change literature data, while solid-phase thermochemistry is based on low-temperature polymer data.

The semi-detailed model serves as the basis for deriving simplified models. Specifically, a semi-detailed reduced model and a fully-lumped multi-step model are obtained. The former employs a lumping procedure to simplify both radical chemistry and volatiles tracked. The latter simplifies radical chemistry into a few global steps, accounting for the main reaction classes.

All the three models undergo validation with an extensive set of experimental data from the scientific literature, including a comprehensive comparison with the detailed model by Ranzi *et al.*⁵⁵. The semi-detailed model demonstrates its capability to accurately describe degradation times, even when compared to more expensive models. The reduced-order models are validated against the semi-detailed one, demonstrating their ability to describe mass-loss profiles with the same accuracy. The semi-detailed mechanism accurately captures volatile distribution, including valuable compounds (e.g., C₃H₆, C₉H₁₈) and long-chain cuts. Conversely, the reduced and multi-step models exhibit differences in volatile distribution profiles due to significant lumping involved. Validation with TG/DSC data proves the model's ability to describe the energy balances of the degradation process despite high experimental scattering.

All three mechanisms are provided in CHEMKIN format and are freely accessible on GitHub².

The proposed models specifically address condensed-phase reactivity, and future work will extend to modelling secondary gas-phase reactivity to assess gasification conditions. Gas-phase cracking, as emphasized throughout this chapter, significantly influences the product distribution, with, for example, gas-residence times of approximately 20 seconds resulting in over 50% cracking of heavy waxes at 500°C¹³³.

² available at <https://github.com/Alocaspi/Polymers-Kinetic-Mechanisms>

POLYSTYRENE

POLOSTYRENE (PS) is a widely used thermoplastic polymer that plays a prominent role in various industries³³³. Known for its versatility and unique properties, polystyrene is primarily used for packaging, household appliances, electronics, building and medical items. It is extensively employed in the food industry, serving as both packaging material and for disposable eating utensils³⁵⁷. PS is also copolymerized or blended with other polymers to increase the hardness and rigidity of the final product.

Historically, polystyrene gained industrial prominence in the 1940s. The primary reasons for its widespread use are its favourable mechanical and dielectric properties, coupled with high processability²²⁴. As styrene can function both as electron donor and acceptor, several polymerization processes can be employed. Radical polymerization is the most relevant industrially, while cationic, anionic or coordination processes are less employed²²⁴. A wide range of grades are obtained combined styrene with other monomers. The main polystyrenes are High-Impact Polystyrene (HIPS), Expanded Polystyrene (EPS) and General-Purpose Polystyrene (GPPS). The first is obtained blending low amounts of polybutadiene to increase toughness and impact resistance and accounts for more than half of PS production³⁵⁷. EPS is the raw material for production of foams and provides both insulation properties and lightweight constructions²²⁴. The label GPPS refers to all variants employed in common applications and are usually clear, hard and brittle materials. Styrene is also employed in a wide range of speciality polymers as acrylonitrile-butadiene-styrene (ABS).

The most common form of PS is the atactic configuration, which has a glass transition temperature of ~100°C. Coordination polymerization produces an isotactic polymer, but it is not industrially viable due to the low rate of crystallization²²⁴. Syndiotactic polystyrene is obtained by special titanium-aluminoxan catalysts and has niche uses in heat-resistant applications.

The thermal behaviour of the different polystyrenes is quite similar. The aromatic rings result in formation of significantly stable radicals and correspondingly larger radical pools. For this reason, it exhibits a lower degradation temperature compared to PE and PP⁵⁷. With appropriate operating conditions, pyrolysis of polystyrene produces monomer yields of ~90 wt.% together with high amounts of styrene dimer and trimer. EPS has lower onset temperatures, possibly due to presence of air trapped inside which results in exothermic phenomena³⁵⁸ by formation of peroxides.

As discussed in Section 2.2 of Chapter 2, polystyrene has received the highest consideration in the past decades. However, neither detailed models (e.g., discrete section⁶⁶ and kMC^{72,158,159,359,360}) nor global models¹³⁷ are suitable for modelling PW respectively because of their high computational cost and low accuracy. While MoM models satisfy these requirements^{61,73,360,361}, they are not suitable to consider mixtures involving PVC as well⁴² as discussed in Chapter 2.

The present Chapter proposes a kinetic mechanism for PS condensed-phase pyrolysis. The model is based on the functional groups approach in line with the other polymers. This Chapter is organized similarly to Chapter 4, describing the model development in a concise form. For the reader who desires a higher level of detail, Chapter 3 reports in-depth the methodology and applications using polyethylene as reference. The content unfolds in a structured manner introducing first the representation of polymer chains and volatiles. Following this, the degradation mechanism is discussed detailing its reaction classes and associated rate constants. An in-depth comparison of the choice of reaction pathways and rate parameters with literature studies is also presented. The semi-detailed kinetic model is then validated, evaluating its performance with data on mass-loss profiles, product distribution, and energy requirements. Building on this model, two additional lumped mechanisms are developed - a semi-detailed and a fully lumped one. The kinetic mechanism is automatically written through a Python code at assigned species. The developed mechanisms are in CHEMKIN format and are available on GitHub as public repositories¹.

5.1 SEMI-DETAILED KINETIC MODEL: PS-55-500

This section delineates the development of the kinetic model. The aim of the proposed mechanism is to reproduce the main features of the degradation process at low computational cost. This refers to describing the characteristic degradation times (mass-loss profiles), product distribution, and heat requirements. The kinetic mechanism is a semi-detailed one and employs a functional group approach. Briefly, long polymer chains are described with functional groups characteristic of the polymer moieties (mid- and end-chain groups). Short chains, i.e., compounds of interest, are described with real species as C₈H₈, C₁₆H₁₆, etc. Starting from elementary reaction families, the network is built following a hierarchical approach. In the following paragraphs are presented first the species definition and then the considered reaction pathways. Comparisons with families employed in other literature models are also discussed.

¹ available at <https://github.com/Alocaspi/Polymers-Kinetic-Mechanisms>

5.1.1 Species Definition

The distribution of polymer chains is distinguished in High and low molecular weight species, respectively labelled HMW and LMW. Although studies measure formation of small amounts of gas-phase tetramer⁷², a threshold carbon number value $N_c^*=32$ is chosen because the total yield of monomer, dimer, and trimer alone is higher than 90 wt.%⁶⁶. The threshold carbon number corresponds to assuming species with $T_{b,n}>500^\circ\text{C}$ as not being able to evaporate.

HMW chains are described as mixtures of mid-chain (MC) and end-chain (EC) moieties, identified by the prefix "P-". MCs account for the chain's length and EC for the terminal chemical functionalities. In the following, the terms "paraffins", "olefins", and "diolefins" denote the backbone unsaturation. Compared to PP, due to the markedly higher stability of benzylic radicals¹⁴⁶, only "head paraffins" and "tail olefins" are considered (Figure 5.1), where the term "tail" refers to the terminal methyl side-group^{66,73}. Given the low degradation temperatures, the phenyl side-groups are assumed inert^{57,72,73,158,159} and the double bonds can form only on the chain-carbons. Since the glass transition has low enthalpy changes²¹, the mid-chain species is assumed to represent both glassy and amorphous state.

LMW compounds are represented like traditional detailed models for the pyrolysis of gases and liquid fuels⁴³, employing two lumping techniques¹⁴⁶ to reduce the number of species. All compounds are lumped together based on the number of aromatic rings, without distinguishing between different head-tail arrangements (see Section 5.1.2.2). Additionally, species with only one aromatic ring (i. e., $N_c<10$) are assumed to stabilize rapidly and not react any further due to their fast evaporation. Therefore, LMW species with $N_c<10$ are labelled unreactive LMW (ULMW), while those with $N_c>10$ are referred to as reactive LMW (RLMW). No vertical lumping is introduced due to the narrow distribution of compounds. The considered reactive carbon numbers are C_{16} and C_{24} , and stable backbone paraffins, olefins, and diolefins are introduced (e. g., $C_{16}\text{H}_{18}$, $C_{16}\text{H}_{16}$, $C_{16}\text{H}_{14}$). The radical pool for both HMW and LMW species is described by internal and position specific radicals. The former are grouped into a single pseudo-species and formation of secondary alkyl radicals is neglected. Position specific reactivity is considered separately through terminal ("_T") and allyl-type radicals ("_A") because of their different selectivity.

The total number of species introduced is 55, with 8 HMW and 47 LMW species. The kinetic mechanism features a computational cost in-line with the reduced model of PE because of the narrower product distribution. Nevertheless, a reduced and a multi-step model are proposed as presented in Section 5.2.

Evaluation of thermodynamic, transport, and critical properties is performed in analogy to Section 3.1.4. Gas-phase properties are estimated with group-contribution methods²⁷⁰⁻²⁷². As the polymer is mostly atactic, only one 1-5 and 1-4 interaction per monomer unit are considered in the group contribution methodology. No experimental

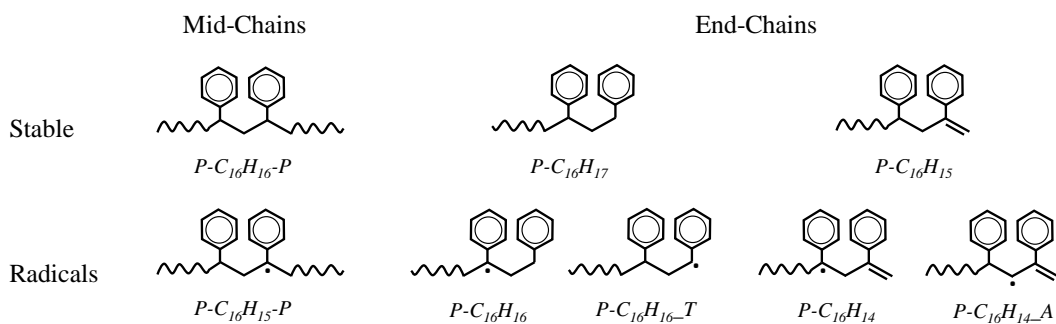


Figure 5.1: Schematic representation of the stable and radical pseudo-species introduced to describe long polymer chains (HMW).

data is available, but the results show good agreement with RMG²⁷³. For liquid-phase species, above the critical temperature the gas-phase parameters are employed, while below the values are evaluated from evaporation enthalpies and correlations^{280,284,287}. The amorphous/molten polymer properties are evaluated with the same approach, except for polymer entropy which is estimated as difference between two fictitious reference carbon numbers C₁₆₀₀ and C₁₇₆₀.

Figure 5.2 shows the comparison of predicted properties of MC with experimental values³⁶². The experimental heat capacity of the glassy state is also reported as comparison in purple. The proposed approach demonstrates good agreement across the experimentally investigated temperature range, except for entropy which is significantly overestimated. Data on solvation energies can improve the agreement with experimental data, but such adjustments do not impact model predictions. Although the absolute values of the heat capacity are well captured, the model predicts a lower increase with temperature. The reason is possibly not accurate estimations of the vaporization enthalpy across the entire temperature range. The same behaviour is observed also for PP and PE, although with a lower discrepancy. Considering a different exponent per class of compound in the Watson correlation could improve the model predictions. The model also overestimates the low temperature specific heat as it does not consider the glass transition. The discrepancies in heat capacities affect the predicted enthalpy, and the model estimates both a lower enthalpy at T<373K and a milder increase with temperature at higher values.

5.1.2 Reaction Classes

A radical chain degradation mechanism is considered, resulting in the formation of backbone alkanes, α -alkenes, and $\alpha - \omega$ dialkenes. The reaction network is built following a hierarchical approach to reaction families. A limited set of classes proposed by other authors^{57,61,66,72,158,159,360} is employed to all liquid-phase species. This section presents the considered reaction classes, their elementary steps, and the associated

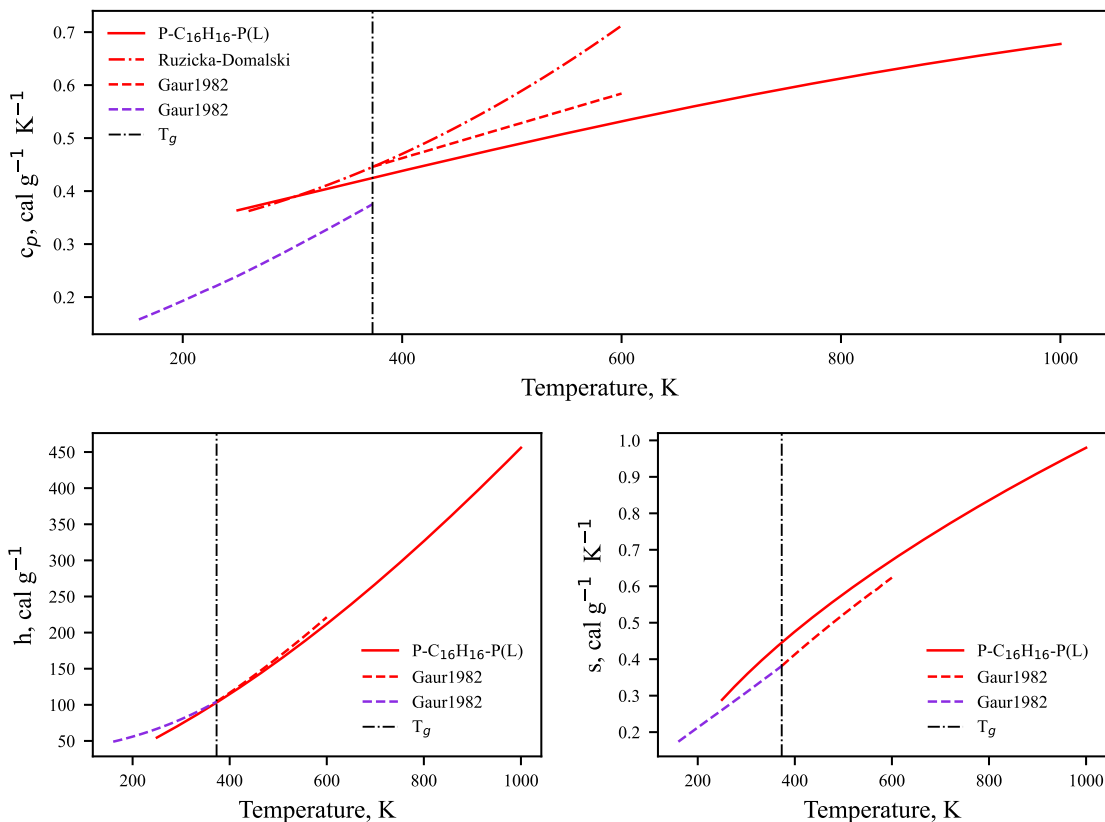


Figure 5.2: Thermodynamic parameters per unit mass evaluated for the mid-chain polymeric species (solid red lines) compared to experimental data³⁶² (dashed lines) and the Ruzicka-Domalski correlation. The glassy state properties are reported in purple.

kinetic parameters. The general random scission mechanism, characteristic of internal radicals reactivity, is then presented. Subsequently, the specific reaction pathways attributed to terminal and allyl-like radicals are discussed. The kinetic mechanism involves ~500 liquid-phase reactions.

5.1.2.1 Elementary Steps

The homogeneous liquid-phase elementary reaction classes, along with their modified-Arrhenius parameters, are reported in Table 5.1. The rate parameters proposed have been slightly revised from the published model³⁶³. The parameters for liquid-phase H-abstraction reactions refer to a tertiary benzylic radical abstracting a tertiary benzylic hydrogen and are the same as in gas-phase¹³³. The selectivity of H-abstraction reactions is also assumed to be equivalent to their gas-phase counterparts^{43,146,245}. Recombination reactions are diffusion-controlled²⁴⁷, and their chain-length dependence is considered based on the approach described by Kruse et al⁶¹, taking into account the flux units evaluated by Faravelli *et al.*⁶⁶ as a lower limit for recombination reactions.

In comparison to other studies^{72,158,159,360}, the higher reactivity of PS in contrast to PE and PP is attributed to a higher radical concentration. Random scission reac-

tions are favoured due to the formation of stable benzylic radicals, while terminations are hindered by the reduced diffusivity of species. Similarly, the proposed rate constants for decomposition are slower because of the enhanced stability of benzylic radicals. Although some authors suggest different rates based on the size of the released molecule^{72,360}, to minimize the number of parameters only one β -scission decomposition parameter is introduced. The same variation in rate parameters between β -scission in PE and PS proposed by Marongiu *et al.*⁵⁷ is employed. Indeed, both the reactant and product radical are significantly more stable compared to the analogous in PE. The higher reactant stability results in an increase in activation energy, while the product's higher stability corresponds to a decrease in E_{act} . Considering gas-phase analogues^{364,365}, a decrease of about 2 kcal mol⁻¹ is observed for β -scissions of alkyl-benzyl radicals compared to secondary alkyl ones. The unzipping rate constant is assumed to have a 2 kcal mol⁻¹ lower activation energy because of the lower stability of the reacting radical as with PE.

Only 1-5 backbiting reaction is introduced because of the higher stability of the benzylic radical and steric hindrance of the phenyl rings. A higher activation energy is also employed in line with the slower H-abstractions because of the higher radical stability. Addition to double bonds are implicitly accounted for in the decomposition rate constants but are not relevant in the considered operating conditions. Similarly, disproportionation is neglected because of the lower importance with respect to recombination. No reaction is introduced to represent the polymer melting or glass transition.

Table 5.1: Modified-Arrhenius parameters for elementary reactions classes (units cm, mol, s, cal). Parameters for recombination reactions refer to the polymer flux unit, while H-abstraction refers to a tertiary benzylic radicals (R_{B3}) abstracting a tertiary benzylic hydrogen (H_{B3}).

Reaction	A	n _A	E _{act}
Random scission	2.00E+13	0	68000
β -scission	2.00E+12	0	26000
Unzipping	2.00E+12	0	24000
H-abstraction $R_{B3}+H_{B3}$	8.00E+10	0	16500
Backbiting 1-5	6.00E+08	0	16000
Radical recombination	1.00E+10	1	14000

5.1.2.2 Backbone Degradation: Lumping and delumping by aromatic ring number

Upon heating polymer, the radical degradation starts through backbone random scission reactions forming terminal radicals¹⁵⁶. The considered propagation reactions are H-abstractions, β -scissions, unzipping, and backbiting, while termination solely occurs

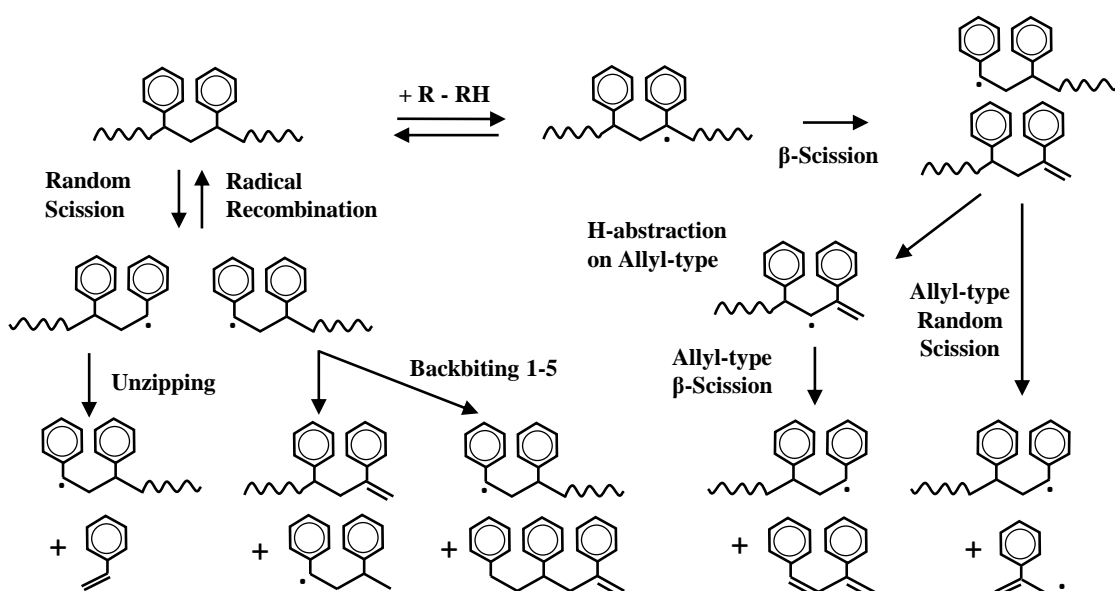


Figure 5.3: Schematic representation of the degradation of the initial mid-chain pseudo-species to form LMW products. The MC species undergoes random scission forming terminal radicals which recombine, backbite, H-abstract, or unzip. The lumping and delumping discussed in the this sections is included in this representation.

through radical-radical recombination reactions^{57,66}. Figure 5.3 schematically shows the reaction pathways leading to the formation of LMW compounds from HMW species. Mid-chains decompose via random or β -scissions, producing end-chains, which subsequently release LMWs capable of either evaporating or undergoing further reactions. The predominant reaction pathway is unzipping from the radical paraffin end-chain. The kinetic mechanism predicts the equimolar formation of backbone paraffins and diolefins and has a high selectivity for styrene.

As discussed in Section 3.1.2.2, multiple simplifying and lumping assumptions are incorporated in the reaction network. For instance, parallel elementary steps with identical rate constants are lumped into a single reaction, releasing all products with stoichiometric coefficients derived from the sum of the coefficients in the grouped reactions⁴³. Species with $N_c < 10$ are assumed to form as stable gas-phase species introducing a stabilization step on any hydrogen available RH (Figure 3.6). Reactions involving degradation of polymer functionalities include neighbouring MCs or ECs group as Support Polymer Units (SPU) to represent the decrease in chain-length (Figure 3.1).

Considering PS pyrolysis, an additional lumping is performed in terms of aromatic ring number. The semi-detailed kinetic model aims at representing the degradation of polymer in terms of liquid mass and the evolution of major products with minimal computational expenses. The primary gas products constituting over 90% of the total gas mass, are the monomer, dimer, and trimer^{15,137,366}, while other valuable compounds such as toluene, α -methyl styrene, diphenyl propane, and small olefins are

present in lower quantities^{75,367}. Overall, the main products are head-tail configurations (HT), accounting for more than 80 wt.%, while head-head (HH) and tail-tail (TT) configurations are present in significantly smaller amounts.

In this work, all configurations are lumped together as HT, reducing the number of low-molecular-weight (LMW) species by approximately 60%. For each carbon number, 10 species are required to describe the backbone paraffins, olefins, and diolefins and their corresponding internal, terminal, and allylic radicals. The introduction of HH and TT configurations would add another 10 species for each structure (i.e., 20 more species per monomer number), without significantly affecting the crucial degradation products. To better understand the lumping procedure, consider the species $C_{24}H_{23}$ formed by random scission of the olefin end-chain. As shown in Figure 5.4, this compound in the mechanism represents all backbone olefin trimer configurations (HH $\dot{C}_{23}H_{21}$, HT $\dot{C}_{24}H_{23}$, and TT $\dot{C}_{25}H_{25}$). Any reaction that would release one of these configurations will instead form only the Head-Tail one¹⁴⁶. A similar distinction is made for end-chain (EC) terminations, but due to the high selectivity towards tertiary benzyl radicals, only HT backbone olefins and backbone paraffins are considered (Figure 5.1). This lumping is further justified by the fast kinetics of phenyl shifts¹⁰⁰, where tail radicals isomerize to form structures with reactivity similar to head ones more rapidly than their stabilization.

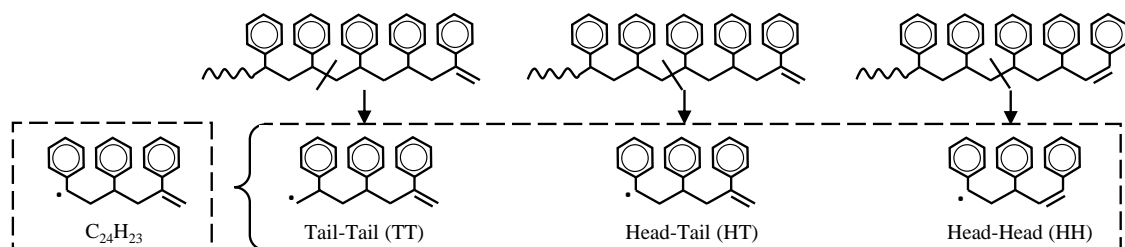
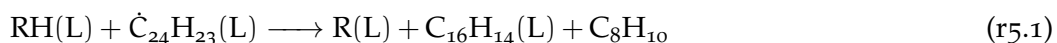


Figure 5.4: Examples of lumping by aromatic ring number for the trimer. Random scission reactions in the represented position leads to formation of three different trimer configurations, which are however represented by a single lumped species labelled $\dot{C}_{24}H_{23}$

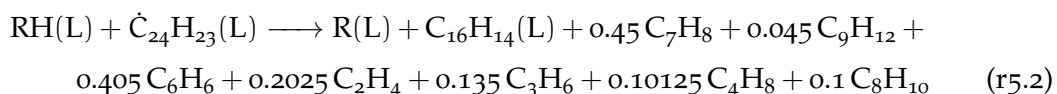
The lumping method outlined here does not enable the prediction of certain products like toluene, α -methyl styrene, and diphenyl propane. To account for the presence of head-head (HH) and tail-tail (TT) configurations from head-tail (HT) moieties, the balancing error is distributed among additional compounds observed experimentally as small olefins and benzene^{75,367}, as illustrated in Figure 5.5. The error introduced by this approach is less than 5% of the total volatile mass, and thus, it is deemed acceptable. In the following paragraphs, the application of delumping to some model reactions is discussed more in detail.

Figure 5.5a illustrates the delumping process for toluene (C_7H_8), which is formed mainly from β -scissions of internal radicals. Head-head paraffins are recovered from

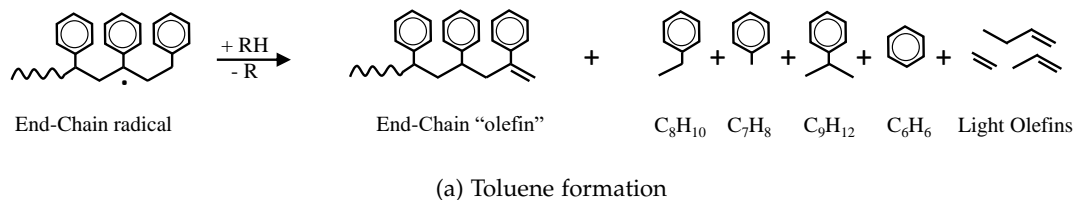
the corresponding HT ones (C_8H_{10}) and the error is redistributed in the formation of benzene, light olefins, and cumene. According to the lumping process, β -scission on the internal trimer radical forms a backbone diolefin and ethylbenzene:



where any stable species RH is converted in its radical R to avoid introducing the ULMW radical C_8H_9 (Section 3.1.2.2). Toluene is recovered explicitly from this reaction through appropriate delumping coefficients that allow to satisfy the elemental balances while representing formation of reasonable compounds. Therefore, any β -scission reaction that forms C_8H_{10} is instead written as:

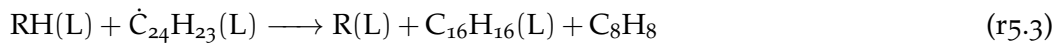


where the main product is toluene and formation of small amounts of the C₈ HT and TT configurations are also included. The balancing error is dumped on benzene and light olefins which can form from low-temperature dealkylation reactions of volatiles. The reaction coefficients are constrained by atomic coefficients and should be considered as adaptive parameters of the model.

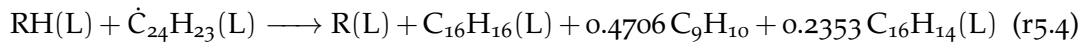


(a) Toluene formation

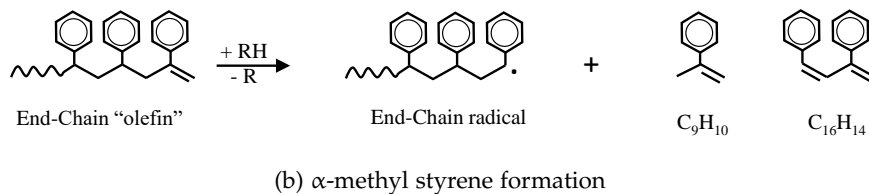
A similar procedure is employed also for α -methyl styrene (C_9H_{10}) as shown in Figure 5.5b. This species is the TT configuration of styrene and forms from the allylic reactivity (Section 3.1.2.2). Specifically, the reactions involved are random and β -scissions enhanced by formation of the resonantly stabilized allylic radicals. Since allylic radicals also result in formation of conjugated double bonds, the balancing error is dumped on the conjugated backbone diolefin ($C_{16}H_{14}$). Considering the β -scission from the secondary alkyl trimer radical, the reaction introduced according to the lumping procedure would be:



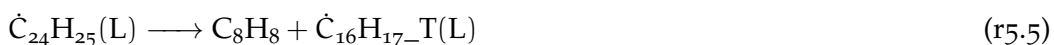
Instead, following the delumping procedure the reaction introduced is:



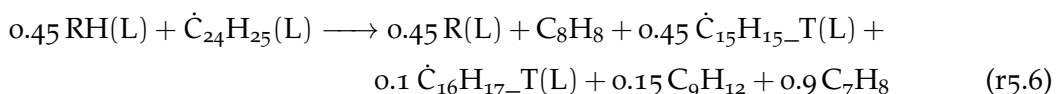
where the stoichiometric coefficients satisfy the carbon and hydrogen balance and stabilization of C_9H_{10} is lumped in its formation.



The last compound of interest is diphenyl propane $C_{15}H_{16}$ which forms both from β -scissions of internal paraffin radicals and backbiting reactions. As this compound is part of the RLMW subset, it forms as a radical species ($C_{15}H_{15}-T$) and its degradation reactions are also considered. Like with toluene, diphenyl propane is recovered from the corresponding HT conformer, i.e., $C_{16}H_{18}$. Since few data on the TT configuration are available, the balancing error is dumped in formation of the HT configuration and toluene and cumene (Figure 5.5c). According to the lumping by aromatic ring, the reaction from the saturated trimer radical $C_{24}H_{23}$ would be:



On the other hand, formation of diphenyl propane is recovered introducing the following reaction for all β -scission and backbiting reactions:



The ratio diphenyl propane (C_{15}) to diphenyl butane (C_{16}) is the same as toluene to ethylbenzene. To satisfy both the hydrogen and radical balances, formation of 0.45 radicals from any stable species is considered as well. This reaction results also in high formation of toluene at low temperatures. The reactions introduced for $C_{15}H_{15}-T$ are H-abstractions, unzipping and terminations. Formation of the radical from H-abstractions on diphenyl propane is also considered.

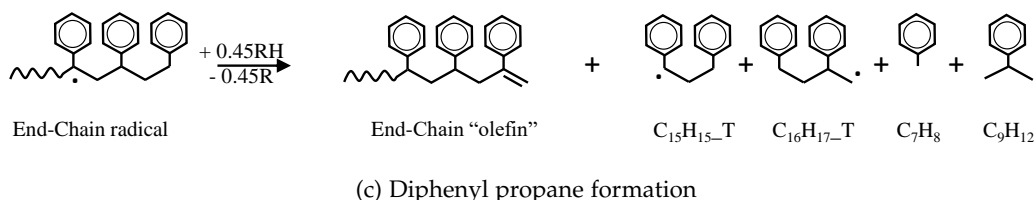
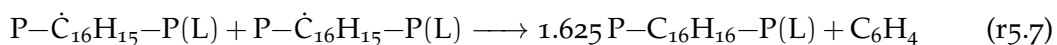


Figure 5.5: Examples of delumped reactions forming: a) toluene (C_7H_8); b) α -methyl styrene (C_9H_{10}); c) diphenyl propane ($C_{15}H_{16}$). The balancing error is dumped on formation of benzene (C_6H_6), ethylbenzene (C_8H_{10}), cumene (C_9H_{12}), diphenyl butane ($C_{16}H_{18}$), and light olefins

An additional highly unsaturated species C_6H_4 is incorporated to represent formation of small highly unsaturated compounds. This species is also utilised to satisfy the balancing error in reactions that form highly branched or unsaturated structures.

For example, the recombination of two mid-chain radicals ($P-C_{16}H_{15}-P$) leads to the formation of quaternary benzyl carbons. However, to simplify the mechanism, these quaternary benzyl carbons are not considered and the considered recombination reaction is:



The C_6H_4 species is a highly unsaturated compound, which acts as a soot precursor. This forms mainly from secondary gas-phase reaction, and the yield from the liquid phase mechanism ranges from 2 to 200 mass ppm from 250 to 1150°C.

5.1.2.3 Terminal and allyl-type radicals

The described backbone mechanism is extended to encompass specific reactive positions such as backbiting isomerisation and the reactivity of allylic radicals.

Backbiting reactions (BB) contribute to an uneven product distribution through the isomerisation of radicals from terminal to any internal position "n" (i.e., 1-n transfer). BB steps are introduced for EC and RLMW terminal radicals, considering SPU and stabilization species when required. Given the high considerable steric hindrance introduced by aromatic rings, only 1-5 BB reactions leading to the preferential formation of diphenyl-propane and styrene trimer are considered^{57,66}. Despite discussions in the literature emphasizing the importance of BB 1-3 and 7-3 in dimer formation^{158,159,360}, these pathways are neglected in this work due to their low relevance⁷². The former is not included as formation of 4-member rings involves high extra strain energy, approximately 20 kcal mol⁻¹ higher than BB 1-5^{72,146}. The latter on the other hand forms from a 1-5 isomerisation from a radical in the 7th position. However, backbiting 7-3 compared to 1-5 has an increased activation energy as the reactant radical is more stable (i.e., less reactive). Moreover, from a mechanistic point of view no preferential formation of radicals in the 7th position is found. With respect to H-abstractions, all internal radical positions are equivalent from the 5th to the 1000th, resulting in no net increase of dimer formation with respect to the trimer, tetramer, and so on. The preferential formation could result from BB 1-7 isomerisation, but formation of 8-member rings has a low entropic contribution (approximately 10^{0.8} times slower per hindered rotor⁴³, i.e., 30 times slower than BB 1-5). The multiple isomerisation combining BB 1-7 followed by 7-3 can be computed through the probability of the second backbiting (see Section 3.1.2.4) but the resulting rate constant has both a low frequency factors and a high activation energy.

The distinct reactivity of the allyl-type radical results in the formation of 1,3-diphenyl-1,3-butadiene (the smallest α - ω backbone diolefin, i.e., $C_{16}H_{14}$) and α -methyl styrene, as depicted in Figure 5.6. The former results from β -scissions of allylic radicals, while the latter stems from random and β -scission reactions that form an allyl-type radical. Table 5.2 reports the corrections for allylic positions with respect to the parameters

presented in Table 5.1. The rate parameters for reactions involving allylic positions are the same previously estimated (Table 3.3), with the corrections described herein referred to benzylic radicals. Allylic radicals have similar stability to benzylic ones^{100,276}, and only random scissions to form allylic radicals are favoured as they result in an allylic and a benzylic radical. On the contrary, allyl-type β -scission results in formation of conjugated double bonds and a primary radical. As the reaction forms an unstable radical from a stable one, an increase in activation energy of 5 kcal mol⁻¹ is considered²⁴⁶. The formation of α -methyl styrene is consequence of β -scission of secondary radicals, which are not considered. While H-abstractions of secondary hydrogens is significantly less favoured, they have a higher reactivity enhanced by formation of a stabilized allylic radical⁴³. Employing the reaction lumping approach¹⁴⁶, a single reaction is introduced to represent the net difference between these two steps. Overall, both a higher and lower activation energy respectively for H-abstraction and β -scission reactions, a correction of 1 kcal mol⁻¹ is proposed, i.e., allylic radical formation is slightly unfavored. In terms of H-abstractions, secondary allyl-type radicals are considered to have similar reactivity to secondary benzylic ones¹³³.

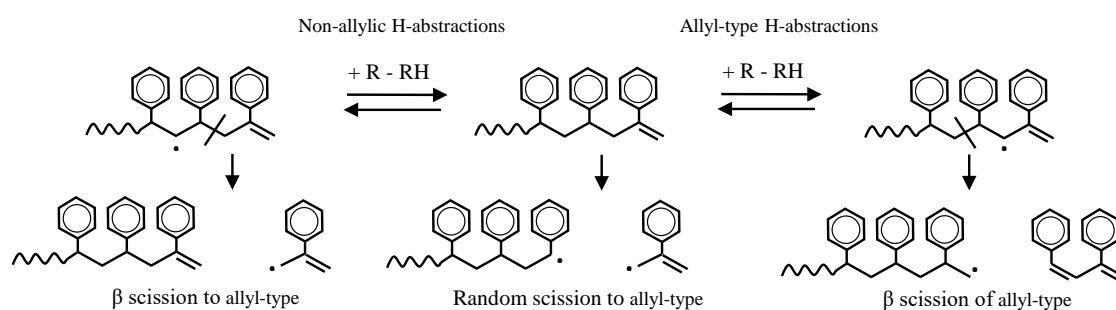


Figure 5.6: Schematic representation of: a) β -scission reaction involving instantaneous stabilization of the LMW product; b) supported β -scission reaction occurring on an end-chain to release a LMW. The end-chain functional group is reformed consuming the “support” mid-chain unit (SPU)

Table 5.2: Allylic corrections to modified-Arrhenius parameters²⁴⁶. The “0” subscript refers to the elementary reference parameters reported in Table 5.1 (units mol, cal).

Reaction	A _{allyl}	n _{allyl}	E _{allyl}
Random scission	0.2·A ₀	0	E ₀ -11000
β -scission of allylic	A ₀	0	E ₀ +5000
β -scission to allylic	A ₀	0	E ₀ +1000
H-abstraction of R _{allylic}	A ₀	0	E ₀ -1000
H-abstraction of H _{allylic}	A ₀	0	E ₀ +2500

5.2 REDUCED-ORDER MODELS

The semi-detailed model features a low number of species, but a further reduction can decrease computational cost in CFD applications including also gas-phase reactivity. In the ensuing sections, two reduced models are introduced in line with Section 3.3. Firstly, a semi-detailed model that simplifies the radical description is presented. Subsequently, the selectivity of various radical isomers is leveraged to derive a multi-step (fully lumped) mechanism. This model neglects all radical intermediates, lumping complex reaction pathways into a few global steps.

5.2.1 Reduced Semi-Detailed Model: PS-40-300

The main computational cost of the proposed kinetic mechanism stems from the detailed characterization of the radical reactivity. In contrast with PE and PP, the same carbon numbers are considered, while radical isomers are lumped in a single species. The resulting model involves 40 gas+liquid species.

As discussed in Section 3.3.1.2, the radical lumping is performed as proposed by Pegurri *et al.*³³². The rate constants obtained are regressed to an Arrhenius form and are reported in Table 5.3. Compared to values obtained for PE (Table 3.6), several differences are observed. Unzipping rate constants are similar, while the lower selectivity to waxes is reflected in a significantly lower rate constant for paraffin β -scissions and H-abstractions. For this reason, backbiting reactions in PS are intermediate temperature reactions contrary to PE. On the contrary, backbone olefin radicals preserve the same kinetic parameters as allyl-type reactions are high temperatures pathways in PS.

Table 5.3: Modified-Arrhenius parameters of radical lumped reactions obtained from regression (units s, cal, mol).

Reaction	A	n _A	E _{act}
Unzipping	2.80E+12	0	24700
Paraffin β -scission	3.00E+06	0	12200
Olefin β -scission	4.00E+10	0	21800
Olefin allylic β -scission	9.00E+12	0	34300
H-abstraction by paraffin	1.10E+11	0	7240
H-abstraction by olefin	1.30E+11	0	16700

To further reduce the number of reactions, the radical pool is assumed not affected by RLMW initiation and recombination. The H-abstraction lumping for decomposition reaction cannot be employed in the present mechanism due to the high disparity in reactivity between backbone paraffins and olefins.

A further reduction can be obtained assuming also the range $10 < N_c < 20$ form directly in gas-phase. While the boiling points are similar to those of the corresponding normal-alkanes ($\sim 30^\circ\text{C}$ higher²⁶¹), the stabilization step is significantly slower. Secondary liquid-phase degradation of the C_{16} species occurs before their evaporation, leading to a non-negligible loss in model accuracy. For specific compounds like the styrene dimer, the secondary reactivity can be entirely neglected. Given that phenyl and vinyl positions involve high energy barriers, only allylic and terminal radicals form at the temperature of interest. β -scission or unzipping of these radicals results in the formation of a phenyl or vinyl radical, respectively, requiring significantly higher activation energies. This selective stabilization has not been implemented in the current work. If the liquid-phase degradation of $C < C_{20}$ is neglected, a mechanism of 30 gas+liquid species and 200 reactions is obtained. The loss in accuracy however significantly off-sets the gain in computational time.

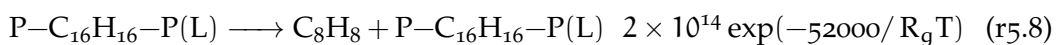
5.2.2 Multi-step Fully Lumped Model: PS-7-6

Both the semi-detailed and reduced mechanisms involve a notably low computational cost. To further decrease the stiffness of the system, a multi-step model that lumps the radical reactivity in few steps is proposed. Again, the multi-step mechanism also aims at describing the key physico-chemical steps of the degradation, i. e., residence times, heat requirements, and product distribution.

The polymer is exclusively represented by the chain species $P-C_{16}H_{16}-P$, and the volatiles are further lumped, considering only the main products, namely styrene, dimer, and trimer. To represent the chain unsaturations, two additional species are introduced, respectively representative of backbone paraffins and diolefins: diphenyl propane ($C_{15}H_{16}$) and 1,3-diphenyl-1,3butadiene ($C_{16}H_{14}$). Allyl-type reactions are neglected due to their minor role. All products form as volatiles species, except for the trimer, which can undergo further degradation in liquid-phase. The resulting model involves 7 gas+liquid species.

As previously mentioned, the complex reactivity is lumped in few single-step reactions representative of the elementary acts involved. Radicals are not explicitly considered but are accounted for through the proposed Arrhenius parameters. The introduced reaction classes and their rate parameters are summarized in Table 5.4.

Upon reaching the degradation temperature, the polymer decomposes according to three pathways. The main decomposition pathway is unzipping to form styrene:



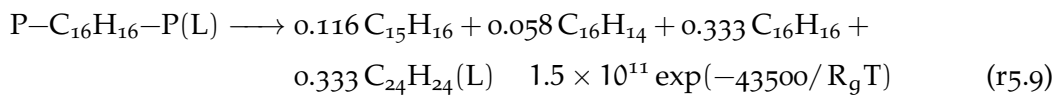
The rate parameters of this reaction are obtained considering the pseudo-steady-state assumption for terminal radicals (Section 3.3.2.2) The same reaction is introduced also for the liquid-phase trimer to form styrene and dimer. Compared to PE and PP, signi-

Table 5.4: Reaction classes of the multi-step model and their modified-Arrhenius parameters (units cm, mol, s, cal)

Reaction (number)	A	E
Unzipping	2.0E+14	52000
Backbone scission mechanism	1.5E+11	43500
Backbiting	1.2E+11	44000
Trimer evaporation	1.2E+12	44000

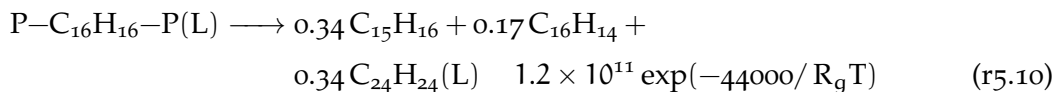
fificantly lower activation energies are obtained due to the lower energy to form stable radicals and higher diffusion limitations.

Like PP, the backbone scission mechanism is a low temperature pathway. The reaction introduced is:



which forms the dimer, trimer, and LMW products with different lower and higher chain unsaturations. The rate parameters of the present reactions are obtained from the selectivity of the reduced model, i. e., from the ratio of paraffin β -scission to unzipping constants (Table 5.3).

The third pathway is backbiting of the terminal radical to form trimer and diphenyl propane:



where the unsaturated species is introduced to preserve the atomic balances. The same selectivity of backbiting to unzipping of the reduced model is employed. The resulting parameters position these isomerisation reactions as mid-temperature processes.

As previously mentioned, 2 reactions are introduced to account for the trimer decomposing through unzipping or backbone degradation. A third additional pathway is included also to represent its volatilisation to stable gas-phase products. The trimer cannot undergo backbiting reactions and therefore the corresponding reaction is not considered.

The multi-step mechanism employs 6 liquid-phase reactions.

5.3 MODEL VALIDATION

The performance evaluation of the proposed kinetic models employ a wide range of experimental data gathered from the scientific literature. This data exhibits notable

variability, attributed potentially to variations in plastic composition and differences in the experimental setups employed¹⁵. The discrepancies arising from plastic composition is linked to distinct quantities of weak links, inorganics, additives, and initial molecular weights present in each polymer. These factors particularly impact the onset temperature⁶⁵, contributing to the observed high scattering in the experimental results. The variability arising from experimental facilities includes variations in carrier gas flow rate, sample pan design, and instrument geometries, potentially leading to temperature shifts of approximately 10°C^{306,307}.

Model validation encompasses characteristic degradation times (i.e., mass-loss profiles), volatile yields, and energy requirements. Setups where transport phenomena and secondary cracking reactions can be reasonably neglected (e.g., TGAs, pyroprobes, micropyrolyzers) are considered in the validation process. If no information on the polymer is reported, an initial number average molecular weight of 160 kg mol⁻¹ is assumed. The initial composition is evaluated from the Schultz or Schultz-Flory distribution according to the polymerization process^{66,236} assuming only olefins are present in the reacting mixture. The same physical and numerical model discussed for PE is employed (see Section 3.2.1). The semi-detailed model performances are assessed comparing with the detailed model of Faravelli *et al.*⁶⁶, while the reduced and multi-step mechanisms are compared with the semi-detailed one. All validations are compared to experimental data, and model performances are quantitatively assessed through the Curve Matching (CM) score³¹² (Section 3.2.2).

5.3.1 Characteristic degradation times: mass-loss profiles

Mass-loss profiles are the main kind of experiments conducted in scientific literature on polymer pyrolysis, and approximately 60 mass-loss profiles^{60,61,115,138,309,318,339,355,358,368–380} have been utilized in the present validation.

Figure 5.7 shows the comparison of mass-loss profiles of polystyrene in different operating conditions. Experimental data show a variability of ~10–20°C according to the experimental study, although average degradation temperatures are quite consistent. The highest scattering is observed at HR=10°C/min and is about 50°C. The semi-detailed proposes a steeper degradation profile compared to the one of Faravelli *et al.*⁶⁶. Indeed, considering dynamic conditions (Figure 5.7a), the semi-detailed mechanism predicts a higher onset and a lower final temperature. The proposed process apparent activation energy is also lower, as at higher heating rates the semi-detailed predicts a global lower reactivity.

Similar behaviours are also observed considering isothermal conditions (Figure 5.7b), where the lumped model has a lower degradation rate. Both detailed and semi-detailed profiles agree with the experimental data as both smoother or steeper degradation are observed according to the study. Nevertheless, according to the curve matching score,

the semi-detailed model has a generally better agreement. Considering the effect of the initial molecular weight, neither model perceives a significant variation in decomposition profiles. The lower reactivity of the 5 kg mol^{-1} sample is possibly related to the average chain length being similar to the unzipping length. If polymer chains fully unzip before any methatesis takes place, the short chain radical can evaporate reducing the total liquid-phase concentration of radicals in a "pseudo-termination" step. This phenomenon results in an unimolecular dependence of termination reactions and has been experimentally verified for PMMA^{381,382}, but both models neglect evaporation of radical species to reduce the stiffness of the reaction system. These behaviours are a limitation of the functional groups approach as it neglects any dependence on the chain-length and is not able to include such effects.

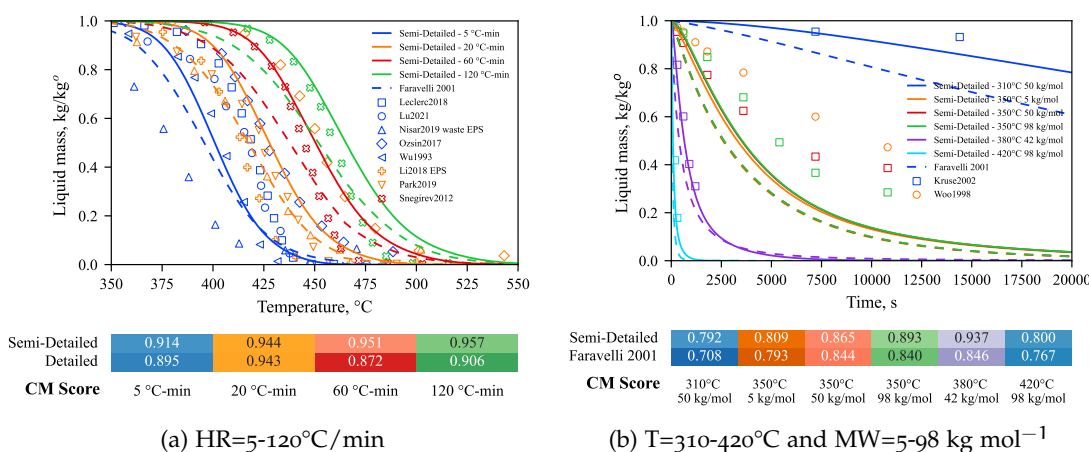


Figure 5.7: Mass-loss profiles of PS subjected to different temperature profiles. Comparison among the semi-detailed model (solid lines), the detailed one of Faravelli *et al.* (dashed lines) and literature experimental data (marks). The Curve Matching score (CM) is also reported.

Figure 5.8 shows the comparison of the three proposed models with PS mass-loss profiles. Comparable behaviours are observed under both dynamic and isothermal conditions, shown in Figure 5.8a and 5.8b respectively. The three models have similar profiles with temperature differences of less than 5°C and align well with experimental data, as indicated by the high CM scores. The reduced model predicts steeper degradation profiles resulting in a delayed onset but higher overall reactivity. All the models correctly capture the process apparent activation energy. Considering isothermal conditions, the reduced model overestimates the final degradation times, while the semi-detailed and multi-step models have better agreement overall. Nevertheless, all mechanisms exhibit high CM scores and reproduce the experimental profiles.

Similar behaviours are shown also in Figure 5.9, which presents parity plots of onset ($m_L = 90\%$), half-conversion ($m_L = 50\%$), and final-conversion ($m_L = 10\%$) temperatures (T) and times (t). All models have similar prediction capabilities, although the detailed

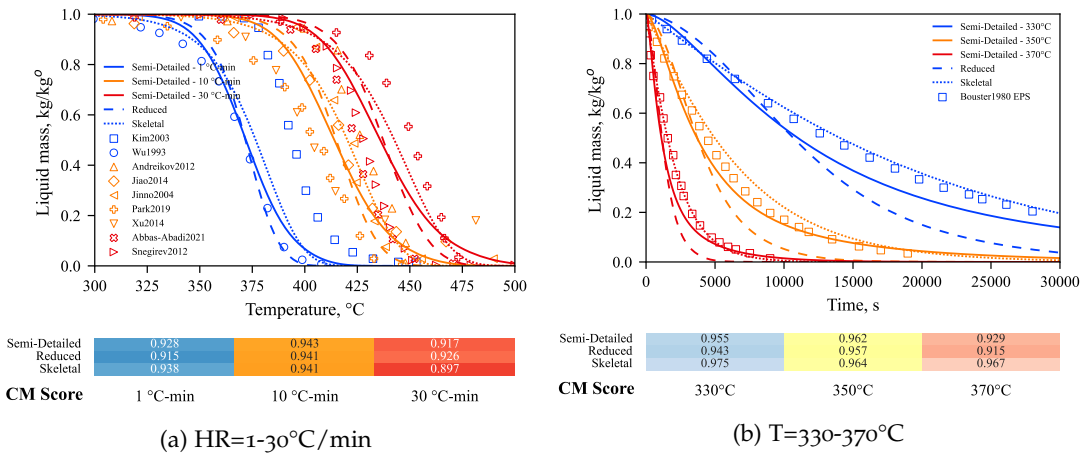
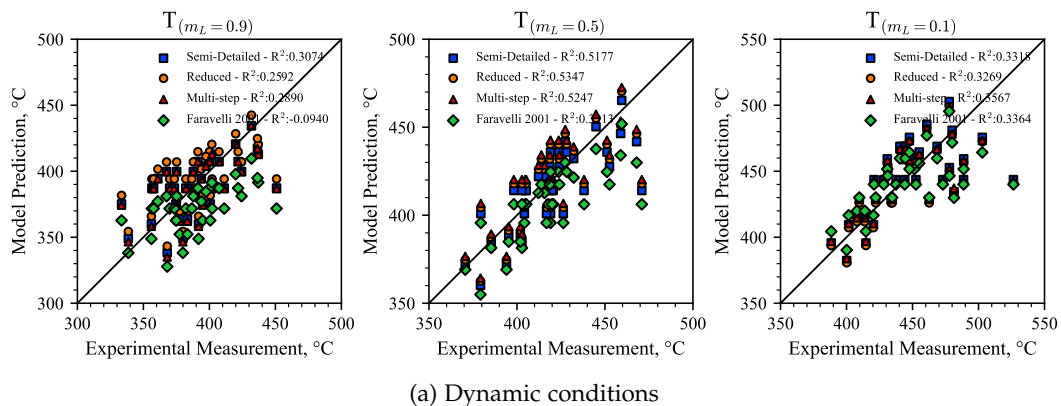


Figure 5.8: Mass-loss profiles of PS subjected to different temperature profiles. Comparison among the present semi-detailed (solid lines), reduced (dashed lines) and multi-step (dotted lines) mechanisms with literature experimental data (marks). The Curve Matching score (CM) is also reported.

one of Faravelli *et al.*⁶⁶ predicts lower apparent activation energies and has lower R^2 scores. Considering dynamic conditions shown in Figure 5.9a, the onset temperatures exhibit a high scattering which no model is able to reproduce. The reduced model predicts the highest onset temperatures and the lowest final-conversion ones as well, still within 5-10°C from the other models. It also has the highest R^2 value for mid-conversion temperatures, although the other models are quite close. The multi-step model has higher R^2 values with respect to the final degradation temperature. With respect to isothermal conditions (Figure 5.9b) the semi-detailed mechanism better represents experimental data in the investigated range compared to the detailed one. The R^2 values of the detailed model are notably lower, but its predictions, although overestimating the reactivity, are not significantly deviant. The reduced and multi-step models show the highest R^2 values, but the semi-detailed model predictions are always quite similar. At high temperatures, all models predict an exponential increase in degradation rates.



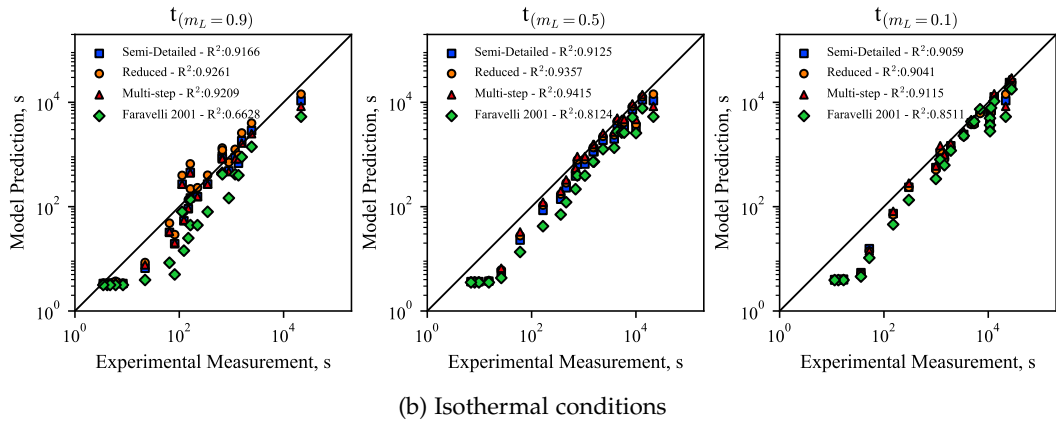


Figure 5.9: Parity plots of the present work prediction (blue squares), the detailed model of Faravelli *et al.* (yellow circles) and literature experimental data for polymer degradation temperatures (top) and times (bottom) at sample mass (m_L) 0.9, 0.5 and 0.1.

Figure 5.10 shows model performances in terms of CM score and the 5 different indices introduced (Section 3.2.2). As discussed in previous paragraphs, individual differences in polymer samples result in variations in degradation temperatures. The semi-detailed and detailed models exhibit similar CM scores, emphasizing the reliability of the proposed approach in terms of characteristic degradation times. The detailed model has comparable indices values but a significantly lower horizontal shift which penalizes it significantly. The reduced and multi-step models have higher CM scores compared to both the semi-detailed and detailed mechanisms. This is mainly due to the higher values for the $d_{L_2}^1$ and shift compared to the semi-detailed model. The former relates to the DTG profiles, while the latter to uncertainties in degradation temperatures. Overall, the proposed lumping approaches even improves model predictions in terms of mass-loss profiles, although volatile yields are less accurate as shown in Figure 5.12.

	0.870	0.953	0.932	0.931	0.899	0.754
Semi-Detailed	0.870	0.953	0.932	0.931	0.899	0.754
Reduced	0.885	0.960	0.954	0.908	0.891	0.798
Multi-step	0.920	0.992	0.986	0.946	0.932	0.831
Faravelli 2001	0.840	0.953	0.927	0.907	0.887	0.683
CM	$d_{L_2}^0$	$d_{L_2}^1$	$d_{P_e}^0$	$d_{P_e}^1$	shift	

Figure 5.10: Comparison of SciExpeM indices (Section 3.2.2) on all mass-loss profiles investigated for the semi-detailed, reduced, and multi-step model. The detailed model of Faravelli *et al.* is also reported as comparison.

Figure 5.11 shows the comparison of predicted and experimental data on number average molecular weight ($MW_{n,\alpha v}$). The average molecular weight is computed on-

the-fly by the detailed model of Faravelli *et al.*⁶⁶ (loosely dashed-dotted lines), while it is post-processed according to Equation 3.5 for the semi-detailed and reduced models (dash dotted and loosely dashed lines). The same comparison of mass-loss profiles is also shown in Figure 5.7b. With respect to the variation in $MW_{n,av}$, the proposed model shows quite good agreement with the predictions of the detailed model, where the discrepancies result from the different kinetic parameters employed. However, all models appear to significantly overestimate the decrease in average chain length compared to the experimental data. The reason is possibly related to transport limitations or pressure effect in the experimental batch-type vessel not described in the model⁶¹, but also to the experimental procedure itself. Since the batch vessel is a closed system, the released gases during cooling of the ampule can undertake condensation and repolymerization reactions. These phenomena result in an increase of the average chain length which is not accounted for in the present model. The reduced model captures with high accuracy the semi-detailed one, where the differences arise from the delayed onset temperatures. Further work to improve the semi-detailed model is expected also to enhance the reduced one.

Considering variation in model predictions at different initial molecular weight (Figure 5.11b), the semi-detailed and detailed models predict similar onset temperatures for MW decrease. While good agreement is observed for the low MW sample, at higher MW the model significantly overestimates the start of the MW decrease. Furthermore, both models predict the lower MW sample to have a higher reactivity, as shorter chains take less steps to decompose to shorter volatile chains. As previously mentioned, experimental data show a different behaviour possibly because short chains fully decompose and evaporate before undergoing any chain-transfer reaction.

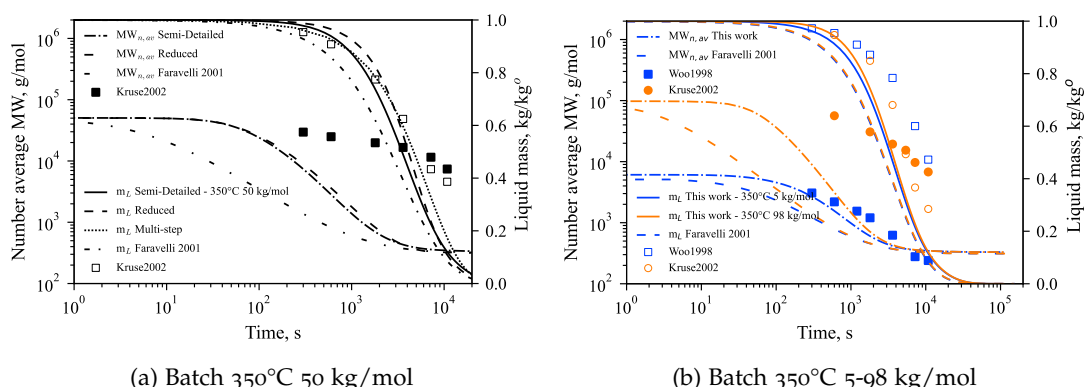


Figure 5.11: PS mass-loss (m_L) and number average molecular weight ($MW_{n,av}$) profiles at 350°C from different initial molecular weights. Comparison among the semi-detailed, reduced, and detailed model of Faravelli *et al.* and mass-loss and number average molecular weight literature experimental data.

5.3.2 Products selectivity: volatile yields

Model predictions are validated in comparison to the detailed model of Faravelli *et al.*⁶⁶ and with 58 speciation data-sets from the scientific literature^{60,61,75,339,367,383–388}. The performances are evaluated through parity plots of final mass yields of C₈, C₁₆, and C₂₄ (Figure 5.12). In the next paragraphs more in-depth analysis of the model predictions are shown. The simulation results are taken at the experiment time to have a proper comparison. Therefore, difference between models and experiments are also due to variations in the degradation times. A significant scattering is observed according to the experimental facility, particularly considering formation of trimer¹⁵⁸. Several experimental data are obtained at T>700°C, where secondary gas-phase reactions can play significant roles³⁷⁹. For instance, according to the CRECK gas-phase model at 900°C the cracking time of styrene is lower than 0.1 s. The trimer is expected to have significantly higher reactivity, possibly explaining the especially wide scattering of data. Pressure effects, which are seldomly discussed, are also believed responsible for inconsistencies between different experimental data.

The proposed models have considerable agreement with the experimental yields. Both C₈ and C₁₆ yields are captured with extremely high accuracy. The models' results are an intricate balance of all the reaction classes considered. Specifically, the competition between evaporation and decomposition of the trimer significantly affects the entire product distribution. Backbiting is also quite important as it relates to formation of the trimer and therefore its secondary degradation. Further reaction classes could also be considered, but the model predictions are not expected to significantly improve. Compared to the detailed model of Faravelli *et al.*⁶⁶, a globally higher agreement is observed in the entire investigated range. The semi-detailed model has the highest R² score, with a 0.7869 value for dimer yields. All mechanisms overestimate styrene formation at high temperatures, which however is probably due to the already mentioned secondary gas-phase cracking reactions. As previously discussed, the detailed model at low temperatures overestimates C₈ yields because of the lower degradation times but underestimates it due to the higher activation energy of unzipping reactions. The reduced and multi-step models also show high agreement over the entire temperature range. The former tends to slightly underestimate styrene yields while the latter overestimates them. Similarly, the dimer yields are respectively overestimated and underestimated by the reduced and multi-step models.

Figure 5.13 shows the comparison between the semi-detailed and detailed models for the predicted and measured yields of volatiles. The difference between measured yields and full mass-closure (100 wt.%) is categorized as "others". For the models, all species not reported experimentally are categorized as "others".

Considering experimental CSTR data at low temperatures (Figure 5.13a), the semi-detailed model correctly captures the yield in styrene and C₁₆. The simplified delumping procedure proves able to describe with high accuracy also formation of toluene

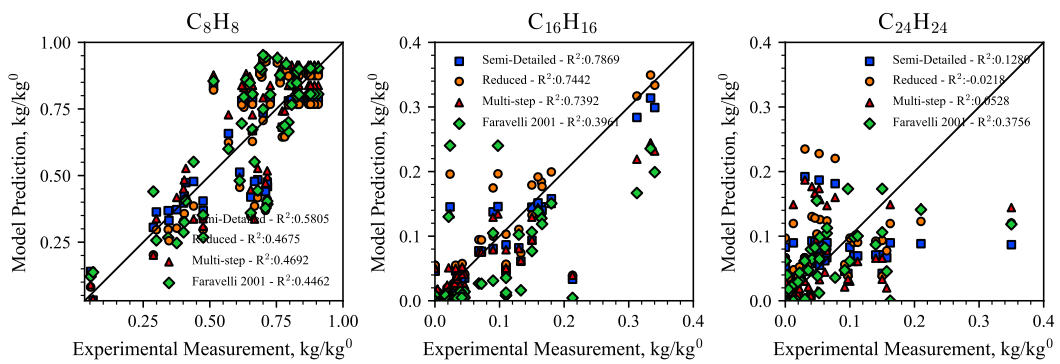
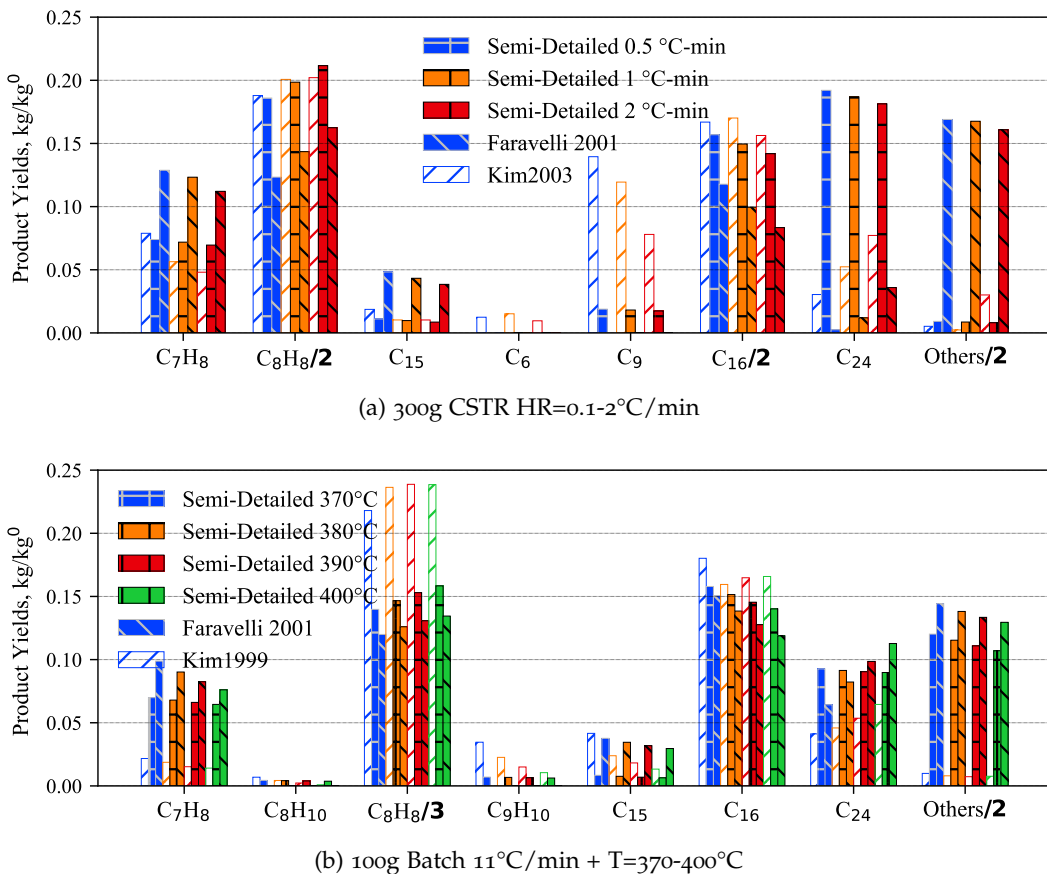


Figure 5.12: Parity plots of final gas-phase yields of C_8 , C_{16} , and C_{24} . Comparison of the present semi-detailed (blue squares), reduced (yellow circles), multi-step (red triangles), and detailed model of Faravelli *et al.* (green diamonds) and literature experimental data.

and diphenyl propane. The detailed model overestimates their formation because of the lower predicted styrene yield. On the other hand, neither model is able to account for preferential formation of C_9 . Indeed, α -methyl styrene is a minor product at normal operating conditions and may form because of secondary gas-phase reactions. However, secondary gas-phase reactions are expected to significantly increase the styrene yield as well. The proposed mechanism correctly overestimates formation of trimer, possibly because of the simplified evaporation reaction employed or secondary reaction in the CSTR reactor.

Figure 5.13b shows experimental data from a batch vessel with a fixed temperature profile. The operating conditions are similar to those shown in Figure 5.13a, but significantly different experimental results are obtained. With respect to these data, both models severely underestimate styrene yield while overestimating toluene formation, even though high agreement is reported shown in the previous Figure. Furthermore, the experimental compounds measure almost full mass closure, while the models predict formation of significant amounts of other compounds. The formation of C_{16} compounds is well captured, while C_{24} is overestimated at low temperatures. Pressure effect could explain the decrease in C_{24} yield. Indeed, at high conversion variation of the initial pressure of ~ 0.5 bar could favour degradation of the trimer.

Mass yields obtained in a broader temperature range are shown in Figure 5.13c. The semi-detailed model correctly captures the variation in product yields in the low-mid temperature range. The detailed model overestimates the styrene yields because of the predicted higher polymer reactivity. On the other hand, it has better agreement with data on trimer formation compared to the semi-detailed one. With respect to dimer and trimer, the present model underestimates both at low temperatures. Experimental data measure a maximum yield in styrene of approximately 75 wt.% while both models predict an increase in styrene yield upto almost 100 wt.%. The reason is probably secondary gas-phase reactions occurring at temperatures above 600°C. Additionally,

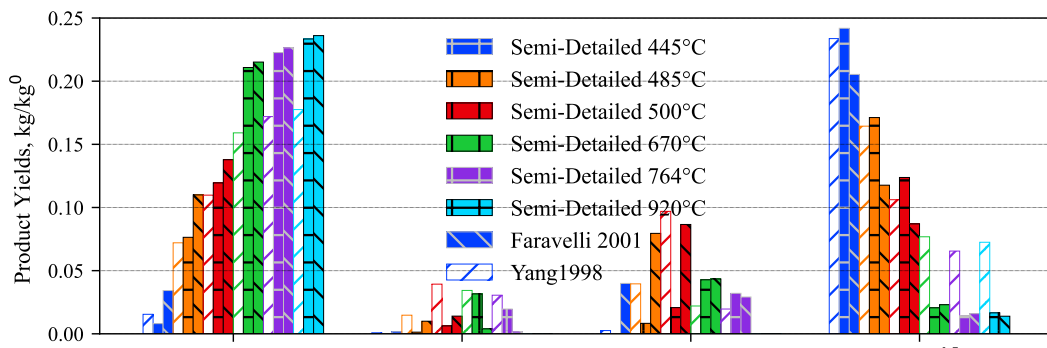


because of the high temperatures the polymer might have fully decomposed before reaching the set value.

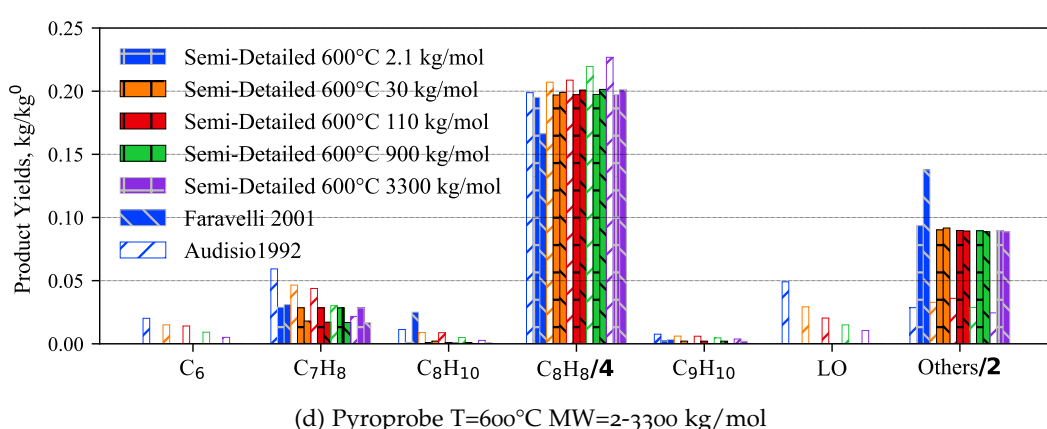
Similar results are observed on waste EPS data as shown in Figure 5.13d. Both kinetic models predict a monotone increase in styrene yield, while experimental data have a maximum at 800°C. Secondary gas-phase reactions are also the reason for the high amounts of non-identified compounds. The semi-detailed model overestimates at low temperature formation of dimer, while underestimating the trimer possibly because of the different evaporation model employed. Better agreement is observed at higher temperatures. Formation of benzene and light olefins (LO) takes place only at high temperatures according to data of Bouster *et al.*³⁶⁷, while Audisio and Bertini⁷⁵ measure them also at 600°C. Once again, these discrepancies are possibly attributed to secondary gas-phase reactions, as the authors do not identify neither dimer nor trimer. Both model predict a decrease in toluene yield at higher temperatures contrary to experimental data.

A more in-depth comparison with data of Audisio and Bertini⁷⁵ is shown in Figure 5.13d. The authors measure variation in compound yields according to the sample initial molecular weight. The semi-detailed model does not perceive any variation due to the simplified description of long-chains. The detailed model on the other hand correctly captures the decrease in toluene and increase in styrene yield. Neither model

accounts for benzene or light olefins formation, while significant amounts are experimentally observed. These are possibly resulting from impurities in the polymer which interact with the aromatic rings. Secondary gas-phase reactions could also be responsible.



(c) Curie-point pyrolysis T=400-920°C



(d) Pyroprobe T=600°C MW=2-3300 kg/mol

Figure 5.13: Comparison of mass yields of volatiles among the semi-detailed model, the detailed one of Faravelli *et al.* and experimental data (patched bars).

Figure 5.14 shows the comparison among the semi-detailed, reduced, and multi-step mechanisms in terms of predicted volatile yields at 500-900°C. The three models exhibit high consistency in predictions, although with specific differences. Considering styrene yield, the reduced model underestimates it at low temperatures, while the multi-step one overestimates it across the entire temperature range. The former is consequence of the significant lumping performed, and is observed also for PE and PP. Further optimization of the kinetic parameters³³² is expected to improve model predictions, but overall all differences are within experimental uncertainty. The multi-step model on the other hand entirely neglects formation of C₉. Similarly, the multi-step mechanism does not predict formation of toluene as it lumps all configurations in the C₁₅. The high yield of C₁₅ also results from neglecting its secondary liquid-phase decompositions. The multi-step model also underestimates formation of C₂₄ compounds, possibly because it lumps also unsaturated configurations (C₂₄H₂₂) which

are significantly less reactive due to the vinyl bonds. As previously discussed, the deviations at high temperatures with experimental data are possibly due to secondary gas-phase reactions not considered at present. The models overestimate the measured toluene yields, but are consistent with the predictions of the detailed model of Faravelli *et al.*⁶⁶.

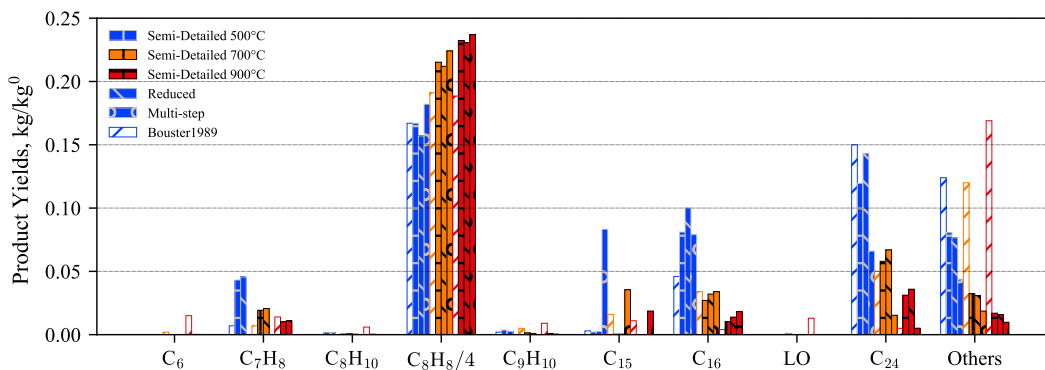


Figure 5.14: Comparison of mass yields of volatiles among the semi-detailed, reduced and multi-step models with experimental data (patched bars).

5.3.3 Energy requirements

The validation of thermodynamic properties relies on experimental data derived from heat profiles, where measurements involve assessing the heat fluxes required to maintain specified temperature profiles for the sample. Commonly, TG/DSC and TG/DTA calorimetry data are employed for this purpose, with the heat release profiles intricately linked to mass-loss profiles.

In Figure 5.15, a comparison is presented between predicted and measured PS heat flux profiles. These data exhibit significant scattering also in this case. Considering HR=10–50°C/min (Figure 5.15a), experimental data have high variability both in the peak value and temperature. The latter is related to the high variability also in degradation profiles. As previously mentioned, the heat related to the phase-change is negligible motivating the choice of not introducing an additional solid state species. The model predicts an asymmetric heat release profile, where a steeper variation occurs first followed by a smoother decrease. This behaviour results from the lower reactivity of allylic radicals, and appears quite consistent with the data of Jinno *et al.*³¹⁸ at both 10 and 50°C/min. Nevertheless, the predicted peak magnitude and location is different although the variation is quite well captured.

Different behaviours are observed with respect to EPS data as shown in Figure 5.15b. An initial exothermic peak is observed, possibly related to interactions of oxygen trapped in the polymer. Additionally, the authors do not measure any variation in peak magnitude at higher heating rates. The model does not account for any exo-

thermic phenomenon currently, and measures a significant increase in heat fluxes at higher heating rates consistently with data of Jinno *et al.*³¹⁸ shown in Figure 5.15a. As with PP, a much broader validation is required, but model predictions are currently well within experimental uncertainty.

Figure 5.15c shows the comparison of predicted and measured heat-fluxes at $10^{\circ}\text{C}/\text{min}$. Overall, the models have comparable results in terms of peak height and width. The different position is however related to the variation in degradation profiles. For instance, the reduced model has a sharper peak due to the steeper mass loss curve.

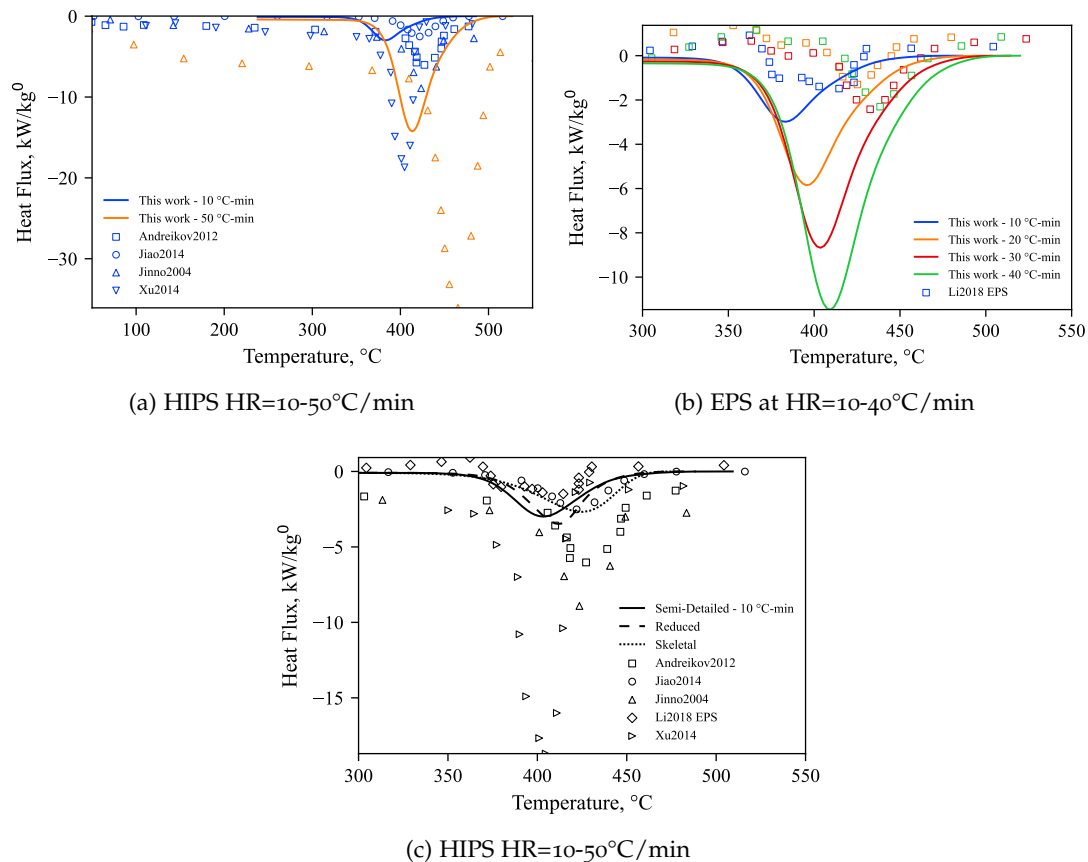


Figure 5.15: Comparison of predicted (solid lines) and measured^{318,358,369,372,374} (symbols) heat-flux profiles.

5.4 CONCLUSIONS AND FURTHER WORK

In the present Chapter a condensed-phase kinetic model for Polystyrene degradation has been proposed. The mechanism is formulated through the functional groups approach to characterize degradation times, released volatiles, and energy requirements. high molecular weight chains are simplified into a few lumped pseudo-species with specific chemical functionalities, while low molecular weight products are treated in greater detail. The kinetic mechanism adopts reaction classes from the scientific liter-

ature, employing various lumping techniques to reduce the number of reactions. An in-depth comparison with reaction classes proposed by other authors and their elementary steps is also reported. The kinetic mechanism is complemented by defining species thermochemistry to account for the heat requirements in the process. Liquid-phase properties are derived from phase-change literature data showing good agreement with data on the molten polymer.

The proposed semi-detailed model serves as the basis for deriving reduced-order models. Specifically, a semi-detailed reduced model and a fully-lumped multi-step model are obtained. The former employs a lumping procedure to simplify the radical chemistry. The latter simplifies further the radical chemistry into a few global steps, accounting for the main reaction classes.

The three models are validated with an extensive set of experimental data from the scientific literature, including a comprehensive comparison with the detailed mechanism by Faravelli *et al.*⁶⁶. The semi-detailed model demonstrates its capability to accurately describe degradation times, even when compared to the more expensive mechanism. The revised kinetic parameters allow achieving considerable agreement with volatiles yield across more than fifty speciation data sets, without the need for additional less probable reaction classes. The lower R^2 for the trimer yield is consequence of the high experimental scattering, possibly resulting from secondary gas-phase reactions. The reduced-order models are validated against the semi-detailed one, demonstrating their ability to describe mass-loss profiles with the same accuracy. However, differences in volatile distribution profiles are observed due to significant lumping involved. Validation with TG/DSC data proves the models' ability to describe the energy balances of the degradation process despite high experimental scattering.

All three mechanisms are provided in CHEMKIN format and are freely accessible on GitHub². The proposed models specifically address condensed-phase reactivity, and future work will extend to modeling secondary gas-phase reactivity to assess gasification operating conditions.

² available at <https://github.com/Alocaspi/Polymers-Kinetic-Mechanisms>

POLY(ETHYLENE TEREPHTHALATE)

POLY(ETHYLENE TEREPHTHALATE) (PET) is a versatile and widely used thermoplastic polymer in the polyester family³³³. This synthetic polymer is known for its exceptional clarity, strength, and recyclability, making it a preferred choice across various industries. PET is synthesized through condensation polymerization of terephthalic acid and ethylene glycol, yielding a high-performance material with remarkable mechanical and chemical properties.

One key attribute of PET is its transparency. This, coupled with its lightweight nature, makes it ideal for producing clear plastic containers, bottles, and packaging materials. The aromatic rings in the polymer backbone contribute to its stiffness and strength, allowing to produce high-performance materials³⁸⁹. PET's robustness, impact resistance, and dimensional stability, make it a suitable option for manufacturing fibres and films used in textiles, packaging, and industrial applications. Its excellent barrier properties against gases, moisture, and aromas further enhance its suitability for the packaging industry, preserving the freshness and integrity of a wide range of products. Additionally, PET's compatibility with diverse processing techniques, such as injection and blow molding, contributes to its widespread adoption in producing a vast array of products.

PET's widespread use extends to its role in sustainability. The material boasts high recyclability, with recycled PET (rPET) finding application in eco-friendly products, thereby reducing plastic waste's environmental burden. Over the past decades, several recycling technologies have emerged²⁵. However, these methods often involve significant purification and separation costs, potentially also deteriorating the material properties. In this context, thermochemical recycling offers a complementary approach for complex and contaminated waste streams, potentially minimizing separation and purification when properly optimized^{7,28}.

Real-world plastic waste samples typically contain 3-7 wt.% PET, varying with location and season.^{15,390}. While the quantities are modest, the presence of oxygen can decrease the quality of pyrolysis oil³⁹¹ and leads to a carbonaceous solid residue (char) that requires further treatment. Most importantly, PET alters the release of chlorinated and nitrogenated compounds from polyvinylchloride (PVC)^{119,120,124} and polyamides (PA)^{50,119,121}. Given that hydrochloric acid (HCl) formation and pollutant release are critical concerns in thermochemical recycling of plastic waste, understanding the degradation of PET and its interactions with other polymers is crucial.

As discussed in Section 2.2 of Chapter 2, the kinetics of PET thermal degradation have received less attention compared to other polymers. Numerous intermediary reaction pathways have been proposed^{85,87,90–93,95–99,392–400}, but, to the author's knowledge, no predictive model able to quantitatively account for the complex product spectra has been developed. This Chapter presents a semi-detailed kinetic model for PET's condensed-phase degradation. The mechanism is developed following the functional group (FG) approach employed also for the other polymers. The content of the chapter unfolds in a structured manner introducing first the representation of polymer chains, volatiles, and char. Following this, the degradation mechanism is discussed detailing both molecular and radical reaction classes and associated rate constants. Model validation, both in terms of mass-loss and product distribution profiles, is performed by comparison with literature experimental data. Additionally, novel micro-pyrolysis speciation data by two-dimensional GC are presented together with elemental characterization of the char residue produced by thermogravimetric analysis. The developed condensed-phase model will be coupled with other subsets to study secondary gas-phase and gas-solid gasification reactions and is available on GitHub as a public repository¹.

6.1 SEMI-DETAILED KINETIC MECHANISM: PET-85-700

The purpose of the present work is to propose a kinetic model that quantitatively explains the condensed-phase chemical phenomena involved in PET pyrolysis (Figure 6.1). As mentioned, the mechanism development follows a first-principles approach, critically assessing potential reaction pathways by means of analogies with smaller compounds with similar chemical functionalities. Small methyl and ethyl esters serve as reference due to the high accuracy of computational methods for these molecules. Bond dissociation energies (BDE) evaluated through the ATcT²⁷⁶ and NIST¹⁰⁰ databases are employed to validate these studies and extrapolate the information to heavier compounds. Fitting methods can also be employed to propose both simple global or complex semi-detailed models. These however often lead to unphysical kinetic parameters and models that rely heavily on over-parametrization to reproduce experimental data. Additionally, these approaches are sensitive to data quality and inconsistencies between theoretical and experimental results. Nevertheless, numerical optimizations techniques are valuable when employed within reasonable uncertainties ranges for the rate constants.

Due to limited and inconsistent data, thermochemical properties of PET are not included in this work. Even for gas-phase phenyl esters, significant discrepancies exist between different estimation methods. For instance, the formation enthalpy (Δh_f^0) of ethylene glycol dibenzoate (one of the PET dimers) estimated with Burke *et al.*²⁷⁰ group

¹ Available at <https://github.com/Alocaspi/Polymers-Kinetic-Mechanisms>

contribution method is ~ 135 kcal mol $^{-1}$. On the other hand, employing the approach implemented in RMG²⁷³ a value of ~ 98 kcal mol $^{-1}$ is obtained. This variation of 40 kcal mol $^{-1}$ highlights the need for further research to improve the reliability of these methods. When compared with available experimental data on benzoic acid^{100,302}, Burke *et al.*²⁷⁰ and RMG²⁷³ underestimate Δh_f^0 of 5 and 10 kcal mol $^{-1}$, respectively.

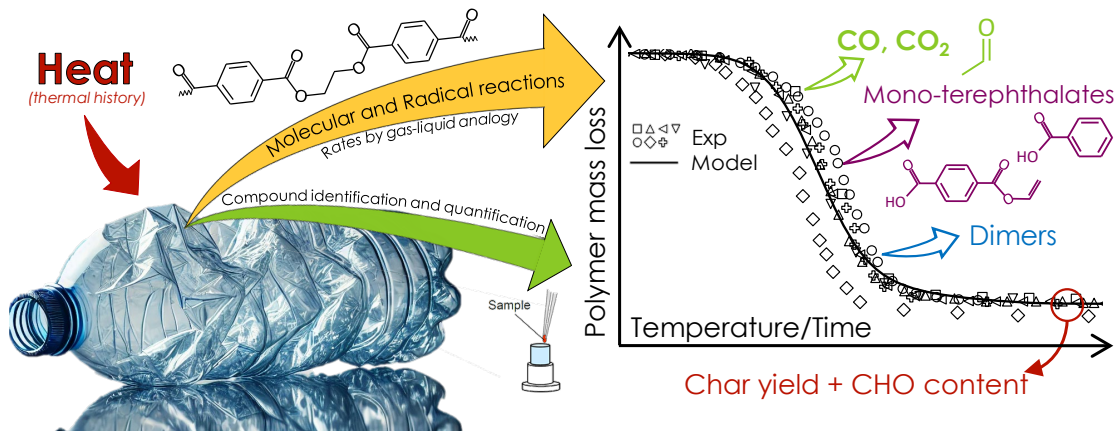


Figure 6.1: Schematic representation of the PET semi-detailed model according to the functional groups approach.

6.1.1 Species Definition

PET degradation is a three-phase system. Polymer degradation occurs mainly in the molten state⁹⁷, resulting in formation of both gas and solid components. In the following, all compounds that evaporate from the molten to the gas- phase at reaction temperature are defined as "gas species". These are further categorized as light or condensable (tars) gases according to their physical state at room temperature. The solid residue is simply referred to as "char" independently of its elemental composition¹⁶⁷. For modelling purposes, char species are incorporated into the liquid phase kinetics, although a separate solid-phase mechanism can be implemented if needed. According to the functional groups approach (FG), the reactivity of macromolecules is captured through pseudo-species characteristic of their chemical moieties. The liquid-phase compounds are distinguished in three different subsets: all polymeric chains longer than the trimer are considered high molecular weight (HMW) species and are described with functional groups characteristic of the polymer moieties; compounds smaller than the PET trimer are modelled as real species and are referred to as low molecular weight (LMW) species; solid-phase species are described through the fully lumped functional groups approach developed for biochar formation¹⁵².

Similar to the other polymers, species representative of HMW mid-chain (MC) and end-chain (EC) moieties are introduced. Figure 6.2 depicts all the pseudo-species considered in the model. MC and EC species are distinguished by the "P" prefix/suffix.

To identify the chemical moieties of pseudo-species from their names, a specific nomenclature is introduced. "Ph" represents the aromatic rings along the chain (-C₆H₄-), while terminal double bonds are labelled "D" (-C₂H₃). Alkyl-like carbon atoms can be methyl groups ("M", i.e., -CH₃), secondary carbons ("C", i.e., -CH₂-), or tertiary ones ("T", i.e., -CH-). The starting polymer comprises only terephthalic and ethylene glycol moieties. Following the nomenclature described, MC species are labelled respectively *P-COPhCO-P* and *P-OCCO-P*, while the corresponding EC counterparts are *P-COPhCOOH* and *P-OCCOH*. Additional species are introduced to represent the chemical moieties formed during the degradation, such as vinyl benzoates (*P-COPhCOOD*), phenyls (*P-COPhH*), and ethyl-idenes (*P-OTMO-P*). The corresponding pseudo-species are introduced to represent these moieties. The model incorporates alkyl, carboxylic, and phenyl radicals to account for radical reactivity. Benzoyl radicals are excluded due to their propensity for rapid decarbonylation and the inherent instability of the hydrogen atom within the benzo-aldehyde functionality. The presence of a radical is denoted by the "dot" within the label. Within the mechanism, the "dot" is replaced by the "r" to conform with the syntax required in OpenSMOKE++ v 0.21³¹⁰. Certain species, such as the ethyl ester end-chain (*P-OCM*), possess two distinct isomer radicals, exhibiting different reactivities. The location of the "dot/r" in the species' label relates to the type of radical. For example, *P-OCM* represents the primary radical, while *P-OC·M* the secondary one.

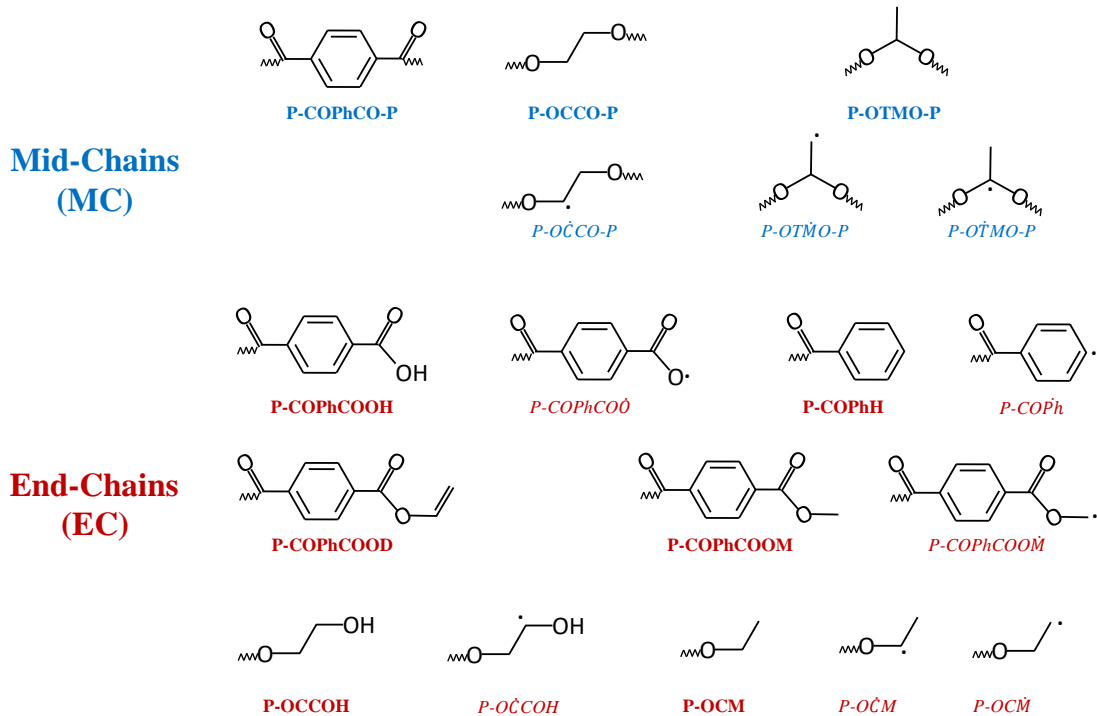


Figure 6.2: Schematic representation of the stable and radical HMW species included in the present kinetic model. Further details on the nomenclature are given in the text.

LMW compounds are described similarly to the other polymers. Species with boiling temperature ($T_{b,n}$) $<200^{\circ}\text{C}$ are assumed to directly enter gas-phase upon stabilization. The degradation products are primarily characterized by terminal phenyl, carboxylic, or vinyl benzoate functionalities. Minor compounds with methyl-ketone or methyl-/ethyl ester ends are also observed⁹¹, but their low abundance justifies their exclusion for model simplicity. Considering the monomers, all combinations of terminal functional groups are explicitly considered. For example, the model includes three monomers with one carboxylic end, namely benzoic acid (BA) for phenyl-carboxylic ends, monovinyl terephthalate (MVT) for vinyl-carboxylic ends, and terephthalic acid (TA) for carboxylic-carboxylic ends. Dimers configurations are limited to cyclic dimers (CYEGDE) and symmetric configurations such as ethylene glycol dibenzoate (EGDB), ethylene glycol divinyl terephthalate (EGDV), and ethylene glycol dibenzoic acid (EGDA). Mixed configurations are represented as equimolar amounts of the corresponding symmetric dimers. For instance, a dimer with one phenyl and one carboxylic end is represented as 0.5EGDB + 0.5EGDA. Figure 6.3 shows the included monomers and dimers (except for the cyclic one for clarity purposes). The same types of radical considered for HMW species are also introduced for LMW ones. Molecules with multiple radical isomers have their specific radical location indicated by the placement of "dot" within the label. For example, $\cdot\text{GDB}$ represents the glycol radical of the EGDB dimer, while $\text{EGD}\cdot\text{B}$ represents the phenyl radical.

PET degradation proceeds through formation of polycyclic aromatic hydrocarbons. Subsequent dealkylation and decarbonylation reactions lead to a carbonaceous solid residue (char). While extensive research has been conducted on coal- and bio-char^{152,167,401}, to the author's knowledge limited characterization data exist for plastic char. Among the char studies performed in controlled conditions, only few focus on char elemental characterizations⁴⁰²⁻⁴⁰⁶, which is crucial for understanding char reactivity and secondary reactions¹⁶⁷. For this reason, the fully lumped approach developed for biochar formation¹⁵² is adopted in the present model. A single pseudo-species labelled CHAR describes the aromatic structure of the solid, while additional pseudo-species represent groups such as ketones, ethers, esters, aliphatics, and other moieties. These are denoted by the "G-" preceding their chemical formula (e.g., G-CO, G-H₂) and represent the evolution of char's elemental composition. These are classified as liquid species to avoid considering a three-phase system. Since the reference biomass model is fully lumped, the radical reactivity is not explicitly accounted for but only the global behaviour of pseudo-components is considered. For instance, phenyl hydrogens are represented by the G-H₂ species, and a single unimolecular reaction represents its release to H₂. Similarly, methyl bridges and toluene-like structures are represented through the species G-CH₄ which decomposes in a single lumped step to gas-phase CH₄. Overall, the char pseudo-species share the same chemical composition as the stable gas-phase molecules they decompose into^{37,152,407}. The total number of liquid-phase pseudo-species introduced to describe PET condensed-phase degradation is 51,

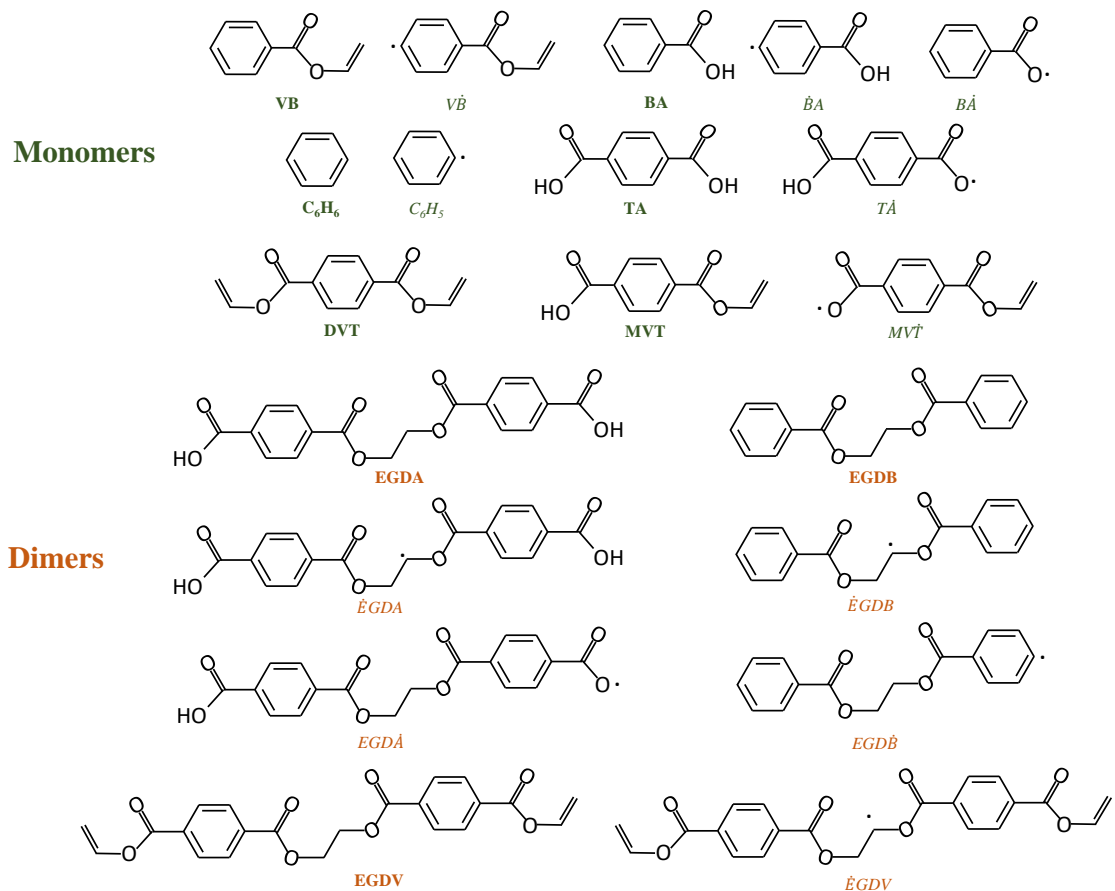


Figure 6.3: Schematic representation of the monomer and dimers considered in the present work (except for the cyclic dimer CYEDGE). Both stable and radical species are presented with their labels.

18 of which are HMW species and 8 are functional groups representing the char composition. Liquid-phase species are identified by “(L)” and the same LMW species are present also in the gas phase, obtaining a total number of 84 species.

6.1.2 Reaction Classes

The thermal degradation of PET has been a subject of study since the 1950s^{91,392}. Considerable work has been performed to investigate the reaction pathways involved, by means of model compounds or introducing other components in the reactive mixture^{90–98}. In recent decades, theoretical studies have explored the gas-phase reactivity of small alkyl esters^{83,397,408–415}, and recently calculations on PET dimers have also emerged^{85,393,398}. While these studies offer valuable insights into polymer degradation, inconsistencies remain, as discussed further below. In general, PET degradation is known to occur through both molecular and radical pathways. Carboxylic acids have been observed to catalyse polymer degradation^{94,95}, further highlighting the complexity of the process.

Figure 6.4 schematically shows the overall degradation mechanism, which is composed by molecular (blue) and radical (red) pathways. The former primarily governs the formation of monomers, dimers, and trimers, while the latter is responsible for small products like CO, CO₂, and char. Other compounds, such as acetaldehyde, arise from the interplay of both mechanisms. Several proposed molecular pathways in the literature will be explained through the lens of radical isomerisation and degradation. The reactions are outlined in more detail through several figures in the following sections. These representations necessarily simplify the complex three-dimensional morphology and accurate relative bond lengths (e.g., C=O bonds are shorter than C=C bonds). The elementary Arrhenius parameters are presented together with each reaction introduced, comparing the proposed value with studies on analogous compounds. Further high-accuracy studies targeting specific assumptions can assist in model refinement. The total number of liquid-phase reactions is 720, where approximately 400 are H-abstractions.

6.1.2.1 Molecular Degradation Mechanism

The importance of concerted molecular reactions has been highlighted in the degradation of both PET^{85,91,98,395,396} and small gas-phase esters^{83,100,411,414}. Table 6.1 reports the considered reaction classes and their Arrhenius parameters. Each family and the corresponding kinetic rates are discussed in the following paragraphs.

Table 6.1: Modified-Arrhenius parameters for molecular elementary reactions classes (units cm, mol, s, cal).

Reaction	A	n _A	E _{act}
Syn elimination (r6.1, r6.2, r6.3)	2.00E+13	o	48000
Assisted molecular decarboxylation (r6.6)	5.00E+10	o	36000
Carboxylic acid dimerization (r6.7)	3.00E+10	o	35000
Vinyl ester isomerisation (r6.8)	2.00E+13	o	50000
Ester-interchange (r6.9, r6.10)	4.00E+07	o	20000
Pseudo Diels-Alder (r6.11)	1.00E+07	o	35000

PET chain cleavage and rearrangement can occur via a concerted 6-centre syn elimination involving hydrogen transfer, as illustrated in Figure 6.5. This reaction converts the initial mid-chain species (blue) into P-COPhCOOH and P-COPhCOOD end-chains (red). The reaction rate is first-order in the concentration of the glycol mid-chain and it employs two neighbouring terephthalic groups as "supporting polymer units" (SPU, dashed lines) to form the two end-chain moieties (see Section 3.1.2.2).

The same reaction can occur near any end-chain forming the corresponding monomer or dimer. Formation of the monomer and dimer involves the same elementary step, and

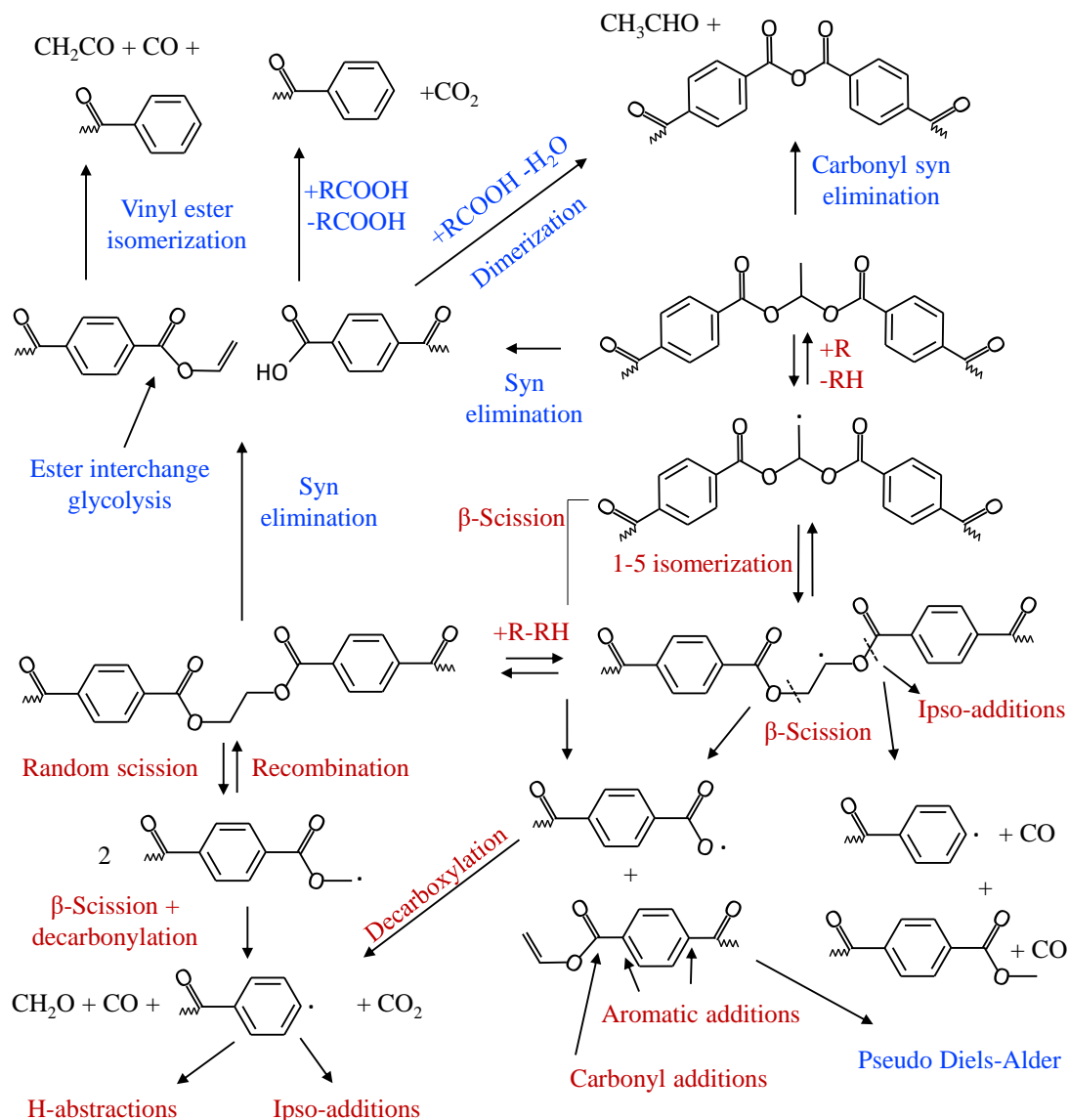


Figure 6.4: Schematic representation of the proposed molecular (blue) and radical (red) degradation mechanism.

the release of the former near a P-COPhCOOH end-chain is shown in Figure 6.6. The reaction introduced in the mechanism (r6.2) lumps the formation of both monomers and dimers in a single step, utilizing the sum of the elementary steps' stoichiometric coefficients. The reaction has an equal probability of forming either a carboxylic or vinyl end on the polymer, reflected by the formation of both types of end-chains in the product distribution. Similarly, the LMW species can have either two acid ends or a combination of one benzoic and one vinyl end. Dimers with different terminations are represented as 0.5EGDA and 0.5EGDV. The reaction rate depends on both the mid-chain and the end-chain SPUs, exhibiting unimolecular behaviour with respect to

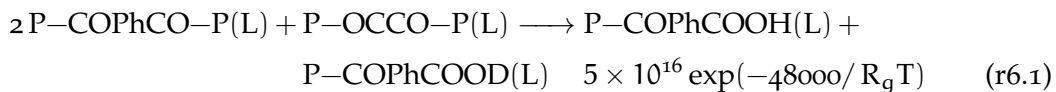
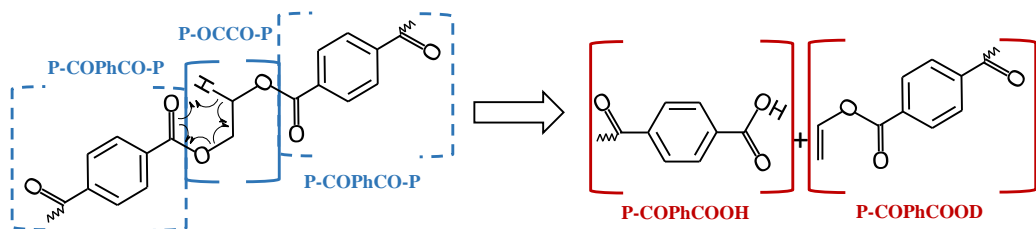


Figure 6.5: Schematic representation of the degradation of the 6-centred syn elimination to form vinyl and carboxylic end-chains employing two terephthalic units as SPUs (dashed lines).

the glycol mid-chain (MC) concentration. Reaction orders are enforced with the *FORD* keyword as dictated by the CHEMKIN format.

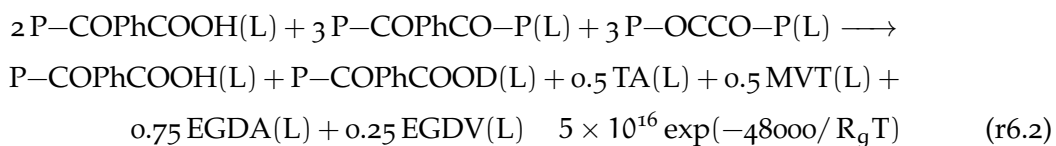
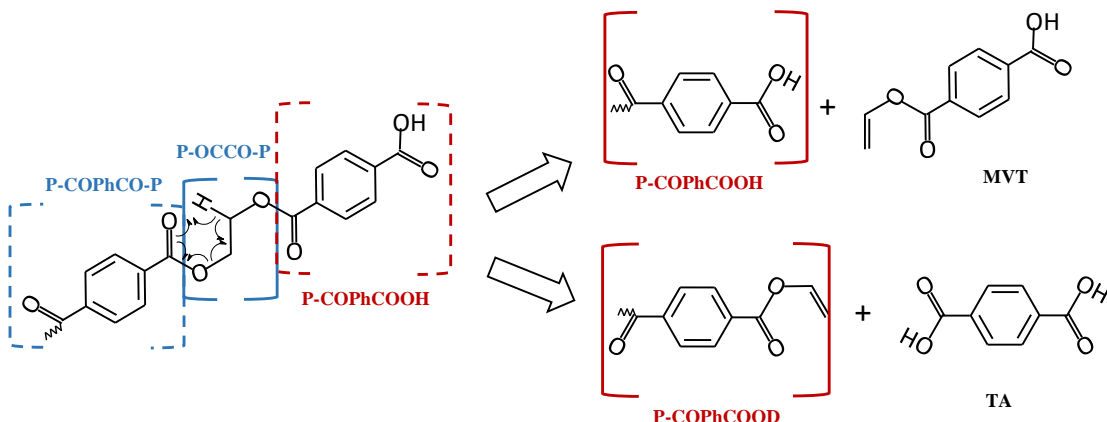
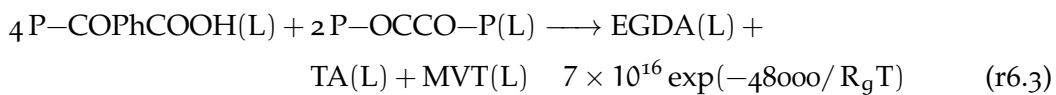


Figure 6.6: Schematic representation of the syn elimination occurring near a carboxylic end-chain.

Degradation of P-OCCO-P can occur also employing two end-chains as support. To simplify the kinetic mechanism, these reactions do not form any chain species but only LMW products. For instance, considering two P-COPhCOOH units as SPUs, the reaction is:



Similar to the case with two mid-chains acting as support, this reaction exhibits a first-order dependence on both SPUs, resulting in a second-order dependence on the concentration of P-COPhCOOH(L). Glycol end-chain moieties can undergo the same pathway, forming carboxylic ends and CH₃CHO, but this route is of minor significance due to the low concentration of P-OCCOH. Likewise, liquid-phase dimers can decompose into their respective monomers through the same reaction mechanism. For cyclic dimers, this corresponds to a ring-opening reaction.

The kinetic parameters of the syn elimination reaction are defined by analogy to gas-phase ethyl ester^{83,100,411,415}. Since the C-H bond in α to the ester is more labile than a primary hydrogen by ~ 4 kcal mol⁻¹^{276,410}, an activation energy of 48 kcal mol⁻¹ is introduced. Huang *et al.*⁸⁵ calculate a gas-phase energy barrier of 43 kcal mol⁻¹ for the PET dimer, which is 7 kcal mol⁻¹ lower than the energy barrier of ethyl metanoate^{83,100,411,415}. While this can be attributed to the weaker C-H bond, the low-accuracy DFT method employed is also a possible source of uncertainty. Ma *et al.*³⁹³ studied free energy surfaces of PET dimers at 435°C, suggesting comparable rates for this concerted pathway and homolytic C-C bond fission. Since initiations do not directly affect polymer degradation due to the relatively low degradation temperature, these results imply that molecular pathways do not significantly affect PET pyrolysis, in contrast with the rest of the scientific literature. Furthermore, the authors do not consider radical propagations (i.e., the pyrolysis rate determining step) but study initiation on radical species forming bi-radicals. These pathways are less probable than initiation on the stable counterparts due to the lower concentration of the radicals. As previously mentioned, the same reaction can occur also on end-chain moieties. For these reactions, a 3 kcal mol⁻¹ decrease in activation energy is adopted for the analogous reaction on glycol end-chain moieties due to the even lower BDE of the C-H bond α to an OH group^{276,410}.

During the thermal degradation ethyldene structures form because of radical and molecular mechanisms. While the radical pathway is discussed in Section 6.1.2.2, the present mechanism does not include the molecular route. Experimental evidence suggests that vinyl ethers and carboxylic acids readily undergo addition reactions at T between 40-70°C, leading to the formation of hemiacetal esters⁴¹⁶. These pathways are often catalysed by salts and strong acids, but can also proceed with the carboxylic acid itself acting as self-catalyst. Notably, Mukaiyama *et al.*⁴¹⁶ observe first-order dependence in vinyl ether and a second-order one in carboxylic acid for the reaction rate. Similar behaviour has been reported also for equimolar amounts of vinyl benzoate and benzoic acid at 260-300°C⁹¹, where the reaction proceeds almost quantitatively. However, Allan *et al.*⁹¹ found no such activity for vinyl acetate and acetic acid without a catalyst. While these addition reactions exhibit low activation energies (15-20 kcal mol⁻¹⁴¹⁶), the termolecular reaction involves a 10-membered cyclic transition states. Because of the high entropic cost, this pathway may be relevant at low temperatures range, but further experimental work is required to investigate those conditions. As

these reactions are not relevant in the investigated conditions, they are excluded from the current model.

Similar to the reaction depicted in Figure 6.5, the ethylenedene diester also undergoes decomposition through two types of concerted 6-centre molecular pathways. The first of these pathways, illustrated in Figure 6.7, is similar to the syn elimination involving glycol end-chain moieties (Figure 6.5). This reaction results in the formation of benzoic and vinyl end-chains, and all combinations of EC and MCs are employed as SPU like the reactions above. Compared to reaction 6.1, a 2 kcal mol⁻¹ higher activation energy is considered because of the stronger BDE of primary hydrogens in line with the values of Sun *et al.* for ethyl metanoate⁸³. The frequency factor is also assumed 3 times higher due to the higher mobility and greater number of hydrogens available.

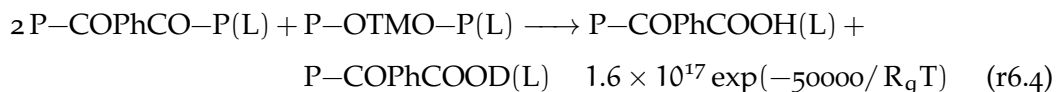
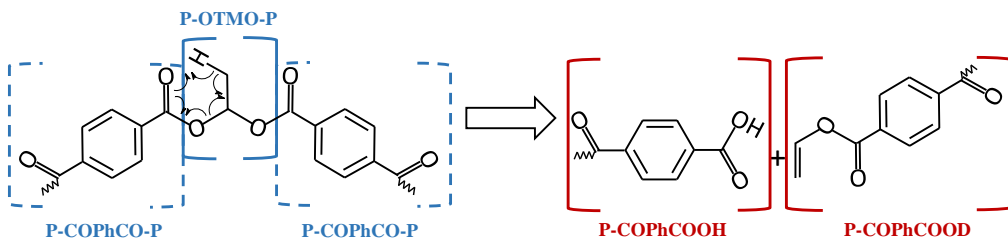


Figure 6.7: Schematic representation of the ethylenedene methyl syn elimination to form vinyl and carboxylic end-chains.

The alternative pathway involves interaction between the oxygen and carbon atoms of two different carbonyl groups (Figure 6.8). This reaction occurs through a 6-membered ring, resulting in CH₃CHO and an anhydride moiety. Due to its thermal stability⁴¹⁷, the phenyl anhydride is categorized as a char functional group. While Carson *et al.*⁴¹⁸ estimate BDE of ~75 kcal mol⁻¹ for this compound, these values are 20 kcal mol⁻¹ lower than those reported for smaller analogous anhydrides^{100,276}. This discrepancy possibly stems from a 10 kcal mol⁻¹ difference for formation enthalpies of benzoyl radicals between Carlson *et al.*⁴¹⁸ and the ATcT database²⁷⁶. Estimating Δh_f^o of the benzoyloxy radical from the energy barriers proposed by Liu *et al.*⁴¹⁹, a value of 95 kcal mol⁻¹ is obtained from ATcT and NIST databases for the BDE of the phenyl anhydride. This value is also consistent with the estimations of Liu *et al.*⁴¹⁹. The phenyl anhydride lacks available hydrogens compared to small analogues and it reacts more slowly, only by chain initiations, radical additions, or hydro/alcoholysis. For these reasons, the anhydride of r6.5 is represented through char pseudo-species, and the two outer phenyl ketone moieties are represented as half terephthalate mid-chains. To avoid introducing additional char species compared to the biomass model⁴⁰⁷, CO₂ is directly released. The remaining oxygen are represented as G-CO and G-COH₂ to account for the partial release

of CO and the remaining oxygen being trapped within the char matrix. The aromatic carbon and hydrogen are represented by G-H₂ and CHAR species. The Arrhenius parameters for this reaction are defined in analogy to the glycol syn elimination. However, a 6 kcal mol⁻¹ decrease in E_{act} is introduced to account for the polarization of the carbonyl groups which is expected to favour the reaction. Conversely, the frequency factor is assumed 30 times lower because of the higher steric hindrance of the bulky aromatic groups.

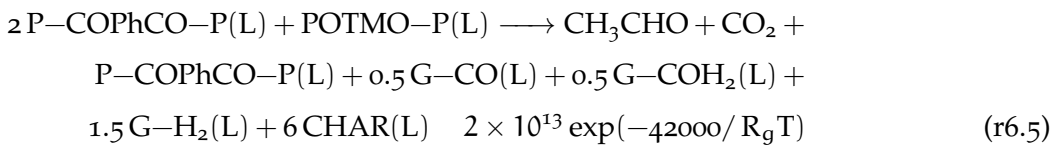
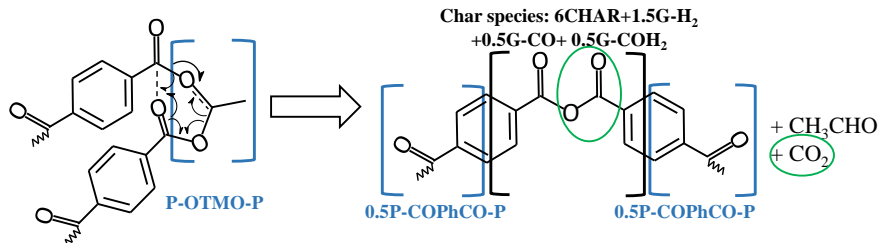
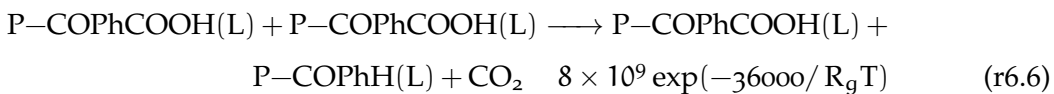


Figure 6.8: Schematic representation of the ethylenedide syn elimination to form phenyl anhydride and acetaldehyde.

The main reaction product of syn elimination reactions are carboxylic and vinyl end-chains. Molecular degradation pathways are considered for both functionalities. The rate of molecular decarboxylation has been considerably studied in gas-phase, highlighting that these are slow high-temperature degradation with E_{act} ≈ 65-75 kcal mol⁻¹^{83,84,100,420}. As the frequency factor is comparable to syn elimination (i.e., 10¹²-10¹³), these pathways do not affect the PET degradation in the conditions of interest and are not included. Conversely, theoretical^{419,421} and experimental^{94,95} literature studies have shown carboxylic acids enhance several degradation pathways, decarboxylation included⁴¹⁹. To account for this phenomenon, bimolecular reactions are included as:



where an additional P-COPhCOOH(L) unit is introduced as catalyst and is not consumed across the reaction. Similar reactions are introduced to account for end-chains catalysing dimer and monomer decomposition and vice-versa. Because of their low liquid-phase concentrations, interactions between LMW compounds are neglected to simplify the mechanism. An activation energy of 35 kcal mol⁻¹ is considered for reaction 6.6 in line with the one reported by Liu *et al.*⁴¹⁹. The introduced frequency factor

is similar to gas-phase addition of a carboxylic acid to a vinyl bond⁸³ and Diels-Alder kinetics³⁵.

Coupling of carboxylic acid results also in acid dimerization/dehydration to form the corresponding anhydride. The reaction is represented in Figure 6.9 and is similar to the catalysed decarboxylation, but it consumes both moieties to form water. The anhydride product is represented as in reaction 6.5. The kinetics of acid dimerization have been studied for poly(acrylic acid), but the rate of the mechanism remains unclear. Different studies^{422–424} report varying E_{act} for the process, ranging from 27 to 38 kcal mol⁻¹. Some suggest a bimolecular mechanism with E_{act} of 27⁴²⁴ or 38⁴²³ kcal mol⁻¹ depending on the study. Eisenberg *et al.*⁴²² propose an unimolecular route $E_{act} \approx 27$ kcal mol⁻¹. This work employs the energy barriers proposed by Liu *et al.*⁴¹⁹, with a 1 kcal mol⁻¹ decrease compared to bimolecular decarboxylation. Additionally, a 10^{0.8} times faster frequency factor⁵⁸ is assumed due to the smaller (6-member) transition state involved in dimerization compared to the 7-member state in decarboxylation.

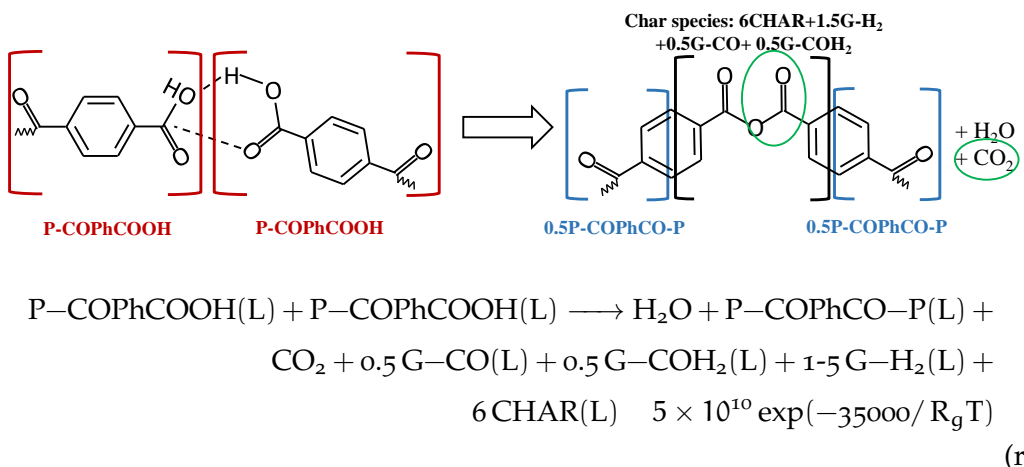


Figure 6.9: Schematic representation of carboxylic acids dimerization.

Vinyl benzoate end-chains can undergo various reaction pathways, similar to those observed for vinyl acetate^{91,411,425}. The analogous syn elimination is excluded due to the 10 kcal mol⁻¹ higher BDE of vinyl hydrogens compared to primary hydrogens²⁷⁶. The primary unimolecular decomposition pathway is schematically represented in Figure 6.10 and involves rearrangement to form a β -keto-aldehyde (benzoylacetaldehyde). This compound then quickly decomposes releasing CO and forming an acetophenone moiety⁹¹. Since the rate-determining step for the vinyl ester molecular degradation is the intramolecular rearrangement, the reaction products are represented through the main compounds derived from acetophenone pyrolysis (i.e., ketene and phenyl rings by radical degradation), with the additional benefit of avoiding an increase in the model size. To avoid considering species representative of the latter moieties, the reaction products are represented through the main species expected from acetophen-

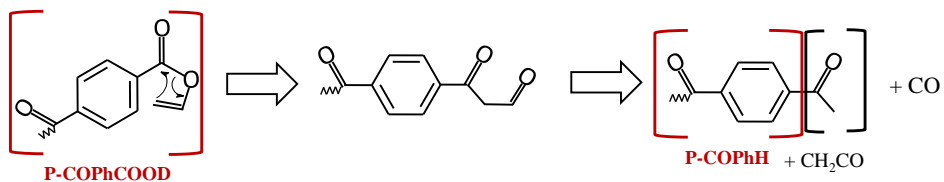
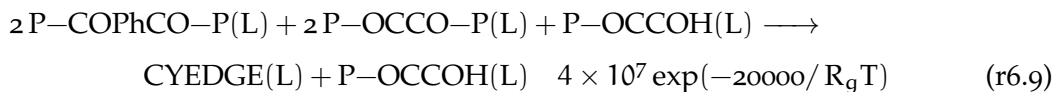


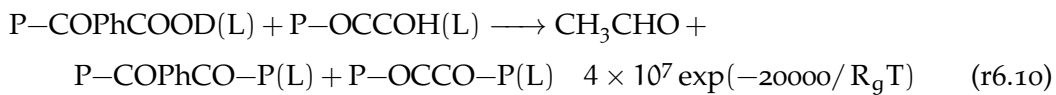
Figure 6.10: Schematic representation of vinyl-ester isomerisation and decarbonylation.

one pyrolysis (ketene and phenyl rings by radical degradation). The rate parameters for the determining step derive from the analogous gas-phase phase keto-enol tautomerization⁴²⁶. A 2 kcal mol⁻¹ decrease in the activation energy is applied to account for the polarization of the carbon atom in the carbonyl group. These parameters involve higher temperatures compared to those proposed by Morsch *et al.*⁴¹¹ for vinyl acetate, which were adjusted to match the selectivity data reported by Allan *et al.*⁹⁰. While Da Silva *et al.*⁴²¹ calculate that carboxylic acids can catalyse keto-enol tautomerization at atmospheric conditions, this phenomenon is not included in the current model.

Glycol end-chains can participate in alcoholysis reactions with both mid-chain and end-chain moieties. These reactions affect the initial stages of degradation and under conditions of low initial molecular weight. Reactions occurring near the end-chain itself result in formation of cyclic dimers as:



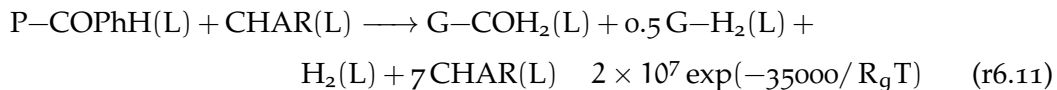
which is an unimolecular autocatalytic reaction that employs the mid-chain units as SPU. The same reaction can take place on the vinyl end to release acetaldehyde and regenerate the initial polymer moiety:



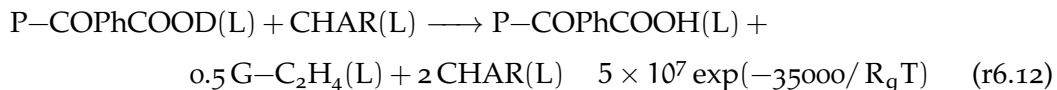
Bimolecular alcoholysis can take place also on the carbonyl group near the end-chains releasing LMW products. Although ester alcoholysis is a well-studied reaction, the existing kinetic analyses primarily focus on acid and basic catalysis within specific solvents. For the present purposes, the kinetic parameters proposed by Reimschuessel *et al.*⁹⁴ are considered.

Diels-Alder reactions represent the final category of considered molecular pathways. These reactions are unique in their ability to facilitate condensation and growth of

polycyclic aromatic carbons. These are the only considered reactions that involve interaction of HMW and LMW species with the char functional groups. For instance, phenyl end-chains get embedded in the char structure according to the following reaction:



As regards kinetic parameters for r6.11, the values of the activation energies are adopted from studies on Diels-Alder reactions³⁵. Instead, pre-exponential factors differ significantly since the reaction presented here describes the molecular addition to an aromatic network within the char, where CHAR is represented by a single carbon atom. This approach leads to high carbon concentrations, but it also neglects that only the surface layer of the aromatic network is actually accessible. The specific surface area of char particles typically falls within the range of $50\text{-}500 \text{ m}^2 \text{ g}^{-1}$ ^{166,167}. To account for this limitation, an adjusted pre-exponential factor of $10^7 \text{ cm}^3 \text{ mol}^{-1} \text{ s}^{-1}$ is employed. The frequency factor of r6.11 is 2 times higher than the elementary step to account for the higher available surface for the charification reaction. The same reaction can also occur on vinyl ends as:



The frequency factor is assumed 5 times higher because of the higher mobility of the terminal vinyl bond.

6.1.2.2 Radical Degradation Mechanism

In analogy with the other polymers, a radical degradation mechanism is incorporated in the PET pyrolysis model. These pathways are dominant at higher temperatures, but also affect product distributions at lower T. Table 6.2 reports all proposed radical reaction classes and their elementary rate parameters. Compared to the other polymers, β -scission reactions have lower importance and radical additions are included. These pathways, in analogy to polyvinylchloride³⁵, lignin¹⁰², and soot¹⁴⁷, result in formation of considerable amounts of char (10-20 wt.%). The onset temperatures are mainly affected by β -scissions, which are the rate determining step, and random scission and recombination reactions, which control the radical pool. H-abstractions and additions control the product distribution together with β -scissions reactions.

The primary initiation pathway involves homolytic scission of the C-C bond within the glycol moiety. Figure 6.11 shows the chain fission forming two methyl ester end-chain radicals. Estimation of the BDE involved is not straightforward. Huang *et al.*⁸⁵ compute a BDE of 81 kcal mol^{-1} , which is 6 kcal mol^{-1} lower than typical values for normal alkanes and gas-phase ethyl esters^{100,276,410,414,415}. Initiation on the gas-phase glycol is assumed to have a 2 kcal mol^{-1} lower energy barrier compared to n-alkanes

Table 6.2: Modified-Arrhenius parameters for radical elementary reactions classes (units cm, mol, s, cal).

Reaction	A	n _A	E _{act}
Random scission OCH ₂ -CH ₂ O (r6.13)	8.00E+14	0	74000
H-abstraction R _{OC} H+HOCH ₂	3.00E+11	0	13500
β-scission COO-CH ₂ (r6.15)	1.00E+13	0	32000
β-scission CO-OCH ₂ (r6.16)	5.00E+13	0	36000
Carboxylic radical decarboxylation	5.00E+13	0	16000
Glycol 1-5 isomerisation (r6.18)	5.00E+10	0	26000
Glycol carbonyl addition (r6.19)	5.00E+09	0	11000
Glycol aromatic addition (r6.20, r6.21)	2.00E+10	0	18000
Phenyl carbonyl addition (r6.22)	5.00E+09	0	2000
Phenyl aromatic addition (r6.23)	1.00E+10	0	6000
Radical recombination (r6.24)	1.00E+08	1	11000

due to the electron withdrawing effect of the neighbouring oxygen atoms⁴¹⁰. The difference in gas-phase E_{act} between initiation and syn elimination is 31 kcal mol⁻¹, which is similar to the selectivity proposed by Huang *et al.*⁸⁵. As with the other polymers, an additional solvation correction⁵⁷ is applied to account for the transition from gas-phase reactions to the liquid phase. This results in a variation of the liquid-phase constant (k_L) with respect to the gas-phase one (k_G):

$$k_L = k_G \times 10^{-2} \exp\left(-\frac{5000}{R_g T}\right) \quad (6.1)$$

where R_g is in cal mol⁻¹ K⁻¹, and the values of viscosity energies (E_η) are adopted from Van Krevelen²¹. Overall, compared to initiation on PE (Table 3.2), a 4 kcal mol⁻¹ lower activation energy is employed. Also initiations employing ECs as SPU are introduced with the appropriate corrections.

Vinyl esters significantly contribute to the radical pool in PET degradation. As highlighted by Morsch *et al.*⁴¹¹ and in-line with BDE computed from the ATcT and NIST databases^{100,276}, the CO-O bond in vinyl esters (Figure 6.12) is 24 kcal mol⁻¹ weaker than that in ethyl esters. This difference arises from the formation of the resonantly stabilized enethol radical (CH₂CH₂O), while the aromatic ring has negligible increase in its resonance stabilization due to the non-planarity of the unpaired electron of benzoyl. The BDE for this scission is similar to allylic scissions, and the correction reported in Table 3.3 is adopted. The proposed values are quite in good agreement with the difference in energy barriers estimated by Huang *et al.*⁸⁵. Initiation reactions on the CO-O bond are introduced assuming that the benzoyl radical readily decarbonylates

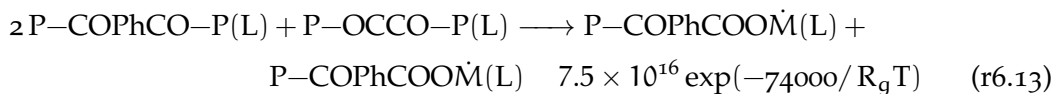
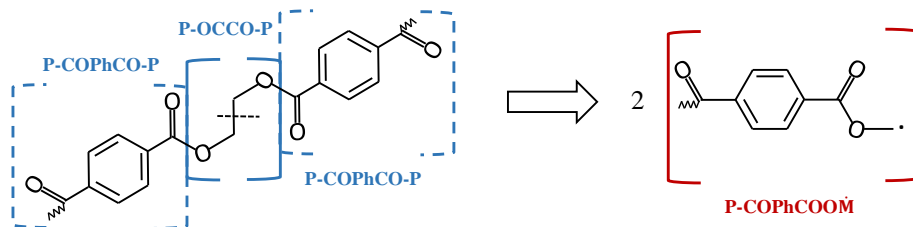


Figure 6.11: Schematic representation of the random scission on the OC-CO bond of the glycol mid-chain moiety to form two end-chain methyl ester radicals.

and that the acetaldehyde radical stabilizes before evaporating. Vinyl ester moieties are the primary products of the molecular degradation mechanism, resulting in the radical mechanism being enhanced by the molecular one.

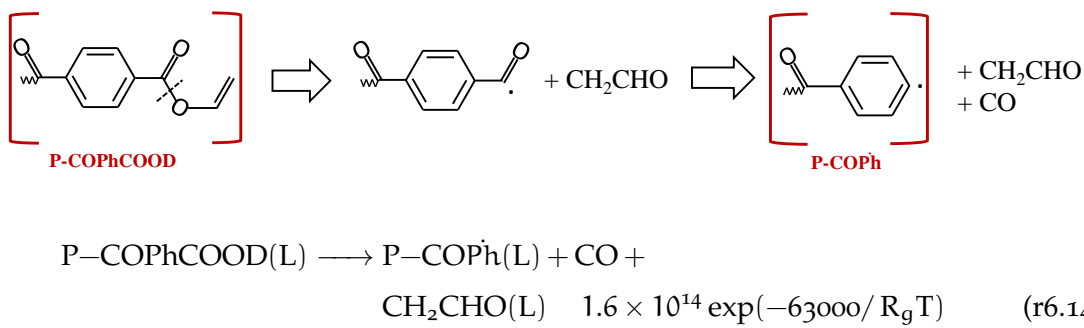


Figure 6.12: Schematic representation of the random scission on the CO-OC bond of the vinyl ester end-chain moiety to form acetaldehyde, CO, and a phenyl end-chain.

The radicals generated by initiation participate in various propagation reactions based on their specific type. The model considers primary, secondary, and tertiary alkyl-like radicals, benzoyloxy radicals, and phenyl radicals. These radicals undergo H-abstraction reactions, with selectivities similar to those proposed by Ranzi *et al.*²⁴⁵, but adjusted for the differing BDEs present in the PET system. H-abstractions to form vinyl radicals are not included⁵⁷, while those on phenyl hydrogens are considered due to their large amounts and the importance of phenyl radical addition pathways. Indeed, phenyl radicals stabilize rapidly, but at $T < 500^\circ\text{C}$ aromatic and carbonyl additions have rates similar to the H-abstraction reactions.

The most abundant radical within the system is the mid-chain glycol radical ($P-OCCO-P$). This radical decomposes along two main routes as schematically shown in Figure 6.13 and 6.14. The first pathway involves breaking the COO-C bond leading

to formation of a vinyl ester and a benzoyloxy radical (Figure 6.13). Similar to the molecular degradation mechanism, all possible combinations of end-chains and mid-chains are considered as SPUs. The reaction energy is 4 kcal mol⁻¹ higher than the corresponding reaction in PE (Table 3.2). This is due to the stabilizing effect of the ester group in the reactant, which increases the BDE by 2 kcal mol⁻¹ as computed by small gas-phase analogues²⁷⁶. Furthermore, the COO-C bond within the ester group of the product is 2 kcal mol⁻¹ stronger than that in typical alkyl radicals²⁷⁶. Consequently, β -scission reactions in PET require higher temperatures compared to PE and an activation energy of 32 kcal mol⁻¹ is employed.

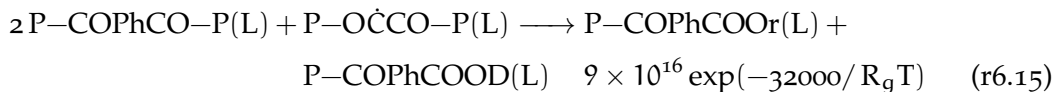
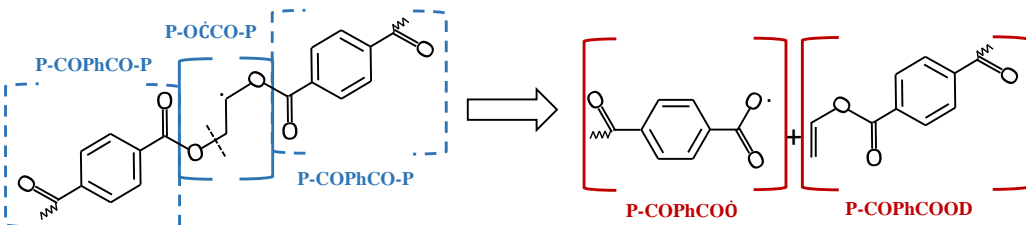


Figure 6.13: Schematic representation of the β -scission of the glycol COO-C bond to form a vinyl ester and a benzoyloxy radical.

The second class of β -scission reactions involves breaking the CO-OC bond to form a benzoyl radical and an aldehyde (Figure 6.14). The benzoyl radical is again assumed to immediately release CO. The β -ester-aldehyde product is represented through its main degradation products, i.e., CO released after decarbonylation and a methyl ester. The selectivity between the two types of β scission reactions affects the high temperature CO-to-CO₂ ratio. A ratio similar to the one proposed for unsaturated ethyl esters by Bennadji *et al.*⁴¹⁵ is employed, resulting in the second pathway being more relevant at high temperatures.

Figure 6.15 shows additional β -scission reactions considered in the present mechanism. The first one is decarboxylation of benzoyloxy radicals, which is among the main responsible for CO₂ release. The considered Arrhenius parameters are similar to other gas-phase acids^{84,420} and align closely with the values proposed by Mielczarek *et al.*¹⁰³ and experimental studies by Barson and Bevington⁴²⁷. The high instability of the radical on the oxygen atom offsets the double bond resonance resulting in activation energies of 16 kcal mol⁻¹.

The other β -scission reactions involve mainly alkyl-like radicals such as methyl and ethyl esters. The former decomposes by breaking the CO-O bond releasing CH₂O and CO, while the latter has two different isomers which decompose according to two different pathways. In ethyl esters, the methyl radicals break the COO-C bond producing

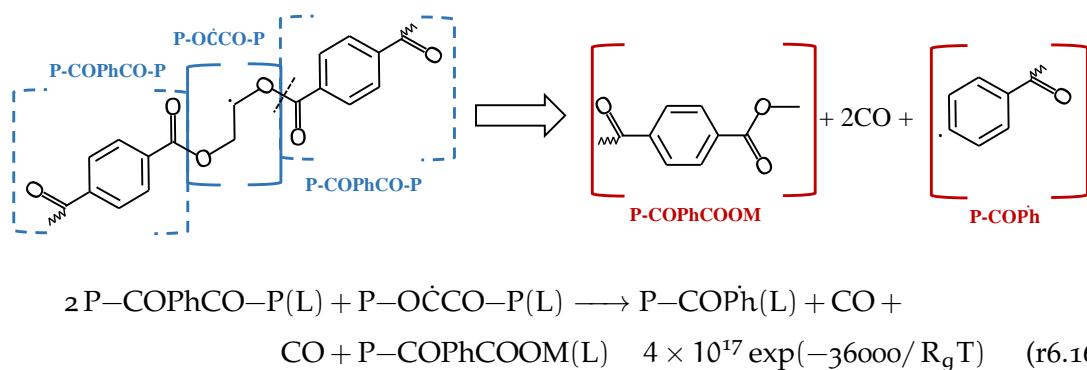


Figure 6.14: Schematic representation of the β -scission of the glycol CO-OC bond a methyl ester, a phenyl radical and 2 CO.

C_2H_4 and CO_2 , while secondary-like ones form CH_3CHO and CO by scission of the CO-O bond. The rate coefficients of these reactions are computed from the elementary classes related to breaking the COO-C or CO-OC bonds. The elementary steps are modified to account for the different stabilities of the starting radical. For instance, decomposition of P-OCM and P-COPhCOOM employ a decrease of 1 kcal mol $^{-1}$ in E_{act} due to the lower stability of primary radicals^{55,74}.

The radical decomposition of glycol end-chains is also considered. The only radicals considered are α -position to the OH group due to their lower BDE. This species decomposes to CH_3CHO and a benzoic radical. Compared to β -scission of the mid-chain glycol radical, a 1 kcal mol $^{-1}$ higher activation energy is considered because of the higher stability of $\text{P-OC}\cdot\text{COH}$.

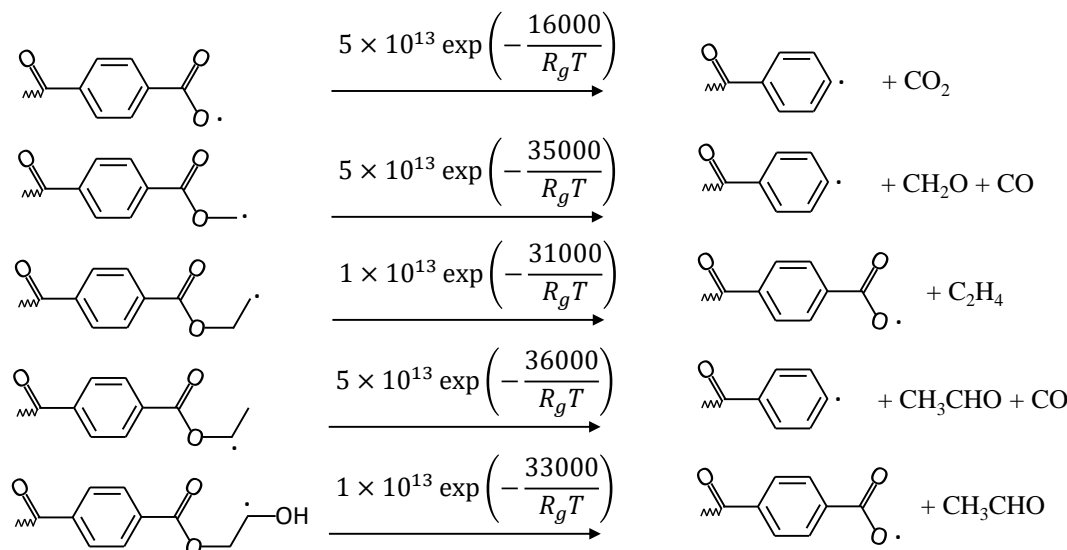


Figure 6.15: Schematic representation of all types of β -scission reactions considered in the present work.

The proposed β -scission parameters lead to an accumulation of glycol radicals within the system. A key pathway herein proposed is isomerisation of the radical through the ester moiety as shown in Figure 6.16. This reaction involves a 5-membered ring and results in formation of a primary ethyldene diester radical ($P\text{-OTMO}$). The rate parameters for this reaction are similar to those of 1-4 backbiting (BB 1-4) in PE (Table 3.2). These coefficients are computed from the reverse reaction, i.e., isomerisation from the primary radical back to the secondary glycol one. With respect to BB 1-4, the reverse reaction has similar energy barriers accounting both for the higher stability of the formed radical but also a more rigid C=O bond. A higher frequency factor is also considered as the double bond keeps the reactants in place requiring one less hindered rotor. The forward reaction is computed from equilibrium. A 4 kcal mol⁻¹ higher E_{act} is introduced considering the BDE differences for primary and secondary hydrogens adjacent to the ester group as reported by El-Nahas *et al.*⁴¹⁰. Additionally, the difference in entropy between isobutyl and 2-butyl is considered, resulting in the reverse step having a 2 times higher frequency factor compared to the forward one.

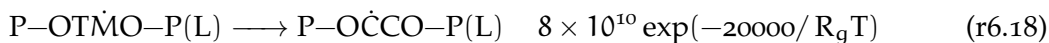
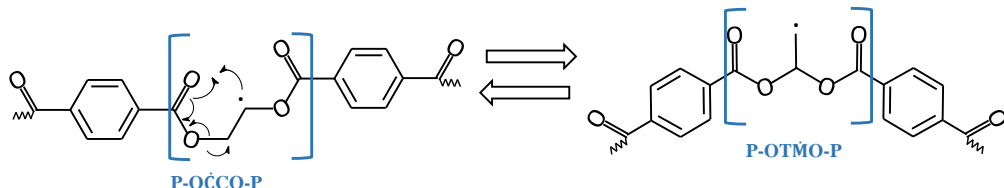


Figure 6.16: Schematic representation of isomerisation of the glycol secondary radical to the primary ethyldene position. The reverse step is represented through a separate reaction.

The ethyldene primary radical can decompose by β -scission of the COO-C bond or stabilize to $P\text{-OTMO-P}$. This stable species can undergo H-abstractions to form the primary radical or the tertiary-like $P\text{-O}\dot{\text{TMO}}$. The latter is the more stable configuration, but it is hindered by the bulky substituents and its formation involves both a lower activation energy and frequency factor compared to the primary one. Furthermore, β -scissions of this radical require to break the CO-O bond and have low importance at reaction conditions. As discussed in Section 6.1.2.1, the main decomposition pathway of the ethyldene are concerted ones (Figure 6.7 and 6.8), which are major contributors to acetaldehyde formation.

A peculiar aspect of PET degradation reactivity compared to other polymers lies in the presence of benzene rings along the backbone. These functionalities slow polymer decomposition because of their high BDEs, but also facilitate the formation of an aro-

matic network. At PET degradation temperatures, glycol radicals decompose slowly, while phenyl radicals are unable to decompose at all, and both can interact with the surrounding electrons by H-abstraction or addition reactions. These reaction classes have been studied for gas-phase species^{104,105} and are among the main responsible for soot growth¹⁴⁷. With respect to PET degradation, the high concentration of both radicals and potential addition sites within a polymeric melt makes these pathways highly relevant. Several reaction pathways are considered to account for the various possible addition positions, leading to the formation of stable polycyclic aromatic structures that gradually evolve into char. Because of the lack of quantitative data, the complex unsaturated and branched products of these reactions are lumped in the CHAR species and its functional groups analogously to the anhydride in Figure 6.8. Only addition of phenyl and glycol radicals to aromatic rings and carbonyl of vinyl esters are considered in the present work. These reactions heavily affect char yield and composition.

Figure 6.17 and 6.18 schematically represent additions of mid-chain glycol radicals to vinyl esters and aromatic rings respectively. The former are seldom considered in gas-phase mechanisms due to the dominance of faster, unimolecular degradation pathways at high temperatures. Existing studies on small radicals suggest that addition typically occurs on the carbon atom side, leading to the formation of short-lived alkoxy radicals¹⁰⁴. In the context of PET, these addition reactions are sterically hindered by the aromatic rings compared to ipso-additions. However, these reactions are significantly favoured by formation of stable products¹⁰⁴ such as the ethenol radical. For this reason, only additions to the vinyl ester carbonyls are considered due to the significantly lower BDE of the CO-O bond.

Figure 6.17 schematically represents carbonyl addition of glycol radicals to vinyl esters. This reaction forms an acetaldehyde radical and an acetophenone-like structure. The latter is represented by incorporating a half-terephthalic moiety alongside a mid-chain alkyl group. The remaining aromatic part is represented through CHAR, ethylene moieties, and gas-phase CO. The latter is not represented as G-CO due to the weaker bond compared to similar structures in biomasses. The kinetic parameters are obtained from analogies to gas-phase studies¹⁰⁴. The frequency factor is the one of the entrance channel, while the activation energy is related to the decomposition of the alkoxy radical¹⁰⁵. As described by Curran¹⁰⁴, the addition of H to styrene is considered as equivalent to addition of H to benzaldehyde (i.e., the analogous compounds with a carbonyl group instead of a vinyl bond). The frequency factor is modified through the ratio of addition of H with respect to isopropyl on alkyl ketones¹⁰⁴. Because of the higher stability of the products, the model introduces a 2 kcal mol⁻¹ lower activation energy compared to formation of CH₃ from tert-butoxy radicals¹⁰⁴. Similar reactions are considered also for all other alkyl-like radicals on all vinyl ester moieties, dimers included. Addition to other carbonyl groups are not considered as they involve a BDE 10 kcal mol⁻¹ higher than the one from acetone.

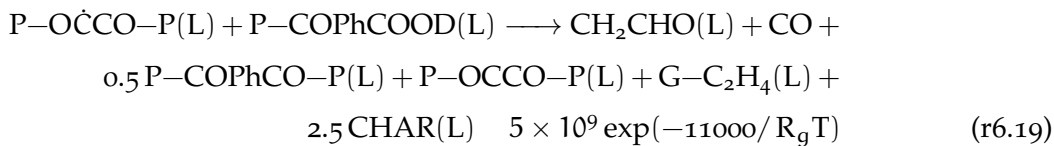
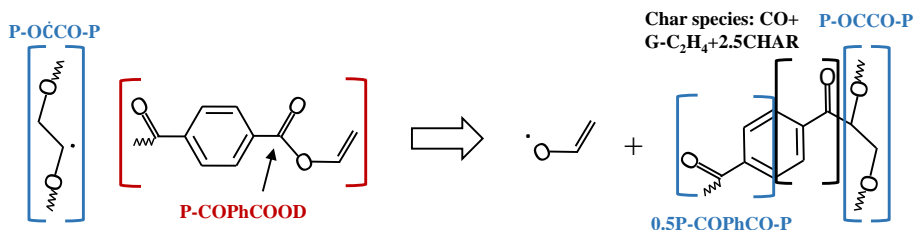


Figure 6.17: Schematic representation of glycol radical additions on carbonyl positions of the vinyl ester end-chain.

Because of the large amounts of mid-chain aromatic rings, aromatic additions of glycol radicals are also introduced as shown in Figure 6.18. These reactions form alkyl aromatic moieties and a formyloxy radical ($\cdot\text{COOCH}_2^-$) which is assumed to instantaneously decarboxylate forming an ethyl ester primary radicals. The glycol MC is not introduced as SPU since it would balance out as a product. On the other hand, the alkyl aromatic is represented by the ethylene moiety pseudo-species ($G-C_2H_4$) and CHAR. The Arrhenius parameters of these reactions are obtained from the analogy to gas-phase additions of alkyl radicals to aromatic rings^{100,105}. A 4 times higher frequency factor compared to carbonyl additions is considered mostly to account for the lower steric hindrance.

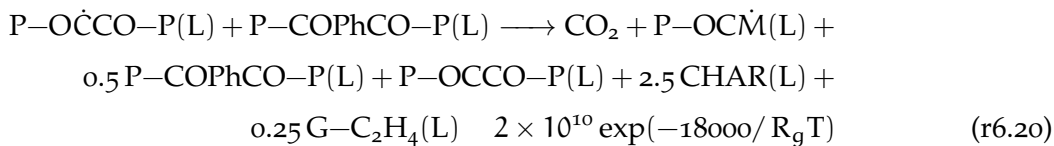
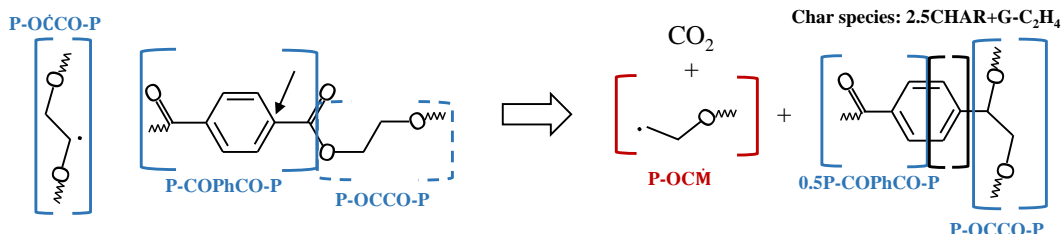
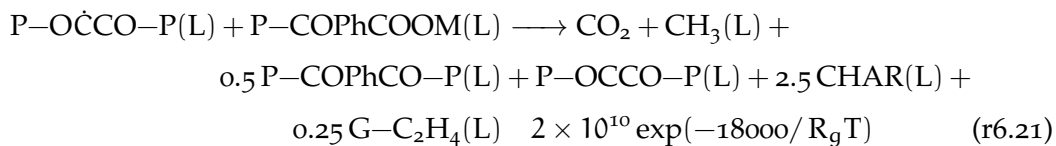


Figure 6.18: Schematic representation of glycol radical aromatic additions on the mid-chain aromatic rings.

Additions to the aromatic rings on end-chains side-groups are also considered. For instance, aromatic addition on methyl ester end-chains is represented as:



where the formyloxy radical is assumed to decarboxylate forming a methyl radical and CO_2 . The same representation of char from the other aromatic additions is employed.

The addition pathway for phenyl radicals mirrors the behaviour of glycol radicals as shown in Figure 6.19 and 6.20. Considering additions to the carbonyl group of vinyl esters (Figure 6.19), the LMW product remains the same as glycol additions (CH_2CHO), while the aromatic structure differs. The latter is characterized by the presence of two moieties derived from the original terephthalic unit, and appropriate functional groups are employed to represent the benzophenone-like structure. Three kinds of oxygen and hydrogen pseudo-species describe the variation of carbon content in char with temperature. G-CO and G-COH₂, respectively, stand for oxygen release at intermediate and high temperatures. The latter also describes the hydrogen release at a mid-temperature as opposed to the high-temperature release by G-H₂. The Arrhenius parameters of this reaction are obtained by analogy. The same frequency factor that is used for glycol carbonyl addition is employed here. On the other hand, the proposed energy barrier is 2 kcal mol⁻¹, i.e., 3 kcal mol⁻¹ lower than the rate of H-abstraction by phenyl radicals from glycol mid-chains employed in the current model. This difference in energy barriers between H-abstraction and carbonyl addition is similar to that of glycol mid-chain radicals herein used.

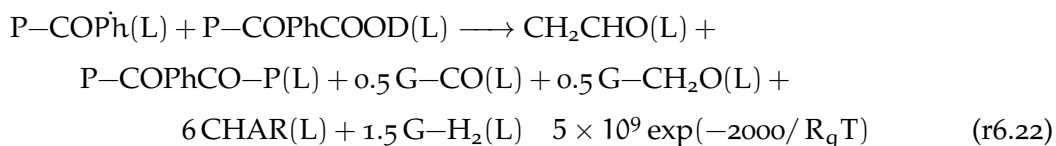
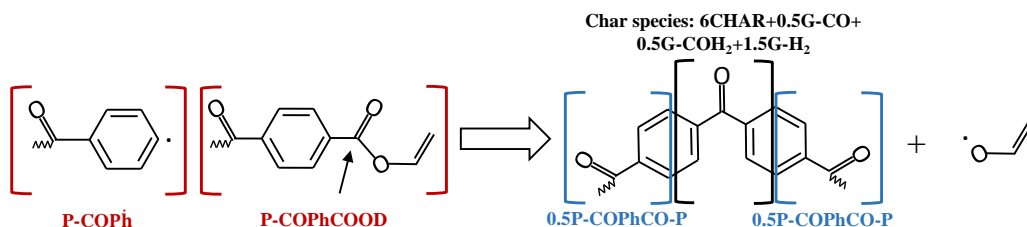


Figure 6.19: Schematic representation of phenyl additions to carbonyl groups considered in the present work.

Figure 6.20 represents the addition of the vinyl benzoate phenyl radical (VB) to a mid-chain terephthalic moiety. The biphenyl structure involves terephthalic moieties on both sides, which are represented by a vinyl ester EC to maintain the radical's functionality. The remaining structure is described by the CHAR and $\text{G}-\text{H}_2$ pseudo-species. Release of gas-phase hydrogen is also included to account for the subsequent dehydrogenation of the structure. The reaction is bimolecular but employs a glycol mid-chain as SPU, where the formyloxyl-like radical (COO) is considered to decarboxylate releasing CO_2 yielding an ethyl ester radical. With respect to the Arrhenius parameters, the frequency factor is similar to aromatic additions of glycol radicals. On the other hand, the energy barrier is 2 kcal mol⁻¹ lower than C_6H_5 ipso-substitution of H in soot growth^{428–430} because of the 6 kcal mol⁻¹ lower BDE of Ph-COO- groups.

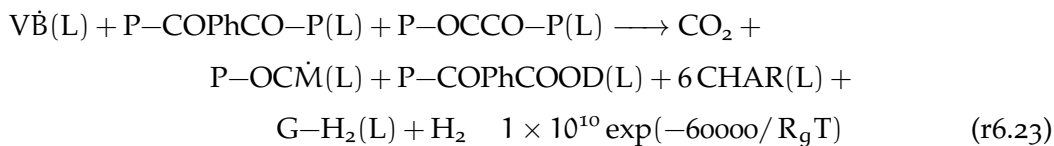
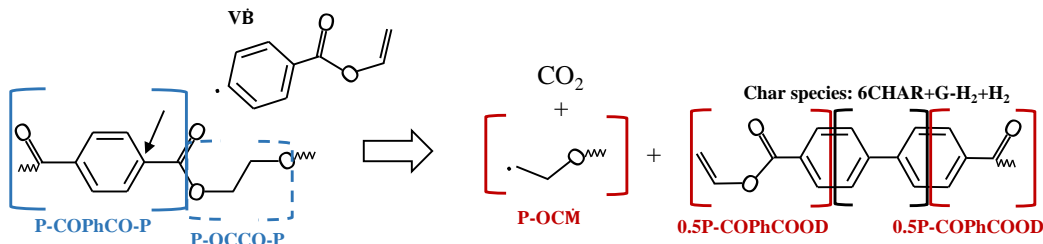
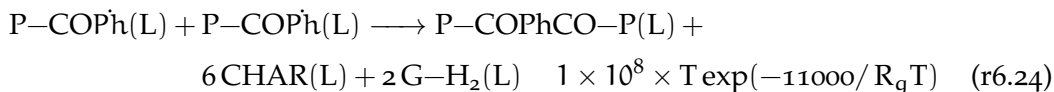


Figure 6.20: Schematic representation of LMW phenyl radicals additions to mid-chain aromatic rings.

Only termination by radical-radical recombination is included in the present mechanism. All combinations of MCs, ECs, and LMW radicals are considered. These reactions lead to an increase in average chain-length and, to represent this behaviour, when the recombination reaction leads to the formation of HMW species, these are represented as a mixture of MC and EC units. These reactions lead to formation of highly unsaturated or ramified structures, which can lead to char formation. In these cases, to simplify the mechanism, these functionalities are represented as mid-chain and char species. For instance, recombination of two phenyl end-chain radicals is represented as:



where the resulting biphenyl-like structure is represented through char pseudo-species similarly to reaction 6.23. Recombination reactions are assumed diffusion-controlled^{55,57,247}, and their kinetic parameters are evaluated according to free volume theory^{43,57} employ-

ing values on viscosity-temperature relations²¹ and symmetry considerations in line with polystyrene⁶⁶.

As previously mentioned, the reactions introduced for HMW pseudo-species are also defined for LMW molecules. For instance, terephthalic acid radicals ($\text{T}\dot{\text{A}}$) can de-carboxylate to the phenyl radical of benzoic acid ($\text{B}\dot{\text{A}}$), which then stabilize. Small radicals such as C_2H_3 and CH_2CHO are accounted for, but are assumed to not undergo further condensed-phase degradation once stabilized, because of their fast evaporation. Conversely, secondary reactions of the stable molecules are considered for molecules with higher boiling points due to their lower evaporation rates. For instance, the present mechanism includes H-abstractions on monovinyl terephthalate to form the carboxyl radicals ($\text{MV}\dot{\text{T}}$) and their decomposition to vinyl benzoate. Similarly, radical additions to vinyl benzoate forming light products and end-chains and char species are included as well.

6.2 MODEL VALIDATION

The kinetic model leverages data from the scientific literature, complemented by an in-house experimental campaign to address potential limitations. The observed variability in literature data is attributed to differences in plastic composition and experimental setups¹⁵. For example, Dhahak *et al.*^{87,99} report a $\sim 10^\circ\text{C}$ discrepancy in degradation temperature between their 2019 and 2020 studies, highlighting the need for careful data analysis. Model validation encompasses characteristic degradation times (i.e., mass-loss profiles) and volatile yields. Due to the high uncertainty in evaluation of aromatic esters' thermodynamics, no investigation is performed on the energy requirements of the process. In cases where no information on the polymer is reported, an initial number average molecular weight of 30 kg mol^{-1} is assumed. The initial polymer composition is determined using the Schultz distribution and considering equimolar amounts of glycol and terephthalate units. The same physical and numerical model discussed for PE is employed (see Section 3.2.1) and performances are evaluated through the Curve Matching (CM) score³¹² (Section 3.2.2). To the best of the author's knowledge, no other kinetic model is available in the scientific literature to compare with.

6.2.1 Methods and Materials

A virgin commercial PET sample is employed for all experimental measurements. The elemental CHNS/O composition of the polymer was analysed with a Thermo Scientific FLASH 2000 analyzer. Five replicates were performed burning 2-3 mg of sample in pure oxygen at 950°C . An elemental composition of $63.74 \pm 1.09\%$ wt C and $4.23 \pm 0.03\%$ wt H is measured, where no nitrogen or sulphur is detected.

The pyrolysis experiments are conducted by using a single-shot tandem micro-pyrolysis facility (Rx-3050tr, Frontier Labs, Japan) coupled with two-dimensional gas chromatography (GCxGC) and a separate customized multicolumn GC (Trace 1300) for the analysis of light gases, illustrated in Figure 6.21. The pressure of the GC inlet and inside the reactor was ~2.7 bara, and the column flow was 2.1 mL/min. The pyrolysis reactor is maintained at 400 °C, 500 °C and 600 °C and loaded with grounded PET into a deactivated stainless steel sample cup (Eco-cup LF). Helium is used as carrier gas at 50 mL/min to purge volatiles into the GCxGC section. Based on the time-resolved data for the release of volatiles, the cryogenic trap (MJT-1035E) was operated sufficiently long (30 minutes for pyrolysis at 400 °C, 5 minutes at 500 °C and 600 °C) to capture the volatiles released during the pyrolysis.

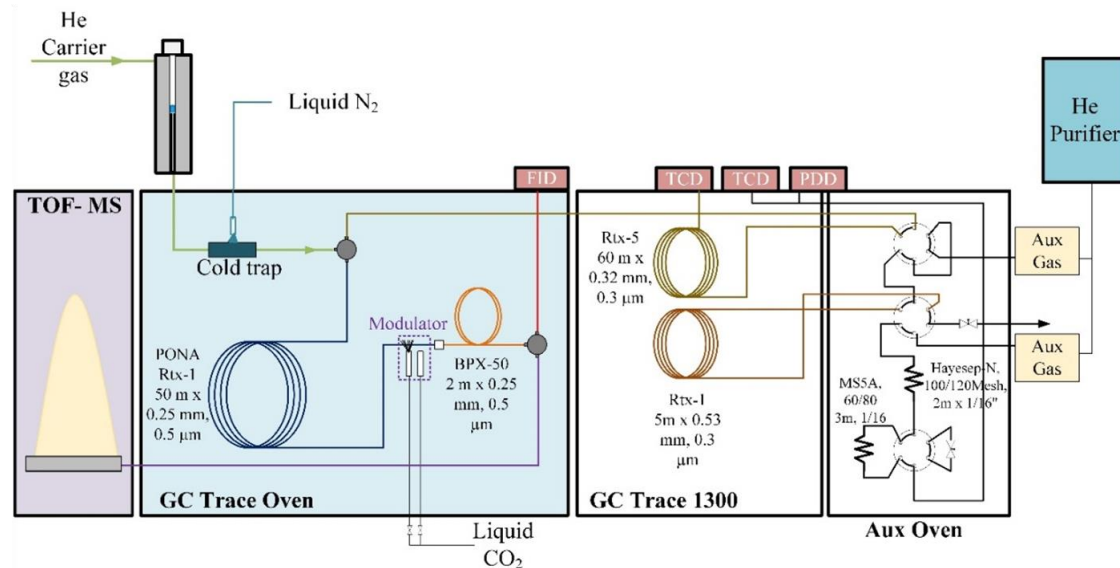


Figure 6.21: Schematic diagram of the micropyrolyzer reactor with a comprehensive analytical section comprising ToF-MS, FID and PDD detectors

Prior to experiments, the GCxGC is calibrated with iso-butane and benzoic acid. Both calibration demonstrated similar results for the product quantification, thus the isobutane calibration is used throughout the campaign. Based on the FID detector response for isobutane and benzoic acid, the yields of all other heteroatom-free products were calculated using the molar response factor approach (MRF). The molar response factor of each compound was calculated based on its combustion enthalpy and molecular structure⁴³. The response of a compound *c* is given by:

$$\text{MRF}_c = -0.071 + 0.000857\Delta H_{\text{comb}} + 0.127n_{\text{Benz}} \quad (6.2)$$

where n_{Benz} is the number of benzene rings present in the molecule. ΔH_{comb} is the heat of combustion, which is approximated as:

$$\Delta H_{\text{comb}} = 11.06 + 103.57N_C + 21.85N_H - 48.18N_O + 7.46N_N \quad (6.3)$$

where N_i is the number of atoms i in each molecule. The moles and yield of compound c (respectively n_c and y_c) are then estimated with respect to the internal standard:

$$n_c = \frac{V_c MRF_{is} n_{is}}{V_{is} MRF_c} \quad (6.4)$$

$$y_c = \frac{MW_c n_c}{m_0} \quad (6.5)$$

where MW is the molecular weight, V is the peak volume, and m_0 is the total sample weight. The subscript c refers to the compound, while is to the internal standard. TOF-MS data is acquired by TOF-DS software. For the GCxGC-FID data, Thermo Scientific's Chrom-Card data system was used. The raw GCxGC-FID data were exported as a .cdf file and subsequently processed by GC Image software (Zoex Corporation, Houston, USA). The obtained peaks were identified using TOF-MS spectra compared with the NIST database's available spectra. Mass closure obtained from the setup increases with temperature, ranging from 30% at 400°C to 70% at 600°C. However, considering ~10-20 wt.% of char formation^{99,101}, and similar results in literature^{87,101}, the results are deemed acceptable.

Thermogravimetric analysis (TGA) is performed for both investigating the PET degradation profiles and char quantification, using the NETZSCH STA 449 F3 Jupiter simultaneous thermal analyzer. Grounded PET samples weighing between 30 to 40 mg are loaded into Al₂O₃ Netzsch Crucibles (0.3ml). The analysis is performed under a continuous flow of nitrogen (N₂) at a rate of 100 mL/min. The initial temperature was raised from 20°C to specific target temperatures (400°C, 500°C, or 600°C) at a heating rate of 10°C/min, followed by a 30-minute isothermal period at the set temperature. Due to limitations, shorter holding times under isothermal conditions were not viable. The recorded data represents the relationship between mass loss and time/temperature. The char obtained from TGA analysis is then analysed in terms of elemental CHNS/O composition with a Thermo Scientific FLASH 2000 analyzer. Three replicates per temperatures are performed burning ~2 mg of char in pure oxygen at 950°C.

6.2.2 Characteristic degradation times: mass-loss profiles

The PET kinetic model is validated with 45 mass-loss profiles^{87,99,139,400,432-437}, as shown in Figure 6.22 and 6.23. According to the model, the degradation starts from mid-chain syn elimination leading to vinyl and carboxylic end groups (r6.1). At low temperatures and MW_{av}, alcoholysis from glycol end-chains slightly affects the initial degradation. Specifically, these result in formation of cyclic dimers (CYEDGE) or regeneration of the polymer mid-chain moiety releasing CH₃CHO or H₂O. As degradation proceeds, syn elimination pathways occurring near the end-chains lead to the formation of monomers and dimers with carboxylic and vinyl functionalities (r6.2 and r6.3). The specific end-chain type dictates the products terminations. For instance, reactions near vinyl ends yield divinyl and monovinyl terephthalate, along with o.75EGDV and

0.25EGDA to represent one out of four carboxylic ends. Consequently, the molecular mechanism alone results in products with equimolar amounts of carboxylic and vinyl ends, i.e., molar ratios of TA-MVT-DVT ~1-2-1. Similar results are observed for the paraffin-olefin-diolefin ratio of PE and PP. Among the available molecular pathways for end-chain moieties, vinyl ester isomerisation is the most significant (r_{6.10}). This reaction explains the experimentally observed lower abundance of vinyl esters⁹¹ and results in formation of ketene (CH_2CO) and phenyl ends groups according to the lumping performed. Syn elimination near phenyl end-chains yields vinyl benzoate and benzoic acid, while also contributing to increased char formation. The presence of vinyl esters initiates the radical mechanism due to the considerably lower BDE (Section 6.1.2.2). The radical degradation is responsible for most of the light molecular products and compounds with phenyl end groups (e.g., benzoic acid). While β -scission of glycol radicals gain importance only at high temperatures, addition and isomerisation reactions contribute to degradation of carboxylic and vinyl ends. Specifically, fast decarboxylation of benzoyloxy radicals and carbonyl additions are responsible for the low observed quantities of TA and DVT, respectively. Additions are the primary drivers of char formation (r_{6.17}, r_{6.18}, r_{6.19}, r_{6.20}), where both the type of radical and addition location influence the degree of char oxygenation.

The model captures correctly the degradation profiles in the entire temperature range, although several specific deviations are observed. Figure 6.22 shows the comparison of mass-loss profiles in dynamic conditions. Most experimental data fall within a 5°C range, with some discrepancies reaching 50°C. For instance, at a HR=5°C/min (Figure 6.22a), the data from Brebu *et al.*⁴³³ exhibit a degradation temperature 40°C higher than other studies. Similarly, Czegeny *et al.*⁴³⁷ measure a reaction temperature 20°C lower than other experimental data at HR=10°C/min. Wide variations in char yields are also observed. Generally, higher temperatures lead to lower char amounts and a higher carbon content. Nevertheless, the variability due to polymer sample is more pronounced than that arising from operating conditions. For example, Czegeny *et al.*⁴³⁷ report a char yield of 11.5 wt.% at HR=10°C/min and 500°C, while other authors measure values of ~ 16 wt.%. Inorganic impurities are also expected to affect the char yield. On the one hand, the amounts of solid residue increase because of the low volatility of metals which are trapped in the carbonaceous matrix. On the other hand, the presence of metals with low volatility trapped within the carbonaceous matrix can increase solid residue amounts. Conversely, inorganics act as catalysts for the molecular degradation of esters, potentially reducing the significance of the radical pathway and leading to lower char yields. However, to the best of the author's knowledge, no dedicated studies on the impact of different inorganic impurities on PET char formation are reported in the literature. Char description remains a key source of uncertainty in the current model. As mentioned in Section 6.1.1, limited data availability necessitates the use of the same functional groups employed for bio-char. While this framework offers robustness, it is primarily geared towards phenolic and ether linkages in the char

matrix which decompose releasing mainly water and CO. PET degradation is expected to yield predominantly phenone and ester linkages, which are only partially accounted for in the proposed mechanism. Further work is required to refine the description of char and its subsequent graphitization. Nevertheless, given that PET is primarily sorted from PW, improvement to this secondary release is expected to have a minor impact on the overall predictions of volatiles.

Similar trends are observed also at higher heating rates (Figure 6.22b). The model exhibits good agreement with most experimental data, as highlighted by the high CM scores. However, a slight underestimation of degradation rate is observed in the later stages of the process. This discrepancy is attributed to the increasing molar fractions of char species, which act as diluents and reduce the overall system reactivity due to the lower concentration of reactive sites. This phenomenon affects mainly bimolecular and supported reactions, while for unimolecular ones a decrease in-line with the degradation behaviour is observed. Charification through Diels-Alder reaction becomes important during these later stages. The wide scattering in experimental data is observed also in these conditions. For instance, Brems *et al.*¹³⁹ and Das and Tiwari⁴³⁴ measure a difference of 20°C in degradation temperatures at HR=50°C/min. Furthermore, Brems *et al.*¹³⁹ show a constant degradation temperature across a heating rate range of 50-120°C/min, while the model predicts a monotonic increase consistently with other HR values. Char yield measurements also exhibit variability, with Brems *et al.*¹³⁹ reporting 9 wt.% residue at 550°C compared to 15 wt.% observed by Das and Tiwari⁴³⁴.

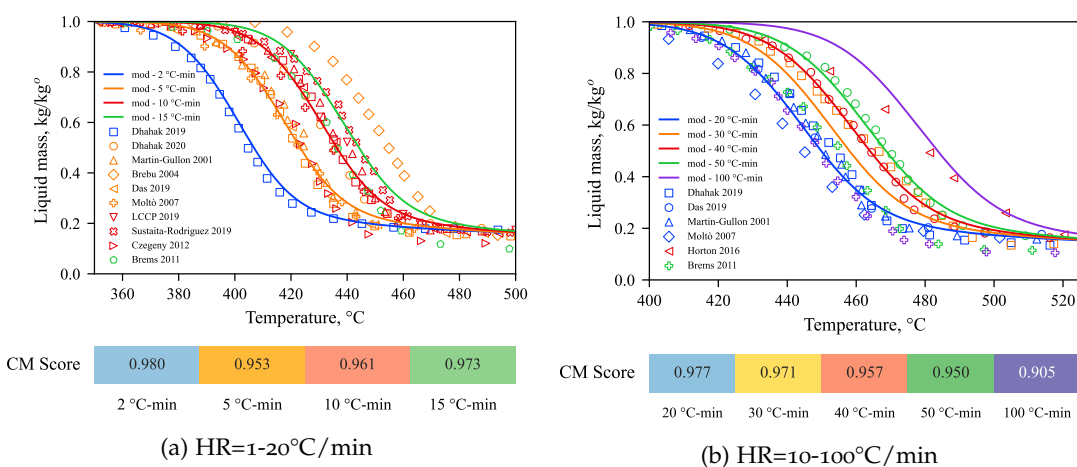


Figure 6.22: Mass-loss profiles of PET in dynamic conditions. Comparison among the present work (solid lines) and literature experimental data^{87,99,139,400,432-437} (marks).

Figure 6.23 shows the mass-profiles in isothermal and quasi-isothermal conditions. At low temperatures (Figure 6.23a), the model slightly underestimates the polymer reactivity as represented by the low CM score, although good agreement is maintained. At 400°C the model overestimates char formation predicting a yield of 19 wt.% at 150

min compared to the experimental 11 wt.%. Nevertheless, the predicted values are consistent with the data of the same authors in dynamic conditions. Since the dynamic degradation measured by Das and Tiwari⁴³⁴ (Figure 6.22) occurs at $T > 420^\circ\text{C}$, the model estimates slightly higher amounts of char at 400°C .

Considering $\text{HR}=5^\circ\text{C}/\text{min}$ with different isothermal temperatures (Figure 6.23b), the model predicts a lower reactivity in the investigated range. Furthermore, a decrease in char yield is observed contrary to experimental data. The non-monotonic decrease is attributed to experimental uncertainty. To aid in model development, new TG experimental data have been performed and are reported in Figure 6.23c. The campaign investigates an $\text{HR}=10^\circ\text{C}/\text{min}$ and different isothermal temperatures to assess char yields and composition. Compared to data reported by Dhahak *et al.*⁹⁹, the model exhibits slight overestimation of reactivity at low temperature and underestimation of yield at high T. As shown in Figure 6.22a, at $\text{HR}=10^\circ\text{C}/\text{min}$ polymer degradation occurs at $\sim 460^\circ\text{C}$. Since experimental data are performed with a heating rate of $10^\circ\text{C}/\text{min}$, the polymer decomposes well before reaching the isothermal plateau of 500 and 600°C . Notably, both model and experimental TG curves display identical behaviours except for the char yields. Nevertheless, the model underestimates char formation at 500°C , although the predicted elemental composition has good agreement with experimental data as discussed in the next Sections. Developing functional groups specific for PET char is expected to improve model predictions, but requires higher amounts of data.

Figure 6.24 presents a parity plot comparing model predictions and experimental results for onset and half-degradation temperatures, along with char yield. Similar observations can be drawn from these plots as from the detailed discussion in the preceding sections. The model exhibits good accuracy in predicting both onset and half-degradation temperatures under dynamic (Figure 6.24a) and isothermal/quasi-isothermal conditions (Figure 6.24b). However, the model's capability in reproducing char yield is limited. As previously mentioned, this discrepancy is likely attributable to inherent variability between different polymer samples, in addition to the influence of operating conditions.

Figure 6.25 presents the model's performances metrics in terms of CM score and the corresponding five indices (Section 3.2.2). The model has better performances compared to the other polymers. This outcome is possibly attributed to a lower scattering of experimental data in terms of temperatures/times. The L^2 indices approach unity, indicating a good match between the predicted and experimental mass-loss profiles. However, other parameters show lower values. Notably, the d_{pe}^1 index is relatively low due to the broader predicted mass-loss observed at the terminal stages of degradation. Additionally, the shift index remains low, reflecting the inherent scattering in experimental degradation temperatures, similar to what was observed with other polymers.

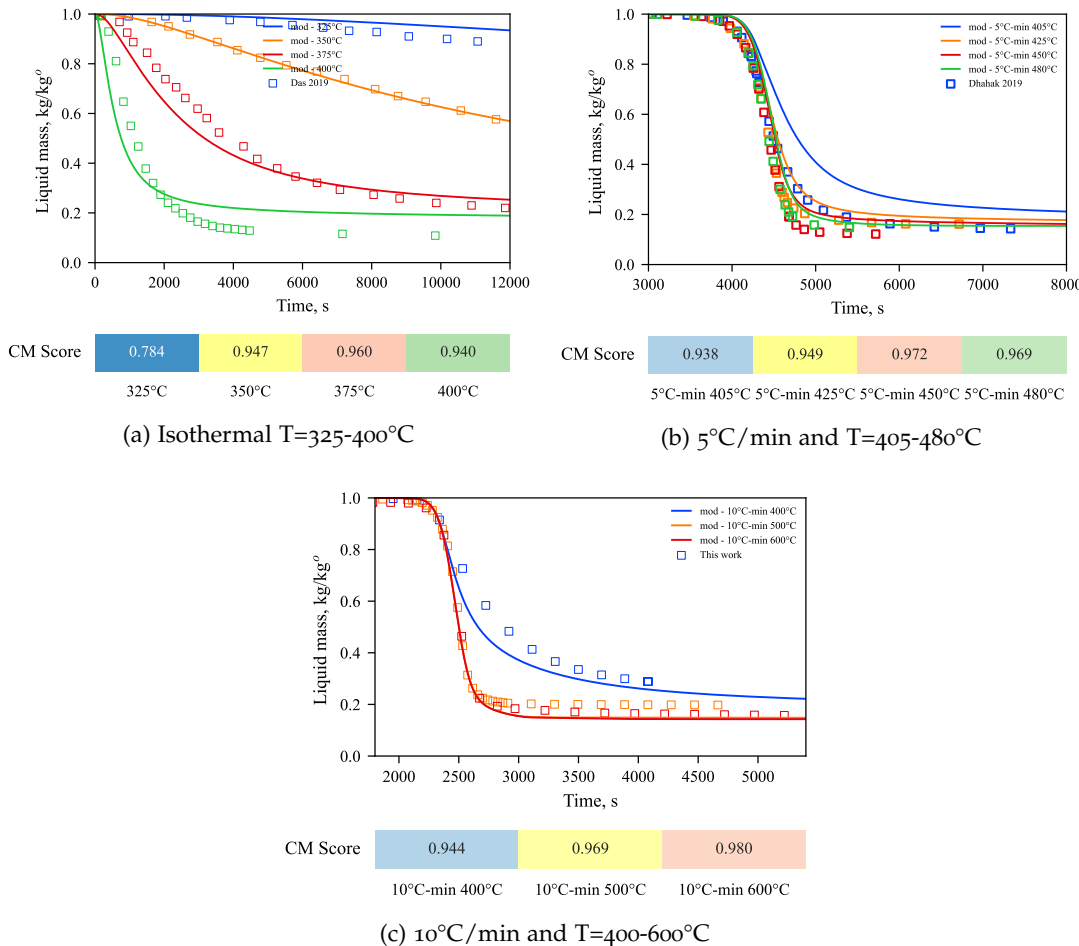


Figure 6.23: Mass-loss profiles of PET in isothermal conditions. Comparison among the present work (solid lines) and both literature^{99,434} and new experimental data (marks).

6.2.3 Products selectivity: volatile yields and char characterization

The degradation products of PET have been investigated in the literature since the 1950s^{91,392}. However, to the author's knowledge, quantitative data under kinetically controlled conditions remains scarce^{99,101}. As previously mentioned, characterizing products provides insights into the reaction mechanisms, but is not directly applicable to kinetic model evaluation. The main volatiles observed are benzoic acid, acet-aldehyde, CO, and CO₂. A key discrepancy exists between predicted and observed amounts of vinyl esters, requiring further investigation.

Figure 6.26 shows the volatiles released from PET pyrolysis at different operating conditions. The comparison involves model predictions and literature experimental results at low temperatures (Figure 6.26b), new experimental results at medium temperatures (Figure 6.26a), and literature results at high temperatures¹⁰¹ (Figure 6.26c). Experimentally, CO₂, CH₃CHO, and benzoic acid are the most abundant products in

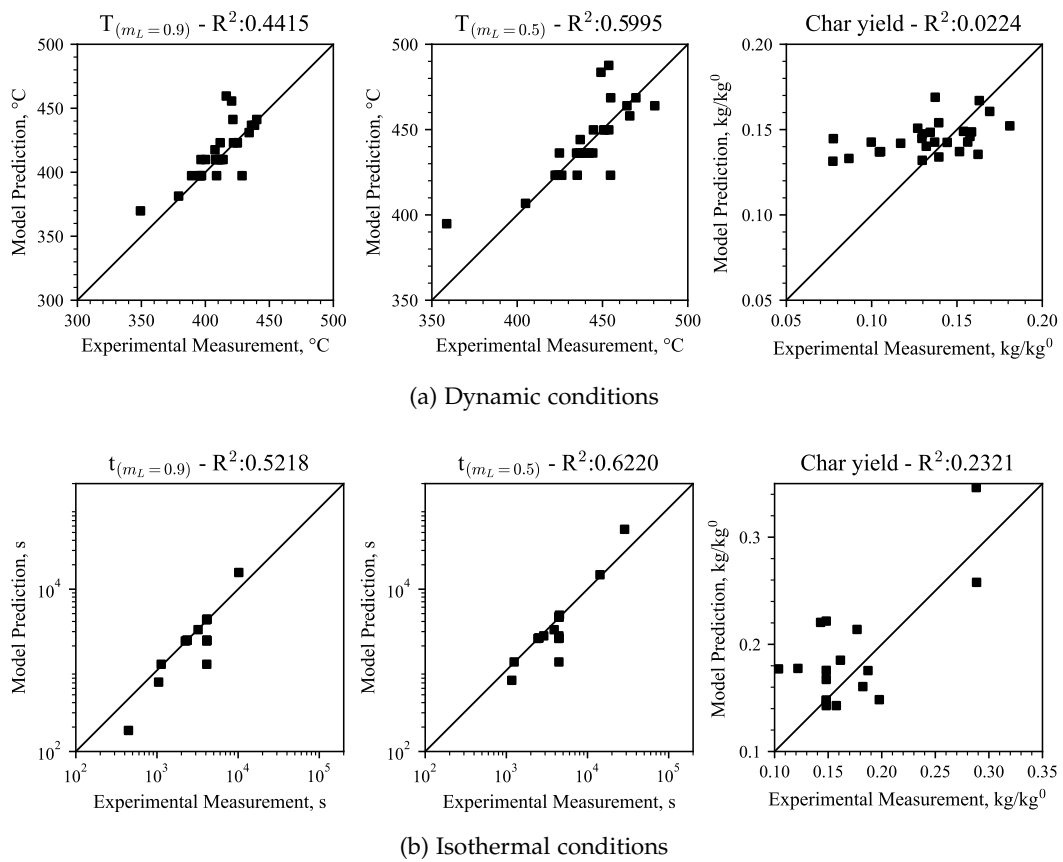


Figure 6.24: Parity plots of model prediction with literature^{87,99,139,400,432–437} and new experimental data for polymer degradation temperatures (top) and times (bottom) at sample mass (m_L) 0.9 and 0.5 and char yield.

the present study, with low amounts of benzene, vinyl benzoate, and ethylene measured. These observations align with values reported by Dhahak *et al.*⁹⁹ and Day *et al.*¹⁰¹. Nevertheless, no CO is detected at 400°C in the present study possibly because of elution through the cryo-trap at long reaction time (25 min), while terephthalic acid is identified only at low temperatures. The reduction in its yield at higher temperatures is consequent to formation of lower molecular weight compounds such as benzene and CO₂. Vinyl benzoate yields are significantly lower compared to Day *et al.*¹⁰¹ (~10 wt.%), while Dhahak *et al.*⁹⁹ do not detect it. Overall, the mass closure is poor at 400°C, although in line with Dhahak *et al.*⁹⁹. This can be attributed to incomplete polymer conversion, as a 29 wt.% solid residue is still present according to both the model and the TGAs experiments (Figure 6.23c). On the other hand, the low mass closure is also due to high boiling products not detected in the equipment employed²²⁸. Compounds such as monovinyl terephthalate (MVT), divinyl terephthalate (DVT), or dimers and trimers are not identified. While Day *et al.*¹⁰¹ measure significant formation of acetylene, it is believed to be ethylene as measured in the present work and by Dhahak *et al.*⁹⁹ and

mod	0.946	0.998	0.996	0.932	0.918	0.917
	CM	$d_{L_2}^0$	$d_{L_2}^1$	d_{Pe}^0	d_{Pe}^1	<i>shift</i>

Figure 6.25: Comparison of SciExpeM indices (Section 3.2.2) on all mass-loss profiles investigated.

misidentified due to the overlapping peaks. Only trace amounts of C₂H₂ were found in the present study and therefore not reported.

The model captures the overall trends in the yields of main compounds, but exhibits some discrepancies with experimental data. Specifically, the reaction families approach employed is not able to correctly represent specific behaviours as the yields of several compounds are intrinsically related (see the sensitivity analysis reported in Section 6.2.4). For instance, benzoic acid, vinyl benzoate, and CO₂ formation are mechanistically linked through decarboxylation reactions (Figure 6.15). Indeed, both result from decarboxylation of benzyloxy radicals (BA from TAr and VB from MVTr) and the same reaction class is also responsible for CO₂. BA and VB are also formed from syn elimination near phenyl end-chains (P-COPhH), which is responsible also for formation of EGDB. The latter is a lumped species which accounts for dimers with phenyl terminations. Since these three compounds are inherently related, the model predicts similar molar yields. Preferential dimer degradation pathways are responsible for the low yields of EGDB at high temperature, but the low vinyl benzoate yields are possibly related to the capability to polymerize similarly to diolefins in PE, PP, and PS. Similarly, CH₃CHO and char yields are intertwined. The model predicts acetaldehyde formation from reactions leading to aromatic precursors, e. g., carbonyl additions and ethylidene degradation (r6.19 and r6.8). Although not reported in the present comparison, the model predicts formation of ketene (i. e., CH₂CO) at increasing temperatures.

The model accurately predicts CO₂ yields at low and high temperatures but underestimates them at intermediate temperatures (500-600°C). In the present model, the main pathways are decarboxylation of benzoic radicals and ipso-additions to mid-chain terephthalic moieties (r6.20 and r6.23). Molecular pathways play a role at low temperatures and at the start of the degradation process. CO formation is reasonably captured at low and medium temperatures but deviates significantly at high temperatures (1000°C). This is likely due to the omission of secondary gas-phase reactions from the model. At present, the main responsible for CO formation are addition reactions and high-temperature β-scissions (r6.19 and r6.14). With respect to the acetaldehyde yield, the model underestimates its formation at low and medium temperatures but captures its variations. Improving the description of the char yield is expected to increase the accuracy of CH₃CHO predictions. Ethylene yield is underestimated by the

model, particularly at higher temperatures. The primary pathway involves degradation of end-chain P-OCM species (Figure 6.15), which is formed from ipso-additions on terephthalic moieties (r6.20 and r6.23). However, an increased contribution from this pathway would also lead to overestimation of CO₂ and char.

With respect to higher molecular weight compounds, more discrepancies are observed even among different experimental data sets. The model predicts comparable amounts of vinyl and carboxylic end groups, while significant vinyl ester formation is only observed by Day *et al.*¹⁰¹ at high T. The model underestimates them, but considering both MVT and DVT in these conditions can explain the high yields of vinyl esters from Day *et al.*¹⁰¹. As previously mentioned, both acids and vinyl esters form as consequence of mid-chain degradations, either from glycol radical beta-scissions (r6.13) or syn elimination pathways (r6.1). Overall, the model predicts lower amounts of carboxylic ends than vinyl esters, consistently with high temperature data of Day *et al.*¹⁰¹. However, it overestimates formation of MVT compared to Dhahak *et al.*⁹⁹ (1-4 wt.%), who detect neither DVT nor vinyl benzoate. Similarly, in the present experimental campaign only low amounts of vinyl benzoate are found (1-3 wt.%) and no MVT or DVT are identified. On the other hand, the model predicts amounts of vinyl benzoate and MVT of 5-15 and 15 wt.%, respectively. Although degradation of vinyl esters could decrease their yields (r6.8), higher amounts of benzene from these reactions are expected. However, the model already overestimates benzene formation because of these reactions. Further experimental and computational work is required to better assess the reactivity of vinyl esters.

Model predictions are assessed also in terms of char elemental composition (Figure 6.27). As previously mentioned, due to limited PET char data availability, the model employs a framework developed for biomass pyrolysis. The elemental analysis of solid residues obtained from the TGA experiments (Figure 6.23c) is included for comparison. Oxygen content is determined by difference with respect to carbon and hydrogen content. In general, increasing the temperature is expected to produce solid residues with high carbon content, while low temperature pyrolysis results in higher oxygen content. The model captures these trends but with slight deviations compared to typical biochars. Specifically, the char has amounts of hydrogen higher than the starting polymer, while most of the oxygen is lost upon pyrolysis. Considerable deviations are observed with respect to the data of Li *et al.*(2022)⁴⁰⁵ and Williams and Williams⁴⁰⁶. The model's higher predicted carbon yields can be attributed to the severe operating conditions. While low and medium heating rates are employed for the pyrolysis, the sample is heated to 600 and 700°C respectively. For this reason, the model predicts high carbon content and low amounts of oxygen.

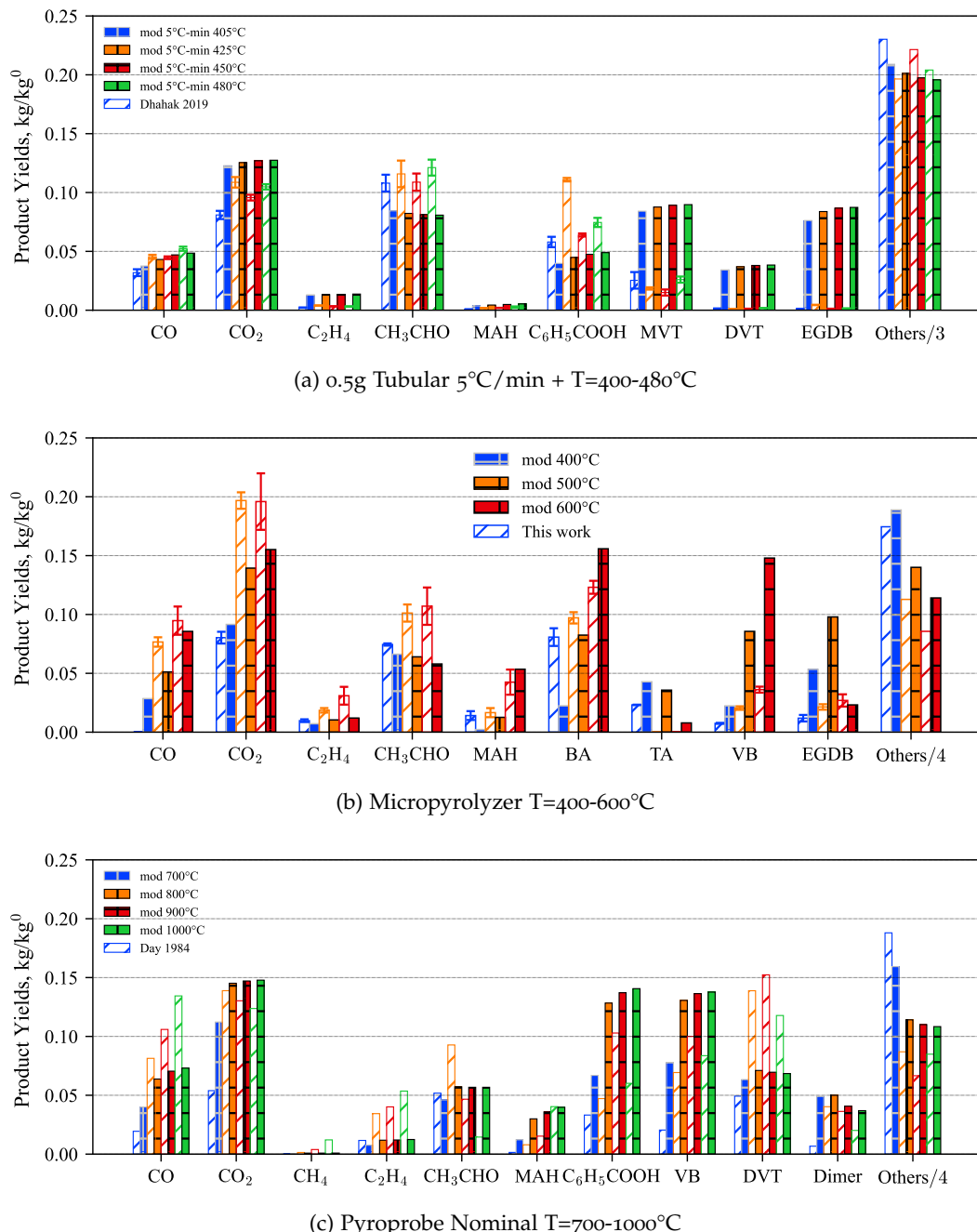


Figure 6.26: Comparison of mass yields of volatiles for the proposed model and both new and literature^{99,101} experimental data (patched bars).

6.2.4 Sensitivity analysis

A brute force sensitivity analysis is performed to assess the effects of the involved parameters on model predictions. The sensitivity coefficient $\sigma_{Y/K}$ of a variable Y to a parameter K is defined as:

$$\sigma_{Y/K} = \ln \left(\frac{Y_{2K}}{Y_{0.5K}} \right) / \ln \left(\frac{2K}{0.5K} \right) \quad (6.6)$$

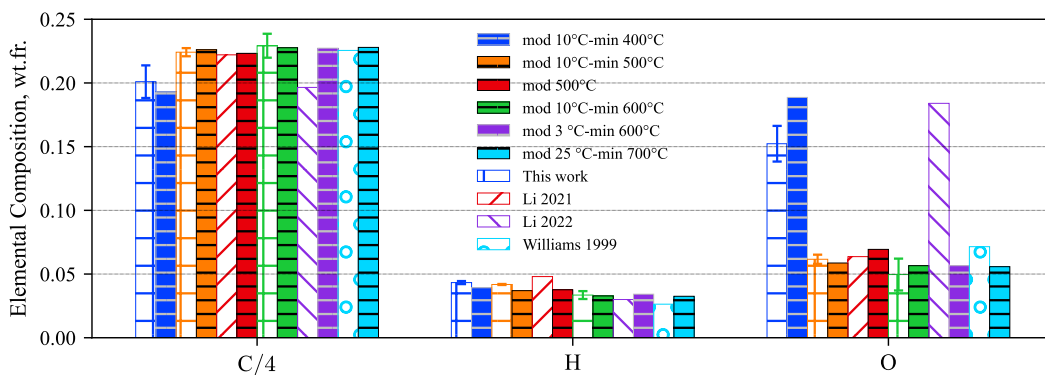


Figure 6.27: Comparison of char elemental composition for the present model (solid bars) and both literature^{405,406,438} and new experimental data (patched bars).

where parameter K is modified by a factor of 2. The absolute value of $\sigma_{Y/K}$ represents the importance of the parameter K in influencing the variable Y. On the other hand, the sign of $\sigma_{Y/K}$ represents if an increase in parameter K corresponds to an increase or a decrease of Y.

The sensitivity is performed considering model predictions at HR=1, 10, 100, 1000 °C/min. The model parameters are the rate constants reported in Table 6.1 and 6.2, but for clarity purposes only the main classes are reported herein. The sensitivity target are both characteristic degradation temperatures and species yields, shown in Figure 6.28 and 6.29 respectively.

Considering the degradation profiles, the reference values are the onset temperature (10% mass loss), the temperature 50% mass loss is reached, and the final char yield. The most important reaction class is the concerted molecular path (Reaction r6.1). The onset temperature is controlled by this reaction and partly by low temperature β -scissions. Random scissions affect the TG profiles as they increase the radical pool, and radical recombination has the same effect but with opposite value. As the degradation proceeds, radical pathways become important affecting the half-degradation temperature but also the char yield. Addition reactions slow the degradation due to formation of char, while β -scission affects it because of the formation of phenyl radicals. The concerted molecular pathway results also in char formation due to degradation of the ethylenediene moiety. H-abstractions affect char yields as they contribute to formation of phenyl radicals through H-abstractions on carboxylic and phenyl ends.

Considering species yields, only the major products are presented for clarity purposes. The interplay between different reaction classes in the model significantly impacts the formation of major products. The concerted molecular pathway (r6.1) favours monomers and vinyl esters, consequently reducing CO₂ yield. While it promotes dimer formation, it also enhances their degradation to monomers. This pathway promotes acetaldehyde formation at low temperatures due to ethylenediene degradation, but at higher temperatures, it hinders it by favouring vinyl ester formation from ethylenediene

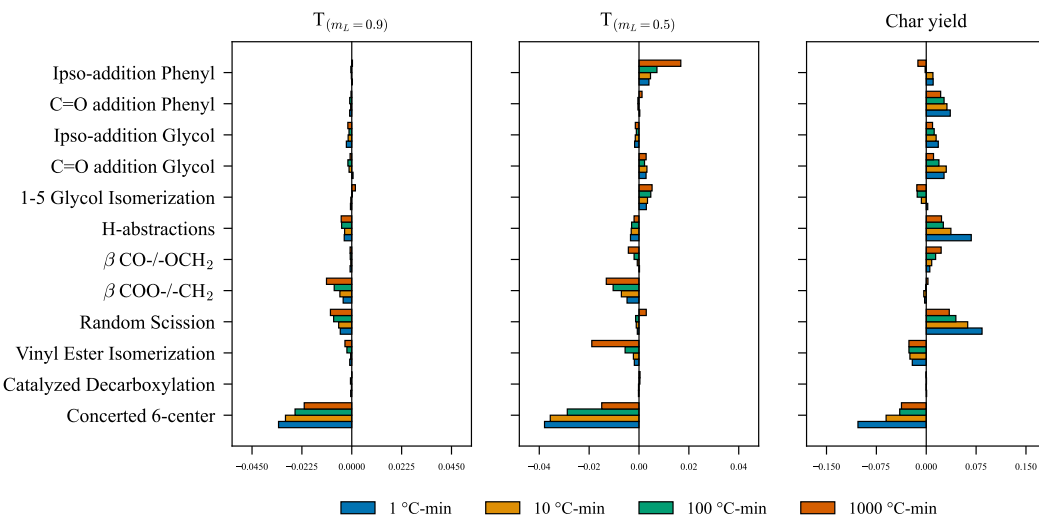


Figure 6.28: Sensitivity analysis for the temperatures 0.1 and 0.5 liquid conversion are achieved ($T_{(m_L=0.9)}$ and $T_{(m_L=0.5)}$) and the final char yield.

groups. Vinyl ester isomerisation reduces the yields of both vinyl esters and acetaldehyde. The reason is that it reduces the availability of vinyl esters for acetaldehyde formation, and carbonyl additions become less important at higher temperatures. The resulting increase in benzoic acid yield is linked to MVT degradation. Similarly, EGDB formation increases due to EGDV degradation. The random scission values represent the global sensitivity to the radical mechanism. The mechanism favours formation of small species and chars with respect to the molecular one. The low temperature β -scission pathway promotes vinyl ester formation but hinders acid formations due to their rapid decarboxylation. Conversely, the high-temperature pathway increases CO yield (not shown) and char formation through phenyl radical generation. Benzoyloxy radical decarboxylation is a key pathway for CO_2 formation, but it is not highly sensitive due to its fast rate. Indeed, the rate-determining steps for CO_2 yields are the formation of the carboxylic radicals, which rapidly decompose. Isomerization of the glycol radical is among the most important pathways for formation of the ethyldene moiety. However, due to the reverse being defined by equilibrium, it does not appear as a sensitive reaction. Acetaldehyde formation involves multiple steps: glycol mid-chain radical isomerisation, H-abstraction to form the ethyldene moiety, and concerted degradation to form the anhydride and acetaldehyde. Isomerization dominates at low temperatures, while concerted degradation controls the reaction at high temperatures. Radical additions significantly affect the product distribution. Vinyl benzoate has a higher sensitivity to these reactions compared to benzoic acid for this reason. Formation of the hydroxy-formyl radical (COOH) from ipso-additions on acid terminations is accounted only for HMW species due to the high BDE involved. Conversely, all vinyl esters can undergo both ipso and carbonyl additions which considerably decrease their yield. These reactions affect the overall monomer yields as they decrease the concen-

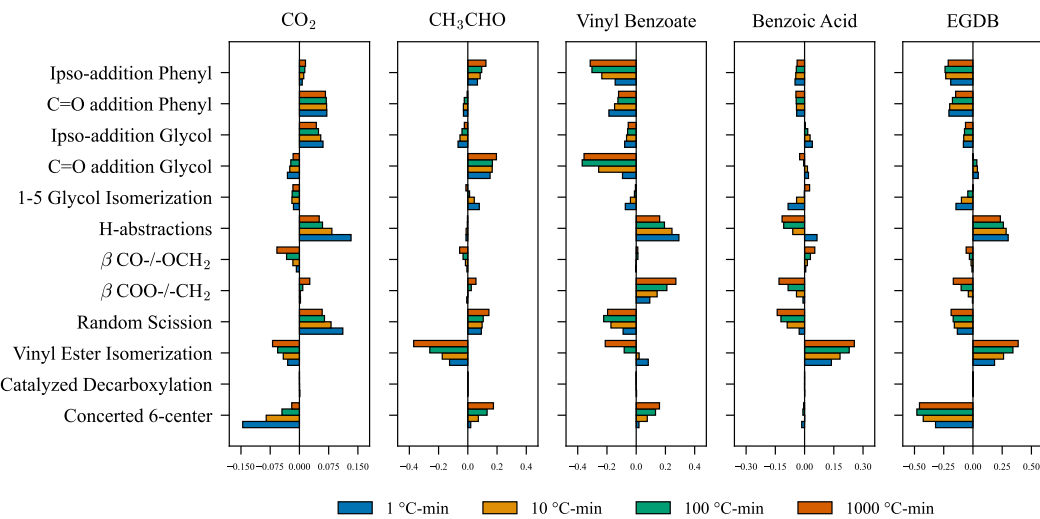


Figure 6.29: Sensitivity analysis for the final mass yields of the major volatiles.

tration of glycol mid-chains. Furthermore, the LMW radicals (e.g., VBr, rBA, EGDBr, rEGDB) can add to polymer chains before evaporating to stable species.

6.3 CONCLUSIONS AND FURTHER WORK

A condensed-phase kinetic model for PET thermal degradation is proposed. Consistently with the other polymers, the mechanism is formulated through the functional groups approach. Polymeric chains are represented through several pseudo-species representative of the chain chemical moieties, while short compounds of interest are represented with higher level of detail. Because of lack of data, the PET char is modelled through the framework developed for biomass pyrolysis. The kinetic mechanism incorporates both molecular and radical pathways and is developed through a first principle approach. Reactions proposed in the scientific literature are critically assessed, employing kinetic parameters obtained from analogous gas-phase compounds through a reaction class based approach. Thermochemical properties are not defined due to the limitations in accuracy for the estimation of aromatic esters in gas-phase.

The model is validated considering literature and new experimental data in terms of mass profiles, volatile yields, and char characterization. To the best of the author's knowledge, this is the first quantitative kinetic mechanism for PET pyrolysis. The model accurately predicts mass loss profiles, although there is significant variability in experimental char yield data that the model cannot fully capture. Regarding volatile products, the model reasonably captures the major components. However, it overestimates the vinyl ester to acid ratio compared to some experimental observations. This discrepancy is likely due to the model predicting similar reaction pathways for both products, while some experiments show predominantly acid formation. The

model proves capable at describing also char elemental composition. Further work is required to develop a description consistent with the ester moieties specific of PET char, but broader validation sets are needed for the purposes. A sensitivity analysis is performed to assess the importance of the reaction pathways. The analysis revealed significant interdependencies between the formation of various products.

The proposed mechanism is provided in CHEMKIN format and is freely accessible on GitHub². The model specifically address condensed-phase reactivity, and future work will extend its application to assess gasification reactivity.

² Available at <https://github.com/Alocaspi/Polymers-Kinetic-Mechanisms>

PLASTIC WASTE THERMOCHEMICAL RECYCLING

PLASTIC WASTE is a complex feedstock of various origins. It is typically classified as post-industrial or post-consumer waste due to their different characteristics⁷. The former originates from manufacturing leftovers and is typically clean and well-defined. It often undergoes recycling within the production facility itself. On the other hand, the latter encompasses mixed plastic streams often contaminated with organic and inorganic materials. The specific composition of post-consumer waste varies depending on the application. For example, PMMA waste collected from automotive applications is often high-purity, single-polymer feedstock⁴³⁹.

Household and municipal plastic waste represent the most complex mixtures. Their composition fluctuates based on seasonal variations and local regulations. Packaging materials are a major contributor to plastic waste due to their widespread use and short lifespans¹⁵. Consequently, the composition of municipal and household plastic waste reflects the commonly used packaging polymers, such as PET and polyolefins. Partial sorting for mechanical recycling separates PET and HDPE from other plastics. This results in a typical composition of 70-75% PE-PP, 5-10% PS, 5-10% PET, and 0-4% PVC²³. However, studies have reported significantly higher PVC content (15-25%) in plastic waste⁷, highlighting the inherent variability in composition.

The present Chapter discusses kinetic models for plastic waste condensed-phase pyrolysis. To this aim, a detailed description on coupling of the mechanisms proposed in the previous Chapters is presented. As discussed, the degradation of each constituent of PW varies according to the study reported in literature. This results from both the polymer intrinsic variability and experimental uncertainties. In PW, the origin and characteristics of the individual components are unknown, further increasing the complexity of the system. A brief introduction on mixture thermodynamics is given, followed by an examination of binary mixtures of different polymers. This approach allows for investigation of pair interactions likely to occur in real-world waste mixtures. Because of the remarkably different behaviours, the discussion is separated between vinyl and condensation polymers.

7.1 MIXTURE THERMODYNAMICS

Plastic waste is a mixtures of multiple polymers and additives. Contrary to gas-phase compounds, the components can be completely or partially immiscible due to their different chemical nature. Polymer miscibility is mostly limited to the amorphous phases, as only few instances of co-crystallization of polymer blends are known⁴⁴⁰. When a polymer mixture is miscible, it forms a homogeneous polymer blend. These blends act as a single phase, exhibiting properties that are a combination of the individual polymers. In contrast, immiscible mixtures are heterogeneous, displaying distinct properties characteristic of each separate component. These immiscible mixtures take on various complex morphologies, such as spherical drops, cylinders, or fibers⁴⁴¹.

Phase behaviours are related to thermodynamic relationships^{21,440-443}. Miscibility is defined through the Gibbs free energy of mixing (ΔG_m) as:

$$\Delta G_m = \Delta G_{\text{mixture}} - \sum_i G_i \quad (7.1)$$

where miscibility is achieved only if $\Delta G_m < 0$. The mixture composition is the one that satisfies the local equilibrium as:

$$\left(\frac{\partial^2 \Delta G_m}{\partial \phi_i^2} \right)_{T,P} > 0 \forall i \quad (7.2)$$

The free energy of mixing is also related to the enthalpy and entropy of mixing as:

$$\Delta G_m = \Delta H_m - T \Delta S_m \quad (7.3)$$

For low molecular weight compounds the entropy contribution favours miscibility at increasing temperature. On the other hand, for polymer chains the entropy terms is negligible, and the free energy of mixing depends mainly on enthalpic contributions. Most polymer-polymer pairs are immiscible^{7,440,441}. As with solvent-solvent mixtures, polymer blends show an upper or lower critical solution temperatures (UCST or LCST). For these blends, a spinodal curve is observed and its location is the one that satisfies the following equality:

$$\left(\frac{\partial^2 \Delta G_m}{\partial \phi_i^2} \right)_{T,P} = 0 \forall i \quad (7.4)$$

which represents the equilibrium condition between the polymer in the homogeneous mixture and the phase-separated ones. For miscible polymers, a single well-defined minimum in ΔG is present. In case of partial miscibility, more local minima are usually observed. These represent the composition of the phases the blend splits into. In case of non-miscibility, the minima of free-energy correspond to the pure polymers.

The most commonly employed theory to describe the mixing energy is the Flory-Huggins lattice theory. For binary systems, the mixing Gibbs free energy is expressed as:

$$\frac{\Delta G_m}{RTV} = \frac{\phi_1}{V_1} \ln \phi_1 + \frac{\phi_2}{V_2} \ln \phi_2 + \chi_{12} \phi_1 \phi_2 \quad (7.5)$$

where ϕ_i is the volumetric fraction of compound i and χ_{12} the Flory-Huggins binary interaction parameter. The molar volume of each component can be estimated from MW_i / ρ_i , while the total Volume V is the sum of the two volumes⁴⁴³. The configurational entropy of polymer blends is usually negligible, resulting in miscibility being mostly related to the enthalpic contribution. While the initial polymerse may not be miscible, their decrease in chain-length upon pyrolysis result in formation of shorter chains with a non negligible mixing entropy contribution. Additionally, oligomers of one polymer may diffuse into the phase of the other polymer. While the Flory-Huggins is the most commonly employed approach, several other theories have been developed to describe the miscibility. Among these, Equation of State models have been validated for several polymeric systems^{441,443}. These models offer improved description of the blend properties but require considerably more information on the constituents. Although mixing rules can be employed to estimate the binary parameters, the model struggles when specific interactions are present in the blend requiring estimation of appropriate parameters.

As previously mentioned, a negative value for ΔG_m corresponds to miscibility at the molecular scale. Nevertheless, for non-miscible blends the interface between two phases shows partial miscibility. The interfacial thickness is related to the interaction parameter (χ_{12}) and corresponds to the volume where both polymers are present. Through mean-field theories^{444–446}, this interfacial thickness (Δl) is expressed as:

$$\Delta l = \frac{2b}{(6\chi_{12})^{1/2}} \quad (7.6)$$

where b is a lattice parameter such as the length of a monomeric unit. This length is of the order of the monomer size, and relates to the adhesive properties of the blend⁴⁴³.

7.1.1 Binary interaction parameters

The literature approaches require estimation of binary interaction parameters. These are performed either experimentally or through theoretical methods. The former usually involves calorimetry or light scattering techniques to measure ΔH_m or interface thickness^{441,443}. While several experimental data are present in the scientific literature, high uncertainty in the estimation of χ_{12} is observed.

The most adopted formalism is the solubility parameter introduced by Hildebrand and Scott. According to this approach, χ_{12} is related to differences in the solubility parameters of the pure components (δ_1 and δ_2) as:

$$\chi_{12} = \frac{V_r}{RT} (\delta_2 - \delta_1)^2 + \beta \quad (7.7)$$

where V_r is the molar volume of a polymer segment, which can be estimated as geometrical average of the monomers' molar volume. Conversely, $\beta \sim 0.34$ is an empirical

constant that is found necessary for polymer-solvent systems and represents a correction to the Flory combinatorial entropy⁴⁴⁷. The solubility parameters are in turn related to the polymer cohesive energy density, which is in turn related to the energy of vaporization. Several group contribution methods have been proposed to predict these²¹, but these approaches are mostly based on data on polymer-solvent pairs. Large errors are observed when these values are applied to polymer blends⁴⁴⁸, possibly because the Hildebrand parameters are applicable to regular solutions, which generally refer to strictly non-polar systems.

An improved approach involves estimating multidimensional solubility parameters as proposed by Hansen⁴⁴⁷. This methodology involves estimating the solubility parameter as composed by three contributions: dispersion (D), polar (P), and hydrogen bonding (H) interactions. Therefore, the corresponding interaction parameter is estimated as:

$$\chi_{12} = \frac{V_r}{RT} \left[(\delta_2^D - \delta_1^D)^2 + 0.25 (\delta_2^P - \delta_1^P)^2 + 0.25 (\delta_2^H - \delta_1^H)^2 \right] \quad (7.8)$$

These parameters allow to understand the various factors influencing the mutual solubility of polymers. The most significant contributor to miscibility is often hydrogen bonding. Polymers containing groups that can both donate and accept hydrogen bonds can self-associate, leading to increased miscibility. Among these groups, carboxylic acid and amine functionalities exhibit the strongest interactions after acid-base ones. For example, the solubility of aliphatic polyesters with PVC is believed to be related to the interaction between the α -hydrogens in PVC and the carbonyl groups of the aliphatic ester. Dipole-dipole interactions also play a significant role, as evidenced by the interactions between poly(caprolactone) (PCL) and chlorinated PVC¹²². Low energy interactions are also observed between hydrogen donors and π orbitals of aromatic rings⁴⁴³. While solubility parameters provide a valuable guideline, the approach lacks the ability to predict specific interactions key for achieving miscibility in several polymer blends⁴⁴³. For instance, this approach is not able to predict the experimentally observed^{122,443,449} miscibility of poly(caprolactone) and PVC blends.

The interaction parameter also has a temperature dependence which is often neglected. This relation follows the form:

$$\chi_{12} = a_1 + \frac{a_2}{T} + \frac{a_3}{T^2} \quad (7.9)$$

where the quadratic term is sometimes replaced by a logarithmic one²¹. Most blends show values of $a_2 > 0$ and $a_3 \sim 0$ ⁴⁴⁸, which corresponds to an UCST behaviours. A dependence on the volume fraction of the constituents has also been proposed²¹, but this is valid only for polymer-solvent systems⁴⁴⁸.

7.2 VINYL POLYMERS

Vinyl polymers have received the highest consideration in the past decades. Both experimental and modelling efforts have been made to investigate the mutual interactions occurring in condensed-phase pyrolysis¹⁵. In general, minor interactions are observed^{113,114}. Nevertheless, the experimental investigation measures quite different types of interactions. For instance, Albano *et al.*⁴⁵⁰ find adding 10–50 % of iPP to HDPE results in a degradation temperature (T_d) mixture similar to pure PP. Conversely, Singh *et al.*⁴⁵¹ measure that T_d for the same mixture is similar to the one of pure PE. Mc Neil and coworkers^{452–462} report that binary interactions depend on the physical state of the system, such as miscibility and degree of phase dispersion¹¹⁶. They proposed that small radicals at the phase boundaries could diffuse into the other polymer. Experimental investigation of Csmorovà *et al.*⁴⁶³ suggested that interactions are primarily related to the mutual solubility of the two polymers.

In the following sections, the main approaches to model mixtures of vinyl polymers are presented. A comparison with experimental data is then presented, highlighting the differences with experimental data.

7.2.1 Literature degradation models

Two primary approaches have been proposed in the literature to model the degradation of polymer mixtures. The first one, proposed by Faravelli *et al.*¹¹³ involves phase-equilibrium calculations. Conversely, Kruse *et al.*¹¹⁴ model mixture degradation through diffusion of LMW radicals at the interface.

Mechanistically, interactions between vinyl polymers during pyrolysis occur through radical-based bimolecular pathways. Radicals generated from one polymer can react and initiate degradation in the other polymer. The main reactions involve hydrogen abstraction, resulting in the transfer of the radical from one chain to another. For polyolefins, this phenomenon translates to a single-step degradation occurring at a temperature between the individual degradation temperatures of the pure polymers ($T_{d,1} < T_{d,mix} < T_{d,2}$). However, this requires the polymer constituents to be intimately mixed at the molecular level. If the polymers are not miscible, radicals must diffuse to the other phase before interacting.

As most polyolefins exhibit limited miscibility, radicals produced in one phase are not readily available to the contrasting polymer-rich phase. The fraction of radicals available for inter-polymer reactions can be estimated based on the phase composition.

Faravelli *et al.*¹¹³ compute the equilibrium composition of PE-PS mixtures. They found that the PE-rich phase contained approximately 2.5% PS, while the PS-rich phase contained 12.5% PE. These values, however, are highly dependent on the initial molecular weights of the polymers⁴⁶⁴, and uncertainties exist regarding the accuracy

of the exponential terms used in the calculations⁴⁶⁵. The proposed two-phases model successfully reproduced the variation in degradation profiles. Nevertheless, also considering completely immiscible polymers was observed to yield good agreement with experimental results. Notably, the degree of mixing was not observed to significantly affect the degradation process, suggesting that phase separation plays a dominant role.

Kruse et al.¹¹⁴ adopted a different approach to model PP-PS mixtures. While acknowledging the immiscibility of the polymers, they focused on the ability of LMW radicals near the interface to diffuse into the other phase. This approach emphasizes the interaction between polymers within the interfacial region. The interaction volume is estimated using a diffusion length, which represents the maximum distance a radical can diffuse within its own phase before stabilizing. Employing this method, they estimated that approximately 0.037% of PS radicals could diffuse into the molten PP phase. Conversely, the estimated percentage of PP radicals diffusing into the PS melt was significantly lower (0.0026%) due to the higher hydrogen abstraction rates of alkyl radicals compared to benzyl radicals. This ternary-phase model successfully captures the observed differences in degradation trends, predicting an enhancement of PP degradation by approximately fourfold.

Both approaches suggest that the degree of mixing has minimal influence on the degradation process. Faravelli et al.¹¹³ attribute this to the inherent equilibrium phase separation, while Kruse et al.¹¹⁴ propose that the prevalence of LMW radicals in PP plays a key role. These readily diffusible radicals can counteract the effect of PS radicals diffusing into the PP matrix, leading to a minimal net effect on degradation behaviour.

7.2.2 Validation of mixture degradation

As discussed earlier, this thesis lays the foundation for modeling thermochemical recycling of plastic waste. Notably, vinyl polymers are predominantly immiscible⁴⁶⁶, with interactions primarily occurring near phase boundaries. Introducing separate phases for each vinyl polymer, along with interactions at these boundaries, would significantly increase model complexity. Furthermore, accurately depicting these phenomena necessitates a robust definition of thermodynamics and phase dynamics.

Despite the increased complexity, such an approach offers only marginal improvements in prediction accuracy. Studies have shown that binary interactions result in degradation temperature deviations of around 5°C compared to a completely segregated mixture model. This difference is relatively small compared to the inherent variability of polymers discussed in previous chapters. Therefore, for the sake of practicality, interactions between vinyl polymers will be neglected in this work.

Careful consideration is required when employing kinetic mechanisms within the appropriate liquid phase. Representing the molten waste as a single pseudo-phase leads to a decrease in the concentration of each polymer species. This is a reasonable

assumption for unimolecular reactions, as the concentration decrease reflects the lower polymer volume compared to the pseudo-phase volume. However, for bimolecular reactions, a single pseudo-phase approach overestimates the dilution effect. This consequently reduces their importance compared to the actual scenario. The multi-step models developed for PE, PP, and PS (Sections 3.3.2, 4.2.2, and 5.2.2) involve only unimolecular reaction rates. As such, they are well-suited for use within a single polymeric pseudo-phase. Conversely, semi-detailed mechanisms incorporate various bimolecular reactions like H-abstractions, as well as reactions representing stabilization and support polymer units (Section 3.1.2.2). Nonetheless, the error introduced by employing a single pseudo-phase for all mechanisms remains within the range of inherent polymer-to-polymer variability.

Figure 7.1 compares predicted and measured degradation behaviours of 50/50 PE/PP mixtures at different heating rates, alongside the degradation profiles of pure PE and PP. The model appears to struggle with capturing the interactions occurring during co-pyrolysis of these polymers. However, inconsistencies are also evident between different sets of experimental data.

At a heating rate of 5°C/min (Figure 7.1a), Waldman *et al.*⁴⁶⁷ report that PE appears to slow down PP degradation in the mixture. The model overestimates the mixture's degradation temperatures by approximately 10°C. This overestimation applies to both PE and PP within the blend. While the model captures the "accelerating" effect of PP on PE degradation, it might be due to an underestimation of PP reactivity.

Figure 7.1b shows the comparison at 10°C/min. Albano *et al.*⁴⁵⁰ observed a PE/PP mixture with a degradation temperature similar to pure PP, while Chowlu *et al.*⁴⁶⁸ reported a similar T_d but with higher mixture reactivity compared to pure PP. The model cannot account for either of these observations. Even considering inter-polymer interactions, PP radicals reacting with PE lead to a slower PP decomposition. Additionally, the model cannot predict a T_d lower than the pure polymers, which represent the upper and lower boundaries.

At 40°C/min (Figure 7.1c), the model accurately predicts the degradation of pure polymers but underestimates the mixture's T_d by approximately 20°C. Singh *et al.*⁴⁵¹ measured a T_d for the mixture similar to pure PE, exhibiting an inhibition effect opposite to that observed at 10°C/min (Figure 7.1b) but more aligned with the findings at 5°C/min (Figure 7.1a). However, the model explains the behaviour at 5°C/min due to the predicted lower T_d difference between PP and PE. The significant discrepancies between experimental data likely stem from both polymer-to-polymer variability and sample preparation methods. Hot press machines used for sample preparation are known to partially initiate polymer degradation¹¹⁴, potentially explaining lower-than-expected degradation temperatures in some mixtures.

Chowlu *et al.*⁴⁶⁸ also reported variations in product distribution based on the PE/PP ratio, observing an increase in light hydrocarbons compared to pure polymers. These cross-interaction effects are beyond the scope of the current model and cannot be pre-

dicted by the radical chain-transfer mechanisms proposed in the literature. Further experimental validation with product distribution data from well-defined binary mixtures is necessary to improve model predictions. However, the observed significant variability even with pure polymers highlights the complexity of the investigation.

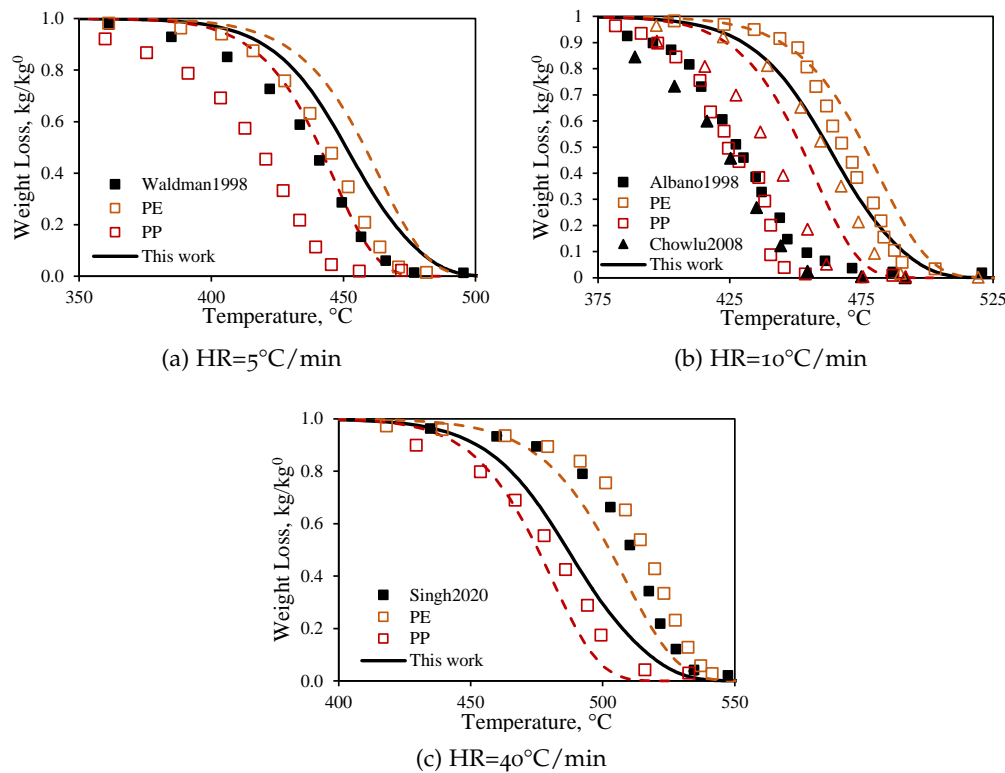


Figure 7.1: Comparison of predicted (solid lines) and measured (symbols) mass-loss profiles for PE, PP, and 50-50 mixtures.

The model's ability to handle binary mixtures is further assessed using experimental data involving PVC (Figure 7.2). The model incorporates the PVC degradation mechanism proposed by Marongiu *et al.*³⁵ while neglecting interactions between vinyl polymers. As shown in Figures 7.2a and 7.2b, the model successfully describes the degradation behaviour of both PS-PVC and PE-PVC mixtures. For PS-PVC mixtures, experimental data from Miranda *et al.*¹¹⁶ and Knumann and Bockhorn⁵⁰ show similar degradation profiles. Knumann and Bockhorn⁵⁰ observed a slight accelerating effect (around 5°C) on the second degradation step for the mixture compared to the pure polymers. Conversely, Dodson *et al.*⁴⁵⁴ reported that adding PS inhibits the second degradation step in the mixture. The model accurately reproduces the degradation profiles of both polymers, although it overestimates the dehydrochlorination temperature by approximately 20°C. This overestimation likely stems from the PVC degradation model, which might underestimate the temperature difference between the first and second degradation steps. Similar results are observed for PE-PVC binary mixtures. The model accurately predicts the second degradation step but overestimates the de-

hydrochlorination temperature, consistent with the behaviour observed for PS-PVC mixtures.

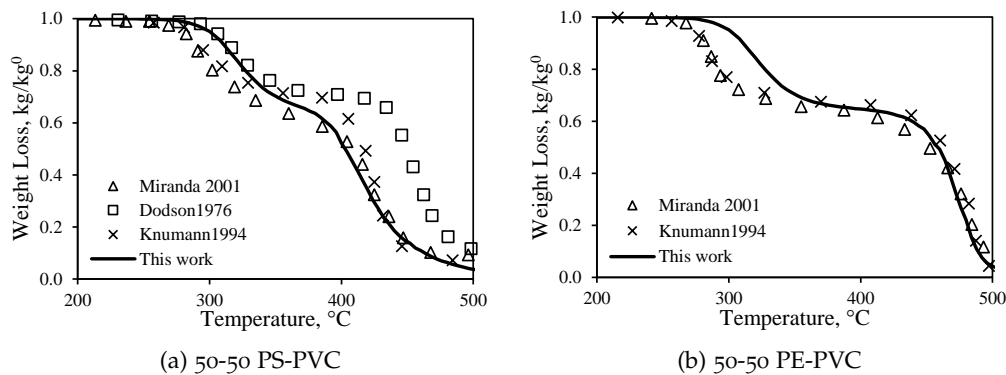


Figure 7.2: Comparison of predicted (solid lines) and measured (symbols) mass-loss profiles for 50-50 mixtures of PE and PS with PVC at $\text{HR}=10^\circ\text{C}/\text{min}$.

The model is assessed also with experimental data on more complex mixtures¹¹⁶ as shown in Figure 7.3. While the model proves able to represent the binary mixtures, it appears to overestimate the degradation temperatures experimentally observed. Considering the polyolefin mixture shown in Figure 7.3a, a difference of $\sim 50^\circ\text{C}$ is observed in terms of onset temperatures. According to Miranda *et al.*¹¹⁶, PS radicals at lower temperatures can diffuse to other polymer phases, initiating their degradation. However, this diffusion phenomenon should also be observed in binary mixtures. As the involved polymers are not miscible, formation of a ternary-mixture is improbable. In these conditions, the three different phases simultaneously touch only at the intersection between phases interfaces. Adding PVC to the mixture does not considerably modify the comparison as shown in Figure 7.3b. The difference in onset temperatures reduces, but this is because of the initial degradation of PVC. The overestimation in T_d observed also in binary mixtures is present also in this case. Nevertheless, the degradation temperature of the second step is still overestimated although by $\sim 30^\circ\text{C}$.

Figure 7.4 presents a comparison of model predictions with experimental data for complex mixtures containing PVC. The data include results from Wu *et al.*¹¹⁵ at heating rates of 2 and $5.5^\circ\text{C}/\text{min}$, alongside the PVC-containing mixture investigated by Miranda *et al.*¹¹⁶ (also shown in Figure 7.3b). Notably, the compositions of the two mixtures examined differ by only 10% in PE content and 5% in PP and PS content.

The model successfully captures the degradation temperatures measured by Wu *et al.*¹¹⁵ and their dependence on heating rate. However, it fails to reproduce the behaviour observed by Miranda *et al.*¹¹⁶ at a higher heating rate ($10^\circ\text{C}/\text{min}$). While the measured degradation temperatures for both mixtures are similar, Miranda *et al.*¹¹⁶ reported an enhancement in degradation for their mixture compared to Wu *et al.*¹¹⁵'s findings. The model is more consistent with the latter data as it neglects cross-interactions.

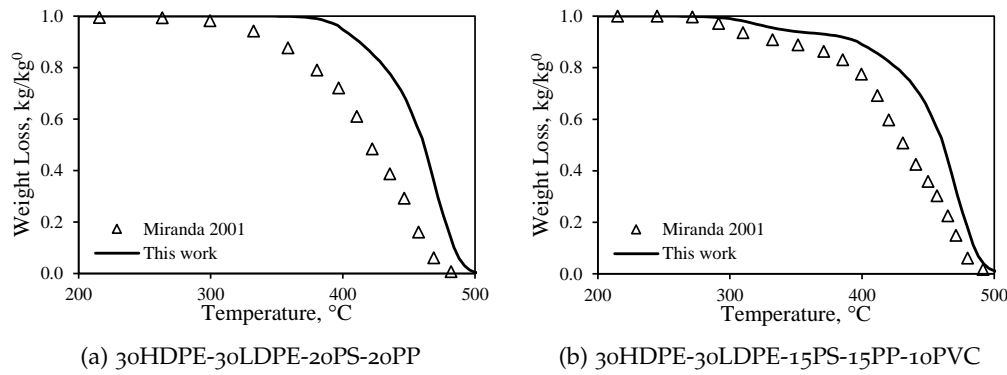


Figure 7.3: Comparison of predicted (solid lines) and measured (symbols) mass-loss profiles plastic mixtures at $\text{HR}=10^\circ\text{C}/\text{min}$.

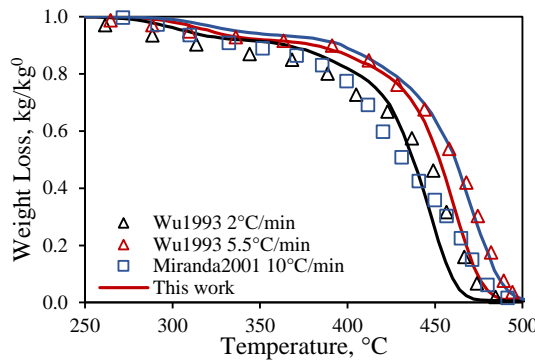


Figure 7.4: Comparison of predicted (solid lines) and measured (symbols) mass-loss profiles of a 35LDPE-35HDPE-10PP-10PS-10PVC mixture at various HR.

The proposed model does not account for the effect of inorganic matter in the mixture. For instance, several salts (e.g., CaCO_3) are known to capture HCl avoiding its release to gas-phase¹⁵. Further work is also required to assess also the mass-transfer from the polymer melt to the inorganic matter.

7.3 CONDENSATION POLYMERS

As shown in the previous sections, several studies on mixtures of vinyl polymers have been proposed in the scientific literature. While some differences are present among different experimental studies, overall only minor interactions are observed. Conversely, condensation polymers received lower attention. From a modelling point of view, to the author's knowledge the present thesis is the first to propose a detailed kinetic model for one of these. The main ones present in plastic waste are PET and polyamides^{7,15,333}. In the present thesis, nitrogen-containing polymers have not been addressed in details and therefore have not been reported. On the other hand, the mechanism for PET

degradation can be coupled with polyolefins. The following paragraphs discuss interactions in mixtures of real plastic waste, which is the main part still to be addressed.

Figure 7.5a shows the predicted and measured mass-loss profiles for a mixture of 25HDPE-25PP-25PS-25PET⁴⁵¹. The model predicts the degradation of the mixture well within experimental variability similarly to the vinyl polymer mixtures previously discussed (<20°C). On the other hand, higher deviations are observed considering mixtures of 20LDPE-20PP-20PS-20PET-20PVC as shown in Figure 7.5b. The data reported in the present Figure are courtesy of Professors A. Beretta and L. Lietti from LCCP group at POLIMI⁴⁶⁹. The main issue is that the kinetic mechanism underestimates the mass-loss at 300°C, i. e., the mass variations occurring during the dehydrochlorination step.

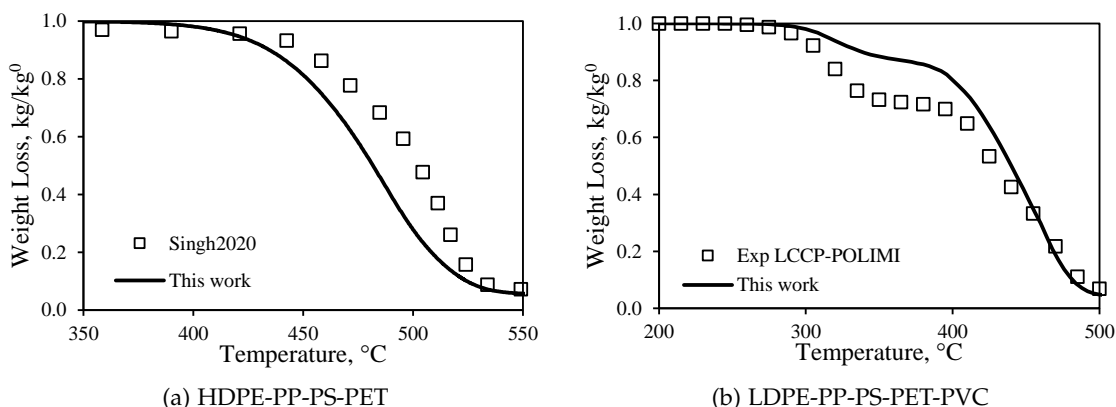


Figure 7.5: Comparison of predicted (solid lines) and measured (symbols) mass-loss profiles for: a) 25HDPE-25PP-25PS-25PET HR=40°C/min⁴⁵¹; b) 20LDPE-20PP-20PS-20PET-20PVC HR=10°C/min⁴⁶⁹.

7.3.1 On the interactions in PET-PVC blends

The presence of both PET and PVC in plastic waste mixtures significantly alters their co-pyrolysis behaviour compared to mixtures lacking PVC (Figures 7.5 and 7.3). Notably, substantial deviations from the expected behaviour arise when polyesters, polyamides, and chlorinated polymers are present together (Figure 7.6).

Figure 7.6a presents experimental data⁴⁶⁹ for a binary PET/PVC mixture. The solid line represents the measured mass loss, while the dashed line depicts a linear combination of the pure components' behaviour (assuming no interaction). Neglecting interactions significantly underestimates the mass loss during the dehydrochlorination step of PVC. More importantly, the presence of PET alters the types of volatile products released during degradation. Studies have observed the formation of various chlorinated compounds^{119,120}, and the release of aromatic esters might lead to unforeseen fouling and clogging issues within processing equipment.

Elucidating the nature of the interactions between PET and PVC is paramount for accurate modeling of complex plastic waste mixtures. While most polymers are immiscible, some highly chlorinated polymers and specific polyesters can form a homogeneous phase^{122,443,449,470,471}. Hydrogen bonding between the α -hydrogen of PVC and the ester carbonyl group of PET is believed to be a key factor¹²². Because of the similar glass transition temperatures and PET melting after PVC degradation, it's challenging to experimentally determine their mutual solubility. Studies by Aubin and Prud'Homme¹²³ suggest solubility of PET and polybutylene terephthalate (PBT) with chlorinated PVC (CPVC), while neither is soluble with low chlorine-content PVC. Considering linear aliphatic polyesters, it is observed that solubility with PVC is achieved only if the ratio of alkyl units (-CH₂-) to carbonyl ones (-COO-) is between 3 and 10^{470,471}. At high numbers of alkyl-to-carbonyl ratios the low concentrations of interaction centres is not enough to guarantee the solubility. Conversely, at low CH₂/COO values chain rigidity hinders rearrangement to favourable interactions¹²². For instance, poly(caprolactone) (PCL) is soluble with PVC and is widely regarded as the aliphatic polyester with highest compatibility with chlorinated polymers^{122,443,449}. To investigate the miscibility of PET with PVC, Ma and Prud'Homme⁴⁴⁹ measured blends of chlorinated polymers with a co-polymer of PCL and PET. Increasing the content of PET, they observed a decrease in the mixture solubility suggesting that PET may not be miscible with PVC. The miscibility is not the only requirement however. For instance, as shown in Figure 7.6b, experimental blends of PVC and PCL¹²⁴ do not exhibit any cross-interaction as the behaviours can be explained through a linear combination of the two pure polymers. On the other hand, Goulet and Prud'Homme¹²⁴ observe significant interactions between PVC and poly(ethylene adipate), which however are not miscible. Considering PCL-PVC blends, there is no consensus in the scientific literature. Pekdemir *et al.*^{472,473} and Demir⁴⁷⁴ experimentally observe significant interactions for PCL-PVC. The measured interaction corresponds to a dehydrochlorination step occurring at higher temperatures involving also decomposition of part of PCL. For PET-PVC, the dehydrochlorination occurs in the same temperature range as pure PVC.

A key prerequisite for significant interactions is the solubility of PET with either PVC or partially degraded PVC. However, conclusive evidence for or against their miscibility remains elusive. Here, potential pathways for these interactions are explored considering both molecular and radical mechanisms. Dehydrochlorination of PVC generates substantial HCl, known to catalyze ester degradation. However, HCl's boiling point (around -85°C¹⁰⁰) implies it acts as a dissolved gas upon formation, hindering interaction with the polymer due to their differing physical states. The dehydrochlorination process involves both autocatalytic radical mechanisms and molecular pathways³⁵. The presence of ester groups might accelerate the latter, potentially allowing interaction with HCl before it's released. However, the rate of unimolecular dehydrochlorination at 400°C is slower than the unimolecular cis-elimination of ethyl esters, rendering it incapable of initiating PET degradation.

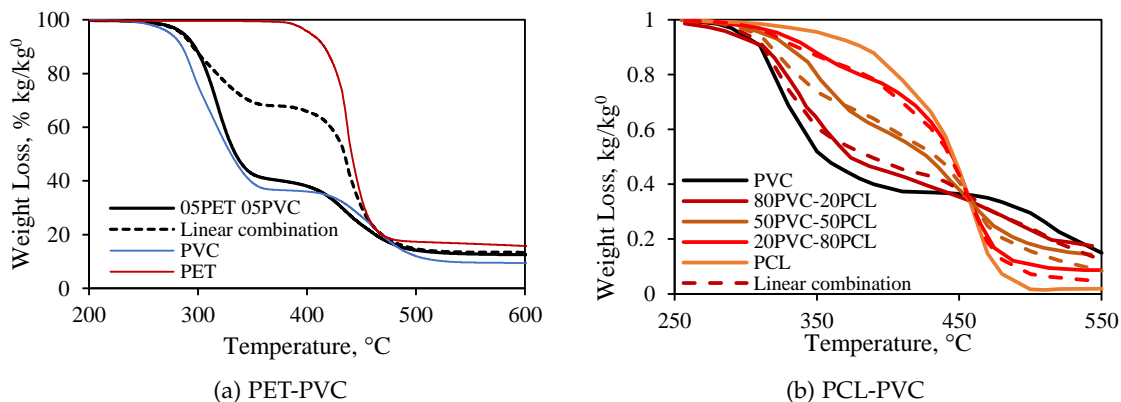


Figure 7.6: Experimental mass-loss profiles at $\text{HR}=10^\circ\text{C}/\text{min}$ for: a) 50PET-50PVC mixture⁴⁶⁹; b) different PCL-PVC mixtures¹²². Solid lines are the experimental results, while dashed lines are obtained as linear combination of the pure polymer behaviours.

Chlorine radicals from PVC, however, can perform H-abstractions on the PET glycol chain. Figure 7.7 schematically represents the proposed interaction mechanism between PVC and PET. As discussed in Section 6.1.2.2, glycol mid-chain radicals favor addition reactions at low temperatures and have slow β -scission rates. They can also abstract hydrogens from PVC chains, forming alkyl radicals that decompose like pure PVC through β -scission, releasing more Cl radicals. PET's glycol radicals can also abstract chlorine atoms due to their low bond dissociation energies, forming a chloro-alkyl ester. This reaction leaves the PVC chain with a secondary alkyl radical unable to undergo β -scission and release Cl atoms, potentially hindering the autocatalytic dehydrochlorination process. The presence of chlorine reduces the bond dissociation energy of the already labile α -hydrogen on the PET glycol unit due to its proximity to the ester group. Considering the difference in BDE between hydrogen in methane and chloromethane²⁷⁶, a decrease of 5 kcal mol⁻¹ is estimated with respect to the glycol unit of PET. This weaker bond facilitates ester cis-elimination, leading to the formation of carboxylic acids and chloro-vinyl aromatic esters. The mechanism can also occur on ethylidene moieties, forming a 1-chlorovinyl ester instead of the 2-chloro variant. While most experimental observations report di-chloro ethyl terephthalate as the cross-interaction product^{119,120}, its formation mechanism remains unclear. Formation of this compound can occur through interaction of the Cl atom with the C group α to the ester, which is however hindered by the hydrogen atoms. Additionally, similar BDE are expected for these compounds with respect to PVC backbones, and therefore they should also decompose rapidly at the dehydrochlorination temperature. The chloroethyl and chlorovinyl terminations however differ by 2 hydrogen. Due to the scarce literature on these peculiar compounds, the degradation spectra may be confused. The presence of chlorine atoms on the glycol unit can also introduce mid-chain unsaturation. H-abstractions at the β -position on these unsaturated units readily undergo β -scission,

releasing Cl atoms. The resulting mid-chain vinyl ester acts as an initiator similar to vinyl benzoate ends, potentially further increasing the radical pool. Further work is required to corroborate the proposed interaction mechanism, the degradation products, and investigate the miscibility of PET and PVC.

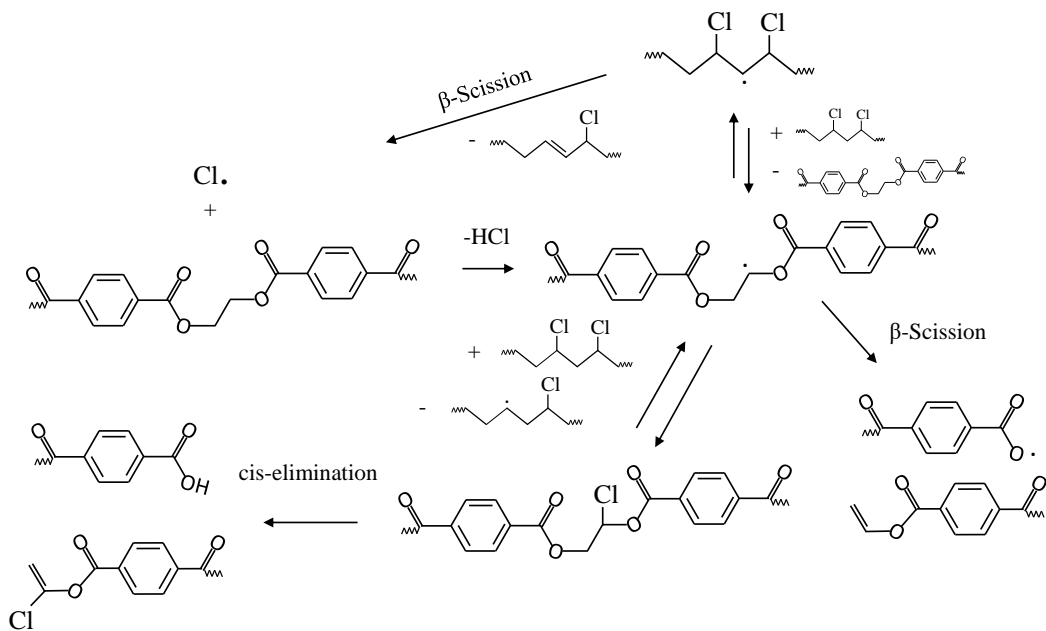


Figure 7.7: Proposed radical-molecular interaction mechanism between PET and PVC.

7.3.2 On the interactions of polyamides with PET and PVC

Polyamides (PA), particularly nylon-6 and nylon-6-6, are common components of plastic waste^{7,15}. In general, polyamides are thought to undergo molecular degradation through formation of cyclic groups^{106,107}. Similar to PET, PAs exhibit interactions with both PVC^{50,117,119,475} and PET during co-pyrolysis^{119,121}. Considering PA-PVC, the dehydrochlorination step involves higher weight loss than expected and formation of nitrogenated aromatics. On the other hand, PET-PA result in a degradation temperature lower than both pure polymers and formation of aromatic amides. The scientific literature on interactions between these polymers is scarce, even in comparison to PET-PVC interactions.

PVC-PA blends are not miscible^{125,127}. Nylon 6 has a similar molecular structure to PCL, only with an amine group instead of the ester. The difference in solubility between PCL and PA is possibly due to the strong hydrogen bonds between amide groups, which is possibly stronger than the one of PCL with PVC. As with PET-PVC interactions, several studies relate the cross-interaction phenomena to the effect of HCl acting as catalyst for the amine group degradation. However, as previously mentioned, the boiling point of hydrogen chloride is ~ -85°C, i. e., 400°C lower than the dehydro-

chlorination temperature. Knumann and Bockhorn⁵⁰ suggest water always present in polyamides in 4–8 wt.% can act as a medium for HCl catalysis.

PET-PA blends are also not miscible^{126,128,129,476}. However, these polymers undergo mutual compatibilisation through interchange reactions^{443,477,478}. This class of reactions is catalysed by inorganic salts and forms a copolymer that improves the phases' dispersion. During co-pyrolysis, cis-elimination or radical degradation can lead to the formation of cross-linked products between the polymer chains. However, this mechanism doesn't explain the observed decrease in degradation temperature compared to the pure polymers.

7.4 CONCLUSIONS

The present Chapter discusses modelling the degradation of plastic waste mixtures. To this aim, the kinetic models previously developed are coupled to predict degradation of laboratory and real plastic waste mixtures. The developed kinetic model successfully predicts the degradation of simulated mixtures containing vinyl polymers (PE, PP, PS, PVC) and PET, with deviations falling within the expected range for vinyl polymer mixtures. This suggests minimal interactions during co-pyrolysis for these specific combinations. These minimal interactions are possibly consequence of mutual immiscibility among the polymers.

However, the model encounters challenges when incorporating PVC and PET together. It underestimates the mass loss observed during the dehydrochlorination step of PVC within mixtures containing both PVC and other polymers. This highlights the model's inability to capture the specific interactions between PVC and other waste components during degradation. An interaction mechanism involving both molecular and radical pathways is proposed to explain the binary interactions. The hypothesis that HCl from PVC dehydrochlorination acts as a catalyst for PET degradation is questionable due to its low boiling point. Conversely, chlorine radicals from PVC can abstract hydrogens on the PET chain, leading to increased cis-elimination and the formation of chloro-vinyl aromatic esters. Nevertheless, further experimental and modelling work is required to quantitatively validate the proposed interaction pathways.

Similar interactions are observed also for PET-PA and PVC-PA blends. As with PET, HCl is not expected to act as a catalyst for PA degradation because of the low boiling point. However, the inherent water content in PAs could potentially act as a medium for such catalysis. PA and PET blends, while immiscible, interact through interchange reactions facilitated by inorganic salts. This improves the dispersion of the phases but doesn't explain the observed decrease in degradation temperature compared to pure polymers. Nevertheless, development of a kinetic degradation model for polyamides is required before assessing their binary interactions.

PERSPECTIVES AND FURTHER WORK

THE present Ph.D. thesis proposes a lumped condensed-phase kinetic model for thermochemical recycling of plastic waste. The main polymers present in PW were first investigated separately, building a total of 13 CHEMKIN-like mechanisms for pure PE, PP, PS, and PET. These models were then combined with a validated literature PVC mechanism³⁵ to assess degradation of real PW mixtures. The resulting kinetic models are freely available as GitHub repositories¹ and can be employed in CFD or process simulators.

8.1 TOWARDS A NEW STATE-OF-THE-ART

The mechanisms developed in this Ph.D. thesis are of the semi-detailed kind, compromising between accuracy and computational cost. Model accuracy is defined as the capability to reproduce the key aspects of the degradation process. The chosen targets are polymer characteristic degradation times, product yields, and heat fluxes. The functional groups approach satisfies these requirements. Furthermore, it allows coupling with other kinetic subsets such as halogenated polymers (e.g., PVC³⁵) and biomass⁴⁰⁷ to address PW and PW/MSW mixtures valorization.

The mixture model builds on degradation mechanisms for the individual components. In real PW samples, no characterization of the constituents can be performed, and therefore the models aim at describing the average polymer degradation behaviour. Following the functional groups methodology, each plastic is modelled by distinguishing the polymer chain distribution in two different subsets. High molecular weight chains (HMW) are represented through pseudo-species characteristic of the polymer chemical functionalities. Conversely, low molecular weight chains (LMW) are described with approaches similar to conventional gas-phase mechanisms. Polymer degradation mechanisms are built on reaction classes proposed in the scientific literature. Considering PE, PP, and PS, existing validated kinetic models serve as a reference for constructing the reaction network. Conversely, for PET the reaction pathways are built following studies on analogous compounds and plausible degradation mechanisms. To the author's knowledge, this model represents the state-of-the-art PET pyrolysis. The reaction mechanisms for PE, PP, and PS are supplemented through the definition of

¹ Available at <https://github.com/Alocaspi/Polymers-Kinetic-Mechanisms>

species thermochemical properties. An approach utilizing established gas-phase and phase-change thermochemistry data is employed for these estimations. The developed kinetic models for PE, PP, and PS are employed to derive reduced-order models. Both reduced semi-detailed and multi-step fully lumped mechanisms are proposed and validated with literature data. With respect to PE, the decrease in computational cost is quantified as being 5 times for the reduced model, and 50 times for the multi-step one.

Extensive validation of the kinetic models is conducted using a broad range of experimental data from the literature. The characteristic degradation times are assessed through plastic mass-loss profiles, and each model proves able to represent the degradation process within the experimental variability of the initial polymer. Accuracy in volatile product prediction is assessed by comparing model outputs with quantitative speciation data available in the literature. Due to the wide spectrum of degradation products, a high scattering of experimental data is observed according to the experimental facility. Nevertheless, the models capture the detailed products released and the variation in volatile yields with the operating conditions. Data on heat fluxes are scarce and show the highest experimental scattering among the investigated profiles. The methodology developed shows satisfactory agreement for PE degradation, but additional experimental data are required to validate it for PP and PS.

The single polymer models are coupled to assess the thermochemical recycling of real PW mixtures. Due to the immiscibility of most plastics, the primary interactions during degradation occur in the gas-phase. The mixture pyrolysis is validated in terms of characteristic degradation times neglecting interactions among vinyl polymers, proving the consistency of the approach. Conversely, interactions become significant when considering mixtures containing PET, PVC, and PA. For these cases, an interaction mechanism is proposed to predict the degradation behaviour of PET-PVC mixtures.

8.2 PERSPECTIVES AND OUTLOOKS

Chemical reactors represent the cornerstone equipment within thermochemical recycling plants. Their configuration and operating conditions significantly affect the downstream purification and upgrading sections. Design and control of the reactors relies on an in-depth knowledge of the variation in target yields according to the reactor type and operating parameters. Computational fluid dynamics (CFD) and kinetic models are complementary tools that aid in designing these processes. On the one hand, CFD simulations allow investigating the effect of transport phenomena and reactor geometry. On the other hand, kinetic models describe the chemical phenomena occurring in the reaction vessels. These methodologies are intrinsically coupled through concentration and temperature profiles. Combining these tools allows identifying regions in the reaction vessel that might lead to out-of-target yields. For instance, it is possible to pinpoint the location of cold-spots or rich-zones that promote tar formation. Min-

imizing these undesired products considerably simplifies the downstream treatment sections.

The kinetic framework proposed in this work targets the condensed-phase degradation of PW within the reaction vessel. The following sections present additional research to expand on the methodology proposed to cover a broader range of waste streams and operating conditions. Recommendations on the methodologies to employ the proposed models are also given and a roadmap for further development is presented. As mentioned in Chapter 1, 2, 7, the model encompasses constituents representing ~80 wt.% of common PW streams. Ad hoc modelling and experimental investigations also aid describing the further degradation of volatiles and chars. While the literature offers various methodologies for modelling both volatiles and chars^{133,142,167,273,479}, the novelty of this field necessitates the acquisition of more comprehensive experimental data.

8.2.1 On the condensed-phase degradation of plastic waste

As previously mentioned, the present thesis proposes condensed-phase kinetic models to account for the most common polymers in PW. The models offer different levels of detail depending on the desired application. While semi-detailed pure polymer models are directly usable in CFD simulations, their high computational cost limits their current applicability in PW valorization. Nevertheless, machine learning methodologies aid in the implementation of complex micro-kinetic models in expensive CFD simulations. Techniques as tabulation and pre-computed data avoid real-time chemistry calculations while preserving comparable accuracy to the coupled model¹⁶².

Reduced-order models allow simulating real PW mixtures. Specifically, the multi-step models can be employed also in process simulators due to their flexibility and lower computational demand. Further work is required to develop reduced-order models for PET, PVC, and PMMA. Additionally, developing multi-step mechanisms based on first order reactions allows addressing PW mixtures through a single pseudo-phase approach. Definition of the thermochemical and physical properties of the species involved are also required to employ the models. Both the reduction and estimation species properties can be developed following the approach used for PE, PP, and PS.

While the condensed-phase models describe the majority of PW, the framework can be further expanded to account for other polymers, additives, and inorganics. To this aim, the model subsets can be complemented for nitrogenated polymers such as polyamides and polyurethanes. A simplified multi-step model has been presented for nylon-6¹⁰⁷, but it requires further refinement to account for the complex radical chemistry and side-products formation. Polyurethanes are more complex, as broadly different degradation profiles are observed according to the polymer's specific chemical functionality⁸⁹. Both polyamides and polyurethanes are significant contributors to

nitrogenated pollutants and must be accounted for similarly to PVC. A crucial step is also assessing the condensed-phase interactions between these polymers, PVC, and PET. As the kinetic framework is completed, appropriate characterization procedures must be developed to surrogate the properties of real PW mixtures. The methodology based on the elemental analysis developed for biomass^{37,480} serves as a reference. Nevertheless, knowledge of specific relationships between polymers, additives, and inorganics can further aid the development. The impact of inorganics and additives on the process also requires investigation as it can significantly alter product yields¹⁵. Considering specific interactions between PW and biomass allows employing the models also for MSW valorization.

8.2.2 On the secondary reaction of volatiles from plastic waste

The proposed models address the condensed-phase degradation of plastic waste. However, industrial reactors typically involve volatiles' residence times of the order of seconds, if not minutes. Secondary gas-phase degradation occurs in the order of 10^1 seconds at 500°C , and 10^{-1} seconds at 700°C . For this reason, higher amounts of light gases and particulate matter are observed compared to smaller vessels. Figure 8.1 shows the comparison of the semi-detailed model with experimental data on HDPE pyrolysis in a spouted bed reactor²²⁹. While the model has satisfactory agreement at low temperatures, high deviations are observed above 650°C . On the one hand, the assumption of no liquid-phase degradation for $\text{C} < \text{C}_{30}$ could be removed to predict the decrease of diesel-cuts yields. On the other hand, the high yield of $\text{C}_2 - \text{C}_4$ is explained only through gas-phase secondary degradation. Because of the lower concentrations compared to liquid-phase, unimolecular degradations such as unzipping and backbiting are favoured. Appropriate gas-phase pyrolysis kinetic models are required to describe the secondary product degradation. Nevertheless, estimation of the gas-phase residence times is complex and often requires complex fluid dynamic simulations. The same models can be employed both for secondary reactions in the reactor and steam cracking product upgrading. Conversely, catalytic upgrading of the volatiles requires appropriate methodologies to assess interactions with the catalyst surface.

Similar considerations are valid also in gasifying conditions. Gasification occurs in gas-phase, and estimation of the secondary reactions and gas-phase residence times is of paramount importance. The interactions of gasifying agents with the volatiles released from plastic are however limited as, because of the low concentrations, unimolecular decomposition is favoured. For instance, H_2O has been observed to affect fuel degradation only in terms of collisional efficiencies^{481,482}. Also, the addition of water in steam cracking process decreases formation of coke but does not affect the unimolecular degradation of long-chain alkanes⁴⁸³. Coupling pyrolysis gas-phase kinetic models with mechanisms for gasification of small hydrocarbons⁴⁸⁴ is expected to yield satis-

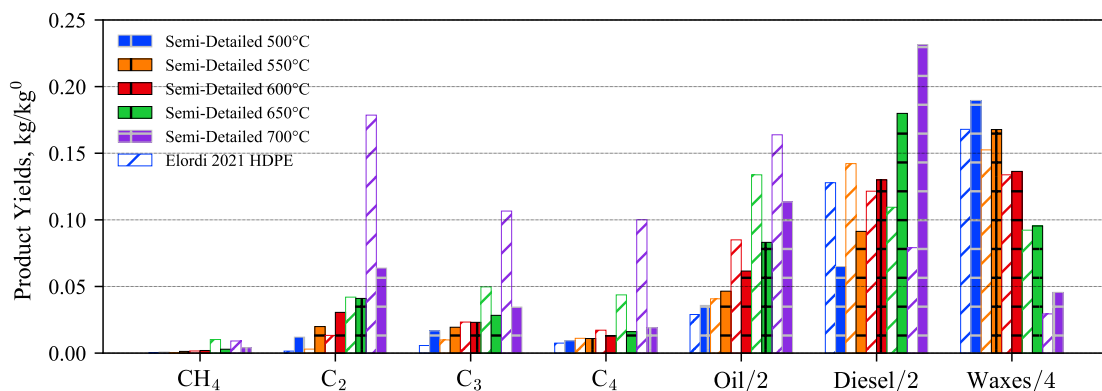


Figure 8.1: Comparison of predicted and experimental yields for HDPE pyrolysis in a spouted bed reactor at different operating temperatures.

factory results. Conversely, modelling plastics combustion requires accounting for the low temperature oxidation pathways of the released volatiles.

8.2.3 On the secondary reaction of plastic char

Gasification and oxidation of plastic char are among the secondary reactions to consider. However, as previously mentioned, data on plastic char are scarce. Appropriate kinetic models are required to consider the secondary heterogeneous reactivity. Because of the intrinsic similarities between plastic, bio-, and coal-chars, the latter can be employed as reference to study the gasification/oxidation behaviour. Compared to bio and coal-chars, most studies focus on direct oxidation of the plastic material. While for polymers like PET the fuel and char oxidation are quite distinct⁴⁸⁵, complex waste mixtures show an overlap of the TGA degradation peaks. Nevertheless, direct oxidation does not yield any information on the char produced. The model developed for biochar oxidation¹⁶⁷ can be employed and updated to account also for plastic chars. This methodology can be first validated for oxidation conditions due to the higher amount of data, and then extended to gasification conditions.

Figure 8.2 shows the comparison of experimental data on char oxidation during PET direct oxidation and the model proposed by Locaspi *et al.*¹⁶⁷. The experimental data are taken considering only temperatures higher than the local minimum of DTG profiles. Polymer devolatilization is modelled with the semi-detailed condensed-phase model described in Chapter 6, as the devolatilization peak is mildly affected by the presence of oxygen^{432,485}. The initial char composition considered is the one predicted by the PET kinetic model at the DTG local minimum, while the correlations developed for biochars are employed to supplement the missing information. These are strong sources of uncertainty for the model. On the one hand, the PET and bio char share a similar aromatic network. A difference in cluster size is present, but the correlation accounts for this through the high hydrogen content of the PET char (~4 wt.%). On the

other hand, the devolatilization processes are possibly significantly different because of the different types of starting materials. PET char has been observed to have high BET surface areas even at low hydrogen content¹⁶⁶, and therefore the wood correlation, i. e., the one with the highest maximum value, is considered.

Figure 8.2 shows the comparison varying the heating rate. Reasonable agreement is observed between experimental data and model predictions, well within the high uncertainties involved, both in terms of elemental composition, structural information, and decoupling of devolatilization-oxidation. While it overestimates the degradation temperatures, it captures the spread of the degradation profiles, i. e., the apparent activation energy of the process. In terms of shapes, the model considers steeper profiles, mainly because all hydrogen is represented as phenyl kind, which involves high activation energies to decompose. The presence of ashes is expected also to smooth the predicted mass profiles. The model exhibits similar results also in terms of oxygen effect (although not shown here). While it overestimates degradation temperatures consistently with the previous case, it captures the effect of the different gaseous environments.

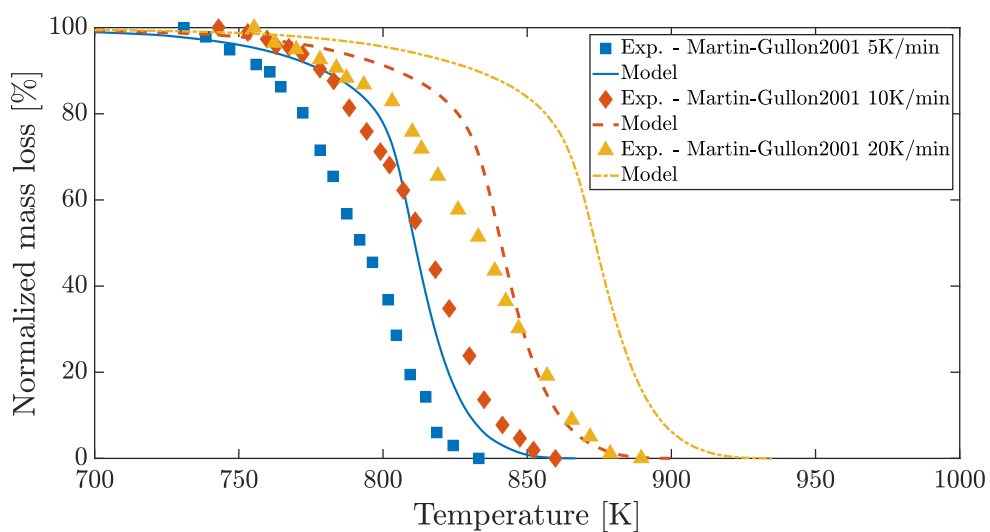


Figure 8.2: Oxidation step of chars obtained by direct oxidation of PET at different heating rates. Comparison of model predictions (lines) and literature⁴³² experimental results (marks)

Further work is required to describe the reactivity of plastic chars, specifically in gasification conditions. Ad hoc experimental data targeted for these studies can aid to improve the model. Additional development is required also to describe the energy balances associated with the degradation profiles. As with oxidation, developing a framework based on biochar gasification is expected to aid in modelling also plastic chars valorization.

8.3 CONCLUSIONS

The kinetic models proposed in the present Ph.D. thesis constitute a step towards a sustainable and circular plastic economy. Business-as-usual is no longer a viable option, and reshaping the current economic system is required to prioritize long-term environmental health. Thermochemical recycling technologies are investigated due to their promising applicability and flexibility to address plastic waste. Converting PW into valuable fuels and chemicals, decreases the reliance on fossil fuels lowering greenhouse gas emissions. Additionally, it avoids landfilling and incineration of PW, preventing plastic pollution from entering the environment. These technologies are complementary approaches to other processes as mechanical and solvent recycling for highly contaminated waste. Chemical kinetics in combination with Computational Fluid Dynamic tools are required to design and optimize these processes.

BIBLIOGRAPHY

1. Andrade, A. L. & Neal, M. A. Applications and societal benefits of plastics. *Philosophical Transactions of the Royal Society B: Biological Sciences* **364**, 1977–1984 (2009).
2. MacArthur, D. E., Waughray, D. & Stuchtey, M. R. *The new plastics economy, rethinking the future of plastics* in *World Economic Forum* **17** (2016).
3. Kearney, A. T. Plastics. *The Future for Automakers and Chemical Companies* (2012).
4. Plastics Europe. The Circular Economy for Plastics, 1–114 (2024).
5. Geyer, R., Jambeck, J. R. & Law, K. L. Production, use, and fate of all plastics ever made. *Science Advances* **3** (2017).
6. OECD. *Global Plastics Outlook: Economic Drivers, Environmental Impacts and Policy Options* tech. rep. (2022).
7. Ragaert, K., Delva, L. & Van Geem, K. Mechanical and chemical recycling of solid plastic waste. *Waste Management* **69**, 24–58 (2017).
8. Thompson, R. C., Moore, C. J., Saal, F. S. & Swan, S. H. Plastics, the environment and human health: current consensus and future trends. *Philosophical Transactions of the Royal Society B: Biological Sciences* **364**, 2153–2166 (2009).
9. Hale, R. C., Seeley, M. E., La Guardia, M. J., Mai, L. & Zeng, E. Y. A Global Perspective on Microplastics. *Journal of Geophysical Research: Oceans* **125**, e2018JC014719 (2020).
10. Cox, K. D., Covernton, G. A., Davies, H. L., Dower, J. F., Juanes, F. & Dudas, S. E. Human Consumption of Microplastics. *Environmental Science and Technology* **53**, 7068–7074 (2019).
11. Law, K. L. & Thompson, R. C. Microplastics in the seas. *Science* **345**, 144–145 (2014).
12. Čverenkárová, K., Valachovičová, M., Mackul'ák, T., Žemlička, L. & Bírošová, L. *Microplastics in the food chain* 2021.
13. OECD. *Global Plastics Outlook: Policy Scenarios to 2060* tech. rep. (2022).
14. Singh, N., Hui, D., Singh, R., Ahuja, I. P., Feo, L. & Fraternali, F. Recycling of plastic solid waste: A state of art review and future applications. *Composites Part B: Engineering* (2017).
15. Dogu, O., Pelucchi, M., Van de Vijver, R., Van Steenberge, P. H., D'hooge, D. R., Cuoci, A., Mehl, M., Frassoldati, A., Faravelli, T. & Van Geem, K. M. The chemistry of chemical recycling of solid plastic waste via pyrolysis and gasification: State-of-the-art, challenges, and future directions. *Progress in Energy and Combustion Science* **84**, 100901 (2021).
16. Directive 2008/98/EC of the European Parliament and of the Council of 19 November 2008 on waste and repealing certain Directives. *Official Journal of the European Union* **312**, 22 (2008).
17. Rahimi, A. R. & Garcíá, J. M. Chemical recycling of waste plastics for new materials production. *Nature Reviews Chemistry* **2017 1:6** 1, 1–11 (2017).

18. Shi, C., Reilly, L. T., Phani Kumar, V. S., Coile, M. W., Nicholson, S. R., Broadbelt, L. J., Beckham, G. T. & Chen, E. Y. *Design principles for intrinsically circular polymers with tunable properties* 2021.
19. Al-Salem, S. M., Lettieri, P. & Baeyens, J. Recycling and recovery routes of plastic solid waste (PSW): A review. *Waste Management* **29**, 2625–2643 (2009).
20. Britannica, T. E. o. E. *Plastic* 2024.
21. Van Krevelen, D. W. *Properties of Polymers: Their Correlation with Chemical Structure; their Numerical Estimation and Prediction from Additive Group Contributions: Fourth Edition* 1–1004 (Elsevier, 2009).
22. Plastics Europe. *Plastics - the fast facts* tech. rep. (2023).
23. Ferrando, A. & Nodari, M. SPW feedstock characterization. *Advances in Chemical Engineering* **60**, 1–20 (2022).
24. Brems, A., Baeyens, J. & Dewil, R. Recycling and recovery of post-consumer plastic solid waste in a European context. *Thermal Science* **16**, 669–685 (2012).
25. Brivio, L. & Tollini, F. in *Advances in Chemical Engineering* 1, 215–267 (Academic Press, 2022).
26. Zia, K. M., Bhatti, H. N. & Ahmad Bhatti, I. Methods for polyurethane and polyurethane composites, recycling and recovery: A review. *Reactive and Functional Polymers* **67**, 675–692 (2007).
27. Brems, A., Dewil, R., Baeyens, J. & Zhang, R. in *Solid Waste as a Renewable Resource: Methodologies* 241–264 (Apple Academic Press, 2015).
28. Arena, U. Process and technological aspects of municipal solid waste gasification. A review. *Waste Management* **32**, 625–639 (2012).
29. Al-Sabagh, A. M., Yehia, F. Z., Eshaq, G. & ElMetwally, A. E. Ionic Liquid-Coordinated Ferrous Acetate Complex Immobilized on Bentonite As a Novel Separable Catalyst for PET Glycolysis. *Industrial and Engineering Chemistry Research* **54**, 12474–12481 (2015).
30. Zhan, L., Jiang, L., Zhang, Y., Gao, B. & Xu, Z. *Reduction, detoxification and recycling of solid waste by hydrothermal technology: A review* 2020.
31. Czajczynska, D., Anguilano, L., Ghazal, H., Krzyzynska, R., Reynolds, A. J., Spencer, N. & Jouhara, H. Potential of pyrolysis processes in the waste management sector. *Thermal Science and Engineering Progress* **3**, 171–197 (2017).
32. Ranzi, E., Faravelli, T. & Manenti, F. in *Advances in Chemical Engineering* 1–94 (Academic Press, 2016).
33. Anderson, J. *Computational Fluid Dynamics: The Basics with Application*. McGrawhill Inc, 1–547 (1995).
34. Madanikashani, S., Vandewalle, L. A., De Meester, S., De Wilde, J. & Van Geem, K. M. Multi-Scale Modeling of Plastic Waste Gasification: Opportunities and Challenges. *Materials* **15**, 4215 (2022).
35. Marongiu, A., Faravelli, T., Bozzano, G., Dente, M. & Ranzi, E. Thermal degradation of poly(vinyl chloride). *Journal of Analytical and Applied Pyrolysis* **70**, 519–553 (2003).

36. Mehl, M., Marongiu, A., Faravelli, T., Bozzano, G., Dente, M. & Ranzi, E. A kinetic modeling study of the thermal degradation of halogenated polymers. *Journal of Analytical and Applied Pyrolysis* **72**, 253–272 (2004).
37. Ranzi, E., Cuoci, A., Faravelli, T., Frassoldati, A., Migliavacca, G., Pierucci, S. & Sommariva, S. Chemical kinetics of biomass pyrolysis. *Energy and Fuels* **22**, 4292–4300 (2008).
38. Solis, M. & Silveira, S. Technologies for chemical recycling of household plastics – A technical review and TRL assessment. *Waste Management* **105**, 128–138 (2020).
39. Chen, D., Yin, L., Wang, H. & He, P. Pyrolysis technologies for municipal solid waste: A review. *Waste Management* **34**, 2466–2486 (2014).
40. Lombardi, L., Carnevale, E. & Corti, A. A review of technologies and performances of thermal treatment systems for energy recovery from waste. *Waste Management* **37**, 26–44 (2015).
41. Ranzi, E., Debiagi, P. E. A. & Frassoldati, A. Mathematical Modeling of Fast Biomass Pyrolysis and Bio-Oil Formation. Note I: Kinetic Mechanism of Biomass Pyrolysis. *ACS Sustainable Chemistry & Engineering* **5**, 2867–2881 (2017).
42. Locaspi, A., Ferri, M., Serse, F., Maestri, M. & Pelucchi, M. *Chemical kinetics of catalytic/non-catalytic pyrolysis and gasification of solid plastic wastes* **1**, 21–76 (Academic Press, 2022).
43. Dente, M., Bozzano, G., Faravelli, T., Marongiu, A., Pierucci, S. & Ranzi, E. Kinetic Modelling of Pyrolysis Processes in Gas and Condensed Phase. *Advances in Chemical Engineering* **32**, 51–166 (2007).
44. Kaminsky, W. Chemical recycling of mixed plastics of pyrolysis. *Advances in Polymer Technology* **14**, 337–344 (1995).
45. Adrados, A., de Marco, I., Caballero, B. M., López, A., Laresgoiti, M. F. & Torres, A. Pyrolysis of plastic packaging waste: A comparison of plastic residuals from material recovery facilities with simulated plastic waste. *Waste Management* **32**, 826–832 (2012).
46. Milbrandt, A., Coney, K., Badgett, A. & Beckham, G. T. Quantification and evaluation of plastic waste in the United States. *Resources, Conservation and Recycling* **183** (2022).
47. Koo, J. K. & Kim, S. W. Reaction Kinetic Model For Optimal Pyrolysis Of Plastic Waste Mixtures. *Waste Management & Research* **11**, 515–529 (1993).
48. Sommariva, S., Grana, R., Maffei, T., Pierucci, S. & Ranzi, E. A kinetic approach to the mathematical model of fixed bed gasifiers. *Computers & Chemical Engineering* **35**, 928–935 (2011).
49. Bhaskar, T., Kaneko, J., Muto, A., Sakata, Y., Jakab, E., Matsui, T. & Uddin, M. A. Pyrolysis studies of PP/PE/PS/PVC/HIPS-Br plastics mixed with PET and dehalogenation (Br, Cl) of the liquid products. *Journal of Analytical and Applied Pyrolysis* **72**, 27–33 (2004).
50. Knümann, R. & Bockhorn, H. Investigation of the Kinetics of Pyrolysis of PVC by TG-MS-Analysis. *Combustion Science and Technology* **101**, 285–299 (1994).
51. Horstemeyer, M. F. Multiscale modeling: A review. *Practical Aspects of Computational Chemistry: Methods, Concepts and Applications*, 87–135 (2010).
52. Hughes, T. J. Multiscale phenomena: Green's functions, the Dirichlet-to-Neumann formulation, subgrid scale models, bubbles and the origins of stabilized methods. *Computer Methods in Applied Mechanics and Engineering* **127**, 387–401 (1995).

53. Maestri, M. & Cuoci, A. Coupling CFD with detailed microkinetic modeling in heterogeneous catalysis. *Chemical Engineering Science* **96**, 106–117 (2013).
54. Wehinger, G. D. *et al.* Quo vadis multiscale modeling in reaction engineering? – A perspective. *Chemical Engineering Research and Design* **184**, 39–58 (2022).
55. Ranzi, E., Dente, M., Faravelli, T., Bozzano, G., Fabini, S., Nava, R., Cozzani, V. & Tognotti, L. Kinetic modeling of polyethylene and polypropylene thermal degradation. *Journal of Analytical and Applied Pyrolysis* **40-41**, 305–319 (1997).
56. Marongiu, A. *Thermal Decomposition of Polymers* PhD thesis (Politecnico di Milano, 2006).
57. Marongiu, A., Faravelli, T. & Ranzi, E. Detailed kinetic modeling of the thermal degradation of vinyl polymers. *Journal of Analytical and Applied Pyrolysis* **78**, 343–362 (2007).
58. Benson, S. W. *Thermochemical kinetics* (1976).
59. Dickens, B. Thermally degrading polyethylene studied by means of factor-jump thermogravimetry. *Journal of Polymer Science: Polymer Chemistry Edition* **20**, 1065–1087 (1982).
60. Woo, O. S. & Broadbelt, L. J. Recovery of high-valued products from styrene-based polymers through coprocessing: Experiments and mechanistic modeling. *Catalysis Today* **40**, 121–140 (1998).
61. Kruse, T. M., Woo, O. S., Wong, H. W., Khan, S. S. & Broadbelt, L. J. Mechanistic Modeling of Polymer Degradation: A Comprehensive Study of Polystyrene. *Macromolecules* **35**, 7830–7844 (2002).
62. Wong, H. W., Kruse, T. M., Woo, O. S. & Broadbelt, L. J. Tertiary resource recovery from waste polymers via pyrolysis: Polypropylene. *ACS Division of Fuel Chemistry, Preprints* **45**, 480–481 (2000).
63. Nising, P. *High-Temperature Radical Polymerization of Methyl Methacrylate in a Continuous Pilot Scale Process* PhD thesis (Ecole Polytechnique Federal de Lausanne, 2006).
64. Moens, E. K. C., De Smit, K., Marien, Y. W., Trigilio, A. D., Van Steenberge, P. H. M., Van Geem, K. M., Dubois, J. L. & D'hooge, D. R. Progress in Reaction Mechanisms and Reactor Technologies for Thermochemical Recycling of Poly(methyl methacrylate). *Polymers* **2020**, Vol. 12, Page 1667 **12**, 1667 (2020).
65. Faravelli, T., Bozzano, G., Scassa, C., Perego, M., Fabini, S., Ranzi, E. & Dente, M. Gas product distribution from polyethylene pyrolysis. *Journal of Analytical and Applied Pyrolysis* **52**, 87–103 (1999).
66. Faravelli, T., Pincioli, M., Pisano, F., Bozzano, G., Dente, M. & Ranzi, E. Thermal degradation of polystyrene. *Journal of Analytical and Applied Pyrolysis* **60**, 103–121 (2001).
67. Levine, S. E. & Broadbelt, L. J. Detailed mechanistic modeling of high-density polyethylene pyrolysis: Low molecular weight product evolution. *Polymer Degradation and Stability* **94**, 810–822 (2009).
68. Kruse, T. M., Wong, H. W. & Broadbelt, L. J. Mechanistic Modeling of Polymer Pyrolysis: Polypropylene. *Macromolecules* **36**, 9594–9607 (2003).
69. Mastral, J. F., Berrueco, C & Ceamanos, J. Theoretical prediction of product distribution of the pyrolysis of high density polyethylene. *Journal of Analytical and Applied Pyrolysis* **80**, 427–438 (2007).

70. Beuermann, S., Harrisson, S., Hutchinson, R. A., Junkers, T. & Russell, G. T. Update and critical reanalysis of IUPAC benchmark propagation rate coefficient data. *Polymer Chemistry* **13**, 1891–1900 (2022).
71. Harmon, R. E., Sribala, G., Broadbelt, L. J. & Burnham, A. K. Insight into Polyethylene and Polypropylene Pyrolysis: Global and Mechanistic Models. *Energy & Fuels* **35**, 6765–6775 (2021).
72. Poutsma, M. L. Further considerations of the sources of the volatiles from pyrolysis of polystyrene. *Polymer Degradation and Stability* **94**, 2055–2064 (2009).
73. Kruse, T. M., Wong, H. W. & Broadbelt, L. J. Modeling the evolution of the full polystyrene molecular weight distribution during polystyrene pyrolysis. *Industrial and Engineering Chemistry Research* **42**, 2722–2735 (2003).
74. Locaspi, A., Pelucchi, M., Mehl, M. & Faravelli, T. Towards a lumped approach for solid plastic waste gasification: polyethylene and polypropylene pyrolysis. *Waste Management* **156**, 107–117 (2022).
75. Audisio, G. & Bertini, F. Molecular weight and pyrolysis products distribution of polymers. I. Polystyrene. *Journal of Analytical and Applied Pyrolysis* **24**, 61–74 (1992).
76. Poutsma, M. L. Reexamination of the Pyrolysis of Polyethylene: Data Needs, Free-Radical Mechanistic Considerations, and Thermochemical Kinetic Simulation of Initial Product-Forming Pathways. *Macromolecules* **36**, 8931–8957 (2003).
77. Poutsma, M. L. Comparison of literature models for volatile product formation from the pyrolysis of polyisobutylene at mild conditions: Data analysis, free-radical mechanistic considerations, and simulation of initial product-forming pathways. *Journal of Analytical and Applied Pyrolysis* **73**, 159–203 (2005).
78. Kaminsky, W. & Eger, C. Pyrolysis of filled PMMA for monomer recovery. *Journal of Analytical and Applied Pyrolysis* **58-59**, 781–787 (2001).
79. Vinu, R. & Broadbelt, L. J. A mechanistic model of fast pyrolysis of glucose-based carbohydrates to predict bio-oil composition. *Energy & Environmental Science* **5**, 9808 (2012).
80. Yu, J., Sun, L., Ma, C., Qiao, Y. & Yao, H. *Thermal degradation of PVC: A review* 2016.
81. Huang, J., Li, X., Zeng, G., Cheng, X., Tong, H. & Wang, D. Thermal decomposition mechanisms of poly(vinyl chloride): A computational study. *Waste Management* **76**, 483–496 (2018).
82. Pelucchi, M., Cavallotti, C., Ranzi, E., Frassoldati, A. & Faravelli, T. Relative Reactivity of Oxygenated Fuels: Alcohols, Aldehydes, Ketones, and Methyl Esters. *Energy and Fuels* **30**, 8665–8679 (2016).
83. Sun, W., Tao, T., Zhang, R., Liao, H., Huang, C., Zhang, F., Zhang, X., Zhang, Y. & Yang, B. Experimental and modeling efforts towards a better understanding of the high-temperature combustion kinetics of C₃C₅ ethyl esters. *Combustion and Flame* **185**, 173–187 (2017).
84. Cavallotti, C., Pelucchi, M. & Frassoldati, A. Analysis of acetic acid gas phase reactivity: Rate constant estimation and kinetic simulations. *Proceedings of the Combustion Institute* **37**, 539–546 (2019).

85. Huang, J., Meng, H., Luo, X., Mu, X., Xu, W., Jin, L. & Lai, B. Insights into the thermal degradation mechanisms of polyethylene terephthalate dimer using DFT method. *Chemosphere* **291**, 133112 (2022).
86. Bockhorn, H., Hornung, A. & Hornung, U. Mechanisms and kinetics of thermal decomposition of plastics from isothermal and dynamic measurements. *Journal of Analytical and Applied Pyrolysis* **50**, 77–101 (1999).
87. Dhahak, A., Grimmer, C., Neumann, A., Rüger, C., Sklorz, M., Streibel, T., Zimmermann, R., Mauviel, G. & Burkle-Vitzthum, V. Real time monitoring of slow pyrolysis of polyethylene terephthalate (PET) by different mass spectrometric techniques. *Waste Management* **106**, 226–239 (2020).
88. Ohtani, H., Kimura, T., Okamoto, K., Tsuge, S., Nagataki, Y. & Miyata, K. Characterization of polyurethanes by high-resolution pyrolysis-capillary gas chromatography. *Journal of Analytical and Applied Pyrolysis* **12**, 115–133 (1987).
89. Oenema, J., Liu, H., Coensel, N. D., Eschenbacher, A., Van de Vijver, R., Weng, J., Li, L., Wang, C. & Van Geem, K. M. Review on the pyrolysis products and thermal decomposition mechanisms of polyurethanes. *Journal of Analytical and Applied Pyrolysis* **168**, 105723 (2022).
90. Allan, R. J. P., Forman, R. L. & Ritchie, P. D. Studies in pyrolysis. Part IV. Model systems for the pyrolysis of poly(ethylene terephthalate) and allied polyesters. *Journal of the Chemical Society (Resumed)*, 2717 (1955).
91. Allan, R. J. P. *A study of the pyrolysis of poly(ethylene terephthalate) by means of model systems* PhD thesis (University of Glasgow, 1956).
92. Allan, R. J., Jones, E. & Ritchie, P. D. 104. Studies in pyrolysis. Part VIII. Competitive routes in the pyrolysis of esters: alkylene and alkylidene dibenzoates and some related substances. *Journal of the Chemical Society (Resumed)*, 524–531 (1957).
93. Buxbaum, L. H. The Degradation of Poly(ethylene terephthalate). *Angewandte Chemie International Edition in English* **7**, 182–190 (1968).
94. Reimschuessel, H. K. Poly(ethylene terephthalate) Formation. Mechanistic and Kinetic Aspects of the Direct Esterification Process. *Ind. Eng. Chem. Prod. Res. Dev* **19**, 117–125 (1980).
95. Dröscher, M. & Georg Schmidt, F. The kinetics of the ester-interchange reaction of poly(ethylene terephthalate). *Polymer Bulletin* **4**, 261–266 (1981).
96. Carlsson, D. J., Day, M., Suprunchuk, T. & Wiles, D. M. Pyrolysis of poly(ethylene terephthalate) fibers: Characterization of involatile residues. *Journal of Applied Polymer Science* **28**, 715–724 (1983).
97. Halek, G. W. Zero-Order Kinetics of acetaldehyde thermal generation from polyethylene terephthalate. *Journal of polymer science. Part C, Polymer symposia*, 83–92 (1986).
98. Montaudo, G., Puglisi, C. & Samperi, F. Primary thermal degradation mechanisms of PET and PBT. *Polymer Degradation and Stability* **42**, 13–28 (1993).
99. Dhahak, A., Hild, G., Rouaud, M., Mauviel, G. & Burkle-Vitzthum, V. Slow pyrolysis of polyethylene terephthalate: Online monitoring of gas production and quantitative analysis of waxy products. *Journal of Analytical and Applied Pyrolysis* **142**, 104664 (2019).

100. Linstrom, P. J. & Mallard, W. G. The NIST Chemistry WebBook: A Chemical Data Resource on the Internet. *Journal of Chemical and Engineering Data* **46**, 1059–1063 (2001).
101. Day, M. & Wiles, D. M. Influence of temperature and environment on the thermal decomposition of poly(ethylene terephthalate) fibres with and without the flame retardant tris(2,3-dibromopropyl) phosphate. *Journal of Analytical and Applied Pyrolysis* **7**, 65–82 (1984).
102. Faravelli, T., Frassoldati, A., Migliavacca, G. & Ranzi, E. Detailed kinetic modeling of the thermal degradation of lignins. *Biomass and Bioenergy* **34**, 290–301 (2010).
103. Mielczarek, D. C., Matrat, M., Amara, A. B., Bouyou, Y., Wund, P. & Starck, L. Toward the Accurate Prediction of Liquid Phase Oxidation of Aromatics: A Detailed Kinetic Mechanism for Toluene Autoxidation. *Energy and Fuels* **31**, 12893–12913 (2017).
104. Curran, H. J. Rate constant estimation for C₁ to C₄ alkyl and alkoxy radical decomposition. *International Journal of Chemical Kinetics* **38**, 250–275 (2006).
105. Pratali Maffei, L., Faravelli, T., Cavallotti, C. & Pelucchi, M. Electronic structure-based rate rules for H ipso addition-elimination reactions on mono-aromatic hydrocarbons with single and double OH/CH 3 /OCH 3 /CHO/C 2 H 5 substituents: a systematic theoretical investigation. *Physical Chemistry Chemical Physics* **22**, 20368–20387 (2020).
106. Bockhorn, H., Hornung, A., Hornung, U. & Weichmann, J. Kinetic study on the non-catalysed and catalysed degradation of polyamide 6 with isothermal and dynamic methods. *Thermochimica Acta* **337**, 97–110 (1999).
107. Locaspi, A., Pelucchi, M., Batista da Silva Junior, R., Mehl, M., Cuoci, A., Frassoldati, A., Beretta, A., Lietti, L. & Faravelli, T. *Thermal Degradation of Nylon-6 and Real Mixtures of Solid Plastic Waste. An Experimental and Kinetic Modeling Study* in *43rd ASICI meeting* (Ischia, 2021).
108. Bockhorn, H., Hornung, A., Hornung, U. & Jakobströer, P. Modelling of isothermal and dynamic pyrolysis of plastics considering non-homogeneous temperature distribution and detailed degradation mechanism. *Journal of Analytical and Applied Pyrolysis* **49**, 53–74 (1999).
109. Kumagai, S., Motokicho, S., Yabuki, R., Anzai, A., Kameda, T., Watanabe, A., Nakatani, H. & Yoshioka, T. Effects of hard- and soft-segment composition on pyrolysis characteristics of MDI, BD, and PTMG-based polyurethane elastomers. *Journal of Analytical and Applied Pyrolysis* **126**, 337–345 (2017).
110. Chattopadhyay, D. K. & Webster, D. C. Thermal stability and flame retardancy of polyurethanes. *Progress in Polymer Science* **34**, 1068–1133 (2009).
111. Ravey, M & Pearce, E. M. Flexible polyurethane foam. I. Thermal decomposition of a polyether-based, water-blown commercial type of flexible polyurethane foam. *Journal of Applied Polymer Science* **63** (1998).
112. Grassie, N., Zulfiqar, M. & Guy, M. I. Thermal degradation of a series of polyester polyurethanes. *Journal of Polymer Science: Polymer Chemistry Edition* **18**, 265–274 (1980).
113. Faravelli, T., Bozzano, G., Colombo, M., Ranzi, E. & Dente, M. Kinetic modeling of the thermal degradation of polyethylene and polystyrene mixtures. *Journal of Analytical and Applied Pyrolysis* **70**, 761–777 (2003).

114. Kruse, T. M., Levine, S. E., Wong, H. W., Duoss, E., Lebovitz, A. H., Torkelson, J. M. & Broadbelt, L. J. Binary mixture pyrolysis of polypropylene and polystyrene: A modeling and experimental study. *Journal of Analytical and Applied Pyrolysis* **73**, 342–354 (2005).
115. Chao-Hsiung Wu, Ching-Yuan Chang, Jwo-Luen Hor, Shin-Min Shih, Leo-Wang Chen & Feng-Wen Chang. On the thermal treatment of plastic mixtures of MSW: Pyrolysis kinetics. *Waste Management* **13**, 221–235 (1993).
116. Miranda, R., Yang, J., Roy, C. & Vasile, C. Vacuum pyrolysis of commingled plastics containing PVC I. Kinetic study. *Polymer Degradation and Stability* **72**, 469–491 (2001).
117. Czégény, Z. & Blazsó, M. Thermal decomposition of polyamides in the presence of poly(vinyl chloride). *Journal of Analytical and Applied Pyrolysis* **58-59**, 95–104 (2001).
118. Kulesza, K. & German, K. Chlorinated pyrolysis products of co-pyrolysis of poly(vinyl chloride) and poly(ethylene terephthalate). *Journal of Analytical and Applied Pyrolysis* **67**, 123–134 (2003).
119. Coralli, I., Giorgi, V., Vassura, I., Rombolà, A. G. & Fabbri, D. Secondary reactions in the analysis of microplastics by analytical pyrolysis. *Journal of Analytical and Applied Pyrolysis* **161**, 105377 (2022).
120. Li, B., Wang, X., Xia, Z., Zhou, W., Wu, Y. & Zhu, G. Co-pyrolysis of waste polyester enameled wires and polyvinyl chloride: Evolved products and pyrolysis mechanism analysis. *Journal of Analytical and Applied Pyrolysis* **169**, 105816 (2023).
121. Perez, B. A., Jayarama Krishna, J. V. & Toraman, H. E. Insights into co-pyrolysis of poly-ethylene terephthalate and polyamide 6 mixture through experiments, kinetic modeling and machine learning. *Chemical Engineering Journal* **468**, 143637 (2023).
122. Prud'homme, R. E. Miscibility phenomena in polyester/chlorinated polymer blends. *Polymer Engineering & Science* **22**, 90–95 (1982).
123. Aubin, M. & Prud'Homme, R. E. A study of aromatic polyester/chlorinated polymer blends. *Polymer Engineering & Science* **24**, 350–354 (1984).
124. Goulet, L. & Prud'Homme, R. E. Dégradation thermique de mélanges miscibles et immiscibles polyester/polychlorure de vinyle. *European Polymer Journal* **22**, 529–536 (1986).
125. Alberda Van Ekenstein, G. O., Deuring, H., Ten Brinke, G. & Ellis, T. S. Blends of caprolactam/caprolactone copolymers and chlorinated polymers. *Polymer* **38**, 3025–3034 (1997).
126. Ellis, T. S. Phase behaviour of polyamide—polyester blends: the influence of aromaticity. *Polymer* **38**, 3837–3841 (1997).
127. Xiong, C., Lu, S., Wang, T., Hong, Y., Chen, T. & Zhou, Z. Study on morphology of compatibilized poly (vinyl chloride)/ultrafine polyamide-6 blends by styrene–maleic anhydride. *Journal of Applied Polymer Science* **97**, 850–854 (2005).
128. Hsiao, K., Shu, Y. C. & Tsen, W. C. Thermal and Mechanical Properties of Polyblends of Polycaprolactam with Cationic Dyeable Poly(ethylene terephthalate). *Journal of Polymer Research* **10**, 161–169 (2003).
129. Serhatkulu, T., Erman, B., Bahar, I., Fakirov, S., Evstatiev, M. & Sapundjieva, D. Dynamic mechanical study of amorphous phases in poly(ethylene terephthalate) /nylon-6 blends. *Polymer* **36**, 2371–2377 (1995).

130. Avella, M., Cosco, S., Di Lorenzo, M. L., Di Pace, E., Errico, M. E. & Gentile, G. Nucleation activity of nanosized CaCO₃ on crystallization of isotactic polypropylene, in dependence on crystal modification, particle shape, and coating. *European Polymer Journal* **42**, 1548–1557 (2006).
131. López, A., De Marco, I., Caballero, B. M., Laresgoiti, M. F. & Adrados, A. Dechlorination of fuels in pyrolysis of PVC containing plastic wastes. *Fuel Processing Technology* **92**, 253–260 (2011).
132. De Oliveira, L. P., Hudebine, D., Guillaume, D. & Verstraete, J. J. A Review of Kinetic Modeling Methodologies for Complex Processes. *Oil & Gas Science and Technology – Revue d'IFP Energies nouvelles* **71**, 45 (2016).
133. Ranzi *et al.* Reduced kinetic schemes of complex reaction systems: Fossil and biomass-derived transportation fuels. *International Journal of Chemical Kinetics* **46**, 512–542 (2014).
134. Aguado, R., Olazar, M., Gaisán, B., Prieto, R. & Bilbao, J. Kinetics of polystyrene pyrolysis in a conical spouted bed reactor. *Chemical Engineering Journal* **92**, 91–99 (2003).
135. Neeft, J. P. A., Hoornaert, F., Makkee, M. & Moulijn, J. A. The effects of heat and mass transfer in thermogravimetical analysis. A case study towards the catalytic oxidation of soot. *Thermochimica Acta* **287**, 261–278 (1996).
136. Zhao, D., Wang, X., Miller, J. B. & Huber, G. W. The Chemistry and Kinetics of Polyethylene Pyrolysis: A Process to Produce Fuels and Chemicals. *ChemSusChem* **13**, 1764–1774 (2020).
137. Westerhout, R. W., Waanders, J., Kuipers, J. A. & Van Swaaij, W. P. Kinetics of the Low-Temperature Pyrolysis of Polyethene, Polypropene, and Polystyrene Modeling, Experimental Determination, and Comparison with Literature Models and Data. *Industrial and Engineering Chemistry Research* **36**, 1955–1964 (1997).
138. Bouster, C., Vermande, P. & Veron, J. Study of the pyrolysis of polystyrenes: I. Kinetics of thermal decomposition. *Journal of Analytical and Applied Pyrolysis* **1**, 297–313 (1980).
139. Brems, A., Baeyens, J., Beerlandt, J. & Dewil, R. Thermogravimetric pyrolysis of waste polyethylene-terephthalate and polystyrene: A critical assessment of kinetics modelling. *Resources, Conservation and Recycling* **55**, 772–781 (2011).
140. Flynn, J. H. & Wall, L. A. General treatment of the thermogravimetry of polymers. *Journal of Research of the National Bureau of Standards Section A: Physics and Chemistry* **70A**, 487 (1966).
141. Wang, L., Chai, M., Liu, R. & Cai, J. Synergetic effects during co-pyrolysis of biomass and waste tire: A study on product distribution and reaction kinetics. *Bioresource Technology* **268**, 363–370 (2018).
142. Tilghman, M. B. & Mitchell, R. E. Coal and biomass char reactivities in gasification and combustion environments. *Combustion and Flame* **162**, 3220–3235 (2015).
143. Sorum, L., Gronli, M. G. & Hustad, J. E. Pyrolysis characteristics and kinetics of municipal solid wastes. *Fuel* **80**, 1217–1227 (2001).
144. Yousef, S., Eimontas, J., Striugas, N. & Abdelnaby, M. A. Modeling of Metalized Food Packaging Plastics Pyrolysis Kinetics Using an Independent Parallel Reactions Kinetic Model. *Polymers* **2020**, Vol. 12, Page 1763 **12**, 1763 (2020).

145. Németh, A., Blazsó, M., Baranyai, P. & Vidóczy, T. Thermal degradation of polyethylene modeled on tetracontane. *Journal of Analytical and Applied Pyrolysis* **81**, 237–242 (2008).
146. Ranzi, E., Dente, M., Goldaniga, A., Bozzano, G. & Faravelli, T. *Lumping procedures in detailed kinetic modeling of gasification, pyrolysis, partial oxidation and combustion of hydrocarbon mixtures* 2001.
147. Nobili, A., Cuoci, A., Pejpichestakul, W., Pelucchi, M., Cavallotti, C. & Faravelli, T. Modeling soot particles as stable radicals: a chemical kinetic study on formation and oxidation. Part I. Soot formation in ethylene laminar premixed and counterflow diffusion flames. *Combustion and Flame* **243**, 112073 (2022).
148. Bamford, C. H. & Tompa, H. The calculation of molecular weight distributions from kinetic schemes. *Transactions of the Faraday Society* **50**, 1097–1115 (1954).
149. Wang, M., Smith, J. M. & McCoy, B. J. Continuous kinetics for thermal degradation of polymer in solution. *AIChE Journal* **41**, 1521–1533 (1995).
150. Mastan, E. & Zhu, S. Method of moments: A versatile tool for deterministic modeling of polymerization kinetics. *European Polymer Journal* **68**, 139–160 (2015).
151. Mueller, M. E., Blanquart, G. & Pitsch, H. Hybrid Method of Moments for modeling soot formation and growth. *Combustion and Flame* **156**, 1143–1155 (2009).
152. Debiagi, P., Gentile, G., Cuoci, A., Frassoldati, A., Ranzi, E. & Faravelli, T. A predictive model of biochar formation and characterization. *Journal of Analytical and Applied Pyrolysis* **134**, 326–335 (2018).
153. Gillespie, D. T. A general method for numerically simulating the stochastic time evolution of coupled chemical reactions. *Journal of Computational Physics* **22**, 403–434 (1976).
154. Gillespie, D. T. Exact stochastic simulation of coupled chemical reactions. *Journal of Physical Chemistry* **81**, 2340–2361 (1977).
155. Gillespie, D. T. Stochastic Simulation of Chemical Kinetics. *Annual Review of Physical Chemistry* **58**, 35–55 (2007).
156. Tobita, H. Simultaneous Long-Chain Branching and Random Scission: I. Monte Carlo Simulation. *J Polym Sci B: Polym Phys* **39**, 391–403 (2001).
157. Iedema, P. D., Remerie, K., Seegers, D. & McAuley, K. B. Tacticity Changes during Controlled Degradation of Polypropylene. *Macromolecules* **54**, 8921–8935 (2021).
158. Dogu, O., Eschenbacher, A., John Varghese, R., Dobbelaere, M., D'hooge, D. R., Van Steenberge, P. H. & Van Geem, K. M. Bayesian tuned kinetic Monte Carlo modeling of polystyrene pyrolysis: Unraveling the pathways to its monomer, dimers, and trimers formation. *Chemical Engineering Journal* **455**, 140708 (2023).
159. Pires da Mata Costa, L., Brandão, A. L. & Pinto, J. C. Modeling of polystyrene degradation using kinetic Monte Carlo. *Journal of Analytical and Applied Pyrolysis* **167**, 105683 (2022).
160. Poutsma, M. L. Mechanistic analysis and thermochemical kinetic simulation of the products from pyrolysis of poly(α -methylstyrene), especially the unrecognized role of phenyl shift. *Journal of Analytical and Applied Pyrolysis* **80**, 439–452 (2007).

161. Moens, E. K., Marien, Y. W., Figueira, F. L., Trigilio, A. D., De Smit, K., Van Geem, K. M., Van Steenberge, P. H. & D'hooge, D. R. Coupled matrix-based Monte Carlo modeling for a mechanistic understanding of poly (methyl methacrylate) thermochemical recycling kinetics. *Chemical Engineering Journal* **475**, 146105 (2023).
162. Bracconi, M. & Maestri, M. Training set design for machine learning techniques applied to the approximation of computationally intensive first-principles kinetic models. *Chemical Engineering Journal* **400**, 125469 (2020).
163. Kashiwagi, T. & Ohlemiller, T. J. A study of oxygen effects on nonflaming transient gasification of PMMA and PE during thermal irradiation. *Symposium (International) on Combustion* **19**, 815–823 (1982).
164. Miandad, R., Nizami, A. S., Rehan, M., Barakat, M. A., Khan, M. I., Mustafa, A., Ismail, I. M. & Murphy, J. D. Influence of temperature and reaction time on the conversion of polystyrene waste to pyrolysis liquid oil. *Waste Management* **58**, 250–259 (2016).
165. Martín-Lara, M. A., Piñar, A., Ligero, A., Blázquez, G. & Calero, M. Characterization and Use of Char Produced from Pyrolysis of Post-Consumer Mixed Plastic Waste. *Water* **2021**, Vol. 13, Page 1188 **13**, 1188 (2021).
166. Gil, M. V., Fermoso, J., Pevida, C., Pis, J. J. & Rubiera, F. Intrinsic char reactivity of plastic waste (PET) during CO₂ gasification. *Fuel Processing Technology* **91**, 1776–1781 (2010).
167. Locaspi, A., Debiagi, P., Pelucchi, M., Hasse, C. & Faravelli, T. A Predictive Physico-chemical Model of Biochar Oxidation. *Energy and Fuels* **35**, 14894–14912 (2021).
168. Smith, I. W. *The combustion rates of coal chars: A review* 1982.
169. Reyes, S. & Jensen, K. F. Estimation of effective transport coefficients in porous solids based on percolation concepts. *Chemical Engineering Science* **40**, 1723–1734 (1985).
170. Jensen, K. F. & Reyes, S. Percolation Concepts in Modelling Gas-Solid Reactions: I. Application To Char in the Kinetic Regime. *Chemical Engineering Science* **41**, 333–343 (1986).
171. Bhatia, S. K. & Perlmutter, D. D. A random pore model for fluid-solid reactions: I. Isothermal, kinetic control. *AIChE Journal* **26**, 379–386 (1980).
172. Bhatia, S. K. & Vartak, B. J. Reaction of microporous solids: The discrete random pore model. *Carbon* (1996).
173. Singer, S. L. & Ghoniem, A. F. An adaptive random pore model for multimodal pore structure evolution with application to char gasification. *Energy and Fuels* **25**, 1423–1437 (2011).
174. Hurt, R. H. & Mitchell, R. E. Unified high-temperature char combustion kinetics for a suite of coals of various rank. *Symposium (International) on Combustion* (1992).
175. Hurt, R. H. & Calo, J. M. Semi-global intrinsic kinetics for char combustion modeling. *Combustion and Flame* **125**, 1138–1149 (2001).
176. Hong, J., Hecker, W. C. & Fletcher, T. H. Modeling high-pressure char oxidation using langmuir kinetics with an effectiveness factor. *Proceedings of the Combustion Institute* (2000).
177. Su, S., Song, Y., Wang, Y., Li, T., Hu, S., Xiang, J. & Li, C. Z. Effects of CO₂ and heating rate on the characteristics of chars prepared in CO₂ and N₂ atmospheres. *Fuel* (2015).

178. Haynes, B. S. & Newbury, T. G. Oxyreactivity of carbon surface oxides. *Proceedings of the Combustion Institute* (2000).
179. Haynes, B. S. A turnover model for carbon reactivity. I. Development. *Combustion and Flame* **126**, 1421–1432 (2001).
180. Tognotti, L., Longwell, J. P. & Sarofim, A. F. The products of the high temperature oxidation of a single char particle in an electrodynamic balance. *Symposium (International) on Combustion* **23**, 1207–1213 (1991).
181. Abbas-Abadi, M. S., Ureel, Y., Eschenbacher, A., Vermeire, F. H., Varghese, R. J., Oenema, J., Stefanidis, G. D. & Van Geem, K. M. Challenges and opportunities of light olefin production via thermal and catalytic pyrolysis of end-of-life polyolefins: Towards full recyclability. *Progress in Energy and Combustion Science* **96**, 101046 (2023).
182. Anuar Sharuddin, S. D., Abnisa, F., Wan Daud, W. M. A. & Aroua, M. K. A review on pyrolysis of plastic wastes. *Energy Conversion and Management* **115**, 308–326 (2016).
183. Daligaux, V., Richard, R. & Manero, M. H. Deactivation and regeneration of zeolite catalysts used in pyrolysis of plastic wastes—a process and analytical review. *Catalysts* **11** (2021).
184. Chester, A. W. Zeolite Characterization and Catalysis: a tutorial. *Focus on Catalysts* **2010** (ed Springer) 8 (2010).
185. Sakata, Y., Uddin, M. A. & Muto, A. Degradation of polyethylene and polypropylene into fuel oil by using solid acid and non-acid catalysts. *Journal of Analytical and Applied Pyrolysis* **51**, 135–155 (1999).
186. Schirmer, J., Kim, J. S. & Klemm, E. Catalytic degradation of polyethylene using thermal gravimetric analysis and a cycled-spheres-reactor. *Journal of Analytical and Applied Pyrolysis* **60**, 205–217 (2001).
187. Lin, Y. H., Yang, M. H., Yeh, T. F. & Ger, M. D. Catalytic degradation of high density polyethylene over mesoporous and microporous catalysts in a fluidised-bed reactor. *Polymer Degradation and Stability* **86**, 121–128 (2004).
188. Miskolczi, N., Bartha, L., Deák, G., Jóver, B. & Kalló, D. Kinetic model of the chemical recycling of waste polyethylene into fuels. *Process Safety and Environmental Protection* **82**, 223–229 (2004).
189. Mastral, J. F., Berueco, C., Gea, M & Ceamanos, J. Catalytic degradation of high density polyethylene over nanocrystalline HZSM-5 zeolite. *Polymer Degradation and Stability* **91**, 3330–3338 (2006).
190. Hernández, M. d. R., Gómez, A., García, Á. N., Agulló, J. & Marcilla, A. Effect of the temperature in the nature and extension of the primary and secondary reactions in the thermal and HZSM-5 catalytic pyrolysis of HDPE. *Applied Catalysis A: General* **317**, 183–194 (2007).
191. Miskolczi, N., Angyal, A., Bartha, L. & Valkai, I. Fuels by pyrolysis of waste plastics from agricultural and packaging sectors in a pilot scale reactor. *Fuel Processing Technology* **90**, 1032–1040 (2009).
192. Marcilla, A., Beltrán, M. I. & Navarro, R. Thermal and catalytic pyrolysis of polyethylene over HZSM5 and HUSY zeolites in a batch reactor under dynamic conditions. *Applied Catalysis B: Environmental* **86**, 78–86 (2009).

193. Elordi, G., Olazar, M., Lopez, G., Artetxe, M. & Bilbao, J. Continuous polyolefin cracking on an HZSM-5 zeolite catalyst in a conical spouted bed reactor. *Industrial and Engineering Chemistry Research* **50**, 6061–6070 (2011).
194. Liu, X., Zhang, Y., Li, Z., Feng, R. & Zhang, Y. Characterization of corncob-derived biochar and pyrolysis kinetics in comparison with corn stalk and sawdust. *Bioresource Technology* **170**, 76–82 (2014).
195. Takuma, K., Uemichi, Y. & Ayame, A. Product distribution from catalytic degradation of polyethylene over H-gallosilicate. *Applied Catalysis A: General* **192**, 273–280 (2000).
196. Gobin, K. & Manos, G. Polymer degradation to fuels over microporous catalysts as a novel tertiary plastic recycling method. *Polymer Degradation and Stability* **83**, 267–279 (2004).
197. Zhang, X., Lei, H., Yadavalli, G., Zhu, L., Wei, Y. & Liu, Y. Gasoline-range hydrocarbons produced from microwave-induced pyrolysis of low-density polyethylene over ZSM-5. *Fuel* **144**, 33–42 (2015).
198. Zhang, H., Liu, J., Wang, X. & Jiang, X. Density functional theory study on two different oxygen enhancement mechanisms during NO-char interaction. *Combustion and Flame* **169**, 11–18 (2016).
199. Huang, W. C., Huang, M. S., Huang, C. F., Chen, C. C. & Ou, K. L. Thermochemical conversion of polymer wastes into hydrocarbon fuels over various fluidizing cracking catalysts. *Fuel* **89**, 2305–2316 (2010).
200. Lin, Y. & M.H., Y. A novel approach for the kinetic and mechanistic modeling of acid-catalyzed degradation of polymers. *Asia-Pacific Journal of Chemical Engineering* **4**, 147–153 (2008).
201. Elordi, G., Olazar, M., Lopez, G., Amutio, M., Artetxe, M., Aguado, R. & Bilbao, J. Catalytic pyrolysis of HDPE in continuous mode over zeolite catalysts in a conical spouted bed reactor. *Journal of Analytical and Applied Pyrolysis* **85**, 345–351 (2009).
202. Renzini, M. S., Lerici, L. C., Sedran, U. & Pierella, L. B. Stability of ZSM-11 and BETA zeolites during the catalytic cracking of low-density polyethylene. *Journal of Analytical and Applied Pyrolysis* **92**, 450–455 (2011).
203. Kunwar, B., Moser, B. R., Chandrasekaran, S. R., Rajagopalan, N. & Sharma, B. K. Catalytic and thermal depolymerization of low value post-consumer high density polyethylene plastic *. *Energy* **111**, 884–892 (2016).
204. Seo, Y. H., Lee, K. H. & Shin, D. H. Investigation of catalytic degradation of high-density polyethylene by hydrocarbon group type analysis. *Journal of Analytical and Applied Pyrolysis* **70**, 383–398 (2003).
205. Garforth, A. A., Lin, Y. H., Sharratt, P. N. & Dwyer, J. Production of hydrocarbons by catalytic degradation of high density polyethylene in a laboratory fluidised-bed reactor. *Applied Catalysis A: General* **169**, 331–342 (1998).
206. Sakata, Y., Uddin, M. A., Koizumi, K. & Murata, K. Thermal degradation of polyethylene mixed with poly(vinyl chloride) and poly(ethyleneterephthalate). *Polymer Degradation and Stability* **53**, 111–117 (1996).

207. Aguado, J., Serrano, D. P., Miguel, G. S., Escola, J. M. & Rodríguez, J. M. Catalytic activity of zeolitic and mesostructured catalysts in the cracking of pure and waste polyolefins. *Journal of Analytical and Applied Pyrolysis* **78**, 153–161 (2007).
208. Artetxe, M., Lopez, G., Amutio, M., Barbarias, I., Arregi, A., Aguado, R., Bilbao, J. & Olazar, M. Styrene recovery from polystyrene by flash pyrolysis in a conical spouted bed reactor. *Waste Management* **45**, 126–133 (2015).
209. Van Grieken, R., Serrano, D. P., Aguado, J., García, R. & Rojo, C. Thermal and catalytic cracking of polyethylene under mild conditions. *Journal of Analytical and Applied Pyrolysis* **58-59**, 127–142 (2001).
210. Marcilla, A., Gómez, A. & Reyes-Labarta, J. A. MCM-41 catalytic pyrolysis of ethylene-vinyl acetate copolymers: Kinetic model. *Polymer* **42**, 8103–8111 (2001).
211. Olazar, M., Lopez, G., Amutio, M., Elordi, G., Aguado, R. & Bilbao, J. Influence of FCC catalyst steaming on HDPE pyrolysis product distribution. *Journal of Analytical and Applied Pyrolysis* **85**, 359–365 (2009).
212. Abbas-abadi, M. S., Nekoomanesh, M., Yeganeh, H. & McDonald, A. G. Journal of Analytical and Applied Pyrolysis Evaluation of pyrolysis process parameters on polypropylene degradation products. *Journal of Analytical and Applied Pyrolysis* **109**, 272–277 (2014).
213. Miskolczi, N. Kinetic Model of the Chemical and Catalytic Recycling of Waste Polyethylene into Fuels. *Feedstock Recycling and Pyrolysis of Waste Plastics: Converting Waste Plastics into Diesel and Other Fuels*, 225–247 (2006).
214. Marcilla, A., Beltran, M. & Conesa, J. A. Catalyst addition in polyethylene pyrolysis: Thermogravimetric study. *Journal of Analytical and Applied Pyrolysis* **58-59**, 117–126 (2001).
215. Marcilla, A., Gómez, A., Reyes-Labarta, J. A., Giner, A. & Hernández, F. Kinetic study of polypropylene pyrolysis using ZSM-5 and an equilibrium fluid catalytic cracking catalyst. *Journal of Analytical and Applied Pyrolysis* **68-69**, 467–480 (2003).
216. Marcilla, A., Gómez, A., Reyes-Labarta, J. A. & Giner, A. Catalytic pyrolysis of polypropylene using MCM-41: Kinetic model. *Polymer Degradation and Stability* **80**, 233–240 (2003).
217. Marcilla, A., Gómez-Siurana, A. & Valdés, F. Catalytic cracking of low-density polyethylene over H-Beta and HZSM-5 zeolites: Influence of the external surface. Kinetic model. *Polymer Degradation and Stability* **92**, 197–204 (2007).
218. Lin, Y. H., Hwu, W. H., Ger, M. D., Yeh, T. F. & Dwyer, J. A combined kinetic and mechanistic modelling of the catalytic degradation of polymers. *Journal of Molecular Catalysis A: Chemical* **171**, 143–151 (2001).
219. Lin, H. T., Huang, M. S., Luo, J. W., Lin, L. H., Lee, C. M. & Ou, K. L. Hydrocarbon fuels produced by catalytic pyrolysis of hospital plastic wastes in a fluidizing cracking process. *Fuel Processing Technology* **91**, 1355–1363 (2010).
220. Artetxe, M., Lopez, G., Amutio, M., Bilbao, J. & Olazar, M. Kinetic modelling of the cracking of HDPE pyrolysis volatiles on a HZSM-5 zeolite based catalyst. *Chemical Engineering Science* **116**, 635–644 (2014).
221. Till, Z., Varga, T., Sója, J., Miskolczi, N. & Chován, T. Kinetic identification of plastic waste pyrolysis on zeolite-based catalysts. *Energy Conversion and Management* **173**, 320–330 (2018).

222. Zavala-Gutiérrez, J., Pérez-Camacho, O., Villarreal-Cárdenas, L. & Saldívar-Guerra, E. Mathematical Modeling of the Catalytic Pyrolysis of High-Density Polyethylene in a Plug-Flow Tubular Reactor. *Industrial and Engineering Chemistry Research* **58**, 19050–19060 (2019).
223. Britannica. *Polyethylene (PE) | Properties, Structures, Uses, & Facts | Britannica* 2023.
224. Ullmann. *Ullmann's Encyclopedia of Industrial Chemistry* (Wiley, 2011).
225. Michajlov, L., Zugemmaier, P. & Cantow, H. J. Structural investigations on polyethylenes and ethylene-propylene copolymers by reaction gas chromatography and X-ray diffraction. *Polymer* **9**, 325–343 (1968).
226. Kee, R. J. *et al.* CHEMKIN Release 4.1, Reaction Design. Inc, San Diego, CA **185** (2006).
227. De Witt, M. J. & Broadbelt, L. J. Binary interactions between high-density polyethylene and 4-(1-naphthylmethyl)biphenyl during low-pressure pyrolysis. *Energy and Fuels* **14**, 448–458 (2000).
228. Eschenbacher, A., Varghese, R. J., Abbas-Abadi, M. S. & Van Geem, K. M. Maximizing light olefins and aromatics as high value base chemicals via single step catalytic conversion of plastic waste. *Chemical Engineering Journal* **428**, 132087 (2022).
229. Elordi, G., Olazar, M., Lopez, G., Artetxe, M. & Bilbao, J. Product Yields and Compositions in the Continuous Pyrolysis of High-Density Polyethylene in a Conical Spouted Bed Reactor. *Industrial & Engineering Chemistry Research* **50**, 6650–6659 (2011).
230. Motawie, M., Hanafi, S. A., Elmelandy, M. S., Ahmed, S. M., Mansour, N. A., Darwish, M. S. A. & Abulyazied, D. E. Wax co-cracking synergism of high density polyethylene to alternative fuels. *Egyptian Journal of Petroleum* **24**, 353–361 (2015).
231. Akin, O., He, Q., Yazdani, P., Wang, Y., Varghese, R. J., Poelman, H., Van Steenberge, P. & Van Geem, K. M. Tailored HZSM-5 catalyst modification via phosphorus impregnation and mesopore introduction for selective catalytic conversion of polypropylene into light olefins. *Journal of Analytical and Applied Pyrolysis* **181**, 106592 (2024).
232. Gaur, U. & Wunderlich, B. Heat capacity and other thermodynamic properties of linear macromolecules. II. Polyethylene. *Journal of Physical and Chemical Reference Data* **10**, 119–152 (1981).
233. Cuoci, A. Numerical modeling of reacting systems with detailed kinetic mechanisms. *Computer Aided Chemical Engineering* **45**, 675–721 (2019).
234. Stagni, A., Frassoldati, A., Cuoci, A., Faravelli, T. & Ranzi, E. Skeletal mechanism reduction through species-targeted sensitivity analysis. *Combustion and Flame* **163**, 382–393 (2016).
235. Gascoin, N., Navarro-Rodriguez, A., Fau, G. & Gillard, P. Kinetic modelling of High Density PolyEthylene pyrolysis: Part 2. Reduction of existing detailed mechanism. *Polymer Degradation and Stability* (2012).
236. Gedde, U. W. *Polymer Physics* (ed Chapman & Hall) (Springer Netherlands, Dordrecht, 1999).
237. Murata, K., Sato, K. & Sakata, Y. Effect of pressure on thermal degradation of polyethylene. *Journal of Analytical and Applied Pyrolysis* **71**, 569–589 (2004).

238. Murata, K., Brebu, M. & Sakata, Y. The effect of silica–alumina catalysts on degradation of polyolefins by a continuous flow reactor. *Journal of Analytical and Applied Pyrolysis* **89**, 30–38 (2010).
239. Rosenstein, I. J. in *Radicals in Organic Synthesis* 50–71 (John Wiley & Sons, Ltd, 2008).
240. Cavallotti, C. Automation of chemical kinetics: Status and challenges. *Proceedings of the Combustion Institute* **39**, 11–28 (2023).
241. Chung, Y. & Green, W. H. Computing Kinetic Solvent Effects and Liquid Phase Rate Constants Using Quantum Chemistry and COSMO-RS Methods. *Journal of Physical Chemistry A* **127**, 5637–5651 (2023).
242. Serse, F., Bjola, A., Salvalaglio, M. & Pelucchi, M. Unveiling Solvent Effects on β-Scissions through Metadynamics and Mean Force Integration. *Journal of Chemical Theory and Computation* (2024).
243. Achilias, D. S. A Review of Modeling of Diffusion Controlled Polymerization Reactions. *Macromolecular Theory and Simulations* **16**, 319–347 (2007).
244. Hong, S. U. Prediction of Polymer-Solvent Diffusion Behavior Using Free-Volume Theory. *Industrial & Engineering Chemistry Research* **34**, 2536–2544 (1995).
245. Ranzi, E., Dente, M., Faravelli, T. & Pennati, G. Prediction of Kinetic Parameters for Hydrogen Abstraction Reactions. *Combustion Science and Technology* **95**, 1–50 (1993).
246. Mehl, M., Vanhove, G., Pitz, W. J. & Ranzi, E. Oxidation and combustion of the n-hexene isomers: A wide range kinetic modeling study. *Combustion and Flame* **155**, 756–772 (2008).
247. Achilias, D. S., Roupakias, C., Megalokonomos, P., Lappas, A. A. & Antonakou, V. Chemical recycling of plastic wastes made from polyethylene (LDPE and HDPE) and polypropylene (PP). *Journal of Hazardous Materials* **149**, 536–542 (2007).
248. Arisawa, H. *Kinetics and pathways of polymer binder/fuel pyrolysis under combustion-like conditions - ProQuest PhD thesis* (University of Delaware, 1996).
249. Ceamanos, J., Mastral, J. F., Millera, A. & Aldea, M. E. Kinetics of pyrolysis of high density polyethylene. Comparison of isothermal and dynamic experiments. *Journal of Analytical and Applied Pyrolysis* **65**, 93–110 (2002).
250. Wang, Y., Hu, Y., Zhao, X., Wang, S. & Xing, G. Comparisons of biochar properties from wood material and crop residues at different temperatures and residence times. *Energy and Fuels* **27**, 5890–5899 (2013).
251. Cozzani, V., Nicolella, C., Rovatti, M. & Tognotti, L. Influence of Gas-Phase Reactions on the Product Yields Obtained in the Pyrolysis of Polyethylene. *Industrial and Engineering Chemistry Research* **36**, 342–348 (1997).
252. Androsch, R., Di Lorenzo, M. L., Schick, C. & Wunderlich, B. Mesophases in polyethylene, polypropylene, and poly(1-butene). *Polymer* **51**, 4639–4662 (2010).
253. Butler, K. M. A numerical model for combustion of bubbling thermoplastic materials in microgravity: (2002).
254. Wichman, I. S. A model describing the steady-state gasification of bubble-forming thermoplastics in response to an incident heat flux. *Combustion and Flame* **63**, 217–229 (1986).

255. Yarin, A. L., Lastochkin, D., Talmon, Y. & Tadmor, Z. Bubble nucleation during devolatilization of polymer melts. *AIChE Journal* **45**, 2590–2605 (1999).
256. Blander, M. & Katz, J. L. Bubble nucleation in liquids. *AIChE Journal* **21**, 833–848 (1975).
257. Tanaka, K. K., Tanaka, H., Angélil, R. & Diemand, J. Simple improvements to classical bubble nucleation models. *Physical Review E - Statistical, Nonlinear, and Soft Matter Physics* **92**, 022401 (2015).
258. Han, J. H. & Dae Han, C. Bubble nucleation in polymeric liquids. II. theoretical considerations. *Journal of Polymer Science Part B: Polymer Physics* **28**, 743–761 (1990).
259. Han, J. H. & Dae Han, C. Bubble nucleation in polymeric liquids. I. Bubble nucleation in concentrated polymer solutions. *Journal of Polymer Science Part B: Polymer Physics* **28**, 711–741 (1990).
260. Epstein, P. S. & Plesset, M. S. On the stability of gas bubbles in liquid-gas solutions. *The Journal of Chemical Physics* **18**, 1505–1509 (1950).
261. Nannoolal, Y., Rarey, J. & Ramjugernath, D. Estimation of pure component properties: Part 3. Estimation of the vapor pressure of non-electrolyte organic compounds via group contributions and group interactions. *Fluid Phase Equilibria* **269**, 117–133 (2008).
262. Vrentas, J. S. & Duda, J. L. Diffusion in polymer—solvent systems. I. Reexamination of the free-volume theory. *Journal of Polymer Science: Polymer Physics Edition* **15**, 403–416 (1977).
263. Ju, S. T., Liu, H. T., Duda, J. L. & Vrentas, J. S. Solvent diffusion in amorphous polymers. *Journal of Applied Polymer Science* **26**, 3735–3744 (1981).
264. Zielinski, J. M. & Duda, J. L. Predicting polymer/solvent diffusion coefficients using free-volume theory. *AIChE Journal* **38**, 405–415 (1992).
265. Ferry, J. D. *Viscoelastic properties of polymers* (John Wiley & Sons, Incorporated, 1980).
266. Lubetkin, S. D. The fundamentals of bubble evolution. *Chemical Society Reviews* **24**, 243–250 (1995).
267. Kulkarni, A. A. & Joshi, J. B. Bubble formation and bubble rise velocity in gas-liquid systems: A review. *Industrial and Engineering Chemistry Research* **44**, 5873–5931 (2005).
268. Ghazivini, M., Hafez, M., Ratanpara, A. & Kim, M. A review on correlations of bubble growth mechanisms and bubble dynamics parameters in nucleate boiling. *Journal of Thermal Analysis and Calorimetry* **2021** *147:11* **147**, 6035–6071 (2021).
269. Ban, Z. H., Lau, K. K. & Shariff, A. M. Prediction of the bubble nucleation rate in a quasi-stable cavitating nozzle using 2D computational fluid dynamics and enhanced classical nucleation theory. *Engineering Applications of Computational Fluid Mechanics* **9**, 247–258 (2015).
270. Burke, S. M., Simmie, J. M. & Curran, H. J. Critical evaluation of thermochemical properties of C₁-C₄ species: Updated group-contributions to estimate thermochemical properties. *Journal of Physical and Chemical Reference Data* **44**, 13101 (2015).
271. Ghosh, M. K., Elliott, S. N., Somers, K. P., Klippenstein, S. J. & Curran, H. J. Group additivity values for the heat of formation of C₂–C₈ alkanes, alkyl hydroperoxides, and their radicals. *Combustion and Flame* **257**, 112492 (2023).

272. Ghosh, M. K., Elliott, S. N., Somers, K. P., Klippenstein, S. J. & Curran, H. J. Group additivity values for entropy and heat capacities of C₂–C₈ alkanes, alkyl hydroperoxides, and their radicals. *Combustion and Flame* **257**, 112706 (2023).
273. Liu, M. *et al.* Reaction Mechanism Generator v3.0: Advances in Automatic Mechanism Generation. *Journal of Chemical Information and Modeling* **61**, 2686–2696 (2021).
274. Dobbelaere, M. R., Ureel, Y., Vermeire, F. H., Tomme, L., Stevens, C. V. & Van Geem, K. M. Machine Learning for Physicochemical Property Prediction of Complex Hydrocarbon Mixtures. *Industrial and Engineering Chemistry Research* **61**, 8581–8594 (2022).
275. Ureel, Y., Vermeire, F. H., Sabbe, M. K. & Van Geem, K. M. Beyond group additivity: Transfer learning for molecular thermochemistry prediction. *Chemical Engineering Journal* **472**, 144874 (2023).
276. Ruscic, B., Pinzon, R. E., Morton, M. L., Von Laszewski, G., Bittner, S. J., Nijsure, S. G., Amin, K. A., Minkoff, M. & Wagner, A. F. Introduction to active thermochemical tables: Several "Key" enthalpies of formation revisited. *Journal of Physical Chemistry A* **108**, 9979–9997 (2004).
277. Ritter, E. R. & Bozzelli, J. W. THERM: Thermodynamic property estimation for gas phase radicals and molecules. *International Journal of Chemical Kinetics* **23**, 767–778 (1991).
278. Landau, L. The theory of phase transitions. *Nature* **138**, 840–841 (1936).
279. Vermeire, F. H. & Green, W. H. Transfer learning for solvation free energies: From quantum chemistry to experiments. *Chemical Engineering Journal* **418**, 129307 (2021).
280. Kolská, Z., Růžička, V. & Gani, R. Estimation of the Enthalpy of Vaporization and the Entropy of Vaporization for Pure Organic Compounds at 298.15 K and at Normal Boiling Temperature by a Group Contribution Method. *Industrial and Engineering Chemistry Research* **44**, 8436–8454 (2005).
281. Mehmoodoust, B., Sanjari, E. & Vatani, M. An efficient reliable method to estimate the vaporization enthalpy of pure substances according to the normal boiling temperature and critical properties. *Journal of Advanced Research* **5**, 261–269 (2014).
282. Nannooolal, Y., Rarey, J., Ramjugernath, D. & Cordes, W. Estimation of pure component properties: Part 1. Estimation of the normal boiling point of non-electrolyte organic compounds via group contributions and group interactions. *Fluid Phase Equilibria* **226**, 45–63 (2004).
283. Nannooolal, Y., Rarey, J. & Ramjugernath, D. Estimation of pure component properties: Part 2. Estimation of critical property data by group contribution. *Fluid Phase Equilibria* **252**, 1–27 (2007).
284. Watson, K. M. Thermodynamics of the Liquid State. *Industrial & Engineering Chemistry* **35**, 398–406 (1943).
285. Poling, B. E., Prausnitz, J. M., O'connell, J. P., York, N., San, C., Lisbon, F., Madrid, L., City, M., Delhi, M. N. & Juan, S. *The Properties of Gases and Liquids* Fifth Edit (McGRAW-HILL, 2001).
286. Thodos, G. Vapor Pressures of Normal Saturated Hydrocarbons. *Industrial & Engineering Chemistry* **42**, 1514–1526 (1950).

287. Rùžika, V. & Domalski, E. S. Estimation of the Heat Capacities of Organic Liquids as a Function of Temperature using Group Additivity. I. Hydrocarbon Compounds. *Journal of Physical and Chemical Reference Data* **22**, 597–618 (1993).
288. Ureel, Y., Vermeire, F. H., Sabbe, M. K. & Van Geem, K. M. Ab Initio Group Additive Values for Thermodynamic Carbenium Ion Property Prediction. *Industrial and Engineering Chemistry Research* **62**, 223–237 (2023).
289. Einstein, A. Planck's theory of radiation and the theory of specific heat. *Ann. Phys.* **22**, 180–190 (1907).
290. Debye, P. Zur Theorie der spezifischen Wärmen. *Annalen der Physik* **344**, 789–839 (1912).
291. Mackle, H. & Mayrick, R. G. A plastic capsule technique for the combustion calorimetry of volatile or chemically reactive compounds: the heat of combustion of polythene. *Journal of Scientific Instruments* **38**, 218 (1961).
292. Parks, G. S. & Mosher, H. P. Enthalpy and free energy changes in some simple polymerization processes. *Journal of Polymer Science Part A: General Papers* **1**, 1979–1984 (1963).
293. Fic, V. No Title. *Chemicky Prumysl* **16**, 607 (1966).
294. Joshi, R. M. & Zwolinski, B. J. Heats of Combustion Studies on Polymers. *Macromolecules* **1**, 25–30 (1968).
295. Splitstone, P. L. & Johnson, W. H. The Enthalpies of Combustion and Formation of Linear Polyethylene. *Journal of Research of the National Bureau of Standards. Section A, Physics and Chemistry* **78A**, 611 (1974).
296. Walters, R. N., Hackett, S. M. & Lyon, R. E. Heats of combustion of high temperature polymers. *Fire and Materials* **24**, 245–252 (2000).
297. Chen, R. S., Ahmad, S., Gan, S. & Tarawneh, M. A. High loading rice husk green composites: Dimensional stability, tensile behavior and prediction, and combustion properties. *Journal of Thermoplastic Composite Materials* **33**, 882–897 (2020).
298. Warfield, R. W. & Petree, M. C. Thermodynamic properties of polyethylene. *Die Makromolekulare Chemie* **51**, 113–122 (1962).
299. Nannoolal, Y., Rarey, J. & Ramjugernath, D. Estimation of pure component properties. Part 4: Estimation of the saturated liquid viscosity of non-electrolyte organic compounds via group contributions and group interactions. *Fluid Phase Equilibria* **281**, 97–119 (2009).
300. Lee, B. I. & Kesler, M. G. A generalized thermodynamic correlation based on three-parameter corresponding states. *AIChE Journal* **21**, 510–527 (1975).
301. Holley, A., You, X., Dames, E., Wang, H. & Egolfopoulos, F. Sensitivity of propagation and extinction of large hydrocarbon flames to fuel diffusion. *Proceedings of the Combustion Institute* **32**, 1157–1163 (2009).
302. Yaws, C. L. *The Yaws Handbook of Physical Properties for Hydrocarbons and Chemicals* 2nd ed., 1–832 (Elsevier, 2015).
303. Elbro, H. S., Fredenslund, A. & Rasmussen, P. Group contribution method for the prediction of liquid densities as a function of temperature for solvents, oligomers, and polymers. *Industrial & engineering chemistry research* **30**, 2576–2582 (1991).

304. Sastri, S. R. & Rao, K. K. A new temperature-thermal conductivity relationship for predicting saturated liquid thermal conductivity. *Chemical Engineering Journal* **74**, 161–169 (1999).
305. Taylor, R. & Krishna, R. *Multicomponent mass transfer* (John Wiley & Sons, 1993).
306. Conesa, J. A., Font, R., Martilla, A. & Garcia, A. N. Pyrolysis of Polyethylene in a Fluidized Bed Reactor. *1238 Energy & Fuels* **8**, 1238–1246 (1994).
307. Khaghanikavkani, E., Mohammed, & Farid, M. Thermal Pyrolysis of Polyethylene: Kinetic Study. *Energy Science and Technology* **2**, 1–10 (2011).
308. Al-Salem, S. M. & Lettieri, P. Kinetic study of high density polyethylene (HDPE) pyrolysis. *Chemical Engineering Research and Design* **88**, 1599–1606 (2010).
309. Jayarama Krishna, J. V., Korobeinichev, O. P. & Vinu, R. Isothermal fast pyrolysis kinetics of synthetic polymers using analytical Pyroprobe. *Journal of Analytical and Applied Pyrolysis* **139**, 48–58 (2019).
310. Cuoci, A., Frassoldati, A., Faravelli, T. & Ranzi, E. OpenSMOKE++: An object-oriented framework for the numerical modeling of reactive systems with detailed kinetic mechanisms. *Computer Physics Communications* **192**, 237–264 (2015).
311. Bernardi, M. S., Pelucchi, M., Stagni, A., Sangalli, L. M., Cuoci, A., Frassoldati, A., Secchi, P. & Faravelli, T. Curve matching, a generalized framework for models/experiments comparison: An application to n-heptane combustion kinetic mechanisms. *Combustion and Flame* **168**, 186–203 (2016).
312. Pelucchi, M., Stagni, A. & Faravelli, T. Addressing the complexity of combustion kinetics: Data management and automatic model validation. *Computer Aided Chemical Engineering* **45**, 763–798 (2019).
313. Ramalli, E., Dinelli, T., Nobili, A., Stagni, A., Pernici, B. & Faravelli, T. Automatic validation and analysis of predictive models by means of big data and data science. *Chemical Engineering Journal* **454**, 140149 (2023).
314. Aboulkas, A., El harfi, K. & El Bouadili, A. Thermal degradation behaviors of polyethylene and polypropylene. Part I: Pyrolysis kinetics and mechanisms. *Energy Conversion and Management* **51**, 1363–1369 (2010).
315. Budrigeac, P. Theory and practice in the thermoanalytical kinetics of complex processes: Application for the isothermal and non-isothermal thermal degradation of HDPE. *Thermochimica Acta* **500**, 30–37 (2010).
316. Conesa, J. A., Marcilla, A., Font, R. & Caballero, J. A. Thermogravimetric studies on the thermal decomposition of polyethylene. *Journal of Analytical and Applied Pyrolysis* **36**, 1–15 (1996).
317. Capote, J., Alvear, D., Abreu, O., Lazaro, M. & Puente, E. *Pyrolysis characterization of a linear low density polyethylene in Fire Safety Science* (2011), 877–888.
318. Jinno, D., Gupta, A. K. & Yoshikawa, K. Thermal Decomposition Characteristics of Critical Components in Solid Wastes. *Environmental Engineering Science* **21**, 65–72 (2004).
319. Mazloum, S., Aboumsallem, Y., Awad, S., Allam, N. & Loubar, K. Modelling pyrolysis process for PP and HDPE inside thermogravimetric analyzer coupled with differential scanning calorimeter. *International Journal of Heat and Mass Transfer* **176**, 121468 (2021).

320. Kumar, S. & Singh, R. K. Recovery of hydrocarbon liquid from waste high density polyethylene by thermal pyrolysis. *Brazilian Journal of Chemical Engineering* **28**, 659–667 (2011).
321. Dubdub, I. & Al-Yaari, M. Pyrolysis of Low Density Polyethylene: Kinetic Study Using TGA Data and ANN Prediction. *Polymers* **2020**, Vol. 12, Page 891 **12**, 891 (2020).
322. Duque, J. V. F., Martins, M. F., Debenest, G. & Orlando, M. T. D. The influence of the recycling stress history on LDPE waste pyrolysis. *Polymer Testing* **86**, 106460 (2020).
323. Kayacan, I. & Doğan, Ö. M. Pyrolysis of low and high density polyethylene. Part I: Non-isothermal pyrolysis kinetics. *Energy Sources, Part A: Recovery, Utilization and Environmental Effects* **30**, 385–391 (2008).
324. Janajreh, I., Adeyemi, I. & Elagroudy, S. Gasification feasibility of polyethylene, polypropylene, polystyrene waste and their mixture: Experimental studies and modeling. *Sustainable Energy Technologies and Assessments* **39**, 100684 (2020).
325. Sezgi, N. A., Cha, W. S., Smith, J. M. & McCoy, B. J. Polyethylene pyrolysis: Theory and experiments for molecular-weight-distribution kinetics. *Industrial and Engineering Chemistry Research* **37**, 2582–2591 (1998).
326. Anderson, D. A. & Freeman, E. S. The kinetics of the thermal degradation of polystyrene and polyethylene. *Journal of Polymer Science* **54**, 253–260 (1961).
327. Rychlý, J & Rychlá, L. Non-isothermal thermogravimetry of polymer - I. General model involving formal termination of active centres. *Journal of Thermal Analysis* **35**, 77–90 (1989).
328. Jellinek, H. H. G. Thermal degradation of polystyrene and polyethylene. Part III. *Journal of Polymer Science* **4**, 13–36 (1949).
329. Ghassemi, H., Baek, S. W. & Khan, Q. S. Experimental study on binary droplet evaporation at elevated pressures and temperatures. *Combustion Science and Technology* **178**, 1031–1053 (2006).
330. Eschenbacher, A., Varghese, R. J., Delikontantis, E., Mynko, O., Goodarzi, F., Enemark-Rasmussen, K., Oenema, J., Abbas-Abadi, M. S., Stefanidis, G. D. & Van Geem, K. M. Highly selective conversion of mixed polyolefins to valuable base chemicals using phosphorus-modified and steam-treated mesoporous HZSM-5 zeolite with minimal carbon footprint. *Applied Catalysis B: Environmental* **309**, 121251 (2022).
331. Pratali Maffei, L., Pelucchi, M., Cavallotti, C., Bertolino, A. & Faravelli, T. Master equation lumping for multi-well potential energy surfaces: A bridge between ab initio based rate constant calculations and large kinetic mechanisms. *Chemical Engineering Journal* **422**, 129954 (2021).
332. Pegurri, A., Dinelli, T., Pratali Maffei, L., Faravelli, T. & Stagni, A. Coupling chemical lumping to data-driven optimization for the kinetic modeling of dimethoxymethane (DMM) combustion. *Combustion and Flame* **260**, 113202 (2024).
333. Plastics Europe. Plastics the fact 2021. *Plastics Europe Market Research Group (PEMRG) and Conversio Market & Strategy GmbH.*, 1–34 (2021).
334. Britannica, T. E. o. E. *Polypropylene* 2023.
335. Grebowicz, J., Lau, S. F. & Wunderlich, B. The thermal properties of polypropylene. *Journal of Polymer Science: Polymer Symposia* **71**, 19–37 (1984).

336. Kiang, J. K., Uden, P. C. & Chien, J. C. Polymer reactions-Part VII: Thermal pyrolysis of polypropylene. *Polymer Degradation and Stability* **2**, 113–127 (1980).
337. Ballice, L. & Reimert, R. Classification of volatile products from the temperature-programmed pyrolysis of polypropylene (PP), atactic-polypropylene (APP) and thermogravimetrically derived kinetics of pyrolysis. *Chemical Engineering and Processing: Process Intensification* **41**, 289–296 (2002).
338. De Amorim, M. T. P., Comel, C. & Vermande, P. Pyrolysis of polypropylene: I. Identification of compounds and degradation reactions. *Journal of Analytical and Applied Pyrolysis* **4**, 73–81 (1982).
339. Kim, S. S. & Kim, S. S. Pyrolysis characteristics of polystyrene and polypropylene in a stirred batch reactor. *Chemical Engineering Journal* **98**, 53–60 (2004).
340. Park, C. & Lee, J. Pyrolysis of polypropylene for production of fuel-range products: Effect of molecular weight of polypropylene. *International Journal of Energy Research* **45**, 13088–13097 (2021).
341. Zhao, W., Hasegawa, S., Fujita, J., Yoshii, F., Sasaki, T., Makuuchi, K., Sun, J. & Nishimoto, S. I. Effects of zeolites on the pyrolysis of polypropylene. *Polymer Degradation and Stability* **53**, 129–135 (1996).
342. Rätzsch, M., Arnold, M., Borsig, E., Bucka, H. & Reichelt, N. Radical reactions on polypropylene in the solid state. *Progress in Polymer Science* **27**, 1195–1282 (2002).
343. Sousa Pessoa De Amorim, M. T., Bouster, C. & Veron, J. Pyrolysis of polypropylene. II. Kinetics of degradation. *Journal of Analytical and Applied Pyrolysis* **4**, 103–115 (1982).
344. Azizi, K., Keshavarz Moraveji, M. & Abedini Najafabadi, H. Characteristics and kinetics study of simultaneous pyrolysis of microalgae Chlorella vulgaris, wood and polypropylene through TGA. *Bioresource Technology* **243**, 481–491 (2017).
345. Ciliz, N. K., Ekinci, E. & Snape, C. E. Pyrolysis of virgin and waste polypropylene and its mixtures with waste polyethylene and polystyrene. *Waste Management* **24**, 173–181 (2004).
346. Das, P. & Tiwari, P. The effect of slow pyrolysis on the conversion of packaging waste plastics (PE and PP) into fuel. *Waste Management* **79**, 615–624 (2018).
347. Dawood, A. & Miura, K. Pyrolysis kinetics of γ -irradiated polypropylene. *Polymer Degradation and Stability* **73**, 347–354 (2001).
348. Farhat Ali, M. & Salman Qureshi E J, M. H. Catalyzed pyrolysis of plastics: A thermogravimetric study. *African Journal of Pure and Applied Chemistry* **5**, 284–292 (2011).
349. Kiran, E. & Gillham, J. K. Pyrolysis-molecular weight chromatography: A new on-line system for analysis of polymers. II. Thermal decomposition of polyolefins: Polyethylene, polypropylene, polyisobutylene. *Journal of Applied Polymer Science* **20**, 2045–2068 (1976).
350. Martínez, M. C., Benavente, R. & Gómez-Elvira, J. M. Molecular weight dependence and stereoselective chain cleavage during the early stages of the isotactic polypropylene pyrolysis. *Polymer Degradation and Stability* **143**, 26–34 (2017).
351. Nguyen, L. T., Poinern, G. E. J., Le, H. T., Nguyen, T. A., Tran, C. M. & Jiang, Z. T. A LaFeO₃ supported natural-clay-mineral catalyst for efficient pyrolysis of polypropylene plastic material. *Asia-Pacific Journal of Chemical Engineering* **16**, e2695 (2021).

352. Sogancioglu, M., Yel, E. & Ahmetli, G. Behaviour of waste polypropylene pyrolysis char-based epoxy composite materials. *Environmental Science and Pollution Research* **27**, 3871–3884 (2020).
353. Wu, X., Wu, Y., Wu, K., Chen, Y., Hu, H. & Yang, M. Study on pyrolytic kinetics and behavior: The co-pyrolysis of microalgae and polypropylene. *Bioresource Technology* **192**, 522–528 (2015).
354. Zhang, Y., Fu, Z., Wang, W., Ji, G., Zhao, M. & Li, A. Kinetics, Product Evolution, and Mechanism for the Pyrolysis of Typical Plastic Waste. *ACS Sustainable Chemistry and Engineering* **10**, 91–103 (2022).
355. Abbas-Abadi, M. S., Van Geem, K. M., Fathi, M., Bazgir, H. & Ghadiri, M. The pyrolysis of oak with polyethylene, polypropylene and polystyrene using fixed bed and stirred reactors and TGA instrument. *Energy* **232**, 121085 (2021).
356. Wong, H.-W. & Broadbelt, L. J. Tertiary Resource Recovery from Waste Polymers via Pyrolysis: Neat and Binary Mixture Reactions of Polypropylene and Polystyrene. *Industrial \& Engineering Chemistry Research* **40**, 4716–4723 (2001).
357. Britannica, T. E. o. E. *Polystyrene* 2023.
358. Xu, Q., Jin, C., Griffin, G. & Jiang, Y. Fire safety evaluation of expanded polystyrene foam by multi-scale methods. *Journal of Thermal Analysis and Calorimetry* **115**, 1651–1660 (2014).
359. Poutsma, M. L. Mechanistic analysis and thermochemical kinetic simulation of the pathways for volatile product formation from pyrolysis of polystyrene, especially for the dimer. *Polymer Degradation and Stability* **91**, 2979–3009 (2006).
360. Levine, S. E. & Broadbelt, L. J. Reaction pathways to dimer in polystyrene pyrolysis: A mechanistic modeling study. *Polymer Degradation and Stability* **93**, 941–951 (2008).
361. Kruse, T. M., Sang Woo, O., Broadbelt, L. J., M. Kruse, T., Sang Woo, O. & J. Broadbelt, L. Detailed mechanistic modeling of polymer degradation: Application to polystyrene. *Chemical Engineering Science. 16th {International} {Conference} on {Chemical} {Reactor} {Engineering}* **56**, 971–979 (2001).
362. Gaur, U. & Wunderlich, B. *Heat Capacity and Other Thermodynamic Properties of Linear Macromolecules. V. Polystyrene* 1982.
363. Locaspi, A., Pelucchi, M. & Faravelli, T. Towards a lumped approach for solid plastic waste gasification: Polystyrene pyrolysis. *Journal of Analytical and Applied Pyrolysis* **171**, 105960 (2023).
364. Tsang, W. Butylbenzene combustion kinetics database. *43rd AIAA Aerospace Sciences Meeting and Exhibit - Meeting Papers*, 869–880 (2005).
365. Husson, B. *et al.* Experimental and modeling study of the oxidation of n-butylbenzene. *Combustion and Flame* **159**, 1399–1416 (2012).
366. Maafa, I. M. Pyrolysis of polystyrene waste: A review. *Polymers* **13**, 1–30 (2021).
367. Bouster, C., Vermande, P. & Veron, J. Evolution of the product yield with temperature and molecular weight in the pyrolysis of polystyrene. *Journal of Analytical and Applied Pyrolysis* **15**, 249–259 (1989).

368. Adnan, Shah, J. & Jan, M. R. Thermo-catalytic pyrolysis of polystyrene in the presence of zinc bulk catalysts. *Journal of the Taiwan Institute of Chemical Engineers* **45**, 2494–2500 (2014).
369. Andreikov, E. I., Amosova, I. S., Dikovinkina, Y. A., Krasnikova, O. V. & Pervova, M. G. Pyrolysis of polystyrene in coal tar and ethylene tar pitches. *Russian Journal of Applied Chemistry* **85**, 89–97 (2012).
370. Bockhorn, H., Hornung, A. & Hornung, U. Gasification of polystyrene as initial step in incineration, fires, or smoldering of plastics. *Symposium (International) on Combustion* **27**, 1343–1349 (1998).
371. Chen, K., Harris, K. & Vyazovkin, S. Tacticity as a Factor Contributing to the Thermal Stability of Polystyrene. *Macromolecular Chemistry and Physics* **208**, 2525–2532 (2007).
372. Jiao, L. L. & Sun, J. H. A Thermal Degradation Study of Insulation Materials Extruded Polystyrene. *Procedia Engineering* **71**, 622–628 (2014).
373. Leclerc, P., Doucet, J. & Chaouki, J. Development of a microwave thermogravimetric analyzer and its application on polystyrene microwave pyrolysis kinetics. *Journal of Analytical and Applied Pyrolysis* **130**, 209–215 (2018).
374. Li, X., jun Yin, Y., xin Zhou, J., Shen, X., guo Xie, M. & Liu, W. Pyrolysis characteristics and thermal kinetics of expanded polystyrene (EPS) and styrene-methyl methacrylate (St-MMA) copolymer in LFC process. *China Foundry* **15**, 428–435 (2018).
375. Lu, C., Xiao, H. & Chen, X. Simple pyrolysis of polystyrene into valuable chemicals. *E-Polymers* **21**, 428–432 (2021).
376. Marcilla, A., Gómez-Siurana, A., Quesada, J. C. & Berenguer, D. Characterization of high-impact polystyrene by catalytic pyrolysis over Al-MCM-41: Study of the influence of the contact between polymer and catalyst. *Polymer Degradation and Stability* **92**, 1867–1872 (2007).
377. Nisar, J., Ali, G., Shah, A., Iqbal, M., Khan, R. A., Sirajuddin, Anwar, F., Ullah, R. & Akhter, M. S. Fuel production from waste polystyrene via pyrolysis: Kinetics and products distribution. *Waste Management* **88**, 236–247 (2019).
378. Özsın, G. & Pütün, A. E. Insights into pyrolysis and co-pyrolysis of biomass and polystyrene: Thermochemical behaviors, kinetics and evolved gas analysis. *Energy Conversion and Management* **149**, 675–685 (2017).
379. Park, K. B., Jeong, Y. S., Guzelciftci, B. & Kim, J. S. Two-stage pyrolysis of polystyrene: Pyrolysis oil as a source of fuels or benzene, toluene, ethylbenzene, and xylenes. *Applied Energy* **259**, 114240 (2020).
380. Snegirev, A. Y., Talalov, V. A., Stepanov, V. V. & Harris, J. N. Formal kinetics of polystyrene pyrolysis in non-oxidizing atmosphere. *Thermochimica Acta* **548**, 17–26 (2012).
381. Inaba, A., Kashiwagi, T. & Brown, J. E. Effects of initial molecular weight on thermal degradation of poly(methyl methacrylate): Part 1—Model 1. *Polymer Degradation and Stability* **21**, 1–20 (1988).
382. Hirata, T., Kashiwagi, T. & Brown, J. E. Thermal and Oxidative Degradation of Poly(methyl methacrylate): Weight Loss. *Macromolecules* **18**, 1410–1418 (1985).

383. De Amorim, M. T. P., Bouster, C., Vermande, P. & Veron, J. Study of the pyrolysis of polystyrenes: II. Study of transfer reactions by identification of the most important by-products. *Journal of Analytical and Applied Pyrolysis* **3**, 19–34 (1981).
384. Cascaval, C. N., Straus, S., Brown, D. W. & Florin, R. E. Thermal degradation of polystyrene: Effect of end groups derived from azobisisobutyronitrile. *Journal of Polymer Science: Polymer Symposia* **57**, 81–88 (1976).
385. Kim, Y. S., Hwang, G. C., Bae, S. Y., Yi, S. C., Moon, S. K. & Kumazawa, H. Pyrolysis of polystyrene in a batch-type stirred vessel. *Korean Journal of Chemical Engineering* **1999** *16*:*2*, 161–165 (1999).
386. Lin, R. *Catalytic cracking of poly (ethylene) and poly (styrene) by silica-alumina, HZSM-5 zeolite and sulfated zirconia* PhD thesis (University of Oklahoma, 1997).
387. Ohtani, H., Tsuge, S., Matsushita, Y. & Nagasawa, M. Pyrolysis gas chromatographic characterization of block copolymers of ordinary and deuterated styrenes. *Polymer Journal* **14**, 495–499 (1982).
388. Yang, M & Shibasaki, Y. Mechanisms of Thermal Degradation of Polystyrene, Poly-methacrylonitrile, and Their Copolymers on Flash Pyrolysis. *J Polym Sci A: Polym Chem* **36**, 2315–2330 (1998).
389. Britannica, T. E. o. E. *Polyethylene terephthalate* 2023.
390. López, A., de Marco, I., Caballero, B. M., Laresgoiti, M. F. & Adrados, A. Pyrolysis of municipal plastic wastes: Influence of raw material composition. *Waste Management* **30**, 620–627 (2010).
391. Talmadge, M. S. *et al.* A perspective on oxygenated species in the refinery integration of pyrolysis oil. *Green Chemistry* **16**, 407–453 (2014).
392. Adelman, R. L. The interchange reaction of vinyl acetate with organic acids. *Journal of Organic Chemistry* **14**, 1057–1077 (1949).
393. Ma, T., Wang, R., Wang, W., Gu, W., Yuan, Y., Zhang, A. & Wei, J. Studies on the thermal degradation mechanism of polyethylene terephthalate and its 2-carboxy ethyl (phenyl) phosphinic acid copolymers. *Polymer Degradation and Stability* **206**, 110185 (2022).
394. Bednas, M. E., Day, M., Ho, K., Sander, R. & Wiles, D. M. Combustion and pyrolysis of poly(ethylene terephthalate). I. The role of flame retardants on products of pyrolysis. *Journal of Applied Polymer Science* **26**, 277–289 (1981).
395. Ravindranath, K. & Mashelkar, R. A. Polyethylene terephthalate—I. Chemistry, thermodynamics and transport properties. *Chemical Engineering Science* **41**, 2197–2214 (1986).
396. Venkatachalam, S. *et al.* Degradation and Recyclability of Poly (Ethylene Terephthalate). *Polyester* (2012).
397. Rhee, D. M., Ha, W. S., Youk, J. H. & Yoo, D. I. Interchange reaction kinetics and sequence distribution of liquid crystalline poly(ethylene terephthalate-co-2(3)-chloro-1,4-phenylene terephthalate). *Fibers and Polymers* **2001** *2*:*2*, 86–91 (2001).
398. Huang, J. B., Zeng, G. S., Li, X. S., Cheng, X. C. & Tong, H. Theoretical studies on bond dissociation enthalpies for model compounds of typical plastic polymers. *IOP Conference Series: Earth and Environmental Science* **167**, 012029 (2018).

399. Holland, B. J. & Hay, J. N. The effect of polymerisation conditions on the kinetics and mechanisms of thermal degradation of PMMA. *Polymer Degradation and Stability* **77**, 435–439 (2002).
400. Horton, S. R., Woeckener, J., Mohr, R., Zhang, Y., Petrocelli, F. & Klein, M. T. Molecular-Level Kinetic Modeling of the Gasification of Common Plastics. *Energy and Fuels* **30**, 1662–1674 (2016).
401. Hasse, C., Debiagi, P., Wen, X., Hildebrandt, K., Vascellari, M. & Faravelli, T. Advanced modeling approaches for CFD simulations of coal combustion and gasification. *Progress in Energy and Combustion Science* **86**, 100938 (2021).
402. Ahmetli, G., Kocaman, S., Ozaytekin, I. & Bozkurt, P. Epoxy composites based on inexpensive char filler obtained from plastic waste and natural resources. *Polymer Composites* **34**, 500–509 (2013).
403. Lee, J., Lee, T., Tsang, Y. F., Oh, J. I. & Kwon, E. E. Enhanced energy recovery from polyethylene terephthalate via pyrolysis in CO₂ atmosphere while suppressing acidic chemical species. *Energy Conversion and Management* **148**, 456–460 (2017).
404. Atashi, F., Gholizadeh, M. & Ataei, F. Pyrolysis of bottle-grade polyethylene terephthalate: Effect of carrier gases on carriage of pyrolysis products. *Polymer Engineering & Science* **62**, 2524–2531 (2022).
405. Li, C., Sun, Y., Li, Q., Zhang, L., Zhang, S., Wang, H., Hu, G. & Hu, X. Effects of volatiles on properties of char during sequential pyrolysis of PET and cellulose. *Renewable Energy* **189**, 139–151 (2022).
406. Williams, E. A. & Williams, P. T. The pyrolysis of individual plastics and a plastic mixture in a fixed bed reactor. *Journal of Chemical Technology and Biotechnology* **70**, 9–20 (1997).
407. Debiagi, P., Faravelli, T., Hasse, C. & Ranzi, E. in, 31–76 (Springer, Singapore, 2020).
408. Coniglio, L., Bennadji, H., Glaude, P. A., Herbinet, O. & Billaud, F. Combustion chemical kinetics of biodiesel and related compounds (methyl and ethyl esters): Experiments and modeling – Advances and future refinements. *Progress in Energy and Combustion Science* **39**, 340–382 (2013).
409. Yang, B., Westbrook, C. K., Cool, T. A., Hansen, N. & Kohse-Höinghaus, K. The Effect of Carbon–Carbon Double Bonds on the Combustion Chemistry of Small Fatty Acid Esters. *Zeitschrift für Physikalische Chemie* **225**, 1293–1314 (2011).
410. El-Nahas, A. M., Navarro, M. V., Simmie, J. M., Bozzelli, J. W., Curran, H. J., Dooley, S. & Metcalfe, W. Enthalpies of formation, bond dissociation energies and reaction paths for the decomposition of model biofuels: Ethyl propanoate and methyl butanoate. *Journal of Physical Chemistry A* **111**, 3727–3739 (2007).
411. Morsch, P., Dörntgen, M. & Heufer, K. A. High- and low-temperature ignition delay time study and modeling efforts on vinyl acetate. *Proceedings of the Combustion Institute* **39**, 115–123 (2023).
412. Grana, R., Frassoldati, A., Cuoci, A., Faravelli, T. & Ranzi, E. A wide range kinetic modeling study of pyrolysis and oxidation of methyl butanoate and methyl decanoate. Note I: Lumped kinetic model of methyl butanoate and small methyl esters. *Energy* **43**, 124–139 (2012).

413. Ning, H., Wu, J., Ma, L., Ren, W., Davidson, D. F. & Hanson, R. K. Combined Ab Initio, Kinetic Modeling, and Shock Tube Study of the Thermal Decomposition of Ethyl Formate. *The Journal of Physical Chemistry A* **121**, 6568–6579 (2017).
414. Metcalfe, W. K., Dooley, S., Curran, H. J., Simmie, J. M., El-Nahas, A. M. & Navarro, M. V. Experimental and modeling study of C₅H₁₀O₂ ethyl and methyl esters. *Journal of Physical Chemistry A* **111**, 4001–4014 (2007).
415. Bennadji, H., Coniglio, L., Billaud, F., Bounaceur, R., Warth, V., Glaude, P. A. & Battin-Leclerc, F. Oxidation of small unsaturated methyl and ethyl esters. *International Journal of Chemical Kinetics* **43**, 204–218 (2011).
416. Mukaiyama, T. & Nohira, H. A Kinetic Study of Addition Reaction of Vinyl Ether with Carboxylic Acids. *Bulletin of the Chemical Society of Japan* **33**, 1716–1720 (1960).
417. Eskay, T. P., Britt, P. F. & Buchanan, A. C. Pyrolysis of aromatic carboxylic acids: Potential involvement of anhydrides in retrograde reactions in low-rank coal. *Energy and Fuels* **11**, 1278–1287 (1997).
418. Carson, A. S., Fine, D. H., Gray, P. & Laye, P. G. Standard enthalpies of formation of diphenyl oxalate and benzoic anhydride and some related bond dissociation energies. *Journal of the Chemical Society B: Physical Organic*, 1611–1615 (1971).
419. Liu, W. J., Zeng, F. X., Jiang, H. & Zhang, X. S. Preparation of high adsorption capacity bio-chars from waste biomass. *Bioresource Technology* **102**, 8247–8252 (2011).
420. Namysl, S., Pelucchi, M., Herbinet, O., Frassoldati, A., Faravelli, T. & Battin-Leclerc, F. A first evaluation of butanoic and pentanoic acid oxidation kinetics. *Chemical Engineering Journal* **373**, 973–984 (2019).
421. Da Silva, G. & da Silva, G. Carboxylic Acid Catalyzed Keto-Enol Tautomerizations in the Gas Phase. *Angewandte Chemie* **122**, 7685–7687 (2010).
422. Eisenberg, A., Yokoyama, T. & Sambalido, E. Dehydration kinetics and glass transition of poly(acrylic acid). *Journal of Polymer Science Part A-1: Polymer Chemistry* **7**, 1717–1728 (1969).
423. Greenberg, A. R. & Kamel, I. Kinetics of anhydride formation in poly(acrylic acid) and its effect on the properties of a PAA-alumina composite. *Journal of Polymer Science: Polymer Chemistry Edition* **15**, 2137–2149 (1977).
424. Blanco-Fuente, H., Anguiano-Igea, S., Otero-Espinar, F. J. & Blanco-Méndez, J. Kinetics of anhydride formation in xerogels of poly(acrylic acid). *Biomaterials* **17**, 1667–1675 (1996).
425. Taylor, R. The mechanism of thermal elimination. Part 17. Rate data for pyrolysis of vinyl acetate and 1,2-diacetoxyethane. *Journal of the Chemical Society, Perkin Transactions 2*, 1157–1160 (1983).
426. Grajales-González, E., Monge-Palacios, M. & Sarathy, S. M. Theoretical Kinetic Study of the Unimolecular Keto-Enol Tautomerism Propen-2-ol - Acetone. Pressure Effects and Implications in the Pyrolysis of tert - And 2-Butanol. *Journal of Physical Chemistry A* **122**, 3547–3555 (2018).
427. Barson, C. A. & Bevington, J. C. A tracer study of the benzoyloxy radical. *Tetrahedron* **4**, 147–156 (1958).

428. Saggese, C., Ferrario, S., Camacho, J., Cuoci, A., Frassoldati, A., Ranzi, E., Wang, H. & Faravelli, T. Kinetic modeling of particle size distribution of soot in a premixed burner-stabilized stagnation ethylene flame. *Combustion and Flame* **162**, 3356–3369 (2015).
429. Pejpichertakul, W., Frassoldati, A., Parente, A. & Faravelli, T. Kinetic modeling of soot formation in premixed burner-stabilized stagnation ethylene flames at heavily sooting condition. *Fuel* **234**, 199–206 (2018).
430. Pejpichertakul, W. Chemical and Physical Pathways of PAH and Soot Formation in Laminar Flames (2019).
431. De Saint Laumer, J. Y., Cicchetti, E., Merle, P., Egger, J. & Chaintreau, A. *Quantification in gas chromatography: Prediction of flame ionization detector response factors from combustion enthalpies and molecular structures* in *Analytical Chemistry* **82** (American Chemical Society, 2010), 6457–6462.
432. Martín-Gullón, I., Esperanza, M. & Font, R. Kinetic model for the pyrolysis and combustion of poly-(ethylene terephthalate) (PET). *Journal of Analytical and Applied Pyrolysis* **58–59**, 635–650 (2001).
433. Brebu, M., Bhaskar, T., Murai, K., Muto, A., Sakata, Y. & Uddin, M. A. The effect of PVC and/or PET on thermal degradation of polymer mixtures containing brominated ABS. *Fuel* **83**, 2021–2028 (2004).
434. Das, P. & Tiwari, P. Thermal degradation study of waste polyethylene terephthalate (PET) under inert and oxidative environments. *Thermochimica Acta* **679**, 178340 (2019).
435. Moltó, J., Font, R. & Conesa, J. A. Kinetic model of the decomposition of a PET fibre cloth in an inert and air environment. *Journal of Analytical and Applied Pyrolysis* **79**, 289–296 (2007).
436. Sustaita-Rodríguez, J. M., Medellín-Rodríguez, F. J., Olvera-Mendez, D. C., Gimenez, A. J. & Luna-Barcenas, G. Thermal Stability and Early Degradation Mechanisms of High-Density Polyethylene, Polyamide 6 (Nylon 6), and Polyethylene Terephthalate. *Polymer Engineering & Science* **59**, 2016–2023 (2019).
437. Czégény, Z., Jakab, E., Blazsó, M., Bhaskar, T. & Sakata, Y. Thermal decomposition of polymer mixtures of PVC, PET and ABS containing brominated flame retardant: Formation of chlorinated and brominated organic compounds. *Journal of Analytical and Applied Pyrolysis* **96**, 69–77 (2012).
438. Li, C., Ataei, F., Atashi, F., Hu, X. & Gholizadeh, M. Catalytic pyrolysis of polyethylene terephthalate over zeolite catalyst: Characteristics of coke and the products. *International Journal of Energy Research* **45**, 19028–19042 (2021).
439. Kaminsky, W. & Franck, J. Monomer recovery by pyrolysis of poly(methyl methacrylate) (PMMA). *Journal of Analytical and Applied Pyrolysis* **19**, 311–318 (1991).
440. Paul, D. R. & Newman, S. *Polymer blends* (Academic Press, 1978).
441. Manias, E. & Utracki, L. A. Thermodynamics of polymer blends. *Polymer Blends Handbook*, 171–289 (2014).
442. Simon, G. P. *Polymer Blends and Alloys* (Routledge, 1999).
443. Robeson, L. M. *Polymer Blends I–XII* (Carl Hanser Verlag GmbH & Co. KG, München, 2007).

444. Helfand, E. & Tagami, Y. Theory of the interface between immiscible polymers. *Journal of Polymer Science Part B: Polymer Letters* **9**, 741–746 (1971).
445. Helfand, E. & Tagami, Y. Theory of the Interface between Immiscible Polymers. II. *The Journal of Chemical Physics* **56**, 3592–3601 (1972).
446. Brosetav, D., Fredrickson, G. H., Helfand, E. & Leibler, L. Molecular Weight and Polydispersity Effects at Polymer-Polymer Interfaces. *Macromolecules* **23**, 132–139 (1990).
447. Hansen, C. M. *Hansen Solubility Parameters* (CRC Press, 2007).
448. Eitouni, H. B. & Balsara, N. P. Thermodynamics of Polymer Blends. *Physical Properties of Polymers Handbook*, 339–356 (2007).
449. Ma, D. Z. & Prud'homme, R. E. Miscibility of caprolactone/ethylene terephthalate copolymers with chlorinated polymers: a differential scanning calorimetry and Fourier transform infra-red study. *Polymer* **31**, 917–923 (1990).
450. Albano, C. & De Freitas, E. Thermogravimetric evaluation of the kinetics of decomposition of polyolefin blends. *Polymer Degradation and Stability* **61**, 289–295 (1998).
451. Singh, R. K., Ruj, B., Sadhukhan, A. K. & Gupta, P. A TG-FTIR investigation on the co-pyrolysis of the waste HDPE, PP, PS and PET under high heating conditions. *Journal of the Energy Institute* **93**, 1020–1035 (2020).
452. McNeill, I. C. & Neil, D. Degradation of polymer mixtures. III.: Poly(vinyl chloride) - poly(methyl methacrylate) mixtures, studied by thermal volatilization analysis and other techniques. The nature of the reaction products and the mechanism of interaction of the polymers. *European Polymer Journal* **6**, 569–583 (1970).
453. Jamieson, A. & McNeill, I. C. Degradation of polymer mixtures. IV. Blends of poly(vinyl acetate) with poly(vinyl chloride) and other chlorine-containing polymers. *Journal of Polymer Science: Polymer Chemistry Edition* **12**, 387–400 (1974).
454. Dodson, B. & McNeill, I. C. Degradation of polymer mixtures. VI. Blends of poly(vinyl chloride) with polystyrene. *Journal of Polymer Science: Polymer Chemistry Edition* **14**, 353–364 (1976).
455. Grassie, N., McNeill, I. C. & Cooke, I. Thermal degradation of polymer mixtures. I. Degradation of polystyrene-poly(methyl methacrylate) mixtures and a comparison with the degradation of styrene-methyl methacrylate copolymers. *Journal of Applied Polymer Science* **12**, 831–837 (1968).
456. Jamieson, A. & McNeill, I. C. Degradation of polymer mixtures. VII. Blends of poly(vinyl acetate) with polystyrene. *Journal of Polymer Science: Polymer Chemistry Edition* **14**, 603–608 (1976).
457. McNeill, I. C., Ackerman, L. & Gupta, S. N. Degradation of polymer mixtures. IX. Blends of polystyrene with polybutadiene. *Journal of Polymer Science: Polymer Chemistry Edition* **16**, 2169–2181 (1978).
458. McNeill, I. C. & Gupta, S. N. Degradation of polymer blends. Part XI. Blends of polystyrene with polyisoprene. *Polymer Degradation and Stability* **2**, 95–111 (1980).
459. McNeill, I. C., Gorman, J. G. & Basan, S. Thermal degradation of blends of PVC with poly(tetramethylene sebacate). *Polymer Degradation and Stability* **33**, 263–276 (1991).

460. McNeill, I. C., Neil, D., Guyot, A., Bert, M. & Michel, A. Thermal degradation of graft copolymers of PVC prepared by mastication with styrene and methyl methacrylate, and of further PVC mixtures and vinyl chloride copolymers. *European Polymer Journal* **7**, 453–469 (1971).
461. McNeill, I. C. & Neil, D. Degradation of polymer mixtures-II: Poly(vinyl chloride) - poly(methyl methacrylate) mixtures, studied by thermal volatilization analysis and other techniques. The effect of mixing on the thermal stability of each polymer and the general nature of their interaction. *European Polymer Journal* **6**, 143–160 (1970).
462. McNeill, I. C., Grassie, N., Samson, J. N., Jamieson, A. & Straiton, T. Thermal Degradation of Blends of PVC with Other Polymers. *Journal of Macromolecular Science: Part A - Chemistry* **12**, 503–529 (1978).
463. Csmorova, K., Rychly, J. & Bucsi, A. Nonisothermal thermogravimetry of polymers III. Thermogravimetry of PE/PP, PE/PMMA and PP/PMMA blends. *Journal of thermal analysis* **39**, 743–753 (1993).
464. Cheung, Y. W. & Guest, M. J. A Study of the Blending of Ethylene-Styrene Copolymers Differing in the Copolymer Styrene Content: Miscibility Considerations. *J Polym Sci B: Polym Phys* **38**, 2976–2987 (2000).
465. Murata, K. & Akimoto, M. Thermal Degradation of Mixed Polymer. *Nippon Kagaku Kaishi* **1979**, 774–781 (1979).
466. Teh, J. W., Rudin, A. & Keung, J. C. A review of polyethylene-polypropylene blends and their compatibilization. *Advances in Polymer Technology* **13**, 1–23 (1994).
467. Waldman, W. R. & De Paoli, M. A. Thermo-mechanical degradation of polypropylene, low-density polyethylene and their 1:1 blend. *Polymer Degradation and Stability* **60**, 301–308 (1998).
468. Chowlu, A. C. K., Reddy, P. K. & Ghoshal, A. K. Pyrolytic decomposition and model-free kinetics analysis of mixture of polypropylene (PP) and low-density polyethylene (LDPE). *Thermochimica Acta* **485**, 20–25 (2009).
469. Beretta, A. & Lietti, L. *Private communication*
470. Ziska, J. J., Barlow, J. W. & Paul, D. R. Miscibility in PVC-polyester blends. *Polymer* **22**, 918–923 (1981).
471. Woo, E. M., Barlow, J. W. & Paul, D. R. Thermodynamics of the phase behaviour of poly(vinyl chloride)/aliphatic polyester blends. *Polymer* **26**, 763–773 (1985).
472. Pekdemir, M. E., Öner, E., Kök, M. & Qader, I. N. Thermal behavior and shape memory properties of PCL blends film with PVC and PMMA polymers. *Iranian Polymer Journal (English Edition)* **30**, 633–641 (2021).
473. Pekdemir, M. E., Kök, M., Qader, I. N. & Aydogdu, Y. Preparation and physicochemical properties of mwcnt doped polyvinyl chloride / poly (ϵ -caprolactone) blend. *Journal of Polymer Research* **29**, 1–9 (2022).
474. Demir, P. Thermal degradation kinetics, mechanism, thermodynamics, shape memory properties and artificial neural network application study of polycaprolactone (PCL)/polyvinyl chloride (PVC) blends. *Polymer Bulletin* **80**, 9685–9708 (2023).

475. Kubatovics, F. & Blazsó, M. Thermal decomposition of polyamide-6 in the presence of PVC. *Macromol. Chem. Phys.* **201**, 349–354 (2000).
476. Ellis, T. S. Interactions and Phase Behavior of Polyester Blends. *Polymer Blends and Alloys*, 209–234 (2019).
477. Pillon, L. Z. & Utracki, L. A. Compatibilization of polyester/polyamide blends via catalytic ester-amide interchange reaction. *Polymer Engineering & Science* **24**, 1300–1305 (1984).
478. Puglisi, C. & Samperi, F. Exchange Reaction Mechanisms in the Reactive Extrusion of Condensation Polymers. *Reactive Extrusion*, 133–177 (2017).
479. Vandewiele, N. M., Van Geem, K. M., Reyniers, M. F. & Marin, G. B. Genesys: Kinetic model construction using chemo-informatics. *Chemical Engineering Journal* **207-208**, 526–538 (2012).
480. Debiagi, P. E. A., Pecchi, C., Gentile, G., Frassoldati, A., Cuoci, A., Faravelli, T. & Ranzi, E. Extractives Extend the Applicability of Multistep Kinetic Scheme of Biomass Pyrolysis. *Energy and Fuels* **29**, 6544–6555 (2015).
481. Zhang, D., Wang, Y., Zhang, C., Li, P. & Li, X. Experimental and numerical investigation of vitiation effects on the auto-ignition of n-heptane at high temperatures. *Energy* **174**, 922–931 (2019).
482. Schmitt, S., Wick, M., Wouters, C., Ruwe, L., Graf, I., Andert, J., Hansen, N., Pischinger, S. & Kohse-Höinghaus, K. Effects of water addition on the combustion of iso-octane investigated in laminar flames, low-temperature reactors, and an HCCI engine. *Combustion and Flame* **212**, 433–447 (2020).
483. Depeyre, D., Flicoteaux, C. & Chardaire, C. Pure n-hexadecane thermal steam cracking. *Industrial & Engineering Chemistry Process Design and Development* **24**, 1251–1258 (1985).
484. Bagheri, G., Ranzi, E., Pelucchi, M., Parente, A., Frassoldati, A. & Faravelli, T. Comprehensive kinetic study of combustion technologies for low environmental impact: MILD and OXY-fuel combustion of methane. *Combustion and Flame* **212**, 142–155 (2020).
485. Biagini, E. & Tognotti, L. Comparison of devolatilization/char oxidation and direct oxidation of solid fuels at low heating rate. *Energy and Fuels* **20**, 986–992 (2006).